②

Bulletin 50
(Part 2 of 4 Parts)

THE
SHOCK AND VIBRATION BULLETIN

Part 2
Measurement Techniques and Data Analysis, Dynamic Measurements, Vibration and Acoustics

SEPTEMBER 1980

A *Publication of*
THE SHOCK AND VIBRATION
INFORMATION CENTER
Naval Research Laboratory, Washington, D.C.

Office of
The Under Secretary of Defense
for Research and Engineering

BLANK PAGES
IN THIS
DOCUMENT
WERE NOT
FILMED

SYMPOSIUM MANAGEMENT

THE SHOCK AND VIBRATION INFORMATION CENTER

Henry C. Pusey, Director
Rudolph H. Volin
J. Gordan Showalter
Carol Healey
Elizabeth A. McLaughlin

Bulletin Production

Publications Branch, Technical Information Division,
Naval Research Laboratory

Bulletin 50
(Part 2 of 4 Parts)

THE SHOCK AND VIBRATION BULLETIN

SEPTEMBER 1980

A Publication of
THE SHOCK AND VIBRATION
INFORMATION CENTER
Naval Research Laboratory, Washington, D.C.

The 50th Symposium on Shock and Vibration was held at the Antlers Plaza Hotel, Colorado Springs, CO on October 16-18, 1979. The U.S. Air Force Academy, Colorado Springs, CO, was host on behalf of the Air Force.

Office of
The Under Secretary of Defense
for Research and Engineering

PAPERS APPEARING IN PART 2

MEASUREMENT TECHNIQUES AND DATA ANALYSIS

A PRECISION INERTIAL ANGULAR VIBRATION MEASURING SYSTEM 1
H. D. Morris and R. B. Peters, Systron-Donner Corporation, Concord, CA and
P. H. Merritt, Air Force Weapons Laboratory, Kirtland AFB, NM

ANGULAR ACCELERATION MEASUREMENT ERRORS INDUCED BY LINEAR ACCELEROMETER CROSS-AXIS COUPLING 11
A. S. Hu, New Mexico State University, Las Cruces, NM

A METHOD FOR EXPERIMENTALLY DETERMINING ROTATIONAL MOBILITIES OF STRUCTURES 17
S. S. Sattinger, Westinghouse–Bettis Atomic Power Laboratory, Pittsburgh, PA

TRANSIENT EFFECTS IN ACOUSTIC SOUND REDUCTION MEASUREMENTS 29
A. J. Kalinowski, Naval Underwater Systems Center, New London, CT

SHOCK MEASUREMENT DURING BALLISTIC IMPACT INTO ARMORED VEHICLES 45
W. S. Walton, U.S. Army Aberdeen Proving Ground, Aberdeen Proving Ground, MD

AUTOMATIC DATA CHANNEL CALIBRATION AND NOISE IDENTIFICATION 57
E. E. Nesbit, Lawrence Livermore Laboratory, Livermore, CA

STATISTICAL ESTIMATION OF SIMULATED YIELD AND OVERPRESSURE 73
P. F. Mlakar and R. E. Walker, U.S. Army Engineer, Waterways Experiment Station, Vicksburg, MS

DYNAMIC MEASUREMENTS

AN ASSESSMENT OF THE COMMON CARRIER SHIPPING ENVIRONMENT 83
F. E. Ostrem, GARD, Inc., Niles, IL

SHOCK AND VIBRATION ENVIRONMENT IN A LIVESTOCK TRAILER 91
M. T. Turczyn, U.S. Department of Agriculture, Beltsville, MD, D. G. Stevens and T. H. Camp,
U.S. Department of Agriculture, College Station, TX

SHOCK INDUCED IN MISSILES DURING TRUCK TRANSPORT 103
D. B. Meeker and J. A. Sears, Pacific Missile Test Center, Point Mugu, CA

DYNAMIC CHARACTERISTICS OF AN INDUCED-DRAFT FAN AND ITS FOUNDATION 121
S. P. Ying and E. E. Dennison, Gilbert/Commonwealth, Jackson, MI

VIBRATION AND ACOUSTICS

A METHOD TO DETERMINE REALISTIC RANDOM VIBRATION TEST LEVELS TAKING INTO ACCOUNT MECHANICAL IMPEDANCE DATA - PART 1) BASIC IDEAS AND THEORY 129
O. Sylwan, IFM Akustikbyran AB, Stockholm, Sweden

A METHOD TO DETERMINE REALISTIC RANDOM VIBRATION TEST LEVELS TAKING INTO ACCOUNT MECHANICAL IMPEDANCE DATA - PART 2: VERIFICATION TESTS 137
T. Hell, SAAB-SCANIA AB, Linkoping, Sweden

VIBRATION ANALYSIS OF A HELICOPTER PLUS AN EXTERNALLY-ATTACHED STRUCTURE 155
D. J. Ewins, Imperial College of Science and Technology, London, England, J. M. M. Silva,
University of Lisbon, Portugal and G. Maleci, Nuovo Pignone, Florence, Italy

IMPROVING VIBRATION TECHNIQUES FOR DETECTING WORKMANSHIP DEFECTS IN ELECTRONIC EQUIPMENT 173
J. W. Burt and M. A. Condouris, U.S. Army Electronics Command, Fort Monmouth, NJ

SINGLE-POINT RANDOM AND MULTI-SHAKER SINE SPACECRAFT MODAL TESTING 191
M. Ferrante, C. V. Stahle and D. G. Breskman, General Electric Company, Space Division, King of Prussia, PA

BIAS ERRORS IN A RANDOM VIBRATION EXTREMAL CONTROL STRATEGY 199
D. O. Smallwood and D. L. Gregory, Sandia Laboratories, Albuquerque, NM

A NEW METHOD OF IMPROVING SPECTRA SHAPING IN REVERBERANT CHAMBERS 207
J. N. Scott, NASA Goddard Space Flight Center, Greenbelt, MD and R. L. Burkhardt, Northrop Services, Inc., NASA, Goddard Space Flight Center, Greenbelt, MD

THE VIBRATION TEST UNIT A UNIQUE RAIL VEHICLE VIBRATION TEST FACILITY 217
R. O. Coupland and A. J. Nintzel, Wyle Laboratories, Colorado Springs, CO

THE APPLICATION OF COMPUTERS TO DYNAMIC RAIL VEHICLE TESTING 229
B. Clark, Wyle Laboratories, Colorado Springs, CO

LOW FREQUENCY STRUCTURAL DYNAMICS OF THE SPACE SHUTTLE SOLID ROCKET BOOSTER MOTOR DURING STATIC TESTS 235
M. A. Behring and D. R. Mason, Thiokol Corporation/Wasatch Division, Brigham City, UT

VIBRATION ENVIRONMENT OF THE SPACE SHUTTLE SOLID ROCKET BOOSTER MOTOR DURING STATIC TESTS 241
D. R. Mason and M. A. Behring, Thiokol Corporation/Wasatch Division, Brigham City, UT

ELIMINATION OF A DISCRETE FREQUENCY ACOUSTICAL PHENOMENON ASSOCIATED WITH THE SPACE SHUTTLE MAIN ENGINE OXIDIZER VALVE-DUCT SYSTEM 247
L. A. Schutzenhofer, J. H. Jones, R. E. Jewell and R. S. Ryan, NASA, George C. Marshall Space Flight Center, Marshall Space Flight Center, AL

PAPERS APPEARING IN PART 1

WELCOME

WELCOME
Brigadier General William A. Orth, United State Air Force Academy

WELCOME
Colonel Ralph L. Kuster, Air Force Flight Dynamics Laboratory

KEYNOTE ADDRESS

U.S. ARMY KEYNOTE ADDRESS
Lieutenant General Robert J. Baer, U.S. Army Material Development and Readiness Command

U.S. NAVY KEYNOTE ADDRESS
Dr. T. T. G. Horwath, Naval Material Command

U.S. AIR FORCE KEYNOTE ADDRESS
Brigadier General Brien D. Ward, Air Force Systems Command

INVITED PAPERS

MEASUREMENT IN PERSPECTIVE
Professor Robert M. Mains, Washington University

DYNAMIC ANALYSIS AND DESIGN-CHALLENGE FOR THE FUTURE
Mr. Robert Hager, Boeing Company

MATERIALS IN DYNAMICS
Mr. Richard Shea and Mr. John Mescall, U.S. Army Materials and Mechanics Research Agency

DYNAMIC TESTING -- HOW FAR WE'VE COME -- HOW MUCH FURTHER TO GO
Dr. Allen J. Curtis, Hughes Aircraft Company

PAPERS APPEARING IN PART 3

DYNAMIC ANALYSIS

THE RELATIVE COMPLEXITIES OF PLATE AND SHELL VIBRATIONS
A. W. Leissa, Ohio State University, Columbus, OH

IN-FLUID CYLINDRICAL BEAM VIBRATION WITH MULTI-DEGREE OF FREEDOM ABSORBERS
B. E. Sandman and J. S. Griffin, Naval Underwater Systems Center, Newport, RI

DYNAMIC STABILITY OF FIBROUS COMPOSITE CYLINDERS UNDER PULSE LOADING
R. J. Stuart and S. Dharmarajan, San Diego State University, San Diego, CA

TRANSFER-MATRIX ANALYSIS OF DYNAMIC RESPONSE OF COMPOSITE-MATERIAL STRUCTURAL ELEMENTS WITH MATERIAL DAMPING
M. M. Wallace and C. W. Bert, The University of Oklahoma, Norman, OK

CONTRIBUTIONS TO THE DYNAMIC ANALYSIS OF MAGLEV VEHICLES ON ELEVATED GUIDEWAYS
K. Popp, Technical University Munich, West Germany

DYNAMICS OF LONG VERTICAL CABLES
F. H. Wolff, Westinghouse R&D Center, Pittsburgh, PA

RESPONSE AND FAILURE OF UNDERGROUND REINFORCED CONCRETE PLATES SUBJECTED TO BLAST
C. A. Ross and C. C. Schauble, University of Florida Graduate Engineering Center, Eglin AFB, FL and P. T. Nash, USAF Armament Laboratory, Eglin AFB, FL

WHIPPING ANALYSIS TECHNIQUES FOR SHIPS AND SUBMARINES
K. A. Bannister, Naval Surface Weapons Center, White Oak, Silver Spring, MD

LIMITATIONS ON RANDOM INPUT FORCES IN RANDOMDEC COMPUTATION FOR MODAL IDENTIFICATION
S. R. Ibrahim, Old Dominion University, Norfolk, VA

STRUCTURAL-DYNAMIC CHARACTERIZATION OF AN EXPERIMENTAL 1200-KILOVOLT ELECTRICAL TRANSMISSION-LINE SYSTEM
Leon Kempner, Jr., Bonneville Power Administration, Portland, OR and Strether Smith and Richard C. Stroud, Synergistic Technology Incorporated, Cupertino, CA

DESIGN TECHNIQUES

ANALYSIS AND DESIGN OF THE SHUTTLE REMOTE MANIPULATOR SYSTEM MECHANICAL ARM FOR LAUNCH DYNAMIC ENVIRONMENT
D. M. Gossain, E. Quittner and S. S. Sachdev, Spar Aerospace Limited, Toronto, Canada

STRUCTURAL DYNAMIC CHARACTERISTICS OF THE SPACE SHUTTLE REACTION CONTROL THRUSTERS
G. L. Schachne and J. H. Schmidt, The Marquardt Company, Van Nuys, CA

MODIFICATION OF FLIGHT VEHICLE VIBRATION MODES TO ACCOUNT FOR DESIGN CHANGES
C. W. Coale and M. R. White, Lockheed Missiles and Space Company, Sunnyvale, CA

EVALUATION OF AIRBORNE LASER BEAM JITTER USING STRUCTURAL DYNAMICS COMPUTER CODES AND CONTROL SYSTEM SIMULATIONS
C. L. Budde and P. H. Merritt, Air Force Weapons Laboratory, Kirtland AFB, NM and
C. D. Johnson, Anamet Laboratories, Inc., San Carlos, CA

FATIGUE LIFE PREDICTION FOR MULTILEVEL STEP-STRESS APPLICATIONS
R. G. Lambert, General Electric Company, Utica, NY

LATERAL INSTABILITY DURING SPIN TESTS OF A PENDULOUSLY SUPPORTED DISC
F. H. Wolff, A. J. Molnar, G. O. Sankey and J. H. Bitzer, Westinghouse R&D Center, Pittsburgh, PA

PAPERS APPEARING IN PART 4

DYNAMIC PROPERTIES OF MATERIALS

MATERIAL DAMPING AS A MEANS OF QUANTIFYING FATIGUE DAMAGE IN COMPOSITES
P. J. Torvik, Air Force Institute of Technology, Wright-Patterson AFB, OH and C. J. Bourne,
Air Force Flight Test Center, Edwards AFB, CA

SONIC FATIGUE TESTING OF THE NASA L-1011 COMPOSITE AILERON
J. Soovere, Lockheed-California Company, Burbank, CA

MODELING A TEMPERATURE SENSITIVE CONFINED CUSHIONING SYSTEM
V. P. Kobler, U.S. Army Missile Command, Huntsville, AL, R. M. Wyskida and J. D. Johannes,
The University of Alabama in Huntsville, Huntsville, AL

APPLICATIONS OF MATERIALS

PRELIMINARY HARDNESS EVALUATION PROCEDURE FOR IDENTIFYING SHOCK ISOLATION REQUIREMENTS
R. J. Bradshaw, Jr., U.S. Army Engineer Division, Huntsville, Huntsville, AL and P. N. Sonnenburg,
U. S. Army Construction Engineering Research Laboratory, Champaign, IL

AN APPLICATION OF TUNED MASS DAMPERS TO THE SUPPRESSION OF SEVERE VIBRATION IN THE ROOF OF AN AIRCRAFT ENGINE TEST CELL
J. L. Goldberg, N. H. Clark and B. H. Meldrum, CSIRO Division of Applied Physics, Sydney, Australia

COMPARISON OF ANALYTICAL AND EXPERIMENTAL RESULTS FOR A SEMI-ACTIVE VIBRATION ISOLATOR
E. J. Krasnicki, Lord Kinematics, Erie, PA

AN EXPERIMENTAL INVESTIGATION OF NOISE ATTENUATING TECHNIQUES FOR SPACE-SHUTTLE CANISTERS
L. Mirandy, General Electric Company, Philadelphia, PA, F. On and J. Scott, NASA Goddard
Space Flight Center, Greenbelt, Md

DYNAMIC INTEGRITY METHODS INCLUDING DAMPING FOR ELECTRONIC PACKAGES IN RANDOM VIBRATION
J. M. Medaglia, General Electric Company, Philadelphia, PA

AN OVERVIEW OF SHOCK ANALYSIS AND TESTING IN THE FEDERAL REPUBLIC OF GERMANY
K. -E. Meier-Dornberg, Institut fur Mechanik, Technische Hochschule Darmstadt,
Federal Republic of Germany

CONSERVATISM IN SHOCK ANALYSIS AND TESTING
T. L. Paez, The University of New Mexico, Albuquerque, NM

MEASUREMENT OF DYNAMIC STRUCTURAL CHARACTERISTICS OF MASSIVE BUILDINGS BY HIGH-LEVEL MULTIPULSE TECHNIQUES
D. G. Yates and F. B. Safford, Agbabian Associates, El Segundo, CA

CONSIDERATION OF AN OPTIMAL PROCEDURE FOR TESTING THE OPERABILITY OF EQUIPMENT UNDER SEISMIC DISTURBANCES
C. W. de Silva, Carnegie-Mellon University, Pittsburgh, PA, F. Loceff and K. M. Vashi,
Westinghouse Nuclear Energy Systems, Pittsburgh, PA

DYNAMIC LOADING OF METAL RIVETED JOINTS
R. L. Sierakowski, C. A. Ross, J. Hoover, University of Florida, Gainesville, FL and
W. S. Strickland, USAF Armament Lab, AFATL/DLYV Eglin AFB, FL

GENERALIZED GRAPHICAL SOLUTION FOR ESTIMATING RECOILLESS RIFLE BREECH BLAST OVERPRESSURES AND IMPULSES
P. S. Westine, G. J. Friesenhahn and J. P. Riegel, III, Southwest Research Institute, San Antonio, TX

PREDICTING THE MOTION OF FLYER PLATES DRIVEN BY LIGHT-INITIATED EXPLOSIVE FOR IMPULSE LOADING EXPERIMENTS
R. A. Benham, Sandia Laboratories, Albuquerque, NM

FRAGMENTS

SCALING OF INITIATION OF EXPLOSIVES BY FRAGMENT IMPACT
W. E. Baker, M. G. Whitney and V. B. Parr, Southwest Research Institute, San Antonio, TX

EQUATIONS FOR DETERMINING FRAGMENT PENETRATION AND PERFORATION AGAINST METALS
I. M. Gyllenspetz, National Defense Research Institute (FOA), Stockholm, Sweden

BREACHING OF STRUCTURAL STEEL PLATES USING EXPLOSIVE DISKS
D. L. Shirey, Sandia Laboratories, Albuquerque, NM

TITLES AND AUTHORS OF PAPERS PRESENTED IN THE SHORT DISCUSSION TOPICS SESSION

NOTE: These papers were only presented at the Symposium. They are not published in the Bulletin and are only listed here as a convenience.

DAMAGE EQUIVALENCE BETWEEN DISCRETELY APPLIED AND COMPLEX HARMONICS
J. J. Richardson, USAMICOM, Huntsville, AL

ON A UNIFIED THEORY OF VIBRATION CONTROL AND ISOLATION
P. W. Whaley, Air Force Institute of Technology, Wright-Patterson AFB, OH

THE VIBRATION OF WELDED PLATES
S. M. Dickinson and M. M. Kaldas, The University of Western Ontario, London, Ontario, Canada

SENSIBLE DISPLAY OF PSD INFORMATION
W. D. Everett, Pacific, Missile Test Center, Point Mugu, CA

RAIL SHIPMENT SHOCK SIMULATION ON A PEACEFUL NUCLEAR EXPLOSION INSTRUMENT VAN
R. O. Brooks, Sandia Laboratories, Albuquerque, NM

FREE FALL TESTING OF ARRESTMENT DEVICES FOR MAN CONVEYANCES IN MINE SHAFTS
F. A. Penning, Colorado School of Mines, Golden, CO, and E. H. Skinner, Spokane Mining Research Center, Spokane, WA

REVERSAL IN TIME DOMAIN EQUALS COMPLEX CONJUGATE IN FREQUENCY DOMAIN
A. J. Curtis, Hughes Aircraft Co., Culver City, CA

ELIMINATION OF INTERFERING ACOUSTIC STANDING WAVES IN A SONIC FATIGUE FACILITY
H. N. Bolton, McDonnel Douglas Corporation, Long Beach, CA

TEST VEHICLE CONFIGURATION EFFECTS ON VIBRO-ACOUSTIC TESTING
C. J. Beck, Jr., Boeing Aerospace Company, Seattle, WA

RANDOM VIBRATION CONCEPTS CLARIFIED
W. Tustin, Tustin Institute of Technology, Inc., Santa Barbara, CA

TRANSMISSION-LINE WIND-LOADING RESEARCH
R. C. Stroud, Synergistic Technology Inc., Cupertino, CA

A METHOD FOR MEASURING END LOAD IN A HOLLOW ROD USING STRAIN GAGE ORIENTATION TO CONCEL UNWANTED STRAIN OUTPUTS
J. Favour, Boeing Aerospace Company, Seattle, WA

CRITICAL ASPECTS OF FIXTURE DESIGN AND FABRICATION FOR 781C
D. V. Kimball, Kimball Industries, Inc., Monrovia, CA

MEASUREMENT TECHNIQUES AND DATA ANALYSIS

A PRECISION INERTIAL ANGULAR VIBRATION MEASURING SYSTEM

H. D. Morris and R. B. Peters
Systron-Donner Corporation
Concord, California

and

Dr. P. H. Merritt
Air Force Weapons Laboratory
Kirtland AFB, New Mexico

Presented by

Harold D. Morris, Systron-Donner Corporation

An instrumentation system is described which permits high precision broadband angular vibration measurements or real time image motion compensation in typical aircraft environments. The system consists of a proprietary dynamic inertial angular displacement sensor calibrated by a special purpose table which is capable of producing and measuring sinusoidal motions up to one milliradian peak amplitude from 1 Hz to over 500 Hz. For a typical flight application, system accuracy is estimated as 0.3 arc seconds, 1σ, for data in the optimum 70 Hz to 500 Hz band, and 1.4 arc seconds from 1 Hz to 1500 Hz. These estimates include environmental effects. Actual flight data is presented which verifies the estimated accuracy.

I. INTRODUCTION

There are a large number of airborne systems that stabilize platforms as inertial references. One such system is an optical pointing system. A small amount of angular disturbance when multiplied by a long line-of-sight distance will result in a large amount of motion at the desired aimpoint. Linear disturbances at the platform affect the aimpoint with no magnification and are usually negligible. For this reason, the primary disturbance that must be measured and compensated is angular vibration, and it must be measured over a wide bandwidth with combined phase and amplitude accuracy on the order of a few microradians. However, on reviewing available instrumentation one finds a large number of linear accelerometers, velocity pickups, and displacement transducers while finding almost a void of inertial angular measurement instrumentation. Gyroscopes are the usual means to measure angular motion, but most inexpensive gyroscopes are found to be noisy and limited in frequency response, while inertial guidance gyroscopes are found to be very expensive. This paper will report on the operation and application of an angular instrumentation system which was built by the Systron-Donner Corporation under contract to the Air Force Weapons Laboratory, using a proprietary angular displacement sensor. This system uses inertial techniques to measure three axes of angular displacement with extreme accuracy over a very wide frequency range, with no need for temperature control.

The basic three axis unit is identified as a 5690-4 Angular Vibration Sensor System, and is a self-contained module enclosed in a cube with outside dimension of 8.4 centimeters (3.3 inches). The user supplies ±15 volt regulated power, and the outputs are three high level buffered bipolar analog signals (5 volts/milliradian) plus temperature of the cube. The unit has a flat frequency response from about 3 Hz to 2000 Hz and can be used to 1 Hz with transfer function compensation. It is relatively insensitive to linear vibration and operates within specifications from −18°C to +68°C (0°F to 155°F). Extensive acceptance tests were performed by Systron-Donner to characterize the frequency response function of each sensor.

The first application of these sensors was as an image motion stabilizer for the FLIR System on the USAF B-1 aircraft. Over the past year, similar units have been utilized by the Air Force to collect considerable vibration data on several aircraft, including a KC-135, a DC-10, a 747, and an L1011. Flight data is included which shows the accuracy of these instruments. One airborne measurement shows a wideband angular displacement of 14.5 microradians RMS, while the corresponding Power Spectral Density (PSD) plot reveals a band from 60 to 500 Hz in which the total indicated motion is only 2 microradians RMS. Further, data is presented from an instrument which was mounted close to a guidance quality rate integrating gyroscope in a quiescent laboratory test. The two overlaid PSD's show excellent agreement even though the total angular motion was less than 2.5 microradians RMS.

II. TECHNICAL DESCRIPTION

Methods of Measuring Inertial Angular Motion

Deriving a signal, electrical or otherwise, proportional to very small inertial displacements at relatively low frequencies is the usual problem faced by a seismologist in designing his seismic instruments. Over the years, two general approaches have evolved based on mass-spring systems. In one case, the natural frequency of the inertial system is made, by a suitable design of the mass and spring, higher than the frequency of the displacement signals. The instrument then produces a signal proportional to the acceleration applied, and must be double-integrated to yield displacement. In the other case, the natural frequency of the system is designed to be much lower than the lowest displacement frequency expected. The instrument then responds with a signal directly proportional to displacement with a single integrator, or a direct displacement sensor which requires no integrators with their associated errors.

When the motions to be measured are angular rather than rectilinear, additional options are introduced. There is a choice to be made between true angular sensors and arrays of linear sensors, and within the angular option an additional choice between gyroscopic sensors, Coriolis rate sensors, and sensors based on response to angular acceleration. For low frequencies, and especially ground based measurements, linear arrays and gyroscopes have been popular. The state of development in the required sensors has been quite high for several years, and their limitations have not been unduly restrictive in the majority of cases. In the former case these limitations included the need for three or more sensors, connected by a rigid structure, and carefully matched in response. In the latter case the limitations were primarily bandwidth and noise level, or at least a marked tradeoff between these aspects of performance and purchase price, along with the necessity to separate small amplitude oscillations from large amplitude low frequency rates.

In designing an inertial angular displacement sensor for airborne applications, one is faced with the same system requirements as the seismologist plus additional stringent requirements on high frequency response, and, in many cases, faithfulness of phase reproduction between the sensor output and its input. For example, when measurements are to be compared at several locations, it is necessary that all sensors be standardized to the same phase response over the useful bandwidth. In the even more demanding application of real time analog stabilization of a line of sight in space, it is necessary that the phase response for all sensors be very nearly zero. It is this last application for which the 8301 ADS was originally designed, after closely examining the possibility of using any of the other options open to the seismologist, including possible gyro-based solutions. Experience in actual applications has shown that the design approach represented by the 8301 indeed yields the desired performance.

Measurement of the vibration environment of an aircraft is a difficult and demanding problem. Linear acceleration measurements at various points in a fuselage will provide information on translatory motions of the mounting points only, and must be made coherent in phase, parallel in sensing axis, and of standardized sensitivity to provide true relative motion of the various parts. Furthermore, the low frequency motions corresponding to rigid body rotations and the first few structural modes of large aircraft seldom involve accelerations of more than a few hundredths of a g. Very sensitive accelerometers are required, then, with the attendant difficulties of accommodating more vigorous modes at higher frequencies, as well as the large translational components of maneuvering accelerations.

Measurement of angular vibration in aircraft fuselages is much less common and certainly less generally understood in industry in terms of measurement capability and attainable accuracy. The required measurements often extend down to the microradian range of amplitude and up to the kilohertz range of frequencies. The previously described use of linear accelerometers is impractical in accomplishing this measurement because the comparatively massive moving systems necessary to make them function as milli-g accelerometers gives rise to mechanical resonances, which make phase reproducibility into the kilohertz region most difficult. Further, the very small wavelengths of structural vibrations of the high frequencies make such measurements necessary to survey a structure. Obviously, a direct measurement of such angular motion is desirable.

Use of Fluid Rotor Angular Sensors

The inertial angular sensor which is the subject of this paper provides just such a direct measurement. It is an unusually practical and versatile outgrowth of angular accelerometer technology, which is in turn largely derived from the technology of closed loop servo force rebalance linear accelerometers. Its mode of operation is most easily understood by looking first at the operation of an idealized solid rotor torque rebalance angular accelerometer shown schematically in Figure 1.

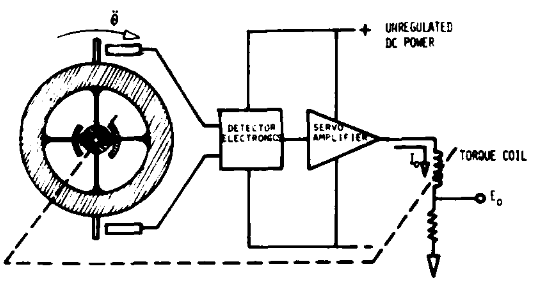

Figure 1:
Operation of a Torque Balance Servo Angular Accelerometer

A large flywheel with moment of inertia J is suspended so that it is free to rotate relative to the sensor case about its cylindrical axis. A pair of angular position detectors is affixed to the case so as to measure and produce an electrical analog of the relative rotation. An amplifier raises the voltage level and drives a resistive load in series with the torquing coil of an electromagnetic D'Arsonval meter movement, producing ultimately a torque proportional to angular displacement. When the case is subjected to a steady angular acceleration θ, equilibrium is reached with a current through the sampling resistor which produces a torque $J\theta$ just sufficient to angularly accelerate the rotor at θ and maintain its position fixed relative to the case.

This electromechanical system provides an analog electrical spring with a built-in read-out of torque. Furthermore, it is a spring with no discernible threshold or resolution limit, no hysteresis, and excellent stability and linearity.

When the angular acceleration is changing so rapidly that equilibrium cannot be achieved, the sensor exhibits a highly repeatable dynamic characteristic. If the amplifier has flat gain, i.e., independent of frequency, the response is second order. Unlike a mechanical spring, the amplifier response is easily modified to give other response curves.

As a second order device, this sensor's dynamic behavior is closely analogous to the traditional seismometer's, producing an output proportional to angular acceleration below its corner frequency, and an output proportional to angular displacement above its corner frequency. That is essentially what we desire, but, the solution described is not yet in a fully practical form. The problem is the large mass which must be supported to produce usable operating torques. Consider, for example, the comparison between a 1 g linear accelerometer and a 1 radian per second squared angular accelerometer. The tangential acceleration associated with 1 radian per second squared is only about a milli-g per centimeter of radius, and to have its active mass acted on by 1 g such an angular accelerometer would require a flywheel a staggering 30 meters in diameter! Obviously, packaging such a sensor would impose great difficulties, and other solutions must be found.

These alternate solutions require typically larger inertial masses than their linear brethren and still have to operate at much lower torque levels, making suspensions much more critical with respect to both error torques and environmental damage. Error torques degrade the bias performance of angular accelerometers and limit the useful low frequency response of angular displacement sensors as well as the linearity of either device, while susceptibility to damage is an obvious problem in any sensor intended for aircraft or missile applications.

A practical solution to this dilemma is the fluid rotor angular sensor, shown schematically in Figure 2. The active inertia is a fluid ring which is viscously coupled to a lightweight moving system so that the suspension needs to support only a small fraction of the total mass, and error torques can be reduced proportionally. If the fluid mass is visualized as being perfectly coupled to the vanes the analogy to the solid rotor device is quite clear, but the fluid rotor is self-supporting and inherently balanced for either linear or centripetal accelerations. It is also entirely free from static hysteresis, while it supplies flotation and damping to the lightweight vane assembly for added protection against environmental damage. In actual fact, leak-free seals to the vanes would be impractical, and fortunately they are not necessary. When the vane assembly and torquer are simply immersed in the fill fluid, as shown, with coupling accomplished by viscous forces alone, the system response remains second order with only minor changes to the designer's scaling equations in all areas except effective damping.

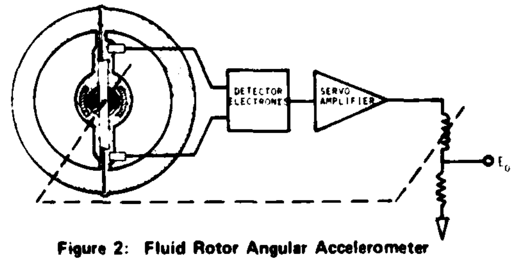

Figure 2: Fluid Rotor Angular Accelerometer

Fluid filled sensors typically experience large changes in damping as the fluid changes viscosity with temperature, but the fluid rotor sensor has inherent built-in compensation for this change. As fluid viscosity becomes very high, coupling to the vane is quite strong and damping increases with viscosity, just as in a viscously damped solid rotor sensor, but at very low viscosities performance is dominated by the long time constant of fluid leaking past the vanes, and effective damping then goes up with decreasing viscosity. In a properly balanced design, there will be a broad intermediate temperature range, centered with respect to the actual use temperatures, in which the rising and falling terms compensate one another and damping changes by only a small amount, typically less than ±20% over a temperature range of 150°F.

Mechanization of Model 8301 ADS

The Model 8301 Angular Displacement Sensor (ADS) which is used in the Triaxis 5690 System, is a fluid rotor angular accelerometer which has been optimized for use above its natural frequency, and has had that natural frequency set at nominally 2 Hz so that it has a high pass filter characteristic. It shares the basic fluid rotor attributes of environmental ruggedness, high rejection of linear acceleration effects, and small temperature sensitivity, and adds some highly significant virtues of its own. In its normal operating frequency range, the fluid mass remains essentially stationary in inertial space along with the vane assembly, so that the non-contacting position sensor is able to provide a direct read-out of angular displacement of the case with a frequency pass band from 2 Hz to above 1000 Hz and no proven upper limit. The fluid rotor which comprises the main mass is inherently free from resonances, while the light weight of the vane assembly and great rigidity of the case structure have pushed anticipated mechanical resonances above 6000 Hz. The light weight of the vane also allows it to be easily balanced to a degree which exceeds any current or projected requirements.

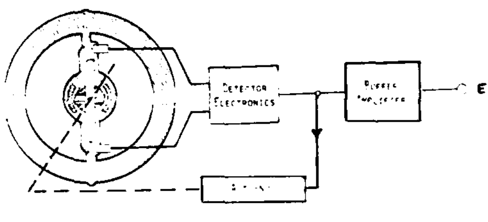

Figure 3: Block Diagram of ADS Servo Loop

The servo system, shown in Figure 3, controls the low frequency motions of both the vane and the fluid and provides adjustable, highly reproducible, low frequency and transient response. It also maintains the mean position of the vane centered between the position pick-offs so that high sensitivity direct position sensors can be used. This characteristic provides a much higher signal-to-noise ratio than would be practical with displacement or integrated velocity pickoffs that were required to cope with the vagaries in zero position characteristic of very low natural frequency purely mechanical suspensions. The low loop gain used in the servo at frequencies higher than

0.1 Hz allows the system noise level to be lower than would be the case with a higher natural frequency angular accelerometer (double integrated to displacement) using otherwise identical technology. The theoretical noise level of the sensor, based on independent noise measurement of its component parts in conjunction with dynamic modeling, is on the order of .001 arc second rms over a 2 KHz bandwidth and is, in fact, thermally rather than electrically limited. No measurements have yet been accomplished in an environment as mechanically quiet as that, but several measurements to date, including some reported in the second half of this paper, have confirmed that the noise level is well below 0.1 arc second.

The position detectors shown are inductive, eddy current loaded coils driven by an internal oscillator at several megahertz and envelope detected with a bandwidth in excess of 10 KHz. They are detected in a differential mode so that common mode oscillator noise cancels out. This proprietary detection system provides a highly linear, high signal-to-noise ratio output, with gain of typically 150 volts per radian before amplification. This high sensitivity allows the buffer amplifier to be placed external to the servo loop so that scaling changes from 1 volt per milliradian to about 10 volts per milliradian may be accomplished without affecting the loop closure.

The loop, labeled "autonull," provides a 2 Hz natural frequency, second order corner, and then integrates position error below 0.1 Hz to give a zero-static-error centering torque with a 2 second time constant.

The suspension for the vane assembly is derived from Systron-Donner's proprietary precision accelerometer technology. In conjunction with the electronics it provides a resolution unmeasurable with state-of-the art test equipment, and a threshold limited only by the very low system noise. Again, measurements to date are consistent

Table 1

Specification Summary

The following is a specification and summary review of the Model 8301 sensor as used in the Model 5690 Tri-Axis Angular Vibration Sensor System:

Spectrum

Frequency Range:	1 Hz - 2000 Hz
Amplitude:	±1 - ±10 millirads peak via external trim resistor

Physical Specifications

Maximum Weight:	<1000 grams
Unit Sensor Size:	See Systron-Donner drawings: 48436, 34084, 48437
Input Voltage and Current:	±15 volts dc ±5% at 20 mA maximum
Linear Acceleration Capability, Operating:	At least 10 g in any direction
Operating Temperature:	0°F to 155°F
Storage Temperature:	-65°F to 165°F
Vibration (Survivability):	
Sine:	20 g peak, 30 Hz to 2000 Hz, 0.5" double amplitude 10 Hz to 30 Hz
Random:	30 g rms, 20 Hz to 2000 Hz
Shock (Survivability):	100 g, 11 ms
Altitude (Operating or Non-Operating):	To 100,000 feet
Humidity:	100% relative humidity acceptable with potted connector

Transfer Function

Transfer function of the following form, within tolerances as detailed below:

$$\frac{E_o}{\theta} = \frac{K_p K_a s^2}{s^2 + 2\zeta\omega_n s + \omega_n^2} \cdot \left(\frac{\tau_1 s}{1 + \tau_1 s}\right)$$

where

E_o = output, volts

θ = input, radians

s = Laplace operator

K_p = pickoff sensitivity, volts/radian

K_a = buffer amplifier gain, volts/volt

ζ = ratio of damping to critical damping (modelable as a function of temperature)

ω_n = natural frequency, radians/second

τ_1 = auto-null time constant

Gain $K_p K_a$ = 0.5 volts/milliradian to 5.0 volts/milliradian

Damping Coefficient, ζ:	0.7 nominal at room temperature 0.25 - 1.25 over temperature
Undamped Natural Frequency, ω_n:	8 to 15 radians/second
Rotor Unbalance, $\frac{ML}{J}$:	0.2 radians/sec^2/g (maximum)
Rotor Angular Freedom:	±20 milliradians (minimum)
Threshold:	0.002 milliradians (maximum)
Crosstalk (Angular Velocity Input on Orthogonal Axis):	0.2% maximum of sensitive axis response
Mounting Alignment:	±2 milliradians
Amplifier Output Impedance:	200 ohms (maximum)
Amplifier/Position Detector Bandwidth:	2000 Hz (minimum)
Room Temperature Amplitude Response Referred to 100 Hz:	±3.5% (maximum), 70 Hz to 500 Hz (absolute) ±10%, 1 Hz to 70 Hz (deviation from stated transfer function)
Room Temperature Phase Response:	±5° maximum at 70 Hz ±3° maximum 140 Hz to 500 Hz (all absolute)
Temperature Coefficient of Scale Factor:	±.05%/°F maximum
Bias:	30 mV maximum
Temperature Coefficient of Bias:	0.05 mV/°F for 0.5 volts/milliradian scale factor
τ_1:	2 seconds ±0.5 seconds
Temperature Sensor:	0.05 to 2.5 volts out in the range 0°F to 155°F

with this theoretical performance. Finally, in 5690 Triax configuration, a circuit is included in each triax block which produces a voltage proportional to block temperature, providing for temperature compensation of data taken at locations where the ambient temperature differs by more than about 10°C from the temperature corresponding to the assumed calibration curve.

As an example of the accuracy to be expected in a typical application, Table 2 summarizes an error budget for an angular vibration survey of a large transport class aircraft. Note that the anticipated accuracy in this typical aircraft environment is 0.3 arc seconds in the optimum 100-500 Hz band, and 1.4 arc seconds over the much wider 1-1500 Hz band, with the dominant errors in the latter case being calibration uncertainty. The flight test data in Section IV of this paper shows that these are realistic estimates.

A summary of 8301-5690 performance specification is provided in Table 1, and the physical configuration of the triax version (5690) is shown in Figure 4.

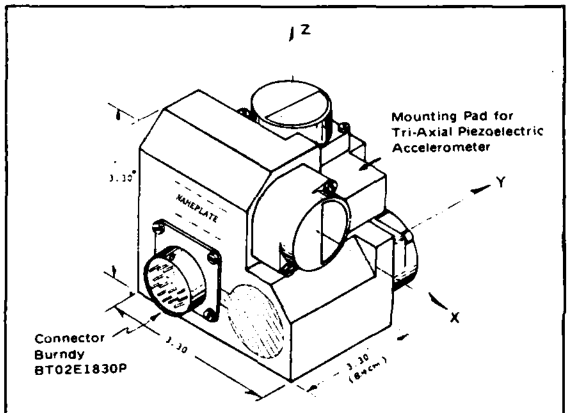

Figure 4: 5690 Tri-Axis Physical Configuration

III. ACCEPTANCE TESTING

Principal Tests Performed

As noted in the error budgets for an aircraft vibration survey, an important part of the reduction to practice of the 8301 ADS concept is the ability to perform accurate wideband inertial angular displacement calibrations.

The 8301 ADS has a high pass characteristic, with no output at DC, so it cannot be tested statically. At high frequencies its transfer characteristic is essentially flat in amplitude (±1%, typically) and zero in phase (±2°, typically), but at frequencies below 70 Hz the nearness of the lower corner asserts itself in the form of variations in amplitude response and steadily increasing phase lead, passing through nominally -3 dB and +90° at the 2 Hz natural frequency. To obtain accurate measurements in this low frequency range it was essential to take measurements of phase and amplitude response of each sensor at enough frequencies to ensure that the response is essentially second order, and to define the natural frequency and damping ratio. In addition, a representative number of sensors, in this case the three first article sensors, were tested over temperature to determine the characteristic variation of damping ratio with temperature. These measurements which characterize the transfer function of each sensor constituted the primary acceptance test activity.

Table 2: ADS Accuracy in a Typical A/C Environment

Error source	100-500 Hz Limit	1σ	μrad in 0.1 mrad	1-1500 Hz Limit	1σ	μrad in 0.1 mrad
Scale	2%	0.5%	0.5	2%	0.5%*	0.5
Linearity	0.5%	0.2%	0.2	0.5%	0.2%	0.2
Amplitude Response	2%	0.7%	0.7	10%	4%*	4.0
Phase Response	3°	0.7°	1.2	--	3°*	5.3
Sensor Noise***	--	--	<0.1	--	--	<0.1
Vibration Response**	6.0	0.7	0.7	6.0	0.7	0.7
RSS Error			1.7 μrad (0.3 arc sec)			6.7 μrad (1.4 arc sec)

*[illegible]
**[illegible]
***[illegible]

The tests which were performed on each sensor were:

- Visual Examination
- Weight
- Insulation Resistance
- Input Current, Null, and Phasing
- Scale Factor, Full Range, and Frequency Range
- Threshold
- Hysteresis, Linearity, and Repeatability
- Amplitude Response and Phase Shift
- Rotor Imbalance

Most of these are self-explanatory, but a few require some comment:

- Null refers to the DC voltage from the sensor in the absence of vibration. Since the vibration output is essentially AC, null is not critical as long as it remains a small fraction of output range.

- Phasing refers to the polarity of the output signal.

- Scale Factor is defined as the amplitude of the transfer function measured at 100 Hz.

- Frequency Range is evaluated by qualitatively observing the sensor output between 100 Hz and 2000 Hz to ensure that it is free from resonances.

- Threshold is demonstrated by attaching each sensor to a lightly damped torsional pendulum and recording essentially sinusoidal output as it decays through the specified level.

- Hysteresis, Linearity, and Repeatability are measured by applying a fixed frequency dynamic angular vibration at a number of different levels up to and including full scale. This test and the frequency response test require some specialized equipment which is described below. Results are given as deviations from at least squares straight line.

- Rotor Imbalance is read statically by tumbling the sensor in a 1 g field and observing the torquing current commanded by the servo to keep the vane assembly centered. A dynamic test would be desirable to confirm that the response is that predicted by static measurements, but the requirements for rotation-free translational motion to separate the linear motion outputs from the true rotational outputs are beyond the current state-of-the-art in shakers.

Specialized Test Equipment

Dynamic testing of inertial angular sensors, i.e., testing in which the angular quantity being measured is changing rapidly with time, is a relatively new discipline with a host of specialized problems (see, for example, Reference No. 4). In the case of the 8301 ADS it was necessary to design and build a broadband angular displacement table capable of producing sinusoidal motions of known amplitude from 1 Hz to greater than 500 Hz. To produce a displacement signal of sufficient amplitude to be measured with precision on the order of 1% at high frequencies, the table has to have a very high angular acceleration capability, e.g., .001 radian peak-to-peak at 500 Hz requires a peak angular acceleration of 5000 radians per second squared (nearly 50,000 RPM per second). It is also necessary, of course, that means be provided to measure the instantaneous angular displacement of the table with accurately known scaling and negligible phase shift.

The table which was constructed to meet these requirements has been dubbed the "Laser Table," and is shown schematically in Figure 5. It is basically a ball-bearing supported vertical axis table operated in an oscillating mode. It has a closed loop angular displacement servo with a bandwidth of 350 Hz. The table is current limited at an acceleration of about 8000 radians per second squared, and has mechanical stops at ±.010 radians. It is normally operated at ±.001 radians or just below current limit, whichever is smaller, and the servo response closely approximates that curve with a constant drive setting.

The name Laser Table is derived from the use of a collimated 5 mW laser reflected from a front surface mirror on the table to perform periodic calibration of the angular displacement detectors. The beam is tracked by a photodetector on a micrometer table at a radius of 4.45 meters, giving a static calibration accuracy of ±1.5 microradians. Dynamic motions are read out electrically by the built-in angular position sensor on the table using the very well established principle of a statically calibrated transfer standard whose bandwidth can easily be shown to be many times greater than the highest frequency to be measured. The position sensor is a pair of coils similar to those used in the 8301 ADS, but with modified circuitry to give a first pole in excess of 75 KHz, so that there is no question of bandwidth limitations at 500 Hz or less. The same differential mode detection is used, giving the bonus that the circuit responds only to table rotation and ignores translational motions, e.g., from bending of the drive shaft.

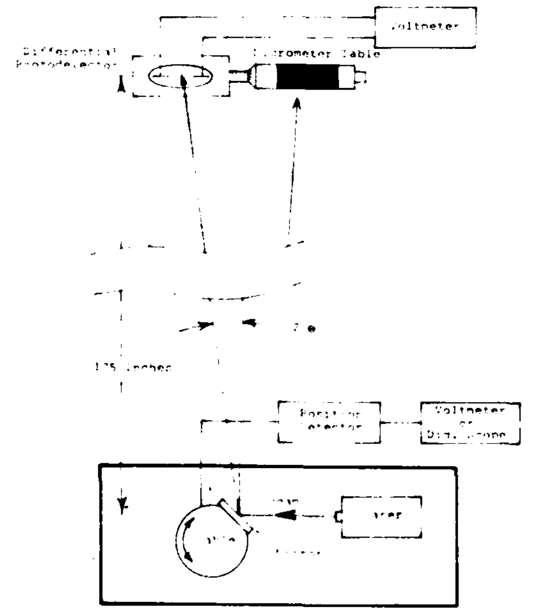

Figure 5: Laser Table

The high loop gain required for a system bandwidth of 350 Hz provides operating convenience at high frequencies, and allows good waveforms down to 10 Hz and useable waveforms down to 1 Hz even though the table uses an unsophisticated suspension system and has a necessarily low polar moment of inertia. In the frequency range from 10 Hz to 500 Hz the estimated absolute accuracy of the table and supporting instrumentation is 0.5%. At lower frequencies the accuracy degrades somewhat due to the effect of waveform distortion on the presently utilized readout instrumentation, as indicated in the two error budgets in Table 2.

Data Reduction

Handling of data taken during acceptance testing was straightforward except for the fitting of a second order response curve to the 1 Hz-100 Hz frequency response data, for convenience in computer modeling of the low frequency transfer function of each sensor. The fitting was done in a least squares sense, percentage weighted with respect to amplitude, using a scheme similar to that described in Reference 6. The assumed transfer function is of the form:

$$\frac{K_1 s^2}{s^2 + 2\zeta\omega_n s + \omega_n^2} \cdot \frac{\tau_1 s}{1 + \tau_1 s} = \frac{P s^2}{1 + Q_1 s + Q_2 s^2} \cdot \frac{\tau_1 s}{1 + \tau_1 s}$$

with $K_1 = \frac{P}{Q_2}$ (Scale Factor)

$\omega_n = \frac{1}{\sqrt{Q_2}}$ (Natural Frequency)

$\zeta = \frac{Q_1}{2\sqrt{Q_2}}$ (Damping Ratio)

The first order corner associated with τ_1 is a small deviation at 1 Hz or higher, since τ_1 corresponds to 0.1 Hz. Further, this portion of the response is assumed accurately known because it is electronically determined, and so is premultiplied out of the data. The parameters P, Q_1, and Q_2 are then fitted in a least squares sense by iteratively solving the matrix equations shown as Equation 1. The weighting function, S, arises from the necessity to frequency weight the cost function in order to obtain a set of linear equations, as described in Reference 6, and is also used to apply percentage weighting with respect to amplitude.

Test Results

The Acceptance Test results which are of primary interest are the frequency response curves taken on each sensor. In Figure 6 are shown a typical set of phase and amplitude

$$\begin{bmatrix} \sum_{i=1}^{n} S_{i,j-1}\omega_i^4 & -\sum_{i=1}^{n} S_{i,j-1}M_i\omega_i^3 & -\sum_{i=1}^{n} S_{i,j-1}R_i\omega_i^4 \\ -\sum_{i=1}^{n} S_{i,j-1}M_i\omega_i^3 & \sum_{i=1}^{n} S_{i,j-1}(M_i^2 + R_i^2)\omega_i^2 & 0 \\ -\sum_{i=1}^{n} S_{i,j-1}R_i\omega_i^4 & 0 & \sum_{i=1}^{n} S_{i,j-1}(M_i^2 + R_i^2)\omega_i^4 \end{bmatrix} \begin{bmatrix} P_j \\ Q_1{}'_j \\ Q_2{}'_j \end{bmatrix} = \begin{bmatrix} -\sum_{i=1}^{n} S_{i,j-1}R_i\omega_i^2 \\ 0 \\ \sum_{i=1}^{n} S_{i,j-1}(M_i^2 + R_i^2)\omega_i^2 \end{bmatrix}$$

EQUATION 1

i represents the ith data point, from i=1 for 1 Hz to i=n for 100 Hz

j represents the jth iteration

$S_{i,j-1} = \left(\frac{A_n}{A_i}\right)^2 \Big/ \left[\left(1-Q_2{}'_{j-1}\omega_i^2\right)^2 + \left(Q_1{}'_{j-1}\omega_i\right)^2\right]$; a weighting function

ω_i = ith test frequency, radians per second

$R_i = A_i \cos\theta_i$; real part of ith response measurement

$M_i = A_i \sin\theta_i$; imaginary part of ith response measurement

measurements taken in the range 70 Hz to 500 Hz, demonstrating the excellent fidelity of the high frequency response of these sensors. Note the amplitude response deviations on the order of 1%, and absolute phase deviations on the order of 2°. For acceptance testing under the present contract, only the range from 1 Hz to 100 Hz needed to be calibrated, since the nominal performance at higher frequencies is well within required limits. A statistical sampling of these acceptance test curves is shown in Figure 7. The solid curves shown are computed second order response curves corresponding to the mean performance of all sensors tested. The broken curves show the plus and minus one sigma limits of deviations from second order performance for a randomly selected sample of ten sensors. The discrete points plotted represent the deviations associated with a particular sensor which was taken as typical on the basis of showing approximately one sigma deviations. The slight rise in amplitude with respect to the second order curve, near 5 Hz, is typical, as well. Subsequent testing has indicated that it is a characteristic of the measurement system, rather than the sensors or the transfer standard. In spite of such minor developmental problems, all contractual requirements were met.

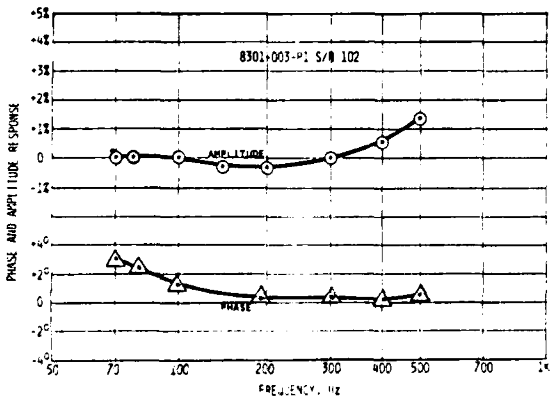

Figure 6: ADS Frequency Response 70 – 500 Hz

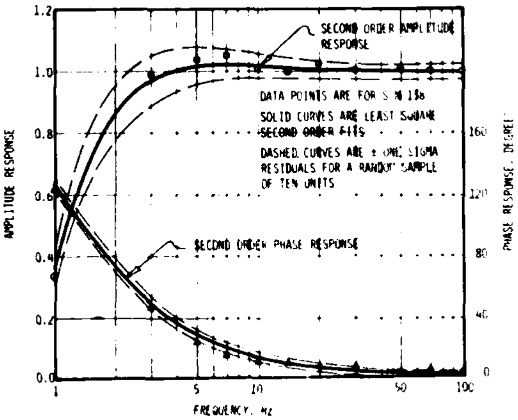

Figure 7: ADS Frequency Response 1 – 100 Hz

IV. FLIGHT TEST DATA FROM THE 8301 SENSORS

The first use of the 8301 ADS was as a real time LOS compensator in a Forward Looking Infrared (FLIR) system flown on the B-1 bomber by Hughes Aircraft Company. It was also used in another FLIR system which was evaluated in the laboratory by Aerojet Electrosystems. Details of these early applications may be found in the references cited. Of particular interest in the Aerojet application is the noise performance achieved by their 500 Hz bandwidth system with the 8301 ADS and with a comparably priced rate gyro which was electronically compensated for its limited bandwidth. With the 8301 ADS, the system showed less than one microradian RMS quiescent noise and seven microradians (1.4 arc seconds) LOS dither when vibrated at 150 microradians (27 dB improvement). With the rate gyro installed, the quiescent noise level was 160 microradians RMS and the vibrated system showed less LOS dither with the system off than when it was on.

The Air Force Weapons Laboratory (AFWL) procured a total of eleven triaxis units such as described in Section II of this paper. These units have been utilized by both the AFWL and the Air Force Flight Dynamics Laboratory (FDL) to measure the vibration of several cargo type aircraft over the last year. The DC-10, L1011, and 747 aircraft have each had extensive test data taken at two locations in the aircraft body, throughout a series of flight conditions and take-off and landing. This data has been documented in test reports, Reference 7, 8, and 9, written by FDL.

The NKC-135 aircraft operated by the AFWL as an Airborne Laser Laboratory (ALL) has been extensively instrumented with these angular measurement systems. The units have provided data to characterize the angular motion of several test equipment locations. The data has also been processed by computer algorithms to difference the signals from the various locations and analyze the bending motions of the aircraft for different flight conditions.

The test data taken at one flight condition of the NKC-135 is shown as Figure 8. The aircraft during this data interval was flying at 5300 meters (17,400 feet), 340 knots calibrated air speed, and straight and level. This is a very low vibration flight regime for this aircraft. The data shown is at the center-of-gravity of the airplane. By observing the Figure there are several interesting characteristics of the data that reflect credit on the measurement system. First, notice the overall yaw measurement shows 14.5 microradians. This is a small angular measurement requiring extremely accurate instrumentation. Moreover, notice the amount of resolution available in the PSD. Noise from a tape recorder or instrumentation is typically "white" or "flat"; this data certainly appears to be representative of mechanical motion, not noise. Notice the yaw level between 60 and 500 Hz. The total RMS level in this frequency band is less than two microradians. Also, notice the small amount of 60 and 400 Hz energy that historically plague the flight test engineer. It is also noticed that the three orthogonal measurements have three distinctly different spectrums. Again, this indicates a good measurement of mechanical motion and not common noise.

The quality of the data is also attested to by the fact that it has been possible for the first time to correlate changes in low level angular vibration with changes in aircraft Mach number, even when dynamic pressure is held constant.

The units have not only been used as airborne instrumentation but have also found use in the various test laboratories at the AFWL to measure disturbance levels during laboratory testing. In one particular test series it was possible to mount an 8301 ADS and an inertial quality gyroscope on the same rigid platform within a few feet of each other. This data is very interesting when the output PSD's are compared in Figure 9. Notice that the overall RMS of the platform is only 2.45 microradians, a very small number, yet the ADS and the gyroscope report essentially the same shape in the PSD's. Notice that the ADS does show several sharp noise spikes in the PSD above 30 Hz. These spikes were almost certainly a function of the data recording system and not a function of the ADS. The ADS output in this data, was run through about 15 meters of single shielded cable, through a buffer unit, a FM VCO, and a tape recorder. The noise spikes were seen on other low level signals not associated with the ADS unit, such as DC logic signals. Therefore, the comparison at this low level is considered an excellent performance demonstration for the ADS.

It should be mentioned that the eleven systems procured by the Air Force have all seen applications during the last year. Some of the systems have been used in flight tests of 5 different aircraft. To present, no failures have been experienced on any of the eleven triad systems.

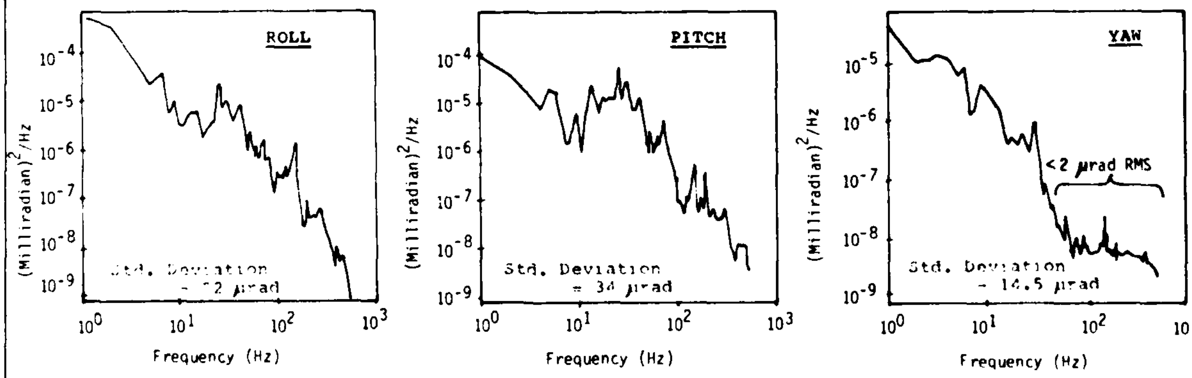

Figure 8: Aircraft C. G. Motion

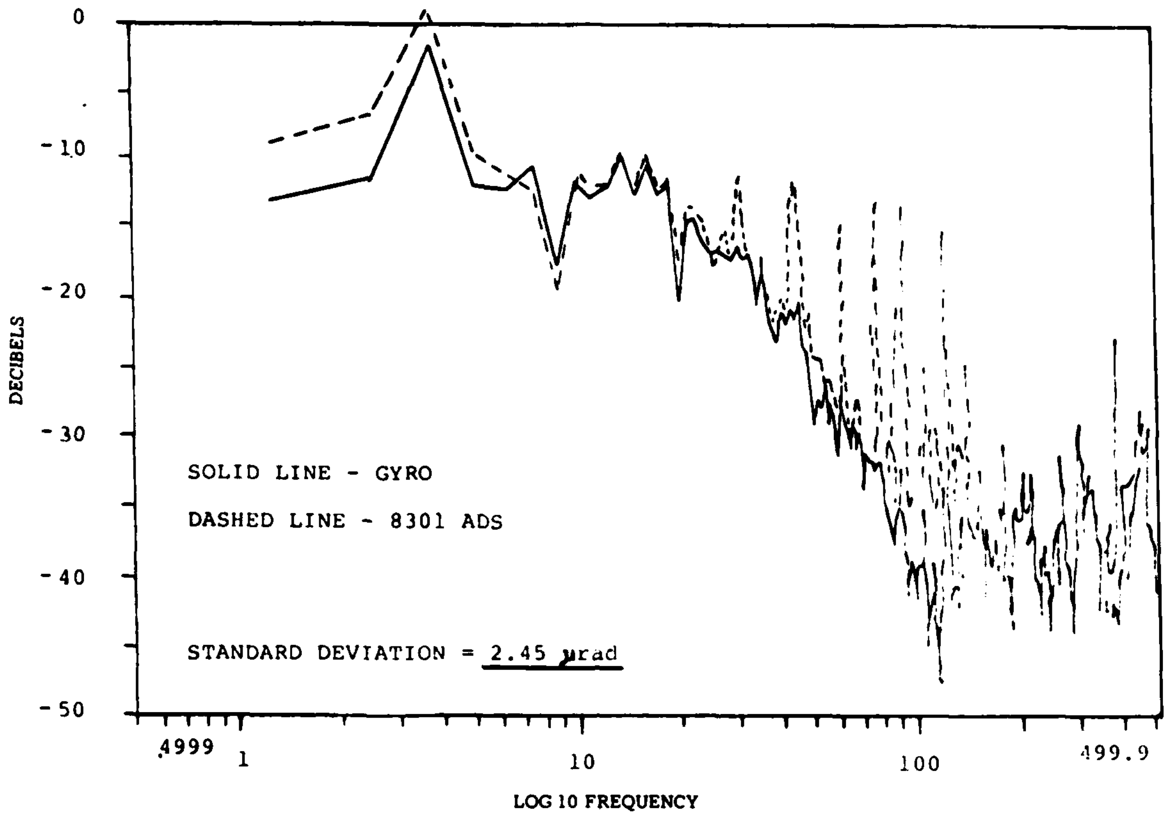

Figure 9: Lab Measurement of ADS and Inertial Gyro

V. CONCLUSIONS

This paper has documented an angular measurement system that has been recently produced by the Systron-Donner Corporation for the Air Force Weapons Laboratory. The design of the instrument is such that it measures angular displacement and requires no integration processing. This is very desirable as it directly yields the quantity of most interest. The detailed tests run by Systron-Donner on each instrument have verified the accuracy and repeatability of the units. Flight test measurements by the Air Force are confirming the accuracy of the systems and to present have indicated a very good reliability record.

In summary, a versatile and very accurate angular vibration measurement system has been built by Systron-Donner for the Air Force. The units have a wide range of applications and fill the need of the Air Force to make wide bandwidth low amplitude angular vibration measurements. Their flat amplitude response and nearly zero phase response over a wide frequency range make them ideally suited to make environmental measurements and as a real time active compensation for angular systems.

REFERENCES

1. Air Force Contract and Specification F29650-77-90248. Issued by AFCMD (PMUS), Kirtland AFB NM 87117, July 14, 1977.

2. C. J. Byrne, "Instrument Noise in Seismometers," Bulletin of the Seismological Society of America, Volume 51, Number 1, pp. 69-84, January 1961.

3. H. B. Ellis, "FLIR High Frequency Stabilization Study Program," Aeroject Electrosystems Company, Final Report, AFAL-TR-76-78.

4. R. B. Peters, "A Dynamic Angular Calibration System for Broadband Microradian Inertial Sensors," Proceedings of the AIAA Guidance and Control Conference, August 1978; Paper Number 78-1253.

5. "Acceptance Test Procedure for Angular Displacement Sensor S-D Model 8301-.001-P4" and Data Sheets, "Final Performance Test for Angular Displacement Sensor S-D Model 5690-4" and Data Sheets, Drawing Numbers 48489-1 through 48489-4 resp. Systron-Donner Corporation, Concord, CA 94518.

6. C. K. Sanathanan and J. Koerner, "Transfer Function Synthesis as a Ratio of Two Complex Polynominals," IEEE Transaction on Automatic Control, 1963, AC-8, 56.

7. "The Boeing 747-100 Airborne Linear and Angular Vibration Measurements," AFFDL/FBG/79-5, May 1979, distribution limited to U.S. Government Agencies.

8. "Douglas DC-10 Airborne Linear and Angular Vibration Measurements," AFFDL/FBG/79-4, May 1979, limited distribution.

9. "Lockheed L-1011 Airborne Linear and Angular Vibration Measurements," AFFDL/FBG/79-7, May 1979, limited distribution.

DISCUSSION

Mr. Foley (Fairchild Republic): You mentioned the measurements being taken on the A-10 aircraft. We have had some problem with low frequency isolation down around 1 Hz or 1¼ Hz and I think we are getting levels up to about 14 milli radians and this was masking out the high frequency angular displacement. Would this saturate your instrument?

Mr. Morris: It would indeed saturate it when it was set for ten milliradians peak input. The unit you utilized had a selectable range from one milliradian full scale to ten milliradians full scale. And as I recall you actually ran into square top saturation of the sensor. That occurred only at infrequent intervals as I recall and I suggested to you that you utilize a low frequency cutoff to cut off your structural information that you did not desire. This was true information being produced by the sensor of the actual motion of the aircraft caused by its low frequency structural modes.

Mr. Foley: We think it was a rigid body pitch mode.

Mr. Morris: But as far as I know the sensor was doing exactly what it was intended to do, namely to measure direct angular displacement.

Mr. Foley: But there was still room for filtering in that low frequency range.

Mr. Morris: Yes, because the sensor was cutting off at 12 db per octave below 2 Hz and you had a very large structural mode at about one Hz as I remember.

Mr. Dyrdahl (Boeing Company): Does the Air Force have a system for using your information to correct the line of sight measurements?

Mr. Morris: The Air Force was investigating the environment since that was totally unknown. They were also investigating whether it was possible to servo a mirror similar to the way Aerojet Electrosystems had demonstrated so that it would take out the line of sight.

Mr. Dyrdahl: Are they making any progress? That would be a great system.

Mr. Morris: I really can't report on that since Dr. Merritt is not present at this meeting.

ANGULAR ACCELERATION MEASUREMENT ERRORS INDUCED BY LINEAR ACCELEROMETER CROSS-AXIS COUPLING

Anthony S Hu, Sc.D.
Physical Science Laboratory
New Mexico State University
Las Cruces, N.M. 88003

In biomechanical experiments, the head angular impact responses of the test subject are usually calculated from the data of linear accelerometers because of their small size and light weight. As many as nine linear accelerometers are sometimes used for a complete three dimensional head kinematic measurement. One major error source of this type of measurement is the cross-axis coupling of the accelerometers. This paper derives the mathematical model of the instrument, defines the cross-axis sensitivity, computes the angular measurement errors caused by the linear accelerometers, and discusses the physical meaning of each error term under various impact motions. The study reveals some insight into the limitations of the measurement technique.

INTRODUCTION

In biomechanical impact experiments, miniature linear accelerometers are often used to measure angular accelerations and angular velocities [1], [2]. As many as nine linear accelerometers can be arranged in various configurations to relate the accelerometer measurements to the angular responses.

Results using both hypothetical and experimental data indicated that good major axis angular acceleration and velocity data may be obtained for planar motion if the state-of-the-art linear piezoresistive accelerometers are used. In oblique runs, especially in near planar motion, minor axis angular accelerations generally contain large errors induced by the cross-axis sensitivity. The purpose of this paper is to explicitly express the angular acceleration errors in terms of the sensitivity coefficients. This provides some insights into the limitations of the measurement technique.

MATHEMATICAL MODEL

Although there are at least eleven possible configurations [1] for angular measurements, this paper discusses only the most commonly used nine-accelerometer module [2]. The 3-2-2-2 nine-accelerometer module is configured as shown in Fig. 1 with the bold arrows indicating the nine accelerometers. The lower case a_1, a_2, ... a_9 indicate the true acceleration when measured with nine ideal acceler-

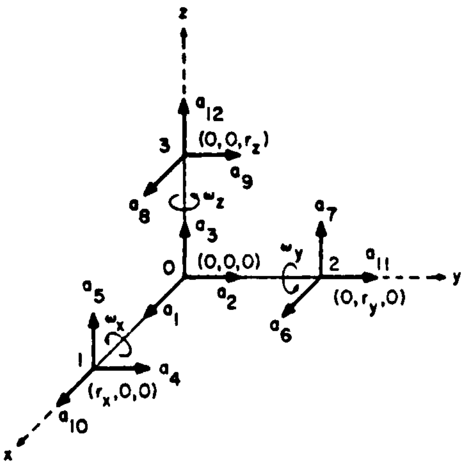

Fig. 1. Nine-accelerometer configuration.

This work was supported by the Department of Transportation, National Highway Traffic Safety Administration under Contract DOT-HS-6-01400. The opinions, findings and conclusions stated herein are those of the author and are not necessarily those of the Department of Transportation.

ometers. Note that a_{10}, a_{11}, and a_{12} are not related to any accelerometers but they represent the true accelerations in axes x, y, and z at cluster locations 1, 2, and 3 respectively. The lower case ω_x, ω_y, and ω_z indicate the true angular velocities about axes x, y, and z respectively. Each cluster of sensors is located in one of the four positions as shown in the figure.

Forward Equations

From Fig. 1, the linear acceleration along a_i, for i = 1, 2, ... 12, can be expressed as follows

$$a_1 = \ddot{x} \tag{1-1}$$

$$a_2 = \ddot{y} \tag{1-2}$$

$$a_3 = \ddot{z} \tag{1-3}$$

$$a_4 = \ddot{y} + \omega_x\omega_y r_x + \dot{\omega}_z r_x \tag{1-4}$$

$$a_5 = \ddot{z} + \omega_x\omega_y r_x - \dot{\omega}_y r_x \tag{1-5}$$

$$a_6 = \ddot{x} + \omega_x\omega_y r_y - \dot{\omega}_z r_y \tag{1-6}$$

$$a_7 = \ddot{z} + \omega_y\omega_z r_y + \dot{\omega}_x r_y \tag{1-7}$$

$$a_8 = \ddot{x} + \omega_x\omega_z r_z + \dot{\omega}_y r_z \tag{1-8}$$

$$a_9 = \ddot{y} + \omega_y\omega_z r_z - \dot{\omega}_x r_z \tag{1-9}$$

$$a_{10} = \ddot{x} - \omega_y^2 r_x - \omega_z^2 r_x \tag{1-10}$$

$$a_{11} = \ddot{y} - \omega_x^2 r_y - \omega_z^2 r_y \tag{1-11}$$

$$a_{12} = \ddot{z} - \omega_x^2 r_z - \omega_y^2 r_z \tag{1-12}$$

Inverse Equations

Using Equations (1-1) through (1-9), $\dot{\omega}_x$, $\dot{\omega}_y$, and $\dot{\omega}_y$ can be calculated [1], [2] to obtain:

$$\dot{\omega}_x = (a_7 - a_3)/2r_y - (a_9 - a_2)/2r_z \tag{2-1}$$

$$\dot{\omega}_y = (a_8 - a_1)/2r_z - (a_5 - a_3)/2r_x \tag{2-2}$$

$$\dot{\omega}_z = (a_4 - a_2)/2r_x - (a_6 - a_1)/2r_y \tag{2-3}$$

Let $r_x = r_y = r_z = r$. Equation (2) is simplified in matrix form

$$\begin{bmatrix} \dot{\omega}_x \\ \dot{\omega}_y \\ \dot{\omega}_z \end{bmatrix} = \frac{1}{2r} \begin{bmatrix} 0 & 1 & -1 & 0 & 0 & 0 & 1 & 0 & -1 \\ -1 & 0 & 1 & 0 & -1 & 0 & 0 & 1 & 0 \\ 1 & -1 & 0 & 1 & 0 & -1 & 0 & 0 & 0 \end{bmatrix} \cdot \begin{bmatrix} a_1 \\ a_2 \\ a_3 \\ a_4 \\ a_5 \\ a_6 \\ a_7 \\ a_8 \\ a_9 \end{bmatrix} \tag{3}$$

If the accelerometers were ideal, then the electrical signals are a_i (i = 1, 2, ... 9), and the calculated angular accelerations will have no error.

EFFECTS OF CROSS-AXIS SENSITIVITY

Definition of Cross-Axis Sensitivity

For an ideal accelerometer, the output signal (bold line) is a cosine function of the angle between the accelerometer principal axis and the acceleration input axis as illustrated in Fig. 2. The output signal should be zero when the acceleration is applied perpendicularly to the sensitive axis ($\theta = \pm 90°$). But for an actual accelerometer, this output signal is not zero, as shown in the dashed curve. The ratio of this value to the value when the applied acceleration is in line with the sensitive axis is defined as the cross-axis sensitivity coefficient s_{ij} where the first subscript is the accelerometer number and the second subscript is the acceleration input axis. Its magnitude may be between 0.01 and 0.05. It is assigned positive if the cross product of the input acceleration and sensor principal axis is positive (right hand rule) and vice versa. For example, if the acceleration along vector a_1(x-axis) creates a positive voltage reading in the accelerometer along vector a_2, then the coefficient s_{2x} is positive.

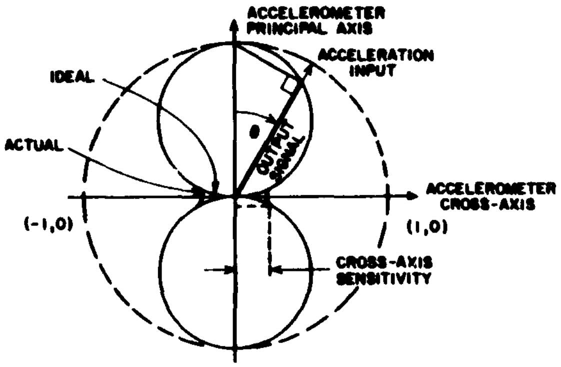

Fig. 2. Cross-axis sensitivity.

Designation of Errors

If the true kinematic acceleration is a_i and the measured acceleration is A_i (for $i = 1, 2, \ldots 9$), then they are related by Equation (4).

$$A_1 = (a_1)+(-s_{1y}a_2 + s_{1z}a_3) \equiv a_1+\Delta a_1 \quad (4\text{-}1)$$

$$A_2 = (a_2)+(s_{2x}a_1 - s_{2z}a_3) \equiv a_2+\Delta a_2 \quad (4\text{-}2)$$

$$A_3 = (a_3)+(-s_{3x}a_1 + s_{3y}a_2) \equiv a_3+\Delta a_3 \quad (4\text{-}3)$$

$$A_4 = (a_4)+(s_{4x}a_{10} - s_{4z}a_5) \equiv a_4+\Delta a_4 \quad (4\text{-}4)$$

$$A_5 = (a_5)+(-s_{5x}a_{10} + s_{5y}a_4) \equiv a_5+\Delta a_5 \quad (4\text{-}5)$$

$$A_6 = (a_6)+(-s_{6y}a_{11} + s_{6z}a_7) \equiv a_6+\Delta a_6 \quad (4\text{-}6)$$

$$A_7 = (a_7)+(-s_{7x}a_6 + s_{7y}a_{11}) \equiv a_7+\Delta a_7 \quad (4\text{-}7)$$

$$A_8 = (a_8)+(-s_{8y}a_9 + s_{8z}a_{12}) \equiv a_8+\Delta a_8 \quad (4\text{-}8)$$

$$A_9 = (a_9)+(s_{9x}a_8 - s_{9z}a_{12}) \equiv a_9+\Delta a_9 \quad (4\text{-}9)$$

Note that A_i can be divided into two parts: The first part is the true kinematic acceleration and the second part is the error acceleration caused by the non-zero cross-axis sensitivity coefficients.

Calculated Angular Accelerations

Since an investigator does not know the true kinematic acceleration a_i, he, therefore, uses the measured value of A_i. Equation (3) becomes Equation (5).

$$\dot{\Omega}_x = \frac{1}{2r}(A_7 - A_3 - A_9 + A_2) \quad (5\text{-}1)$$

$$\dot{\Omega}_y = \frac{1}{2r}(A_8 - A_1 - A_5 + A_3) \quad (5\text{-}2)$$

$$\dot{\Omega}_z = \frac{1}{2r}(A_4 - A_2 - A_6 + A_1) \quad (5\text{-}3)$$

where $\dot{\Omega}_j$ ($j = x, y, z$) is the calculated angular acceleration.

Using Eqs. (1), (4), and (5), the calculated angular acceleration in matrix form becomes

$$\dot{\Omega} = \dot{\omega} + \Delta\dot{\omega} \quad (6)$$

where

$$\dot{\omega} = \begin{bmatrix} \dot{\omega}_x \\ \dot{\omega}_y \\ \dot{\omega}_z \end{bmatrix} = \frac{1}{2r} \begin{bmatrix} 0 & 1 & -1 & 0 & 0 & 0 & 1 & 0 & -1 \\ -1 & 0 & 1 & 0 & -1 & 0 & 0 & 1 & 0 \\ 1 & -1 & 0 & 1 & 0 & -1 & 0 & 0 & 0 \end{bmatrix} \cdot \begin{bmatrix} a_1 \\ a_2 \\ a_3 \\ a_4 \\ a_5 \\ a_6 \\ a_7 \\ a_8 \\ a_9 \end{bmatrix} \quad (7)$$

and

$$\Delta\dot{\omega} = \begin{bmatrix} \Delta\dot{\omega}_x \\ \Delta\dot{\omega}_y \\ \Delta\dot{\omega}_z \end{bmatrix} = \frac{1}{2r} \begin{bmatrix} (s_{2x} + s_{3x} - s_{7x} - s_{9x}) & -(s_{3y} - s_{7y}) & -(s_{2z} - S_{9z}) \\ -(s_{3x} - s_{5x}) & (s_{1y} + s_{3y} - s_{5y} - s_{8y}) & -(s_{1z} - s_{8z}) \\ -(s_{2x} - s_{4x}) & -(s_{1y} - s_{6y}) & (s_{1z} + s_{2z} - s_{4z} - s_{6z}) \end{bmatrix} \cdot \begin{bmatrix} \ddot{x} \\ \ddot{y} \\ \ddot{z} \end{bmatrix}$$

$$+ \frac{1}{2} \begin{bmatrix} -(s_{7y} + s_{9z}) & -s_{9z} & -s_{7y} \\ -s_{8z} & -(s_{5x} + s_{8z}) & -s_{5x} \\ -s_{6y} & -s_{4x} & -(s_{4x} + s_{6y}) \end{bmatrix} \cdot \begin{bmatrix} \omega_x^2 \\ \omega_y^2 \\ \omega_z^2 \end{bmatrix}$$

$$+ \frac{1}{2} \begin{bmatrix} -s_{7x} & 0 & -s_{9x} \\ -s_{5y} & -s_{8y} & 0 \\ 0 & -s_{6z} & -s_{4z} \end{bmatrix} \cdot \begin{bmatrix} \omega_x \omega_y \\ \omega_y \omega_z \\ \omega_z \omega_x \end{bmatrix}$$

$$+ \frac{1}{2} \begin{bmatrix} 0 & -s_{9x} & s_{7x} \\ s_{8y} & 0 & -s_{5y} \\ -s_{6z} & s_{4z} & 0 \end{bmatrix} \cdot \begin{bmatrix} \dot{\omega}_x \\ \dot{\omega}_y \\ \dot{\omega}_z \end{bmatrix} \qquad (8)$$

Equation (7) is identical to Equation (3), which is the true angular acceleration. Equation (8) is the angular acceleration errors due to the non-zero cross-axis sensitivity of the actual accelerometers. These errors are functions of linear accelerations, squares of angular velocities, cross products of angular velocities, and angular accelerations. The cross coupling effect is obvious.

DESCRIPTION OF MOTION

Planar Motion

Assume that the nine-accelerometer module undergoes a planar motion in the x-z plane. This implies the following:

$$\ddot{y} = 0 \qquad (9\text{-}1)$$

$$\omega_x = \omega_z = 0 \qquad (9\text{-}2)$$

$$\dot{\omega}_x = \dot{\omega}_z = 0 \qquad (9\text{-}3)$$

The true and the error angular accelerations are expressed in Equations (10) and (11) respectively.

$$\dot{\omega}_x = 0 \qquad (10\text{-}1)$$

$$\dot{\omega}_y = \frac{1}{2r} (-a_1 + a_3 - a_5 + a_8) \qquad (10\text{-}2)$$

$$\dot{\omega}_z = 0 \qquad (10\text{-}3)$$

$$\Delta\dot{\omega}_x = \frac{1}{2r} \left[(S_{2x}+S_{3x}-S_{7x}-S_{9x})\ddot{x} - (S_{2z}-S_{9z})\ddot{z} \right]$$

due to linear acceleration

$$+ \frac{1}{2} \left[-S_{9z}\ \omega_y^2 \right]$$

due to angular velocity squared

$$+ \frac{1}{2} \left[-S_{9x}\ \dot{\omega}_y \right] \qquad (11\text{-}1)$$

due to angular acceleration

$$\Delta\dot{\omega}_y = \frac{1}{2r} \left[-(S_{3x}-S_{5x})\ \ddot{x} - (S_{1z}-S_{8z})\ \ddot{z} \right]$$

$$+ \frac{1}{2} \left[-(S_{5x} + S_{8z})\ \omega_y^2 \right] \qquad (11\text{-}2)$$

$$\Delta\dot{\omega}_z = \frac{1}{2r} \left[-(S_{2x}-S_{4x})\ddot{x} + (S_{1z}+S_{2z}-S_{4z}-S_{6z})\ddot{z} \right]$$

$$+ \frac{1}{2} \left[-S_{4x}\ \omega_y^2 \right]$$

$$+ \frac{1}{2} \left[S_{4z}\ \dot{\omega}_y \right] \qquad (11\text{-}3)$$

Although $\Delta\dot{\omega}_x$ and $\Delta\dot{\omega}_z$ are not considered under the planar motion assumption, they are never zero.

Pure Rotational Planar Motion

An investigator may ignore $\dot{\Omega}_x$ $(\dot{\Omega}_x = \dot{\omega}_x + \Delta\dot{\omega}_x)$ and $\dot{\Omega}_z$ $(\dot{\Omega}_z = \dot{\omega}_z + \Delta\dot{\omega}_z)$, and consider $\dot{\Omega}_y$ $(\dot{\Omega}_y = \dot{\omega}_y + \Delta\dot{\omega}_y)$ as his only measurement. Thus, his experiment has an error of $\Delta\dot{\omega}_y = -\frac{1}{2}(s_{5x} + s_{8z})\omega_y^2$ under pure rotational planar motion conditions.

Let the angular velocity be $\omega_y(t) = \omega_{ymax}\sin(\omega t)$, where ω is the oscillating frequency, then $\dot{\omega}_y(t) = \omega\omega_{ymax}\cos(\omega t)$. Equation (11-2) becomes

$$\Delta\dot{\omega}_y(t) = -\frac{1}{2}(s_{5x}+s_{8z})\;\omega^2_{y\,max}\sin^2(\omega t)$$

$$= \underbrace{-\frac{(s_{5x} + s_{8z})\;\omega^2_{y\,max}}{4}}_{\text{constant error}}$$

$$+ \underbrace{\frac{(s_{5x} + s_{8z})\;\omega^2_{y\,max}}{4}\cos(2\omega t)}_{\text{second-harmonic error}} \qquad (12)$$

The constant error term in $\dot{\omega}_y$ will create errors proportional to time-squared in angular displacement.

The second-harmonic distortion is illustrated in Fig. 3. Maximum errors occur when ω_y passes through its zeros and peaks but does not affect the peak-to-peak value of $\dot{\omega}_y$. This often misleads the investigator to believe that his experiment has very little error.

Pure Translational Planar Motion

Again, Equation (11) can be simplified by resticting the planar motion to a pure translational motion in the x-z plane. In this case, the measured angular acceleration has an error of

$$\frac{-1}{2r}\left[(s_{3x} - s_{5x})\ddot{x} - (s_{1z} - s_{8z})\ddot{z}\right]$$

For example, if r = 7.62 cm (3 inches), $\ddot{x} = \ddot{z}$ = 50g, and the magnitude of the cross-axis sensitivity is 0.01, then the worst case is $\Delta\dot{\omega}_y$ = 128 rad/sec^2.

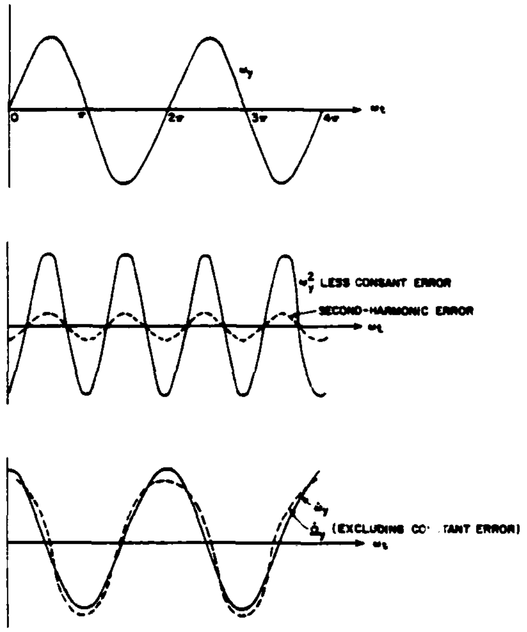

Fig. 3. Second-harmonic distortion.

Near Planar Motion

If this module undergoes an oblique motion but is dominated by the x-z plane motion, then Equation (11) is also valid for the near planar motion where the cross product terms are much less than the squared angular velocity terms. The error analysis of $\Delta\dot{\omega}_y$ is identical to that in the planar motion but the values of $\Delta\dot{\omega}_x$ and $\Delta\dot{\omega}_z$ can no longer be ignored. The following discusses the nature of $\Delta\dot{\omega}_x$. Similar discussion applies for $\Delta\dot{\omega}_z$.

The error $\Delta\dot{\omega}_x$ for a pure rotational motion is derived from Eq. (11-1).

$$\Delta\dot{\omega}_x \simeq \frac{-1}{2}\;(s_{9x}\dot{\omega}_y - s_{9z}\omega_y^2\;) \qquad (13)$$

where the term $(s_{9z}\omega_y^2)$ consists of a constant error and a second-harmonic error similar to those of Equation (12). The additional term $(s_{9x}\dot{\omega}_y)$ may appear to be insignificant when compared with $\dot{\omega}_x$ but it is significant when compared with $\dot{\omega}_x$ since this is a near planar motion.

The error $\Delta\dot{\omega}_x$ for a pure translational motion is shown in Equation (14).

$$\Delta\dot{\omega}_x \simeq \frac{1}{2r}(s_{2x}+s_{3x}-s_{7x}-s_{9x})\ddot{x} - (s_{2z}-s_{9z})\ddot{z} \quad (14)$$

Again, this error may be insignificant when compared with $\dot{\omega}_y$, but it is significant when compared with $\dot{\omega}_x$ since this is a near planar *motion. For example*, if r=7.62 cm (3 inches), $\ddot{x} = \ddot{z} = 50g$, and the magnitude of the cross-axis sensitivity is 0.01, the worst case is $\Delta\dot{\omega}_x = 192$ rad/sec^2.

CONCLUSIONS

This paper discussed the angular acceleration measurement errors induced by the cross-axis coupling of linear accelerometers. Other error sources involve the accelerometer principal axis error (alignment, linearity, hysteresis, resolution, threshold, noise, drift, frequency responses, etc.), seismic mass center error, data channel error, and computational error.

It should be noted that there are many other configurations [1] can be used to calculate angular acceleration as well as angular velocity directly. The impact response data are often subjected to integration and differentiation procedures. These procedures are low- and high-pass filtering processes where the frequency harmonics are weighted at -6 dB/octave and +6 dB/octave respectively [3]. Therefore, the angular acceleration measurement requires higher frequency response than the angular velocity measurement.

It appears that the linear accelerometer cross-axis sensitivity imposes limitations on the measurement of angular data. Some of them are:

Planar Motion -- The rotational kinematics creates two error terms in the calculated angular acceleration, Eq. (12). The constant error accumulates angular velocity and angular displacement errors while the second-harmonic error creates distortion in the calculated angular acceleration. The translational kinematics creates an error in the calculated angular acceleration, Eq. (11-2), proportionally.

Oblique Motion -- In oblique experiments, the calculated angular accelerations have errors due to the non-zero cross-axis sensitivity or the principal axis misalignment of the accelerometers. See Eq. (8). This is especially true for oblique but near planar motion where the kinematics in one plane dominates the others. The rotational kinematics creates three error terms in the minor axis angular acceleration, Eqs. (11) and (12). The first term is coupled from the major axis angular acceleration; the second term is a constant error; and the third term is the second-harmonic distortion. The translational kinematics creates an error in the calculated angular acceleration, Eq. (11), proportionally. These errors become significant in the minor axes but not necessarily in the major axis because of the near planar nature.

REFERENCES

(1) A. S. Hu, "Rotational Measurement Techniques using Linear Accelerometers," Proc. International Instrumentation Symposium, ISA, pp. 349-354, May, 1977.

(2) A. J. Padgoankar, K. W. Krieger, and A. I. King, "Measurement of Angular Acceleration of a Rigid Body Using Linear Accelerometers," J. of Applied Mechanics, pp. 552-556, September 1975.

(3) A. S. Hu and H. T. Chen, "Frequency Response and Differentiation Requirements for Impact Measurements," Shock and Vibration Bulletin, vol. 48, pp. 123-130, September, 1978.

A METHOD FOR EXPERIMENTALLY DETERMINING
ROTATIONAL MOBILITIES OF STRUCTURES

Stanley S. Sattinger
Westinghouse-Bettis Atomic Power Laboratory
Pittsburgh, Pennsylvania

A mobility function is a transfer function relating the complex amplitude of vibratory response velocity at some point on a structural component to the complex amplitude of an excitation applied at any point on the same component. The vibratory response can be either a translational or a rotational velocity, and the excitation can be either a force or a moment. Translational velocity/force mobilities for structural components are commonly used to generate dynamic response predictions for assemblages wherein the components may be assumed to have only translational interactions. However, rotational mobilities, i.e. those involving rotational velocities and/or moments, are needed for assemblages in which rotational interactions among the components are important. This study deals with the experimental determination of such mobilities.

Previous investigators have approached the difficult task of experimentally measuring rotational mobilities with the use of special fixturing attached to the components. It is shown here that rotational mobilities of structures are equivalent to spatial derivatives of their translational mobilities. The method of finite differences is adapted to the approximation of these derivatives. By this method the rotational mobilities are derived from sets of conventionally measured translational mobilities, eliminating the need for special fixturing.

This approach to determining rotational mobilities is demonstrated in a set of experiments on a free-free beam. Good agreement is obtained between experimentally and theoretically generated versions of two rotational velocity/force mobilities. An experimentally derived rotational velocity/moment mobility is found to give reasonably good indications of resonances but exhibits large amounts of scatter in some frequency bands. This scatter is attributed to the subtraction of translational mobility quantities which are nearly equal in magnitude. Further investigation is needed to determine an effective method of smoothing the translational mobility data before the differencing calculations to eliminate this scatter.

INTRODUCTION

A mobility or admittance function is a transfer function relating the complex amplitude of motion at some point on a structure in response to the complex amplitude of an excitation force applied at any point on the same structure. The most common type of mobility is the ratio of a translational component of velocity to a translational force as illustrated in the transfer mobility example of Figure 1(a). However, the concept of mobility can be extended to rotational velocities and moment excitations as shown in the examples of Figures 1(b) through 1(d). A matrix relationship involving the transfer mobilities thus defined between two points is shown in Figure 1(e). This formulation could be specialized to the case where the response measurement point, B, is coincident with the excitation point, A, i.e., each matrix element is a driving point mobility; or it could be generalized to include the existence of motions and excitations at both points. In the latter instance the second order mobility matrix shown would be expanded to the fourth order.

Mobility and impedance concepts are readily used in generating dynamic response predictions for assemblages of two or more component structures. In particular applications ([1], [2], [3]) the components may be assumed to have only translational interactions. This kind of analytical treatment can be realistic if the actual moment reactions among components at each interface are small due to joint configurations, symmetry, or other factors. However, in cantilevered assemblages the rotational interactions can be of dominant importance. Applications of mobility and impedance methods in such cases have been hampered by difficulties in experimentally measuring the rotational mobilities of components. Whereas the measurement of translational velocities and forces is routine, apparatus for the measurement of rotational velocities and moments in structural dynamics applications is not commercially available.

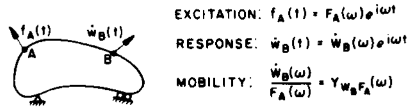

(a) TRANSLATIONAL VELOCITY/FORCE MOBILITY

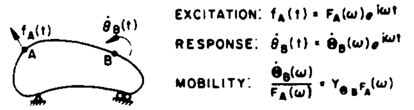

(b) ROTATIONAL VELOCITY/FORCE MOBILITY

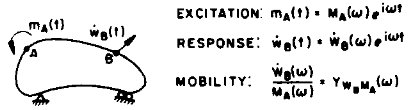

(c) TRANSLATIONAL VELOCITY/MOMENT MOBILITY

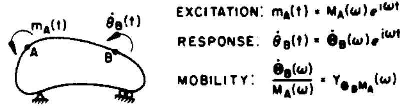

(d) ROTATIONAL VELOCITY/MOMENT MOBILITY

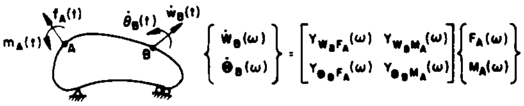

(e) MATRIX EQUATION INVOLVING COMBINED MOBILITIES

Fig. 1 - Transfer Mobilities Involving Various Combinations of Translational and Rotational Effects

Explorations of techniques for the measurement of moment excitations and rotation responses are described in [4], [5], and [6]. In each of these studies special fixtures have been attached to the structures, and accelerometers and/or force transducers have been, in turn, mounted at various locations on the fixtures. Rotational mobilities have been obtained with varying degrees of success using algebraic manipulations on the sensor outputs. Corrections for the dynamic influences of the fixturing have been required in some cases.

The present study was conducted to develop a method of generating experimental rotational mobility functions using conventional measurement techniques without a requirement for the use of special fixturing. The approach taken is to represent mobilities involving rotational velocities and moment excitations as spatial derivatives of conventional translational mobilities; the derivatives are approximated as finite difference sums of sets of these translational mobilities. The theoretical basis and calculations used for these representations are given, and the method is demonstrated in a set of experiments conducted on a free-free beam.

DERIVING ROTATIONAL MOBILITIES FROM TRANSLATIONAL MOBILITIES

Rotational Velocity/Force Mobility

Figure 2(a) depicts a segment of a structure which is being driven by a sinusoidal translational force applied to Point A and in which the resultant sinusoidal translational velocity is being measured at Point B. Considering momentarily that the excitation is at a particular frequency ω_M, the value of the translational mobility at that frequency is the complex quantity $\dot{W}_B(\omega_M)/F_A(\omega_M)$. Now suppose that the velocity measurement is made in turn at each point of a set of points adjacent to Point B with the excitation maintained at Point A as shown in Figure 2(b). The resulting complex amplitude ratios $\dot{W}(\omega_M;\eta)/F_A(\omega_M)$ could be plotted as functions of the position coordinate, η, of the measuring point as shown in Figure 2(c).

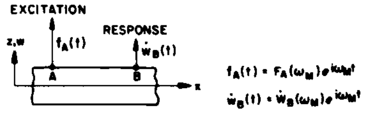

(a) FIXED RESPONSE MEASUREMENT LOCATION

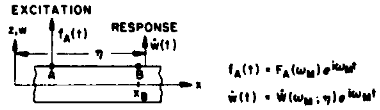

(b) VARYING RESPONSE MEASUREMENT LOCATION

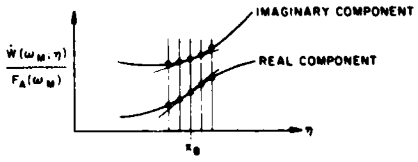

(c) PLOT OF RESULTANT COMPLEX AMPLITUDE RATIOS

Fig. 2 - Relationship of Rotational Velocity/Force Mobility to Translational Mobility at a Single Frequency

In principle the real and imaginary mobility data would lie on smooth curves by virtue of the continuity of the wave fields comprising the vibration of the structure. Tangent lines could be drawn to these curves at the coordinate x_B of Point B. The slopes of these tangents would have the following significance.

The instantaneous angular displacement of the structure relative to its rest position at a location η is given by:

$$\theta = \frac{\partial w}{\partial \eta} .$$

The time rate of change of this slope is given by:

$$\dot{\theta} = \frac{\partial}{\partial t}\frac{\partial w}{\partial \eta} = \frac{\partial}{\partial \eta}\frac{\partial w}{\partial t} = \frac{\partial}{\partial \eta}\dot{w} . \tag{1}$$

But, because the excitation is sinusoidal, this angular velocity can be written as:

$$\dot{\theta} = \dot{\Theta}(\omega_M)e^{i\omega_M t}. \tag{2}$$

By combining Eq. (2) and the expression

$$\dot{w} = \dot{W}(\omega_M;\eta)e^{i\omega_M t}$$

with Eq. (1), it is found that

$$\dot{\Theta}(\omega_M;\eta) = \frac{\partial}{\partial \eta}\dot{W}(\omega_M;\eta), \tag{3}$$

from which is formed the ratio of complex amplitudes

$$\frac{\dot{\Theta}_B(\omega_M)}{F_A(\omega_M)} = \frac{\partial}{\partial \eta}\frac{\dot{W}(\omega_M;\eta)}{F_A(\omega_M)}\Bigg|_{\eta=x_B} \tag{4}$$

$$= \left\{\frac{\partial}{\partial \eta}\operatorname{Re}\left[\frac{\dot{W}(\omega_M;\eta)}{F_A(\omega_M)}\right] + i\frac{\partial}{\partial \eta}\operatorname{Im}\left[\frac{\dot{W}(\omega_M;\eta)}{F_A(\omega_M)}\right]\right\}\Bigg|_{\eta=x_B} .$$

If these derivatives are evaluated over a band of driving frequencies, ω, of interest, the rotational velocity/force mobility is thus derived from the translational mobility:

$$Y_{\dot{\Theta}_B F_A}(\omega) = \frac{\partial}{\partial \eta} Y_{\dot{W}F_A}(\omega;\eta)\Bigg|_{\eta=x_B} . \tag{5}$$

Translational Velocity/Moment Mobility

In Figure 3(a) the structure is again shown with translational excitation and response vectors at Points A and B, respectively. Again with the excitation frequency set at ω_M, suppose that the excitation force is applied in turn at each of a set of points adjacent to A with responses measured at Point B as shown in Figure 3(b). The resulting complex amplitude ratios $\dot{W}_B(\omega_M)/F(\omega_M;\xi)$ could be plotted as functions of the position coordinate, ξ, of the excitation point as shown in Figure 3(c). The real and imaginary mobility components would again lie on smooth curves to which tangent lines could be drawn at the coordinate x_A of Point A.

It is seen in Figure 3(d) that an instantaneous moment applied to the structure at Point A can be represented as a pair of equal and opposite parallel forces separated a small distance, ϵ. The response of the structure at Point B to a sinusoidally varying moment at Point A is then:

$$\dot{w}_B = \dot{W}_B(\omega_M)e^{i\omega_M t} = \lim_{\epsilon\to 0}\left\{\frac{\dot{W}_B(\omega_M)}{F(\omega_M;\xi)}\Bigg|_{\xi = x_A+\epsilon} P(\omega_M)e^{i\omega_M t} - \frac{\dot{W}_B(\omega_M)}{F(\omega_M;\xi)}\Bigg|_{\xi = x_A} P(\omega_M)e^{i\omega_M t}\right\} . \tag{6}$$

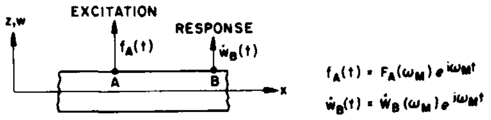

(a) FIXED EXCITATION LOCATION

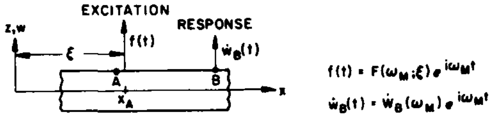

(b) VARYING EXCITATION LOCATION

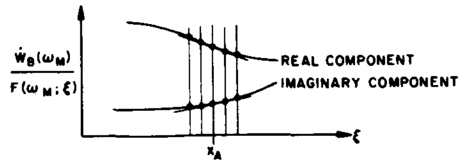

(c) PLOT OF RESULTANT COMPLEX AMPLITUDE RATIOS

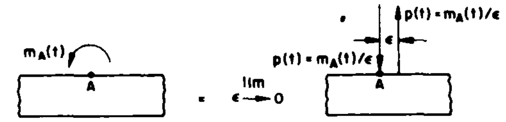

(d) SUBSTITUTION OF EQUIVALENT FORCE PAIR FOR MOMENT

Fig. 3 - Relationship of Translational Velocity/Moment Mobility to Translational Mobility at a Single Frequency

Then

$$\dot{W}_B(\omega_M) = \lim_{\epsilon\to 0}\left\{\left[\frac{\left.\dfrac{\dot{W}_B(\omega_M)}{F(\omega_M;\xi)}\right|_{\xi = x_A+\epsilon} - \left.\dfrac{\dot{W}_B(\omega_M)}{F(\omega_M;\xi)}\right|_{\xi = x_A}}{\epsilon}\right].P(\omega_M)\epsilon\right\} \tag{7}$$

$$= \frac{\partial}{\partial\xi}\left.\frac{\dot{W}_B(\omega_M)}{F(\omega_M;\xi)}\right|_{\xi = x_A} .M_A(\omega_M) \quad ,$$

from which is formed the ratio of complex amplitudes

$$\frac{\dot{W}_B(\omega_M)}{M_A(\omega_M)} = \frac{\partial}{\partial\xi}\left.\frac{\dot{W}_B(\omega_M)}{F(\omega_M;\xi)}\right|_{\xi = x_A}$$

$$= \left\{\frac{\partial}{\partial\xi}\,\mathrm{Re}\left[\frac{\dot{W}_B(\omega_M)}{F(\omega_M;\xi)}\right] + i\,\frac{\partial}{\partial\xi}\,\mathrm{Im}\left[\frac{\dot{W}_B(\omega_M)}{F(\omega_M;\xi)}\right]\right\}\Bigg|_{\xi = x_A} . \tag{8}$$

If these derivatives are evaluated over a band of driving frequencies, ω, of interest, the translational velocity/moment mobility is thus derived from the translational mobility:

$$Y_{W_B M_A}(\omega) = \frac{\partial}{\partial\xi}\,Y_{W_B F}(\omega;\xi)\Big|_{\xi = x_A} . \tag{9}$$

Rotational Velocity/Moment Mobility

The structure is again excited by a sinusoidal translational force of frequency ω_M at Point A. If the location coordinate ξ of the force application point is made to vary about x_A, the resultant derivative of translational mobility relates the complex amplitude of translational velocity at Point B to the complex amplitude of applied moment at Point A in accordance with Eq. (7). If Eq. (3) is written for the case $\eta = x_B$ and is combined with Eq. (7), the result

$$\frac{\dot{\Theta}_B(\omega_M)}{M_A(\omega_M)} = \frac{\partial}{\partial\eta}\frac{\partial}{\partial\xi}\frac{\dot{W}(\omega_M;\eta)}{F(\omega_M;\xi)}\Bigg|_{\substack{\eta = x_B\\ \xi = x_A}}$$

$$= \left\{\frac{\partial^2}{\partial\eta\partial\xi}\,\mathrm{Re}\left[\frac{\dot{W}(\omega_M;\eta)}{F(\omega_M;\xi)}\right]\right. \tag{10}$$

$$\left. + i\,\frac{\partial^2}{\partial\eta\partial\xi}\,\mathrm{Im}\left[\frac{\dot{W}(\omega_I;\eta)}{F(\omega_M;\xi)}\right]\right\}\Bigg|_{\substack{\eta = x_B\\ \xi = x_A}}$$

is obtained. If these derivatives are evaluated over a band of driving frequencies of interest, the rotational velocity/moment mobility is thus derived from the translational mobility:

$$Y_{\Theta_B M_A}(\omega) = \frac{\partial^2}{\partial\eta\partial\xi}\,Y_{WF}(\omega;\eta,\xi)\Bigg|_{\substack{\eta = x_B\\ \xi = x_A}} . \tag{11}$$

Summary of Derivative Relationships

The mobility matrix relating the translational and rotational velocity amplitudes at the response measuring Point B to the amplitudes of force and moment at the excitation Point A on a structure was shown in Figure 1(e). In accordance with Eqs. (5), (9), and (11) each element of this mobility matrix is a function which can be expressed in terms of the translational velocity/force mobility function, yielding the following:

$$\begin{Bmatrix}\dot{W}_B\\ \dot{\Theta}_B\end{Bmatrix} = \begin{bmatrix} Y_{W_B F_A} & \dfrac{\partial}{\partial\xi}\,Y_{W_B F_A}\\ \dfrac{\partial}{\partial\eta}\,Y_{W_B F_A} & \dfrac{\partial^2}{\partial\eta\partial\xi}\,Y_{W_B F_A}\end{bmatrix}\begin{Bmatrix}F_A\\ M_A\end{Bmatrix} . \tag{12}$$

This equation only summarizes the above findings; the matrix of mobilities on the right hand side is not a complete mobility matrix in that excitations are not represented at each of the degrees of freedom and vice-versa. Whereas complete mobility matrices are symmetric, this matrix is not.

FINITE DIFFERENCE EVALUATION OF DERIVATIVES

The calculation of spatial derivatives of translational velocity/force mobilities is the essence of this approach to generating rotational mobilities. To experimentally determine the rotational mobilities, these derivatives are calculated from conventional mobility measurements made at discrete locations on the structure. The method of finite differences [7], [8] is used for this purpose.

Let the symbol Y denote one of conventional velocity/force mobilities from which rotational mobilities will be derived. These conventional mobilities will be determined from velocity measurements at locations ..., η_{m-1}, η_m, η_{m+1},... spaced $\Delta\eta$ apart, and force measurements at locations ..., ξ_{n-1}, ξ_n, ξ_{n+1},... spaced $\Delta\xi$ apart. Thus the notation $Y_{m,n}$ will represent the mobility function $Y(\omega;\eta_m,\xi_n)$. Each of the following expressions approximate the continuous first partial derivative of Y:

Central Difference:

$$\left.\frac{\partial Y}{\partial \eta}\right|_{\eta_m, \xi_n} \approx \frac{Y_{m+1,n} - Y_{m-1,n}}{2\Delta\eta} ;$$

$$\left.\frac{\partial Y}{\partial \xi}\right|_{\eta_m, \xi_n} \approx \frac{Y_{m,n+1} - Y_{m,n-1}}{2\Delta\xi}$$

Forward Difference:

$$\left.\frac{\partial Y}{\partial \eta}\right|_{\eta_m, \xi_n} \approx \frac{-3Y_{m,n} + 4Y_{m+1,n} - Y_{m+2,n}}{2\Delta\eta} ; \qquad (13)$$

$$\left.\frac{\partial Y}{\partial \xi}\right|_{\eta_m, \xi_n} \approx \frac{-3Y_{m,n} + 4Y_{m,n+1} - Y_{m,n+2}}{2\Delta\xi}$$

Backward Difference:

$$\left.\frac{\partial Y}{\partial \eta}\right|_{\eta_m, \xi_n} \approx \frac{3Y_{m,n} - 4Y_{m-1,n} + Y_{m-2,n}}{2\Delta\eta} ;$$

$$\left.\frac{\partial Y}{\partial \xi}\right|_{\eta_m, \xi_n} \approx \frac{3Y_{m,n} - 4Y_{m,n-1} + Y_{m,n-2}}{2\Delta\xi}$$

The choice of the approximation to be used from among these three would depend on whether the location where the derivative is desired happens to be an inboard location, or if an end location, whether at the positive end or the negative end of the η or ξ interval. These expressions are directly useable in evaluating the rotational velocity/force mobility and the translational velocity/moment mobility as indicated in Eqs. (5) and (9) given that $\eta_m = x_B$ and $\xi_n = x_A$, or $Y_{m,n} = Y_{W_B F_A}$. All six expressions in Eqs. (13) are of equivalent accuracy.

The mixed second partial derivative is approximated by each of the following expressions for use in conjunction with Eq. (11):

Central Difference:

$$\left.\frac{\partial^2 Y}{\partial \eta \partial \xi}\right|_{\eta_m, \xi_n} \approx \frac{Y_{m+1,n+1} - Y_{m+1,n-1} - Y_{m-1,n+1} + Y_{m-1,n-1}}{4\Delta\eta\Delta\xi}$$

Forward Difference:

$$\left.\frac{\partial^2 Y}{\partial \eta \partial \xi}\right|_{\eta_m, \xi_n} \approx \frac{1}{4\Delta\eta\Delta\xi}\Big[9Y_{m,n} - 12Y_{m,n+1} + 3Y_{m,n+2} \qquad (14)$$

$$-12Y_{m+1,n} + 16Y_{m+1,n+1} - 4Y_{m+1,n+2} + 3Y_{m+2,n}$$

$$-4Y_{m+2,n+1} + Y_{m+2,n+2} \Big]$$

Backward Difference:

$$\left.\frac{\partial^2 Y}{\partial \eta \partial \xi}\right|_{\eta_m, \xi_n} \approx \frac{1}{4\Delta\eta\Delta\xi}\Big[9Y_{m,n} - 12Y_{m,n-1} + 3Y_{m,n-2}$$

$$-12Y_{m-1,n} + 16Y_{m-1,n-1} - 4Y_{m-1,n-2}$$

$$+3Y_{m-2,n} - 4Y_{m-2,n-1} + Y_{m-2,n-2} \Big]$$

The central difference expression may be used to evaluate any rotational velocity/moment mobility in which the moment excitation is located at a point inboard of the ends and the rotational velocity response is at the same point or any other inboard point. The forward difference expression applies only to the case in which both η_m and ξ_n are at the negative ends of their ranges; i.e., the hypothetical moment excitation is applied and the rotational velocity response is measured at the left end of the structure. Similarly, the backward difference expression applies only in the case where both the moment excitation and the rotational velocity response locations are at the right (positive) end of the structure. Such end-located rotational mobilities would be of main importance in analyzing the dynamic response of end-connected composite structures. In instances where the moment excitation is located at an end point and the rotational velocity response is at some other location, or vice-versa, none of the above difference expressions would be applicable. Other finite difference formulations which would apply in these instances are available [8].

In summary, the evaluation of a particular rotational mobility using the above finite difference approximation methods requires the prior determination of between two and nine conventional translational mobilities, the quantity depending on the location and type of rotational mobility desired. For driving point rotational velocity/moment mobilities the number of translational mobilities needed may be cut almost in half by use of the reciprocity relation $Y_{m,n} = Y_{n,m}$ [9]. Also, several different rotational mobilities can be evaluated using a common set of translational mobilities.

The selection of response measurement and excitation location spacings, $\Delta\eta$ and $\Delta\xi$, must achieve a balance between resolution and proper approximation of derivatives across the number of natural modes of vibration to be encompassed in the band of frequencies. Some analytically or experimentally obtained crude knowledge of mode shapes is useful in the determination of the point spacings. The discussion of the demonstration results shows that this balance is achievable with latitude in the selection, at least in cases where a limited number of resonances are included in the frequency band.

MOBILITY MEASUREMENTS ON A FREE-FREE BEAM

Figure 4 depicts the beam used to demonstrate the method described. Excitation and response monitoring locations were established for measurements of all the conventional translational mobilities needed to generate the types of rotational mobilities identified above using backward differences. The mobilities to be generated would enable predictions of the translational motion at A (Figure 5) due to cantilever attachment of the beam to a moving foundation or other component at B.

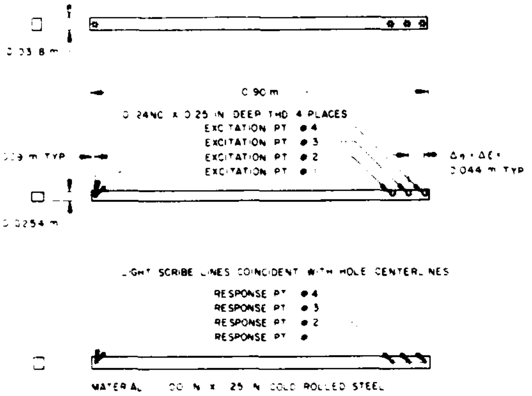

Fig. 4 - Test Beam Details

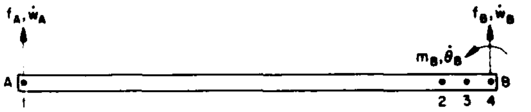

$$\begin{Bmatrix} \dot{w}_A \\ \dot{w}_B \\ \dot{\theta}_B \end{Bmatrix} = \begin{bmatrix} Y_{w_A F_A}(\omega) & Y_{w_A F_B}(\omega) & Y_{w_A M_B}(\omega) \\ Y_{w_B F_A}(\omega) & Y_{w_B F_B}(\omega) & Y_{w_B M_B}(\omega) \\ Y_{\theta_B F_A}(\omega) & Y_{\theta_B F_B}(\omega) & Y_{\theta_B M_B}(\omega) \end{bmatrix} \begin{Bmatrix} F_A \\ F_B \\ M_B \end{Bmatrix}$$

Fig. 5 - Matrix of Mobilities Describing Motion of Test Beam

Reciprocity dictates that mobility matrices be symmetric. Thus the conventional mobilities needed to completely establish the test beam mobility matrix shown in Figure 5 by the present method are as follows:

Translational Mobilities:

$Y_{W_A F_A}(\omega): Y_{1,1}$

$Y_{W_B F_A}(\omega): Y_{4,1}$

$Y_{W_B F_B}(\omega): Y_{4,4}$

Rotational Mobilities:

$Y_{\theta_B F_A}(\omega): Y_{4,1}, Y_{3,1}, Y_{2,1}$

$Y_{\theta_B F_B}(\omega): Y_{4,4}, Y_{3,4}, Y_{2,4}$

$Y_{\theta_B M_B}(\omega): Y_{4,4}, Y_{4,3}, Y_{4,2}, Y_{3,4},$
$Y_{3,3}, Y_{3,2} Y_{2,4}, Y_{2,3}, Y_{2,2}.$

With the use of geometric symmetry and further application of the reciprocity principle it is found that nine distinct conventional mobilities must be measured to determine the nine-element mobility matrix, of which five of the elements are rotational.

Test Setup

The tapped holes shown in Figure 4 were used for stud attachment of an impedance head for force measurements at each drive point location. Because most of the required translational mobilities were to be transfer mobilities, all motion measurements were made by attaching an accelerometer to the opposite side of the beam from the impedance head using beeswax. Accurate placement of the accelerometer was facilitated by lines scribed on the surface coincident with the driving stud hole centers. The outer-most drive points were located as close to the beam ends as possible with assurance of proper seating of the instrumentation. The .044m spacing of the driving and measuring points at B was established by sketching the mode shape of the expected highest resonance with the test frequency band of 0-2000 Hz. The three driving points were set at the widest distance where the backward difference method could be expected to approximate the slope of this mode shape reasonably well. This spacing was chosen as wide as possible for accuracy in the approximation of slopes at the lowest resonance.

The mobility tests were conducted using broad band stationary random excitation. The force and acceleration signals were recorded and processed by a minicomputer using a fast Fourier transform coherence/cross spectral density program. The test beam, which weighed 5.64 kg, was suspended vertically from one end by elastic bands and was driven by a small horizontally oriented electrodynamic shaker connected to the impedance head via a slender rod. The accelerometer mass was 2 grams, and the mass of the impedance head below the force gage was 22 grams. The transducer mass values must either be very small compared to the test item mass, as in this instance, or be compensated electronically to achieve accurate rotational mobility results.

Results

Figures 6 and 7 show plots of two of the measured conventional mobilities and the corresponding calculated mobilities based on Bernoulli-Euler beam theory for an assumed equivalent viscous damping ratio of .005 in each elastic mode. Calculation showed that use of the more refined Timoshenko model was not warranted over the 2000 Hz frequency range shown.

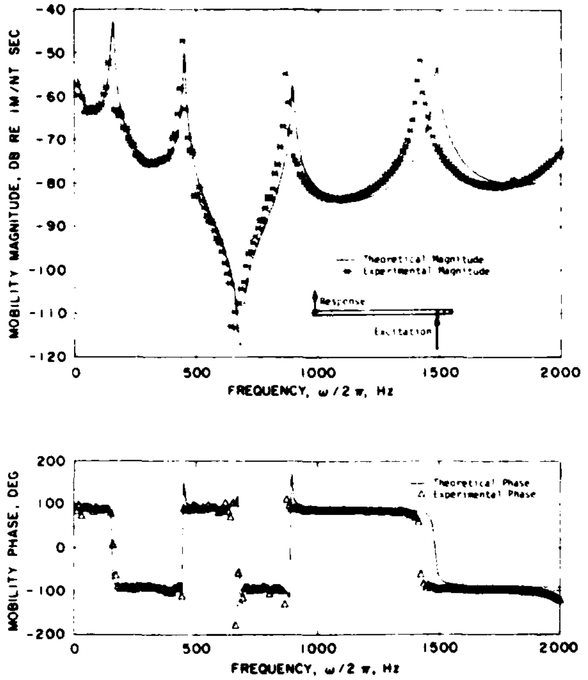

Fig. 6 - Test Beam Translational Mobility $Y_{1,2}$

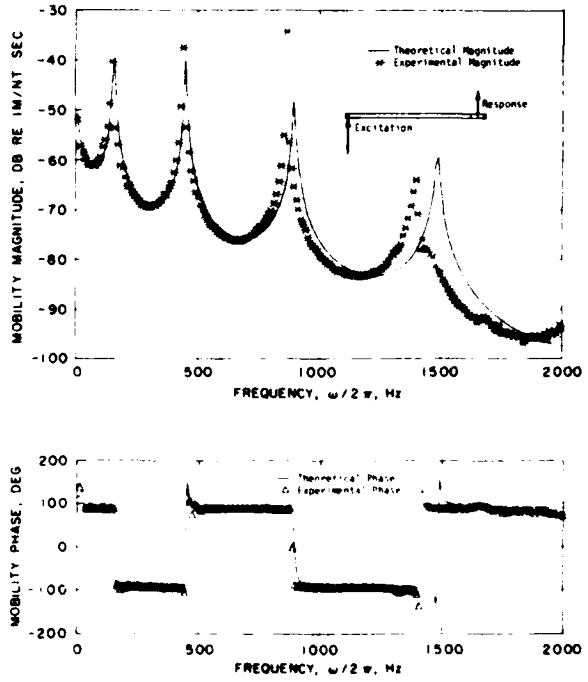

Fig. 7 - Test Beam Translational Mobility $Y_{3,1}$

The plots shown are representative of all nine conventional mobilities with respect to the agreement between measured and theoretical values. Because the agreement was good below the fourth resonance, the experimental data below 1000 Hz were regarded as favorable data for generating rotational mobilities; satisfactory results were not expected above 1000 Hz.

The two rotational velocity/force mobilities $Y_{\theta_B F_A}(\omega)$ and $Y_{\theta_B F_B}(\omega)$, which were derived from the measured conventional mobilities, are shown in Figures 8 and 9. Reasonably close agreement is seen over the 0-1000 Hz band with the corresponding theoretical mobilities, which were again calculated from Bernoulli-Euler beam theory with .005 damping assumed.* Although the experimentally derived rotational velocity/moment mobility $Y_{\theta_B M_B}(\omega)$ gives reasonably clear indications of resonances, Figure 10, it exhibits a great deal of scatter in both magnitude and phase in some regions. This latter mobility function and its constituent translational mobilities were examined closely in the frequency band 230 to 300 Hz, where there was a marked degree of scatter in both the magnitude and phase plots.

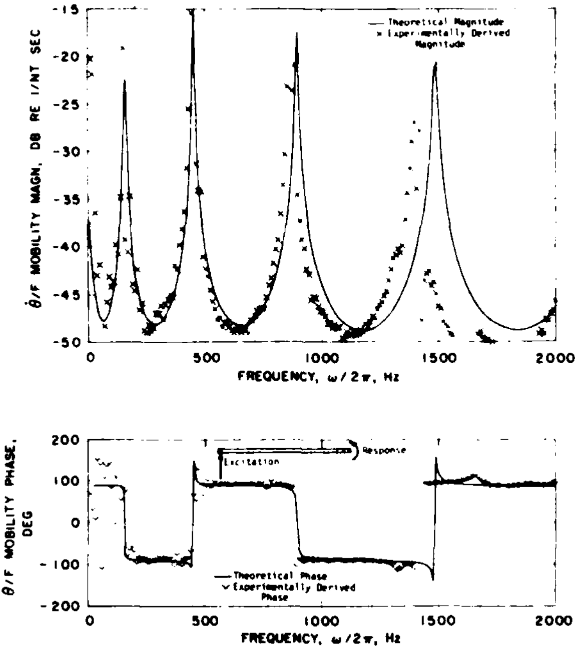

Fig. 8 - Test Beam Rotational Velocity/Force Mobility $Y_{\theta_B F_A}(\omega)$

REMOVING SCATTER FROM THE RESULTS

The scatter in the derived mobility data in this band seems at first inconsistent with the smoothness of the translational mobility data,

---

* All rotational mobility curves identified as theoretical in the figures were obtained by direct calculation rather than by the method of differencing.

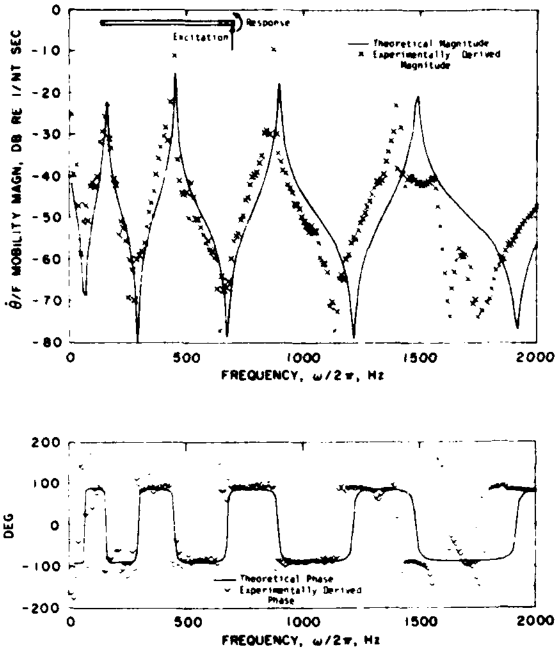

Fig. 9 - Test Beam Rotational Velocity/Force Mobility $Y_{\theta_B F_B}(\omega)$

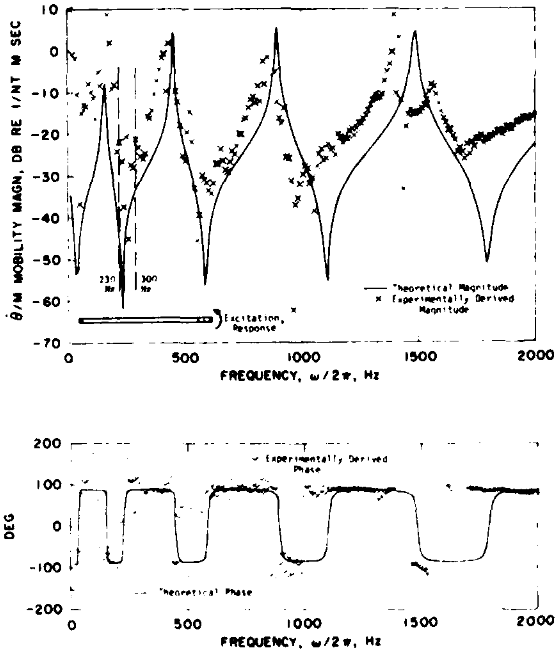

Fig. 10 - Test Beam Rotational Velocity/Moment Mobility $Y_{\theta_B M_B}(\omega)$

e.g. Figures 6 and 7, within the same band. The quadrature components of the constituent translational mobilities over this band are plotted on expanded scales in Figures 11 and 12, and the quadrature components of the resultant rotational mobility are shown in Figure 13. It is seen that the translational mobilities are almost purely imaginary, but the algebraic summation of these numbers gave a resultant imaginary component which was much smaller than most of the individual constituents, magnifying the minor degrees of irregularity present in them. The scatter in the real components of the constituents, Figure 11, had been present due to minor deviations in measured phase from the ideal value, -90°. The scatter in the quadrature components of the resultant mobility $Y_{\theta_B M_B}(\omega)$, Figure 13, is the source of the scatter in the magnitude and phase noted in Figure 10.

This examination of scatter shows that the stability of derived rotational mobilities would be enhanced by performing smoothing operations on the translational mobility data before the differencing calculations. An effective approach to smoothing might be to fit analytical mobility expressions to a number of data points in each experimental mobility by a method such as described in [2] and [6]. Examples of rotational mobilities obtainable by the differencing method from translational mobilities which are smooth and accurate are shown in Figures 14 and 15. The smoothness of the translational mobilities used for deriving these plots was effected by calculating them from beam theory. With the exception of small deviations in anti-resonant frequencies seen in Figure 15, the agreement between the theoretical and derived rotational mobilities is excellent.

Further investigation will be required to determine efficient procedures for smoothing the measured translational mobility data prior to differencing and to evaluate their effectiveness in reproducing the magnitudes and trends that may characterize the data.

ACCOMMODATION OF POINT SPACING VARIATIONS

Figures 16 and 17 show $Y_{\theta_B M_B}(\omega)$ rotational velocity/moment mobility results which were derived in the same manner as Figure 15. The theoretical translational mobilities in these instances, however, were calculated at locations corresponding to $\Delta\eta = \Delta\xi = .088$m and $\Delta\eta = \Delta\xi = .022$m, or twice and one-half the spacing of the measurement points on the test beam. The results for the wide spacing, Figure 17, show an added extent of the antiresonant frequency deviation noted in Figure 15, but more importantly, the matching of resonant frequencies is again achieved. The results for the close spacing, Figure 16, show excellent agreement throughout. The agreement between

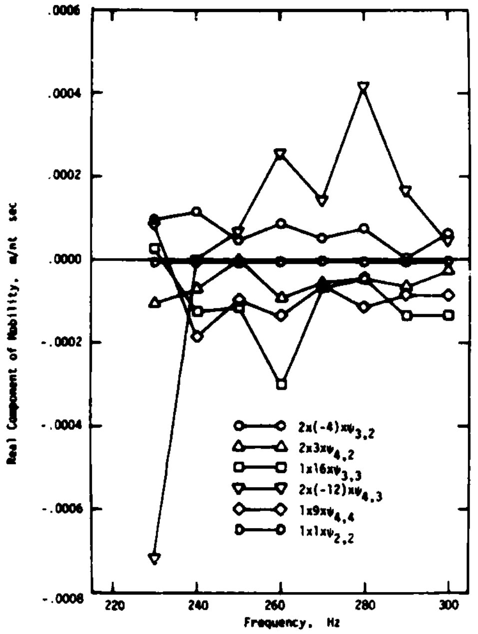

Fig. 11 - Constituent Terms of Derived Experimental Mobility $Y_{\Theta_B M_B}(\omega)$ Over a Frequency Band of Large Scatter: Real Components

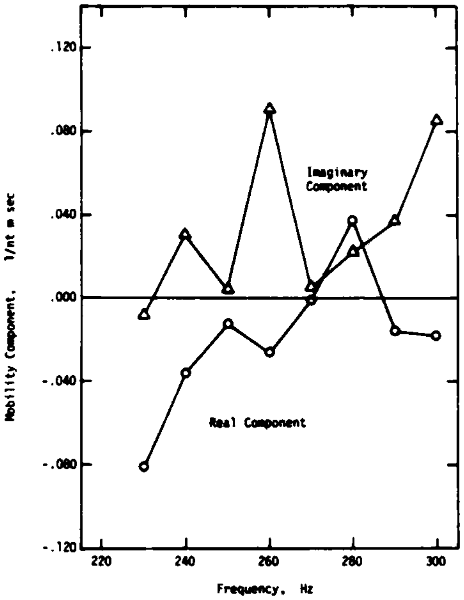

Fig. 13 - Quadrature Components of the Derived Experimental Mobility $Y_{\Theta_B M_B}(\omega)$ Over the Frequency Band of Figures 11 and 12

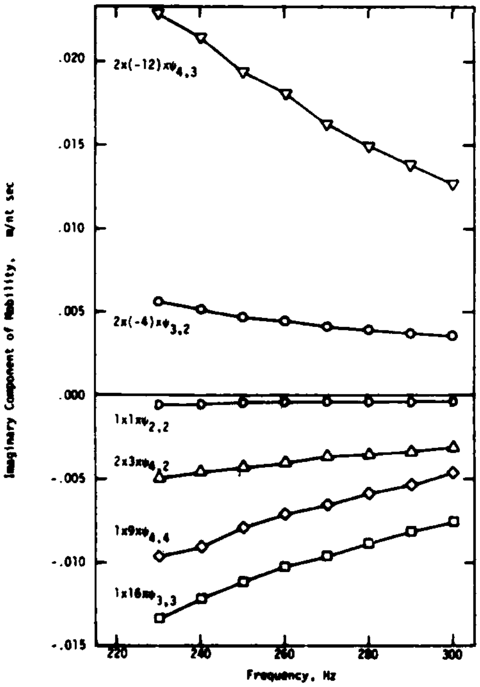

Fig. 12 - Constituent Terms of Derived Experimental Mobility $Y_{\Theta_B M_B}(\omega)$ Over a Frequency Band of Large Scatter: Imaginary Components

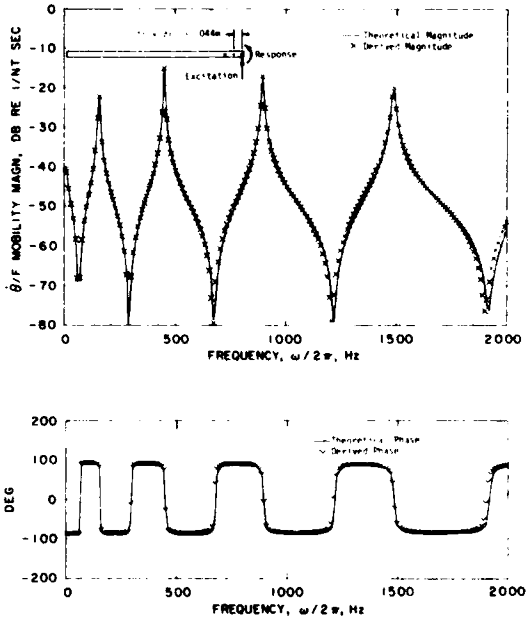

Fig. 14 - Rotational Velocity/Force Mobility $Y_{\Theta_B F_B}(\omega)$ Derived by Differencing Theoretical Translational Mobilities: $\Delta\eta = \Delta\xi = .044$ m

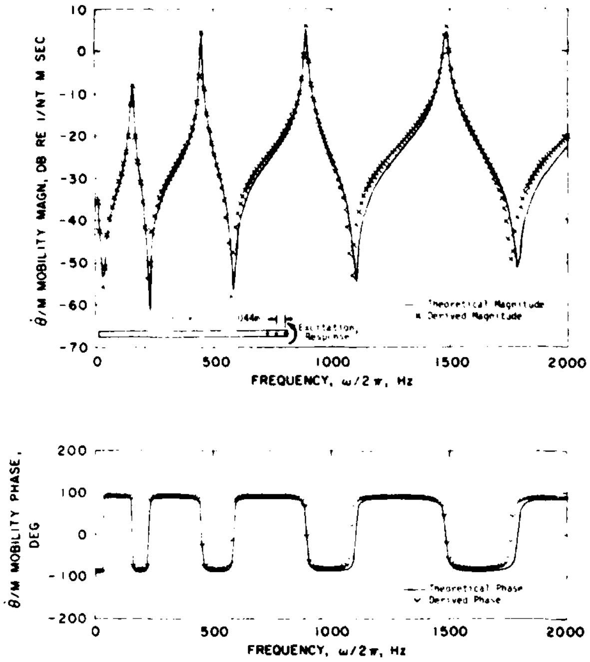

Fig. 15 - Rotational Velocity/Moment Mobility $Y_{\dot{\theta}_B M_B}(\omega)$ Derived by Differencing Theoretical Translational Mobilities: $\Delta\eta = \Delta\xi = .044m$

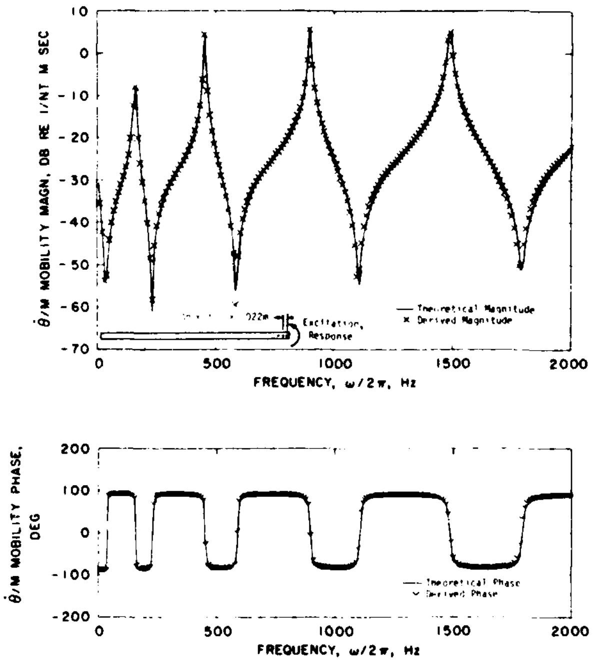

Fig. 16 - Rotational Velocity/Moment Mobility $Y_{\dot{\theta}_B M_B}(\omega)$ Derived by Differencing Theoretical Translational Mobilities: $\Delta\eta = \Delta\xi = .022m$

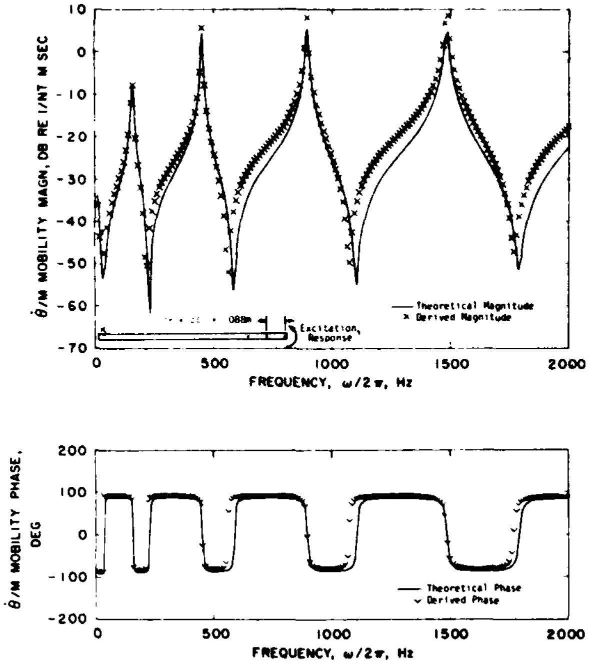

Fig. 17 - Rotational Velocity/Moment Mobility $Y_{\dot{\theta}_B M_B}(\omega)$ Derived by Differencing Theoretical Translational Mobilities: $\Delta\eta = \Delta\xi = .088m$

derived and theoretical rotational velocity/force mobilities for both point spacings (not shown) is also very close throughout. The differencing method is thus seen to accommodate considerable variation in measurement location spacings in instances where a limited number of resonances are included in the frequency band.

CONCLUSIONS

Rotational mobilities of structures are equivalent to spatial derivatives of their translational mobilities and can be determined experimentally by finite difference approximations involving sets of measured translational mobilities. Good agreement was obtained between experimentally and theoretically generated versions of two rotational velocity/force mobilities of a free-free beam. An experimentally derived rotational velocity/moment mobility gave reasonably good indications of resonances but exhibited large amounts of scatter in some frequency bands. This scatter was found to result from the subtraction of nearly equal translational mobility quantities in the differencing operation, magnifying minor irregularities that are present in their variation with frequency.

This scatter in the rotational mobility results can be eliminated if the translational mobility data can be smoothed by a means such as curve fitting before the differencing calculations. However, further investigation will be required to determine an efficient algorithm for performing the smoothing and to evaluate its effectiveness in reproducing the magnitudes and trends that may characterize the experimental data.

The differencing method of determining rotational mobilities offers the advantage that conventional mobility measurement equipment and techniques are used without a requirement for special fixturing. It has been shown that this method can accommodate considerable variation in the spacings of the points where the conventional mobilities are measured.

ACKNOWLEDGEMENTS

This paper is based on the results of a thesis submitted to the Department of Mechanical Engineering, Massachusetts Institute of Technology, during a study program supported by a Westinghouse B. G. Lamme grant. Portions of the laboratory apparatus and computing equipment and software used in this study had been made available to MIT by National Science Foundation grants. The author is grateful to Prof. Richard H. Lyon, thesis advisor, and to Prof. Emmett A. Witmer of the MIT Department of Aeronautics and Astronautics for their helpful suggestions relating to this study.

REFERENCES

1. R. M. Mains, "The Application of Impedance Techniques to a Shipboard Vibration Absorber, "Shock and Vibration Bulletin, 33, 4, March 1964.

2. A. L. Klosterman and J. R. Lemon, "Dynamic Design Analysis Via the Building Block Approach," Shock and Vibration Bulletin, 42, 1, January 1972.

3. R. DeJong, "Vibration Energy Transfer in a Diesel Engine," ScD Thesis, MIT, Dept. of Mechanical Engineering, 1976.

4. F. J. On, "Preliminary Study of An Experimental Method in Multidimensional Mechanical Impedance Determination," Shock and Vibration Bulletin, 34, 3, December 1964.

5. J. E. Smith, "Measurement of the Total Structural Mobility Matrix," Shock and Vibration Bulletin, 40, 7, December 1969.

6. D. J. Ewins and P. T. Gleeson, "Experimental Determination of Multidirectional Mobility Data for Beams," Shock and Vibration Bulletin, 45, 5, June 1975.

7. E. Isaacson and H. B. Keller, "Analysis of Numerical Methods," John Wiley & Sons, Inc., New York, 1966.

8. J. W. Leech, L. Morino, and E. A. Witmer, "PETROS 2: A New Finite-Difference Method and Program for the Calculation of Large Elastic-Plastic Dynamically-Induced Deformations of General Thin Shells," U. S. Army Ballistic Research Laboratories, ASRL TR152, Contract Report No. 12, December, 1969.

9. S. Timoshenko, D. H. Young, and W. Weaver, Jr., "Vibration Problems in Engineering," 4th Ed., John Wiley & Sons, Inc., New York, 1974.

NOMENCLATURE

$f_A(t)$	Concentrated force applied at Point A
$F_A(\omega), F(\omega;\xi)$	Complex amplitude of sinusoidal force
i	$\sqrt{-1}$
$m_A(t)$	Concentrated moment applied at Point A
$M_A(\omega)$	Complex amplitude of sinusoidal moment at Point A
$p(t)$	One member of a force couple
$P(\omega)$	Complex amplitude of sinusoidal force $p(t)$
$w_A(t)$	Translational displacement at Point A
$\dot{W}_A(\omega), \dot{W}(\omega;\eta)$	Complex amplitude of translational velocity
x	Coordinate of axial position
$Y_{W_A F_B}(\omega)$	Translational velocity/force mobility: velocity at A, excitation at B
$Y_{W_A M_B}(\omega)$	Translational velocity/moment mobility: velocity at A, excitation at B
$Y_{\theta_A F_B}(\omega)$	Rotational velocity/force mobility: velocity at A, excitation at B
$Y_{\theta_A M_B}(\omega)$	Rotational velocity/moment mobility: velocity at A, excitation at B
ϵ	Spacing of members $p(t)$ of a force couple
η	Axial coordinate of point of velocity measurement
$\theta_A(t)$	Rotational displacement at Point A
$\dot{\theta}_A(\omega)$	Complex amplitude of sinusoidal rotational velocity at Point A
ξ	Axial coordinate of point of excitation
$Y_{m,n}$	Translational velocity/force mobility
ω	Angular frequency

DISCUSSION

Mr. Mains (Washington University): When you made the measurements and compared the items in the mobility matrix it should have been symmetric, how close did you come?

Mr. Sattinger: I didn't do that. I only measured the nine components. I did not check the symmetry of the results. I relied on the comparison between the measured results and the theory to give me an indication of how good the results were.

Mr. Mains: Did you get symmetry when you substituted the measured components? The elements that should have been symmetric in the matrix were made up of calculations from the measured items. Were they symmetric?

Mr. Sattinger: I did not take it that far. I did not determine all of the elements of the matrix.

Mr. Ewins (Imperial College): You obviously ran into the same difficulty that we did with the rotation moment mobility being by far the most difficult. Once you have the rotation force mobility and the translation force mobility you have enough information to calculate the rotation moment mobility using the orthogonality properties of the two different coordinates x and theta at that point. Have you tried to derive the rotation mobility from the other two?

Mr. Sattinger: No. I saw in your paper that you did this, but I thought you used the curve fitting method of Klosterman and I didn't think I could do this without using his method of curve fitting.

Mr. Ewins: Okay, as you said you must smooth the data at some stage but you have to be careful at what stage you smooth it. If you smooth it before you have taken the difference you might have difficulties. But did you try this derivation rather than measure it? We have more or less abandoned the attempt at trying to measure it directly because of the small errors that would occur.

Mr. Baade (Carrier Corporation): I think we have clearly seen that some of the elements of a mobility matrix can be very easily determined experimentally, some can be determined with considerable more difficulty and some cannot be determined experimentally at all. You may wonder whether this is because we insist on measuring the elements of the mobility matrix; perhaps it might be better to set up an experiment to determine the elements of an impedance matrix. The answer is no, you can't measure the elements of an impedance matrix at all.

TRANSIENT EFFECTS IN
ACOUSTIC SOUND REDUCTION MEASUREMENTS

A. J. KALINOWSKI
NAVAL UNDERWATER SYSTEMS CENTER
NEW LONDON, CONNECTICUT

(U) Experimental problems associated with the measurement of transmitted and/or reflected sound for test panels coated with a homogeneous viscoelastic layer are treated through the application of analytical techniques. The goal of the experimentalist is to measure the steady state transmitted and/or reflected sound pressure for a coated, submerged flat plate, subject to a train of normally incident harmonic waves. Specifically, the paper addresses the questions of (1) what are the minimum number of incident wave cycles required to reach steady state, (2) what are the minimum number of cycles required for the transmitted or reflected response to reach steady state and (3) how far can the peak transient response deviate from the steady state response if minimum acceptable input and output pulse lengths defined by (1) and (2) are not met?

INTRODUCTION

This paper treats problems associated with experimentally measuring the steady state echo reduction and related insertion loss of coated plates emersed in a fluid medium. A typical test configuration is illustrated in Fig. 1 wherein a steel backing plate of thickness, L_3, is coated with a homogeneous viscoelastic dissipative material of thickness L_2. The overall dimension of the coated square plate are $L_p \times L_p$, where a typical value for L_p is 30 inches. A projector at range, R, generates an incident spherical pressure wave of driving frequency f_d and finite pulse length of N_d cycles (pulse length in time units = N_d/f_d). The object of the experimentalist is to measure both the reflected pressure, p_r, and the transmitted pressure, p_t, for a duration of time that is long enough to be representative of the steady state response. By the term steady state response, we refer to the response that would be achieved in a situation where the echo reduction and/or insertion loss is independent of the incident pulse length N_d/f_d. The steady state response state is not always an easy thing to achieve experimentally, particularly when the incident pressure wave length, λ_d, is large relative to the plate dimension L_p. The complication arises when the diffracted edge wave disturbance, p_d, propagates towards the echo reduction or the insertion loss hydrophone (e.g., see the Fig. 1 sketch). The experimentalist desires echo reduction and insertion loss results that are independent of the lateral plate dimensions, L_p. Unfortunately, at the arrival of the edge wave pressure, p_d, this disturbance eventually superimposes on the undisturbed reflected pressure, p_r, (and transmitted pressure, p_t), and consequently destroys the usefulness of the remaining post edge disturbance arrival portion of the transient measurement. Depending on the incident wave frequency and plate dimension L_p, the experimentalist must adjust the locations of the projector, echo reduction measuring hydrophone and insertion loss hydrophone (R, D_r, D_t respectively) so that the arrival of the diffracted edge wave is postponed as long as possible. The reader is referred to reference [1] for further details regarding adjusting these

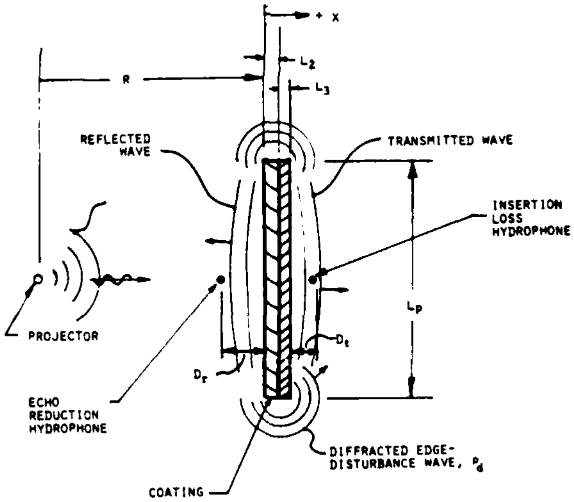

Figure 1 Typical Test Configuration For Submerged Coated Plate

length parameters. As the frequency of the incident wave is lowered, the time duration for recording undisturbed data is also shortened; consequently, the system may not have enough time to reach the steady state condition. When experiments are performed within a fixed dimension tank or enclosure, there is also an additional constraint on the maximum dimension of the incident pulse length, $c_1 N_d/f_d$, (where c_1 = wave speed in fluid). Finally there is the added complication of separating the reflected pressure from the incident pressure. When the echo reduction hydrophone location distance, D_r, is too small, the hydrophone records the superimposed reflected and incident pressure. By making D_r large enough to separate the incident and reflected pressure, but small enough to reasonably postpone the arrival of the diffracted edge disturbance, one can eventually record a separated reflected pressure, (free of edge disturbance effects) for at least some finite amount of time, say Δt_r. Correspondingly, we shall let the variable N_r denote the number of "good data" response cycles for taking echo reduction response measurement of the reflected pressure and let N_t denote the number of "good data" response cycles for taking the insertion loss response measurement of the transmitted pressure.

STATEMENT OF THE PROBLEM

The introduction has set the stage for various complications that arise during the running of a routine echo reduction and/or insertion loss experiment. The experimentalist often finds himself in the position of needing information on the following issues:

PROBLEM 1: Assuming the plate sample length, L_p, is large enough to avoid diffracted edge waves, what is the minimum number of incident wave cycles, $(N_d)_{min}$ that are needed to achieve a steady state response situation for either the echo reduction measurement or the insertion loss measurement?

PROBLEM 2: Assuming N_d is made large enough to allow the system to reach the steady state (i.e., $N_d \geq (N_d)_{min}$) how many response cycles ($(N_r)_{min}$ in the case of reflected pressure and $(N_t)_{min}$ in the case of transmitted pressure) does it take the system to settle down to the steady state response situation?

PROBLEM 3: How bad can the steady state echo reduction or transmission loss results be when the experimentalist operates with too small of an incident pulse length ($N_d < (N_d)_{min}$) and/or too small of a "good data" response window ($N_r < (N_r)_{min}$ or $N_t < (N_t)_{min}$)?

SOLUTION APPROACH

To be sure, the solution to the three problem statements defined earlier is quite complicated, and no explicit formula type answer will be given to completely answer the three questions posed. Instead, we shall approach the problem from a "by example" demonstration point of view. A sample configuration of the type represented by Fig. 1 is selected, whereby a controlled sequence of example solutions are examined in order to get a feel for the type of answers one might expect in typical situations.

The problems are treated from a combined analytical-computational point of view. The mathematical model of the standard test configuration is first simplified by eliminating edge diffraction effects by virtue of letting the plate be infinite ($L_p \to \infty$) and by making the incident input wave planar ($R \to \infty$). The steady state solution (both reflected pressure and transmitted pressure) to a submerged infinite plate, coated with a homogeneous linear viscoelastic coating and subject to a normally incident plane wave, $p_i = p_o e^{i(\omega t-kx)}$, is extracted from a solution in reference [2] (where p_o = pressure amplitude, $\omega = 2\pi f_d$, t = time, $k = \omega/c_1$, x = distance measured from water-coating interface). The steady state solution is converted into the desired transient solution by processing the input (incident pressure wave) in conjunction with the system transfer function via a Fourier integral. More specifically, let the transient input be described by the modulated sine curve

$$\begin{aligned} p_i(t) &= 0.0 && -\infty \leq t < o \\ p_i(t) &= p_o \sin (2\pi f_d t) && o \leq t \leq N_d/f_d \\ p_i(t) &= 0.0 && (N_d/f_d) < t \leq \infty \end{aligned} \tag{1}$$

from reference [2], the steady case reflected wave off of the coating into the fluid medium is given by

$$p_{s_1} = B_1 \, e^{i(\omega t+kx)}, \; k = \omega/c_1 \tag{2}$$

and the steady state transmitted wave into the back side fluid is given by

$$p_{t_4} = A_4 \, e^{i(\omega t-k(x-L_2-L_3))} \tag{3}$$

where $B_1(\omega)$ and $A_4(\omega)$ are the system transfer functions for the reflected and transmitted pressures respectively; the specific formulae for these two expressions are specified later. The reflected pressure transient solution, $p_r(t)$, is obtained from the standard convolution formula (reference [5])

$$p_r(t) = \frac{1}{2\pi} \int_{-\infty}^{\infty} F(p_i(t)) \, p_{s_1}(\omega) e^{+i\omega t} d \tag{4}$$

and the transmitted pressure transient solution, $p_t(t)$, is similarly obtained from

$$p_t(t) = \frac{1}{2\pi} \int_{-\infty}^{\infty} F(p_i(t)) \, p_{t_4}(\omega) e^{+i\omega t} d\omega \tag{5}$$

where the Fourier transform of the input record is given by

$$F(p_i(t)) = \int_{-\infty}^{\infty} p_i(t) e^{-i\omega t} dt \tag{6}$$

Upon substituting Eq. (1) into Eq. (6) and then subsequently substituting Eq. (6) into Eq. (4) or Eq. 5, as appropriate, the desired transient solutions are obtained. The integrations of Eq. (4) or Eq. (5) become rather complicated when viscoelastic dissipation is introduced into the system transfer functions (Eqs. (2) and (3) are complicated functions of the frequency parameter ω). The integrations of Eqs. (4) and (6) are thusly performed numerically employing fast Fourier transform techniques described in reference [6]. The software package employed is a modified version of the programming used to process the data in reference [4].

The introduction of viscoelasticity into the mathematical modeling is of great importance, for it is the viscoelastic effects that account for the energy absorption and hence the echo reduction characteristics of the coating. Therefore to be confident that the ultimate conclusions drawn in this paper are not strongly dependent upon the mathematical form of the viscoelastic model selected, it was decided to process the analytical results for two different viscoelastic models which are subsequently described.

VISCOELASTIC MODELS IN TIME DOMAIN

The Kelvin-Voigt linear dynamic viscoelastic equations of motion are typically used to model coating layers (references [7], [8]). The one-dimensional time dependent form of these equations is *given by*

- Frequency dependent complex modulii form

$$c_d^2 \left[1 + \eta^* \frac{\partial}{\partial t}\right] \frac{\partial^2 u}{\partial x^2} = \frac{\partial^2 u}{\partial t^2}, \ \eta^* = \text{constant} \qquad (7)$$

where c_d is the real elastic dilatational wave sound speed, u is the particle displacement in the direction of wave propagation, t is time, η^* is a frequency independent constant and is related to the more familiar Lamé elastic constants (λ_2, μ_2) and their corresponding complex modulii values (λ_2', μ_2') through the relations

$$\eta = \eta^* \omega \qquad (8)$$

where

$$\eta = \frac{\lambda_2' + 2\mu_2'}{\lambda_2 + 2\mu_2} \qquad (9)$$

and the ω refers to the steady state driving frequency when the viscoelastic material is excited by a harmonic loading proportional to $e^{i\omega t}$. The nondimensional dissipation variable, η, is a quantity that can be indirectly measured experimentally (e.g., reference [9]) by the separate determination of the individual constants λ_2, μ_2, λ_2', μ_2'. The implication of Eq. (8) is that the dissipation constant linearly increases with the frequency ω. The elastic modulii (λ, μ) appearing in the denominator of Eq. (9) are normally frequency independent; thus, Eq. (8) implies that the complex modulii components λ', μ' linearly increase with the frequency ω.

Indeed, some viscoelastic materials do not have continued linearly increasing complex constants λ_2', μ_2' for all ω, but rather the variation of these constants with frequency levels off and they become weakly dependent on frequency over some range of ω. Thus, for frequency independent complex moduli, λ_2', μ_2', the counterpart to Eq. (7) is given by

- Frequency independent complex modulii form

$$c_d^2 \left[1 + i\eta\right] \frac{\partial^2 u}{\partial x^2} = \frac{\partial^2 u}{\partial t^2} \qquad \eta = \text{constant} \qquad (10)$$

Eq. (10) is analogous to the energy absorption model discussed in reference [11], page 1486. Upon multiplying the $\vec{\nabla}$ ( ) operator on both sides of the scalar potential wave equation, on page 1486 of reference [11], and noting $\vec{\nabla}\psi = \vec{u}$, when $\vec{u}$ is the displacement vector, one arrives at a form like our Eq. (10), namely one with a complex, but frequency independent, wave speed.

Eq. (7) or alternatively Eq. (10) is used to solve for the transient response of the system. Both of these partial differential equations are forms of the wave equation in that they both support traveling wave type solutions of the type $u = u\,(x \pm ct)$ (reference [10]). Further, either Eq. (7) or Eq. (10) can also be used to represent the wave propagation through the elastic backing plate (or through the fluid medium) by simply setting η^* (or η), as appropriate, equal zero and setting c_d = the backing *plate's dilatational* wave speed in the case of the elastic backing plate or setting c_d = the fluid compressional wave speed in the case of the front or back side fluid.

VISCOELASTIC MODELS IN FREQUENCY DOMAIN

The implementation of solution Eq. (4) for the reflected pressure, $p_r(t)$, or solution Eq. (5) for the transmitted pressure, $p_t(t)$, requires the solution of the system in the frequency domain form of Eq. (7) or Eq. (10) must be obtained. This is accomplished in the standard way of expressing the response in the form

$$u(x,t) = \overline{u}(x) e^{i\omega t} \qquad (11)$$

and substituting the Eq. (11) form into either Eq. (7) or Eq. (10) as appropriate. Doing this, we arrive at the form

- Frequency dependent complex modulii form

$$c_d^2 \left[1 + i\eta\right] \frac{d^2\overline{u}}{dx^2} = -\omega^2 \overline{u} \qquad (12)$$

where

$$\eta = \omega\eta^* \qquad \text{with } \eta^* = \text{constant}$$

for the frequency dependent complex modulii model; or alternatively we arrive at the form

- Frequency independent complex modulii form

$$c_d^2 \left[1 + i\eta\right] \frac{d^2\overline{u}}{dx^2} = -\omega^2 \overline{u} \qquad (13)$$

where $\qquad \eta = \text{constant}$

for the frequency independent complex modulii model. At this point, we make the following observations:

(i) The form of the frequency domain governing differential equation is exactly the same for both viscoelastic models, except for the fact that in the first model (Kelvin-Voigt model), the dissipation parameter η linearly depends on ω and in the second model, the dissipation parameter η is constant.

(ii) The form of Eqs. (12) or (13) is exactly like the one-dimensional frequency domain form of the elasticity field equations, except that in place of the dilatational wave speed parameter c_d^2 normally found in the elasticity field equations, there now appears the quantity $c_d^2(1 + i\eta)$.

Thus in view of observations (i) and (ii), it follows that an elasticity solution in the frequency domain can be immediately converted into a viscoelastic frequency domain solution by simply replacing* the wave speed parameter, c_d, appearing in the elastic solution with $c_d\sqrt{1 + i\eta}$.

DETERMINATION OF REFLECTION AND TRANSMISSION AMPLITUDES B_1, A_4

The steady state solution for the reflected and transmitted pressure amplitudes ($B_1(\omega)$, $A_4(\omega)$ appearing in Eqs. (2) and (3)) are derived in reference [2] and are converted into solutions for an infinite plate coated with a viscoelastic layer by making the complex wave speed substitution described above. Thus from reference [2], it follows that

Reflected pressure amplitude $\equiv B_1 =$

$$p_o(C_2A_{12}-C_1A_{22})/(A_{21}A_{12}-A_{11}A_{22}) \quad (14a)$$

Transmitted pressure amplitude $\equiv A_4 =$

$$p_o(A_{21}A_{32}C_1 - A_{32}A_{11}C_2)/(A_{21}A_{12}-A_{11}A_{22}) \quad (14b)$$

where

$$C_1 = -\cos(\overline{k}_2\ell_2) + i\, r_{12}\text{Sin}(\overline{k}_2\ell_2);$$

$$r_{12} = \rho_2\overline{c}_{d2}/\rho_1c_{d1};\ r_{34} = \rho_4c_{d4}/\rho_3c_{d3}$$

$$C_2 = r_{23}i\,\text{Sin}(\overline{k}_2\ell_2) - r_{23}r_{12}\cos(k_2\ell_2);$$

$$r_{23} = \rho_3c_{d3}/\rho_2\overline{c}_{d2}$$

$$A_{12} = \Big[[1 + r_{34}][\cos(2k_3\ell_3) + i\,\text{Sin}(2k_3\ell_3)]/[1 - r_{34}]\Big] - 1$$

$$A_{21} = -r_{23}i\,\text{Sin}(\overline{k}_2\ell_2) - r_{23}r_{12}\cos(\overline{k}_2\ell_2)$$

$$A_{11} = \cos(\overline{k}_2\ell_2) + i\, r_{12}\,\text{Sin}(\overline{k}_2\ell_2)$$

$$A_{22} = 1 + [1 + r_{34}][\cos(2k_3\ell_3) + i\,\text{Sin}(2k_3\ell_3)]/[1 - r_{34}]$$

$$A_{32} = -2r_{34}[\cos(k_3\ell_3) + i\,\text{Sin}(k_3\ell_3)]/[1 - r_{34}]$$

$$k_1 = \omega/c_{d1};\ \overline{k}_2 = \omega/\overline{c}_{d2};\ k_3 = \omega/c_{d3};\ k_4 = \omega/c_{d4}$$

where

ρ_1 = incident (front) side fluid mass density

ρ_2 = viscoelastic layer mass density

ρ_3 = backing plate mass density

ρ_4 = back side fluid mass density

c_{d1} = incident side fluid compressional wave speed $= \sqrt{\lambda_1/\rho_1}$

$\overline{c}_{d2}$ = complex viscoelastic layer wave speed $= c_{d2}\sqrt{1 + i\eta}$

c_{d2} = real elastic viscoelastic layer wave speed $= \sqrt{(\lambda_2 + 2\mu_2)/\rho_2}$

c_{d3} = backing plate dilatational wave speed $= \sqrt{(\lambda_3 + 2\mu_3)/\rho_3}$

c_{d4} = back side fluid wave speed $= \sqrt{\lambda_4/\rho_4}$

λ_1 = bulk modulus of incident side fluid

λ_2, μ_2 = elastic Lamé constants for viscoelastic layer

λ_2', μ_2' = complex Lamé constants for viscoelastic layer

λ_3, μ_3 = elastic Lamé constants for backing plate

λ_4 = bulk modulus of back side fluid

ℓ_2 = viscoelastic layer thickness

ℓ_3 = backing plate thickness

The same solution represented by Eqs. (14) (in conjunction with Eqs. (4) and (5)) can be used to exercise both the frequency dependent complex moduli viscoelastic model (represented by Eq. (10)). For the frequency dependent complex moduli case, simply substitute Eq. (8) into the η expression appearing in Eqs. (14). The value of η^* in Eq. (8) is a given constant determined from separate material experiments and is physically the constant slope of the $(\lambda_2' + 2\mu_2')$ vs. ω curve. Next, for the frequency independent complex moduli case, simply substitute η = constant into the η expression appearing in Eqs. (14), where the constant is determined from separate material measurement experiments.

SOLUTION PARAMETERS

Model Dimensions:

The fixed problem parameters are the projector range ($R = \infty$), plate laterial dimensions ($L_p = \infty$), echo reduction hydrophone location ($D_r = 0$), insertion loss hydrophone location ($D_t = 0$), backing plate thickness (L_3 = 1.25 in.), coating thickness (L_2 = 2.4 in.). The incident and reflected waves have been separated analytically (i.e., the reflected pressure is directly

---

*In situations where the driving term is $e^{-i\omega t}$, then $c_d\sqrt{1 - i\eta}$ constitutes the proper replacement for c_d.

computed), consequently there is no need to place the hydrophones away from the plate surface.

Input Wave Constants:

The incident wave frequency, f_d, and number of pulse length cycles, N_d, are parameters that vary for different computer runs. The f_d takes on values of 10.0 KHz, 5.0 KHz, 4.75 KHz, and 1.0 KHz, and N_d takes on values of 1, 2, and 8.

Model Material Constants:

All numerical examples presented in this paper employ the same mass density and real wave speed parameters, namely

ρ_1 = .000096 lb. sec/in^4,

ρ_2 = .0003599 lb. sec/in^4,

ρ_3 = .000735 lb. sec/in^4,

ρ_4 = ρ_1;

c_{d1} = 60000. in/sec,

c_{d2} = 15542. in/sec,

c_{d3} = 234400. in/sec,

c_{d4} = c_{d1}.

For the frequency independent complex moduli viscoelastic model, three values of the dissipation parameter, η = constant, are considered, namely $\eta = 0$, $\eta = .48$, $\eta = .96$.

For the frequency dependent complex moduli viscoelastic model, the η value varies with ω according to Eq. (8), consequently some properly comparable means of selecting the viscoelastic constant, η^*, must be made in order to meaningfully test the sensitivity of the results with regard to which viscoelastic model is used. To this end, a value of η^* is selected so that the η values evaluated at the driving frequency, $\omega_d = 2\pi f_d$, are equal for both the frequency independent model, Eq. (12), and the frequency dependent model, Eq. (13). For example, suppose the frequency independent model was exercised at a driving frequency of f_d = 5000 Hz and the dissipation parameter was η = .48; then the frequency dependent model, employing Eq. (8), would be run for a $\eta^* = .48/(2\cdot\pi\cdot 5000)$. Later in the paper, all other things being held constant, comparisons between both viscoelastic models are made. In order to distinguish one viscoelastic model result from another, the phrase "constant damping" is used to represent the constant moduli case, and the phrase "variable damping" is used to represent the variable moduli case. In both cases, the value of η at the driving frequency will be used to label the curves so that proper comparisons between similar cases can easily be made.

CHECKOUT PROBLEM

Before proceeding to problems of concern to this study, a demonstration sample problem was used to illustrate that the basic computational tools are all in order. The example problem is to determine the transmitted pressure through a submerged steel plate subject to a normal incident, step exponential transient input wave, i.e., $p_i = p_o e^{-\beta t}H(t)$ where β is the decay constant and H(t) the unit step function. A reduced form of the system transfer function, Eq. (3), is also used for this demonstration problem, wherein the coating material constants are set equal to the fluid (water) constants. For reference, the system transfer function is shown in the lower half of Fig. 2. Throughout this paper, all results are plotted in nondimensional form. All incident input pressures, p_o, are unity; nondimensional time is used for transient plots, where the actual time is divided by some convenient scale factor, TSCALE; nondimensional frequency is used for all transfer function plots where actual frequency in Hz is multiplied by TSCALE. In all transfer function plots, the positive frequency range is plotted from zero to FREQ/2.0 and the negative frequency range from -FREQ/2.0 to 0.0 repeats duplicate information and is therefore omitted from the plots.

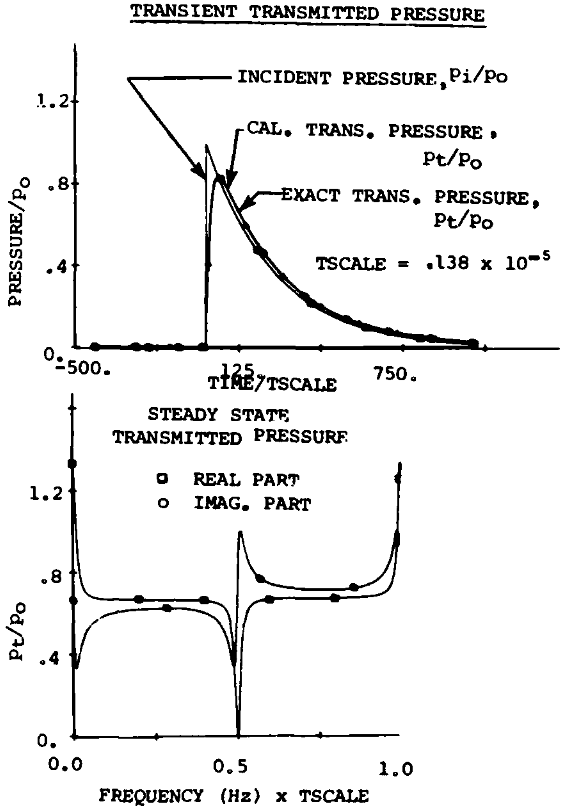

Figure 2 Check Problem Solution

The scale factor, TSCALE = $.138 \times 10^{-5}$, used in Fig. 2 corresponds to the time it takes a compressional wave (in the steel plate) to travel the thickness of the plate. Later, all subsequent plots use a different scale factor explained later. The input curve is shown in Fig. 2 plotted alongside the corresponding transmitted pressure. The curve labeled EXACT TRANS. PRESSURE is the exact solution to the same problem (taken from reference [3]). As can be seen, the agreement is very good, wherein both solution processed by FFT's (denoted by o symbol) and the exact solution, (denoted by □ symbol) fall on top of each other.

PARAMETRIC RESULTS

A set of numerically simulated laboratory experiments are performed using the methodology described in the solution approach section. In actuality, a set of 3 x 5 x 3 x 2 = 90 runs were made using three values of damping (η = 0.0, η = .48, η = .96), five frequency values (10.0 KHz, 5.0 KHz, 4.75 KHz, 2.5 KHz, 1.0 KHz), three pulse lengths (N_d = 1, 2, 8) and two viscoelastic damping models. From this collection of runs, thirteen cases are presented here. It is felt that the omitted ones add no new information already found in the cases presented here. Interesting highlights are pointed out as each case is discussed. Finally, based on this particular sample, we attempt to establish some rules of thumb that are inferred by the numerical experiments. Comments regarding the notation of the figures are discussed in the CHECK-OUT PROBLEM description and will not be repeated here. The scale factor, marked on each plot, corresponds to the transit time, i.e., the amount of time it takes a compressional wave (having the wave speed of water) to travel through a distance equal to the sum of the plate plus the coating thickness; for Figs. 3 through 18, TSCALE = $.6083 \times 10^{-4}$.

On the incident side of the coated plate, the total acoustic pressure is made up of the sum of the incident pressure wave plus the reflected pressure wave. In all coated plate transient results, only the reflected pressure component of the total pressure is plotted (shown in the top half of the figure). The pressure in the fluid existing on the back side of the plate (transmitted pressure) is plotted on the bottom half of the same figure.

- Frequency Domain Plots

Of prime importance in this paper are the transient plots, however, it is also informative to exhibit the transfer function plots for the reflected pressure, $B_1(\omega)$, and transmitted pressure, $A_4(\omega)$. The zero damping case is shown in Fig. 3; the constant damping model in Fig. 4 and finally a variable damping model in Fig. 5. These three curves were used to process the f_d = 1.0 KHz results used in this study; they are representative of other transfer function curves used at other driving frequencies hence no others need be illustrated (others having larger FREQ ranges, e.g., FREQ = 12.2 @ f_d = 5.0 KHz, FREQ = 24.3 @ f_d = 10.0 KHz).

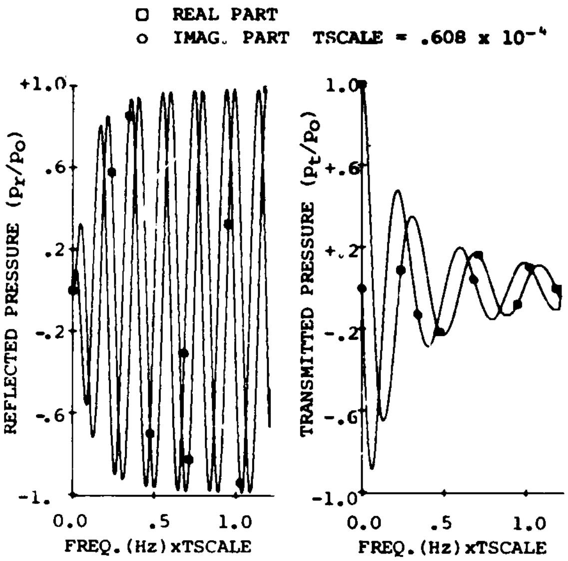

Figure 3 Transfer Function for ZERO DAMPING Case, η = 0 0

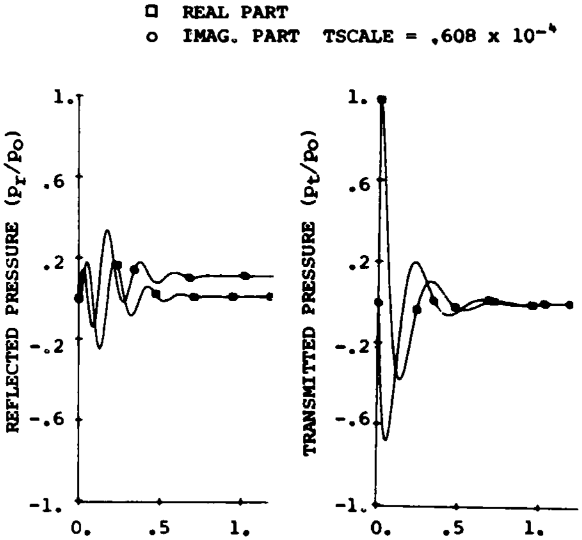

Figure 4 Transfer Function for CONSTANT DAMPING Viscoelastic Model, η = .48

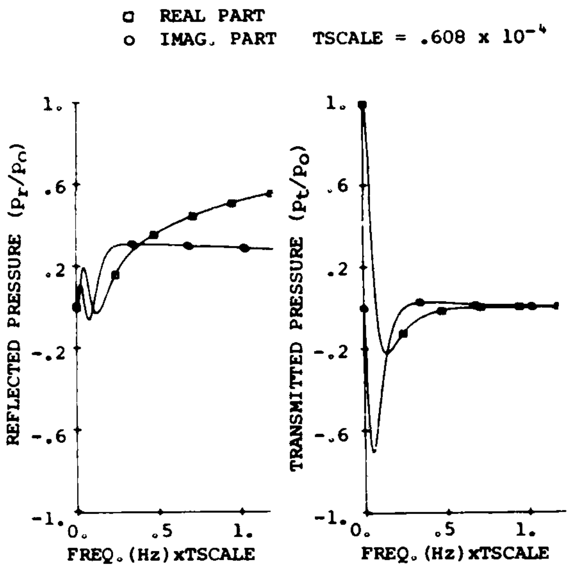

Figure 5 Transfer Function for VARIABLE DAMPING Viscoelastic Model, $\eta^* = 7.64 \times 10^{-5}$ (e.g., $\eta = .48$ @ $\omega = 2\pi \cdot 1000$)

- Incident Frequency = 10.0 KHz, No Damping

This case is shown in Figs. 6 and 7, for 2 and 8 cycles of input respectively. Note that *the input and response is separated by a finite* amount of time. In the case of the reflected pressure, this is due to the fact that it takes a finite amount of time for the wave to pass through the coating (the $\rho_2 c_{d2}$ of the coating is very close to the $\rho_1 c_{d1}$ of the water, thus there is very little initial reflection), strike the backing plate and reflect back to the response measurement point on the wet surface of the coating. In the case of the transmitted pressure, it takes time for the incident wave to pass through the coating and backing plate before reaching the response measurement point on the back (wet) side of the backing plate. The two cycle input, Fig. 6, results in a response that is adequately close to the steady state (i.e., for the last response cycle) and the eight cycle input achieves a response (both transmitted and reflected) very close to steady state after the third cycle of response is recorded. In cases where the experimentalist places the echo reduction hydrophone too close to the plate surface, he may not even see the first reflected response cycle (i.e., it is still unseparated from the incident wave) consequently, only the second cycle of the Fig. 6 reflected pressure may be available to the experimentalist for echo reduction interpretation. This same comment would apply to all similar plots (e.g., Figs. 8, 10, 12, 14, 16).

- Incident Frequency = 10.0 KHz, Variable Damping ($\eta = .48$ @ $\omega = 2\pi \cdot 10000$)

The two and eight cycle input runs of the previous case are repeated, except that the variable damping viscoelastic model is employed. The damping constant of $\eta^* = 7.64 \times 10^{-9}$ used for this run corresponded to the actual damping constant of the coating material; the $\eta = 0.0$ case was run just for comparative purposes. For this variable damping case, the two cycle input, Fig. 8, achieved a value fairly close to the steady state for the last response peak in the case of the reflected pressure; however, in the case of the transmitted pressure, a substantial deviation still exists between the peak response and steady state. Examination of Fig. 9 for eight cycles of input show that about two and one-half cycles of response are needed to reach the steady state. It is interesting to note, upon comparing Figs. 6 and 8, that when damping is present in the coating, all other things equal, there is no lag time between the reflected pressure and input pressure. This is due to the fact that when damping is present, there is a greater mismatch between the fluid and coating impedance due to the complex nature of the coating wave speed. Consequently the reflected pressure begins to build up immediately.

- Incident Frequency = 10.0 KHz, Constant Damping, ($\eta = .48$ for all ω)

Again the two and eight cycle input runs of the two previous cases are repeated in Figs. 10 and 11 except that here the damping parameter η is held constant for all ω in the transfer function. Here, our goal is to investigate the sensitivity of the transient wave form response to a different type of viscoelastic damping model. Examination of the results show that the Figs. 10 and 11 transients are remarkably close to the variable damping case of Figs. 8 and 9, and the observation of requiring about two and one-half cycles to reach the steady state holds again. It is interesting to note that even though the system transfer functions for both viscoelastic models are quite different in appearance (e.g., Figs. 4 and 5), except for the fact that both transfer functions have the same value at the driving frequency, they still produce transient solutions that are quite similar in appearance.

- Incident Frequency = 4.75 KHz, Variable Damping, ($\eta = .48$ @ $\omega = 2\pi \cdot 4750$)

This is a repeat of the earlier Figs. 8 and 9 case, except that here the driving frequency is 4.75 KHz rather than 10.0 KHz. The new results are shown in Fig. 12 for the two cycle input and in Fig. 13 for the eight cycle input. In the two cycle input case, clearly the Fig. 12 reflected pressure plot shows that the steady state is not nearly reached, in fact, if the ending response cycle is mistakenly taken for the steady state, it could lead to an under estimation of the steady state response by a factor of 350% (based on taking the average amplitude of the last output cycle, excluding the tail off portion beyond (TIME/TSCALE) = 12.5). The transmitted pressure, Fig. 12, doesn't deviate as far

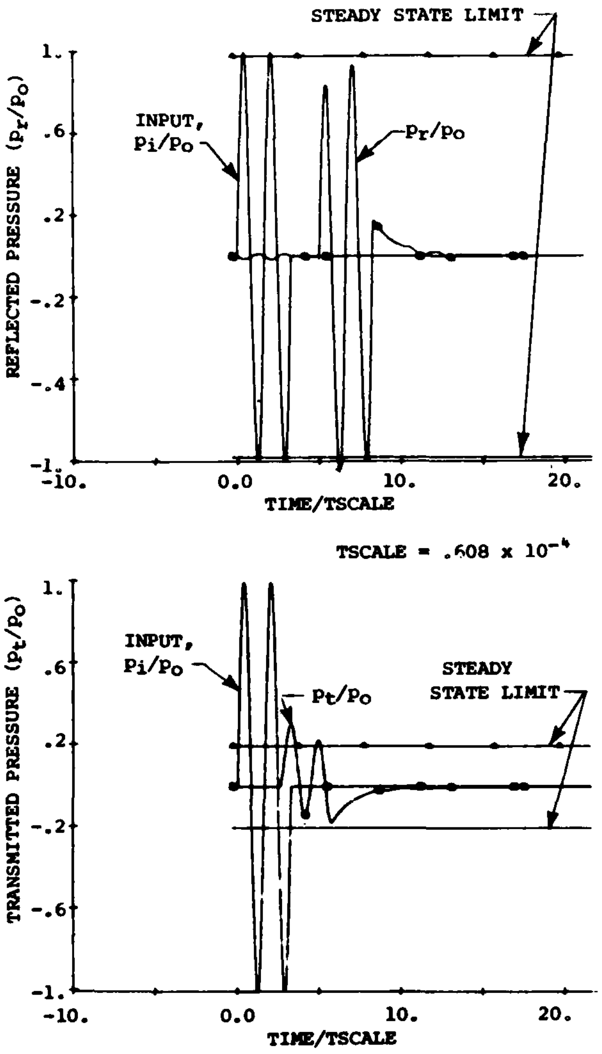

Figure 6 10 KHz, 2-Cycle Input, NO DAMPING; $\eta = 0.$

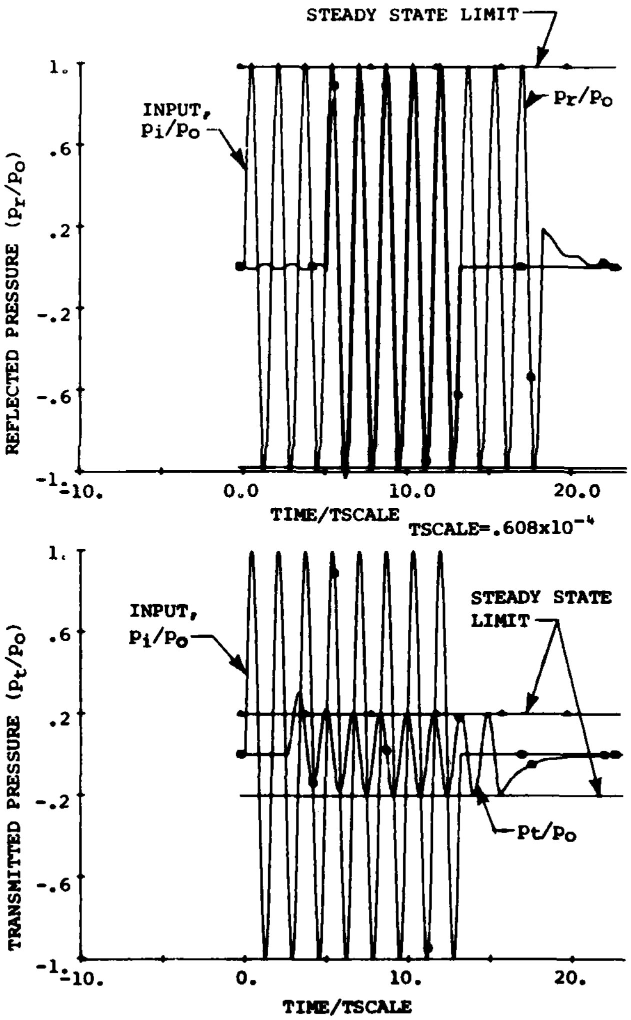

Figure 7 10 KHz 8-cycle Input, NO DAMPING, $\eta = 0.0$

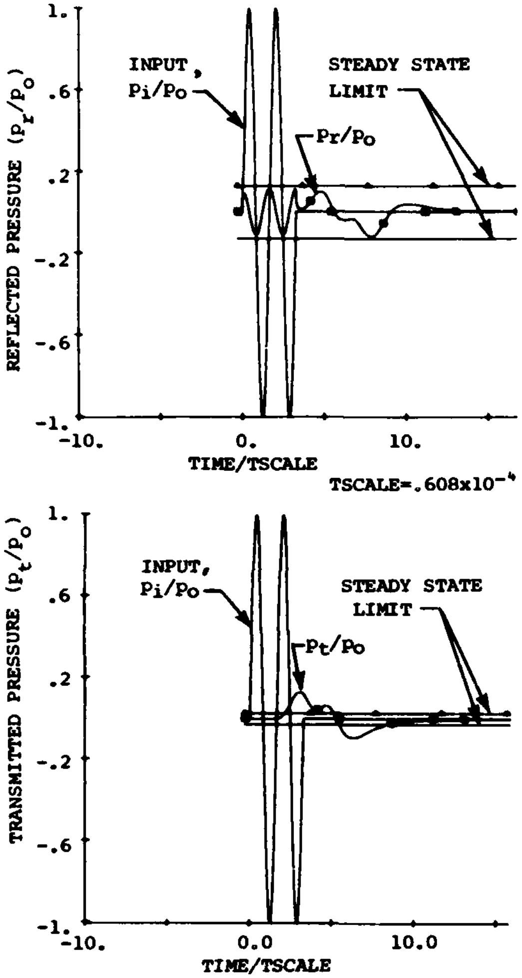

Figure 8 10 KHz, 2-Cycle Input; VARIABLE DAMPING, $\eta = .48$ @ $\omega = 2\pi \cdot 10000$.

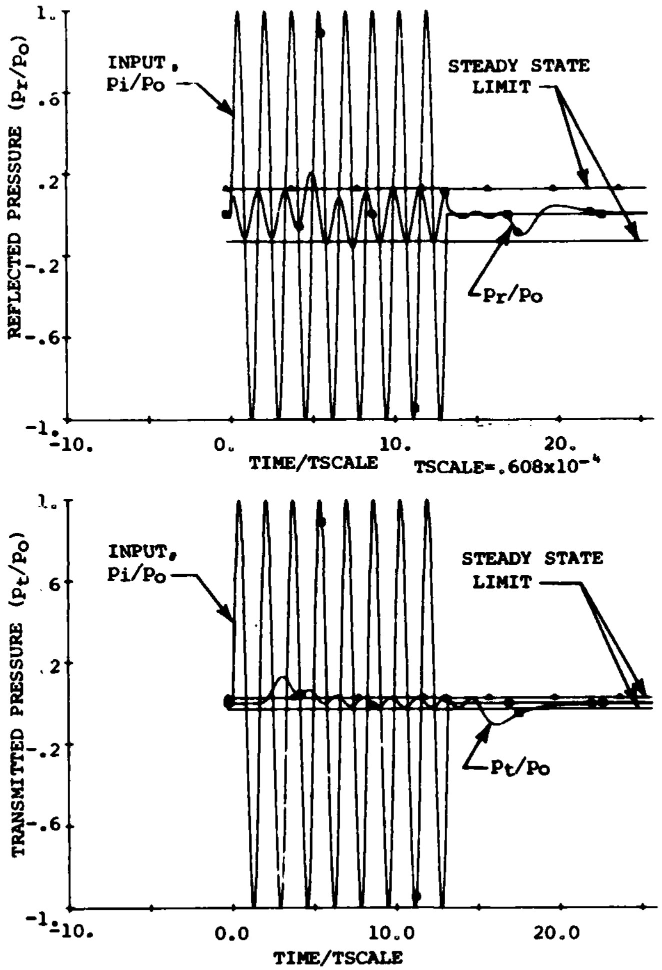

Figure 9 10 KHz, 8-Cycle Input; VARIABLE DAMPING, $\eta = .48$ @ $\omega = 2\pi \cdot 10000$.

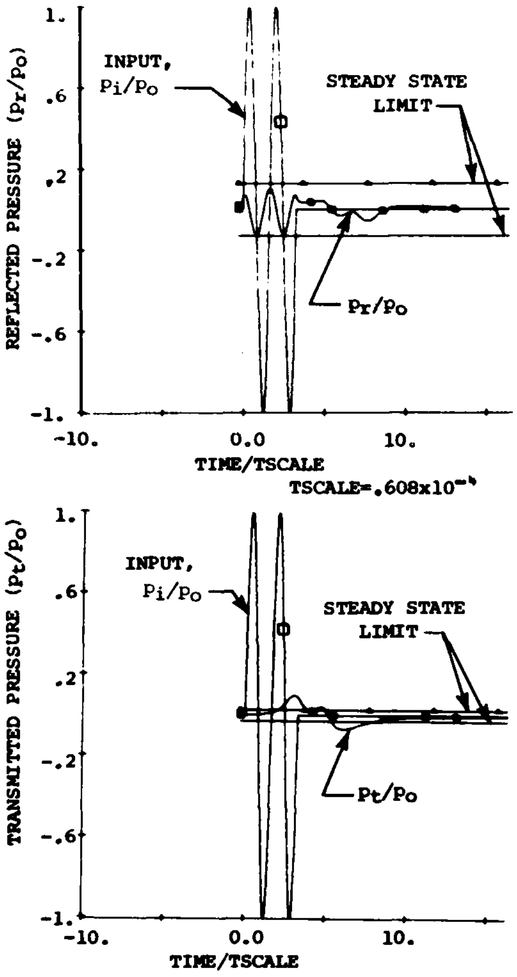

Figure 10 10KHz, 2-Cycle Input; CONSTANT DAMPING (η = .48 @ all ω)

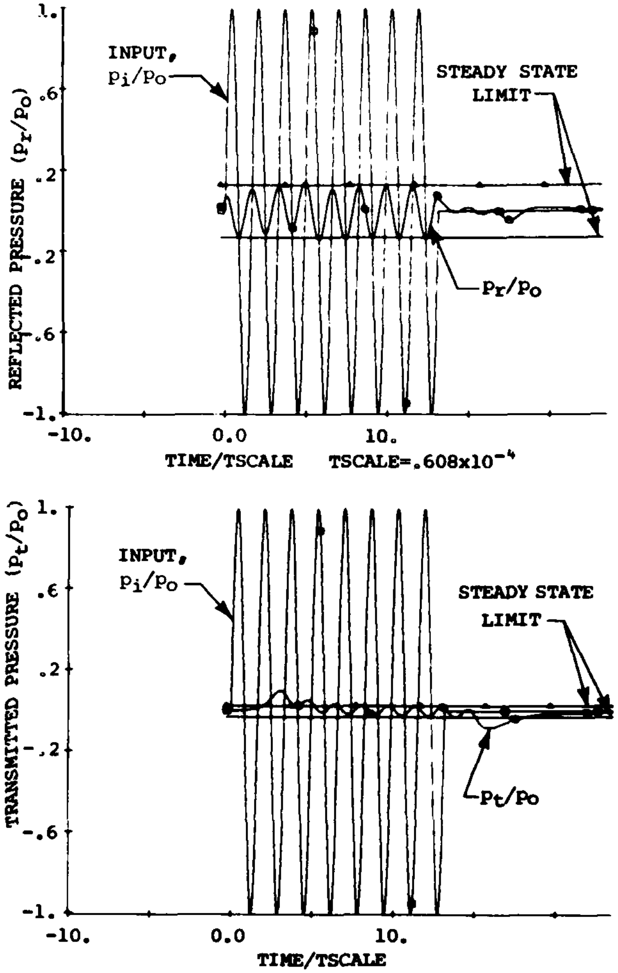

Figure 11 10 KHz, 8 Cycle Input; CONSTANT DAMPING, (η = .48 @ all ω)

from reaching the steady state as the reflected pressure, and in fact for this particular case, an adequate prediction would have been made for steady state transmitted pressure. In the eight cycle input case, Fig. 13, it is seen that the steady state reflected pressure is achieved after approximately 3 cycles of response and the steady state transmitted pressure is achieved after approximately 1½ cycles of response.

This case demonstrates that substantial errors can be experienced by not allowing the input wave form to have a sufficient number of input cycles. Based on additional runs not presented here, four cycles of input would be the minimum amount in order to reach the steady state for both the reflected and transmitted pressure waves. The reason why the reflected pressure takes longer to reach steady state is partially explained by making the observation that in some cases, the sudden termination of an input results in a transient overshoot of the steady state analogous to the overshoot of steady state experienced by the sudden starting of the input pressure. In the eight cycle input case, Fig. 13, we observe that the startup overshoot (TIME/TSCALE = 0.0 → 5.0) of reflected pressure is well separated from the shutdown overshoot (TIME/TSCALE = 27.0 → 32.0). However for the two cycle input case, Fig. 12, we observe the startup overshoot and shutdown overshoot blend into each other, which gives the erroneous appearance that some sort of steady state has been achieved. Possible reasons for obtaining overshoots in some cases while not obtaining them in others is explained in the next constant damping example.

The percent of energy absorbed by the viscoelastic layer is given by the expression, $\frac{\Delta E}{E_I} = 1 - \frac{E_t}{E_I} - \frac{E_r}{E_I}$ where, E_t is the transmitted energy, E_r the reflected energy, E_I the incident energy and $\Delta E/E_I$ the percent energy absorbed. Since for plane waves, energy is proportional to pressure squared, the above expression is also written as

$$\Delta E/E_I = 1 - (|A_4|/p_0)^2 - (|B_1|/p_0)^2 \quad (15)$$

Thus substituting the steady state amplitudes $|A_4|$ and $|B_1|$ from the Fig. 12 plots we see that approximately 97 percent of the energy is absorbed once steady state is achieved. A trend that appears throughout the sequence of parametric runs that were made is: the more energy absorbed by the system, the more cycles one needs to reach the steady state.

- Incident Frequency = 4.75 KHz, Constant Damping, (η = .48 all ω)

Again we wish to verify the sensitivity of the response waveforms to a second type of viscoelastic model. Comparison of the constant damping results (Figs. 14 and 15) to the variable damping results (Figs. 12, 13) show that very similar responses are achieved, including the overshoot in response that occurs at the startup and shutdown of the incident wave. All comments made earlier on the variable damping model would apply equally well here, however, we add one additional observation regarding the occurrence of the response overshoot.

A similar overshoot at both startup and shutdown of the incident wave was observed by reference [12] in situations where elastic spheres were submerged in a fluid and subjected to an incident pressure wave of the type described by Eq. (1). The overshoots occurred whenever the system was driven near a frequency where the reflected pressure wave transfer function had a sharp dip towards zero in the magnitude of the reflected pressure. It is noted that we have a similar situation here. For example, if one observes the reflected pressure transfer function, Fig. 4, at a frequency corresponding to 4.75 KHz (this corresponds to a nondimensional frequency of FREQUENCY*TSCALE = .289 in Fig. 4), it is seen that both the real and imaginary part of B_1 (and hence the magnitude of B_1) takes a sharp dip towards zero at this driving frequency. This is in contrast to the value of $|B_1|$ at 10.00 KHz (i.e., FREQUENCY*TSCALE = .608 in Fig. 4) where no sharp dip towards zero occurs in the Fig. 4 reflected pressure transfer function and also no corresponding significant overshoot exists at either the startup or shutdown of the reflected pressure transient, Fig. 11. Thus the presence of strong overshoots parallel the experience reported in reference [12].

- Incident Frequency = 1.0 KHz, Variable *Damping*, (η = .48 at $\omega = 1000 \cdot 2\pi$

This is similar to the earlier runs in Fig. 8 or Fig. 12, except that here the problem is run at a much lower driving frequency, namely 1.0 KHz. The results are shown in Fig. 16 and reveal that in this case, only two cycles of input are required and the response reaches the steady state within one-half of the first cycle of response for both the reflected and transmitted pressure. This is the ideal situation for the experimentalist, however, this favorable situation does not occur very often. The application of Eq. (15) reveals that only 49% of the energy is absorbed and is in keeping with the trend that the greater the energy absorption, the more cycles it takes to reach steady state.

- Incident Frequency = 5.0 KHz, η^* Sensitivity

In the last example solutions, we investigate the sensitivity of the variable damping model to the change in the η^* parameter (Eq. (8)). The base case is shown in Fig. 17 and corresponds to a run with η^* such that η = .48 at $\omega = 2\pi 5000$. The comparitive run is one with twice the value of η^* of the previous Fig. 17 case and is shown for comparison purposes in Fig. 18. The number of cycles to reach steady state are about the same in each case. It is interesting to note that even though the damping constant is higher in the Fig. 18 case, it still produces a higher reflection pressure than the Fig. 17 case. The reason is that the higher η^* value resulted in worst impedance mismatch between the coating and front fluid than that which exists in the Fig. 17

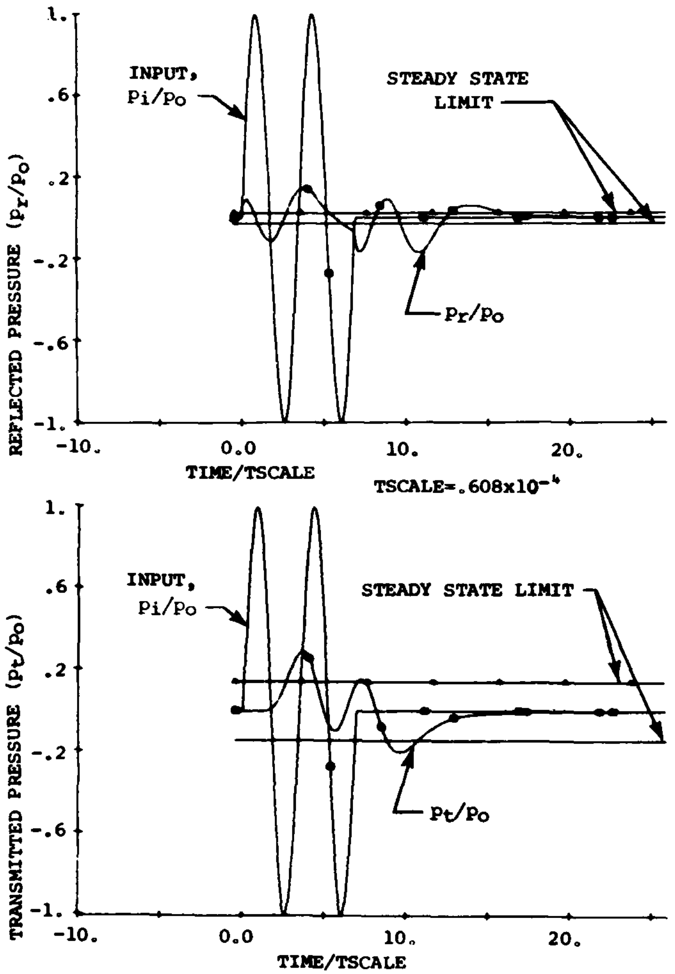

Figure 12 4.75 KHz, 2-Cycle Input; VARIABLE DAMPING, (η = .48 @ ω = $2\pi\cdot10000.$)

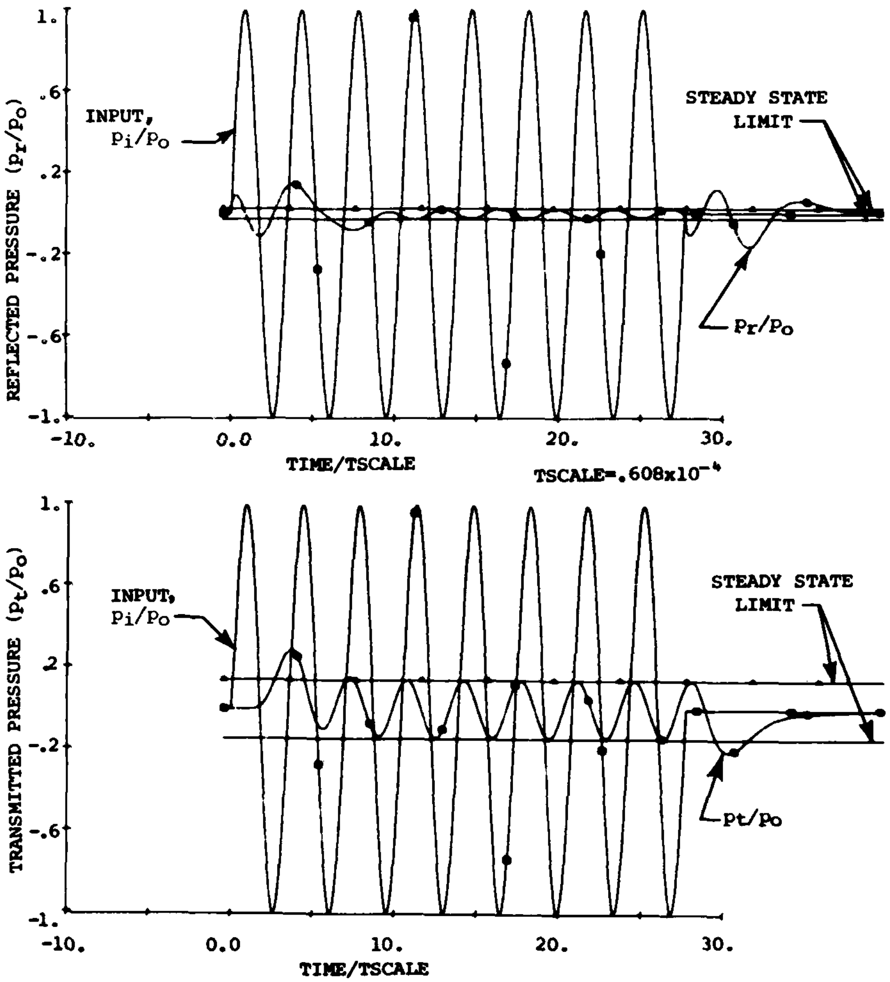

Figure 13 4.75 KHz, 8-Cycle Input; VARIABLE DAMPING, (η = .48 @ ω = $2\pi\cdot4750.$)

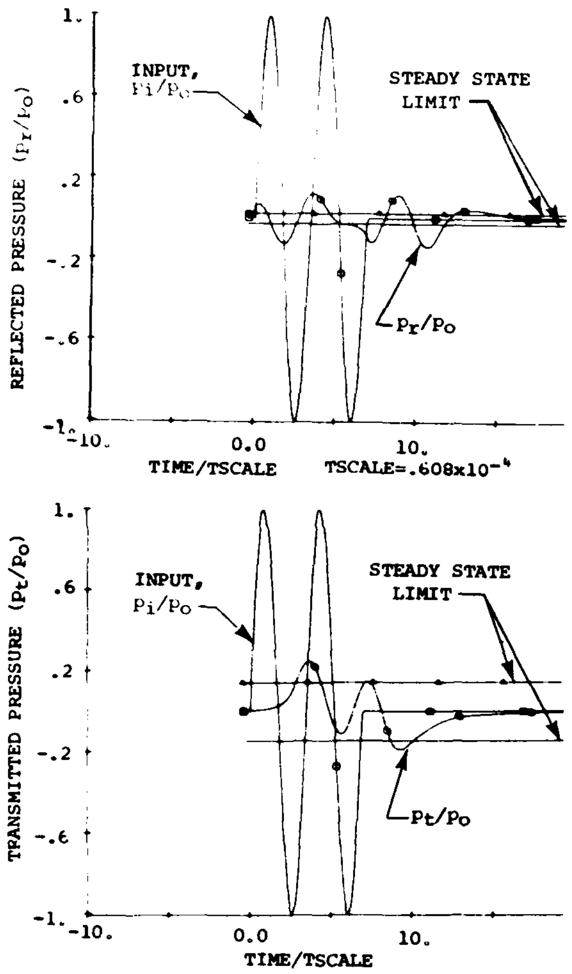

Figure 14 4.75 KHz, 2-Cycle Input; CONSTANT DAMPING, (η = .48 @ all ω)

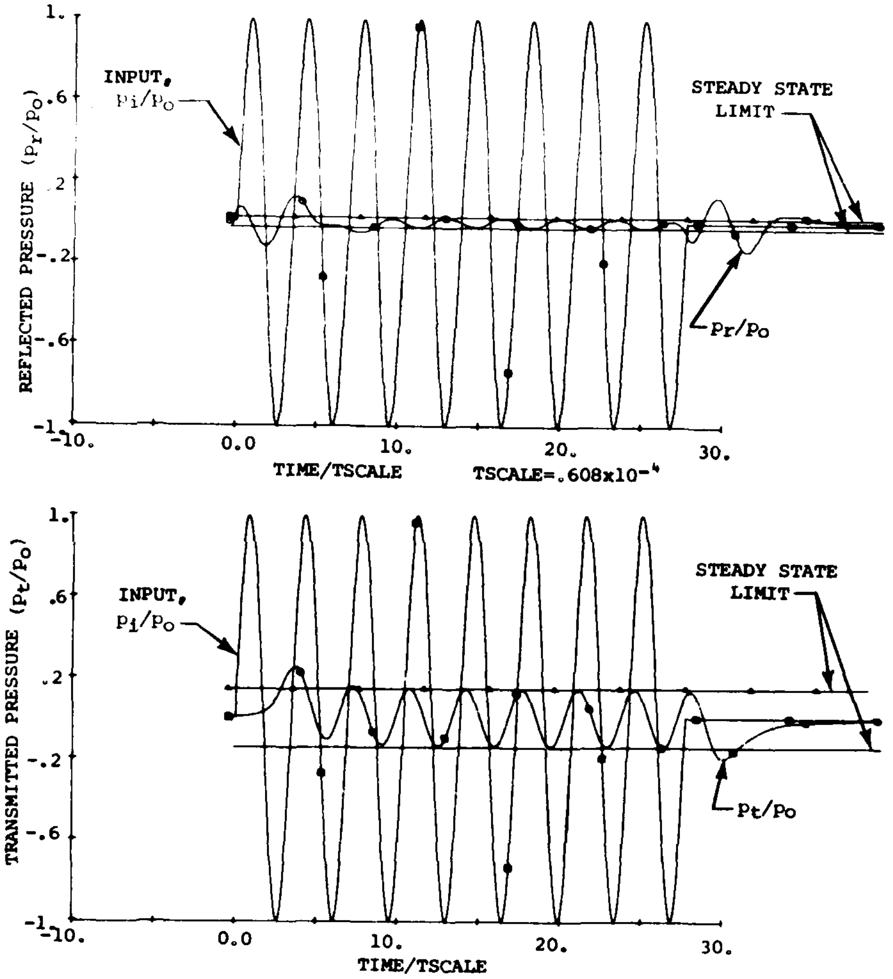

Figure 15 4.75 KHz, 8-Cycle Input; CONSTANT DAMPING, (η = .48 @ all ω)

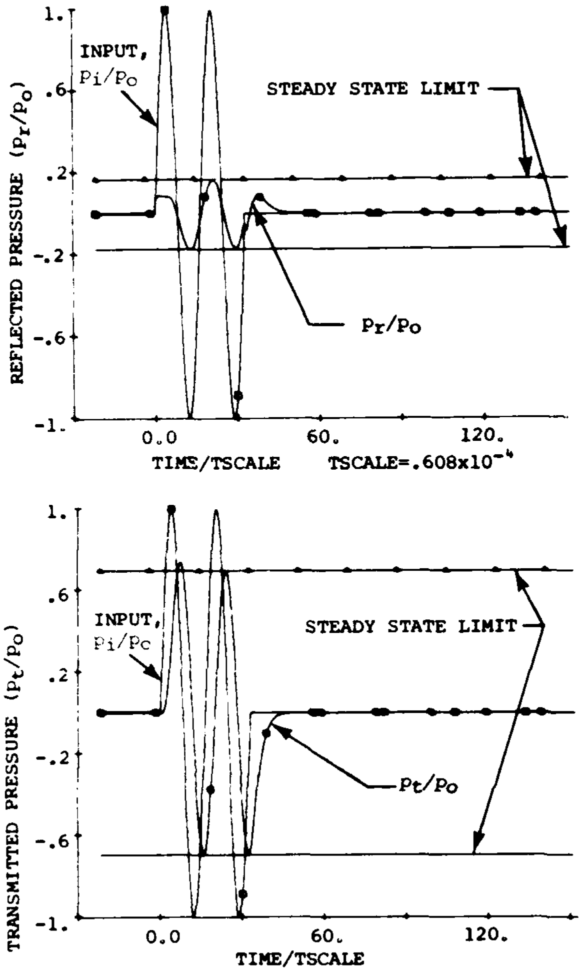

Figure 16 1.0 KHz, 2-Cycle Input; VARIABLE DAMPING, (η = .48 @ ω = $2\pi\cdot1000$)

case. Correspondingly, the greater impedance mismatch resulted in a greater reflected pressure, even though the damping constant was higher.

CONCLUDING REMARKS

As a forward to the conclusions, it is pointed out that the discussion presented next cannot be taken as general rules, but rather apply to the class of materials, and associated frequency levels considered in this limited study. What the results do point out, even in this limited study, is that processing response data based on two cycles of input, which is often done in practice, can sometimes lead to misleading steady state prediction results for both echo reduction and insertion loss.

- With regard to Problem Statement 1, it is recommended that at least four cycles of input be used for running echo reduction or insertion loss experiments. Experiments run with less than four cycles of input may possibly lead to misleading results of the type that usually infer reflected and/or transmitted pressures larger (in absolute magnitude) than the desired steady state pressure values. In the case of an echo reduction experiment, this would tend to make a potentially good coating look bad or marginal.
- With regard to Problem Statement 2, it is recommended that at least three cycles of undisturbed, (i.e., free of edge diffraction effects) pressure response be measured.
- With regard to Problem Statement 3, as much as a 350% error in measuring the incorrect reflected pressure is possible if the above two guide lines are not met. Of course, this is an extreme case, not the average or typical. Similar, but less severe cases were experienced during the course of this study where a 100% error deviation between the peak transient response and steady state pressure was experienced.
- Large overshoots of the transient reflected pressure (both at the startup and shutdown of the incident pressure wave) are experienced when driven at sharp dips in the reflected pressure transfer function. Conversely, if one is trying to measure a reflected pressure transfer function, one could miss these dips if the above recommended 4 cycle input, 3 cycle output rule is violated.

As a final comment, it is emphasized that we are not suggesting that violating the recommended minimum four input cycles and minimum three response cycles rule will always lead to bad results. We only point out that it is possible, in certain situations, to run into problems. The results tend to show that the more energy dissipation that takes place, the longer one has to wait for the transient response to reach the steady state level.

If one has a good idea (say from some analytical model of the transfer function) of what the coating transfer function looks like, then, one can simulate the experiment numerically as we have done here in order to make a pre-experiment judgment regarding how many cycles of input and how many corresponding cycles of "good data" response are needed to achieve a good measurement of the steady state response.

ACKNOWLEDGEMENT

The author would like to acknowledge the help of Miss Christina Nebelung, who assisted in performing the numerical calculations used in this paper.

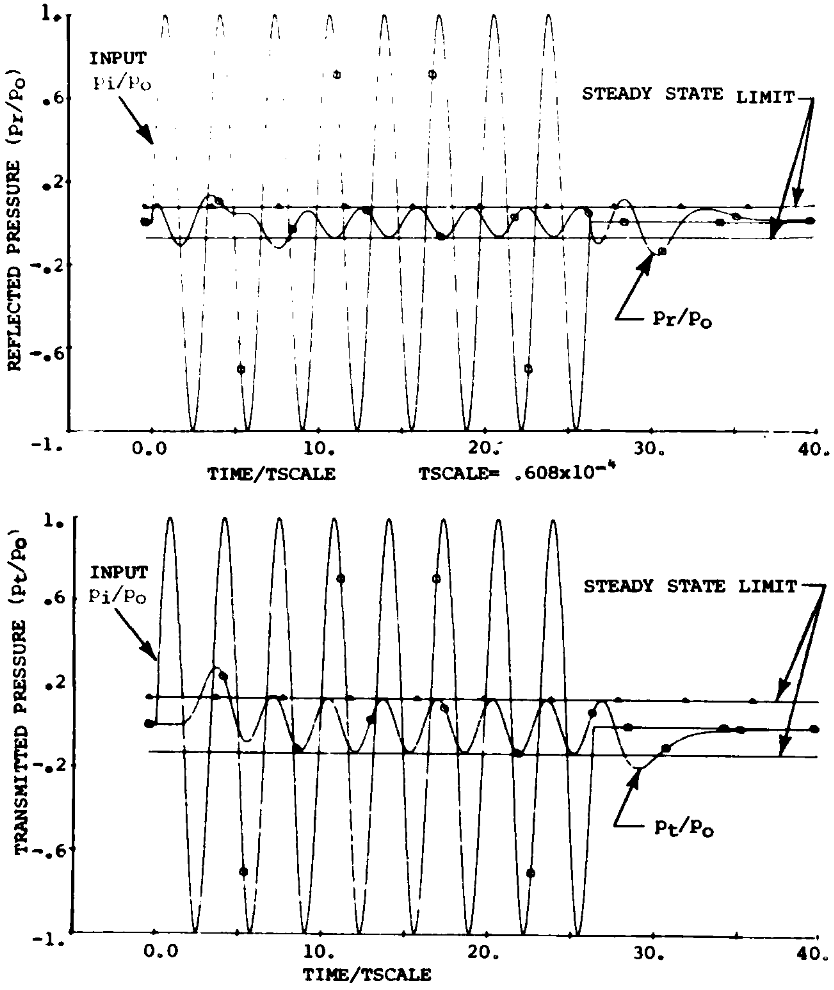

Figure 17 5.0 KHz, 8-Cycle Input; VARIABLE DAMPING (η = .48 @ $\omega = 2\pi \cdot 5000$)

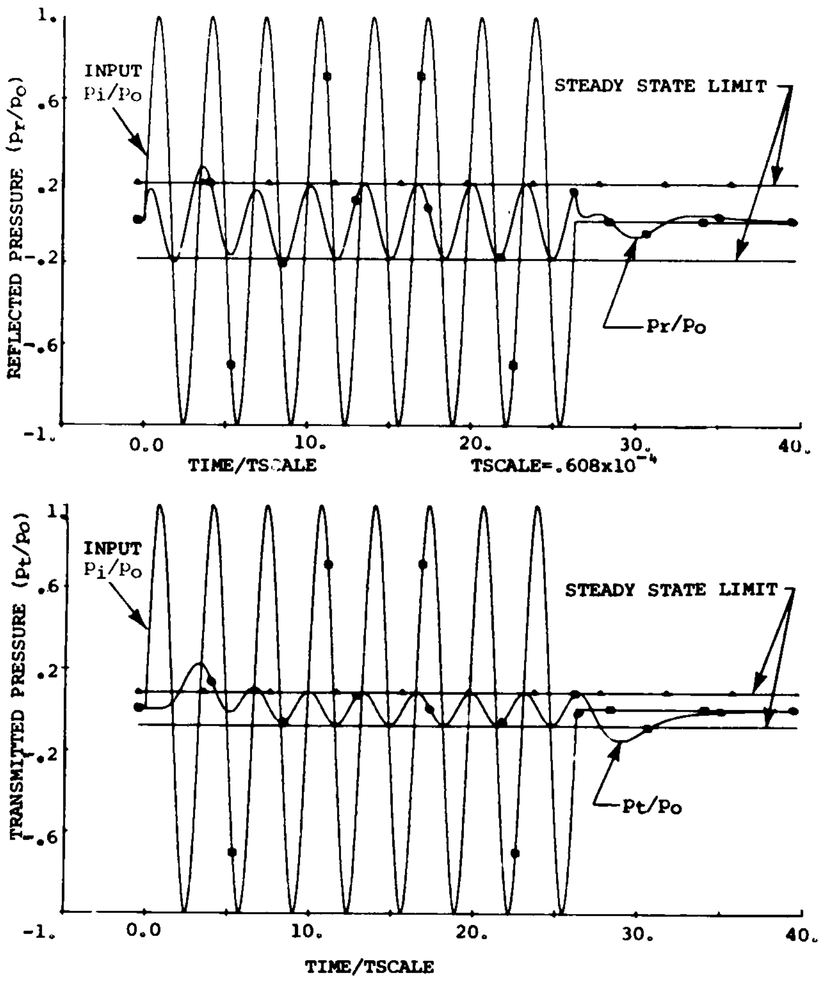

Figure 18 5.0 KHz, 8-Cycle Input; VARIABLE DAMPING, (η = .96 @ $\omega = 2\pi \cdot 5000.$)

REFERENCES

[1] Boffer, R. J., Underwater Electroacoustic Measurements, Naval Research Laboratory, Washington, DC, July, 1970.

[2] Kalinowski, A. J., "Modeling Structural Damping for Solids Having Distinct Shear and Dilatational Loss Factors", Seventh NASTRAN User's Colloquium, NASA CP-2062, October, 1978.

[3] Kalinowski, A. J., "Fluid Structure Interaction Phenomena in Pressure Vessel and Piping Systems", ASME Publication PVP-PB-026, 1977.

[4] Kalinowski, A. J., "Stress Wave Measurement Technique", The Shock and Vibration Bulletin, Vol. 43, June, 1973.

[5] Papoulis, A., The Fourier Integral and its Applications, McGraw-Hill, NY, 1962.

[6] Cooley, W. J., Lewis, D. A., and Welch, D. D., "Application of the Fast Fourier Transform to Computation of Fourier Integrals, Fourier Series and Convolution Integrals", IEEE Transaction on Audio and Electroacoustics, AU-15(2), June, 1967.

[7] Gaunard, G. C., "Sonar Cross Section of a Coated Hollow Cylinder in Water", J. Acoust. Soc. Am., Vol. 61, No. 2, February, 1977.

[8] Flax, L., and Neubauer, W. G., "Acoustic Reflection from Layered Elastic Absorptive Cylinders", J. Acoustic Soc. Am., Vol. 61, No. 2, February, 1977.

[9] Strakna, R. F., Determination of Complex Young's Modulus of Selected Polymers Using WLF Transformation, NUSC Technical Report 5251, October, 1975.

[10] Main, I. G., Vibrations and Waves in Physics, Cambridge Univ. Press, 1978.

[11] Morse, P. M., Feshback, H., Method of Theoretical Physics, McGraw-Hall Book Co., 1953.

[12] Neubauer, W. G., Vogt, R. H., and Dragonette, L. R., "Acoustic Reflection From Elastic Spheres. I. Steady State", J. Acoust. Soc. Am., Vol. 55, No. 6, June 1974.

DISCUSSION

Mr. Dikker (Army Materials & Mechanics Research Center): Could you interpret your results in terms of relaxation time? Since your frequency varies in some multiples you have said that it takes a certain amount of time for material to come to a steady state. At a higher frequency you need a larger number of cycles at a lower frequency you need a fewer number of cycles.

Mr. Kalinowski: There were exceptions to that rule also, it didn't always follow that trend.

Mr. Dikker: Could you possibly interpret it in that way?

Mr. Kalinowski: Actually these results are very new. I'm still in the process myself of understanding exactly the mechanism of what happens, why is it that in some cases two cycles are enough while in other cases it takes much longer. I'm not really sure one can do what you just said.

Mr. Showalter (Shock and Vibration Information Center): You said most experiments are done with two cycle waves and you predicted that you will need four cycles. Does this mean that you will have to double the size of the experimental tanks?

Mr. Kalinowski: Okay, let me qualify that. If you are in the frequency range where you find yourself back up against the wall because the tank is only so long then you have to draw the cutoff at two cycles. But if you have a higher frequency then you can afford more cycles and of course then you do it. I only emphasized two cycles because that is the limit at which a lot of experimental data are quoted. But if you can afford it many times the frequency runs are much higher than the numbers I have given and then you just simply make the length of the train of waves as long as you please. It is in the low frequency problems where you run into trouble. Also it is probably saying that we shouldn't make bigger tanks too. Or you can run them into a lake or something like that. The only trouble with a lake is that you can't control the temperatures or the pressures as you can in the controlled environment of a tank.

SHOCK MEASUREMENT DURING BALLISTIC IMPACT INTO ARMORED VEHICLES

W. Scott Walton
US Army Aberdeen Proving Ground
Aberdeen Proving Ground, MD

Data from piezoelectric and piezoresistive accelerometers subjected to short duration shocks were analyzed. The best measurements were obtained with piezoresistive (strain gage) type accelerometers with filtering. The worst measurements were obtained with piezoelectric (crystal) type accelerometers and no filtering. The most reasonable interpretation was obtained by comparing velocity changes (integral of the acceleration). The worst interpretation was obtained by comparing peak accelerations. It was concluded that ballistic shock is an impulsive phenomenon.

INTRODUCTION

Tests are conducted at Aberdeen Proving Ground to evaluate the vulnerability of armored vehicles to projectile impact. Figure 1 shows the impact of an anti-tank round.

FIGURE 1. Impact of Anti-Tank Projectile Into Right Side of Tank

The primary objective of these tests is to determine if the armor will be penetrated. If the armor is penetrated it must be redesigned. If the armor is not penetrated, survival of the equipment inside the vehicle becomes the question of interest. Accelerometers mounted inside the vehicle are used to measure the shock level and document the environment for future design work. Figure 2 shows accelerometers mounted in the crew compartment of a tank.

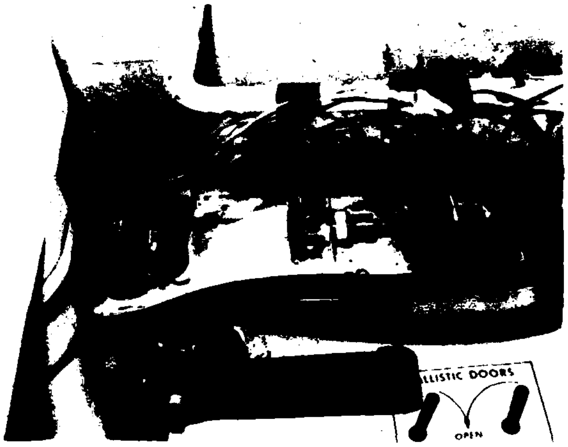

FIGURE 2. Accelerometers Mounted Inside Tank

PROBLEMS WITH BALLISTIC SHOCK DATA

A typical test will consist of 5 to 20 shots fired into a vehicle instrumented with 18 to 48 accelerometers. A typical ballistic shock record obtained from a piezoelectric accelerometer is shown in Figure 3.

The acceleration measurements obtained during ballistic tests have two significant problem areas. The first problem is interpreting the meaning of data like Figure 3. The second problem is that as much as a third of the data is lost due to baseline shift, signal loss, excessive noise or other problems. An example of an unusable acceleration measurement is shown in Figure 4.

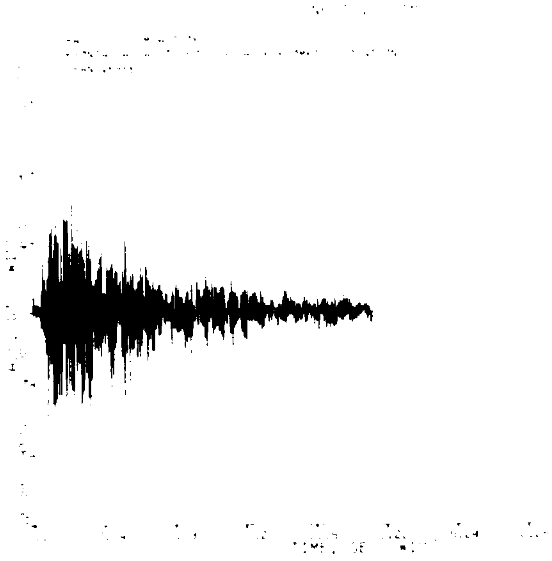

FIGURE 3. Typical Ballistic Shock Record

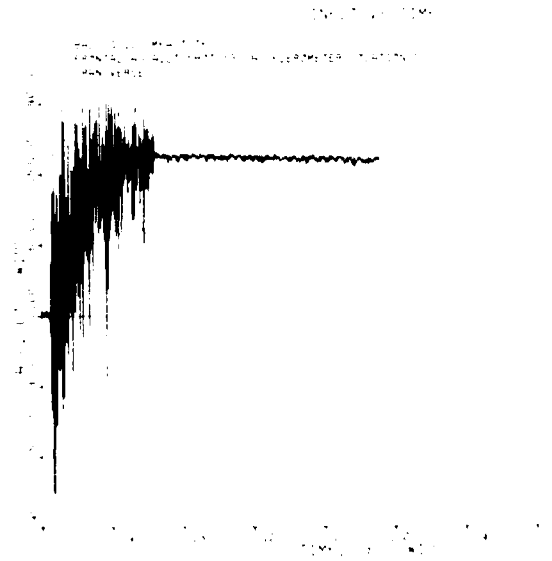

FIGURE 4. Example of Ballistic Shock Data That Cannot Be Used Due to Baseline Shift and Signal Loss

The shock record in Figure 3 shows high frequency ringing (∿ 20 KHz) well above the usable frequency range of the accelerometer (∿ 9 KHz). Little useful information is available from this presentation of the data. A poor way of interpreting the data is to pick the largest "whisker" (∿ 9,000 g's) and simply state 9,000 g's are present, thereby implying that objects in this position should be designed to withstand 9,000 times their own weight!

There are several errors in this interpretation. First, the frequency range of the signal is well above the useful frequency range of the accelerometer, which for an undamped accelerometer means that the signal will be amplified. Second, in this frequency range the type of mounting as well as the type of accelerometer used will cause the result to vary considerably from test to test. Third, and most important, few structures known to man have a first resonance high enough to respond to a 20 KHz transient.

TYPES OF IMPACT

Impact can be divided into several categories. The category is determined by the impact velocity, and the response of the mechanical system of interest to the impact. If the category of impact is known in advance, shock measurement and analysis can be simplified.

a. Quasi-static Impact - The frequency content of the shock is well below the natural frequency of the system, and the system motion duplicates the input shock motion. The maximum system acceleration is the peak acceleration of the input shock. The best single number to describe the shock input is the peak acceleration. An example of quasi-static impact is a parachute drop of a tank onto its suspension system.

b. Dynamic Impact - The frequency content of the shock is approximately equal to the natural frequency of the system. The motion of the system is a combination of the shock input and the natural resonance of the system. There is no simple way to determine the motion (response) of the system and no single number can be used to describe the shock input. An example of dynamic impact is the firing of the main gun of a tank.

c. Impulsive Impact - The frequency content of the shock is considerably higher than the system natural frequency. The system motion is the natural resonance. The amplitude of this motion depends only on the integral (acceleration x time = velocity change) of the input shock. The best single number to describe this kind of shock is the velocity change. Ballistic shock typically contains very high frequency acceleration (20 kHz and above). Even the most "rigid" components mounted on a combat vehicle, such as gun sights, have a first resonance below 2 kHz. Since the shock input frequency is ten times the structure resonant frequency, ballistic impact causes an impulsive response in structures; hence, the velocity change of a ballistic shock is a good number to describe the shock -- peak acceleration is a poor number to use in describing the shock.

d. High Velocity Impact - The velocity of the impact becomes high enough that individual stress waves are significant. The amplitude of the stress wave is determined by the equation:

$\sigma = \rho C V$

Where: σ = stress
ρ = density

C = wave propagation velocity ("speed of sound" in the material)
V = local particle velocity (or change in local particle velocity)

These stress waves can be considered as a discontinuity traveling through the armor plate. As this discontinuity travels past an accelerometer, an "instantaneous" change in displacement occurs which results in an "infinite" acceleration.

e. Hypervelocity impact (also called "fluid impact") - the impact velocity becomes so large that the resulting stresses are far enough above the material yield strength that both the projectile and target can be considered fluids. Density is a dominant parameter, and material strength can be neglected. At the upper limit of this category, material compressability becomes important. Impact velocities exceeding the fluid impact category result in vaporization of colliding solids and are not applicable to armored vehicle studies.

The effect of stress-wave induced acceleration on a structure varies greatly with the structure's mounting, number and type of joints, flatness, and surface finish because the displacements are so small. Only items with high natural frequencies (such as accelerometers) are affected significantly by this type of motion.

Typical recording equipment has a signal to noise ratio of approximately 100:1. Because of this limitation, one must decide in advance whether to record the high frequency, high amplitude (>10,000 g's) acceleration or the low frequency, low amplitude acceleration (∿ 100 g's). Both kinds of accelerations are present. Because the natural resonant frequency of most structures of interest is relatively low (<2,000 Hz), it is reasonable to filter out the high frequency, high amplitude acceleration so that a faithful recording of the low frequency acceleration can be obtained.

COMPARISON OF PIEZOELECTRIC AND PIEZORESISTIVE ACCELEROMETERS

Steel accelerometer mounting blocks were welded to a piece of steel armor plate .64cm (¼ inch) thick as shown in Figure 5. A ball bearing was dropped from a fixed height to strike an impact point in the center of the plate, approximately equidistant to all accelerometers.

Figure 6 shows the response of all four accelerometers to drop 8. In this drop, several layers of tape were placed over the impact point. This modification allowed a smooth, long time duration (∿ 200 microseconds) application of the shock. For this kind of shock, all accelerometers respond in a similar manner. Figure 7 is provided for conversion of velocity in feet per second to velocity in meters per second.

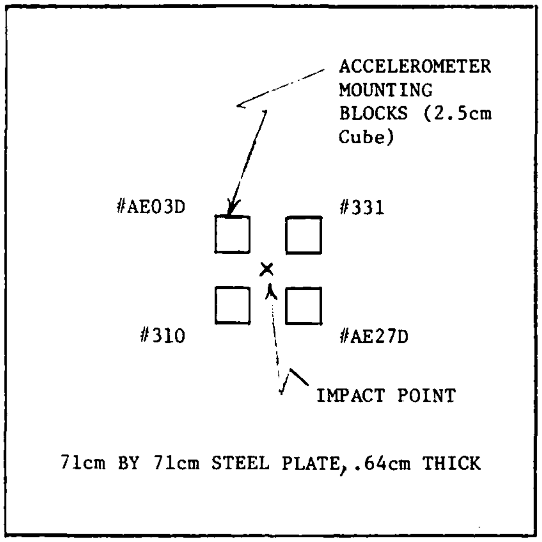

FIGURE 5. Configuration of Accelerometers On Armor Plate; 331 and 310 Are Piezoelectric Accelerometers;AE03D and AE27D Are Piezoresistive

Figure 8 shows the response of the accelerometers to a ball bearing impact on the bare plate. All four accelerometers indicate that the ball bearing was in contact with the plate for approximately 30 microseconds. The piezoelectric accelerometers produced the largest peak accelerations (7,700 g's from 331 and -2,800 g's from 310). The piezoresistive accelerometers produce significantly lower peak acceleration (1,000 g's from AE03D and 930 g's from AE27D).

Because of the configuration of the accelerometers, it is impossible for the ball bearing to have hit closer to both the piezoelectric accelerometers; it is, therefore, not likely that the actual acceleration level was higher on both piezoelectric accelerometers than it was on either of the piezoresistive accelerometers.

The peak accelerations indicated by the piezoelectric accelerometers occur well after the actual impact of the ball bearing. In the case of accelerometer 331, the peak acceleration is almost twice the amplitude that was obtained while the ball bearing was in contact with the plate. Also note the baseline shift in accelerometer 331.

Manufacturers of undamped accelerometers warn against using the accelerometer to measure acceleration with a pulse width below a specified value. During ballistic testing it is impossible to control the acceleration pulse width that will be present. The previous

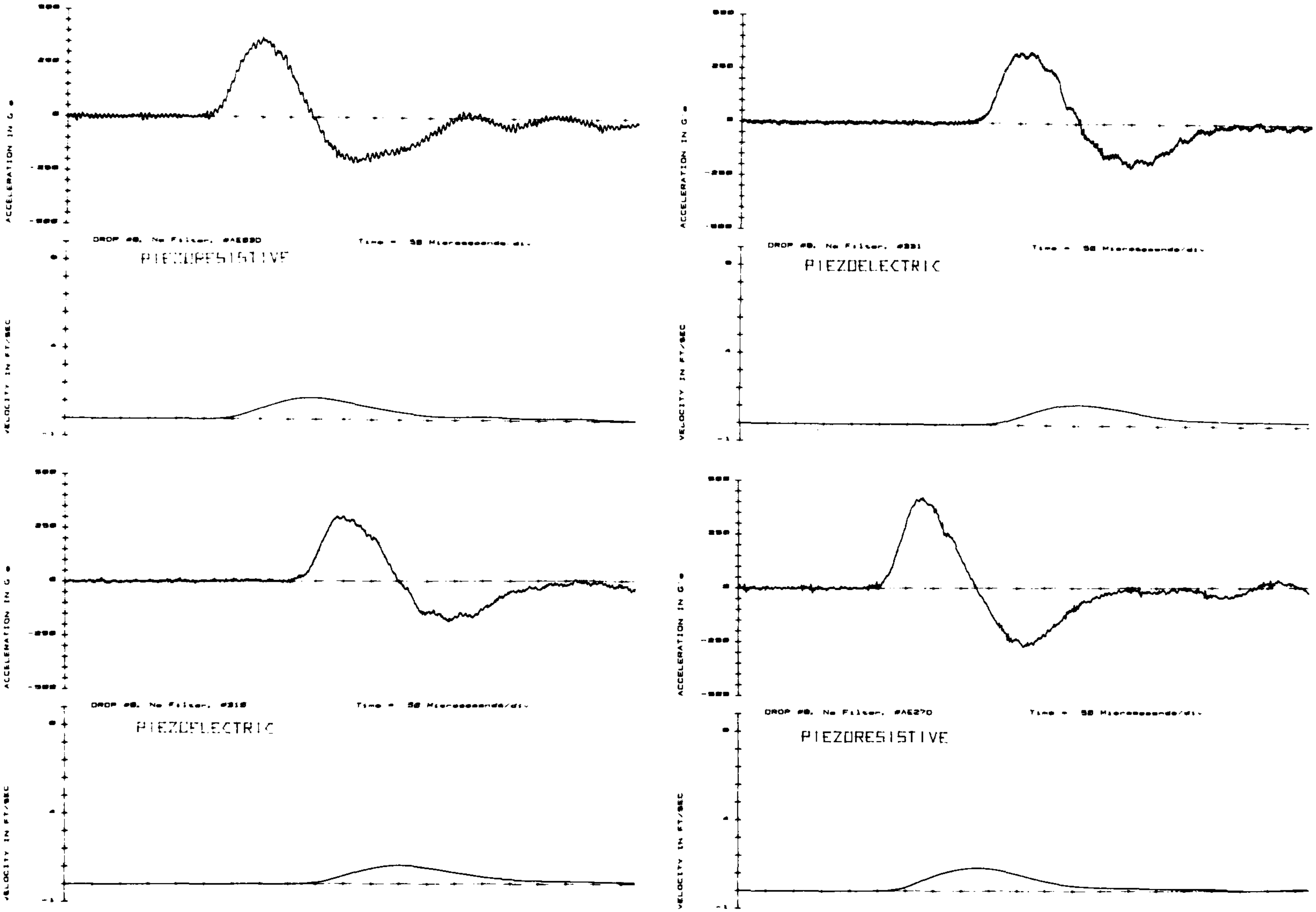

FIGURE 6. Response of Accelerometers to Impact of a Ball Bearing when Several Layers of Tape Were Placed Over the Impact Point

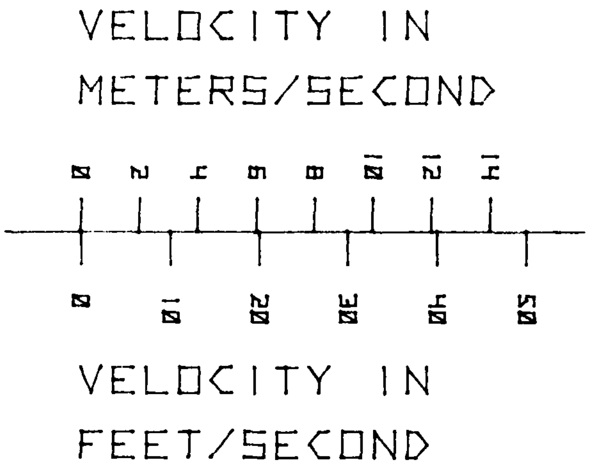

FIGURE 7. Scale for Converting Velocity In Feet Per Second to Velocity In Meters Per Second

experiment shows that piezoresistive accelerometers are more tolerant to misuse (i.e., excessively short pulse width) than piezoelectric accelerometers.

If it were possible to provide damping in the accelerometers that measure high level shock (10,000 to 100,000 g's), the accelerometer ringing problem could be eliminated and better measurements could be obtained. Unfortunately, because of the small displacements made by the seismic mass of the accelerometer, traditional oil or gas damping techniques are not practical.

In general, piezoresistive accelerometers have been more reliable, more consistent, and easier to work with than piezoelectric accelerometers. The excessive ring and baseline shift characteristics of piezoelectric accelerometers are easily documented. A problem not well documented, but often present, is the tendancy of charge amplifiers to drift when cables are subjected to the wet and dirty conditions typical of field testing, or when moisture condenses within the electronics because the instrumentation trailer cools overnight. This problem causes delays in testing or the use of questionable techniques, such as offsetting the amplifier so it will be drifting through zero when the test round is fired.

Figure 9 illustrates a poor acceleration-measurement technique. Note that the peak acceleration in both channels is approximately 1,000 g's, even though one accelerometer is mounted in the direction of fire and the other is perpendicular to the line of fire of the weapon. Obviously, using peak acceleration from these signals to describe the shock would be meaningless. The signal from channel 8 (perpendicular to the line of fire) consists almost entirely of oscillation at the natural frequency of the accelerometer. The velocity change is the most useful information available from the data and shows immediately which channel is in the line of fire (and receiving a significant shock) and which channel is perpendicular to the line of fire (receiving insignificant shock).

An example of much better acceleration-measurement technique is in Figure 10. Notice that the difference between a high velocity round and a low velocity round is immediately obvious from both the acceleration and the velocity change plots. Further evidence that the type of data shown in Figure 10 is good includes: (1) three different accelerometers agreed to within 5% and (2) the velocity change indicated by the accelerometers agreed to within 3% of the recoil velocity obtained from displacement-measuring instrumentation.

SOFT MOUNT TESTS

A test fixture, shown in Figure 11 was constructed. Various materials were tried in an attempt to mechanically isolate the piezoresistive accelerometer from high frequency acceleration. The materials were tested by dropping a steel ball bearing from a fixed position, allowing it to strike an aluminum block, and examining the accelerometer output. The mounting block was held on five sides by the test material; the accelerometer was mounted on the sixth side of the block.

Uncalibrated qualitative plots of the results are presented. Figure 12 shows the signal obtained when no soft mount was used. In this case the accelerometer was mounted directly to the aluminum block.

It is noticeable that the accelerometer rings at its own natural frequency for the entire record. The only part of the signal that is not accelerometer ring appears to be the first two cycles, where the signal does not pass through zero. When the signal is low-pass filtered at 10 kHz, the damped 10 kHz ringing of the filter is obtained. The velocity changes for both the unfiltered record and the record filtered at 10 kHz are approximately the same.

Figure 13 shows the results obtained when room temperature vulcanized (RTV) silicone rubber was used. The ringing of the accelerometer at its own natural frequency is not significantly reduced, but a new resonance at about 2 kHz has been introduced. This new resonance is the response of the soft mount mechanical system. The velocity changes of both the filtered and unfiltered signals are approximately the same as the velocity change obtained with the hard mount.

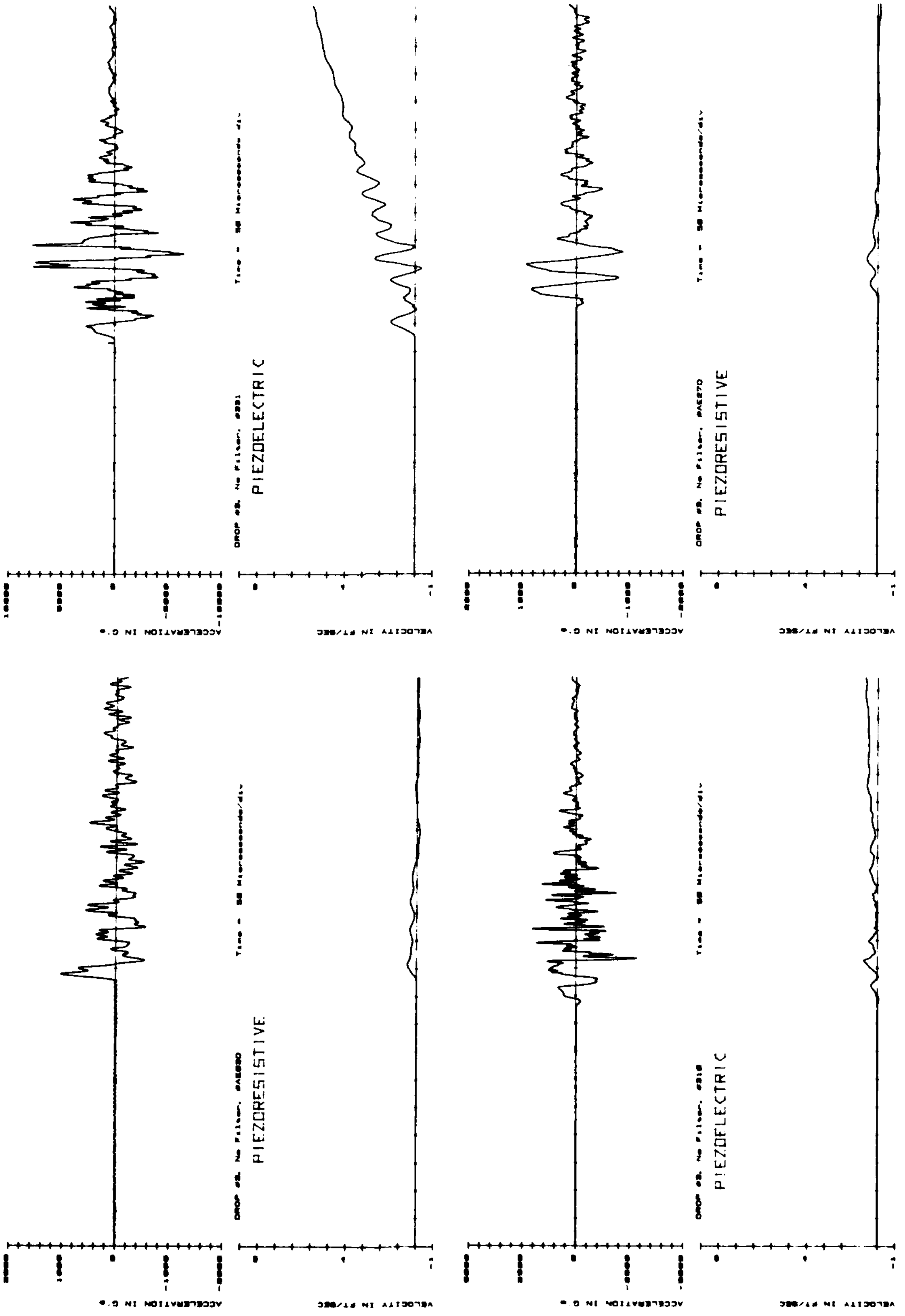

FIGURE 8. Response of Accelerometers to Impact of a Ball Bearing on Bare Plate

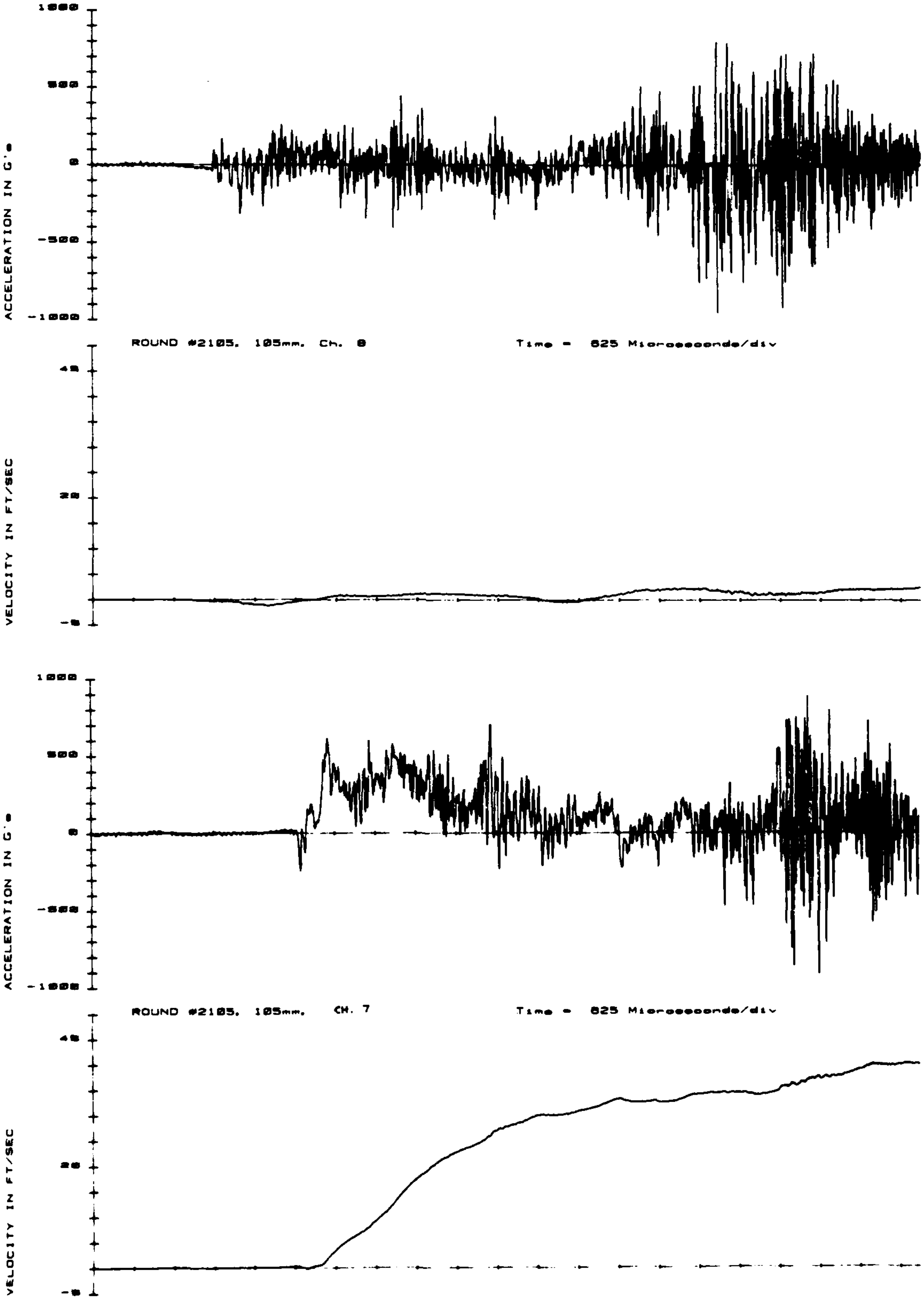

FIGURE 9. Acceleration Measured on a 105mm Howitzer Using Piezoelectric Accelerometers and No Filtering, Channel 7 is in the Line of Fire and Channel 8 is Perpendicular to the Line of Fire

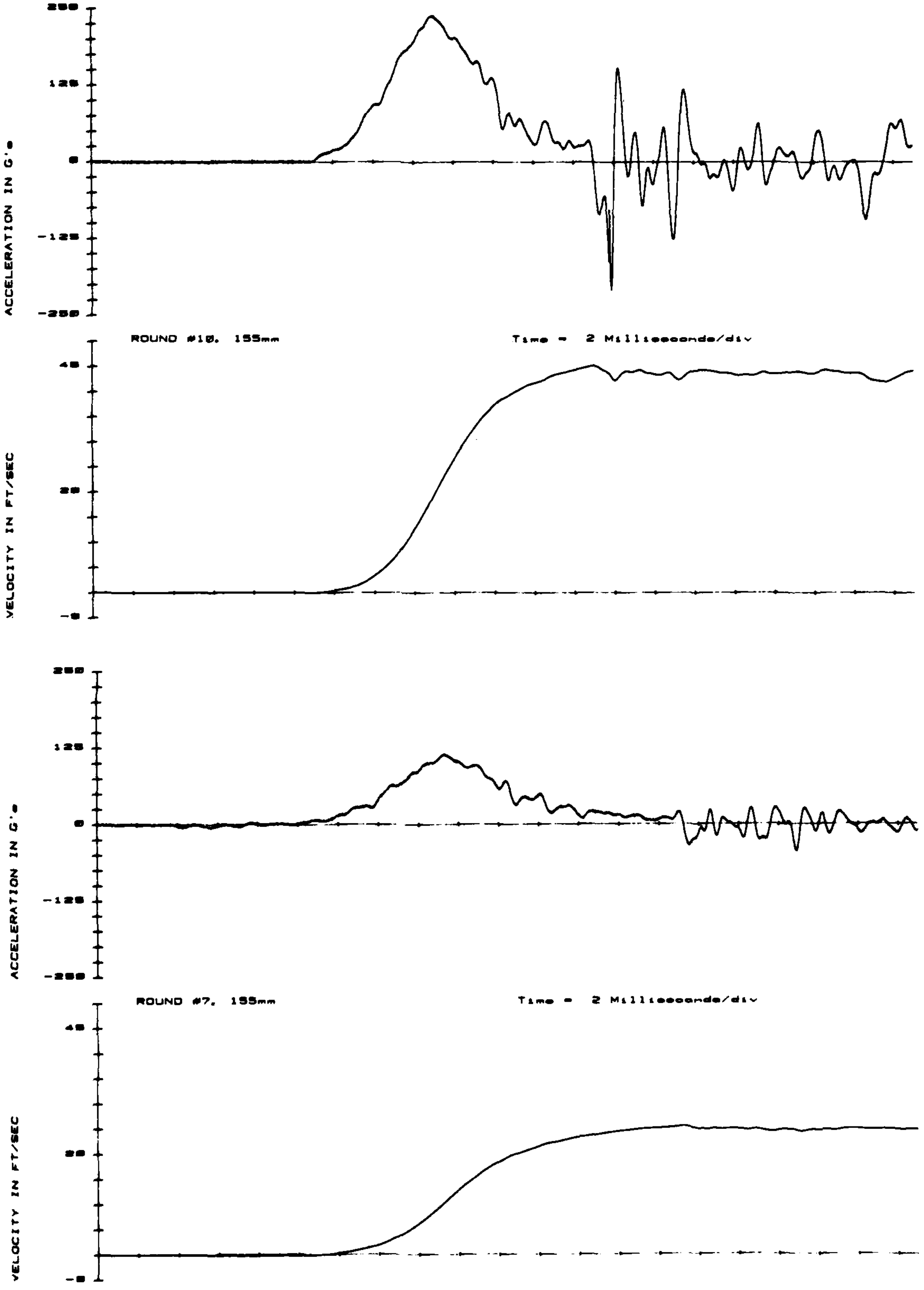

FIGURE 10. Acceleration Measured on a 155mm Howitzer Using Piezoresistive Accelerometers and Low Pass Filtering at 1 kHz. Round 10 is a High Velocity (Zone 8) Shot and Round 7 is a Lower Velocity Shot (Zone 7)

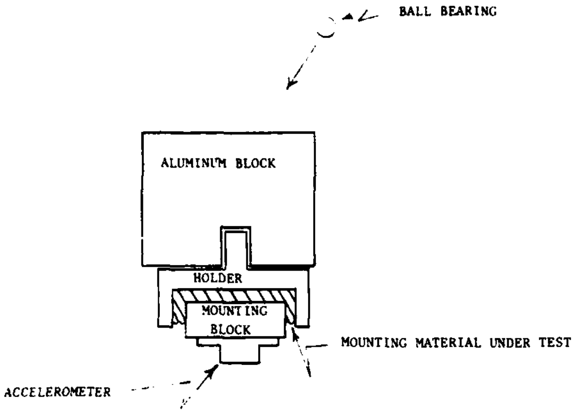

FIGURE 11. Test Fixture Used In Soft Mount Experiments

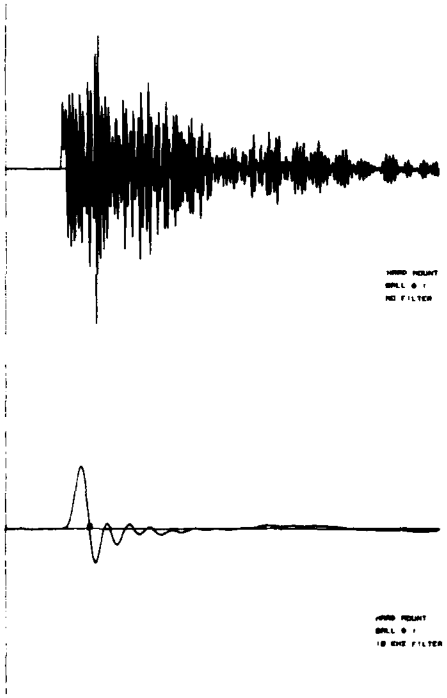

FIGURE 12. Acceleration Versus Time Using Hard Mounted Accelerometer

Figure 14 shows the response obtained when a wax-like substance (Py-Seal) was used. The accelerometer ringing was suppressed with this material and a new resonance of approximately 2 kHz was introduced. The velocity change of both the filtered and unfiltered signals is approximately 15% greater than the velocity change obtained with the hard mount.

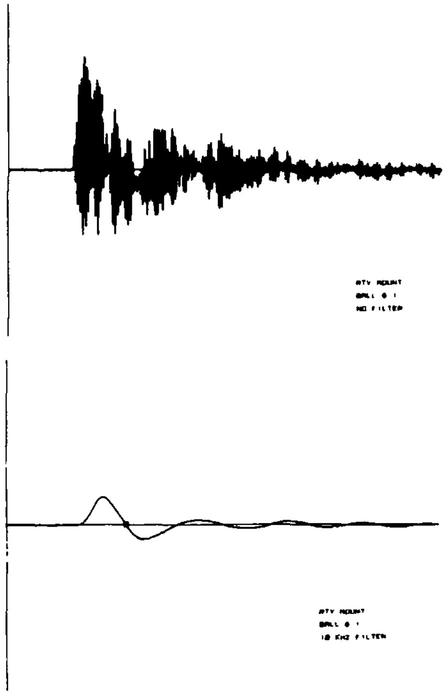

FIGURE 13. Acceleration Versus Time For The RTV Soft Mount

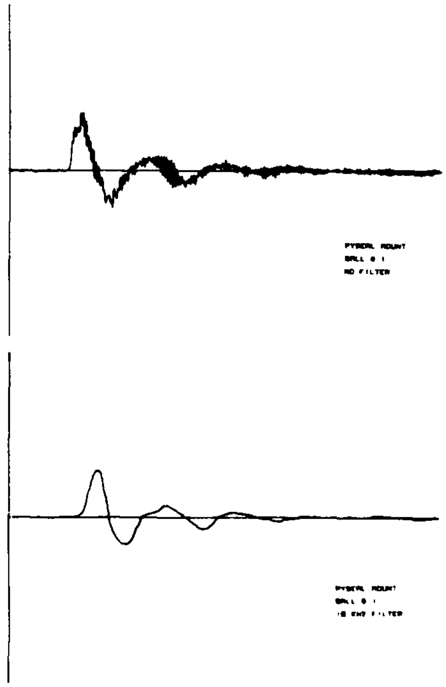

FIGURE 14. Acceleration Versus Time for the Py-Seal Soft Mount

Figure 15 shows the response obtained when a nonhardening putty (Duxseal) was used. Accelerometer ringing was suppressed and no new resonance was introduced. When the signal was filtered at 10 kHz, only the damped ringing of the filter was present. The velocity change from both the filtered and unfiltered signals is approximately 15% lower than the velocity change using the hard mount.

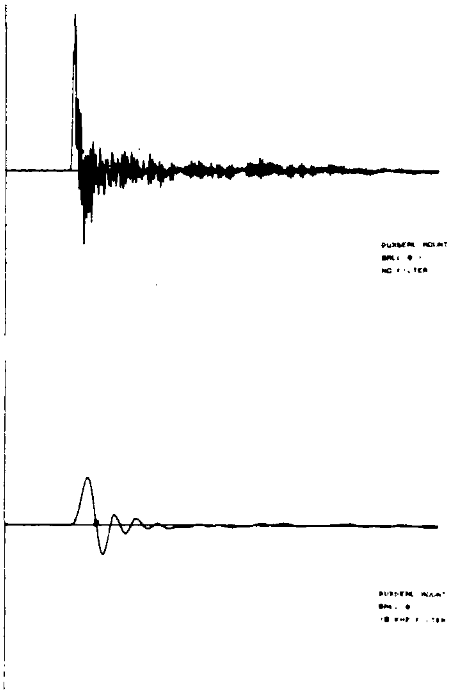

FIGURE 15. Acceleration Versus Time for the Duxseal Soft Mount

The good agreement (±15%) of velocity change despite the large variation in the acceleration signals is encouraging. Since the excitation (a ball bearing hitting an aluminum block) was the same throughout the experiments, some measure of the shock should be the same. In these experiments the only quantity that indicated that the shock level was the same regardless of what type of instrumentation was used (i.e., what kind of mount) was the velocity change.

CONCLUSIONS

a. Ballistic shock is an impulsive phenomena; therefore, techniques for measuring and analyzing an impulse should be used.

b. Depending on the mounting, filtering and type of accelerometer used, almost any number can be obtained for peak acceleration during ballistic shock.

c. Peak acceleration is therefore an almost meaningless number in the evaluation of ballistic shock. Peak velocity change is a much more meaningful number to use in evaluating ballistic shock.

d. In controlled shocks where the pulse width of the shock is above a certain critical value, piezoelectric accelerometers agree quite well with piezoresistive accelerometers.

e. In ballistic shock, where pulse width cannot be controlled, piezoelectric (crystal) accelerometers with no filtering produce the worst results; piezoresistive (strain-gage) accelerometers with filtering produce the best results.

DISCUSSION

Mr. Galef (TRW Systems): When you put a small mass on a spring and you have some way to measure the force in the spring you call it an instrument. That instrument is really too stupid to know whether it's an accelerometer or a seismograph. The difference comes about in the natural frequency of the instrument. If it is a good deal higher than the frequency content of what you are trying to measure it is an accelerometer. If the reverse is true it is a seismograph. It seems when you try to measure these very high very short duration pulses with a strain gage accelerometer you are probably really measuring displacement and you have to be careful about your calibration.

Mr. Walton: The strain gage accelerometers are now available in a very high frequency response range and the important part of what I was trying to say is that during ballistic impact, since it is an impulse, I am not really interested in acceleration. I want a velocity change. I don't have a good inertial velocity transducer, but somehow I can isolate or use my strain gage accelerometer to measure this velocity change or measure acceleration and integrate it to obtain a velocity change.

Mr. Galef: Yes, I quite agree that you can use it but I think some care in its calibration is necessary. The instrument may not be reading acceleration directly or the low frequency component of acceleration. It may read the displacement multiplied by some calibration factor.

Mr. Baade (Carrier Corporation): I think it goes without saying one always has to be careful of calibration.

Mr. Bort (Naval Research Laboratory): I think you ought to come down to NRL. You and Merve Oleson can change ideas with great profitability because he is working on exactly the same sort of thing that you are working on, namely strain gage accelerometers, soft mountings and integration of the signal.

Mr. Walton: I admit that not all of these ideas are my own. I have talked to Mr. Oleson and also to Val Devost. I started from their work.

Mr. Sevin (Defense Nuclear Agency): Perhaps this is nit-picking but when you call something an accelerometer and you soft mount it you can't possibly be measuring the applied acceleration so you have only the velocity gage therefore you must integrate.

Mr. Walton: That is correct and that's the object.

AUTOMATIC DATA CHANNEL CALIBRATION AND NOISE IDENTIFICATION

Edwin E. Nesbit
Lawrence Livermore Laboratory
Livermore, California

As part of an overall upgrade of dynamic testing facilities, an automatic data channel calibration system has been implemented that uses microcomputer-based hardware and a parameter identification algorithm derived from optimal control theory. Analyses are performed using sine and square wave calibration signals (at user-specified frequencies) to determine channel gain and offset, and known constant calibration signals to determine 60, 120, and 180 Hertz channel noise.

INTRODUCTION

As the digital computer has assumed a greater role in data acquisition and reduction, the field of parameter identification has become extremely sophisticated. As a result, reliable models can often be made of quite complicated systems. Sometimes, however, the results are misleading in that a model will fit a particular set of data quite well but then will be shown through extrapolation to other data to be an inadequate representation of the real system. Consequently, there is often a reluctance to use parameter identification as a tool and a skepticism of results obtained when it is used.

For data adhering to two quite restrictive conditions, these reservations should not apply and a particularly simple parameter identification technique has shown to be fast, accurate, and easily realized on a minicomputer. The conditions are that the data constituents to be estimated are known as to type a priori and that the contribution of these modelled components is large with respect to the data.

The Computer System Applications (CSA) group at Lawrence Livermore Laboratory is presently engaged in developing an interactive computer-run control, calibration, and data acquisition system for its dynamic test facility. This paper briefly describes this system, derives the parameter identification equations, and discusses the design and implementation of the program to perform automatic calibration and 60, 120, and 180 Hertz noise identification on the data acquisition and control feedback channels.

APPLICATION AND DESIGN PHILOSOPHY

In its design and evaluation work for the Department of Energy, Lawrence Livermore Laboratory maintains a considerable dynamic testing capability both at the Laboratory itself and at its high explosive test complex (Site 300) outside of Livermore. A large part of the Site 300 capability is housed in Building 854. There, test hardware includes two one-dimensional shakers and two (soon to be three) HYGE (hydraulically actuated, gas energized) shock test machines. The system computer, a MODCOMP IV, controls a Shaker Control Unit (SCU), a Calibration Unit (CBU), and several Data Capture Units (DCU) to conduct the tests, record the data, and present realtime results on a CRT console. (See Figure 1)

D-DAC HOST COMPUTER SYSTEM, BLDG. 854

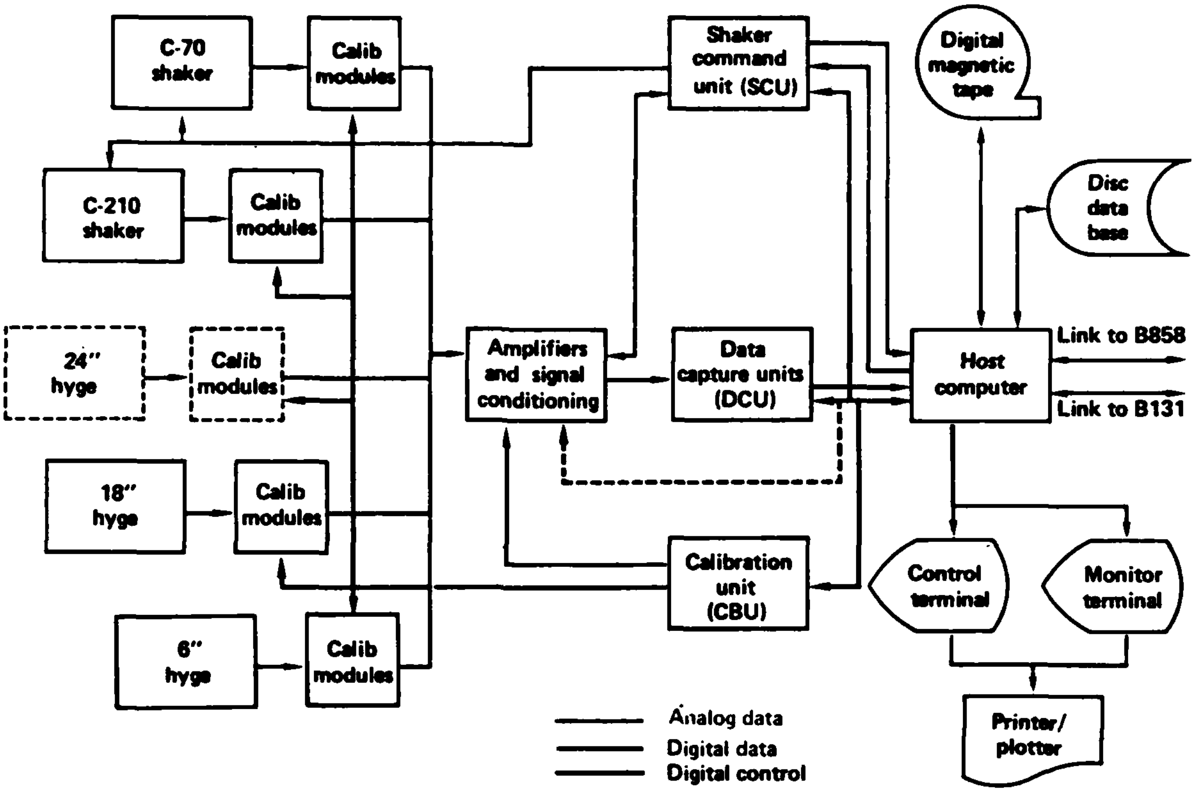

Figure 1

The SCU, DCU and CBU are all system hardware components designed and built within the Laboratory. While specifically designed to meet the requirements of the dynamic test facility, the capabilities and modes of operation of these components were kept flexible enough to permit use at various test locations within the Laboratory.

SCU- The Shaker Control Unit is the nexus for control lines to and from the shakers. It has three analog-to-digital converters arranged in two sets of three inputs for feedback signals and/ or test data. The signal is digitized at a sample rate selectable by the user and the information is captured via direct memory accessing.

The SCU has a digital-to-analog converter on its one output channel. Calculation of the control signal is done by the MODCOMP IV in one of several control programs (swept sine, random, and others). The resulting values are then output to the SCU where they are converted to an analog signal and sent to the shaker.

DCU- The Data Capture Unit is an eight-channel digital data acquisition subsystem based on an LSI-11 microcomputer. Each channel has a programmable filter and amplifier, a 12-bit A/D converter, and a 4096-word memory. Triggering criteria are selectable by the user, memories can be chained or used independently, and the captured data is retrieved by direct memory addressing.

CBU- The Calibration Unit is a set of twenty interchangeable modules that simulate charge, voltage, and strain transducers. An included waveform generator outputs a user-defined digital signal to each module where it is converted to a simulated transducer output. It then traverses the normal data path where it is captured by the SCU or DCU for subsequent channel calibration.

To coordinate this hardware, control and calibration programs have been written for execution on the MODCOMP IV. Each of the control programs calls the calibration routine as an overlay, providing the user with a consistent execution sequence for all tests.

In conceptualizing the calibration function, it was felt that because various hardware component characteristics were known to change with signal frequency, a dynamic calibration was preferable to one that was static and that variable-frequency sine and square waves and variable duty cycle pulses would suffice for the great majority of applications. A user-defined calibration waveform option was also included for the rare situation when these were not adequate. In addition, it was felt that a determination of the 60, 120, and 180 Hertz noise present in a channel was a desirable capability within the calibration function. In both the calibration and noise identification routines, the channel's offset is calculated as well.

In selecting the technique to realize these functions, it was noted that two important criteria would be met in the data:

> The calibration signals are known as to their type (e.g., sine or square wave) and because they are produced digitally in the CBU, there would be negligible uncertainty or variation in the frequency value.
>
> For a good channel, the known signal (including offset) would completely dominate the waveform.

The meeting of these conditions presented an ideal application for a fast, simple, and accurate parameter identification technique that is derived from optimal control theory.

ESTIMATION OF PARAMETERS USING WEIGHTED LEAST SQUARES [Reference 1]

If a set of data can be modelled as the sum of known components (with unknown magnitude and phase) and if the error between this model and the data can be said to be independent of the model, the task of determining each component's contribution to the data is equivalent to estimating the state vector of a static system using system measurements. The matrix equation expressing this relationship is

$$y = Ax + \nu , \qquad (1)$$

where y is the n-component measurement vector; A is a known (n x p)-matrix, the model; x is the unknown p-component state vector, the parameters and ν is the unknown n-dimension error (noise) vector.

One method of making this estimate is to construct a non-negative scalar function of the state that attains its minimum value when x meets some prescribed criteria. This can be done with a quadratic cost function, J, that has as its magnitude the weighted sum of the squares of the differences between the unknown state and a prior state estimate (if one exists), $\bar{x}$, and between the system modelled with this state and the measurements (data):

$$J = \frac{1}{2} \Big[(x - \bar{x})^T K_1 (x - \bar{x}) + (y - Ax)^T K_2 (y - Ax) \Big]$$

where the factor of 1/2 is included for algebraic convenience.

In this expression for J, K_1 and K_2 are weighting matrices that reflect the relative value the analyst wishes to put on a state deviation in the two differences. Typically, they are selected in accordance with the analyst's confidence in the validity of the prior state estimates and of the measurements - the larger the value, the greater the confidence. A minimum J can be thought of as defining the state vector that minimizes its deviation from a prior expected value subject to the data, or more reasonably, that minimizes the deviation of the model from the data subject to the state's expected value.

A derivation of the least sum square estimate of x, $\hat{x}$, is included as Appendix I. There it is shown that if the weighting matrices are picked to be the (assumed known) covariance matrices of x and y, and if the system noise is assumed to be random, then for the case where no prior estimate of the state is known, the least sum squares estimate is

$$\hat{x} = \left(A^T A\right)^{-1} A^T y \,. \qquad (2)$$

SOFTWARE DESCRIPTION

Equation (2) is easily solved for $\hat{x}$ either by a straightforward matrix inversion or by any of a number of elimination schemes. As the matrix $A^T A$ has dimension (p x p), the speed of solution is strongly dependent on the number of parameters, p, and through the row-by-row construction of A, only weakly influenced by the number of data, n.

Practical considerations in realizing this analytical technique on a digital computer include the two previously-mentioned criteria - knowledge of the signal type and dominance of the modelled constituents. In addition, $A^T A$ must be well behaved and no one parameter should be allowed to be much larger (greater than three orders of magnitude or so), than the rest. These last two conditions are usually not a problem. Good behavior of $A^T A$, i.e., non-singularity, usually occurs naturally in real systems; practices to be avoided in the model formulation and data acquisition are a sampling time less than one period of the slowest constituent and the inclusion of more than one waveform of nearly equal frequency, although this last restriction can sometimes be circumvented by the selection of a sample time that is long enough for significant phase differences to manifest. One-parameter dominance of x, with consequent degradation in the solution accuracy of the smaller elements, can be avoided by defining the large parameter to be some nominal constant with a correction as the parameter to be solved for. If this nominal value is not known prior to the analysis, the parameter identification can be performed in two sweeps, the first providing this value. In all cases, test data with known parameter values should be analyzed to insure accurate identification.

Designing the software for implementing this technique at the dynamic test facility involved the construction of three models corresponding to sine wave calibration; square wave calibration; and 60, 120, and 180 Hertz noise identification. The desired parameters were in each case the signal's amplitude and the bias.

SINE WAVE CALIBRATION

This signal was assumed to be composed of a sinusoid at the calibration frequency, a bias, and 60 cycle noise:

$$\begin{aligned} y\,(t) = {} & K_1 \sin\,(\omega_c t) + K_2 \cos\,(\omega_c t) \\ & + K_3 \sin\,(\omega_{60} t) \\ & + K_4 \cos\,(\omega_{60}\, t) + K_5 \end{aligned}$$

where ω_c is the calibration frequency and ω_{60} is 120 π radians/sec (60 Hertz). For the sinusoids, both sine and cosine terms are included to accommodate arbitrary phase. This equation, evaluated at some time t, is the m^th^ row of the matrix equation (1):

$$y_m\,(t) = \sum_{i=1,5} A_{m,i}\,(t)\; x_i + \nu\,(t)$$

$$= \underbrace{\begin{bmatrix} \sin\omega_c t & \cos\omega_c t & \sin\omega_{60} t & \cos\omega_{60} t & 1 \end{bmatrix}}_{A} \cdot \underbrace{\begin{bmatrix} K_1 \\ K_2 \\ K_3 \\ K_4 \\ K_5 \end{bmatrix}}_{x} + \nu\,(t)$$

Solution of equation (2) for this model results in the least squares estimate for the five elements of x. The desired values of calibration and 60 cycle amplitudes and the bias are:

Calibration amplitude = $A_c = \sqrt{K_1^2 + K_2^2}$

60 cycle amplitude = $A_{60} = \sqrt{K_3^2 + K_4^2}$

Bias = K_5

SQUARE WAVE CALIBRATION

This analysis presented some initial difficulty in that the calibration signal is not continuous. It was decided to use the Fourier series approximation of a square wave as the model, then to facilitate rapid solution, determine the smallest number of series terms that provided an acceptable solution.

It turned out that the first two non-zero terms were sufficient for an excellent determination of the square wave amplitude and phase. This somewhat surprising result is due to the fact that a good point-by-point approximation to the data is not required; instead, it is only necessary that the model waveform, whatever its character, have as its minimum least square error to the data, parameters related to the desired square wave parameters. Because the Fourier series has as its first term the sinusoid with frequency equal to that of the square wave and hence is of comparable amplitude to the square wave, it and the third term (all even terms are identically zero) are sufficient to define the data. Figure 2 shows a captured square wave signal and its two-term Fourier approximation.

With only a two-term Fourier series representation, it is not necessary to have summations as the elements of A. Instead, the two terms are treated as unrelated components. These, with 60 cycle noise and bias, constitute the model:

$$\begin{aligned} y(t) = {} & K_1 \sin(\omega_c t) + K_2 \cos(\omega_c t) \\ & + K_3 \sin(3\omega_c t) + K_4 \cos(3\omega_c t) \\ & + K_5 \sin(\omega_{60} t) + K_6 \cos(\omega_{60} t) \\ & + K_7 + \nu(t) . \end{aligned}$$

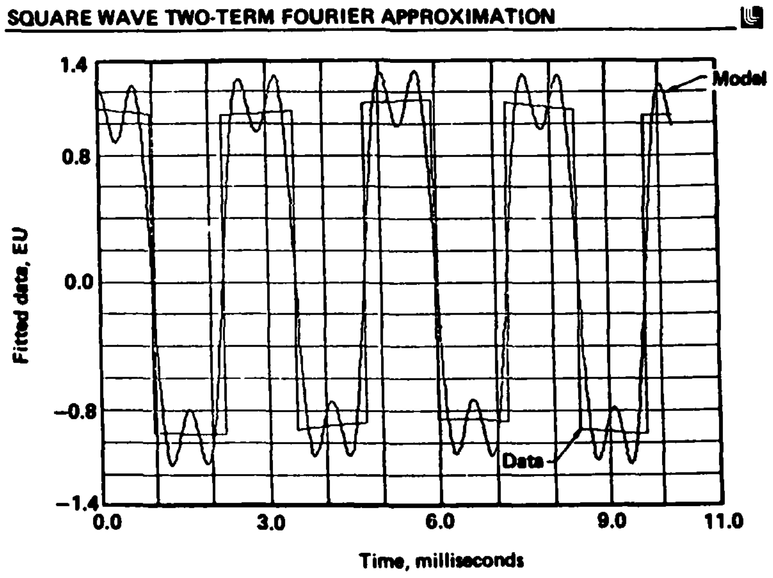

Figure 2 - Two-term Fourier Approximation to a Square Wave Corrupted by 60-cycle Noise

As with the sine wave calibration, A and x are then defined as

$$A = \left[\sin\omega_c t \quad \cos\omega_c t \quad \sin 3\omega_c t \quad \cos 3\omega_c t \quad \sin\omega_{60} t \quad \cos\omega_{60} t \quad 1\right]$$

$$x = \begin{bmatrix} K_1 \\ K_2 \\ K_3 \\ K_4 \\ K_5 \\ K_6 \\ K_7 \end{bmatrix}$$

and the desired values are then

$$A_c = \frac{\pi}{4}\sqrt{K_1^2 + K_2^2}$$

$$= \frac{3\pi}{4}\sqrt{K_3^2 + K_4^2}$$

$$A_{60} = \sqrt{K_5^2 + K_6^2}$$

$$\text{Bias} = K_7 .$$

The factors $\pi/4$ and $3\pi/4$ result from the Fourier coefficients. See, for example, reference 2, page 201.

NOISE IDENTIFICATION (60, 120, AND 180 HERTZ)

This analysis was included to identify the types of noise known to be present in the system. From discussions with facility operators, it was determined that under ordinary circumstances, 60 cycle noise was invariably present with lesser amounts of 120 and 180 Hertz noise also in evidence. A model was designed correspondingly and a calibration signal consisting of a bias of known amplitude B was chosen. The resulting model equation at some time t is

$$y(t) - B = K_1 \sin(\omega_{60} t) + K_2 \cos(\omega_{60} t) + K_3 \sin(\omega_{120} t) + K_4 \cos(\omega_{120} t) + K_5 \sin(\omega_{180} t) + K_6 \cos(\omega_{180} t) + K_7 + \nu(t)$$

where ω_{60} is 120π as before, $\omega_{120} = 240\pi$, and $\omega_{180} = 360\pi$ radians/ sec. The desired values are determined as before:

$$A_{60} = \sqrt{K_1^2 + K_2^2}$$

$$A_{120} = \sqrt{K_3^2 + K_4^2}$$

$$A_{180} = \sqrt{K_5^2 + K_6^2}$$

$$\text{Bias} = K_7 .$$

Program interaction with the operator has been made as self-explanatory as possible. Throughout the execution of a calibration or noise identification analysis, any time a user input is required, an appropriate menu presents the available options.

Figures 3a, 3b, and 3c present representative program menus and result tables. Not shown is the control program menu from which an analysis is initially requested. In it, a choice of calibrating the SCU or DCU is made. This causes entry of the calibration program and branching to the appropriate section. Figure 3a shows the menu resulting from a request for an SCU calibration/noise identification. Selection of item 3, 4, or 5, followed by a channel or a list of channels, causes the generation, capture, and retrieval of the input waveform, conversion to floating point format and scaling to least squares parameter identification, storage of data and results on disc,

```
                    SCU CALIBRATION OPTIONS

        ENTER THE LINE NUMBER OF THE DESIRED OPTION.

        FOR OPTIONS 3 THROUGH 6, IF A LIST OF CHANNELS IS TO BE
        CALIBRATED, TYPE THE MENU NUMBER FOLLOWED BY '0'.

             1.  ALL DONE, RETURN TO MAIN OPTIONS
             2.  CHECK SIGNAL PATCHING
             3.  PERFORM A NOISE IDENTIFICATION (ENTER 3,I)
             4.  PERFORM A SINUSOIDAL CALIBRATION (ENTER 4,I)
             5.  PERFORM A SQUARE WAVE CALIBRATION (ENTER 5,I)
             6.  PERFORM A PULSE CALIBRATION (ENTER 6,I)
             7.  DISPLAY THE SCU TABLE
```

Figure 3a - Main SCU Calibration Menu

```
           NOISE IDENTIFICATION RESULTS (ENGINEERING UNITS)

   CHANNEL        60 HERTZ       120 HERTZ      180 HERTZ      OFFSET

   1 (P1)          0.206          0.117          0.020          0.169
   2 (P2)          0.413          0.241          0.048          0.290
   3 (P3)          0.447          0.258          0.048          0.164
   4 (A1)          0.815          0.507          0.093          0.647
   5 (A2)          0.289          0.182          0.030          0.190
   6 (A3)          0.261          0.167          0.030          0.088

                     NOISE I. D. SUMMARY OPTION LIST

           1.  RETURN TO SCU NOISE I. D. OPTION LIST
           2.  PLOT A CHANNEL'S NOISE I. D. RESULTS (ENTER 3,I)
           3.  TABULATE A CHANNEL'S NOISE I. D. RESULTS (ENTER 3,I)
           4.  SAVE THE NOISE I. D. RESULTS ON TAPE (ENTER 4,I)
           5.  UPDATE A CHANNEL'S SCU TABLE VALUES (ENTER 5,I)
           6.  DISPLAY THE SCU TABLE
```

Figure 3b - Summary Table of a Noise Identification

```
                          SINE WAVE CALIBRATION RESULTS

  SCU             PREDICTED                 CALCULATED               60 CYCLE
CHANNEL    SCALING(EU/V)  OFFSET(EU)     SCALING     OFFSET         EU         DB
 1 (P1)        5.00          0.00          5.38      -0.32         0.01     -38.98
 2 (P2)       10.00          0.00         10.46      -0.57         0.01     -39.07
 3 (P3)       11.00          0.00         11.50      -0.47         0.01     -39.84
 4 (A1)       20.00          0.00         21.53      -1.21         0.02     -35.51
 5 (A2)        7.00          0.00          7.32      -0.38         0.02     -35.92
 6 (A3)        6.50          0.00          6.80      -0.26         0.02     -35.97

                         CALIBRATION SUMMARY OPTION LIST

             1.  RETURN TO SCU CALIBRATION OPTION LIST
             2.  PLOT A CHANNEL'S CALIBRATION RESULTS (ENTER 2,I)
             3.  TABULATE A CHANNEL'S CALIBRATION RESULTS (ENTER 3,I)
             4.  SAVE THE CALIBRATION RESULTS ON TAPE (ENTER 4,I)
             5.  UPDATE A CHANNEL'S SCU TABLE VALUES (ENTER 5,I)
             6.  DISPLAY THE SCU TABLE
```

Figure 3c - Summary Table of a Sine Wave Calibration conversion to engineering units, and presentation of the results to the user. For the dynamic test facility, total elapsed time is about fifteen seconds for six SCU channels or eight DCU channels. The result tables for six-channel noise identification and sine wave calibration are Figures 3b and 3c, respectively.

Figures 4a, 4b, 4c, and 4d show plotted results for sine wave, square wave, and noise identification analyses of artificial data. In each case the data are shown in engineering units e.g., g's for an accelerometer, vs. time. Included in each plot is the captured data, the model data, and the residual, or difference in the two. Note that the calibration models include the 60-cycle noise component but not its 120 and 180 Hertz harmonics; this model inaccuracy is evident in the residual patterns in Figures 4a and 4b. Figure 4c is the same analysis as Figure 4a except there was no 120 and 180 noise present; as expected, the corresponding residual is flat and the scaled data is indistinguishable from the model. Figure 4d, which is a plot of a noise identification and analysis, shows a similarly good fit.

In all the plots shown, the parameters were set to their nominal values:

Calibration Signal A_c = 1.0 volt

Bias = 50.0 milivolts

60 Hertz noise = A_{60} = 50.0 milivolts

120 Hertz noise = A_{120} = 10.0 milivolts

180 Hertz noise = A_{180} = 25.0 milivolts

Known Bias (noise I.D. only) = B = 15.0 milivolts

RESULTS

Evaluation of parameter identifications performed on both artificial and actual calibration data indicate the software written for the dynamic test facility satisfies all foreseeable requirements.

Artificial data, generated within the calibration program, have been used to provide a quantitative measure of the fit quality for various parameter combinations. In particular, the consequences of large disparities in relative parameter size and inexact modelling, specifically unmodelled noise and calibration frequency errors, were documented.

Partial results of these evaluations are presented in Tables 1a and 1b and Figures 5a and 5b. In general, the parameter variation test cases show a degradation in identification accuracy for relatively small parameters, modest in terms of absolute values, though not necessarily in terms of percent error. Estimation errors showed some increase with the addition of unmodelled noise while a complete loss of identifying capability resulted from the introduction of errors in the calibration signal frequency.

In Table 1a, the desired parameters for sine and square wave calibrations were successively set to 1/10, 1, and 10 times their nominal values and the percent errors in the resulting solutions were tabulated. For each input parameter combination, identification was performed first with only the selected parameters contributing to the signal (rows preceded by "a") and then with the data corrupted by unmodelled contributions of the nominal values of 120 and 180 Hertz noise (rows preceded by "b").

For the sine wave analysis it can be seen that with no 120 and 180 Hertz noise, identification is accurate to better than 0.005% (0.00 in the table) for the calibration signal amplitude. The corresponding bias estimates were accurate to 0.04% except one error of 0.28% for a bias value 1/2000 as large as the signal amplitude. Introduction of the unmodelled noise degraded these results somewhat but errors are still within 0.01% for the amplitude and 0.16% for bias, except for two cases where bias is 1/10 its nominal value (1.28% and 1.53%). It should be noted that results will vary with the computer being used. These values are for the MODCOMP IV with 48-bit floating point representation.

For the square wave analysis a similar pattern is seen. Errors in this case are typically an order of magnitude greater than for the sine wave analysis, presumably reflecting the inexact Fourier approximation.

Table 1b presents a similar error profile for the noise identification.

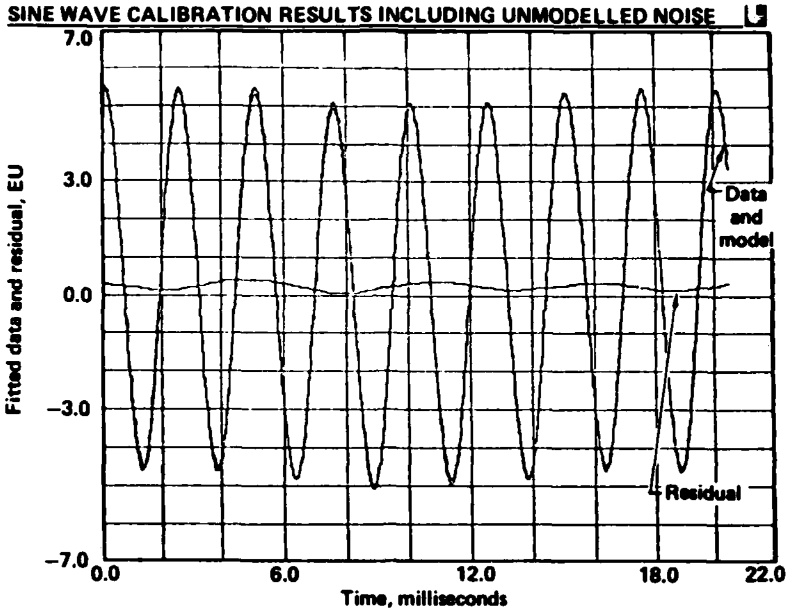

SINE WAVE CALIBRATION RESULTS INCLUDING UNMODELLED NOISE

Figure 4a - Sine Wave Calibration Including Unmodelled 120, 180 Hertz Noise
Data, Model, and Residual

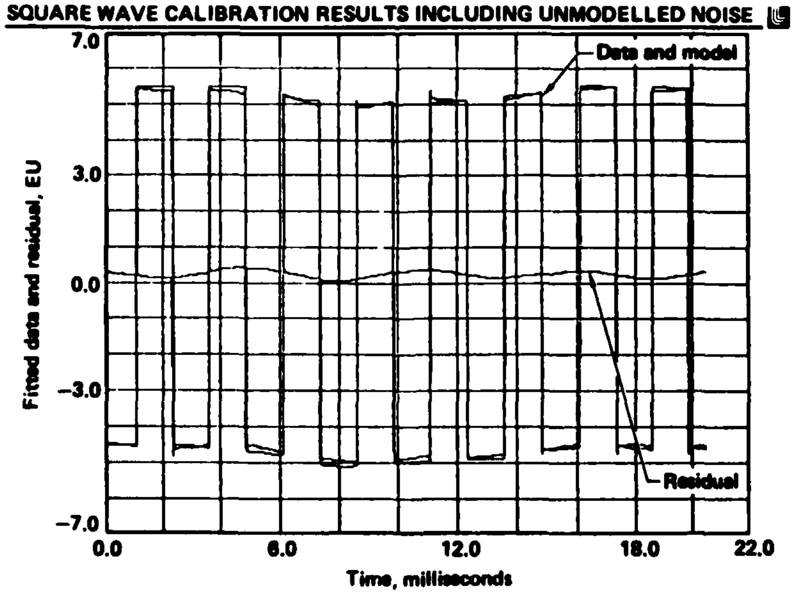

SQUARE WAVE CALIBRATION RESULTS INCLUDING UNMODELLED NOISE

Figure 4b - Square Wave Calibration Including Unmodelled 120, 180 Hertz Noise
Data, Model, and Residual

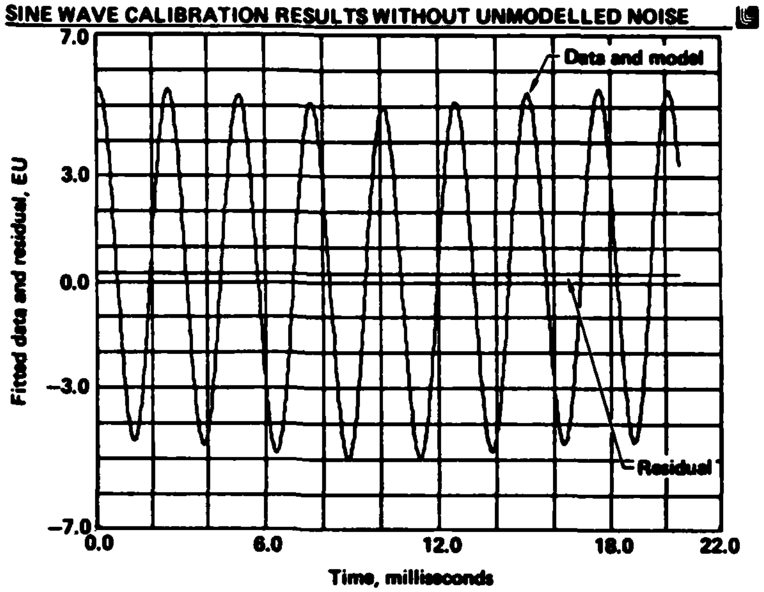

Figure 4c - Sine Wave Calibration with No Unmodelled 120, 180 Hertz Noise
Data, Model, and Residual

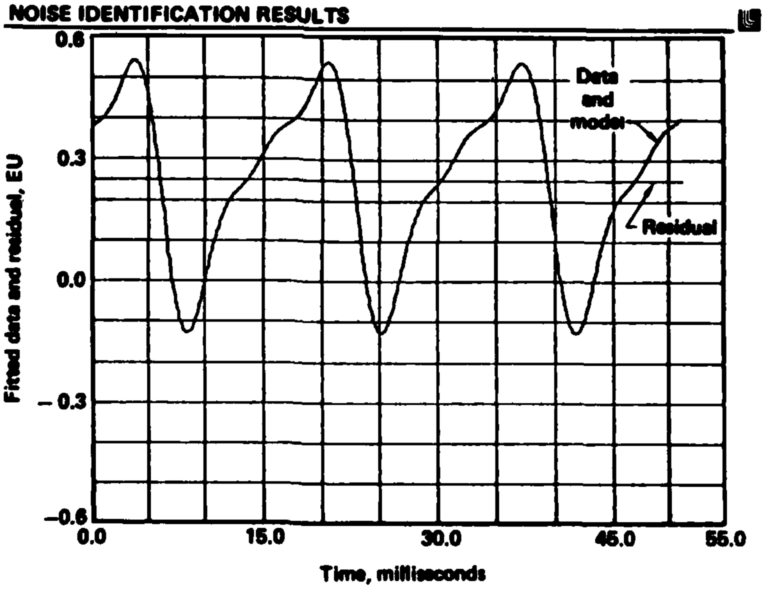

Figure 4d - 60, 120, and 180 Hertz Noise Identification
Data, Model, and Residual

Nominal Input Values: Calibration Signal Amplitude Amp = 1.0 volt
Bias = 50.0 milivolts
60-cycle Noise Amplitude A60 = 50.0 milivolts

Actual Values				Calibration Solution Percent Error					
Amp (v)	Bias (mv)	A60 (mv)		Sine Wave			Square Wave		
				Amplitude	Bias	60-cycle	Amplitude	Bias	60-cycle
1.0	50.0	50.0	(Nominal) (a)	0.00	0.01	0.00	0.13	0.01	0.41
			(b)	0.01	0.14	0.48	0.13	0.13	0.88
1.0	5.0	50.0	(Bias Varied) (a)	0.00	0.04	0.00	0.13	0.03	0.41
			(b)	0.01	1.28	0.48	0.13	1.22	0.89
1.0	500.0	50.0	(a)	0.00	0.01	0.01	0.13	0.01	0.41
			(b)	0.01	0.02	0.48	0.13	0.02	0.88
1.0	50.0	5.0	(A60 Varied) (a)	0.00	0.01	0.03	0.13	0.01	3.32
			(b)	0.01	0.14	4.74	0.13	0.13	7.70
1.0	50.0	500.0	(a)	0.00	0.01	0.00	0.13	0.00	0.04
			(b)	0.01	0.14	0.05	0.13	0.13	0.09
0.10	50.0	50.0	(Amp Varied) (a)	0.00	0.01	0.00	0.13	0.01	0.04
			(b)	0.08	0.13	0.48	0.07	0.13	0.52
10.0	50.0	50.0	(a)	0.00	0.04	0.03	0.13	0.03	3.32
			(b)	0.06	0.16	0.45	0.13	0.10	3.76
0.10	500.0	50.0	(Minimum/ Maximum Values of Amp and Bias) (a)	0.00	0.01	0.00	0.13	0.01	0.04
			(b)	0.08	0.02	0.48	0.07	0.02	0.52
10.0	5.0	50.0	(a)	0.00	0.28	0.03	0.13	0.33	3.32
			(b)	0.00	1.53	0.45	0.13	0.92	3.76

Table 1A - Evaluation of Fit Quality - Sine and Square Wave Calibrations

In this case all expected sources of error are intrinsically included so there is only one solution for each input parameter combination. In all cases, errors are very small, consistently equal to 0.01% for the bias and better than 0.005% (0.00% in the table) for the various noise amplitudes except for a 0.02% error when the smallest component, 120 Hertz, was entered at 1/10 times its nominal value.

The error values and patterns shown in Tables 1a and 1b verify predictions that the minimum identification errors occur when the model includes all non-negligible terms and when the parameters are nearly equal in size. For the constituents present in the data acquisition system at Building 854, it appears that calibrations performed on channels with nearly nominal signals will identify the channel scaling and offset to better than 0.15%. In general, parameter identifications of similar constituents can be expected to be accurate to considerably better than 0.5%, and more like 0.1%, if the parameters are within an order of magnitude of each other. Relative amplitude disparities of up to three orders

Nominal Input Values: Bias = 50.0 milivolts
60 Cycle = 50.0 milivolts
120 Cycle = 10.0 milivolts
180 Cycle = 25.0 milivolts

Actual Values				Noise I.D. Solution Percent Error			
Bias mv)	60 Cycle (mv)	120 Cycle (mv)	180 Cycle (mv)	Bias	60 Cycle	120 Cycle	180 Cycle
50.0	50.0	10.0	25.0	0.01	0.00	0.00	0.00
50.0	50.0	10.0	2.5	0.01	0.00	0.00	0.00
50.0	50.0	10.0	250.0	0.01	0.00	0.00	0.00
50.0	50.0	1.0	25.0	0.01	0.00	0.02	0.00
50.0	50.0	100.0	25.0	0.01	0.00	0.00	0.00
50.0	5.0	10.0	25.0	0.01	0.00	0.00	0.00
50.0	500.0	10.0	25.0	0.01	0.00	0.00	0.00
5.0	50.0	10.0	25.0	0.01	0.00	0.00	0.00
50.0	50.0	10.0	25.0	0.01	0.00	0.00	0.00

Table 1B - Evaluation of Fit Quality - Noise Identification

of magnitude and the presence of modest unmodelled data corruption can be expected to increase these errors to a couple percent at worst.

As mentioned in the Software Description, a significant reduction in errors attributable to grossly different parameter magnitudes can be achieved by using the results of a first analysis to provide parameter estimates for a second pass. The parameters to be solved for would then be corrections to these estimates, and would presumably be comparable in size. Similarly, errors due to unmodelled components can be reduced by expanding the model to include them automatically, if possible noise sources are known, or as an iterative procedure for the operator if they are not. The likelihood of improving the identification by modifying the model would be apparent from the presence of a pattern in the residuals (differences between the data and the model) while the value of the residual standard deviation would indicate if improved identification results were necessary. In this way, the simplest and hence fastest algorithm would be used in the calibration.

Examination of the artificial data results indicates these error reduction techniques are not necessary for the dynamic test facility. In that system the SCU digitizes the signal with 12 bits corresponding to a ± 10-volt analog input. This results in a quantization level of 2.5 milivolts which is 0.25% and 5.0% of the nominal values for calibration signal amplitude and bias respectively. As can be seen, all errors in Tables 1a and 1b fall below this quantization level and therefore do not influence the parameter identification. Consequently, the recommended identification improvements have not been implemented and their effectiveness is not documented in this paper.

Figures 5a and 5b show a far more serious threat to the successful use of this technique for data channel calibration. In these plots, percent errors in identification of the calibration signal amplitude are plotted vs. unmodelled variations in the nominal calibration signal frequency. As can be seen, very small excursions about the nominal input frequency result in massive identification errors. For the test case shown, an error of three Hertz, or less than 1% of the

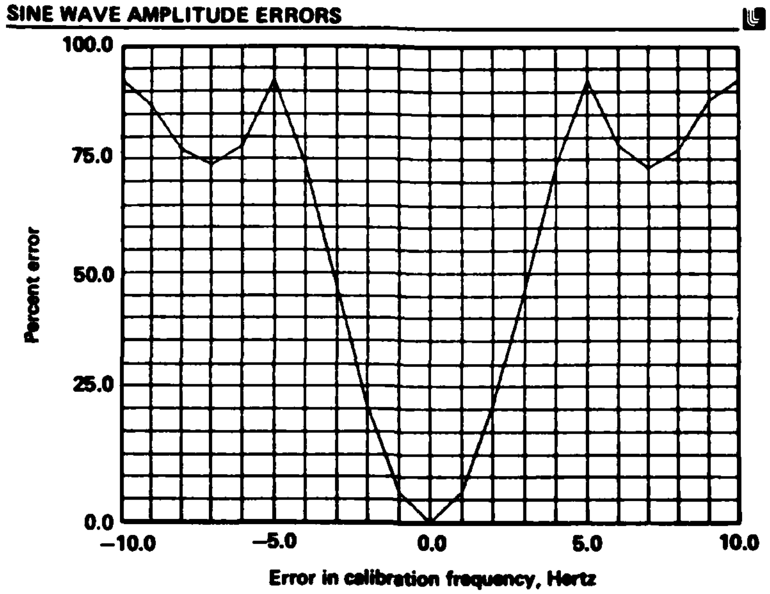

Figure 5a - Sine Wave Amplitude Identification Errors Due to Unmodelled Calibration Frequency Errors

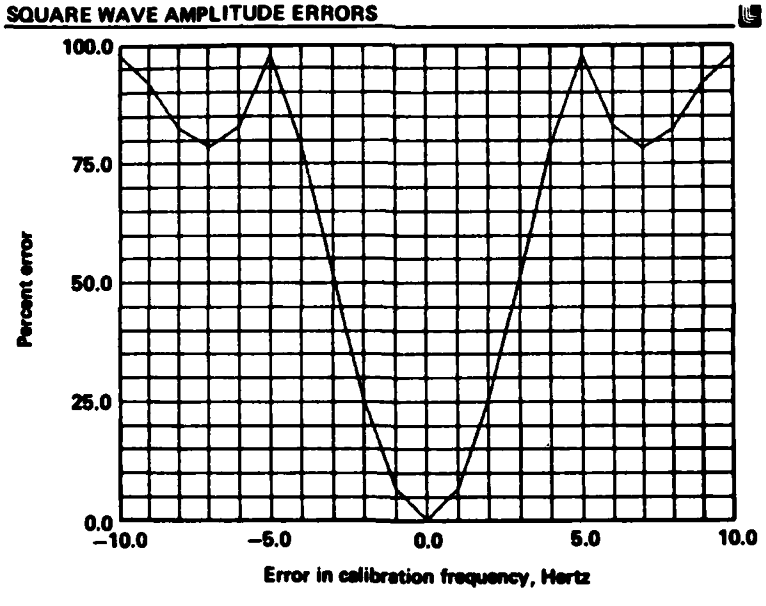

Figure 5b - Square Wave Amplitude Identification Errors Due to Unmodelled Calibration Frequency Errors nominal value of 400 Hertz, was sufficient to cause a 50% error in amplitude identification for both sine and square wave analyses.

The implication of this strong dependence on a known calibration frequency is that the calibration signal must be generated digitally or with only the most reliable analog equipment. In the application at the dynamic test facility, all calibrations are generated digitally by the CBU so no significant frequency error appears. Noise identification is similarly unimpaired as 60-cycle noise and its harmonics can be confidently modelled.

CONCLUSIONS

For a limited class of data analysis problems, the weighted least squares estimation technique offers an accurate and easily-implemented method of solution. Applied to digital data that can be analytically modelled such that the nature of the modelled constituents is known precisely, and the modelled portion of the data is dominant, this technique can identify the magnitude and phase (if appropriate) of each constituent to accuracies considerably better than 1%.

Modelled constituents need not be continuous, periodic, or linear with respect to the independent variable (usually, but not necessarily time). What is necessary is that the data be modelled such that all parameters to be solved for appear linearly in the model equation.

Implementing the equations and arriving at a solution for an arbitrary set of data is straightforward. Solution time depends weakly on the number of data and strongly on the number of model parameters. Iterative solutions, with or without an operator in the loop, are effective in reducing errors caused by inadequate compliance with the above criteria.

A program that applies this weighted least squares technique to evaluate the results of an automatic calibration and noise identification at Lawrence Livermore Laboratory's dynamic test facility has been written and installed on the facility's computer. Evaluations of the program's performance show that for the current and expected signal types (bias, sine wave, square wave), the program, without iterative correction, identifies the desired parameters as accurately as the analog-to-digital quantization allows. These results, achieved with fast execution times, satisfy all calibration requirements at building 854 and indicate this method will be considered in any future data analysis tasks of an appropriate nature.

APPENDIX I

Derivation of the Simplified Weighted Least Squares Parameter Estimation Technique [1]

Given a set of system measurements formulated as an n-component vector y and containing errors ν, if these measurements can be adequately expressed as the matrix product of a known model A (n x p) and an unknown p-component state vector x,

$$y = Ax + \nu , \qquad (A1)$$

then the weighted least squares estimate of x can be found using standard optimal control techniques. If the state vector is defined so as to correspond to physically meaningful parameters, solution for this fitted state vector can provide the precise characteristics of each component of a data signal.

This appendix derives the equation defining the desired state vector estimate including the simplifying assumptions that give this method its value as a fast and easily-realized identification technique. Basic to the method is the assumption that the degree of uncertainty in an initial estimate of the state and in the measurements is known. Specifically, it is assumed that the covariance matrices of x and y are known, where the expected values of x and y are, respectively, the prior state estimate and the model Ax. A cost function is defined such that its value is increased by any variation in the state from that provided in the prior estimate and from that which yields modelled data equal to the measurements. The value of the state that minimizes this cost function is the desired least squares state estimate.

In equation A1, if the measurement bias is included in the model, then if the model error is uncorrelated with time, the expected value of the error, $E(y - Ax) = E(\nu)$, is identically zero. Assuming that the magnitude of the error can be estimated, the (n x n) covariance matrix, R, is

$$E\left[(y - Ax)(y - Ax)^T\right] = E(\nu\nu^T) \doteq R .$$

Similarly, if there is an expected value (prior estimate) of the state, x, then assuming that the magnitude of the deviations of the state from this prior estimate can be estimated, the (p x p) covariance matrix, M, is

$$E\left[(x - \bar{x})(x - \bar{x})^T\right] \doteq M .$$

If a quadratic cost function is defined such that errors in the state (calculated with respect to the prior estimate), and errors in the model increase its value in proportion to known weighting matrices, the state vector that minimizes this cost function is that which minimizes deviations of the model from the data subject to the state's expected value.

Including a factor of 1/2 for algebraic convenience, the cost function, J, is

$$J = \frac{1}{2}\left[(x - \bar{x})^T K_1 (x - \bar{x}) + (y - Ax)^T K_2 (y - Ax)\right] , \quad (A2)$$

where K_1 and K_2 are the weighting matrices. As the construction of any cost function is necessarily arbitrary, the only constraint on the choice of K_1 and K_2 is that they logically reflect the analyst's relative confidence in the validity of the prior estimate x and the noise-corrupted measurements y. If K_1 and K_2 are chosen to be M^{-1} and R^{-1} respectively, the resulting weighted least squares estimate is identical to the conditional expected value estimate assuming Gaussian distributions of x and ν and to the maximum likelihood or minimum variance estimate. Choice of the inverse of the covariances of $(x - \bar{x})$ and $(y - Ax)$ to be the weighting matrices for the $(x - \bar{x})$ and $(y - Ax)$ quadratic terms in J is appealing as a very natural way to include the analyst's knowledge of the state and the measurement.

The equation for J is then

$$J = \frac{1}{2}\left[(x - \bar{x})^T M^{-1} (x - \bar{x}) + (y - Ax)^T \cdot R^{-1} (y - Ax)\right] . \quad (A3)$$

It is clear that an extremum of J will occur when the differential of J is zero for arbitrary variations of the state. Differentiating J yields

$$\partial J = \partial x^T \left[M^{-1} (x - \bar{x}) - A^T R^{-1} (y - Ax)\right].$$

If the value of the state that sends ∂J to zero is defined as $\hat{x}$, then the necessary condition is

$$M^{-1} (\hat{x} - \bar{x}) = A^T R^{-1} (y - A\hat{x})$$

or

$$(M^{-1} + A^T R^{-1} A)\, \hat{x} = M^{-1} \bar{x} + A^T R^{-1} y .$$

Solving this for $\hat{x}$,

$$\hat{x} = \bar{x} + (M^{-1} + A^T R^{-1} A)^{-1} \cdot A^T R^{-1} (y - A\bar{x}) \quad (A4)$$

which is the desired general expression for the weighted least squares state estimate.

A considerably simpler expression for $\hat{x}$ can be written if the following assumptions are made:

No prior estimate exists for x .

This assumption means that M must be considered arbitrarily large, reflecting no confidence in the state's expected value and consequently, M^{-1} is arbitrarily small.

The error is random and independent of the state.

This implies that the error at one time is uncorrelated with that at any other time. As a result, the covariance of the measurement is diagonal with constant elements.

Summarizing the effects of these assumptions:

$$M = \infty \rightarrow M^{-1} = 0$$

$$E\left[(y - Ax)(y - Ax)^T\right] = R = \gamma I$$

where γ is a known constant and 0 and I are properly-dimensioned Zero and Identity matrices.

Applying these assumptions reduces equation (A4) to

$$\hat{x} = x - \left[\frac{1}{\gamma}\left(A^T A\right)^{-1} \cdot \gamma \left(A^T A\right)\right] \bar{x} + \left[\frac{1}{\gamma}\left(A^T A\right)^{-1} \cdot \gamma A^T\right] y$$

or

$$\hat{x} = \left(A^T A\right)^{-1} A^T y , \qquad (A5)$$

which is the expression for the state estimate (parameters) used in the automatic calibration and noise identification program implemented at the dynamic test facility.

REFERENCES

1. A. Bryson and Y. Ho. Applied Optimal Control. Waltham, Massachusetts: Ginn and Company, 1969, Chapter 12.
2. C. R. Wylie, Jr. Advanced Engineering Mathematics. New York, New York: McGraw-Hill Book Company, 1966, Chapter 6.

DISCUSSION

Mr. Piersol (Bolt Beranekand Newman Inc.): You said there was a difficulty some times in inverting the A transpose A matrix. I assume it was because of the singularity. Is the singularity caused by the fact that you have hypothesized two signals that are closing in frequency and that go singular when they reach the same frequency?

Mr. Nesbit: Yes. You will find rows that are very similar and when you invert the matrix you get tremendous values. That can be circumvented also by not inverting but by bringing them to the other side of the equation.

STATISTICAL ESTIMATION OF SIMULATED YIELD AND OVERPRESSURE

Paul F. Mlakar and Robert E. Walker
U.S. Army Engineer Waterways Experiment Station
Vicksburg, Mississippi

Estimates of the nuclear weapon yield and overpressure which most closely correspond to the overpressure history observed in an airblast simulation are found using the principle of least squares. Point estimates of these nonlinear parameters are computed with an algorithm based on search by golden section. Approximate confidence intervals are then estimated using a Taylor series expansion about these point estimates. This estimation technique is verified by a Monte Carlo simulation of observed overpressure histories. Thereafter, estimates are calculated for actual simulations of assorted yields and overpressures obtained by various experimental techniques.

INTRODUCTION

A variety of experimental methods have been used to simulate the airblast loading of nuclear weapons on structures. A hypothetical overpressure as a function of time $p'(t)$ measured in one of these simulations is illustrated in Fig. 1a. This function is not identically equal to any nuclear weapons effects model of the overpressure function $p(t;W,p_o)$ for any values of the yield W and peak overpressure p_o parameters due to the scatter inherent in obtaining this measurement and because of peculiarities associated with the particular simulation technique employed. Nonetheless, the experimenter is often required to estimate a yield and a peak overpressure which most closely describe the results of his simulation. Herein, least squares point estimates are calculated for these parameters along with confidence interval estimates which quantify the experimenter's degree of belief in these point estimates.

STATISTICAL ANALYSIS

Suppose that n observations (p_i', t_i) of overpressure as a function of time are available from an experimental simulation. It is assumed that these observations are such that

$$\ln p_i' = \ln p(t_i;W,p_o) + \epsilon_i \qquad i = 1,\ldots n \tag{1}$$

In this equation the overpressure (psi) as a function of time (msec) for the surface burst of yield W (kt) at the range r (kft) corresponding to the peak overpressure $p_o = p(t_a)$ is modeled by [3] to be

$$p(t;W,p_o) = \left(\frac{1483\ m}{0.0135\ m + t}\right)$$
$$\left[0.417 + 0.583\left(\frac{t_a}{t}\right)^6\left(\frac{40\left(\frac{t_a}{t}\right)^6 + \left(\frac{t_a}{m}\right)}{40 + \left(\frac{t_a}{m}\right)^2}\right)^2\right]$$
$$\left(1 - \frac{t-t_a}{D_p^+}\right)\left(\frac{m^2 + 0.6715\ mt + 0.00481\ t^2}{m^2 + 1.8836\ mt + 0.02161\ t^2}\right) \tag{2}$$

in which $m = (2W)^{1/3}$, the positive phase duration is

$$D_p^+ = m\,\frac{(820350m^2 + 15515mt_a + 330.3t_a^2)}{(6854m^2 + 491.9mt_a + t_a^2)} \tag{3}$$

and the time of arrival is

$$t_a = (0.54291m^3 - 21.185rm^2 + 361.8r^2m$$
$$+ 2383r^3)/(m^2 + 2.048rm + 2.6872r^2) \tag{4}$$

The ϵ_i in Eq. (1) represent the scatter in overpressure observations and are assumed to be a series of n normally distributed, independent random variables with zero means and common variance σ^2. These assumptions imply that the standard deviation of each overpressure observation is proportional to its mean value. This implication will be

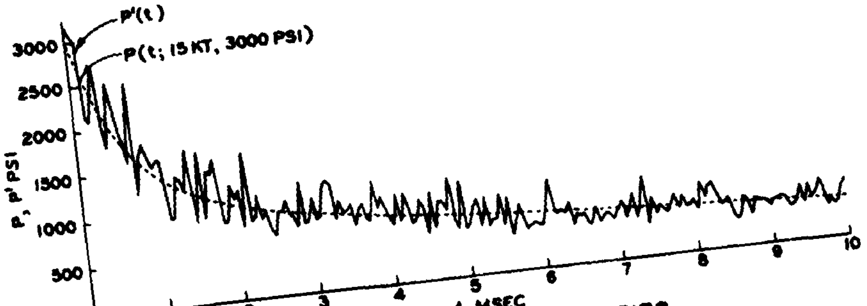

a. OVERPRESSURE HISTORIES

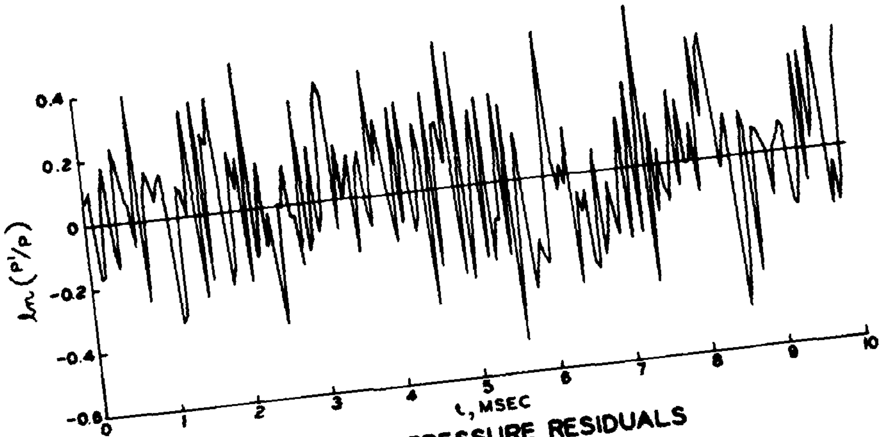

b. OVERPRESSURE RESIDUALS

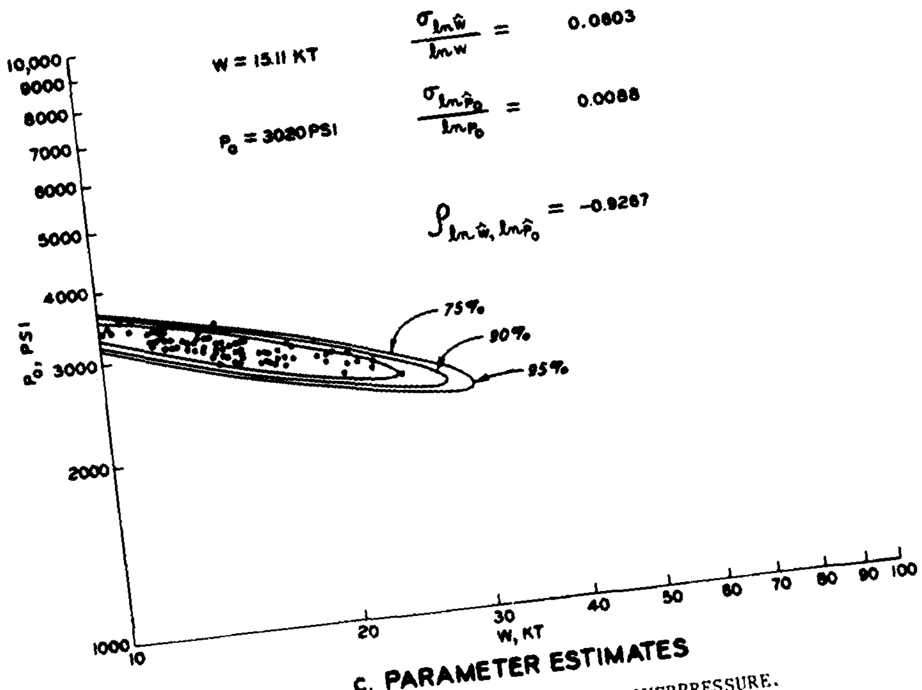

c. PARAMETER ESTIMATES

FIGURE 1. NUMERICAL SIMULATION OF OVERPRESSURE.

subsequently examined for actual data obtained in various experiments.

Under these conditions, by choosing point estimators of yield $\hat{W}$ and overpressure $\hat{p}_o$ to be those values which minimize the sum of the squared differences between the observed and model values of the logarithm of overpressure

$$\Phi(W,p_o) = \sum_{i=1}^{n} (\ell n\, p_i' - \ell n p(t_i;W,p_o))^2 \qquad (5)$$

these estimators are also the maximum likelihood estimators of the yield and overpressure [4]. Because of the form of the overpressure model in Eqs. (2) through (4), differentiation of the error sum of squares Φ leads to a pair of simultaneous normal equations which are nonlinear in the estimators $\hat{W}$ and $\hat{p}_o$. Only limited success was achieved in solving these equations using linearization, steepest descent or a hybrid approach [9]. Eventually, an elimination technique for directly minimizing the error sum of squares was devised which efficiently converged to the values of the point estimators for a variety of actual experimental data. In this scheme, the optimum Φ is found by minimizing with respect to W the minimum value of Φ with respect to p_o for a given W. Both of these single variable optimizations are accomplished in turn through a golden section search [10].

Once these point estimates of yield and peak overpressure have been calculated, it is desirable to compute confidence intervals to emphasize that these values are not known precisely and to quantify the magnitude of this uncertainty. Unfortunately, the distribution properties for the overpressure model of Eqs. (2) through (4) required to compute exact confidence regions are not known. However, the Taylor series expansion of $\ell n p(t;W,p_o)$ about the point estimates $\ell n\hat{W}$ and $\ell n\hat{p}_o$ can be truncated after the first order terms to obtain an approximate overpressure model which is linear in the estimators $\ell n\hat{W}$ and $\ell n\hat{p}_o$. It follows that $\ell n\hat{W}$ and $\ell n\hat{p}_o$ are jointly normally distributed and that the statistic

$$\frac{1}{(1-\rho^2_{\ell n\hat{W},\ell n\hat{p}_o})}\left[\left(\frac{\ell n\hat{W}-\ell nW}{\sigma_{\ell n\hat{W}}}\right)^2 - 2\rho_{\ell n\hat{W},\ell n\hat{p}_o}\left(\frac{\ell n\hat{W}-\ell nW}{\sigma_{\ell n\hat{W}}}\right)\left(\frac{\ell n\hat{p}_o-\ell n p_o}{\sigma_{\ell n\hat{p}_o}}\right) + \left(\frac{\ell n\hat{p}_o-\ell n p_o}{\sigma_{\ell n\hat{p}_o}}\right)^2\right] = \chi^2_2 \qquad (6)$$

is chi-square distributed with 2 degrees of freedom where the variances and correlation coefficient of the estimators are given by

$$\sigma^2_{\ell n\hat{W}} = \frac{\sigma^2}{\Delta}\sum_{i=1}^{n}\left(\frac{\partial\ell n p(t_i)}{\partial\ell n\hat{p}_o}\right)^2 \qquad (7)$$

$$\sigma^2_{\ell n\hat{p}_o} = \frac{\sigma^2}{\Delta}\sum_{i=1}^{n}\left(\frac{\partial\ell n p(t_i)}{\partial\ell n\hat{W}}\right)^2 \qquad (8)$$

$$\rho_{\ell n\hat{W},\ell n\hat{p}_o}\cdot\sigma_{\ell n\hat{W}}\cdot\sigma_{\ell n\hat{p}_o} = -\frac{\sigma^2}{\Delta}\sum_{i=1}^{n}\left(\frac{\partial\ell n p(t_i)}{\partial\ell n\hat{p}_o}\right)\left(\frac{\ell n p(t_i)}{\partial\ell n\hat{W}}\right) \qquad (9)$$

with

$$\Delta = \sum_{i=1}^{n}\left(\frac{\partial\ell n p(t_i)}{\partial\ell n\hat{p}_o}\right)^2\cdot\sum_{i=1}^{n}\left(\frac{\partial\ell n p(t_i)}{\partial\ell n\hat{W}}\right)^2 - \left[\sum_{i=1}^{n}\left(\frac{\partial p(t_i)}{\partial\ell n\hat{p}_o}\right)\left(\frac{\partial p(t_i)}{\partial\ell n\hat{W}}\right)\right]^2 \qquad (10)$$

Further, the exact $(1-\alpha)$ confidence region for this approximate model is given by [4]

$$\frac{1}{2\,(1-r^2_{\ell n\hat{W},\ell n\hat{p}})}\left[\left(\frac{\ell n\hat{W}-\ell nW}{s_{\ell n\hat{W}}}\right)^2 - 2r_{\ell n\hat{W},\ell n\hat{p}_o}\left(\frac{\ell n\hat{W}-\ell nW}{s_{\ell n\hat{W}}}\right)\left(\frac{\ell n\hat{p}_o-\ell n p_o}{s_{\ell n\hat{p}_o}}\right) + \left(\frac{\ell n\hat{p}_o-\ell n p_o}{s_{\ell n\hat{p}_o}}\right)^2\right] \leq v_{1-\alpha}(2,n-2) \qquad (11)$$

where $v_{1-\alpha}(2,n-2)$ is the upper $(1-\alpha)$ point of the variance ratio distribution for 2 and $(n-2)$ degrees of freedom and where the variances and correlation coefficient of the estimators are themselves estimated from the standard error of estimate

$$s = \sqrt{\frac{\min\Phi}{n-2}} \qquad (12)$$

using

$$s^2_{\ell n\hat{W}} = \frac{s^2}{\Delta}\sum_{i=1}^{n}\left(\frac{\partial\ell n p(t_i)}{\partial\ell n\hat{p}_o}\right)^2 \qquad (13)$$

$$s^2_{\ell n\hat{p}_o} = \frac{s^2}{\Delta}\sum_{i=1}^{n}\left(\frac{\partial\ell n p(t_i)}{\partial\ell n\hat{W}}\right)^2 \qquad (14)$$

$$r_{\ell n\hat{W},\ell n\hat{p}_o} s_{\ell n\hat{W}} s_{\ell n\hat{p}_o}$$

$$= -\frac{s^2}{\Delta}\sum_{i=1}^{n}\left(\frac{\partial \ell np(t_i)}{\partial \ell n\hat{p}_o}\right)\left(\frac{\partial \ell np(t_i)}{\partial \ell n\hat{W}}\right) \qquad (15)$$

Note that the variance of each estimator depends on the underlying scatter in the observations through σ^2 and also on the sensitivity of the overpressure model to each parameter through the derivatives of overpressure with respect to the parameters. In actual computations, it has been convenient to evaluate these derivatives from first order finite difference expressions.

NUMBERICAL VERIFICATION

Before applying the foregoing estimation technique to actual experimental data, it is instructive to examine the validity of the linearization used to calculate the confidence regions. This was accomplished by a Monte Carlo simulation of the scatter in the observation of overpressure at 3000 psi for a 15-kt surface burst as shown in Fig. 1. In this numerical experiment, the model overpressure was first computed from Eqs. (2) through (4) at each of $n = 201$ times equally spaced between t_a and $t_a + 10$ msec. Values of the ε_i for $\sigma = 0.2$ were next obtained using the uniform pseudo-random number generator RANDX [7] and a coordinate transformation [2]. Then, the artificial overpressure observations p_i' were determined in accordance with Eq. (1). Fig. 1a illustrates the overpressures $p(t)$ and $p'(t)$ while the corresponding ε_i are shown in Fig. 1b. Subsequently, the point estimates of yield and peak overpressure which minimized Eq. (5) were found through the search by golden section previously described. This entire process was then repeated until 100 such overpressure histories were generated and their parameters so estimated.

The sample means of these estimates were a yield of 15.11 kt and a peak overpressure of 3020 psi which are reassuringly near the model values selected for these simulations. The distribution of these estimates is compared to the confidence contours corresponding to Eq. (6) in Fig. 1c. The coefficients of variation tabulated in this figure imply that the peak overpressure is estimated with less uncertainty than is the yield. The coefficient of correlation denotes a very strong negative linear relation between $\ell n\hat{W}$ and $\ell n\hat{p}_o$ in this numerical simulation. The accuracy of the linearization introduced to compute these confidence intervals can be assessed by comparing the cumulative distribution function of Eq. (6) for this sample of 100 simulations to that of χ_2^2. A Kolmogorow-Smirnov goodness-of-fit test [6] indicates that these functions are significantly different only at the $\alpha = 0.79$ level. In other words, for the hypothetical model overpressure and observation scatter combinations, nonlinearities in the overpressure model do not increase the scatter beyond that which is exceeded with probability $\alpha = 0.79$. This estimation technique should be similarly applicable to actual data involving comparable combinations of overpressure and scatter and not significantly violating the assumption of Eq. (1).

EXPERIMENTAL APPLICATIONS

Having thus validated the estimation techniques with a numerical simulation, example applications of this technique to actual experimental data will now be presented. These examples span a wide range of yields and peak overpressures and also involve a variety of simulation methods.

The first application is an overpressure which was simulated in the MISERS BLUFF (II - 1) test by the surface detonation of 120 tons of ammonium nitrate and fuel oil [1]. Fig. 2a shows the overpressure history which was recorded on the middle of the span of one scale model of a continuous steel girder bridge in this simulation. The yield and peak overpressure corresponding to this history were estimated by performing the least squares fit of Eq. (5) to 1619 equally-spaced data points in the first 90 msec after the arrival of the blast overpressure. The overpressure history corresponding to these point estimates is shown in Fig. 2a while the residuals of this fit appear in Fig. 2b. These residuals ε_i do not seriously violate the assumption that they are independently, normally distributed with a common variance. Thus, the confidence regions drawn in Fig. 2c from Eq. (11) should be meaningful measures of the uncertainty in the point estimates of yield and peak overpressure. The low coefficients of variation given in this figure indicate a high degree of confidence in these estimates while the coefficient of correlation indicates a strong positive linear relation between $\ell n\hat{W}$ and $\ell n\hat{p}_o$.

The next application of the estimation technique is shown in Fig. 3. This overpressure history was recently recorded at the ground surface in the test of a shallow-buried protective shelter by a foam and high-explosive simulation technique [5]. The surface burst parameters were estimated as described previously using 1001 equally-spaced data points in the 10 msec duration shown. The residuals of this estimation appear to satisfy Eq. (1) except for a slight correlation during the first 5 msec due to overpressure reflections from the foam cavity employed in this simulation technique. The confidence regions computed from these residuals connote a high degree of certainty in the estimated yield, an even higher degree of certainty in the estimated peak overpressure, and a very strong negative linear relation between $\ell n\hat{W}$ and $\ell n\hat{p}_o$

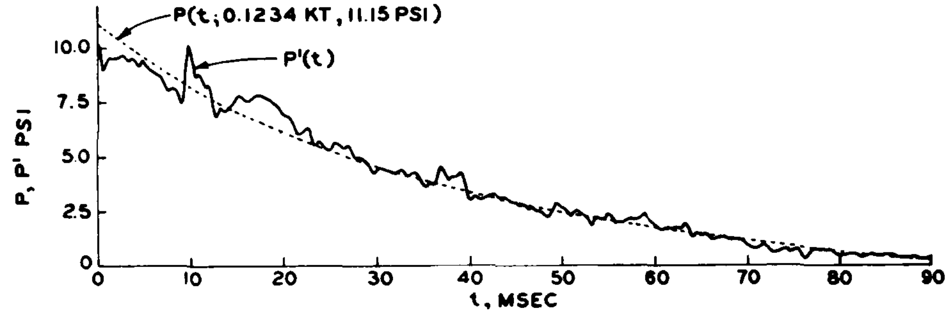

a. OVERPRESSURE HISTORIES

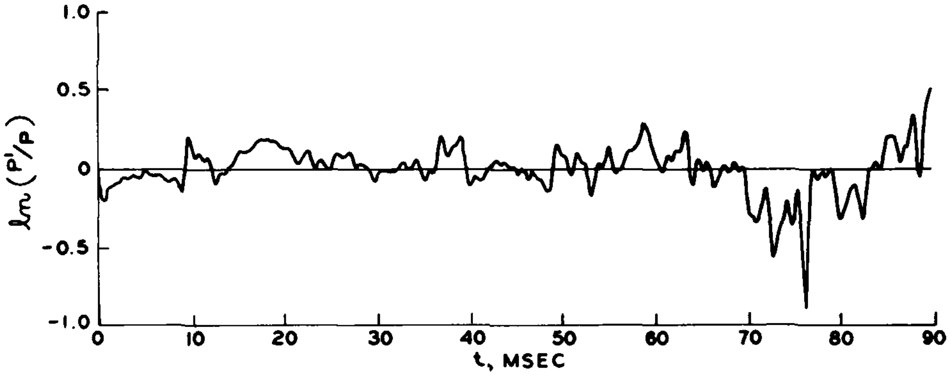

b. OVERPRESSURE RESIDUALS

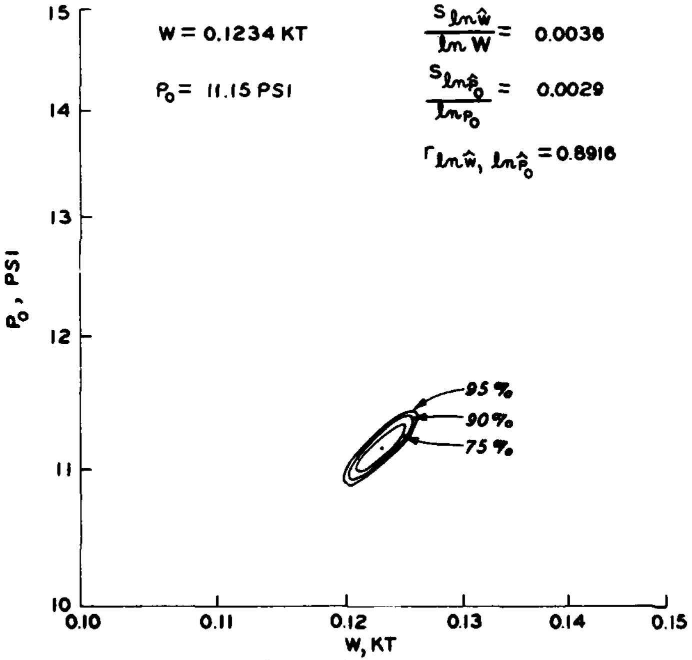

c. PARAMETER ESTIMATES

FIGURE 2. SIMULATION OF OVERPRESSURE BY AMMONIUM-NITRATE AND FUEL OIL.

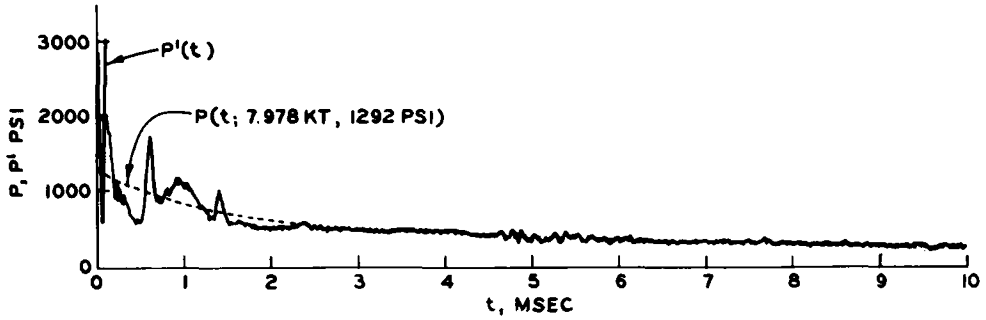

a. OVERPRESSURE HISTORIES

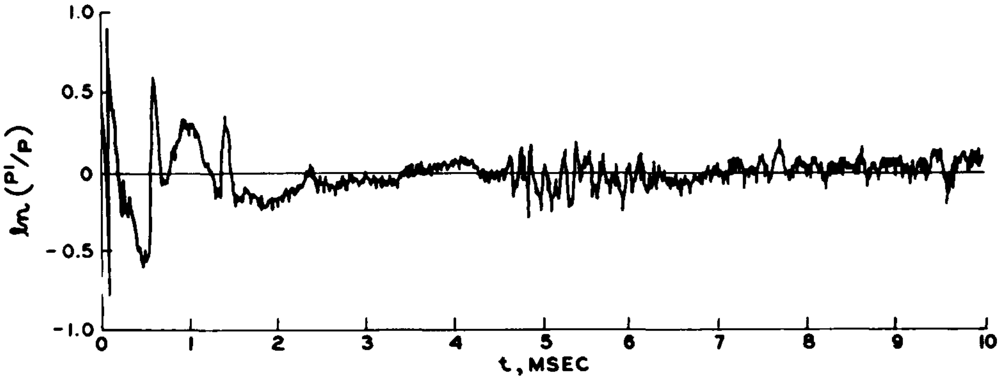

b. OVERPRESSURE RESIDUALS

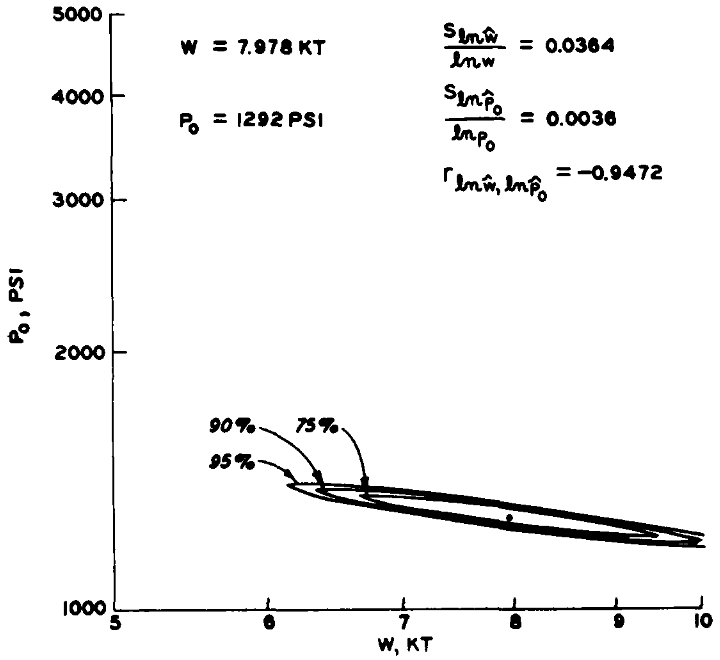

c. PARAMETER ESTIMATES

FIGURE 3. SIMULATION OF OVERPRESSURE BY FOAM AND HIGH EXPLOSIVE.

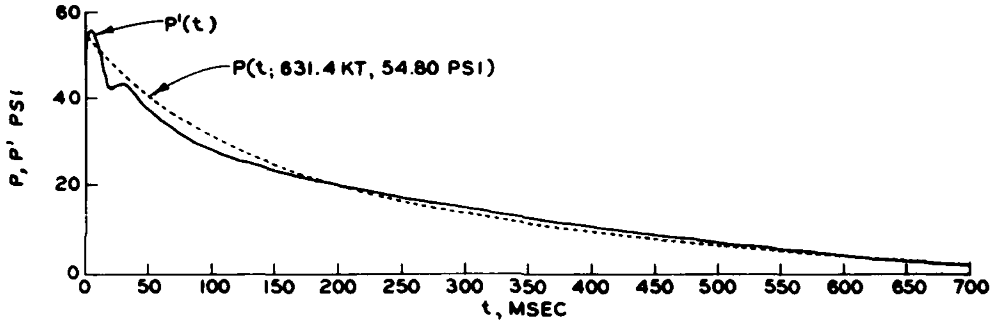

a. OVERPRESSURE HISTORIES

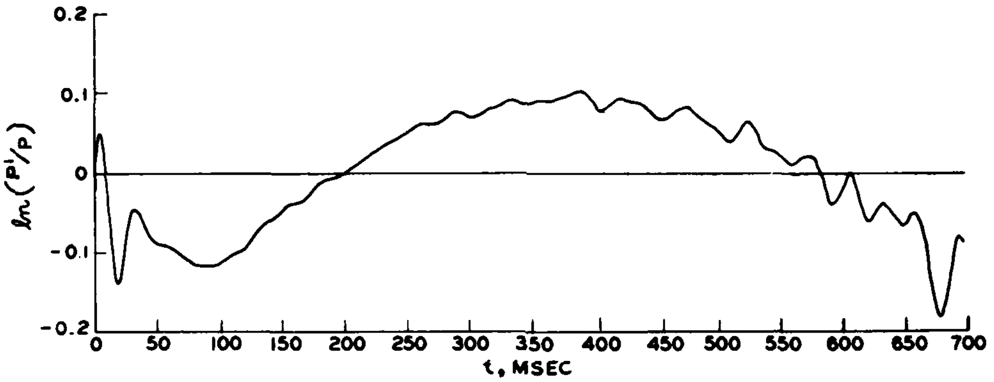

b. OVERPRESSURE RESIDUALS

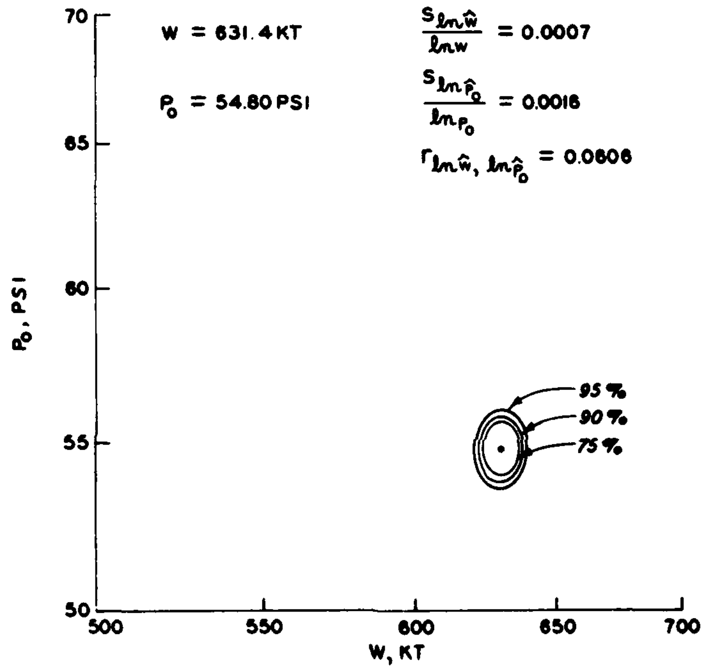

c. PARAMETER ESTIMATES

FIGURE 4. SIMULATION OF OVERPRESSURE BY FIRING TUBES OF PRIMACORD EXPLOSIVE.

The final application of the statistical estimation is to an overpressure which was lately simulated on a floor slab using firing tubes of primacord explosive 8 . This estimation is exhibited in Fig. 4. The yield and peak overpressure were computed from 700 equally-spaced data points in the 700 msec duration. The overpressure residuals of this computation show some correlation which nonetheless may not seriously effect the confidence regions calculated from Eq. (11). These regions show that the peak overpressure is estimated very reliably, that the yield is estimated even more reliably, and that these two estimates are virtually uncorrelated with one another.

CONCLUSIONS

Point estimators of the nuclear yield and peak overpressure have been derived which concisely summarize the result of an experimental simulation. Confidence internal estimators have also been developed which effectively communicate the experimenter's degree of belief in these results. These estimation techniques are applicable to simulations of assorted yields and peak overpressures obtained by various experimental methods.

ACKNOWLEDGEMENTS

This investigation was supported by the Defense Nuclear Agency under the monitorship of Dr. Kent Goering. Several helpful discussions of this study were held with Dr. Robert Port of R&D Associates.

NOMENCLATURE

D_p^+	Positive phase duration
i	Index of observations
$\ell n()$	Natural logarithm function
m	$(2W)^{1/3}$
n	Total number of overpressure versus time observations
$p(t)$	Nuclear weapons effects model overpressure function
$p'(t)$	Observed overpressure function
P_O	Nuclear weapons effects model peak overpressure
r	Range in kft; estimate of correlation coefficient
s	Estimate of standard deviation; standard error of estimate (unsubscripted)
t	Time
t_a	Time of arrival
$v_{1-\alpha}(2,n-2)$	Variance ratio random variable for 2 and n-2 degrees of freedom
W	Nuclear weapons effects model surface burst yield
Δ	Quantity defined by Eq. (10)
ε	Residual
ρ	Correlation coefficient
σ	Standard deviation; standard deviation of ε (unsubscripted)
Σ	Summation
Φ	Error sum of squares
χ^2	Chi-square random variable with 2 degrees of freedom
$\hat{}$	Estimator of

REFERENCES

1. J. W. Ball, In preparation. "MISERS BLUFF; Phase II, Event 1 Bridge Test. Pretest Analysis, Construction, and Test Data," Miscellaneous Paper, U.S. Army Engineer Waterways Experiment Station, CE, Vicksburg, MS.
2. G. E. Box, and M. E. Muller, 1958. "A Note on the Generation of Random Normal Deviates," Annals of Mathematical Statistics, v 29, pp 610-611.
3. H. L. Brode, 1978, "Improvements and Corrections to DASA 2506, 'Height of Burst Effects at High Overpressures'," R&D Associates, Marina del Ray, CA.
4. N. R. Draper and H. Smith, 1966. Applied Regression Analysis, Wiley, NY.
5. J. A. Earickson, 1979. "Simulation Development for Target Assessment," TR 78-158, Air Force Weapons Laboratory, Kirtland Air Force Base, NM.
6. M. Fisz, 1963. Probability Theory and Mathematical Statistics, Wiley, NY.
7. Honeywell Information Systems, 1971. Time-Sharing Applications Library Guide Volume II - Statistics, Wellesley, MA.
8. W. L. Huff, 1969, "Test Devices Blast Load Generator Facility," Miscellaneous Paper N-69-1, U.S. Army Engineer Waterways Experiment Station, CE, Vicksburg, MS.
9. D. W. Marquardt, 1963. "An Algorithm for Least-Squares Estimation of Nonlinear Parameters," J. Soc Indust and Appl Math, v 11, No. 2, pp 431-441.
10. R. L. Zahradnik, 1971. Theory and Techniques of Optimization for Practicing Engineers, Barnes & Noble, NY.

DISCUSSION

Mr. Piersol (Bolt Beranek & Newman, Inc.): I assume that when the regression analysis is done that you have to take data at discrete times. Were you concerned about the spacing and what sort of spacing did you use? How many data points were used in the regression?

Mr. Mlaker: It varied depending on the particular experiment. We obviously used a faster digitizing rate when we only had 10 milliseconds of data than when we had 700 milliseconds of data. The particular regression analysis is such that the confidence intervals are uninfluenced once you get past 200 points. You are summing the square of more and more terms but you are dividing by N-2 in estimating those confidence intervals so that all comes out the same.

Mr. Piersol: I still don't understand why the correlation co-efficient goes negative? This obviously is not the correlation coefficient between yield and over pressure because that has to be positive. That must be a correlation coefficient between residuals of some sort. When the yield goes up doesn't the overpressure have to go up?

Mr. Mlaker: No, there is a negative correlation between the logarithm of yield and peak overpressure. This is the one that had that apparently strong negative correlation. In other words to get that same particular record we could come close to it with a model if we went away from 15 kilotons and 3000 PSI. But if we went to a higher yield it would roughly increase the area under the curve; to get the same degree of fit to the particular data curve we would have to lower the peak overpressure since we have increased the area.

DYNAMIC MEASUREMENTS

AN ASSESSMENT OF THE COMMON CARRIER SHIPPING ENVIRONMENT

Fred E. Ostrem
GARD, INC.
Niles, Illinois

An assessment of available data and information describing the common carrier shipping environment is presented. The assessment includes the mechanical shipping hazards of shock and vibation associated with the handling and transportation of typical distribution cycles. Data for these hazards are summarized in a format considered most useful to packaging engineers. Application of the data to support an ASTM Proposed Recommended Practice for Performance Testing of Shipping Container is described.

INTRODUCTION

Periodically it is desirable to review and assess available environmental data and information for the purpose of defining a particular aspect of an environment or for an up-to-date description of the overall environment. This is particularly true for the transportation environment which is composed of many hazardous shock and vibration elements, each requiring lengthy investigations for proper description. The effect of this situation has been piecemeal investigation with the data being scattered and fragmented.

This paper presents as assessment of available data on the transportation shock and vibration environment, but more specifically the common carrier shipping environment. It is based on the results of a study (1) conducted in cooperation with the Forest Products Laboratory, USDA, and was prompted by their desire to extend and conserve one of our natural resources - wood. Since wood and wood-based products are used extensively in the packaging field, especially for common carrier shipments, this represented an area for large potential savings either through more efficient and effective package design or through recycling of used material.

Essential inputs for optimum package design is information describing all hazards of the common carrier shipping environment. In addition to its use as design information, the same data can be used in support of test procedures to evaluate completed package designs. It is in this latter category that the data has most recently been applied. It has provided background to support the test levels used in a recently approved performance-based ASTM Standard entitled: Proposed Recommended Practice for Performance Testing of Shipping Containers (2). A discussion of the data and the philosophy used in interpreting and applying it to test levels is presented.

HANDLING

Handling of shipping containers, either manually or by mechanical means or assistance, has always been considered to impose the severest loads on cargo. Such operations occur at terminal or transfer points and are a result of physically removing or loading a vehicle or moving it within a transfer or terminal facility. The main hazard from these operations is the impact resulting from dropping, throwing or just plain rough or accidental handling. Intuitively and from experience it is known that the severity of these impacts are affected by such factors as size, weight and the shape of the shipping unit. What is not known is the variability in the magnitude of these drops, the number of drops or the angular orientation at impact.

Currently available data on the handling environment is shown in Figure 1. This data represents the results of two of the most extensive measurement programs conducted in the United States. Curve A applies to shipments of 43-lb. cleated plywood boxes and represents data from an early U.S. Air Force study (3) of their supply channels involving primarily Railway Express shipments. Curve B applies to a more recent study by the U.S. Army Natick Development Center (4) involving shipments of 25-lb. fiberboard boxes. The Natick study is based on a compilation of data from numerous shipments via truck, aircraft, Parcel Post, United Parcel Service and overseas shipments aboard Navy ships. The latter shipments were made with the package positioned at the bottom center of a unitized load. In neither study was the data separated to describe the effect of a particular distribution cycle (i.e., UPS, truck, ship, etc.) or operation. The data includes fork lift, cargo net, conveyor sorting, semi-automated depot operation as well as manual handling.

The data is plotted on log probability paper and indicates the percentage of drops over indicated drop heights. Although completely different instrumentation was used in each study, the data shows good correlation with regard to drop height probability and effect of package weight.

The very sparse data represented by the above studies is due in part to the lack of a low cost, self-contained instrument capable of accurately recording drops over some extended time period. Many of the design problems are related to the variability of the impact surface and package orientation at impact.

Similar type data on handling impacts is available from studies conducted in Europe (5). This data is summarized in Figure 2 and is seen to cover package sizes ranging from 40 to 500 pounds. The data is plotted in the same format used with the previous data. As shown, the same trend in distribution of drop heights as reported in U.S. studies is apparent. Instrumentation in these studies consisted of threshold indicators which were set to record the number of drops above discrete heights. The straight line relationship had previously been established and thus the instruments did not have to record continuously. Although the effect of package weight and the distribution of drops for both studies are similar, the drop heights and corresponding probabilities of occurrence are significantly different. No explanation for the difference could be established.

OPTIMUM DESIGN HEIGHT

Assuming sufficient data of the above type were available, one could specify some acceptable risk level and the design drop height would be specified for each package weight, i.e., following a vertical line at the assumed risk. This would probably be the approach adopted for military items or high value items. Industry on the other hand, would operate under economic considerations for large quantity shipments and would seek an optimum design level or a level resulting in minimum cost.

Figure 3 is a graphical presentation of the optimizing process. C_p represents the

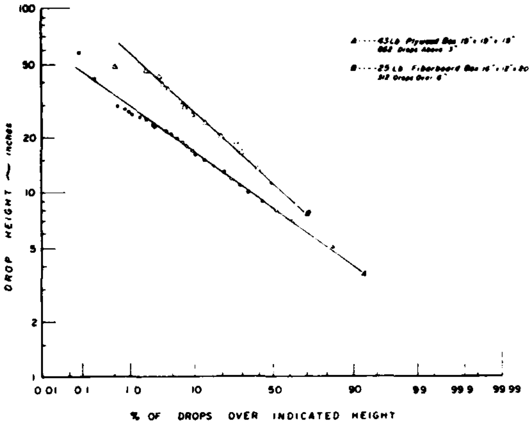

Figure 1 DROP HEIGHT VERSUS PROBABILITY OF OCCURRENCE (U.S. Studies)

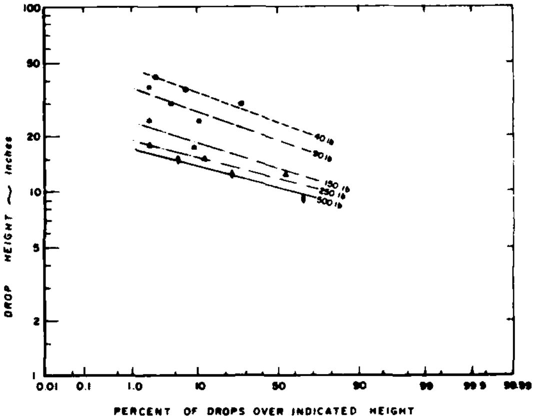

Figure 2 DROP HEIGHT VERSUS PROBABILITY OF OCCURRENCE (European Studies)

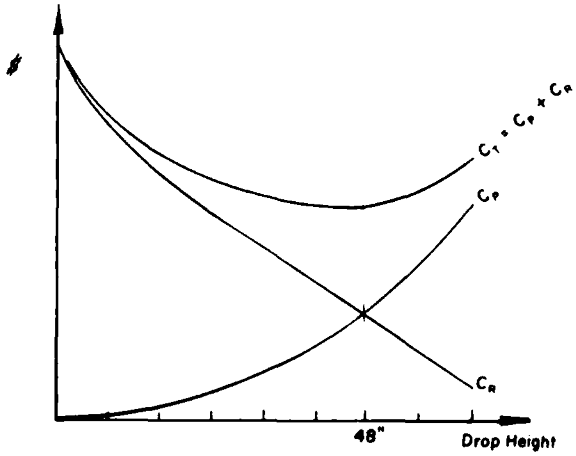

Figure 3 DESIGN FOR MEDIUM VALUE PRODUCTS

packaging cost which is shown to increase with design drop height to reflect added cushioning, a larger container, and resulting greater shipping costs. C_R represents the damage cost or cost to repair or replace the product and is shown to decrease as design drop height increases due to the reduced probability that packages will be dropped from a height greater than the design height. This latter curve can also include costs assigned to customer good will as a result of reduced damage. The total cost curve, C_T, is the sum of the two costs and represents total packaging cost. The optimum design point is the point of minimum total cost. In this case, it is shown as 30 inches.

The process is repeated in Figure 4 for a very similar item, but one with a higher product dollar value. Here we assume the same drop height statistics apply regardless of product value and that the fragility rating or sensitivity to damage is the same for all products. The packaging costs are the same, but because of the higher product value, the product damage cost curve C_R is higher, resulting in a shift of the minimum cost curve to a higher value. In this case, 48 inches.

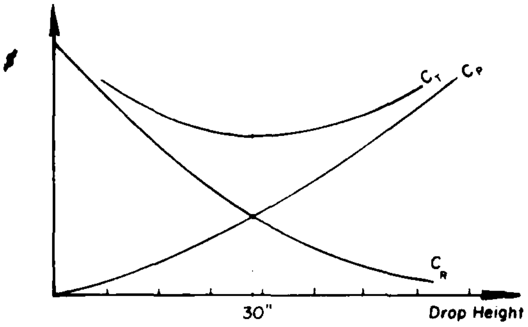

Figure 4 DESIGN FOR HIGH VALUE PRODUCTS

Similar arguments apply to a lower value product as shown in Figure 5. In this case the product damage curve shifts to the left, resulting in a shift of the total cost curve to a lower optimum design height. Ideally, one could arrive at an optimum design level for any product if the required statistical data were available for the anticipated handling operations. Unfortunately, this is usually not the case, and for the recommended drop levels to be used in the proposed ASTM performance standard, historical data developed through shipping experience was used.

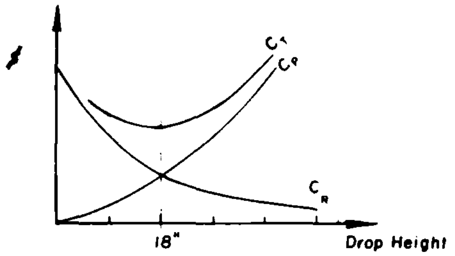

Figure 5 DESIGN FOR LOW VALUE PRODUCTS

PROPOSED TEST SCHEDULE

A summary of drop height specifications from some 30 industrial and military organizations is shown in Figure 6. These specifications have been developed through trial and error, for the most part, but demonstrate the same pattern of decreasing drop height for increasing package weight as would occur from a statistical approach. The plot shows only maximum, minimum, and average values. The relatively narrow band between maximum and minimum could be considered as being in essential agreement with the previous discussion and suggests the possibility of establishing three drop height "design" or "test" levels. This approach was adopted in specifying test levels in the newly proposed ASTM Proposed Recommended Standard for Performance Testing in the form of three Assurance Levels for each package weight category. The assurance level allows the user to specify one of three levels based on product value and probability of damage. The recommended test levels follow the historical data and are as follows for packages weighing less than 200 pounds.

Shipping Weight (lbs)	Drop Height (in) Assurance Level		
	I	II	III
0-20	24	15	9
20-40	21	13	8
40-60	18	12	7
60-80	15	10	6
80-100	12	9	5
100-200	10	7	4

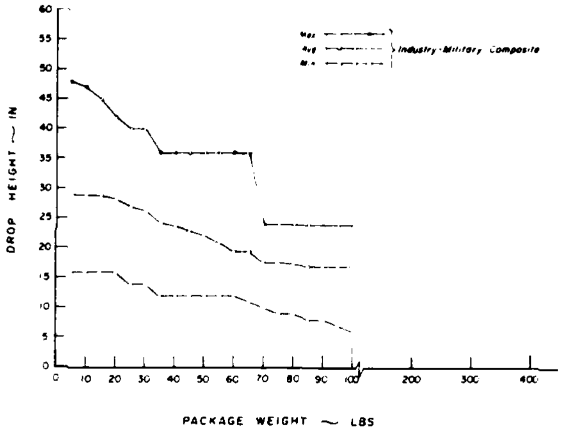

Figure 6 DROP HEIGHT SPECIFICATION - COMPOSITE

NUMBER OF DROPS

A replot of the measured data for the 43 lbs box is presented in Figure 7. In this case the data is plotted to show the number of drops *recorded at the various drop heights. The* data shows a large number of low-level drops and few drops at the higher levels.

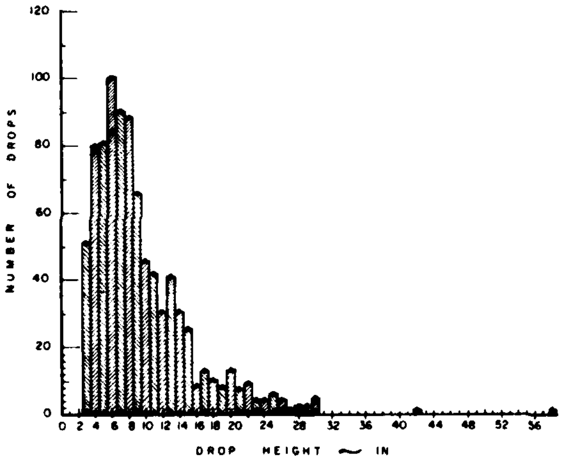

Figure 7 DROP HEIGHT VERSUS NUMBER OF DROPS (43 Lb. Container)

Data for the 25-lb container is plotted in the same manner in Figure 8. As shown, it correlates well with the data of Figure 7.

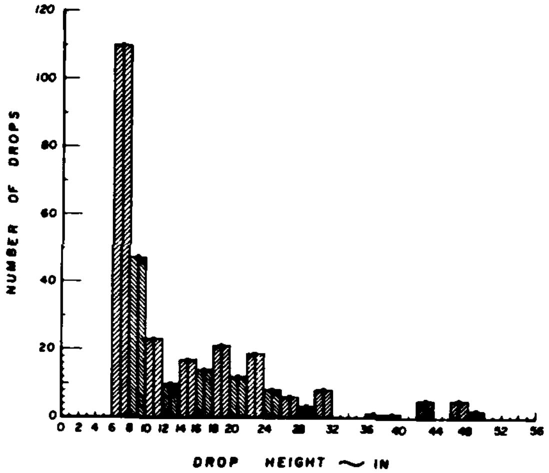

Figure 8 DROP HEIGHT VERSUS NUMBER OF DROPS (25 Lb. Container)

Based on the above data, it appeared that a container would be overtested if it were subjected to high level drops on all faces, edges and corners. Accordingly, a drop schedule was chosen to reflect conditions that occur in the field. The drop schedule proposed is shown in Table 1.

TRANSPORTATION

Transportation implies the transport or in-transit phase of a distribution cycle. During this phase the container is exposed to a vibration environment that is influenced by many factors including load, suspension, road profile, etc. The vehicle vibration environment cannot be estimated in the same manner as handling loads and for this reason has been monitored more extensively than any other shipping hazard. However, the data reduction or processing procedures have not been standardized with the result that data are summarized in various formats.

TRUCK VIBRATION

A summary of truck data reported in terms of power spectral density (6,7,8,9) and involving primarily tractor-trailer combinations is shown in Figure 9. These plots which include data from trailers with a number of different suspensions (air ride,steel leaf spring, coil spring, etc.) and cargo loads do not exhibit peaks and notches at discrete frequencies. Rather, the peaks occur at different frequencies which cover a rather broad frequency range. The peaks, however, are approximately equal in magnitude and could easily be enveloped by a straight horizontal line of constant power spectral density. This procedure of

TABLE 1

Drop Schedule

Number of Drops	Impact Surface		
	Box	Bag	Pail
One at twice specified height	Bottom	Face	Bottom
Five at specified height	Two on adjacent bottom edges	Two sides	Two sides 90^0 apart
	Two on diagonally opposite bottom corners	Two on ends	Two on bottom edge 90^0 apart
	One on top	One opposite face	One on top

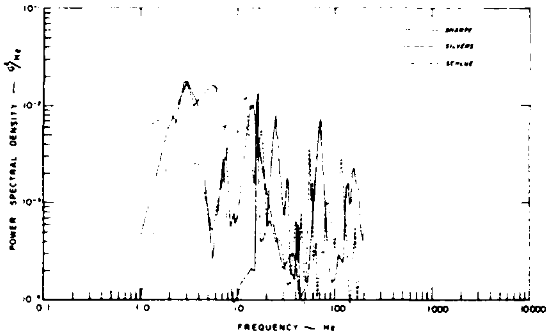

Figure 9 TRUCK FREQUENCY SPECTRA-SUMMARY OF PSD DATA

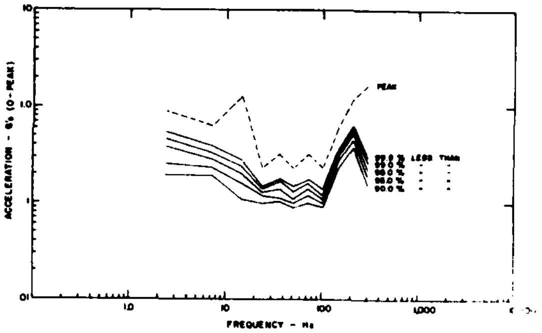

Figure 10 FREQUENCY SPECTRA FOR VARIOUS PROBABILITIES-2½ TON FLATBED TRUCK

(Vertical Direction, Composite of Normal Conditions)

course, results in a conservative specification, since specific vehicles do exhibit peaks and notches. However, for a container, which could ride on any vehicle, this seems a reasonable specification.

Another summary plot of truck vibration data is shown in Figure 10. In this study (10) the data has been reported in terms of acceleration versus frequency and the probability of occurrence. The data applies to a 2½-ton truck and is a composite of data from numerous operating conditions. Again, a constant acceleration over a broad frequency range could be specified.

TRUCK VIBRATION TEST LEVEL

The majority of existing package vibration test equipment is designed for sinusoidal testing. To accommodate this equipment the data has been summarized in terms of a constant or sinusoidal acceleration and corresponding frequency. The summary curve is shown in Figure 11. The shape of the curve was guided by the envelope power spectral density curve described previously. The peak acceleration level is based on the PSD peak of .02 g^2/Hz. Assuming a 1 Hz bandwidth, $g_{rms} = \sqrt{.02} = .15g$. A true random signal will have a peak value corresponding to 3 to 4 times the rms value.

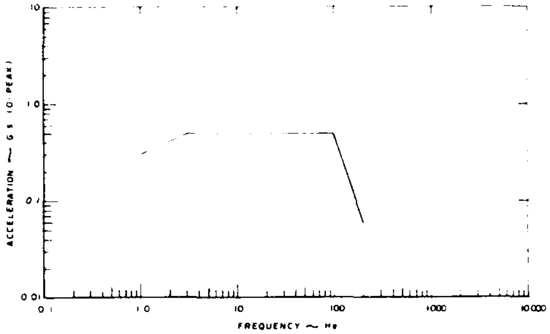

Figure 11 VIBRATION ENVELOPE CURVE - TRUCK SUMMARY

Applying this rationale to the computed rms value, a value of .5g (zero to peak) from 2½ to 100 Hz is specified.

The specified acceleration level correlates well with the data of Figure 10 if the occasional high peaks, not considered representative of continuous vibration, are excluded. Further, it is unlikely that cargo would respond to an occasional high acceleration unless it persisted for several cycles. The upper frequency range is shown to cut off at 200 Hz. Although some activity does occur at higher frequencies, surveys of typical containers and palletized loads have shown little response to these high frequency inputs.

RAIL VIBRATION

A summary of railcar vibration data reported in terms of Power Spectral Density (PSD) is shown in Figure 12. The summary includes data from three independent studies. Byrne's (11) data covers the low frequency range, while Foley's (10) and Sharpe's (12) data covers the intermediate and high frequency ranges. Foley's data is a summary of many tests and therefore appears as straight lines on the summary plot. The other data is plotted in terms of the highest reported levels. Although the data covers a wide frequency range, there is not much overlap between the data sources to give confidence to the results. However, the data does show a relatively constant PSD level over the reported frequency range and this correlates with the acceleration data shown in Figure 13.

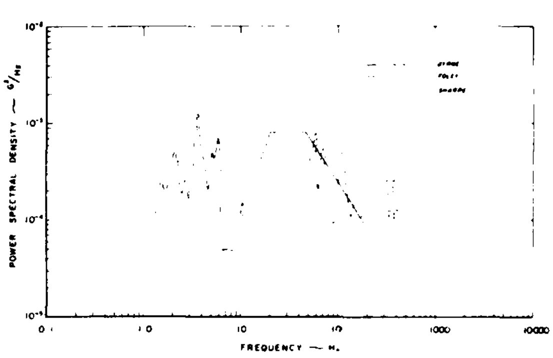

Figure 12 RAILCAR FREQUENCY SPECTRA-SUMMARY OF PSD DATA

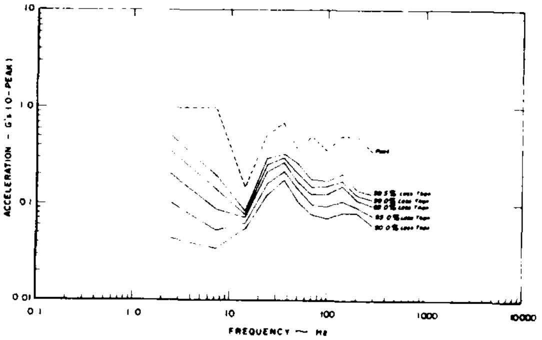

Figure 13 FREQUENCY SPECTRA FOR VARIOUS PROBABILITIES - RAILROAD

(Vertical Direction, Composite of Various Conditions)

The reasons for the variations in reported frequencies and levels of acceleration cannot be determined. However, Foley reports that the data below 10 Hz shows no relation to vibration-like distributions, although this is the frequency range in which the highest amplitudes are found. Further effort is required to better characterize the environment in the low frequency range as well as defining the vibration levels more confidently at all frequencies.

RAIL VIBRATION TEST LEVELS

In spite of the deficiencies noted above, an interim vibration test schedule can be developed based on available data. If we assume the data of Figure 12 is valid, an envelope curve corresponding to a constant

PSD level of 10^{-3} g^2/Hz can be drawn. Following the guidlines used in developing the truck envelope curve, the curve shown in Figure 14 is developed. Although this curve is based on rather sparse data, it compares favorably with the statistical summary shown in Figure 13.

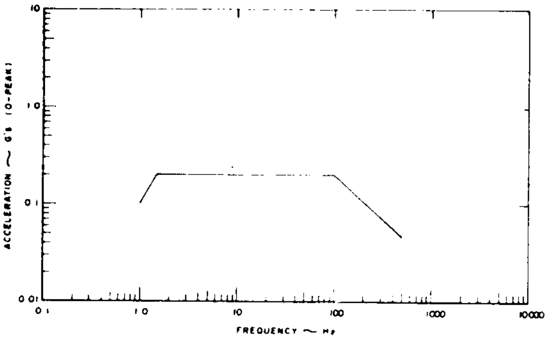

Figure 14 VIBRATION ACCELERATION ENVELOPE - RAILCAR

The vibration levels encountered by cargo are assumed to be a function of the mode of transportation only. Although it is recognized that different suspension system, vehicle load, position on the vehicle, etc. will influence the vibration levels, these will generally be beyond the control of the user or shipper. Thus the specification as developed from the data is assumed to apply to all the cargo. However, a significant variable is the distance traveled and therefore the time duration or exposure to the acceleration levels.

Again relying heavily on experience, the vibration test levels are specified in the ASTM document as follows:

Assurance Level	Frequency Range (Hz)	Sweep & Dwell Amplitude (0 - Peak) (g's)		Dwell Time (min)
		Rail	Truck	
I	3-100	.25	0.5	15
II	3-100	.25	0.5	10
III	3-100	.25	0.5	5

Dwell time is for each noted product or package resonance up to four.

Additional data concerning vehicle shock, railcar coupling impacts and loose-load vibration or repetitive shock are presented in reference 1.

CONCLUSION

An assessment of available data on the common carrier shipping environment in terms of shock and vibration has been presented. The assessment covered vehicle vibration and handling operations. These were selected to show the difference in the rationale to select test levels. Whereas individual containers are handled separately and therefore subjected to impacts depending on a chance phenomenon, containers on vehicles are subjected to essentially the same environment. Their variability is the distance transported or in terms of testing, the time duration. It is known that not all packages are designed to protect their contents to the same level even through the comment is made that the shipping environment is the same regardless of product or product value. The approach adopted by ASTM allows a variation in protective packaging depending on product value, risk or other considerations selected by the designer or user.

Although much information is available concerning the common carrier shipping environment, additional effort is required. This is particularly true for the rail coupling environment in which both the shock input and compressive loading from adjacent containers must be defined.

REFERENCES

(1) Ostrem, F.E., and Godshall, W.D., An Assessment of the Common Carrier Shipping Environment, General Technical Report FPL22, U.S. Forest Products Laboratory, 1979.

(2) ASTM Proposed Recommended Practice for Performance Testing of Shipping Containers, Annual Book of ASTM Standards, Part 20.

(3) Bull, K.W. and Kossack, D.F.: Measuring Field Handling and Transportation Conditions. WADD Technical Report 60-4, Feb., 1960.

(4) Barca, F.D.: Acquisition of Drop Height Data During Package Handling Operations, Report N. 75-108-AMEL, June, 1975.

(5) Allen, D.C.: Maximum Drops Experienced by Packages in Transit. Shock Environment of Packages in Transit - Society of Environmental Engineers Symposium, London, England, Feb. 24, 1971, pg 2.

(6) Schlue, J.W.: The Dynamic Environment of Spacecraft Surface Transportation, Tech Report No. 32-876, Jet Propulsion Laboratory, March, 1966.

(7) Sharpe, W.N. and Kusza, T.J.: Preliminary Measurement and Analysis of the Vibration Environment of Common Carrier Motor Carriers. Michigan State University, School of Packaging, Tech Report No. 22, September, 1973.

(8) Silvers, II, W. and Caruso, H.: Advances in Shipping Damage Prevention. The Shock and Vibration Bulletin No. 46, Part 4, August 1976.

(9) Schlue, J.W. and Phelps, W.D.: A New Look at Transportation Vibration Statistics. The Shock and Vibration Bulletin No. 37, Part 7, January 1968.

(10) Foley, J.T., Gens, M.B. and Magnuson, C.I.: Current Predictive Models of the Dynamic Environment of Transportation, Proceedings of the Institute for Environmental Sciences, 1972, pp. 35-44.

(11) Byrne, R. and Andresen, J.A.: Performance Characteristics of Freight Car Trucks Determined Through Road Testing, ASME Paper No. 76-WA/RT-4.

(12) Sharpe, W.N. Jr.: Preliminary Investigation of Freight Car Vibration, Report No. 20, School of Packaging, Michigan State University, November, 1972.

DISCUSSION

Mr. Galef (TRW Systems): There is no particular drop height for light weight packages that can be picked up and thrown and that surprised me. Seeing some of these 20 inch or more drop heights for packages over 100 pounds, say 500 pounds, also surprised me. What happens when these packages are subjected to drops like that?

Mr. Ostrem: The data I've seen from the U.S. studies showed generally low levels of drop height for the heavier packages. The data from the European study show higher levels. The historical data that we have leaned heavily on shows very low level drops for the heavier packages and this is what we are using in the recommended practice. The source of these high level drops from the European studies are difficult to define. They involve some handling at the ship loading dock and possibly that is where some of the higher drops occured.

Mr. Meeker (Pacific Missile Test Center): Was there some particular duration associated with your curves showing probabilities of various peak accelerations? Do you have some separate indication how frequently these occurred? I suppose these are shock rather than vibrations.

Mr. Ostrem: This was more of an attempt by Sandia to show the distribution of shocks or how the peak levels are distributed. Unfortunately the PSD data doesn't do that although it is a rapid method for analyzing data. This is a very lengthy process in which each frequency band has to be analyzed to determine the distribution of peaks. They plotted curves at Sandia that show the probability of encountering different road conditions, or bridge conditions during a cross country trip; they blended that into an estimated normal exposure and then they drew up a composite plot. They have this type of data for each category of road, operation, speed or vehicle load. It is very lengthy and time consuming. In plotting those curves you see a peak value at a significantly higher level and these could be attributed to shock. If you plot this on log normal probability paper when you get down to the ninety percent it assumes a straight line, almost a Gaussian distribution, and then it jumps up which would imply a shock type event. We seem to get correlation at the ninety percent level if we reduce the PSD test data down to the 3.5 rms value.

Mr. Frydman (Harry Diamond Laboratories): You indicated that most of the road data are random in nature, yet for the ASTM code you recommended a sine dwell at several characteristic frequencies. Why did you recommend a sine test, that is not really part of the real world?

Mr. Ostrem: I hated to do that after that last speech; but we have taken one giant step backward. Most of the equipment that is available in package evaluation laboratories is only capable of sinusoidal testing. Many of those even have trouble in sweeping the frequency range. To introduce random vibration, which I think will be the next step, will mean a large investment in equipment. If you look at relatively simple cartons of ketchup or "Clorox" in plastic bottles you pick up the two essential frequencies; one is a stacked vibration frequency and the other is the vibration of the contents in the containers at some natural frequency. We feel that there has been good correlation between field experience and laboratory test experience using these levels. Convenience I guess.

SHOCK AND VIBRATION ENVIRONMENT IN A LIVESTOCK TRAILER

M. T. Turczyn
Transportation and Packaging Research Branch
Office of Transportation
U.S. Department of Agriculture
Beltsville, Maryland

D. G. Stevens and T. H. Camp
Transportation and Marketing Research Unit
Science and Education Administration
U.S. Department of Agriculture
College Station, Texas

Measurements indicate that the intensity of the shock and vibrational inputs to cattle being transported by livestock trailer are dependent upon tire pressure, load weight, and position within the trailer. Cattle positioned at the rear of the trailer will experience the highest shock and vibrational amplitudes. At this position, as in all locations, under fully loaded conditions the vertical axis usually dominated. Cattle experience simultaneous vibrational energy inputs having peaks at 4-6 Hz, 15 Hz, and 30 Hz with magnitudes up to 0.08 g rms in the vertical axis and substantially lower in the lateral and logitudinal axes. Cattle experience simultaneous shock energy inputs having frequence components below 20 Hz which have acceleration values up to 6 g in the vertical axis, and up to 3 g in the longitudinal and lateral axes. The frequency content and amplitude levels of these vibrational and shock inputs may stress the animals enough to enhance their susceptibility to disease.

INTRODUCTION

Cattle being transported by a tractor/trailer are subjected to a number of stressors. These stressors include: Vehicle shock and vibration, temperature fluctuations, crowding, noise, and handling. The compounding of these stressors weakens the animals, subjecting them to increased disease problems. One disease is so closely linked to the transport of the animal that it commonly is called "shipping fever." Shipping fever is a respiratory disease contacted by cattle that have been transported long distances and is recognized as the most significant health problem in the feedlot industry. There is a general agreement among animal scientists and veterinarians that three agents combine to cause shipping fever: Viral pathogens, bacterial pathogens, and stress [1]. In an attempt to study the causes of shipping fever, each of the stressors must be studied individually to determine its magnitude and effect on transported animals. These experiments were conducted to accomplish the first point--to define the composition and intensity of the shock and vibrations generated by a tractor and a 44-foot livestock trailer traveling over a typical interstate highway at 55 mph, or impacting over railcrossing or road imperfections at 35 mph.

The bulk of the published data on shock and vibration environments associated with similar type transport vehicles has dealt with the carriage of hazardous or delicate cargo on flatbed or dry cargo van trailers [2,3]. While this information provided insight on the range of frequencies and energy levels that may be encountered, we decided to confirm that this data were relevant to livestock transport vehicles through our own measurements.

ELECTRONIC EQUIPMENT

A triaxial* piezoelectric accelerometer, B&K Model 4321**, was used to measure the vibration levels at three different locations

---

*Time, money, size, and power restrictions precluded the use of three triaxial accelerometers as desired.

**Trade names and companies are mentioned in this publication solely for the purpose of providing specific information. Mention of a trade name or organization does not constitute a guarantee of the product by the U.S. Department of Agriculture or an endorsement over other products or companies not mentioned.

on the frame of the livestock trailer. The 3 locations were on the center line of the trailer: 8 inches behind the kingpin, midpoint of the trailer, and 24 inches from the rear of the trailer, as shown in figure 1. Since the measurements were to be used as a comparison to actual cattle shipments, the accelerometer was attached to the underside of the frame, as it would be damaged if attached to the floor when transporting cattle.

The accelerometer was mounted by two means--at the rear location it was stud-mounted directly to a frame member, and at other locations the accelerometer was stud-mounted to a 1/2-inch steel plate which then was bolted to an I-beam crossmember. The accelerometer signals were amplified by a charge amplifier, B&K Model 2634, and the signals were recorded on a 4-channel B&K Model 7003 portable magnetic tape recorder, with 3 data tracks and a voice track.

The frequency response of the accelerometer was flat from 0.3 to 10,000 Hz, with an output of 10 pC/g. The charge amplifiers had a flat frequency response from 1 to 20,000 Hz, with an adjustable gain of from 1 to 10 mv/pC. The amplifiers were adjusted to provide maximum gain. The amplifier signal was AC-coupled to the recorder (tape speed was 1.5 inches/sec.). The recorder has a maximum input level with a range of 1 to 50 v rms with a dynamic range of 39 dB, and a flat frequency response from 4 to 1000 Hz. The input level was adjusted to a 1 v rms maximum.

The entire system has a flat frequency response from 4 to 1000 Hz with an input signal of 0.1 v/g, thus allowing the recording of a signal as small as 0.16 g to a maximum of 14 g. The system was calibrated on an accelerometer calibrator with an output of 1 g peak at 100 Hz.

TEST RUNS

A series of 33 test runs was made, involving different combinations of load, tire pressure, and accelerometer location (table I). A new Merritt Central Standard aluminum trailer having a Hutchens single leaf suspension was used. The test runs were made over a 7.2-mile stretch of continuous, reinforced concrete highway. A plank, nominal 2x4, was placed on the highway at a point where the tractor/trailer would run over it at 35 mph. This speed was chosen as a compromise between the fastest speed experienced when crossing over rail tracks and the slowest speed experienced when hitting highway imperfections. A range of speeds would have generated a worse case condition for this particular suspension, but time and money restrictions precluded doing this. After running over the plank, the tractor accelerated to 55 mph and completed the test run. This gave a minimum of 3 minutes of continuous data at 55 mph.

The load, consisting of filled sandbags, was added, as shown in figure 1, with the first increment, 9,200 lbs, for runs 11-16 being placed in the lower center compartment. The second increment, 9,280 lbs, for runs 17-22, was divided between the lower rear and lower front compartments. The third increment, 9,840 lbs, for runs 23-28, was placed in the upper center compartment. The last increment, 9,840 lbs, for runs 29-34, was divided between the upper front and upper rear compartments. The total load added up to 37,780 lbs. The range of tire pressure and loads chosen represent conditions common while hauling cattle. Often the trailer is partially loaded--40 percent of the time, trailers are hauled empty or nearly empty. This condition may lead to premature wear of the trailer, thus empty trailer data were gathered.

ANALYSIS TECHNIQUES

The data signal was taken from the 1/4-inch, 4-channel tape and then dubbed onto a 1-inch, 14-channel tape to allow compatibility with the analysis equipment. One channel was time-coded with a 36-bit NASA time code for ease of reference. The tape signal was played through a 7-channel galvanometer to extract hard-copy time history and a time code.

From each section of time history for analysis, the x-, y-, and z-axes time histories were taken together as a matched set. We can, therefore, compare what occurred in each axis during the tractor-trailer's impact with the plank or during travel. The z-axis is vertical, the x-axis is longitudinal, and the y-axis is lateral.

For vibration analysis, power spectral density (PSD) plots were made using 26 seconds of data from the 55-mph section of each run,

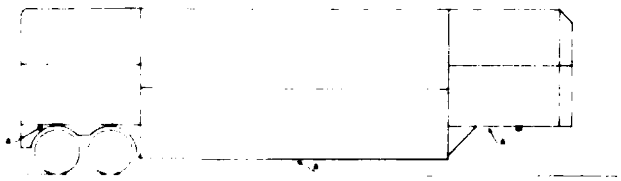

Fig. 1 - Cross section of test trailer showing placement of accelerometer.

TABLE I

Experiments to determine shock and vibration--at various load levels, tire pressure at three locations on livestock semi-trailers

Test number	Accelerometer location	Speed	Tire pressure	Actual truck load
		(mph)	(psi)	(lbs)
2	front	55	90	0
3	middle	55	90	0
4	rear	55	90	0
5	rear	55	80	0
6	middle	55	80	0
7	front	55	80	0
8	front	55	70	0
9	middle	55	70	0
10	rear	55	70	0
11	rear	55	90	9,280
12	middle	55	90	9,280
13	front	55	90	9,280
14	front	55	80	9,280
15	middle	55	80	9,280
16	rear	55	80	9,280
17	rear	55	90	18,300
18	middle	55	90	18,300
19	front	55	90	18,300
20	front	55	80	18,300
21	middle	55	80	18,300
22	rear	55	80	18,300
23	rear	55	90	28,140
24	middle	55	90	28,140
25	front	55	90	28,140
26	front	55	80	28,140
27	middle	55	80	28,140
28	rear	55	80	28,140
29	rear	55	90	37,780
30	middle	55	90	37,780
31	front	55	90	37,780
32	front	55	80	37,780
33	middle	55	80	37,780
34	rear	55	80	37,780

which was free from dropouts and inconsistencies. The 99 PSD plots, x-, y-, and z-axes for each run, were generated using a TDA 53 L spectral analysis system manufactured by Time Data Corporation. This system computes the PSD of the sample using the Fast Fourier Transform (FFT) technique. The band width for analysis was 0.3125 Hz and the frequency limits were set at DC to 300 Hz.

Shock spectrums using 2 seconds of data generated when the tractor-trailer impacted with the 2x4 plank were plotted using the same analysis equipment used to create the PSD plots. We used 2 full seconds of data so that all 5 impacts with the 2x4 plank would be captured. The damping coefficient was 0.05 and the frequency resolution was 1/12 octave. The spectrums were maxi-max, and frequency limits were set at DC to 100 Hz.

RESULTS

Vibration Data

The PSD plots in figures 2 and 3 were generated from the signals produced from the rear accelerometer location. We chose to present these plots as examples because for any combination of dead load weights, tire pressures, and accelerometer location, the rear of the trailer generally produced the highest overall vibrational energy levels. Figure 2 outlines the energy levels in the x-, y-, and z-axes of a trailer loaded with 37,780 lbs, having a 90-psi tire pressure. Figure 3 represents an overlay of the energy level present in the z- or verticle plane for three conditions: Empty trailer with a 90-psi tire pressure, a fully loaded trailer with a 90-psi tire pressure, and an empty trailer with a

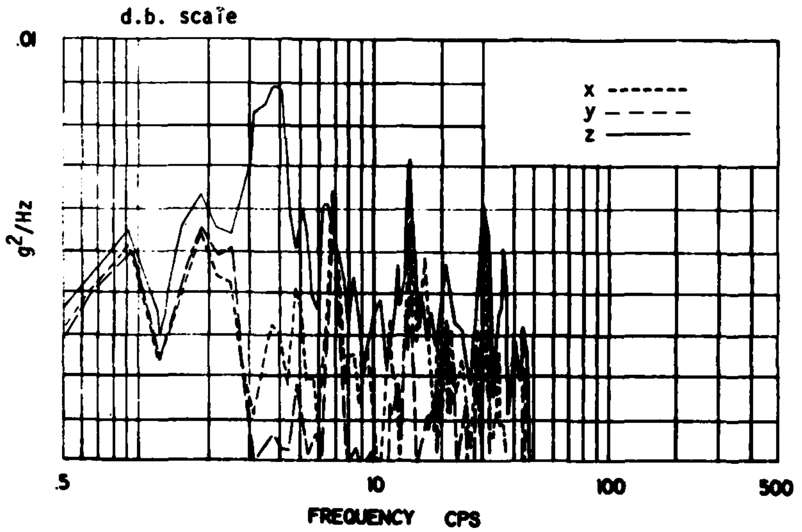

Fig. 2 - PSD, rear of van loaded with 37,780 lbs. with 90-psi tire pressure.

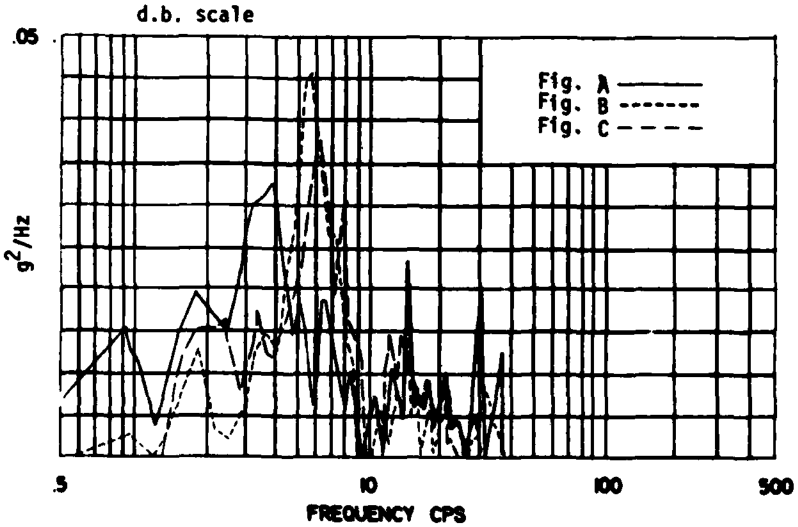

Fig. 3 - PSD, overlay of vertical axis for three conditions: (A) Empty trailer with a 90-psi tire pressure, (B) Fully loaded trailer with a 90-psi tire pressure, and (C) Empty trailer with a 70-psi tire pressure.

tire pressure of 70 psi. The major features are:

1. The major peaks exist at 4 to 6 Hz (the suspension frequency), 15 Hz (the unsprung mass), and 30 Hz.
2. The z-axis generates the highest energy levels (peaks measured at 0.03 to 0.08 g rms).
3. Every axis generally follows the same peaks and valleys in each matched set of plots.
4. As the dead load increases, the overall energy levels decrease, and the lower frequency, 4 to 6 Hz, shifts downward as predicted for any classical spring-mass system. The unsprung mass frequency remained at 15 Hz.
5. Lowering the tire pressure generally decreases the energy levels in the z-axis. Tire pressure seemed to have more effect on lightly loaded trailers than on heavily loaded trailers.
6. Vibration amplitudes at frequencies above 40 Hz are generally insignificant.

Shock Data

The following sample shock-response spectra reflect trends shown in other test runs. Figures 4 and 5 are composite shock-response spectra representing responses in the x-, y-, and z-axes at the three locations. Figure 4 represents a trailer loaded with 37,780 lbs, with a 90-psi tire pressure. Figure 5 represents an empty trailer having a tire pressure of 70 psi.

The shock-response spectra generally confirmed work previously published [4]. The vertical axis dominated at all locations under most load and tire pressure conditions. The only exception to this was in an unloaded trailer. In this case, response accelerations of the longitudinal axis at the front location were extraordinarily high and, therefore, dominated. This probably was due to looseness in the coupling between the tractor and the trailer. This looseness may cause premature wear, since trailers are hauled empty 40 percent of their lifetime.

The rear location over the rear tandem axles usually generated the highest overall vertical response accelerations between 0 to 40 Hz.

Response accelerations of the longitudinal axis often were quite close numerically at all locations for the same load and tire pressures.

Lateral axis response accelerations usually had the lowest values except when the trailer was unloaded. Unloaded, the trailer exhibited a large amount of rear sway.

The shock-response spectra indicated that as the load weight increased, overall response acceleration values tended to decrease. The effect of tire pressure is harder to determine. At the lower load weights, a decrease in tire pressure appears to reduce response accelerations in the vertical axis at all locations. As the load weight goes up, this tendency is not as clearcut. Tables II to IV are charts of the shock-response spectra reduced to shortened tabular form. The effects of load and tire pressure are depicted.

DISCUSSION OF DATA

The vibration data indicated that the vertical axis at the rear location generated the highest energy levels. The dominating frequencies in all axes at every location under various loads and tire pressures were those associated with the leaf-spring suspension system, 4 to 6 Hz, and the unsprung mass, 15 Hz. The g rms values for the 4 to 6 Hz peaks ranged between 0.03 and 0.08, which is slightly lower than other reported data [5]. Our instrument limitations and newness of the trailer may explain this.

Whole-body vibration studies performed on humans and animals infer that suspension frequencies of 4 to 6 Hz may be harmful to the cattle. The first resonance for a person standing upright falls between 5 and 12 Hz [6]. Transmissibility for different sections of a standing person's body may run as high as 2 times [7]. The combination of low-frequency resonance and large amplification factors could cause anything from mild nausea and sickness to ruptured organs and death depending upon the vibration input's amplitude, frequency content, and exposure time [8]. Due to the cattle's large mass, the visceral organs very well may resonate at the lower frequencies found in transport (4 to 6 Hz). The high mobility of these organs allows them to move considerably during resonance; therefore, during even mild resonance, breathing and bodily functions can be impaired [9]. This is reinforced by the fact that ISO Standard 2631, Guide for the Evaluation of Human Exposure to Whole-Body Vibration, 1974, contains charts showing recommended limits for both long-duration, low-amplitude vibrational inputs, as well as short-duration, high-amplitude vibrational inputs.

While the studies cited dealt mainly with sinusoidal vibration and did not specifically examine cattle, they do infer that before any type of vibration exposure can be ruled out as a stressor to the animal, weakening shipping fever resistance, work first must be done to

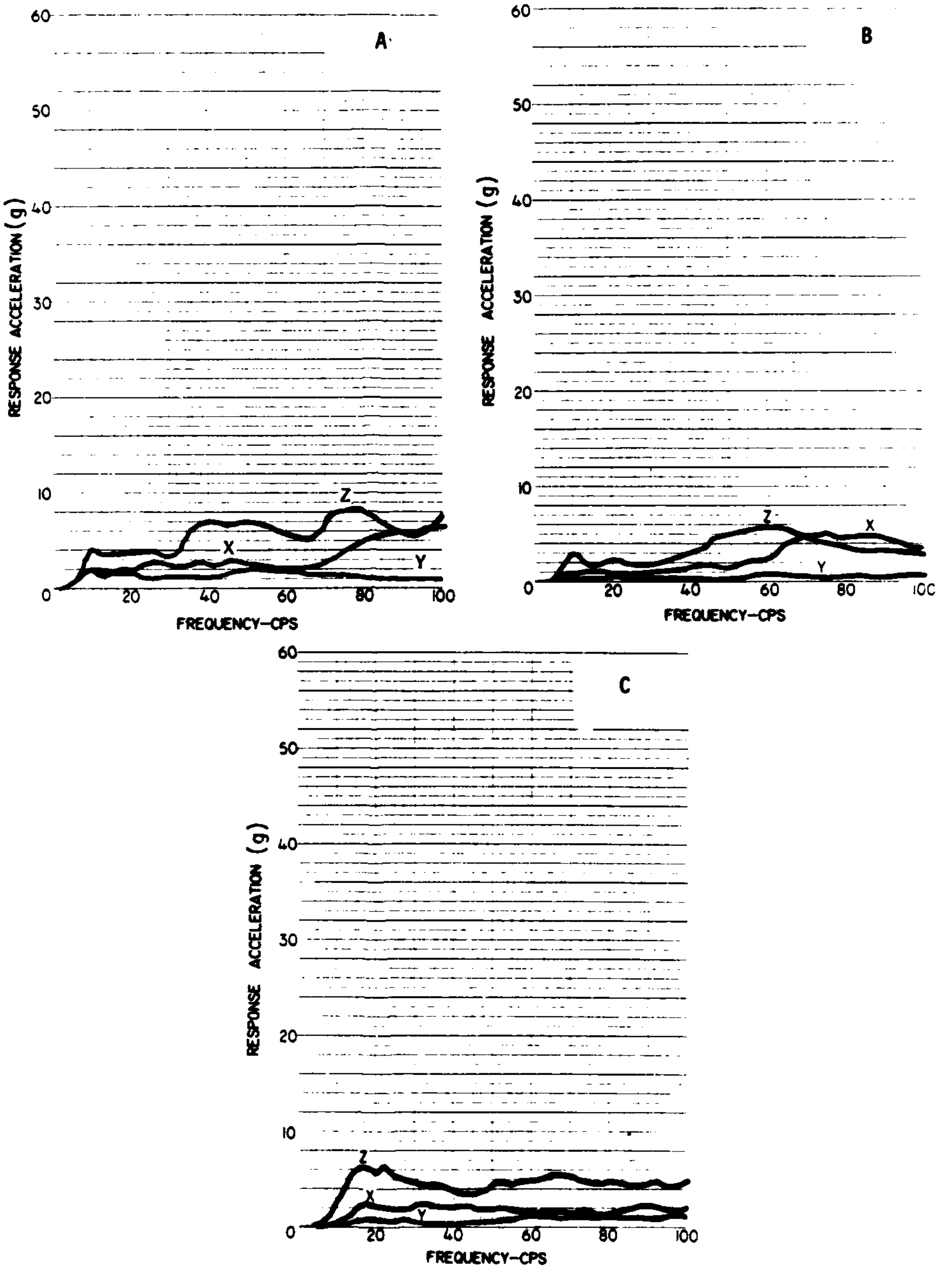

Fig. 4 - Shock spectrum of a trailer van loaded with 37,780 lbs. with a 90-psi tire pressure: A, front; B, middle; C, rear.

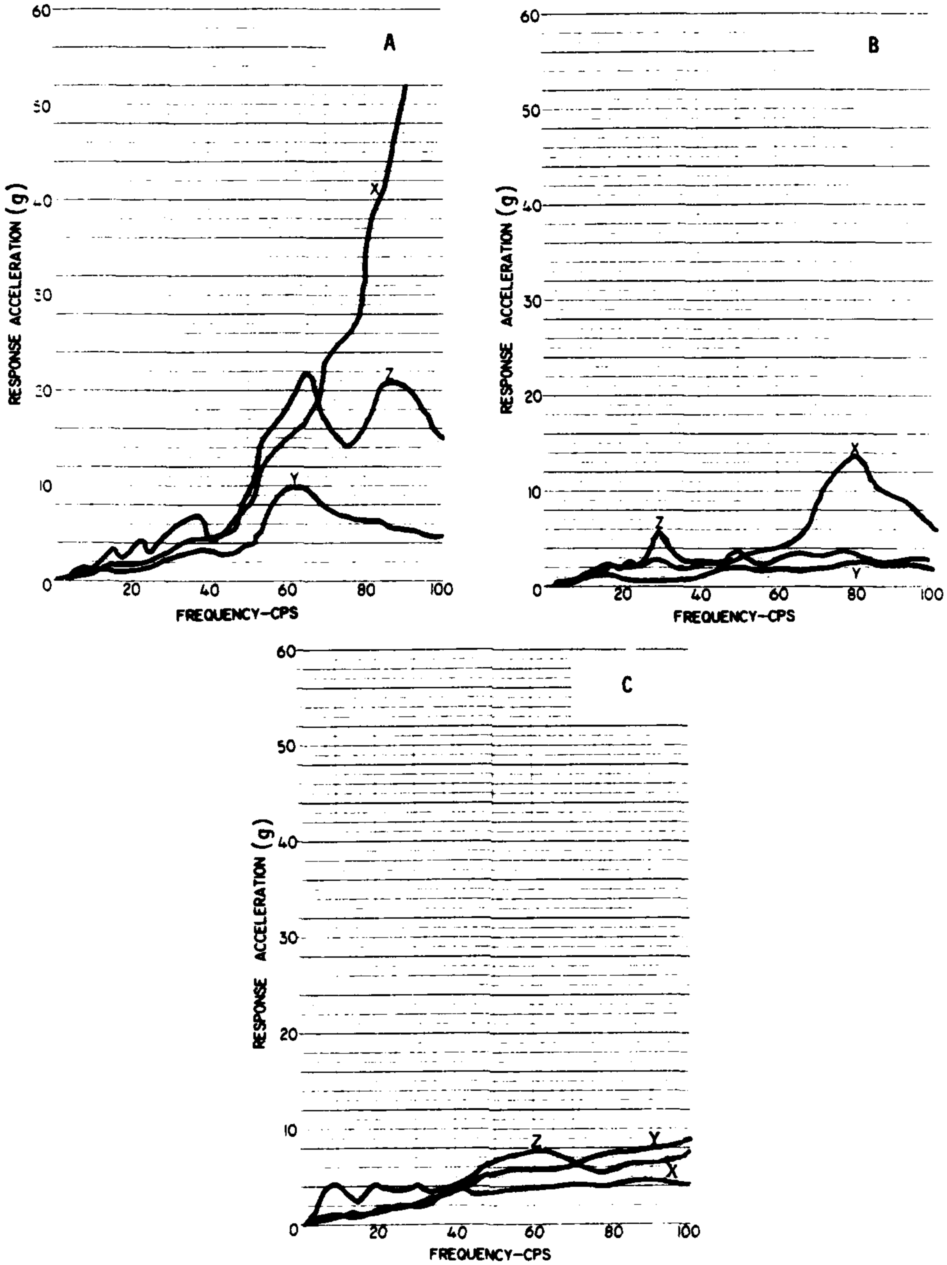

Fig. 5 - Shock spectrum of an empty trailer van having a 70-psi tire pressure: A, front; B, middle; C, rear.

TABLE II

Response acceleration values (g) for trailer with 90-psi tire pressure and various dead loads

Location	Hz	0 lbs			9,280 lbs			18,300 lbs			28,140 lbs			37,780 lbs		
		x	y	z	x	y	z	x	y	z	x	y	z	x	y	z
Front:	10	3.03	0.48	1.45	0.52	0.22	3.29	1.18	0.39	2.36	1.15	0.18	2.38	1.90	2.08	3.98
	20	7.03	0.62	2.84	1.00	0.27	1.87	0.80	0.42	1.47	1.26	0.37	1.93	2.00	1.45	3.73
	30	1.15	1.20	4.46	1.18	0.45	1.94	1.99	0.62	2.83	2.14	0.48	2.86	2.27	1.27	3.34
	40	13.16	1.62	6.56	2.12	0.48	2.60	2.21	0.44	2.15	3.46	0.41	3.86	2.50	0.97	7.13
Middle:	10				1.01	0.32	4.00	0.51	0.28	1.98	0.59	0.27	0.88	0.79	0.29	2.96
	20				1.95	0.54	8.40	0.93	0.46	2.65	1.34	0.33	0.57	0.81	0.46	2.41
	30				2.61	0.50	8.06	1.35	0.43	3.27	1.13	0.33	0.45	0.88	0.43	1.97
	40				3.21	0.48	13.36	1.79	0.37	4.35	1.07	0.47	0.39	1.52	0.44	3.08
Rear:	10	0.71	2.52	4.49	0.47	0.85	2.73	0.40	0.33	2.03	0.37	0.29	2.00	0.52	0.59	2.19
	20	1.85	7.03	9.96	1.93	2.01	3.97	1.00	0.39	3.38	1.51	0.63	7.00	2.33	0.52	5.64
	30	1.79	7.83	10.31	2.45	1.48	5.13	1.27	0.90	3.45	1.44	0.60	5.86	2.37	0.44	4.67
	40	2.26	10.48	11.28	2.19	2.05	4.93	3.29	0.60	3.45	2.11	0.84	4.73	2.17	0.45	3.97

TABLE III

Response acceleration values (g) for trailer with 80-psi tire pressure and various dead loads

Location	Hz	0 lbs			9,280 lbs			18,300 lbs			28,140 lbs			37,780 lbs		
		x	y	z	x	y	z	x	y	z	x	y	z	x	y	z
Front:	10	0.76	0.43	0.53	0.57	0.49	2.87	1.32	3.60	3.01	0.18	0.08	0.73	1.02	0.41	2.26
	20	0.93	0.82	1.28	1.40	0.86	3.41	1.41	0.42	1.64	0.32	0.23	0.60	2.10	0.51	2.51
	30	1.15	0.78	1.97	2.48	1.25	4.64	1.53	0.48	2.92	0.47	0.29	0.50	1.58	0.30	2.18
	40	2.18	1.19	2.71	3.19	2.71	5.89	3.31	0.40	2.54	0.42	0.18	0.35	1.85	0.46	1.91
Middle:	10	1.22	0.76	0.75				0.28	0.13	1.96	0.43	0.15	1.11	0.41	0.17	1.10
	20	2.10	0.92	1.58				1.05	0.43	5.78	1.39	0.39	2.34	0.83	0.29	1.11
	30	2.59	2.71	4.74				1.97	0.68	8.31	0.93	0.33	1.56	0.92	0.38	1.09
	40	2.55	3.16	2.94				3.71	0.42	11.78	1.17	0.34	1.15	1.08	0.21	1.44
Rear:	10	0.50	1.35	3.23	0.64	0.27	3.92	0.66	0.32	2.98	0.80	0.38	2.33	0.74	0.22	2.37
	20	1.18	3.51	5.23	1.19	0.38	4.89	0.85	0.39	4.47	1.61	0.65	5.71	2.08	0.47	2.93
	30	0.97	4.71	7.02	1.44	0.46	5.92	2.17	0.55	5.00	1.93	0.65	5.00	1.81	0.48	3.18
	40	1.30	6.13	7.12	2.23	0.55	6.65	2.70	0.48	4.45	2.43	1.05	3.71	4.11	0.45	3.36

TABLE IV

Response acceleration values (g) for trailer with 70-psi tire pressure with no dead load

			0 lbs	
Location	Hz	x	y	z
Front:	10	1.38	0.73	0.96
	20	3.16	1.02	1.48
	30	5.44	2.48	3.17
	40	4.57	3.31	4.32
Middle:	10	1.27	0.69	1.01
	20	1.90	0.69	1.90
	30	2.86	0.66	5.68
	40	2.45	1.06	2.70
Rear:	10	0.71	1.01	4.33
	20	1.22	1.54	4.16
	30	1.82	2.31	4.21
	40	2.94	3.41	1.11

determine cattle's body resonances and transmissibility values.

The shock response data indicated that for various loads and tire pressures, the vertical axis generally dominated at all locations, with the rear location experiencing the highest low frequency energy. The shock inputs in a loaded trailer had frequency components between 0 to 40 Hz, with acceleration values up to 6 g below 15 Hz.

Experiments performed on humans and animals show that before a rapid deceleration will cause fatal injury, the forces must have high deceleration values and be of substantial impact duration [8,10]. Shock input, therefore, must have a rather large velocity change. While the trailer-response spectra show the cattle will experience low frequency-shock input content, which may coincide with resonance of visceral organs, i.e., 4 to 10 Hz, the duration of shock impulses is probably far too short to incite the organs to maximum displacement. They would probably fall outside of any Damage Boundary Curve [11,12] generated for cattle. Practical field observation seems to confirm that cattle rarely suffer internal mechanical damage during transit. It is possible that these low-energy shock inputs do stress the animal and a repetitive shock situation, such as running over expansion joints at a specific speed, could cause stress-producing body resonances.

The shock-response data show that the cattle experiences three axis-shock impacts having low frequency components, with acceleration up to 6 g. These simultaneous forces may cause unstable conditions for the cattle when the trailer rides over road imperfections. Field observations tend to confirm this. Many haulers try to load the cattle in the trailer as tightly as practical to prevent them from falling during road impacts and brake deceleration.

CONCLUSIONS

The intransit vibration that cattle experience contains the low frequencies that coincide with first body-cavity resonances occurring in humans and other animals. Cattle-body resonances and transmissibility values presently are not known, so concrete conclusions are not in order. Past whole-body vibration studies seem to indicate that these low transport frequencies may have some adverse effects. Therefore, to completely eliminate low-amplitude transport vibration as a stressor contributing to the contraction of shipping fever, is premature without more study.

Elementary steps such as lowering tire pressure or using air-ride suspensions, can be taken to lower overall vibration energy levels that cattle will experience. It is also possible to raise the suspension's primary frequency, but until the cattle primary-body resonances are isolated, the benefits of doing this are hard to estimate.

The shock inputs experienced by the cattle do not appear to have enough velocity change to cause any substantial internal damage, but repetitive inputs may cause undue stress. Additional damping may be obtained through the use of air-ride suspensions, but this may be unwarranted. Loading the cattle in as tightly as practical, as done currently, will reduce the chance of cattle going down during shock inputs.

REFERENCES

1. Hoerlein, A. B., "Preconditioning of beef cattle," Jour. Amer. Vet. Med. Assoc., 163:825-826.

2. Ostrem, F. E. and Godshall, W. D., "An Assessment of the Common Carrier Shipping Environment," Gen. Tech. Rept., Forest Products Lab 22, 1979.

3. Ostrem, F. E., "A survey of the transportation shock and vibration input to cargo," Shock and Vibration Bulletin No. 42, Part 1, pp. 137-151, Jan. 1972.

4. Foley, J. T., "Transportation Shock and Vibration Descriptions for Package Designers," Sandia Lab Rept. SC-M-72 0076, July 1976.

5. Silver, V. and Caruso, H., "Advances in Shipping Damage Prevention," Shock and Vibration Bulletin No. 46, Part 4, pp. 41-48, Aug. 1976.

6. Coermann, R. R., Human Factors, 4:227, 1962.

7. Dieckmann, D., Intern. Z. Angew. Physiol. Einschl. Arbeitsphysiol., 16:519, 1957.

8. Von Gierke, H. E. and Goldman, D. E., "Effects of Shock and Vibration on Man," Shock and Vibration Handbook, 44:22-45, 1976.

9. Coermann, R. R., et al, Aerospace Medicine, 31:443, 1960.

10. Rushmer, R. F., Green, E. L. and Kingsley, H. D., Jour. Av. Med., 17:511, 1946.

11. Kornhauser, M., "Prediction and Evaluation of Sensitivity to Transient Accelerations," J. Appl. Mech., 37:4, p. 371, 1954.

12. Newton, R. E., "Fragility Assessment Theory and Test Procedure, Monterey Res. Lab., Monterey, Calif., 1968.

DISCUSSION

Mr. Szymkoviak (Westinghouse): You probably don't have the full 40,000 pound dynamic load on the cattle because of their isolation system. I would suggest that you pack them tighter because that would seem to keep them from falling down since they have no way of holding on. Your relationship between all three axes and the vertical direction is obvious because the input is vertical; the wheels go up and down and you get some rocking. This is all related to the vertical inputs and this data duplicates the data we have seen on trucks; the only way you can get around it is to lower the suspension frequencies below the internal organ resonance frequencies.

Mr. Turczyn: Thank you. That is something we are going to start studying because we have looked at a lot of data on human organ vibrations and I have yet to talk a vet into vibrating cattle and measuring their organ resonances. This is truely an exploratory project.

Mr. Galef (TRW Systems): When I see the fairly prominent undamped natural frequency, I wonder if there are shock absorbers in the system.

Mr. Turczyn: There are, but I don't know whether they are effective. I don't think the levels were really that high compared to other data I have seen. In fact some of the peaks in the four to six Hz range were rather low.

Mr. Galef: What was the condition of the trailer?

Mr. Turczyn: Supposedly it was brand new with fully new equipment that could be something I could look into.

Mr. Kana (Southwest Research Institute): You mentioned that you had a 30 Hz component in your data and you weren't exactly sure where it came from. That is 1800 rpm and that may very well come from the engine input itself.

Mr. Turczyn: I was thinking that it might be the shaft or the engine itself.

Mr. Kana: You might check the engine rpm at the speed your truck was running.

SHOCK INDUCED IN MISSILES DURING TRUCK TRANSPORT

D. B. Meeker and J. A. Sears

Pacific Missile Test Center
Point Mugu, California

The response of three different types of missiles during four truck trips was measured using an Endevco TEMARS (Transportation Environment Measurement and Recording System). The shock response peaks were found to have an exponential distribution in amplitude. The spectrum of the shocks was defined in terms of the level which is exceeded at a given rate. Formulae are given for designing both Qualification Tests and MTBF (Mean Time Between Failure) Tests based on this data.

I. INTRODUCTION

During the past three years, PMTC personnel have measured the shock response of missiles during four trips by truck. In each case the measurement was at the behest of those concerned with the missile and the results went out to three different groups corresponding to the three kinds of missiles that were carried. My co-author and I were interested, not in the specific missiles, but in a more general description of truck transport shock. So it fell to us to collate and summarize the data from these four trips.

Our interest arose directly from a desire to define laboratory tests simulating missile environments. Such tests are of two kinds, serving two purposes. First are those usually known as Qualification Tests, which prove the capability to survive the worst. Since the worst occurs but once, such tests usually consist of subjecting one missile to the most severe stress expected and seeing whether it survives. If the stress is repeated a few times, it is for statistical replication rather than fidelity to the environment. So, roughly speaking, a Qualification Test for truck transport shock is defined by the shock whose magnitude and duration make it, among all those to be experienced by all missiles of a kind, the most damaging. More precisely, it is allowed that some small percentage of the missiles may fail and the Qualification Test is set, not to the maximum but, to a certain high percentile of the distribution of shocks.

The second kind of laboratory test seeks to determine the missile's reliability or failure rate or MTBF (Mean Time Between Failures). Here the stress to be survived is not the worst one but the common one. The common stresses are low but, being common, they occur over and over; thus causing failure by an accumulation of damage or of coincidences. In the case of truck transport shock, an MTBF test needs to reproduce the lower level shocks in numbers, amplitudes, and durations corresponding to all the trips that a missile will make by truck. Because the number of shocks is large and there are ranges of amplitude and duration to be reproduced, the shock environment is best represented probabilistically. At a minimum this representation assigns a certain frequency of occurence to each shock duration-magnitude pair. Refinements treating the sequence of pulses as a stochastic process with certain time correlations (spectra) could be useful, but finding the minimal representation will prove challenge enough for this paper. Since our interest is primarily the definition of laboratory tests, the derivation of test conditions will be described also.

Before entering into a description of the data and how it was obtained, it will be instructive to see how present tests are defined. Figure 1 is excerpted

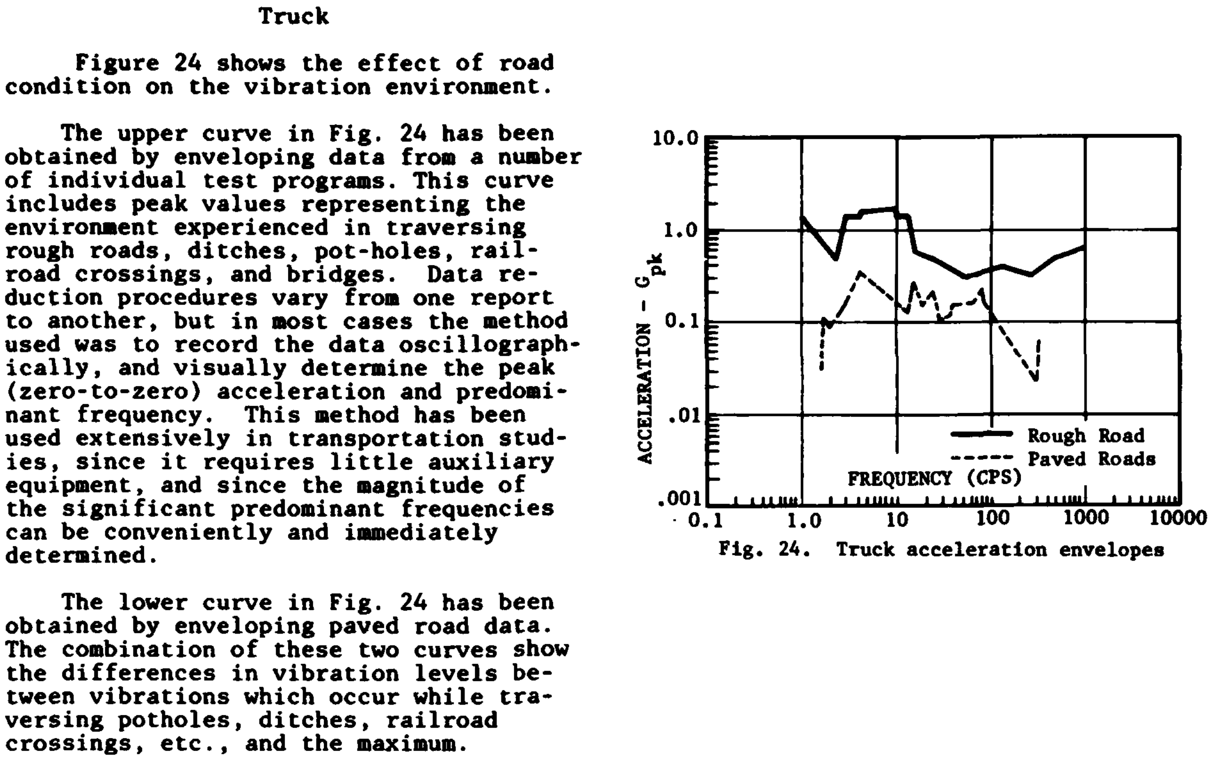

Truck

Figure 24 shows the effect of road condition on the vibration environment.

The upper curve in Fig. 24 has been obtained by enveloping data from a number of individual test programs. This curve includes peak values representing the environment experienced in traversing rough roads, ditches, pot-holes, railroad crossings, and bridges. Data reduction procedures vary from one report to another, but in most cases the method used was to record the data oscillographically, and visually determine the peak (zero-to-zero) acceleration and predominant frequency. This method has been used extensively in transportation studies, since it requires little auxiliary equipment, and since the magnitude of the significant predominant frequencies can be conveniently and immediately determined.

The lower curve in Fig. 24 has been obtained by enveloping paved road data. The combination of these two curves show the differences in vibration levels between vibrations which occur while traversing potholes, ditches, railroad crossings, etc., and the maximum.

Fig. 24. Truck acceleration envelopes

Figure 1. Excerpt from a review paper by Schock and Paulson.

from a NASA funded review by Schock and Paulson [1]. The graph shows peak acceleration as a function of a frequency which, for shocks, may be interpreted as the inverse of twice the duration of the peak pulse. The text explains that it is the envelope of data from various investigations and that different data reduction methods may have been used. The text does not explain whether the accelerations are those of the truck bed or of some equipment being carried; perhaps both were included in the various investigations. Deriving a Qualification Test from figure 1 is fairly straightforward. If, for example, the equipment to be tested resonated highly at 100 Hz, subjecting it to a 5 msec wide 0.35 g high shock pulse should prove its ability to withstand truck transport. There is no information given as to how allowance might be made for less than the worst case or, for that matter, as to how extrapolation might be made to worse than the worst observed case. Also, there is uncertainty as to where the shock should be reproduced, as input or response.

The paper by Schock and Paulson, which covered other forms of transport as well as trucks, was the referenced source of the text and graph of figure 2. Figure 2 is excerpted from a general specification for missile environments. Note the changes. From top to bottom:

1. The graph ends at 50 Hz; the higher frequency part has been elided.
2. The ordinate unit has changed from "G_{pk}" to "g."
3. The figure title has changed from "Truck Acceleration Envelopes" to "Truck Transportation Vibration Envelopes."
4. The text is now explicit: the graph is input to the thing carried, not its response.
5. The text refers to the figure as showing "typical vibration levels" rather than an upper envelope.

Although these changes and additions have removed some uncertainty (the shock, or vibration, is assumed to be input) others have been introduced. If the graph defines vibration but the ordinate is not explicitly peak acceleration then what is it? It might be RMS acceleration level, either Gaussian

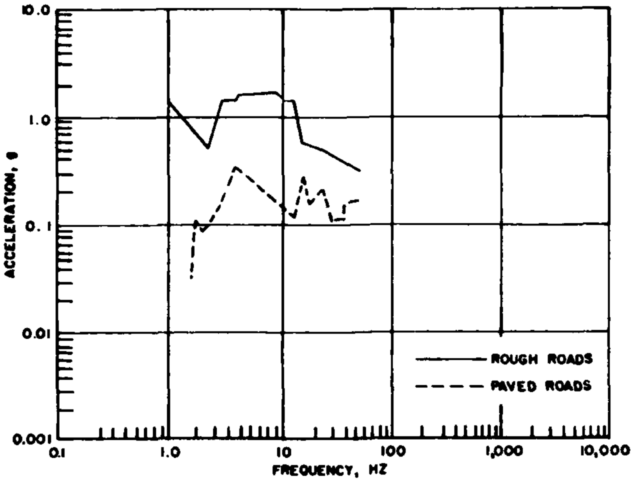

Figure 22. Truck Transportation Vibration Envelopes.

70.1 Transportation vibration, truck. The weapon is packaged or containerized during transportation by truck; hence the vibration is input to the package or container. Vibration during truck transportation is caused by truck passage over rough roads or terrain and by unbalanced rotating portions of the truck power train. The magnitude of the induced vibrations depends on the type of truck used, the load condition of the truck, and the skill of the operator. Figure 22 shows typical vibration levels for this environment.

Figure 2. Excerpt from a general specification for air-launched missiles.

random or sinusoidal. Or of course it might be peak (3δ) random or peak sinusoidal; the deletion of "peak" in the axis label being an oversight. A design specification must of course be more explicit than a general specification, and we would expect these uncertainties to be removed.

This expectation has been realized. Figure 3 is excerpted from a design specification which references the general specification discussed above. The changes have now made it as definite as a design specification can be:

1. The word "PEAK" has reappeared in the ordinate lable.
2. The figure title now spells out "Sinusoidal Vibration."

Thus having arrived at something usable, there is some doubt whether it represents the physical events from which it so remotely descended. Also, while figure 3 is satisfactory for design, it would have to be further supplemented to arrive at a test. Most likely this supplement would specify a sine-sweep test at a certain rate, possibly with certain periods of dwell at resonances. If the total duration of such a test were short it would be regarded as a Qualification Test. On the other hand, seizing on the word "typical" in the general specification, one might specify a test of long duration which would be an MTBF test, i.e., some number of failures would be acceptable. So, even though the specification is sufficiently definite for design, there is still more information needed to define a test.

The lesson of the three figures is whoever undertakes to collect, summarize, and present data on environmental stresses should keep before him the two ultimate uses:

1. Definition of design stress levels
2. Definition of test stresses, both Qualification and MTBF.

The process of data reduction should preserve the information needed for these two ends. This report began with the collection of data from four truck trips. At the end is a prescription for the design of a truck transport MTBF test. A test designer or specification writer using this prescription will still need to exercise judgement and critical selectivity, but not the faculty of creative assumption.

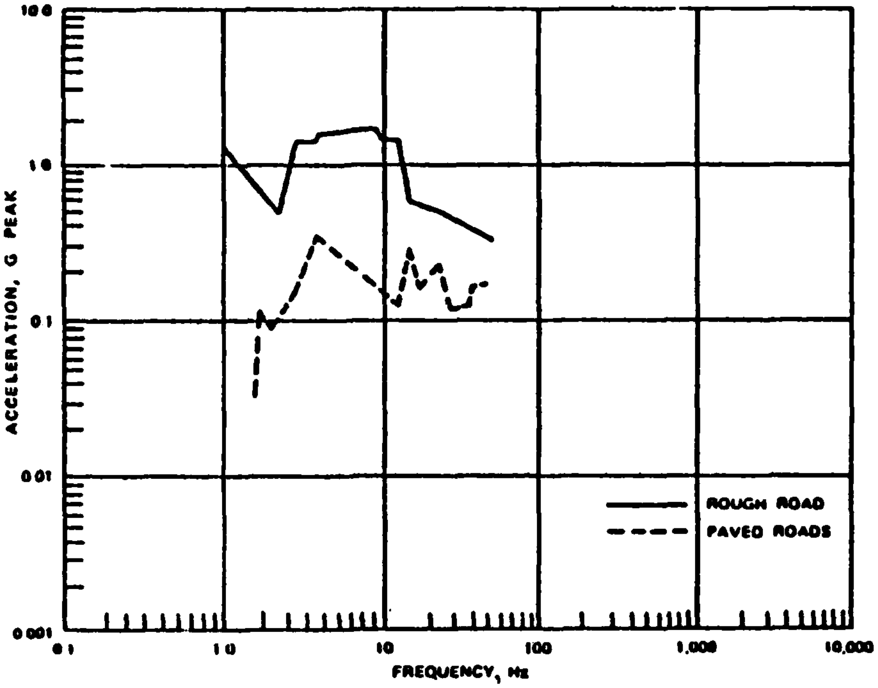

(U) Figure 10-8. Truck Transportation Sinusoidal Vibration Envelopes.

Figure 3. Excerpt from the design specification for an air-launched missile.

II. MEASUREMENTS

Instrumentation

On each of the four trips accelerometers were attached to the external surface of a missile. The attachment points were at major structural bulkheads so as to avoid localized resonances. The specific locations and orientations of the accelerometers are given in table 1. The accelerometers were of the strain gage type so that they responded to steady acceleration. However, an AC amplifier system was used so that measured response was attenuated below 1/2 Hz. The high frequency limit was about 500 Hz.

The accelerometer responses were recorded digitally by an Endevco TEMARS (Transportation Environment Measurement and Recording System). The TEMARS records an acceleration pulse, provided it exceeds a threshold, by first storing in one of three registers its peak value and the time it was above the threshold. This is then read from the register and the pulse is recorded on magnetic tape as having had an amplitude in a certain range (one of 128, 64 positive and 64 negative) and a time between threshold crossings, or width, in a certain range (also one of 64). The register is then free to accept new pulses. Because of the delay in transferring the data from a register to the tape a second pulse may arrive before the first register used, A, is free. In that case the pulse is recorded in the B-register. If another pulse arrives while A and B are full, the pulse goes into the C-register which however only records the pulse height and not width. The register deadtime is approximately 750 msec.

The threshold and maximum values of acceleration used are listed in table 1. The increments in which the amplitude is recorded are 1/64 of the maximum. The pulse widths to which a pulse is assigned were, in each case, 2 msec wide from 1 to 124 msec plus an increment 0-1 msec and a greater-than-124 msec assignment.

The Trips

The particulars of the trips are summarized in table 2. The first trip, in the vicinity of Pt. Mugu, CA, was a shakedown trip with a side objective of obtaining measurements over secondary roads. The other trips were over actual shipping routes. In each case the truck was lightly loaded relative to its rated capacity. The minimum load was deliberately chosen for the Canadian and WSMR

Table 1. Accelerometer Locations, Orientations, and Ranges

Trip	Missile	Accelerometer	Location	Orientation (+)	Threshold g*	Maximum g*
Pt. Mugu	1200 lb air-to-air	X	forward hook	forward	0.3	3.0
		Y	"	left	0.3	3.0
		Z	"	up	0.5	5.0
Tucson	1200 lb air-to-air	X	forward hook	forward	0.3	3.0
		Y	"	left	0.4	4.0
		Z	"	up	0.5	5.0
Canada	60 lb rocket mtr	X	forward bulkhead	left	0.4	4.0
		Y	"	up	0.5	5.0
		Z	"	forward	0.4	4.0
WSMR	1800 lb air-to-ground	X	forward hook	up	1.5	15.0
		Y	center	"	1.5	15.0
		Z	after hook	"	1.5	15.0

*These are nominal values; actual values differ by a calibration factor which varied from 0.85 to 0.88.

Table 2. Trips Over Which Shock Data Were Collected

Trip	Route	Driving time (hr)	Truck/trailer	Load	Location of Instrumented Missile
Pt Mugu	Pt Mugu CA to Camarillo CA to Oxnard CA to Pt Mugu CA	1.33	Commercial 40 ft flatbed 18 wheeler	Two 1200 lb air-to-air missiles in a standard two-missile container	Container was centered on the bed. Right missile was instrumented.
Tucson	Pt Mugu CA to Tucson AZ	14.45	"	Eight 1200 lb air-to-air missiles in four two-missile containers	Containers were in rectangular array centered on the bed. Instrumented missile was the rightfront.
Canada	Trenton, Ontario to Rocky Point B.C.	80	Covered military 6 X 6	Wooden pallet of 20 rocket motors	Pallet was centered over rearmost axle. Center missile was instrumented.
WSMR	Seal Beach CA to White Sands Missile Range NM	11.8	Commercial 40 ft van 18 wheeler	Single 1800 lb air-to-ground missile in a standard container	Centered in van.

trips as a worst case. However, this is not unrealistic since light loads are the rule for explosives. Except for the Canadian trip, the trucks were driven straight through, without overnight stops. On the Canadian trip overnight stops were made because local laws prohibited carrying explosives after dark. It being summer at the time, the layovers were relatively short. The roads were major highways except at the end of the WSMR trip where several miles of poorly maintained and very rough secondary road were transversed. This section continually saturated the instrumentation (±15 g) and had to be eliminated in analysis of the data. Thus the analyzed data refers only to paved, maintained, secondary and major highways.

Data

The data was read off the tapes and compiled by computer. This yielded a set of arrays like that of figure 4. For convenience the pulse width bins were combined in pairs to give bins 4 msec wide (except for the first and the last). The pulses read from the C-register are shown separately since they cannot be assigned a pulse width. Also, the sign of the amplitude was neglected in compiling the C-register data. Each entry in the array is the *number of* shock events recorded with that amplitude and that pulse width. Where the entry is *** it means the number was greater than 999. (This is due to interference between columns in the output format.) Notice that there are some entries below the threshold. This is because whenever the threshold is exceeded by any one of the three accelerometer outputs, all other non-zero outputs are also recorded. The totals for each amplitude bin are printed at the right and the totals for each pulse-width bin are printed at the bottom. These printed arrays of data were the final product sent to each of the missile groups that had asked for a measurement.

Looking at these arrays it is immediately noticed that some data has been lost at the outset. The C-register, which does not record pulse width, provided the following fraction of the recorded data:

Trip	% of Pulses in C-Register
Pt. Mugu	23%
Tucson	5%
Canada	24%
WSMR	13%

The loss of pulse width is far from the worst of it though. Filling the C-register 24 percent of the time, out of a possible 33 percent, suggests that had there been a D-register it might also have been filled a significant part of the time and perhaps even registers E, F, and G might be required to capture all the data. Hypothesizing a geometric decrease from register to register (which likely exaggerates the loss) the fraction of pulses missed can be estimated.

Trip	Estimated Data Loss
Pt. Mugu	37%
Tucson	2%
Canada	40%
WSMR	10%

Also, on all the trips, the C-register seemed to account for an even greater percentage of the high pulses than the overall percentages given above. This would imply that in many cases the C-pulse was higher than the A- or B-pulse, thus the data loss on the Pt. Mugu and Canadian trips may be even more severe in terms of estimating maxima. On the other hand, the Tucson and WSMR data should yield a fairly good description of Interstate Highway travel. To extract this description requires some further analysis of the data.

Analysis

The analysis of the data has two objects: to normalize the data so that the trips may be compared with one another and possibly with previous data such as figure 1. Second, the analysis aims at a description of the truck shock environment from which test conditions easily and directly derive. The analysis which follows begins with the usual assumption that the data of each trip is a sample from a stationary, ergodic random process.

Normalization of data proceeds from recognition that a longer trip will produce more pulses and, as the number of pulses is greater, so the highest pulse will be higher. So the first step in normalization is to scale the number of pulses of each height and width according to some standard trip length. The length would most naturally be measured in kilometres (the number of bumps in the road between two cities is proportional to the distance between them) but for test design it is more convenient to use trip duration. This is actually no less fundamental a measure than distance, since the number of perceived bumps in the road depends on the speed in any case. Whether in terms of time or distance, though, simply ratioing the number of pulses up or down doesn't work at the extremes where the number is 1, 0 or some other small integer. Instead, the number of pulses above a given

```
X COORDINATE DATA FROM 78 11 27 12  0 TO 78 11 29  0  0 (YR MO DA HR MN)

    PULSE   0       5.0     13.0     21.0     29.0     37.0     45.0     53.0     61.0     69.0     77.0
    WIDTH       1.0     9.0     17.0     25.0     33.0     41.0     49.0     57.0     65.0     73.0     8

AMPLITUDE
   8.37   0   0   0   0   0   0   0   0   0   0   0   0   0   0   0   0   0   0   0   0   0         0
   8.17   0   0   0   0   0   0   0   0   0   0   0   0   0   0   0   0   0   0   0   0   0         0
   7.96   0   0   0   0   0   0   0   0   0   0   0   0   0   0   0   0   0   0   0   0   0         0
   7.76   0   0   0   0   0   0   0   0   0   0   0   0   0   0   0   0   0   0   0   0   0         0
   7.56   0   0   0   0   0   0   0   0   0   0   0   0   0   0   0   0   0   0   0   0   0         0
   7.35   0   0   0   0   0   0   0   0   0   0   0   0   0   0   0   0   0   0   0   0   0         0
   7.15   0   0   0   0   0   0   0   0   0   0   0   0   0   0   0   0   0   0   0   0   0         0
   6.94   0   0   0   0   0   0   0   0   0   0   0   0   0   0   0   0   0   0   0   0   0         0
   6.74   0   0   0   0   0   0   0   0   0   0   0   0   0   0   0   0   0   0   0   0   0         0
   6.53   0   0   0   0   0   0   0   0   0   0   0   0   0   0   0   0   0   0   0   0   0         0
   6.33   0   0   0   0   0   0   0   0   0   0   0   0   0   0   0   0   0   0   0   0   0         0
   6.13   0   0   0   0   0   0   0   0   0   0   0   0   0   0   0   0   0   0   0   0   0         0
   5.92   0   0   0   0   0   0   0   0   0   0   0   0   0   0   0   0   0   0   0   0   0         1
   5.72   0   0   0   0   0   0   0   0   0   0   0   0   0   0   0   0   0   0   0   0   0         0
   5.51   0   0   0   0   0   0   0   0   0   0   0   0   0   0   0   0   0   0   0   0   0         0
   5.31   0   0   0   0   0   0   0   0   0   0   0   0   0   0   0   0   0   0   0   0   0         0
   5.11   0   0   0   0   0   0   0   0   0   0   0   0   0   0   0   0   0   0   0   0   0         0
   4.90   0   0   0   0   0   0   0   0   0   0   1   0   0   0   0   0   0   0   0   0   0         1
   4.70   0   0   0   0   0   0   0   0   0   0   0   0   0   0   0   0   0   0   0   0   0         0
   4.49   0   0   0   0   0   0   0   0   1   0   0   0   0   0   0   0   0   0   0   0   0         1
   4.29   1   0   0   0   0   0   0   0   0   0   0   0   0   0   0   0   0   0   0   0   0         1
   4.08   3   0   0   0   0   0   0   0   0   0   0   0   0   0   0   0   0   0   0   0   0         3
   3.89   1   0   0   0   0   0   0   0   0   0   0   0   0   0   0   0   0   0   0   0   0         1
   3.68   0   0   0   0   0   0   0   0   0   1   1   0   0   0   0   0   0   0   0   0   0         2
   3.47   0   0   0   0   0   0   0   0   1   0   2   0   0   0   0   0   0   0   0   0   0         3
   3.27   2   0   0   0   0   0   0   0   1   2   1   0   0   0   0   0   0   0   0   0   0         6
   3.06   6   1   0   0   0   0   1   0   0   0   1   0   0   0   0   0   0   0   0   0   0         9
   2.86   5   0   0   1   0   0   0   0   3   5   0   0   0   0   0   0   0   0   0   0   0        14
   2.65   6   0   0   0   0   0   0   0   2   3   0   0   0   0   0   0   0   0   0   0   0        11
   2.45  11   0   0   0   0   0   0   2   4   2   0   0   0   0   0   0   0   0   0   0   0        19
   2.25   6   1   1   0   1   0   6   3   7   5   1   0   0   0   0   0   0   0   0   0   0        36
   2.04  18   0   2   0   2   0  10  17  13   2   0   0   0   0   0   0   0   0   0   0   0        64
   1.84  23   0  19  10   8   6  47  30  12   0   0   0   0   0   0   0   0   0   0   0   0       155
   1.63  56    0145  22  69  58  87  37   5   0   0   0   0   0   0   0   0   0   0   0   0       479
   1.43157    6998122227115  49  17   0   0   0   0   0   0   0   0   0   0   0   0   0      1691
   1.23459******186  51  16   3   0   0   0   0   0   0   0   0   0   0   0   0   0   0      4352
   1.02  97  15   0   0   0   0   0   0   0   0   0   0   0   0   0   0   0   0   0   0   0       112
   0.82   0   0   0   0   0   0   0   0   0   0   0   0   0   0   0   0   0   0   0   0   0         0
   0.61   0   1   0   0   0   0   0   0   0   0   0   0   0   0   0   0   0   0   0   0   0         1
   0.41   0   0   0   0   0   0   0   0   0   0   0   0   0   0   0   0   0   0   0   0   0         0
   0.20  16   0   0   0   0   0   0   0   0   0   0   0   0   0   0   0   0   0   0   0   0        16
  -0.20   0   0   0   0   0   0   0   0   0   0   0   0   0   0   0   0   0   0   0   0   0         0
  -0.41   0   0   0   0   0   0   0   0   0   0   0   0   0   0   0   0   0   0   0   0   0         0
  -0.61   0   0   0   0   0   0   0   0   0   0   0   0   0   0   0   0   0   0   0   0   0         0
  -0.82   0   0   0   0   0   0   0   0   0   0   0   0   0   0   0   0   0   0   0   0   0         0
  -1.02   0   1   0   0   0   0   0   0   0   0   0   0   0   0   0   0   0   0   0   0   0         1
  -1.23   0  15  70  18   4   0   0   0   0   0   0   0   0   0   0   0   0   0   0   0   0       107
  -1.43   0   0  11  22  16   2   4   0   5   0   0   0   0   0   0   0   0   0   0   0   0        60
  -1.63   0   0   0   4   7   2   0   3   2   0   0   0   0   0   0   0   0   0   0   0   0        18
  -1.84   0   0   0   1   2   4   2   0   1   3   0   0   0   0   0   0   0   0   0   0   0        13
  -2.04   0   0   0   0   0   0   0   0   0   3   0   0   0   0   0   0   0   0   0   0   0         3
  -2.25   0   0   0   0   0   1   0   0   0   1   0   0   0   0   0   0   0   0   0   0   0         2
  -2.45   0   0   0   0   0   0   0   0   0   0   1   0   0   0   0   0   0   0   0   0   0         1
  -2.65   0   0   0   0   0   0   0   0   0   0   0   0   0   0   0   0   0   0   0   0   0         0
  -2.86   0   0   0   0   0   0   0   0   0   0   1   0   0   0   0   0   0   0   0   0   0         1
  -3.06   0   0   0   0   0   0   0   0   0   0   0   0   0   0   0   0   0   0   0   0   0         0
  -3.27   0   0   0   0   0   0   0   0   0   0   0   0   0   0   0   0   0   0   0   0   0         0
  -3.47   0   0   0   0   0   0   0   0   0   0   0   0   0   0   0   0   0   0   0   0   0         0
  -3.68   0   0   0   0   0   0   0   0   0   0   0   0   0   0   0   0   0   0   0   0   0         0
  -3.88   0   0   0   0   0   0   0   0   0   0   0   0   0   0   0   0   0   0   0   0   0         0
  -4.08   0   0   0   0   0   0   0   0   0   0   0   0   0   0   0   0   0   0   0   0   0         0
  -4.29   0   0   0   0   0   0   0   0   0   0   0   0   0   0   0   0   0   0   0   0   0         0
  -4.49   0   0   0   0   0   0   0   0   0   0   0   0   0   0   0   0   0   0   0   0   0         0
  -4.70   0   0   0   0   0   0   0   0   0   0   0   0   0   0   0   0   0   0   0   0   0         0
  -4.90   0   0   0   0   0   0   0   0   0   0   0   0   0   0   0   0   0   0   0   0   0         0

TOTAL         1188     388     205     114      27       0       0       1       1       0
          878     3743    391     208      57       9       0       1       0       0       0
```

Figure 4. Compiled TEMARS shock data for WSMR trip.

height were plotted as in figure 5. This is the sample approximation to one minus the distribution function. Ratioing down to a shorter time then corresponds to sliding the curve down relative to the logarithmic ordinate; and similarly, up for a longer time. From the adjusted curve one may read off the (expected) number of pulses exceeding say 2 g in 500h of trucking (35, according to figure 5). In order to generate a graph like that of figure 1, the distribution function must be read the other way around; i.e. the level which is exceeded once per hour is 1.13 g, the level exceeded once per 500h is 4.82 g. The last of course requires extrapolation since the measurement period was less than 500h.

The use of a straight-line extrapolation on the semi-logarithmic plot has some theoretical justification. It is a theorem of extreme-value statistics [2] that near the highest value of a sample of n from a distribution F(x), the distribution is approximated by:

$$F(x) = 1 - \frac{1}{n} \exp [-\alpha_n(x-U_n)]$$

where U_n and α_n are constants depending on the sample size n and the form of the distribution functions. Assuming this equation, the ordinate in figure 5 is given by:

$$\ln [n(1- F(x))] = - \alpha_n (x - U_n)$$

which is linear. It is also a theorem of extreme value statistics that, at the mode of the largest value of a sample of

$n, \tilde{x}_n,$

$$F(\tilde{x}_n) = 1 - \frac{1}{n}$$

hence the parameter U_n is just that mode. The parameter α_n, which is the negative of the slope in figure 5, is found by differentiation to satisfy.

$$\alpha_n = n f (U_n)$$

where f(x) is the density corresponding to F(x). In the case of an exponential distribution, α_n is just the rate parameter and does not depend on n.

Insofar as the linear extrapolation holds near the highest value, one may infer the distribution of the highest value in a longer trip. This is complicated slightly by the fact that the sample size (number of pulses) for the measured trip is unknown. The complication is overcome by writing the distribution in terms of parameters U_n and α_n of the measured sample and, K, the ratio of the trip length of interest to the measurement trip length. In the case of trucking this will be the ratio of trip durations:

$$P [\text{"largest of } K_n\text{"} < x] = F (x)^{Kn}$$

$$= \{ 1 - \frac{1}{n} \exp [-\alpha_n(x-U_n)]\}^{Kn} \text{ for}$$

$n>>1$ and x not much smaller than U_n.

$$= \exp [-\exp (-\alpha_n(x-U_n)]^K$$

$$= \exp [-K \exp (-\alpha_n(x-U_n))].$$

Using this distribution, extreme values can be estimated. For example taking from figure 5, $\alpha_n = 0.97$ 1/g and $U_n = 3.38$ g and putting K = 500h/80h = 6.25 one may calculate that level which has only 5 percent chance of being exceeded in 500h.

$$0.95 = \exp [-6.25 \exp (-0.97(x-3.38))]$$

solving for x yields

x (exceeded 5% in 500h) = 8.33 g.

This is the sort of information relevant to design and to qualification tests. However, in all the preceding, the normalization and scaling has been relative to trip length or duration. This neglects another important scale factor.

When the pulses were counted by the TEMARS they were assigned to bins corresponding to a certain pulse width as well as a certain height. Just as traveling further would increase the number of pulses expected in a bin, so combining two bins corresponding to the same height, but adjacent widths, would increase the number of pulses associated with the psuedo-frequency at the center width of the two. Hence the data should be normalized with respect to bandwidth as well as trip duration. Of course the measured data was all relative to 4 msec intervals and so was already comparable, one trip to another. However in the derivation above, one step requires that n>>1 (a condition to be desired in all statistical inference) and so it was necessary in most cases to sum together the counts over certain ranges of pulse width. Except for the WSMR trip those summed were 37-41 msec, 45-61 msec, and 65-125 msec. For the WSMR trip 29-37 msec pulses were counted together. (No longer pulses were recorded.) Having summed together adjacent bands it was then necessary to normalize the results. Also, shock data is usually presented as a function of frequency,

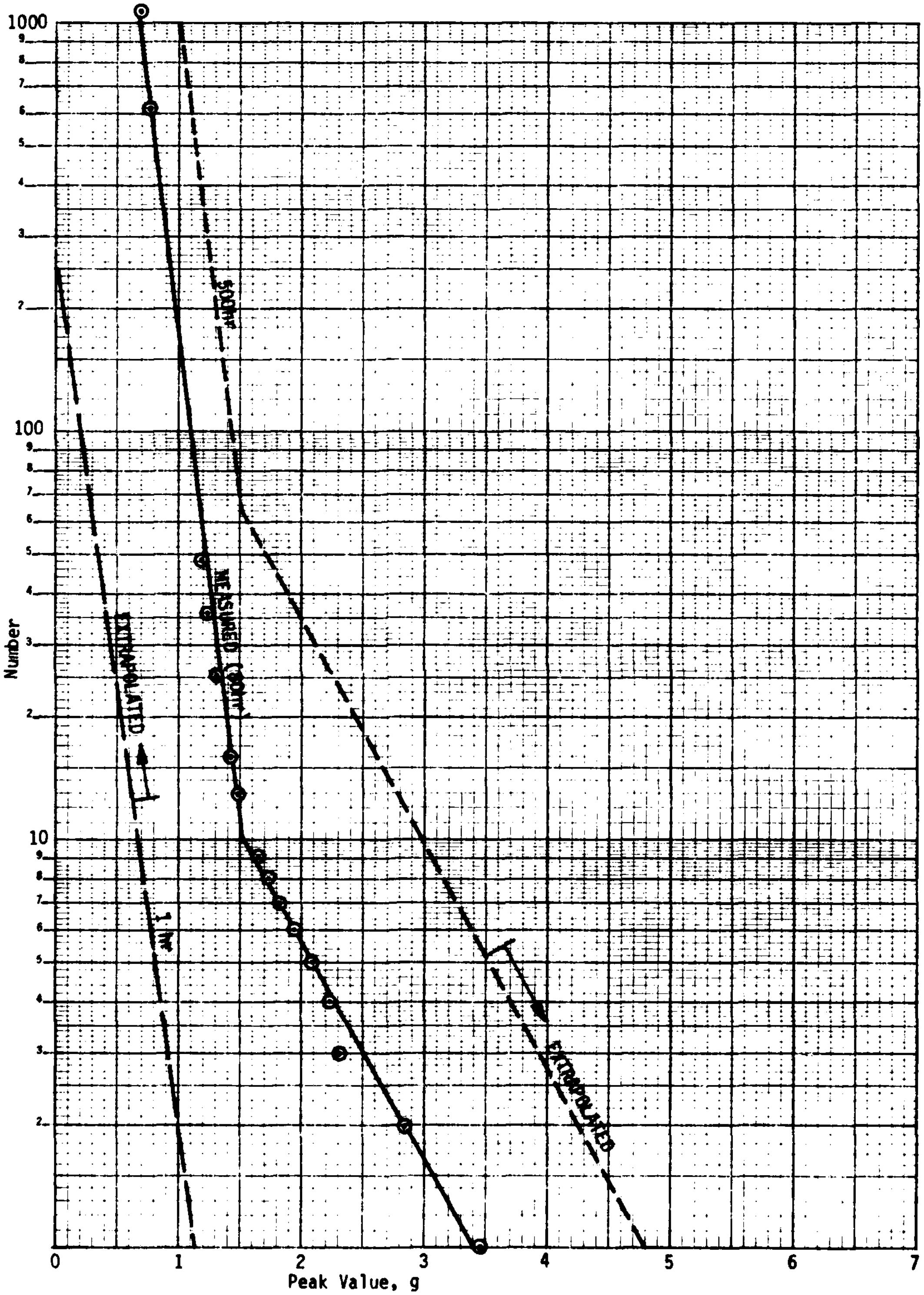

Figure 5. Number of Shocks whose peak value is less than a given acceleration level. Measured values are for the Canada trip, Y-axis, 21 msec pulse width.

as in figure 1. So the final normalization of the data was made, not to a standard pulse width, but to a standard 1 Hz bandwidth of psuedo-frequency (one divided by twice the pulse width). Since, in the equation above, it made no difference where the ratio of sample sizes K came from, the same equation holds when K is interpreted as including a bandwidth factor.

$$K = \left(\frac{\text{Duration}}{\text{Measurement Duration}}\right)$$

$$\left(\frac{\text{Bandwidth}}{\text{Measurement Bandwidth}}\right)$$

Taking the same example as before, note that figure 5 is for 21 msec ±2 msec wide pulses. So,

$$\text{Measurement Bandwidth} = \frac{1}{2\text{x}0.019}$$

$$- \frac{1}{2\text{x}0.023}$$

$$= 4.6 \text{ Hz}$$

Then for pulses resolved into 1 Hz bands and a 500h trip,

$$K = \frac{500}{80}\,\frac{1}{4.6} = 1.36.$$

The level exceeded on only 5 percent of such trips is

x (exceeded 5% in 500h Hz) = 6.76 g.

This is considerably smaller than the previous estimate of 8.33 g; the difference being that before, any pulse with a psuedo-frequency of 23.8 Hz ±2.3 Hz would have been counted, whereas the latter result would only count pulses of psuedo-frequency 23.8 Hz ±0.5 Hz.

Having resolved the method of normalization and extrapolation, curves similiar to the graph of figure 1 were generated as follows:

1. For each trip and each pulse-width band (grouping some together as mentioned above) the cumulative number below a given level was plotted as in figure 5.
2. The resulting plot was fitted by a straight line or a once-broken line as in figure 5.
3. From the slope, $-\alpha_n$, and the intercept with $n=1$, U_n, of this line, the normalized values of U for 1 Hz bandwidth and 1h and 100h trips were calculated. These are plotted as functions of the psuedo-frequency in figures 6 through 9. The values of U (100h) and $1/\alpha$ are given in table 3. Where a broken line fit was used the value for the higher level part of the line is given followed by the lower level value in parantheses.
4. Also using α_n and U_n the 95th percentile level for a 500h trip and 1 Hz bandwidth was calculated and plotted in figures 6 through 9.

The two lower curves of figures 6 through 9, being values of U, are the most likely amplitude of the highest pulse to occur in a 1 Hz wide band over a trip of the specified duration (1h or 100h). The mean amplitude and the median amplitude are slightly higher. Within the context of the same assumptions and approximations as before, they are respectively:

$$\text{Mean } x = U + 0.576\ (1/\alpha)$$

$$\text{Median } x = U + 0.367\ (1/\alpha)$$

The trip duration of 500h was chosen for the extreme value calculation because, as shown in figure 10, this is approximately the 95th percentile of the time a missile may spend in rail/truck transport. Hence the 95th percentile of the 500h trip is the 95th percentile level of the 95th percentile trip duration. Thus it is the 90th percentile over all missile histories.

Comparison of the data for the four trips finds them to be similar. The 100h curves differ by no more than a factor of three. This occurs despite the fact that the measurements were made on different missiles, carried by different trucks over different roads. Comparison with the previous data of figure 1, seems at first to show a great difference; the present data is a factor of ten above that assigned to paved roads in figure 1. Actually it is the upper, or rough-road, curve of figure 1 that should be compared to the present data. The paved-road curve is the vibration alone, leaving out potholes, railroad crossings etc. The upper curve leaves them in, as does the present data. On this basis the old and new data are seen to be very close; the rough-road curve of figure 1 pretty well follows the Pt. Mugu TEMARS data normalized to 1h Hz. Thus it appears that, while the lower curve of figure 3 may be an appropriate test vibration level (although whether it should be sinusodoidal or not is unresolved), the upper curve certainly

Table 3. Estimated Value of the Mode for the Highest Shock in 100h Hz, U, and the Inverse of the Slope α

Center Psuedo-Frequency Hz	PT. MUGU		TUCSON	
	U (100h Hz) g	1/α g	U (100h Hz) g	1/α g
6	3.72	0.53	1.61	0.137
10	2.95	0.32	1.14	0.092
13	1.60	0.128	1.18	0.091
15	1.77 (1.16)	0.19 (0.080)	1.01	0.076
17	1.33	0.113	1.02	0.069
20	1.09	0.078	0.96	0.067
24	0.78	0.048	1.40 (0.81)	0.304 (0.048)
29	0.76	0.074	1.23 (0.68)	0.261 (0.041)
38	0.80	0.060	1.08 (0.65)	0.256 (0.037)
56	0.51	0.030	0.90 (0.62)	0.278 (0.039)
100	0.94 (0.55)	0.21 (0.024)	0.97	0.119
500	0.51	0.056	0.50	0.087

Center Psuedo-Frequency Hz	CANADA		WSMR	
	U (100h Hz) g	1/α g	U (100h Hz) g	1/α g
6	2.81	0.39		
10	2.85	0.56		
13	3.66	0.46		
15	3.46	0.44	4.91	0.75
17	3.36	0.41		
20	2.26 (1.73)	0.33 (0.19)	2.68	0.18
24	2.26	1.03	2.69	0.19
29	1.39	0.22	2.20	0.15
38	1.11 (1.10)	0.54 (0.098)	2.13	0.12
56	0.82 (0.96)	0.43 (0.109)	2.20	0.22
100	0.40 (0.75)	1.32 (0.078)	1.90	0.11
500	0.41 (0.48)	0.33 (0.065)	0.75 (1.32)	0.72 (0.041)

Where a broken-line fit was used, the parameters for the lower level part of the line are included in parentheses.

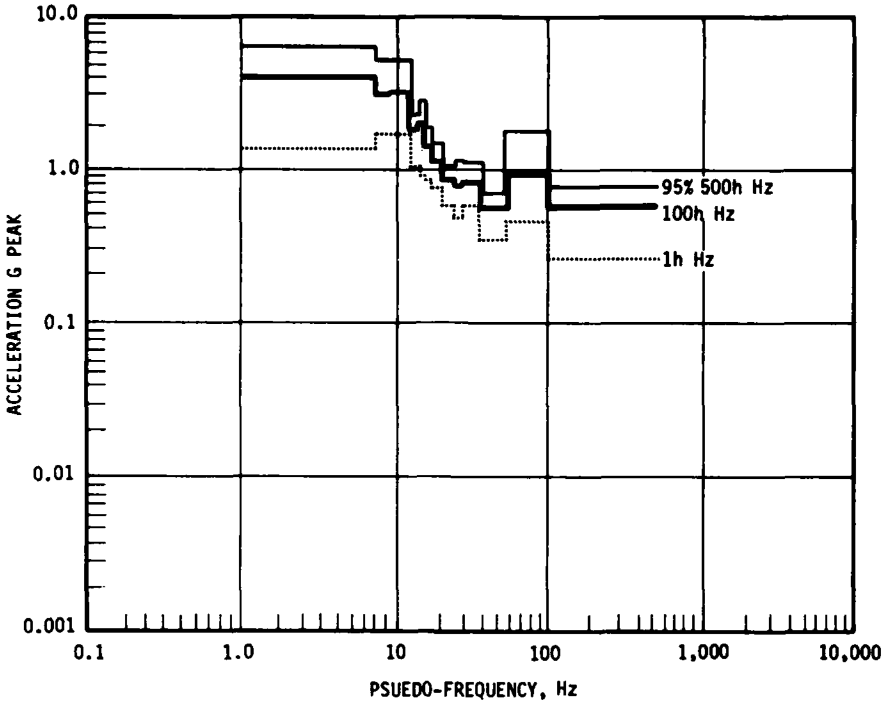

Figure 6. Peak shock spectrum for Pt. Mugu trip, Z-axis.

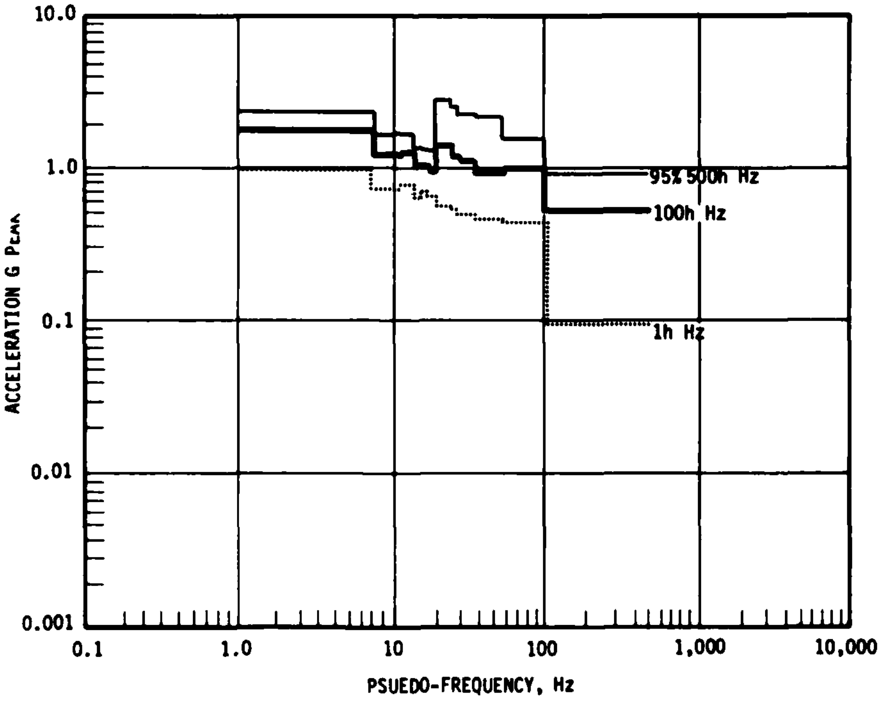

Figure 7. Peak shock spectrum for Tucson trip, Z-axis.

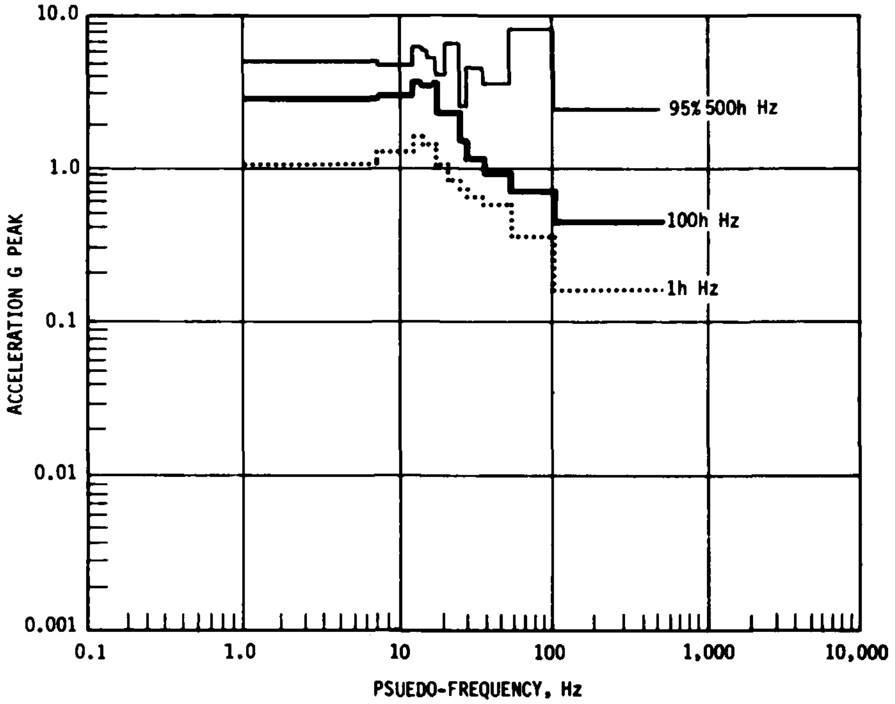

Figure 8. Peak shock spectrum for Canada trip, Y-axis.

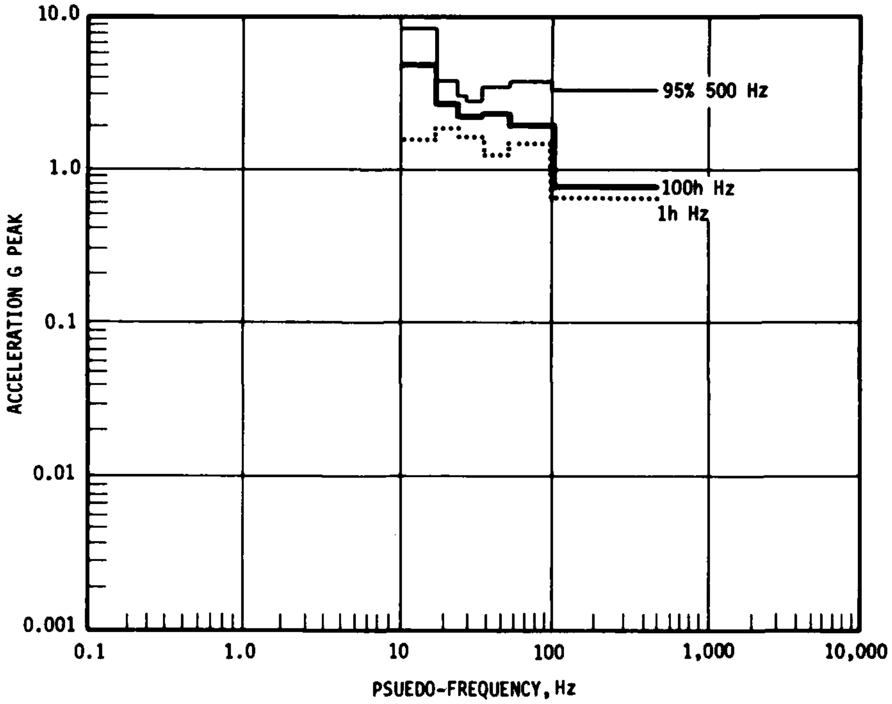

Figure 9. Peak Shock Spectrum for WSMR
(White Sands Missile Range Trip), X-accelerometer.

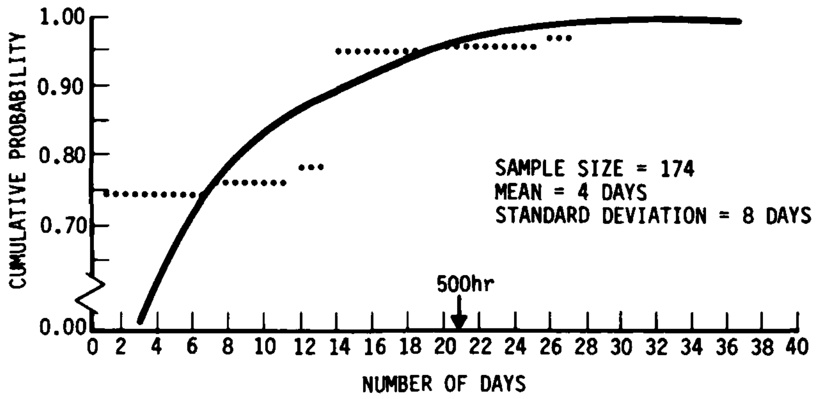

Figure 10. Cumulative Probability of Time Spent in Truck/Rail Transport by an Air-Launched Missile.

is not. The upper curve is a level exceeded about once per hour in driving over paved roads. The short piece of record at the end of the WSMR trip showed that, on a rough road, the level would be at least ten times higher.

TESTS

Finally comes the question of deriving test levels from the data. The upper curves, representing the 90th percentile extremes are close to what is needed. However they are normalized to 1 Hz bandwidth. If a missile and container were to be tested and they were known to have a resonance at 10 Hz with a width of 3 Hz, then the test level should take account of this greater bandwidth.

$$x_{\text{test}} = x(\text{exceeded 5\% in 500h Hz}) + \frac{\ln 3}{\alpha}$$

or, using the Pt. Mugu data,

$$\begin{aligned} x_{\text{test}} &= 4.40 + 0.317 \times 1.099 \\ &= 4.75 \text{ g}. \end{aligned}$$

The missile/containers might be tested at several different psuedo-frequencies taking into account the response bandwidth at each frequency and keeping the center frequencies separated so that each frequency tests different structural modes.

The design of an MTBF test is somewhat more complex and depends on how the shocks are to be induced. Suppose that the shocks are to be induced at intervals, $\Delta\tau$, chosen sufficiently long so that the response dies out between shocks. Further, suppose the shocks to be applied are of I discrete center frequencies, f_i, with associated bandwidths.

$$W_i = \tfrac{1}{2} (f_{i+1} - f_{i-1}).$$

Further, suppose there is a threshold, h, so that only pulses greater than h are to be reproduced in the test. Then the number of pulses of a given kind is what must be determined in designing the test. The order of the pulses applied in the test should be in some way randomized, but exactly how is not important. Assume the number of pulses of frequency f_i, above a level x is given by

$$M_i (x) = M_i \exp [-a_i(x-h)],$$

where M_i is the (unknown) total number in the test and a_i is a scale factor of the random amplitude generator used in the test.

The time to accumulate M_i pulses, above a level x, in actual travel is given by

$$t_i(M,x) = \frac{M_i}{(\text{rate of exceeding } x).}$$

Assume that over the range of interest the distribution can be approximated by a single exponential. This can be written out explicitly,

$$= \frac{Mi}{W_i \exp - \alpha_i \ (x - U_i)}$$

Taking U to be the 1 Hz level, the result, t_i, will be in hundreds of hours. Substituting for M_i yields

$$t_i = \frac{Mi}{Wi} \exp \left[-a_i(x-h) + \alpha_i \ (x-U_i)\right]$$

$$= \frac{M}{W} \ \exp x \ (\alpha_i - a_i) + a_i h - \alpha_i u_i + \ln \left(\frac{M_i}{M} \frac{W}{W_i}\right)$$

where $M = \Sigma M_i$ and $W = \underset{i}{\Sigma} W_i$.

This time, t_i will be the amount of travel time simulated by the M_i shock pulses applied in test. The constraint on the design is that the time simulated must be the same for each frequency of pulse; thus the exponent must be independent of i. This independence must hold regardless of the value of x, so two equations are implied,

$$x \ (\alpha_i - a_i) = \text{constant for all } x$$

$$a_i h - \alpha_i \ ui + \ln \left(\frac{M_i}{M} \frac{W}{W_i}\right) = \text{constant.}$$

The first of these immediately reduces to $a_i = \alpha_i$, a condition to be satisfied by the random amplitude scale a_i. Let the constant in the second be denoted ln b; then it can be solved for the desired quantity, $\frac{Mi}{M}$.

$$\frac{Mi}{M} = b \frac{Wi}{W} \exp \alpha_i \ (U_i - h)$$

The condition,

$$\underset{i}{\Sigma} \frac{Mi}{M} = 1,$$

allows the value of b to be determined.

$$b = [\underset{i}{\Sigma} \frac{Wi}{W} \ \exp \alpha_i \ (U_i - h)]^{-1}.$$

This then fixes the apportioning of the M test pulses among the different psuedo-frequencies,

$$M_i = \frac{M \frac{W_i}{W} \exp \alpha_i(U \quad - h)}{\underset{i}{\Sigma} \ W_i \exp \alpha_i \ (U_i - h)} \quad .$$

The same form holds when different thresholds, h_i, are chosen for each psuedo-frequency. If the above formula for b is substituted for the exponent in the expression for the simulated time, t_i, the result is

$$t_i = \frac{M}{W} b.$$

Since the total number of pulses M is just the total test time, T, divided by the time interval, Δτ, between pulses,

$$t_i = T \ \frac{b}{W\Delta\tau} \quad .$$

So the factor (b/WΔτ) is the acceleration of the testing. A simple example is given in table 4. In this example the acceleration is 302, i.e., only 1h 40 minutes of testing is required to simulate 500h of truck transport. If the lowest frequency pulses (6 Hz) could be deleted because, for example, they were known not to cause damage, then the acceleration would be 863 and only 35 minutes of testing would be required to simulate 500h. The test could also be simplified by deleting the 15, 17, 20 and 500 Hz pulses since they account for less than 1 percent of the total.

Finally, in the above it has been assumed that each pulse observed in service is to be reproduced by a single input pulse in test. Since the pulses measured were not inputs but responses, either the shocks must be induced directly in the missile during test, or allowance must be made for the container/fixture transfer function. This transfer function may be such as to provide several response peaks for one input peak. In that case all of the response peaks above the threshold must be counted against the desired total for the test.

Summary

The shock responses of three kinds of missile were measured during four different truck trips. The responses were counted in intervals of amplitude and duration. These counts were found to correspond well with an exponential distribution; at least at the larger

Table 4. A Simple MTBF Test Design for Truck Transport Shock (Based on Tucson Data)

Center Psuedo-frequency Hz	Band Width Hz	U(100h Hz) g	$1/\alpha$ g	exp $\alpha(U-h)$ h = 1.2 g	$\frac{W_i}{W}$	$\frac{M_i}{M}$
6	4	1.61	0.137	19.24	0.0077	0.650
10	4	1.14	0.092	0.52	0.0077	0.018
13	3	1.18	0.091	0.80	0.0057	0.020
15	2	1.01	0.076	0.08	0.0038	0.001
17	2	1.02	0.069	0.07	0.0038	0.001
20	3	0.96	0.067	0.03	0.0057	0.001
24	4	1.40	0.304	1.93	0.0077	0.065
29	6	1.23	0.261	1.12	0.0115	0.056
38	10	1.08	0.256	0.63	0.0192	0.053
56	21	0.90	0.278	0.34	0.0402	0.060
100	63	0.97	0.119	0.14	0.1207	0.074
500	400	0.50	0.087	0.0003	0.7663	0.001
	W = 522			b = 4.384		

$$\text{Let } \Delta\tau = 10 \text{ sec} = 2.78 \times 10^{-5} \text{ 100 h}$$

$$\text{Acceleration factor } \left(\frac{b}{W\Delta\tau}\right) = 302$$

values. Using the exponential distribution as our approximation the levels which are exceeded once per hour, once per hundred hours, and with only 5 percent chance in 500 hours have been determined. Formulae have been derived for the specification of qualification tests levels and for the specification of MTBF tests from these data. The levels arrived at for smooth roads are higher than those recently specified for rough-road truck transport. It seems that a smooth road is just a rough road with a lot of smooth places in it.

REFERENCES

(1) Schock, R. W. and W. E. Paulson "A Survey of Shock and Vibration Environments in the Four Major Modes of Transportation," The Shock and Vibration Bulletin No. 35, Part 5, February 1966.

(2) Gumbel, E. J. - Statistics of Extremes, New York, Columbia University Press, 1958.

DISCUSSION

Mr. Ostrem (GATX): I would like to apologize for some of that data. That was a study we did for NASA and it encompassed data from some 500 different sources, so there was no particular vehicle and we are working in a vague area. Most of the input was measured at the cargo floor. I understand your data is response. I am surprised that there is such good correlation between the two.

Mr. Lifer (Jet Propulsion Laboratory): You talked about the specification of the test that you reproduced. How do you write your specifications to result in the spectrum to represent the shock environment? Is it in terms of a shock spectrum or is it in terms of a transient input?

Mr. Meeker: It depends on whether we are writing a specification that is intended for use in design or test. In the case of design we try to specify the most severe shock as a function of frequency that it would have to survive one time. We don't define the shock in the terms of the spectrum alone but in terms of the time history. In the case of a test we would get much more explicit. We would describe how we would generate the test pulses.

Mr. Kana (Southwest Research Institute): How does one decide what is shock and what is vibration whenever one looks at data of that type? You may have implied it in an answer to the question here and perhaps I didn't pick it up; could you do it by defining it in terms of the number of incidents of very high acceleration levels, say greater than three times an rms level?

Mr. Meeker: In this case it was kind of controlled by our instrumentation. If you have something that is vibration where you have several in a row then it would fill the A register, the B register, the C register and then it would miss the others. We can see that on the readout although I didn't show it in this printout. You can see how many times it would fill the C register so in that sense you have some measure of when you are looking at several peaks in a row that are closely spaced in time as opposed to isolated peaks; of course the higher the level the less often that happens. So when you are talking about the highest level data there are almost always isolated peaks and that would be the case even if it were random vibration.

Mr. Kana: I guess the answer to my question is that this is generally left up to the specification writer, he more or less answers that for himself depending on how he wants to design the test.

Mr. Meeker: The specification can be either a design specification or a test specification they are not always the same. I don't know how a person writing the design specification would choose between them. Whoever writes the test specification doesn't have to since he can arbitrarily make the division between shock and vibration anywhere he wants to.

DYNAMIC CHARACTERISTICS OF AN INDUCED-DRAFT FAN AND ITS FOUNDATION

S. P. Ying and E. E. Dennison
Gilbert/Commonwealth
Jackson, Michigan 49201

Vibration problems of large induced-draft fans and dynamic responses of their foundations were investigated experimentally. The work included analyses of fan vibration spectra and determinations of vibration mode shapes. The natural resonant frequencies of the foundation were measured by using the transfer function technique with a dual channel Fast Fourier Transform (FFT) analyzer. The resonant behavior of the entire fan and foundation system was observed during start-up of a fan. The resonant characteristics are discussed with a theoretical model and the critical speed of the fan shaft. A problem of an unbalanced fan rotor which caused excessive vibration is described and has been corrected to a normal condition.

INTRODUCTION

A flow of air and combustion gases in steam generating systems is required to supply the proper amount of combustion air and to remove the gaseous combustion products. When air and combustion products flow under the influence of a progressively decreasing pressure below atmospheric, the system is operating under induced-draft (ID). This is the case where stacks are supplemented with induced-draft fans to meet higher pressure differentials between the boilers and the stacks in electric power plants.

Many economic benefits are derived from a unit's increased power-generating capacity. However, predictable problems are inherent in these large units. Vibration in large ID fans is one such problem. We studied the vibration problem and dynamic characteristics of four identical ID fans and their concrete foundations in two oil-fired units. Each unit is capable of generating approximately 660 megawatts of electrical power. Figure 1 illustrates the entire fan and foundation system.

DYNAMIC CHARACTERISTICS OF INDUCED-DRAFT FAN

Critical Speed of Fan Shaft

A theoretical model of the entire fan and foundation system is presented in the section on Discussion. When the fan rotor (consisting of the shaft and the fan wheel) is mounted on completely rigid bearing supports at the bearing journals, the natural frequency of this system is the critical speed of the shaft. The critical speed can be calculated by a finite element method. However, it can also be found by an analytic solution of self-excited lateral vibration of a rotor.

The analysis of self-excited lateral vibration of a shaft only need include the effects of the bending stress, shaft rotation and shear deflection. According to Timoshenko's theory, the natural frequency of the vibration with a correction factor for these effects is given by[1]:

$$f_o = \frac{a\pi}{2(\ell/n)^2}\left[1 - \frac{\pi^2 n^2}{2}\left(\frac{\rho}{\ell}\right)^2\left(1 + \frac{E}{KG}\right)\right] \qquad (1)$$

where

$a^2 = EIg/S\sigma$
E = modulus of elasticity
G = modulus of rigidity
S = cross section area of shaft
σ = weight density
g = gravitational acceleration
I = moment of intertia of shaft = $\pi r^4/4$,
where r is the shaft radius
ℓ = length of shaft
$\rho = \sqrt{I/S}$
$K = F_s/GS\beta$
F_s = total lateral shear force at any section
β = angle which a cross section makes with the axis of the shaft

Under the assumption made in the usual elementary beam theory, K is 3/4 for a circular beam. More refined analysis shows that K = 9/10. The values of n depend on boundary conditions:

1) vibration amplitude = 0, at both ends of the shaft, n = 1, 2, 3, . . .
2) vibration amplitude = 0 at one end, maximum at the other end,

$$n = 1/2, 3/2, \ldots$$

In the above calculation, the mass of the fan wheel has not been taken into account. There are three methods to calculate lateral vibration frequency of beams with masses attached. Those three methods, namely, exact method, spring method and Rayleigh's method, all provide high accuracy. By Rayleigh's method, the natural frequency of the shaft with mass attached becomes[2]:

$$f_n = f_o \, (1 + 2\, m/m_b)^{-1/2} \qquad (2)$$

Where m = attached mass
m_b = mass of the beam itself.

In Equation 2, f_o is given by Equation 1. The boundary conditions for Equation 1 are also valid for Equation 2.

For a steel shaft $E = 2.07 \times 10^8$ kPa, $G = 7.93 \times 10^7$ kN/m^2 and $\sigma = 76000$ N/m^3. For the ID fan, $\ell = 7.24$ m, $mg = 115209$ N and $m_b g = 180153$ N. Using $K = 0.9$, for normal boundary condition $n = 1$, the critical speed calculated from Equations 1 and 2 is

$$f_1 = 15.6 \text{ Hz}$$

Which reasonably agrees with the value of 16 Hz obtained by using matrix transfer functions. The ratio of the critical speed to the running speed is 1.35.

Fan Vibration

A pair of accelerometers was utilized simultaneously to measure vibration accelerations in orthogonal directions on the fan bearings and the foundation pedestals. Holding one accelerometer in a fixed location, the second accelerometer was moved through the several positions; a phase relationship was established in addition to the acceleration time history. The outputs from the pair of accelerometers, through charge amplifiers, were simultaneously recorded on individual channels of an FM tape recorder. The data stored in the tapes were analyzed by using a dual channel Fast Fourier Transform (FFT) analyzer (Nicolet 660) to obtain narrow band frequency spectra of accelerations and displacements.

Figure 2 is an acceleration frequency spectrum obtained from a fan inboard bearing in the horizontal direction, transverse to the fan shaft. The corresponding displacement frequency spectrum which is obtained by using the double integration of acceleration in the FFT analyzer is shown in Figure 3. Both spectra were sampled in a logarithmic scale from 1 Hz to 1 kHz with 800 frequency components; the frequency resolution (bandwidth) is 1.25 Hz. It is clear that the significant vibration frequency component is in the 11.5 Hz band which includes 11.9 Hz of the fan running speed (714 RPM).

Figure 1. Illustration of induced draft fan and foundation.

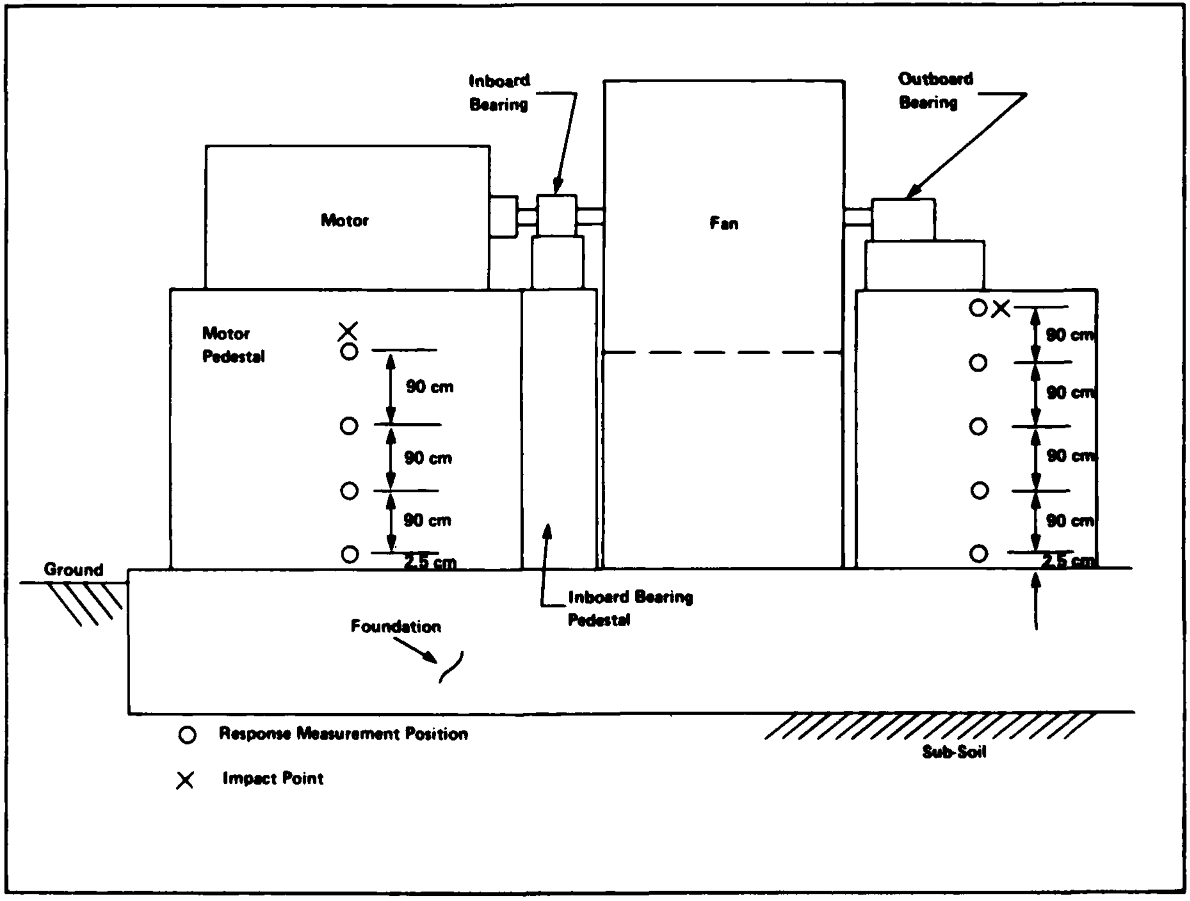

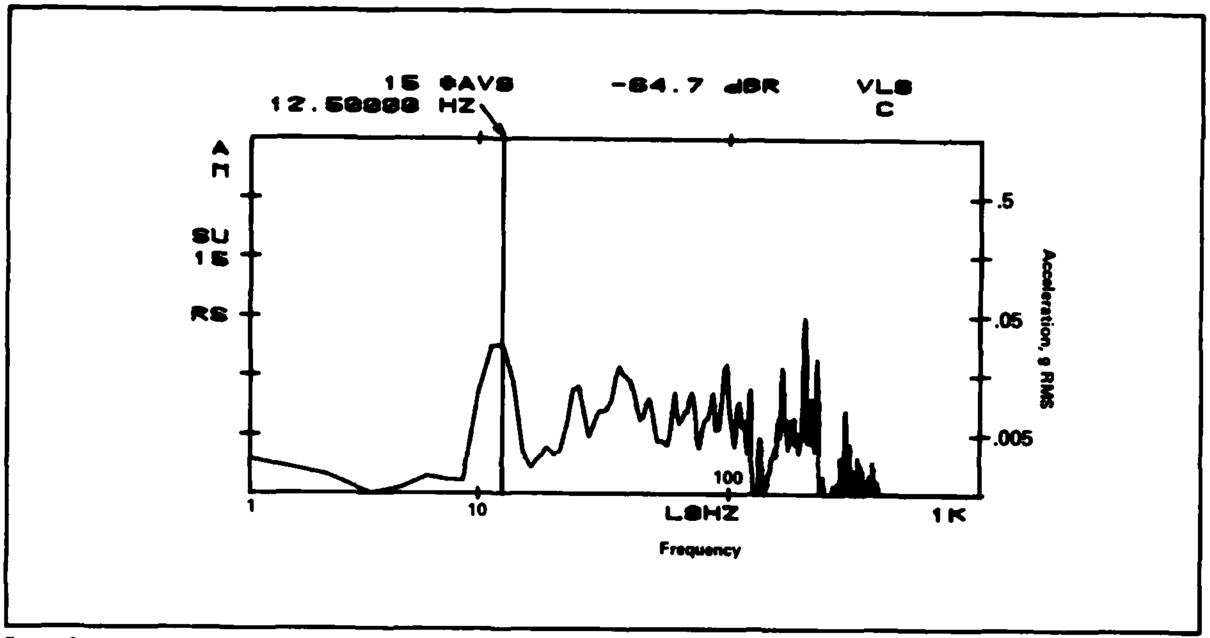

Figure 2. An acceleration spectrum on fan bearing, horizontal, transverse to shaft.

Probable causes for the 11.9 Hz vibration are unbalance or off-center rotor. A relatively small peak at 23.8 Hz, which is the second harmonic of the running speed, indicated a slight misalignment between the shafts of the fan and the driving motor. Occasionally, a subharmonic at 3 Hz appears in a spectrum obtained from a fan bearing in the horizontal direction, transverse to the shaft. As discussed in the preceding section, this subharmonic vibration component reflects an abnormal boundary condition of a concentrated mass rotor, i.e., a problem in a bearing.

Comparing the measured results with acceptable vibration criterion for rotating machinery[3], it was found that an ID fan had excessive vibration of 7 mils (0.18 mm) peak-to-peak at 11.9 Hz.

DYNAMIC RESPONSE OF FOUNDATION

Dynamic Response Profiles

Dynamic responses of the foundation and foundation pedestals were measured by using the same procedures

Figure 3. A displacement spectrum on fan bearing, horizontal, transverse to shaft.

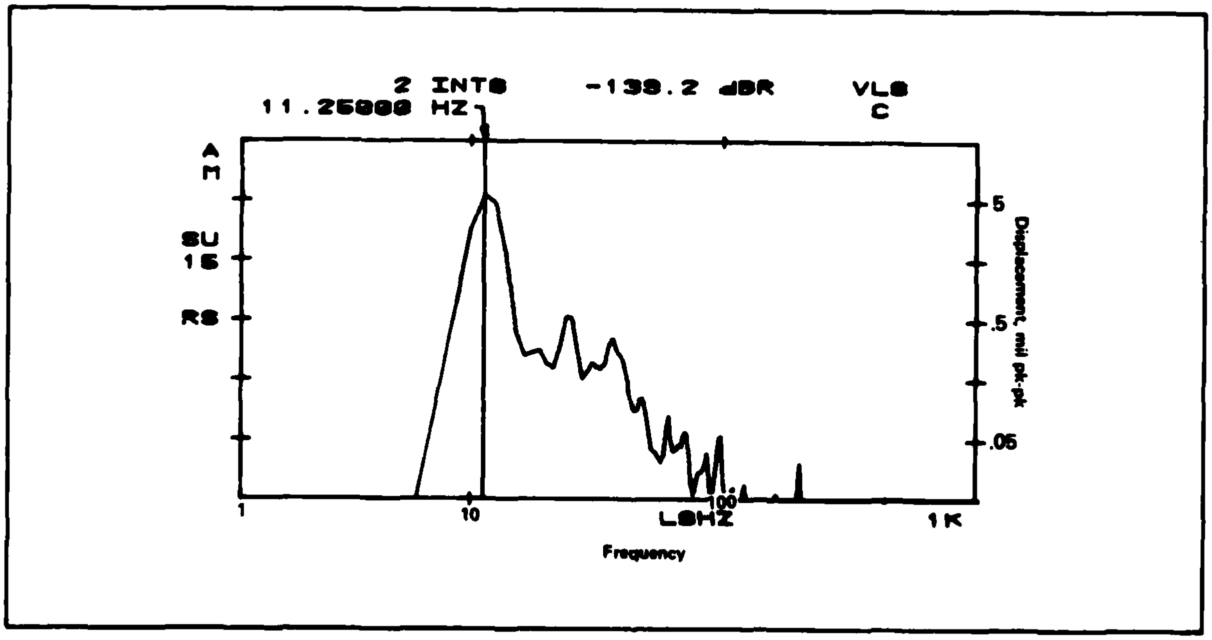

described at the beginning of the preceding section. Figure 4, for example, is an *acceleration frequency spectrum in a linear* scale from 0 to 50 Hz obtained near the top of a motor pedestal in the horizontal direction, transverse to the shaft during excessive vibration of the fan. The spectra obtained from the foundations and foundation pedestals *are essentially* the same as those obtained from the fan bearings. The significant peak in each spectrum is 11.9 Hz. The accelerations on the foundations and foundation pedestals represent their dynamic responses resulting from the forcing function due to the unbalance of the fan rotor.

Collecting the dynamic displacement data at 11.9 Hz, the horizontal displacements, trnasverse to shaft, measured on a fan inboard-bearing pedestal, were plotted as the height of the pedestal in Figure 5. The corresponding accelerations at 11.9 Hz in a time domain are all in phase. As shown in the sketch in Figure 5, the inboard bearing is supported by a steel support, reinforced concrete pedestal, foundation mat and subsoil. Based on the curve fitted to the data points, the horizontal vibration component approaches zero (not absolutely zero) at the interface between the reinforced concrete foundation mat and the subsoil. Furthermore, the portion of the curve corresponding to the displacement of the steel support has a variation of curvatures, but the displacements on the concrete pedestal form a straight line. The displacement curve of the steel support portion reflects the forced elastic response. The two dashed straight lines with junction at the interface between the bearing metal support and the concrete pedestal represent a simplification to two linear springs.

The straight line mode shape was also found in motor concrete pedestals and concrete foundations. Figures 6 and 7 *show the dynamic response profiles* of a motor pedestal and at the top of a foundation, respectively, during excessive fan vibration at 11.9 Hz. The displacements in each curve in Figure 6 are in phase, but the displacements in Figure 7 on the left are 180° out-of-phase with the displacements on the right. As shown in Figure 6, the displacements parallel to the shaft are much smaller than the transverse components. All the curves in Figures 6 and 7 were fitted to the data by the method of least squares.

Combining all the facts pointed out above it is not *difficult* to visualize that the concrete pedestal and foundation had a forced rocking vibration with respect to the horizontal axis, parallel to the shaft at the center of the interface between the foundation and the subsoil.

In Figure 7, the solid line is fitted to the data obtained at the top of the foundation mat; the measured displacement on the center line (0 cm distance) should not be exactly equal to zero. The dashed line which represents the displacements of a rocking mode indicates zero displacement at the center. However, part of the differences between the solid line and the dashed line is an in-phase vertical displacement of the foundation.

Similarly in Figure 6, the horizontal displacements transverse to the shaft were measured at one side of the pedestal, far away from the center line. The extrapolation of the curve which represents the underground displacements along the side of the pedestal has a finite horizontal component. Part of the horizontal component resulted from an in-phase horizontal vibration of the pedestal.

Natural Frequency

The impulsive test technique was used to determine the natural resonance frequency of the foundation including its pedestals. Figure 1 shows the positions of impacts and the locations on the pedestals where the responses were measured. The impact force was produced by a 12-lb hammer with a soft tip. While an accelerometer monitored the dynamic response of the foundation pedestal, another accelerometer measured the forcing function of an impact applied at the top of the pedestal. Both accelerometer signals - through two charge amplifiers - were fed into the dual channel FFT analyzer. The analyzer is able to calculate the transfer

Figure 4. An acceleration spectrum on motor pedestal horizontal, transverse to shaft, from 1 to 50 Hz.

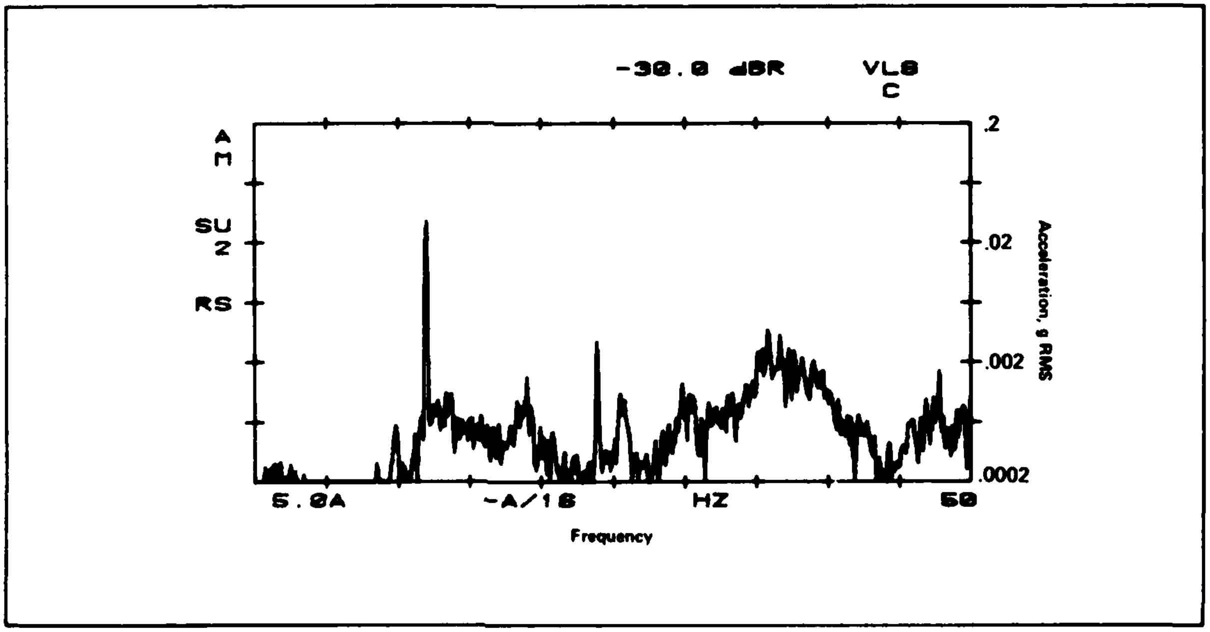

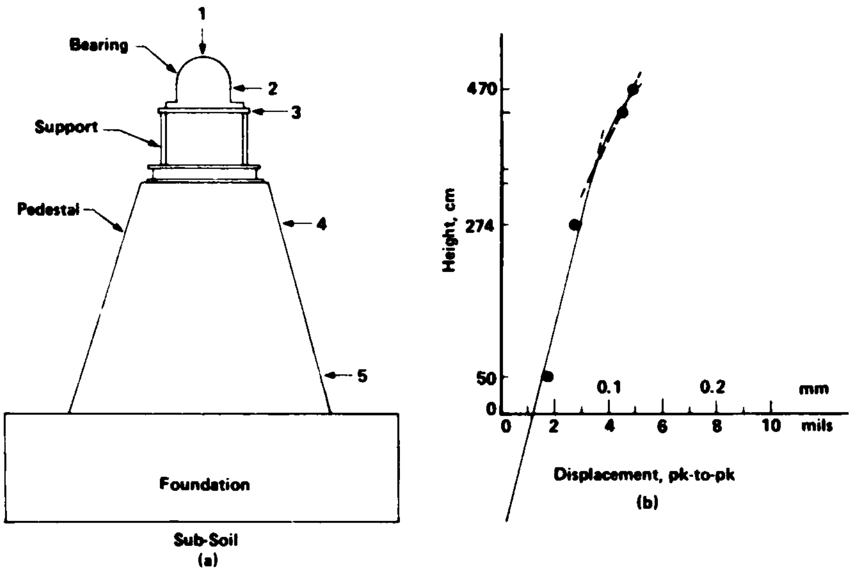

Figure 5. Dynamic response of inboard bearing, steel support and foundation pedestal, horizontal, transverse to shaft. Two dashed straight lines with junction at about 335 cm represent a simplification to two linear springs.

Figure 6. Dynamic response of motor pedestal.

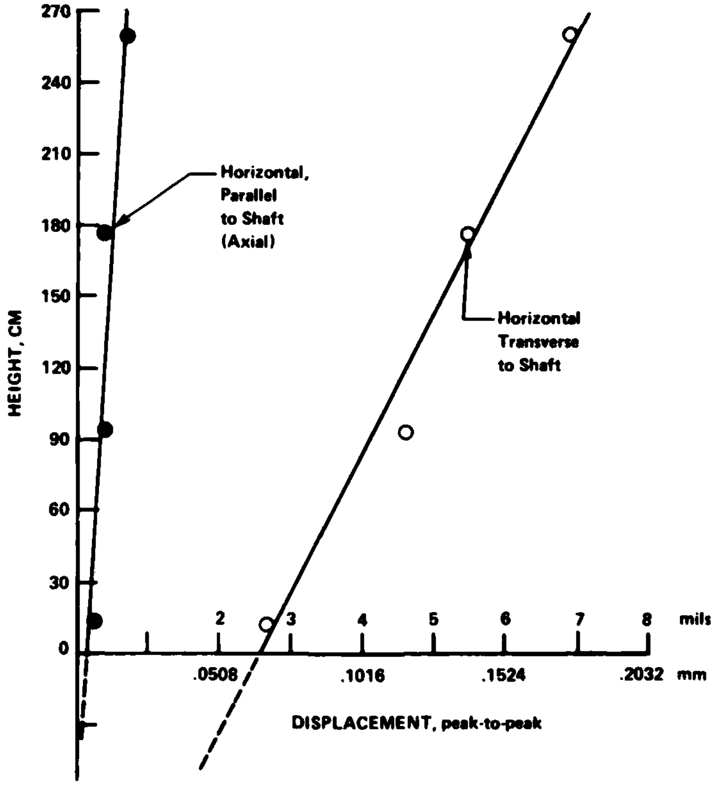

functions (TF) of the two inputs and provides true frequency response spectrum.

Let G_{AA} be the autocorrelation of impact force and G_{AB} be the cross-correlation between the impact force and the acceleration of the response. The definition of the transfer function is[4]

$$f_T = \frac{G_{AB}}{G_{AA}}$$

The dual channel FFT analyzer provides TF in a frequency domain, which is equivalently the frequency spectrum of the response acceleration per unit force. In other words, although all frequency components of the impact force exciting a foundation pedestal are not equal, the TF normalizes this input. The resultant spectrum (TF) represents the response of a force with an equal amplitude for all frequency components. A typical natural resonance spectrum is presented in Figure 8. The vertical axis represents relative values of acceleration in dB, and the values of the horizontal axis are frequencies from 0 to 50 Hz. From this curve, the 11.9 Hz vibration acceleration of the ID fan rotor which can be attributed to resonance of the subject foundation is approximately 2-3 dB.

The impulsive test was conducted during the fan shutdown period, but the ID fans of the second unit were running. The peak at 11.9 Hz in Figure 8 is caused by the fan vibration from the other unit. It was also determined that the peaks at 2.4 Hz and 25.6 Hz are the electric noise in the recording system.

As shown in the spectrum in Figure 8, the frequency of the first mode is about 4 Hz and the higher order mode peaks are at approximately 8 Hz, 13 Hz and 17 Hz. These values are in reasonable agreement with the results from theoretical calculation. Therefore, from the measured natural frequency

Figure 7. Vertical dynamic response at top of foundation. The horizontal axis lies on the top of foundation mat in the horizontal direction, transverse to shaft. The origin (0 cm) is located at the motor end of the foundation center line, parallel to the shaft (see Figure 1).

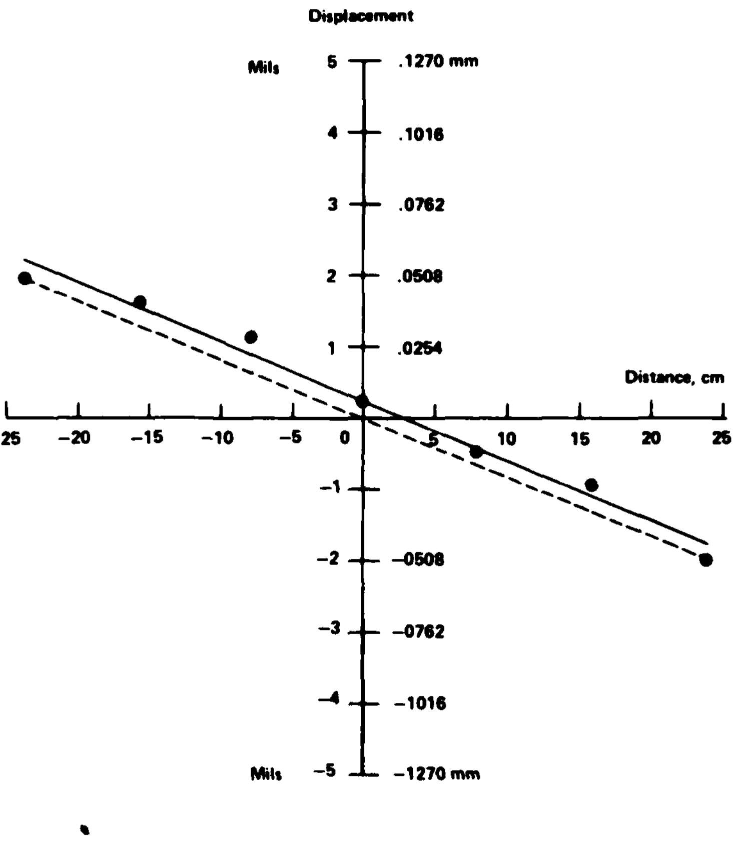

Solid Line Represents Superposition of Vertical Response and Vertical Component of Rocking Mode.
Dashed Line is Vertical Component of Rocking Mode.

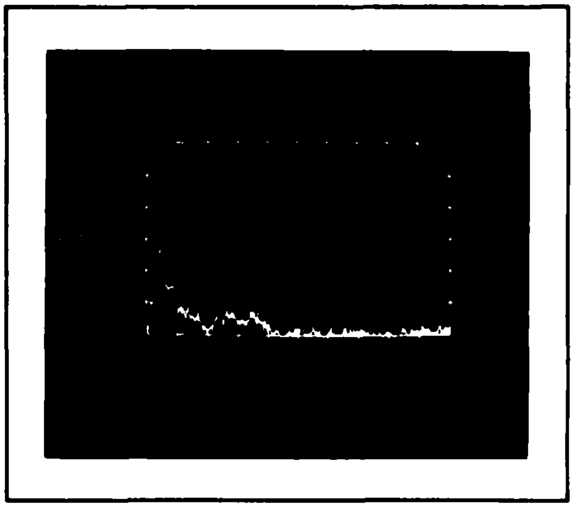

Figure 8. Natural resonant curve of foundation and foundation pedestal.

and the total mass of the foundation and pedestals, the effective stiffness of the subsoil can be calculated.

Additionally, the frequency bandwidth at -3dB point referred to peak acceleration of each mode can be found from the measured curve. For the mode with peak frequency $f_r = 13$ Hz, the bandwidth $\Delta f = 6$ Hz, hence the quality factor

$$Q = \frac{f_r}{\Delta f} = 2.17$$

and the damping ratio

$$\xi = \frac{1}{2Q} = 0.23$$

Thus the response acceleration of the structure can be predicted for a given forcing function F from[5]

$$a = \frac{1 - \xi^2}{(1 + (2\xi)^2)^{1/2}} \frac{F}{m_o}$$

Where m_o is the mass of the structure.

Concrete Properties

Because the velocity of sound in solids depends on the elastic modulus of the material and because the elastic modulus of reinforced concrete determines its quality,[6] this property of the reinforced concrete of the foundation pedestals was juged by sound velocity measurements. The concrete was still in good condition after it experienced excessive vibration.

DISCUSSION

The entire fan and foundation system includes the fan rotor, bearing oil film, bearing housings and steel pedestals, concrete pedestals, foundation mat and subsoil. The total system response to an unbalance weight in the fan wheel must be calculated from all the flexibilities and damping properties of individual portions of the system. A theoretical model of the entire system is presented in Figure 9. The flexibility and damping effect of subsoil should also be considered. Figure 5 suggests simplification to a bi-linear system with a soil spring for concrete pedestal and mat;

Figure 9. A theoretical model of the entire fan and foundation system. The dashed straight lines in Figure 5 (b) represent bilinear springs, i.e., soil spring for concrete pedestal and mat; and spring for metal support, bearing and shaft.

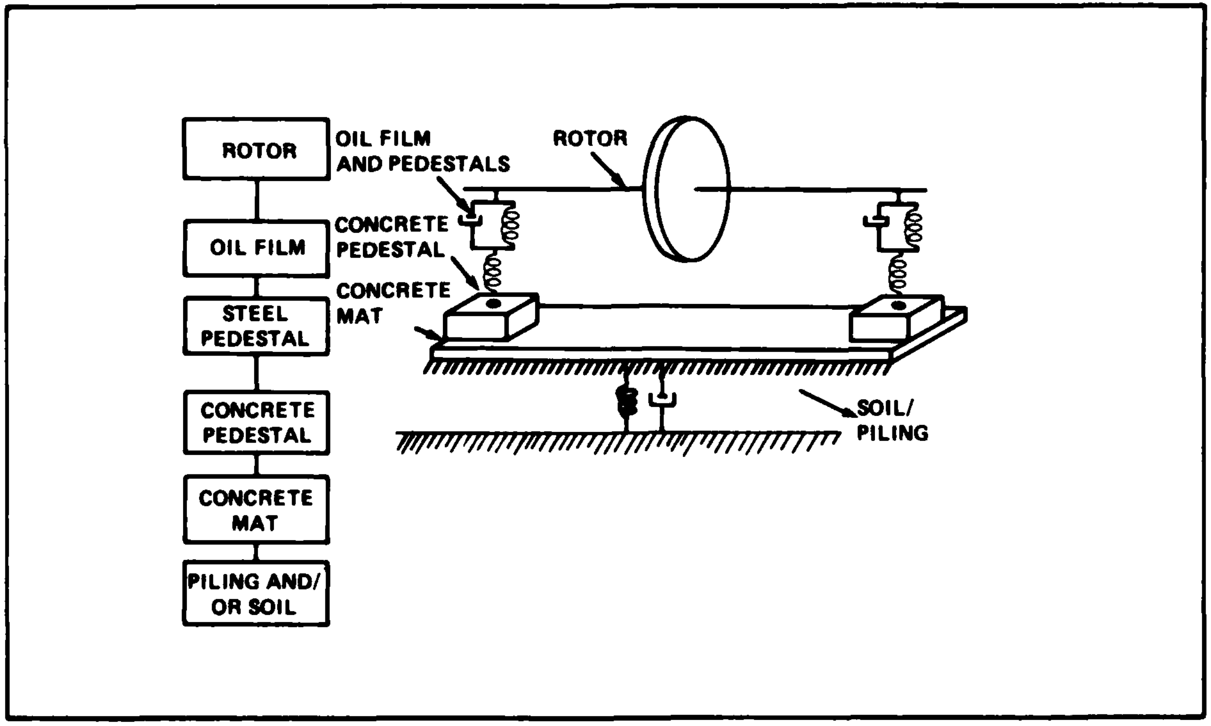

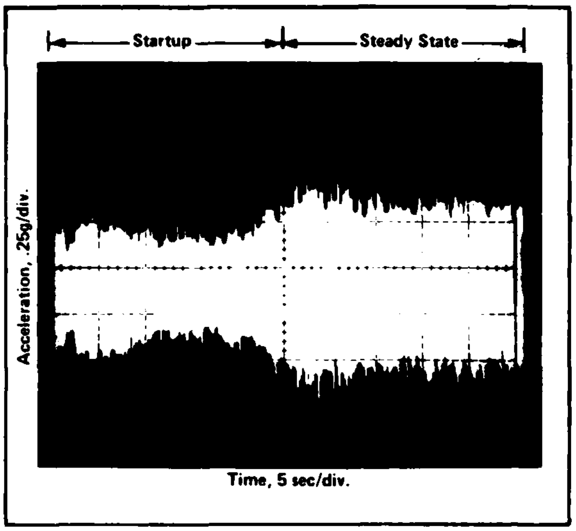

Figure 10. Acceleration time history at fan inboard bearing during start-up.

and another spring for the shaft, bearing, and the bearing metal support.

At a normal fan operating temperature of 535°F, the critical speed is less because of the flexibilities and damping effect of the heated oil film in the bearing. The natural resonant frequency of the entire system is a combination of this reduced critical speed and the natural frequency of the foundation system discussed in previous sections.

The natural frequency of the entire system was investigated experimentally during start-up of an ID fan. An accelerometer monitored the response at a bearing housing during start-up and an FM recorder recorded the signals from the accelerometer through a change amplifier continuously. Figure 10 is the acceleration time history during start-up. During this period, the dominate frequency component of acceleration increases as the fan running speed rapidly increases. As shown in the oscilloscope photograph in Figure 10, the gradual increase of acceleration relates to the increase of angular momentum of the rotor. The fluctuation of acceleration amplitudes reflects the resonant behavior of the entire system. Fortunately, the acceleration does not increase peculiarly prior to nor at the steady speed of 714 RPM. That is, the entire system does not resonant at the fan operating speed.

The excessive vibration of an ID fan at 11.9 Hz really resulted from an unbalance of weight of the rotor, because the wheel was shifted in the axial direction due to thermal distortion of the rotor at operating temperature 535°F.

Although the critical speed of the shaft and natural frequency of the foundation are different from the combined resonant frequency of the entire system, these two parameters are still very important for the design of fan and foundation. The fan rotor dynamic criteria for airfoil ID fans requires that the ratio between the critical speed and the operating speed be 1.35 or greater. The rotor vibration attributed to the high order resonance of the foundation should be equal to or less than 2-3 dB.

CONCLUSIONS

Three basic parameters which are very important for a satisfactory operation are the ratio of the critical speed of the shaft to its running speed, the natural resonance of the foundation, and the natural resonance of the entire system. These parameters of the ID fans and their foundations as investigated here are suitable.

The shift of a wheel which caused excessive vibration has been corrected to a normal condition by the fan manufacturer.

REFERENCES

1) S. Timoshenko, Phil. Mag. (ser. 6), 41, 744 (1921); 43, 125 (1922).

2) W. F. Stokey, "Vibration of Systems Having Distributed Mass and Elasticity," Ch. 7, Shock And Vibration Handbook, edited by C. M. Harris and C. E. Crede, 2 Ed., McGraw-Hill (1976).

3) ISO Standard 2372, "Mechanical Vibration of Machines with Operating Speeds from 10 to 200 Rev./Sec. Basis for Specifying Evaluation Standards," (1974).

4) G. F. Lang, "Understanding Vibration Measurements," Sound and Vibration, Vol. 10, No. 3 (1976).

5) J. T. Broch, "Mechanical Vibration and Shock Measurements," Bruel & Kjaer, Naerum, Denmark, June 1973.

6) D. F. Orchard, "Concrete Technology," Vol. 2, p. 200, John Widey & Son, New York (1970).

VIBRATION AND ACOUSTICS

A METHOD TO DETERMINE REALISTIC RANDOM VIBRATION TEST LEVELS TAKING INTO ACCOUNT MECHANICAL IMPEDANCE DATA

PART 1: BASIC IDEAS AND THEORY

Odd Sylwan
IFM Akustikbyrån AB
Stockholm, Sweden

Saab-Scania and IFM Akustikbyrån in Sweden have developed and tested a new method to determine more realistic random vibration test levels based on measured acceleration spectral densities. It takes into account the differences between the mechanical impedances of the system equipment - supporting structure in service and under test conditions.

A very important feature of the method is that the vibration test can still be performed in accordance with standard test procedures.

In this paper the basic ideas and theory behind the method are presented.

INTRODUCTION

The resistance of airborne equipment to vibrations during flight is an important design factor. Well formulated and realistic vibration requirements are therefore important in order to get a sound design.

The normally used method to determine random vibration test levels for airborne equipment is based on the envelope of acceleration spectral densities in points close to the mountings of the equipment.

It is obvious, that an envelope test spectrum contains more power than the corresponding measured spectrum during flight. However, the corresponding test responses of the equipment often contain still more power than what could be explained by the differences between the power of the envelope test spectrum and the measured spectrum. The reason is, that the mechanical impedance of the fixture during test is different from that of the supporting structure in service.

Several techniques have been suggested taking into account the interaction between the test item and its supporting structure. For example, techniques based on Response Control, Input Force and Power Control have been proposed /1/. The main disadvantage of these methods is that the tests cannot be performed in accordance with standard test procedures.

This new method takes into account the differences in mechanical impedances between test and service conditions, so that the vibration test can still be performed in accordance with standard test procedures.

The method is designed for calculations of vibration test levels without safe margins and acceleration factors (= nominal vibration test levels). Such margins and possible acceleration factors should be added when establishing the final test level.

The reported activities were performed under contract from the Swedish Defence Material Administration.

BASIC IDEAS BEHIND THE METHOD

It is well known, that mechanical resonances are very important for vibration levels of lightly damped mechanical systems. For example, a mechanical system consisting of an airborne equipment and its supporting structure in service vibrates with the vibration power focused on the resonance frequencies of this compound system. If the mechanical impedance of the equipment mountings is of the same order of magnitude as the point impedance of the supporting structure the resonance frequencies and mode shapes of the compound system will be highly affected by the two subsystems. This is often true for airborne equipment and their supporting structures.

When performing vibration tests, the test item will be mounted to a shaker, which excites the item to predetermined vibration levels. Obviously,the mechanical properties of the fixture mounted to the shaker are quite different from those of the supporting structure in service. From theory these differences do not influence the vibration responses of the equipment, if the test levels are identical to the levels of the equipment mountings in service.

In practice,it is not possible to excite the test item exactly in the same complicated way as in service (6-degrees of freedom of each mounting and complicated acceleration spectral densities). It is necessary to simplify the test procedure and composition of test levels. The differences between the mechanical properties of the supporting structure in service and of the fixture will be important when any simplification of this kind is introduced.

The normally used envelope method to determine vibration test levels for use in standard test procedures does not take into account these differences. At test the use of an envelope test spectrum thus will result in rather accurate vibration responses of the test item only close to the resonance frequencies of the above mentioned compound system in service. At all other frequencies, the response levels may be too high particulary close to the resonance frequencies (fixed-base) of the equipment mounted to the shaker, as illustrated in figure 1 for a simple mass-spring system.

At test a flat envelope spectrum will mainly excite these fixed-base frequencies. Thus in some cases it would be better to use a test spectrum based on the notches rather than the peaks of the measured spectrum. In most practical cases the correct vibration test levels are located somewhere between the peaks and notches of the measured spectrum.

DAMAGE CRITERION

Normally,the vibration response levels during test cannot be made equal to that of service conditions in all parts of the test item and for all types of response quantities. However, in many cases it would be possible to get equal response levels at least in most critical areas of the test item and for one response quantity.

The new method to determine random vibration test levels is based on the assumption that the risk of damage or malfunction of a critical area is governed mainly by the RMS-value of one response quantity. Consequently,it is necessary to find a common response quantity,which is rather well related to the risk of damage and malfunction of all critical areas. For example, this quantity can be acceleration or strain.

In most cases,the mean value of the response quantity is 0. Then the RMS value and the standard deviation of the response quantity are identical. In

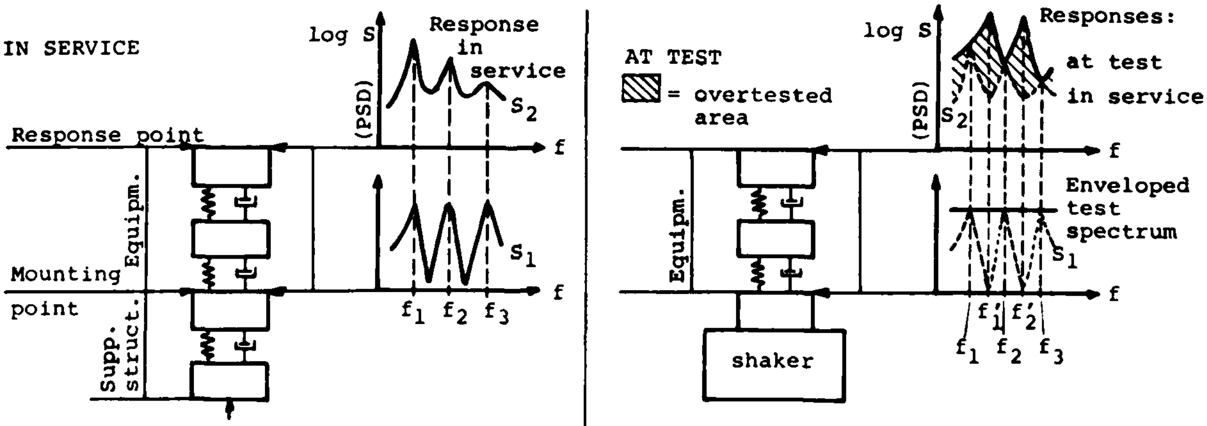

f_1; f_2; f_3 = Resonance frequencies of the compound system in service

f'_1; f'_2 = Resonance (fixed-base) frequencies of the test item

Figure 1 Simple mass-spring system in service and at test.

practice, the use of the RMS-criterion means, that the response quantity will be equally distributed in service and at test, if the probability density functions are Gaussian.

In order to simulate the stress (fatigue) acting in the item, it is important to apply the RMS-criterion at least on a few frequency bands $[f_\nu, f_{\nu+1}]$ (up to approximately 5 bands) within the total frequency range of interest. Then the stresses (levels and frequencies) will be distributed in a reasonably correct way during the test. This is not necessary for the simulation of the vibration environment in cases where the expected damages and malfunctions only depend on the magnitude of the response quantity.

Probably, the mechanical stresses of resonant components of critical areas in airborne equipment are often directly or indirectly controlled by inertia, which is related to force by acceleration. So if the details of the damage mechanism is unknown for a specific test item, it seems to be reasonable to use acceleration as the best measure for a common response quantity.

CALCULATION OF VIBRATION TEST LEVELS

The exact theory of calculating correct vibration test levels (in the sense discussed above), for linear equipment, is based on matrix representation of mechanical impedances and other transfer functions. Unfortunately, a very great number of spectra must be measured (or predicted) to make full use of the exact theory. Normally, it is not feasible to acquire that number of spectra. Consequently, the theory has been simplified to a level, where the accuracy seems to be reasonable, although the number of necessary input spectra is reduced to a minimum.

Thus the mechanical compound system of service conditions and corresponding test system are treated as if the excitation and responses can be determined for one direction at a time. This is always true for test excitations but of course not always for service conditions. For example, it is always true for cases like those described in figure 1.

Since acceleration spectral densities in service are normally available only for points close to equipment mountings, a calculated response quantity S_2 of each critical area often have to be determined. This quantity may be calculated from

$$S_2 = S_1 \cdot |H_{21}|^2 \quad \ldots\ldots\ldots\ldots\ldots\ldots (1)$$

where

S_1 = the acceleration spectral density representing the levels of the mountings

H_{21} = transfer function from mountings (acceleration) to a critical area of the equipment (response quantity) determined in the laboratory. (If the response quantity is acceleration, the transfer function can be expressed as the ratio between the point impedance of the mounting and the corresponding transfer impedance to the critical area. Note that H_{21} at test and H_{21} in service are identical for cases like those described in figure 1).

The transfer function H_{21} of each critical area is determined in the laboratory using shaker or impulse excitation. To optimize the accuracy of the vibration test level calculations, these transfer functions should preferably be measured when the test item is mounted to the same fixture and shaker as it will be when it is tested.

Vibration test levels $S_{p\nu}$ will be calculated from equation (2) for a number of frequency bands $[f_\nu, f_{\nu+1}]$, all together covering the total frequency range $[f_\ell, f_h]$.

$$\underbrace{\int_{f_\nu}^{f_{\nu+1}} S_{p\nu} \cdot |H_{21}|^2 \cdot df}_{\text{Mean square value of response quantity at test}} = \underbrace{\int_{f_\nu}^{f_{\nu+1}} S_1 \cdot |H_{21}|^2 \cdot df}_{\text{Mean square value of calculated response quantity } S_2 \text{ in service}} \quad \ldots\ldots (2)$$

If the vibration test level $S_{p\nu}$ is held constant within each frequency band $[f_\nu, f_{\nu+1}]$, it can be expressed in explicit form

$$S_{p\nu} = \frac{\int_{f_\nu}^{f_{\nu+1}} S_1 \cdot |H_{21}|^2 \cdot df}{\int_{f_\nu}^{f_{\nu+1}} |H_{21}|^2 \cdot df} \quad \ldots\ldots\ldots\ldots (3)$$

Vibration test levels from (3) may be accurate only if the response levels of the critical areas are mainly caused by vibrations in the supporting structure passing through the mountings of the equipment, and if the mountings do not stiffen the supporting structure too much. (This must also be satisfied for the envelope approach).

More accurate vibration test levels $S'_{p\nu}$ than those of (3) can be calculated from (4), if there is a measured response quantity S'_2 (instead of S_2 calculated from (1)).

$$S'_{p\nu} = \frac{\int_{f_\nu}^{f_{\nu+1}} S'_2 \cdot df}{\int_{f_\nu}^{f_{\nu+1}} |H_{21}|^2 \cdot df} \quad \ldots\ldots\ldots\ldots\ldots(4)$$

Vibration test levels from (3) or (4) are calculated for all critical areas (up to approximately 3 areas) and freguency bands. The highest level of each frequency band is chosen as the common test level. Thereby none of the critical areas will get too low vibration responses. (Note that $S_{p\nu} = S_1$ for <u>all parts</u> of the equipment if S_1 = const. in the frequency band $[f_\nu, f_{\nu+1}]$).

CHOICE OF FREQUENCY LIMITS

From the laboratory tests (see part II), it has been found that a suitable number of frequency bands $[f_\nu, f_{\nu+1}]$ is approximately 3 in the frequency range 20-500 Hz and 2 in the range 500-2000 Hz. By chosing these numbers

- the vibration power will mostly be allocated to the main resonances of the test item in a correct way
- an averaging effect is achieved, which should be sufficient with respect to resonance densities and relative bandwidth of the resonances (loss factors) of the present mechanical system

Different ways of selecting the frequency limits f_ν have been tested. The best way found is based on the calculated spectral density of the response quantity $S_2 = S_1 \cdot |H_{21}|^2$ or measured S'_2. It is illustrated in figure 2.

If the number of frequency limits f_ν tends to be great, a few of them can be neglected. The frequency bands containing comparatively little power (small surface under the S_2-curve) is put together with the neighbouring band.

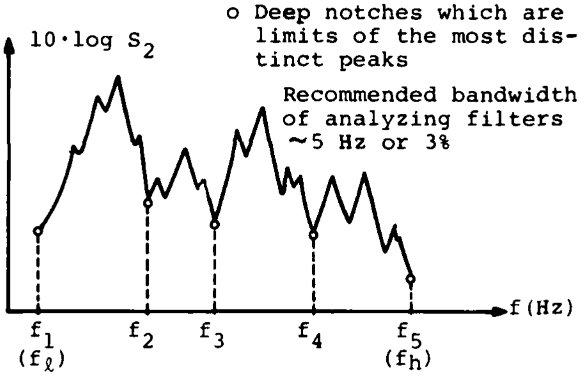

Figure 2 The best way found of chosing the frequency limits f_ν.

SIMPLIFIED METHOD TO CALCULATE VIBRATION TEST LEVELS

The use of H_{21}-data does not always result in better accuracy of the test level calculations than with the envelope approach. If the number of critical areas are >3, or comparable frequencies f_ν of the critical areas are too different, then nothing is gained by basing the test level calculations on H_{21}-data. However, it is still not necessary to use the envelope approach.

This problem can be solved by applying a statistical approach to the variable $(S_{p\nu}/\langle S_1\rangle)$ of a frequency band $[f_\nu, f_{\nu+1}]$ and equipment chosen by random, where $\langle S_1\rangle$ is given as

$$\langle S_1\rangle = \frac{1}{(f_{\nu+1}-f_\nu)} \cdot \int_{f_\nu}^{f_{\nu+1}} S_1 \cdot df \quad \ldots\ldots\ldots(5)$$

Theoretical and test results have given support to the hypothesis, that the expected value of $(S_{p\nu}/\langle S_1\rangle)$ can be expressed as

$$E\,(S_{p\nu}/\langle S_1\rangle) \approx 1 \quad \ldots\ldots\ldots\ldots\ldots\ldots\ldots(6)$$

It also represents the most probable value of $(S_{p\nu}/\langle S_1\rangle)$.

The dispersion from the expected value in (6) is small, if the average bandwidth of $[f_\nu, f_{\nu+1}]$ is large.

From for example test results, it should be possible to determine the maximum value k_ε, which is exceeded by $(S_{p\nu}/\langle S_1\rangle)$ only in arbitrary ε% of the frequency bands $[f_\nu, f_{\nu+1}]$ for a specific group of equipment. Conservative vibration test levels can then be calculated from

$$S_{p\nu} = \langle S_1\rangle \cdot k_\varepsilon \quad \ldots\ldots\ldots\ldots\ldots\ldots (7)$$

If the bandwidth of $[f_\nu, f_{\nu+1}]$ is large, the value of k_ε will be close to 1.

Most of these vibration test levels should be lower than the corresponding envelope levels, although (7) does not include H_{21}-data.

PROPOSAL FOR A NOMINAL VIBRATION TEST LEVEL

A vibration level used at test consists of a nominal level and some margins. However, a nominal test level based on the envelope approach can be considered having an extra margin of an unknown magnitude included. In practice, this may be true also for a test level calculated from the new impedance based method, but in this case the magnitude of the enclosed margin is on an average much smaller than in the envelope approach. Of course, this is an advantage to the impedance based method.

As an alternative to the envelope and impedance approaches (when H_{21}-data are not available or cannot be used), it is proposed that the vibration test level calculations should be based on a nominal test level

- which is defined so that a well known extra margin can be determined (instead of the unknown one of the envelope approach)
- which represents the most probable vibration test level

It can be concluded from the paper, that it would be convenient to define the nominal level as $\langle S_1\rangle$ of each frequency band $[f_\nu, f_{\nu+1}]$ and the extra margin from the factor k_ε, where f_ν must be based on S_1 instead of S_2.

The vibration test levels in dB based on (7) (other safety factors than k_ε and acceleration factors are not included) should then be calculated from

$$10\cdot\log S_{p\nu} = 10\cdot\log \langle S_1\rangle + 10\cdot\log k_\varepsilon \ldots (8)$$

A general magnitude of k_ε cannot be given. Essentially it depends on the group of equipment, the average bandwidth of $[f_\nu, f_{\nu+1}]$ and the ε-value chosen.

For the equipment studied, where the average bandwidth of $[f_\nu, f_{\nu+1}]$ is a few hundred Hz, the value of k_ε has been found to be approximately 1.6 for $\varepsilon < 2\%$. Then the vibration test levels in dB based on (8) can be expressed as

$$10\cdot\log S_{p\nu} = 10\cdot\log\langle S_1\rangle + 2 \quad \ldots\ldots\ldots (9)$$

(Note that from (3) $S_{p\nu} = S_1$ for all parts of the test item, if S_1 = const. in the frequency band $[f_\nu, f_{\nu+1}]$. Then (9) gives levels which are 2 dB too high).

COMPARISON BETWEEN VIBRATION TEST LEVELS DETERMINED IN DIFFERENT WAYS

If the statistical distribution of log $(S_{p\nu}/\langle S_1\rangle)$ is approximately symmetric and its expected value 0, most of the vibration test levels (100-2ε%) would be within the limits of

$$\langle S_1\rangle/k_\varepsilon < S_{p\nu} < k_\varepsilon \cdot \langle S_1\rangle \quad \ldots\ldots\ldots\ldots (10)$$

This is approximately true for the structures studied.

The span between the lower and upper limits of (10) indicates the maximum possible extra gain if H_{21}-data can be used. For the equipment studied under present conditions (k_ε= 1.6), this extra gain in dB is 4 dB (2+2 dB) or a factor of 2.6.

The overall gain of applying this new impedance based method to the equipment studied is in average 5 dB or a factor of 3, when the analysis bandwidth is 3.9 Hz. Thus most of the gains are between 3 and 7 dB (5-2 and 5+2 dB). Roughly speaking, the gain span 0-3 dB can be achieved when using vibration test levels calculated from (9). The extra gain span 3-7 dB can be achieved only if H_{21}-data in (3) is used for the calculations.

EXTENSIONS OF THE METHOD

Impedance or transfer function methods may be of help for solving other dynamic problems concerning vibration tests e.g.

- to transform known vibration data of a supporting structure into vibration data of a slighty different structure
- to give a tool for classification (zoning) of structures with respect to vibration levels and dynamic properties for prediction of vibration test levels

Since the vibration levels and dynamic properties of the measured supporting structure are sometimes slightly different from the present one, it is important to find a mathematical tool to transform the measured data to what they would have been for the present structure.

On the same level of simplification as before, the spectral densities S_1 of the mountings can be roughly calculated from the spectral densities S_1' of the corresponding mounting point in another slighty different supporting structure than the present one as follows

$$S_1 = S_1' \cdot \left|\frac{Z_t'}{Z_t}\right|^2 \quad \dots\dots\dots\dots\dots\dots (11)$$

where Z_t = total mechanical impedance of the present supporting structure with the equipment mounted

Z_t' = the same as Z_t but for the similar supporting structure

Of course the vibration test levels calculated from (3) with S_1 based on (11) will be less accurate than if S_1 was measured.

Often measurements have not been performed on the present structures at all points of interest. Sometimes the present structures do not even exist physically. Then it is necessary to base the calculations on simplified, rough data. These data could be either calculated from a more or less complicated mathematical model of the total system (equipment/supporting structure) or selected among classified data based on a great number of measurements on similar structures. The classification of vibration levels and dynamic properties of structures must be based on quantities convenient for classification.

Theoretically it can be shown, that the quantity $E = S_1 \cdot |Z_t|^2$ (which is a spectrum) would be convenient to classify and to describe the vibration levels of supporting structures in a proper way. On the same level of simplification as before this E-spectrum is supposed

- to be rather independent of the impedance level of the equipment mounted to the supporting structure (increasing the level of Z_t tends to decrease the level of S_1)
- to have equal levels on equal distances from the main vibration sources

The S_1-spectrum, which is necessary for calculations with (3), is determined from (12) and (13)

$$S_1 = E \,/\, |Z_t|^2 \quad \dots\dots\dots\dots\dots\dots (12)$$

$$Z_t = Z + Z_e \quad \dots\dots\dots\dots\dots\dots (13)$$

where Z_e = the mechanical point impedance of a representative mounting of the equipment (freely suspended)

Z = the mechanical point impedance of the supporting structure, when the equipment is not mounted

Z seems to be convenient to classify and to describe the dynamic properties of the supporting structure. It has to be known for the calculation of S_1 from (12).

The described extensions of the method have not yet been sufficiently tested. Therefore they should be considered rather as ideas and future possibilities than as completed results.

CONCLUSIONS

It has been possible to develop a method, designed for standard test procedures, to determine more realistic random vibration test levels taking into account mechanical impedance data. It is based on rather few impedance (or transfer function) data of the equipment. These data can be determined when the equipment is mounted to an ordinary shaker for vibration testing. Vibration test levels, calculated from this new method, are on an average lower and more accurate than for the envelope approach, at least for equipment studied according to part II.

A simplified method has been developed, which does not require impedance data, as an alternative to the envelope and impedance approaches. It has been proposed, that the vibration test level calculations should be based on a nominal vibration test level $\langle S_1 \rangle$ and, that a well known margin will be added to compensate for the lack of impedance (H_{21}) data. Of course the vibration test levels calculated from this method are less accurate than if the calculations were based on impedance data. Still these test levels should be lower and more accurate than those of the envelope based method.

The impedance approach of the vibration test level calculations may be extended to other closely related dynamic problems. It has been proposed that, impedance data should be used

- to transform known vibration data of a supporting structure into vibration data of a slightly different structure
- as a tool for classification of structures with respect to vibration levels and dynamic properties for prediction of vibration test levels.

The described methods were originally developed for airborne equipment, but they can probably be used to determine vibration test levels for other types of equipment.

REFERENCE

1. W.C. Fackler, "Equivalence Techniques for Vibration Testing", SVIC publication SVM-9, Washington, D.C., U.S.A., 1972

A METHOD TO DETERMINE REALISTIC RANDOM VIBRATION TEST LEVELS TAKING INTO ACCOUNT MECHANICAL IMPEDANCE DATA

PART II: VERIFICATION TESTS

Tryggve Hell
SAAB-SCANIA AB
Linköping, Sweden

The new method to determine more realistic random vibration test levels based on measured acceleration spectral densities has been tested on the SAAB-SCANIA built antiship missile Rb 04E and four of its electronic equipment items.

In this paper the different phases of the test program are presented:

- Tests
- Measurements
- Signal analysis
- Test results

INTRODUCTION

SAAB-SCANIA and IFM-Akustikbyrån in Sweden have developed a new method to determine more realistic random vibration test levels for airborne equipment taking into account mechanical impedance data. In the preceding paper (part I) the basic ideas and the theory behind the method have been given.

In this paper the different phases are presented of a program to test the new method on some selected airborne equipment items.
These phases are:

- Tests
- Measurements
- Signal analysis
- Test results

The reported activity was performed under contract to the Swedish Defense Material Administration.

IDEAS BEHIND THE NEW METHOD

The basic ideas of the method are:

- the vibration test levels are determined in such a way that the responses of a few selected critical areas of the equipment will be realistic in comparison to service
- the response levels are expressed as mean square values of a small number of rather wide frequency bands $[f_\nu, f_{\nu+1}]$

Since measured or predicted acceleration spectral densities are normally available only for points close to equipment mountings a calculated response quantity S_2 of each selected critical area has to be determined from

$$S_2 = S_1 \left|H_{21}\right|^2$$

where S_1 = acceleration spectral density representing the levels of the mountings

H_{21} = transfer function from mountings to a critical area of the equipment. H_{21} is determined in the laboratory.

The transfer functions H_{21} of the equipment is determined using shaker or impulse excitation.

The constant vibration test levels $S_{p\nu}$ within the frequency bands $\left[f_\nu, f_{\nu+1}\right]$ are expressed by the following equations

$$\underbrace{\int_{f_\nu}^{f_{\nu+1}} S_{p\nu}\left|H_{21}\right|^2 df}_{\text{Mean square value of response quantity at test}} = \underbrace{\int_{f_\nu}^{f_{\nu+1}} S_1\left|H_{21}\right|^2 df}_{\sim\text{ Mean square value of response quantity in service}}$$

or

$$S_{p\nu} = \frac{\int_{f_\nu}^{f_{\nu+1}} S_1\left|H_{21}\right|^2 df}{\int_{f_\nu}^{f_{\nu+1}} \left|H_{21}\right|^2 df}$$

This new method is based on the measured acceleration spectral density at mounting points of the equipment in service.

To study the new method, there was also a need of measurements inside the equipment at areas considered dynamically critical.

The method has been applied to some selected equipment items of the SAAB-SCANIA built antiship missile Rb 04E. In figure 1 this missile is shown, when carried on the AJ37 Viggen aircraft.

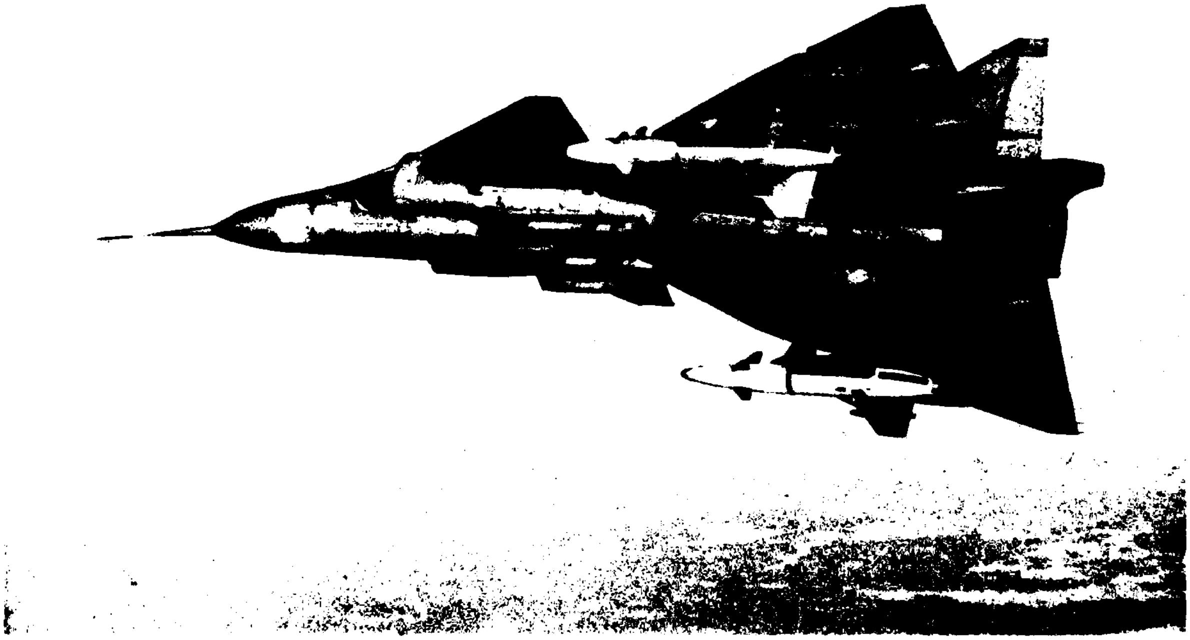

Figure 1. Missile Rb 04E carried on the AJ Viggen aircraft

To test the new method, it was not necessary to have results from measurements in service, for instance flight tests. As the main purpose of the tests was to study the interaction between the equipment and the supporting structure in the missile, it was quite sufficient to generate an approximate flight vibration and acoustic environment in the laboratory. No measurements were available from flight to compare with measurements made within the test program.

TEST ITEMS

The tests have been performed on a missile Rb 04E and four of its equipment items. The missile weighs 600 kg (1320 lbs), has a length of 4.5 m (14.8 ft) and a diameter of 0.5 m (1.6 ft).

The missile used was a prototype, but it was structurally and mechanically almost like a production missile. It was fully equipped in its forward fuselage.

During the tests the motor was replaced by an inert one. Wings, canards and the aft shell of the missile were dismantled.

When testing the missile on a shaker a fixture was used as shown in figure 2. This fixture clamped the missile both at the mid bulkhead and at the spindles for the wings. The total weight of this assembly was approximately 1000 kg (2200 lbs).

To keep the same mechanical system throughout the tests, the missile was mounted to the fixture even during the acoustic testing and when measurements of mechanical impedances were made.

At the end of the test program four equipment items of the missile were vibrated with test levels determined according to the new method and to an envelope approach. These items were: Power Unit (P.U.), Altimeter (A.M.), Autopilot (A.P.), and Electronic Unit (E.U.). The location of these items in the missile is shown in figure 2.

MEASURING POINTS AND EQUIPMENT

During the tests vibration measurements were made at 36 points in the forward fuselage of the missile as shown in table 1. Measurements were performed at mountings of equipment items (17 points), at critical areas inside the equipment (13 points) and at the primary structure of the missile (6 points).

In addition to these measurements recordings were also made of vibrations at the control point for the vibration tests, of the exciting acoustical noise during the acoustical testing and exciting forces during measurement of the mechanical impedances.

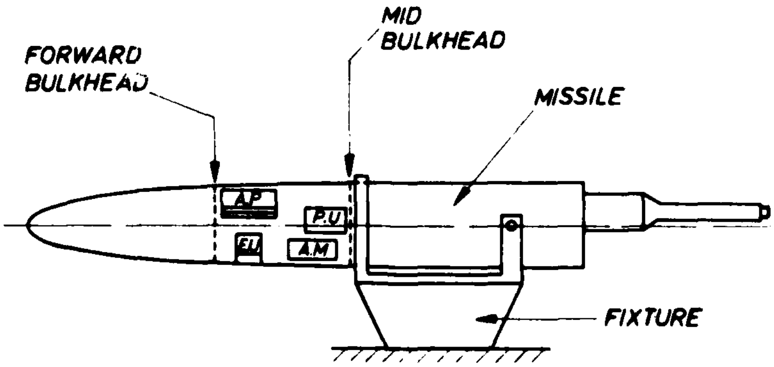

Figure 2. Test configuration

TABLE 1
Measurement points

No	Location		Type of point *	Direction
1	Power unit	Circuit board 2	I	Lateral
2		Component bracket	I	Lateral
3		Component bracket	I	Vertical
4		Transformer T5	I	Lateral
5		Transformer T1-T3	I	Vertical
6		Aft, low	M	Lateral
7		Forward, low	M	Lateral
8		Forward, low	M	Vertical
9		Aft, high	M	Vertical
10		Forward, high	M	Lateral
11		Forward, high	M	Vertical
12	Altimeter	Electronic valve	I	Lateral
13		Electronic valve	I	Vertical
14		Circuit board 1	I	Lateral
15		Circuit board 2	I	Lateral
16		Aft	M	Lateral
17		Aft	M	Vertical
18		Forward	M	Lateral
19		Forward	M	Vertical
20	Autopilot	Circuit board 1	I	Vertical
21		Circuit board 2	I	Axial
22		Rate gyro	I	Vertical
23		Aft	M	Axial
24		Aft	M	Lateral
25		Aft	M	Vertical
26		Forward	M	Lateral
27		Forward	M	Vertical
28	Electronic unit	Aft	M	Vertical
29		Circuit board 4	I	Vertical
30		Aft	M	Lateral
31	Forward bulkhead		S	Lateral
32	Forward bulkhead		S	Vertical
33	Structure close to power unit		S	Lateral
34	Structure close to power unit		S	Vertical
35	Mid bulkhead		S	Lateral
36	Mid bulkhead		S	Vertical

* I = Internal point of equipment, M = Mounting point of equipment, S = Primary structure of missile

In figure 3 a block diagram is presented of the measuring system. Standard type of equipment was used. The piezoelectric accelerometers used were mostly of miniature size due to limited space. The force transducers used for measurements of mechanical impedances were also of piezoelectric type. The acoustic noise was measured with a microphone of condenser type.

The recordings of the measurements were made on a 14-channel and on a 4-channel tape recorder with FMWB-technique. The frequency range of the recordings was 0-5000 Hz and 0-2500 Hz respectively.

An important part of the measuring system was the quick-look instruments. All recordings were checked in the time domain during the tests by oscilloscope. Immediately after the recordings frequency analysis was done with a "time-compression" analyzer.

VIBRATION TEST OF MISSILE

Vibration testing was performed of the missile in two directions: lateral (y) and vertical (z). In figure 4 testing in the vertical direction is shown. When testing the missile in the lateral direction the missile and the fixture were attached to a slip table. The capability of the electrodynamic shaker was 45000 N (10000 lbs).

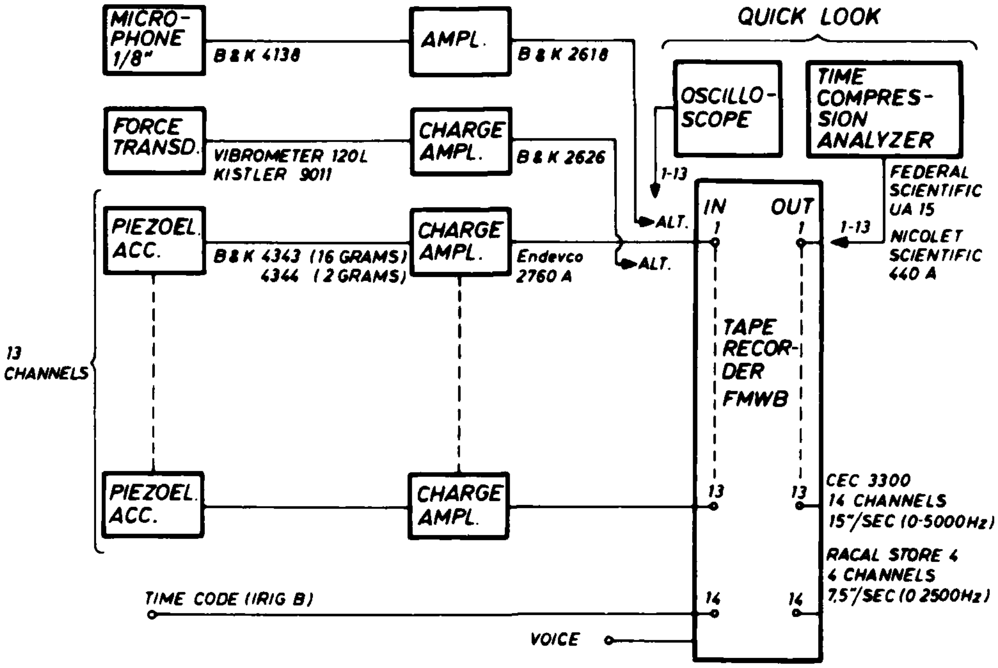

Figure 3. Block diagram of the measuring system

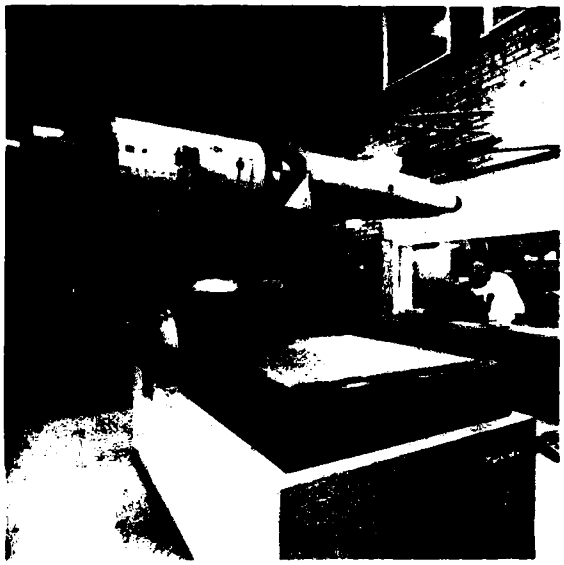

Figure 4. Vibration testing of missile. Vertical direction

The missile was vibrated with shaped random vibration test spectra in the frequency range 20-500 Hz as shown in table 2. The test levels were intentionally held at such a low level, that the mechanical strength of the missile was not affected. They were also reduced around 100 Hz to avoid severe excitation at a vibration mode of the forward fuselage of the missile.

ACOUSTIC TEST OF MISSILE

The missile was installed in a reveberation chamber of rectangular shape with the following size: 3.7x5.5x2.3 m (8.9x18x7.6 ft).

The missile was exposed to random noise with an overall sound level of 143 dB, which was mainly distributed in the frequency range 100-2000 Hz. The noise was generated by two sources, an electropneumatic device and nozzles with upstream bends.

In figure 5 a frequency spectrum is shown of the acoustical noise close to the missile. This spectrum also indicates the density of the acoustical modes in the chamber.

The vibration levels excited in the missile during the acoustical testing were much lower than those excited during the vibration testing in the corresponding frequency band.

TABLE 2
Vibration test levels. Missile

Excitation	Test level
Vibration. Lateral direction	20-70 Hz 0.0025 G^2/Hz 70-120 Hz 0.0008 G^2/Hz 120-500 Hz 0.006 G^2/Hz
Vibration. Vertical direction	20-100 Hz 0.002 G^2/Hz 100-130 Hz 0.0002 G^2/Hz 130-200 Hz 0.005 G^2/Hz 200-500 Hz 0.01 G^2/Hz

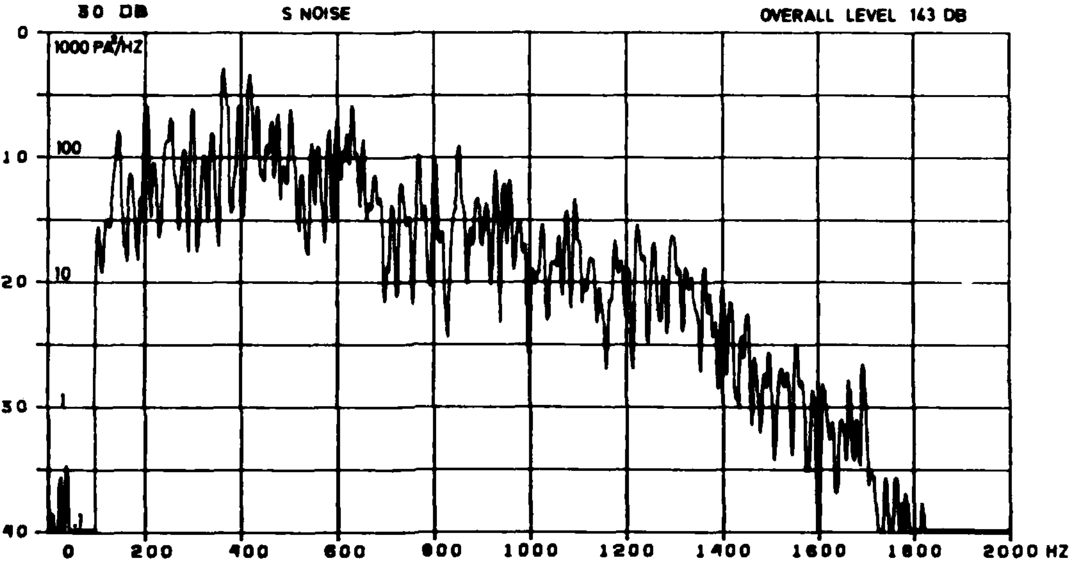

Figure 5. Acoustical excitation spectrum

MEASUREMENTS OF MECHANICAL IMPEDANCE

Measurements of mechanical impedance were made in the missile by exciting its structure with a small hammer and recording the impulse force and the response acceleration in the point of excitation. This is illustrated in figure 6.

This method was the only one possible to use due to the very limited space for the measurements in the missile and the large number of measurement points.

Up to 20 impulse excitations were recorded for each measurement point. This made it possible to get a good signal to noise ratio of the subsequent signal analysis, after averaging the signals in the frequency domain.

To shape the impulse force for different frequency bands the hammer was fitted with adapters of different materials as rubber and plastic.

VIBRATION TESTING OF THE INDIVIDUAL EQUIPMENT ITEMS

To be able to determine vibration test levels for the individual equipment items with the new method the transfer functions H_{21} from the mountings of the equipment to the critical areas inside the equipment had to be determined. This was done by vibrating each of the four equipment items on the shaker and recording input vibrations and response vibrations at the critical areas. The input level was in each case: 20-2000 Hz 0.01 g^2/Hz.

Testing of the individual equipment items were also performed with test levels determined both with the new method and with an envelope approach. The vibration response was recorded for each critical area of the equipment even at this occasion.

SIGNAL ANALYSIS

The aim of the signal analysis was to bring the large quantity of recordings to a comprehensible format to facilitate the subsequent work and interpretation of the data.

The analysis was performed on a HP 5451B Fourier Analyzer, which is described in block form in figure 7. The central unit of the analyzer is a minicomputer. This system has a Fast Fourier Transform (FFT) facility, which quickly brings digitalized time data to the frequency domain. In the frequency domain different kinds of frequency analyses can be made. Analysed data can be stored on a magnetic disc for short-time use and on a digital tape for longtime use.

The parameters for the signal analysis are shown in table 3.

Figure 6. Measurement of mechanical impedance

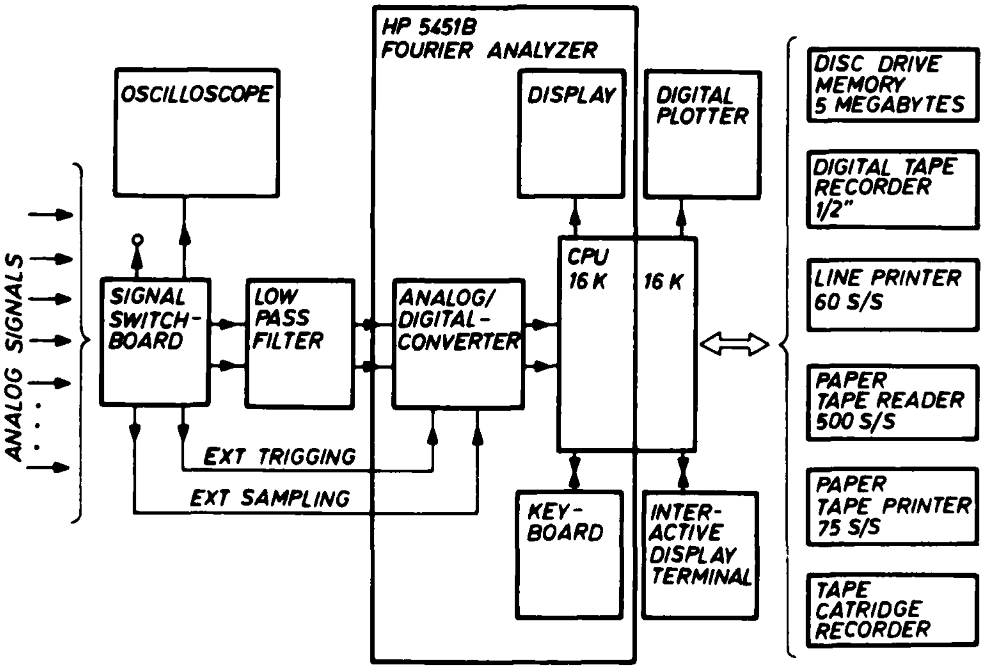

Figure 7. Block diagram of the signal analysing system

TABLE 3
Signal analysis parameters

Parameter	Value
Frequency range (Hz)	2000
Low-pass filter cutoff frequency (Hz)	1500
Low-pass filter rolloff (dB/octave)	48
Sample rate (Hz)	5000
Blocksize	2048
Frequency resolution (Hz)	2.44
Effective noise bandwidth (Hz)	3.9
Number of blocks: S_1	60
Number of blocks: H_{21}	120
Number of blocks: Z	10

As final results of the signal analysis frequency spectra were presented in the form of:

acceleration spectral density (S)

transfer functions (H_{21})

cumulative integrals of spectra in spectral form ($\int S \cdot df$, $\int |H_{21}|^2 \, df$, $\int S |H_{21}|^2 df$)

mechanical impedances (Z)

combinations of spectra ($S \cdot Z^2$, $S \left|\frac{Z_1}{Z_2}\right|^2$)

These spectra were presented in plotted form and in some cases listed.

The results of the signal analysis were mainly used to determine random vibration test levels for the equipment items in the missile. The test levels were determined according to the new method and to an envelope approach.

EXAMPLES OF FREQUENCY SPECTRA

In figure 8-18 examples of different kinds of frequency spectra are presented for some representative points in the missile.

These points are: No. 6, one of the mounting points for the power unit and No. 1, inside the power unit on a printed circuit board.

Figure 8 and 9 show vibrations excited during the vibration testing of the missile and figure 10 and 11 corresponding vibrations excited during the acoustical testing.

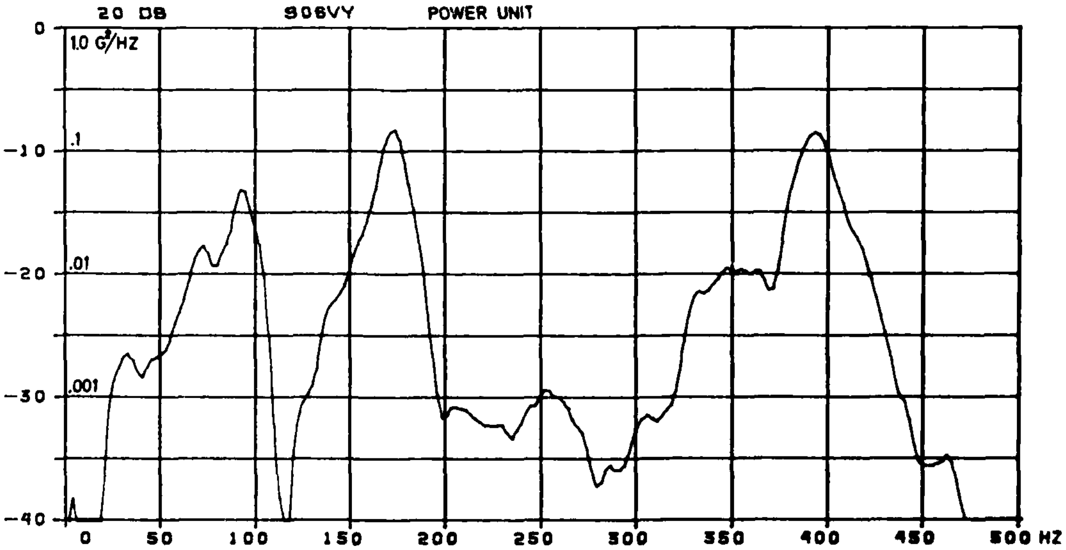

Figure 8. Acceleration spectral density (S_1) for meas. point 6

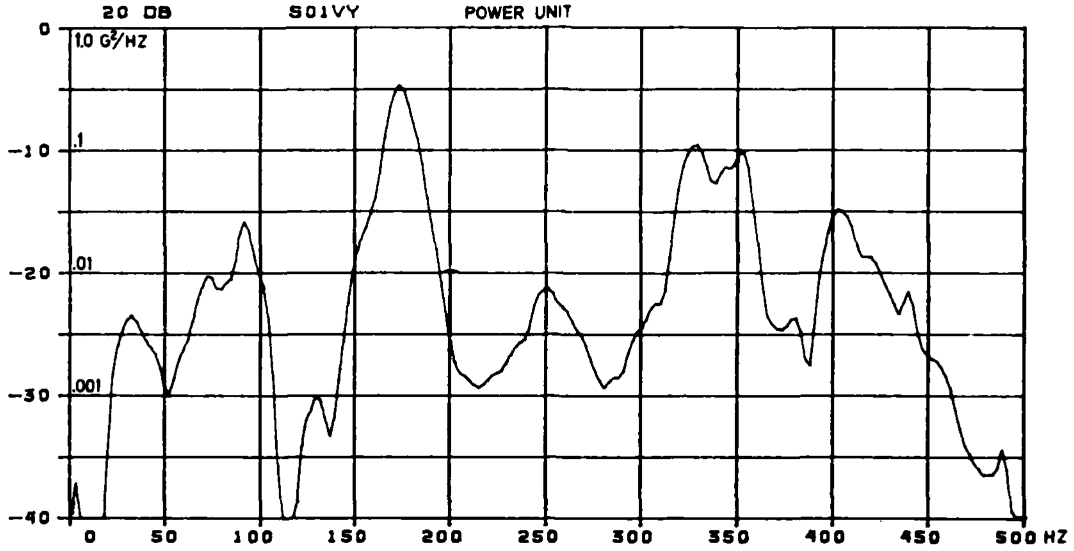

Figure 9. Acceleration spectral density (S_2) for meas.point 1

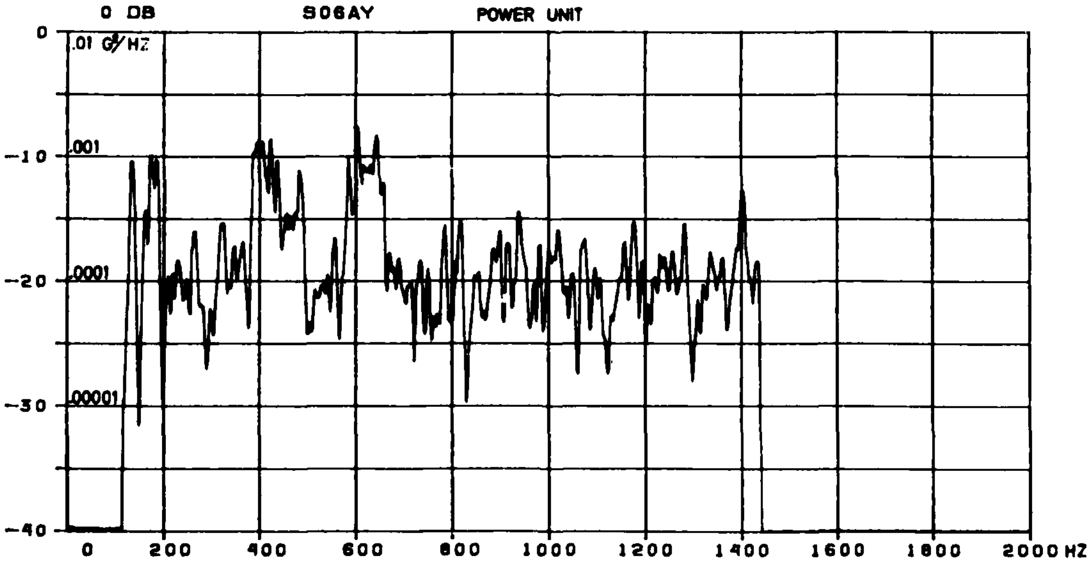

Figure 10. Acceleration spectral density (S_1) for meas.point 6

In figure 12 the transfer function H_{21} between points No. 6 and 1 is presented, as determined from the vibration test of the power unit. The frequency range has in this case been limited to 1500 Hz.

Figures 13 and 14 show combinations of spectra $(S|H_{21}|^2)$. These spectra were used to determine frequency bands $[f_\nu, f_{\nu+1}]$ for the vibration test levels.

In figures 15 and 16 cumulative integrals of spectra $(\int S\cdot|H_{21}|^2 df)$ are presented. These integrals were used to determine vibration test levels $S_{p\nu}$ according to the equation:

$$S_{p\nu} = \frac{\int_{f_\nu}^{f_{\nu+1}} S_1|H_{21}|^2 \cdot df}{\int_{f_\nu}^{f_{\nu+1}} |H_{21}|^2 \cdot df}$$

Test levels $S_{p\nu}$ can also be determined from listed versions of the cumulative integrals.

In figure 17 the mechanical impedance (Z) for point No. 6 is shown. This figure gives information of the magnitude, the phase $(\emptyset_Z)$ and the coherence function (γ^2) of the mechanical impedance.

In figure 18 a spectrum is shown of the combination $S\cdot Z^2$. This type of spectrum, which has been averaged in frequency bands with a width of 78 Hz, is intended to be used for certain extensions of the new method.

STATISTICAL REDUCTION OF TEST RESULTS

Test levels $S_{p\nu}$ have been determined for each equipment item for a number of frequency bands $[f_\nu, f_{\nu+1}]$ and each case of flight simulation.

These levels have been determined from acceleration spectral densities S_1 at the mountings of the equipment in the missile according to the new method $(S_{pi\nu})$ and according to an envelope approach $(S_{pe\nu})$. The envelope test level was determined as the largest value of S_1 in each frequency band $[f_\nu, f_{\nu+1}]$. In figure 19 an example of test levels determined according to the two approaches are presented.

The average value $<S_{1\nu}>$ have been calculated for each frequency band $[f_\nu, f_{\nu+1}]$. In figure 19 the average levels $<S_{1\nu}>$ are also shown.

The response levels at the critical areas of the equipment items have also been determined on an average basis, both for the flight simulations $(<S_{2\nu}>)$ and for the testing of the individual equipment items with test levels determined according to the new method $(<S_{2i\nu}>)$. In figure 20 an example is presented of the average response levels.

The following variables have been observed and treated as random variables by statistical means:

"Test level" $x=S_{pi\nu}/<S_{1\nu}>$, which is the test level determined according to the method normalized to the average value in corresponding frequency bands.

"Reduction factor" $y=S_{pi\nu}/S_{pe\nu}$, which is a comparison between test levels determined according to the new method and to an envelope approach.

"Response level" $z=<S_{2i\nu}>/<S_{2\nu}>$, which expresses differences in response levels when testing to levels determined according to the new method and during the flight simulations. (Theoretically this value should be 1, but in practice it can deviate from this value).

The quantity $\sigma_z/<z>$, which is the standard deviation of the variable z, normalized to the average value <z>. This is a measure of the relative deviation from the average value.

The quantity $\sigma_{ez}/<z_e>$, which has the same meaning as above but with values of z determined according to the envelope approach.

"Energy distribution": $(\sigma_{ez}/<z_e>/(\sigma_z/<z>)$, which can be regarded as a measure of the difference in deviation from the correct vibration responses at critical areas of equipment, when testing according to the envelope approach and to the new approach.

RESULTS

Arthmetic mean values and standard deviations have been calculated for the random variables defined in the preceding section of the paper. The results of these calculations are compiled in table 4.

The value <x> is very close to 1, which indicates that the test levels $S_{p\nu}$ determined with the new method is on

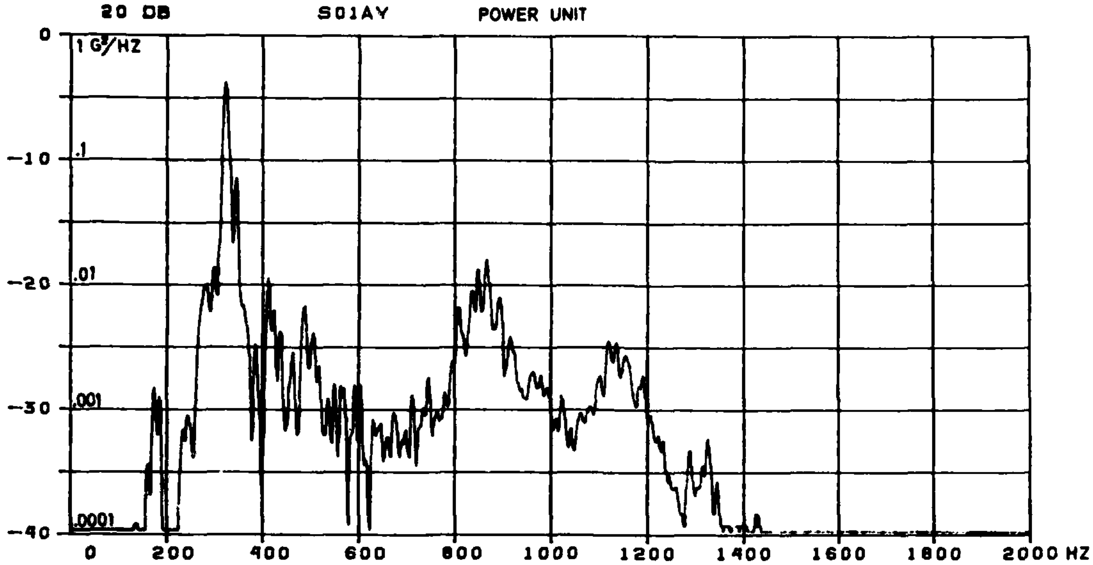

Figure 11. Acceleration spectral density (S_2) for meas.point 1

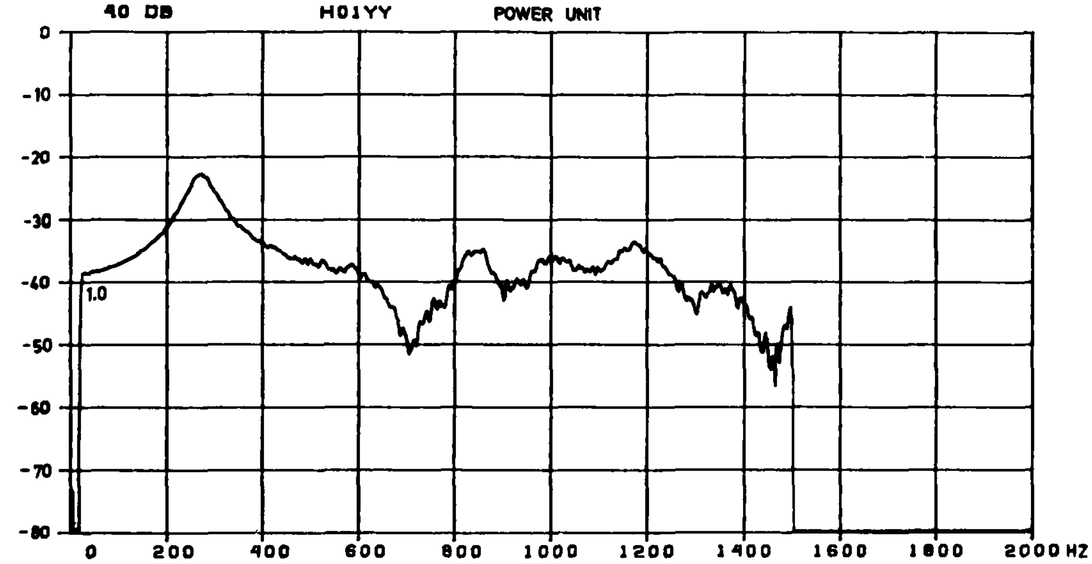

Figure 12. Transfer function ($|H_{21}|$) between meas.points 6 and 1

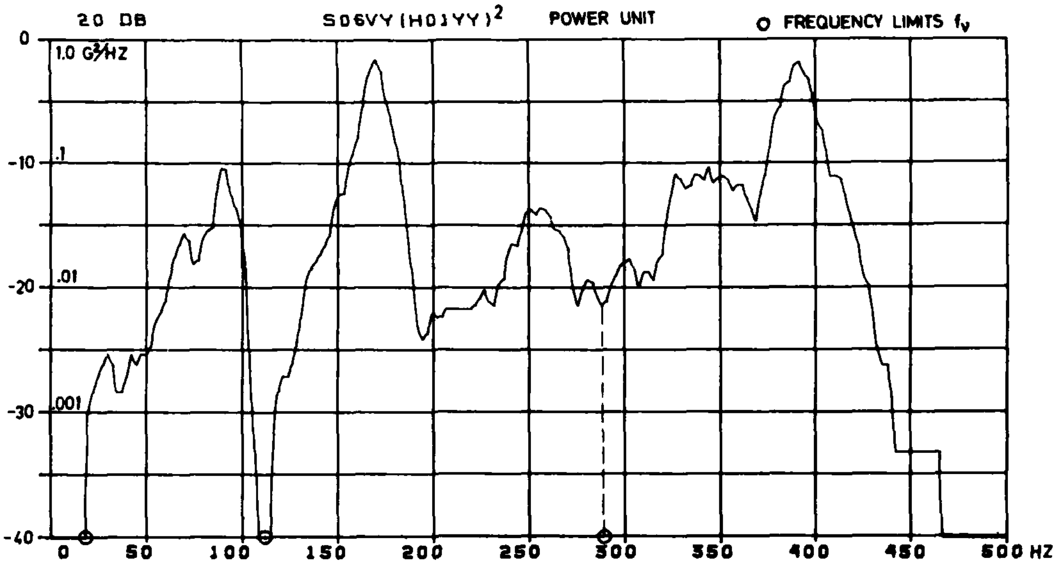

Figure 13. Acceleration spectral density ($S_{2p\nu}$) for meas.point 1

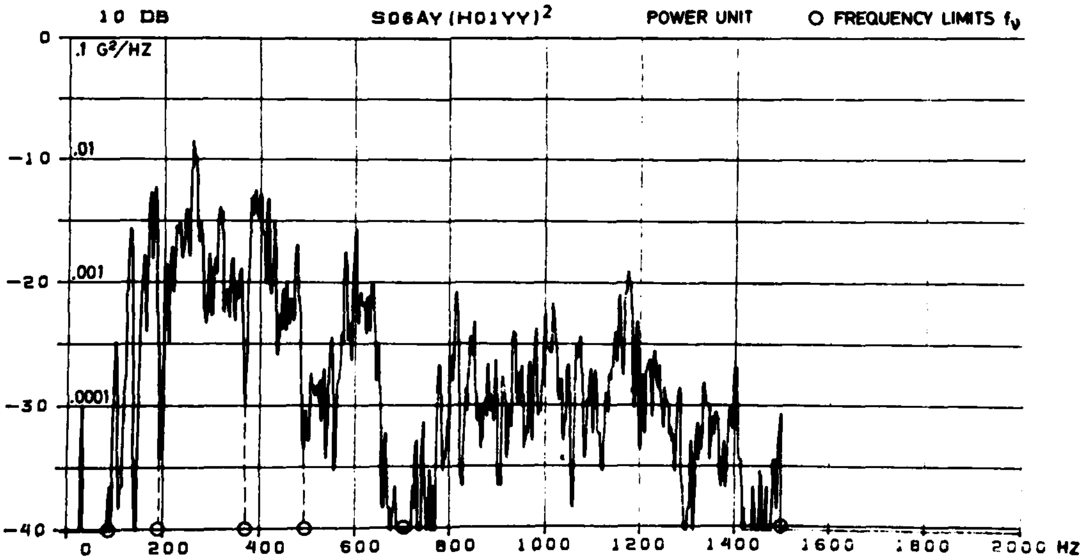

Figure 14. Acceleration spectral density ($S_{2p\nu}$) for meas.point 1

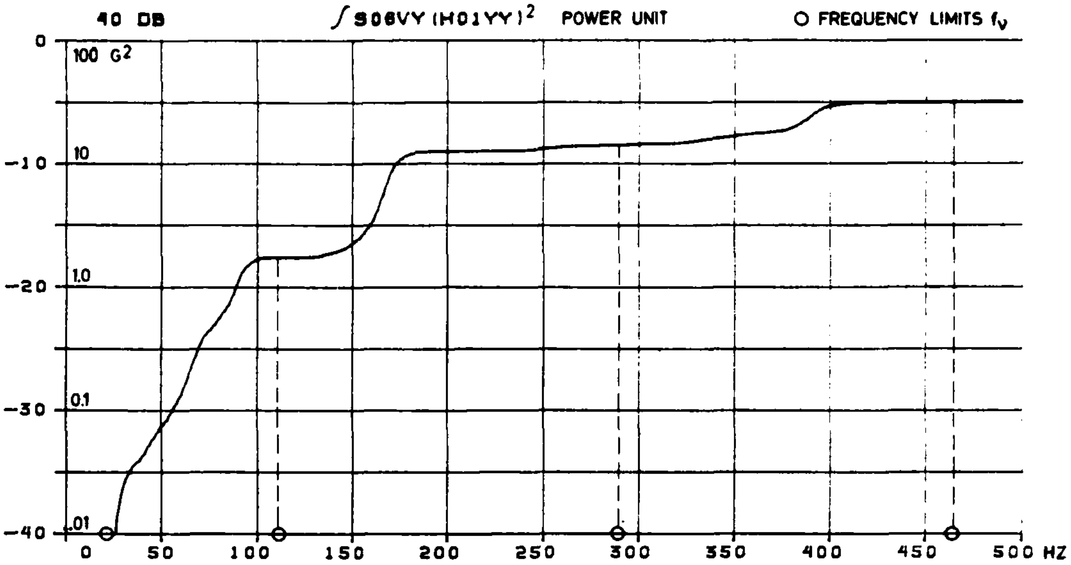

Figure 15. Cumulative integral of acceleration spectral density ($S_{2p\nu}$) for meas.point 1

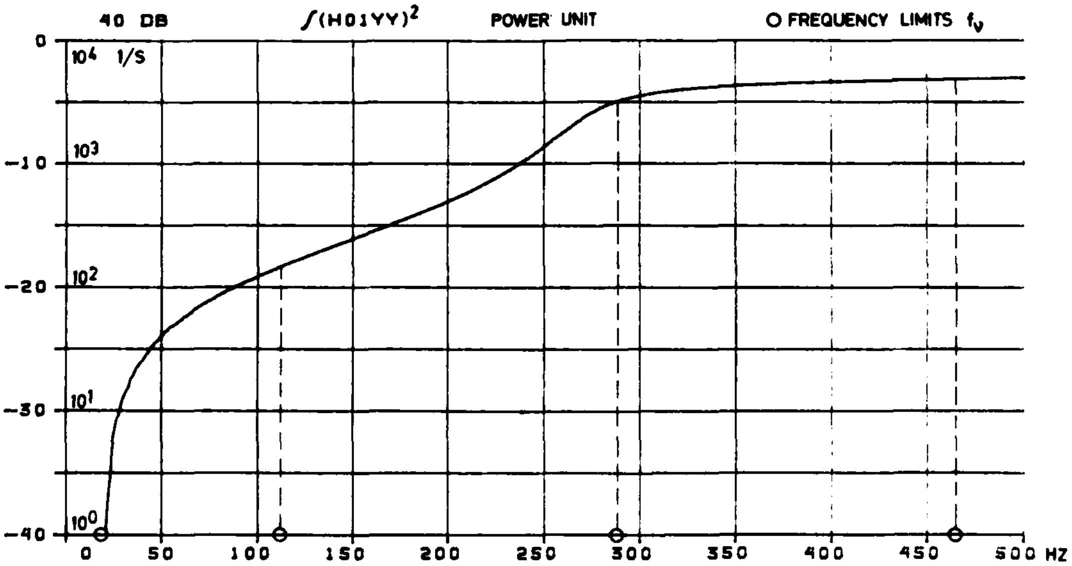

Figure 16. Cumulative integral of transfer function ($|H_{21}|^2$) between meas.points 6 and 1

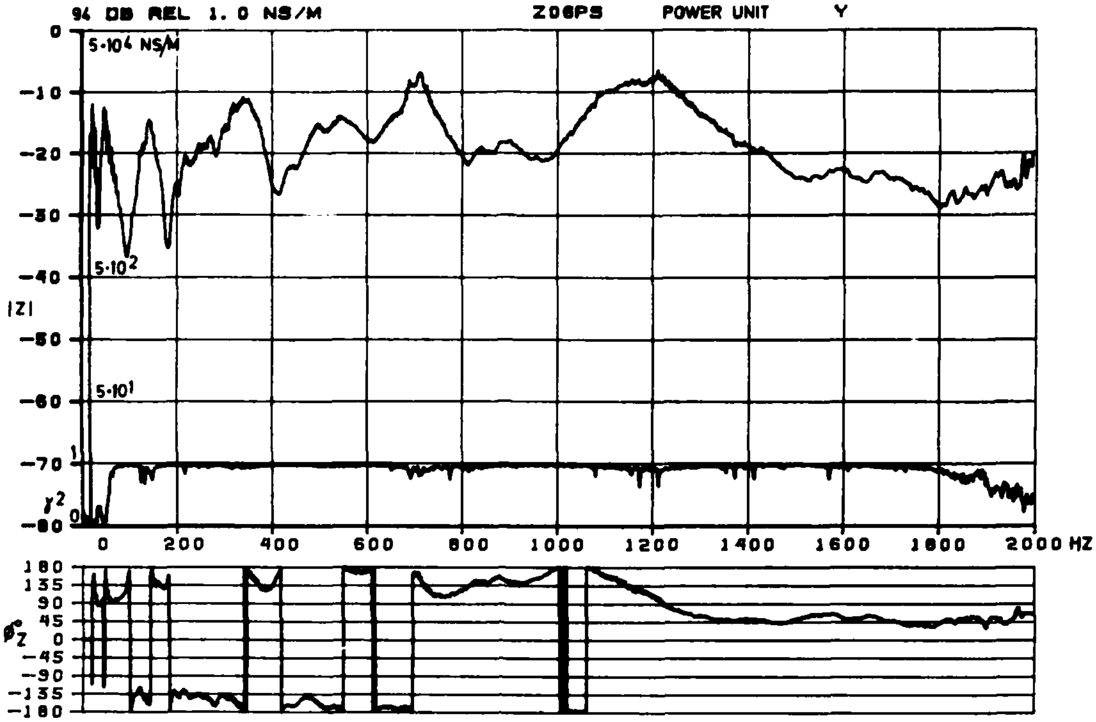

Figure 17. Mechanical impedance of meas. point 6

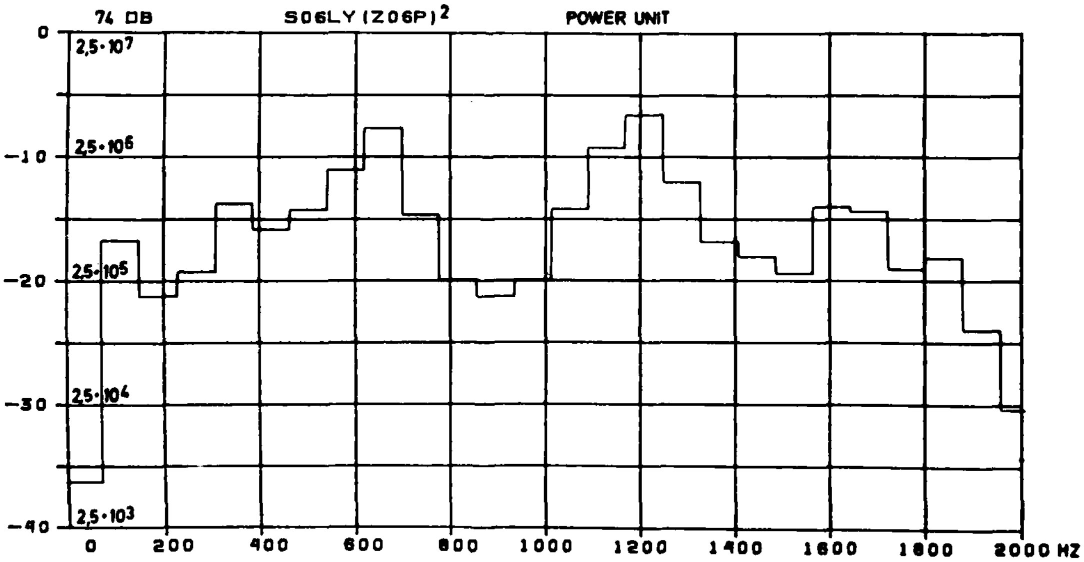

Figure 18. E-spectrum for meas. point 6

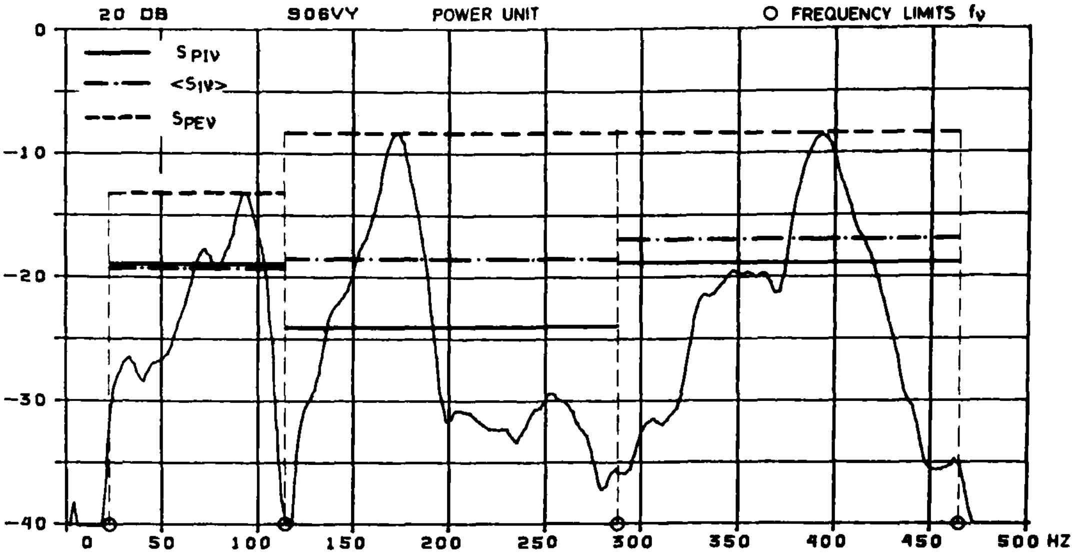

Figure 19. Example of vibration test levels

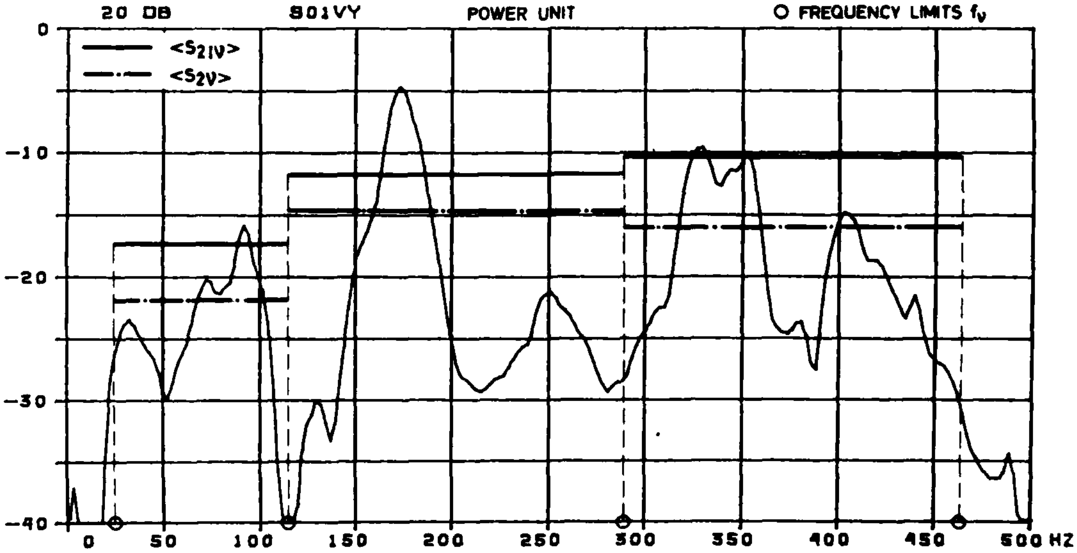

Figure 20. Example of vibration response levels

an average for all frequency bands close to the value $<S_{1\nu}>$. The standard deviation σ_x is 0.2-0.3, which indicates that most test levels fall in the band $0.7<x>1.3$.

If there is no information of the transfer function H_{21} in an actual case, $x>1.3$ should be chosen, say $x=1.6$. This corresponds to the following test level as expressed in dB:

$$10 \log S_{p\nu} = 10 \log<S_{1\nu}> + 2$$

In the column of table 4 titled "Reduction factor" it is shown that the test levels determined with the new method is on an average three times lower than the test levels determined with the envelope approach, when the analysis bandwidth is 3.9 Hz.

For an individual frequency band $[f_{\nu}, f_{\nu+1}]$ the variable y could vary quite a lot. Most of the "reduction factors" will be in the band $0.1 <y< 0.6$.

The column of table 4 titled "Response level" shows that the use of the new method still gives on an average higher responses at critical areas of equipment during vibration testing compared to the flight simulations. The value $<z>$ is 3.4 for the vibration excitation case and 11.8 for the acoustic excitation case.

The very high value for the acoustic excitation case is supposed to be caused by a more complicated type of excitation (strongly multiaxial) compared to the vibration excitation case.

The high value of the standard deviation σ_z for the acoustical excitation case indicates that many frequency bands will be undertested. This is supposed to be caused by a large influence of more direct acoustical excitation of the critical areas inside the equipment. The problem in this case, to find a representative input spectrum, is common to both the new method and an envelope approach.

In the column of table 4 titled "Energy distribution" it is shown that the ratio has a value larger than 1. This indicates that the vibration energy at critical areas was on an average distributed in a better way with respect to the response levels during the flight simulations, when testing with levels determined with the new approach than with the envelope approach.

The results for one of the equipment items, the autopilot, have been quite different from those presented in table 4 and area not included. This is assumed to be caused by the very close mechanical integration of the autopilot in the primary structure of the missile. The autopilot stiffens considerably the supporting structure of the missile.

CONCLUSIONS

The tests have shown that the new impedance based method to determine vibration test levels:

- is easy to handle.
- requires a dual channel frequency analyzer.
- gives test levels $S_{p\nu}$, which on an average are very close to the value $<S_{1\nu}>$ in corresponding frequency bands.
- gives acceleration responses at the critical areas inside the equipment, which on an average are distributed in a better way over the frequency range compared to an enveloped approach.
- gives responses at the critical areas, which on an average still exceed the corresponding responses of the simulated service case.

TABLE 4
Statistical results from the tests

Excitation of missile	"Test level" $x = S_{pi\nu}/<S_{1\nu}>$			"Reduction factor" $y = S_{pi\nu}/S_{pe\nu}$			"Response level" $z = <S_{2i\nu}>/<S_{2\nu}>$			"Energy distribution"	Number of frequency bands[†] $[f_\nu, f_{\nu+1}]$	
	$<x>$	σ_x	10 log$<x>$	$<y>$	σ_y	10 log$<y>$	$<z>$	σ_z	10 log$<z>$	$\frac{\sigma_{ez}/<z_e>}{\sigma_z/<z>}$	M	I
Vibration	1.05	0.19	0.2	0.34	0.2	-4.7	3.44	6.0	5.4	1.48	46	100
Acoustical noise	0.99	0.3	0	0.33	0.24	-4.8	11.8	48.4	10.7	1.25	69	95
Vibration + Acoustical noise	1.02	0.26	0.1	0.34	0.23	-4.7	7.5	34.2	8.8	1.29	115	195

[†] M = Mounting point of equipment
I = Internal point of equipment

DISCUSSION

Mr. Kana (Southwest Research Institute): Your method appears that it would work very well for a case where you have measured an input at one location. If the input were measured at several locations, such as at the base of the instrument, it is possible that you may get a different measurement of input at each one of those locations. If that is true would this method work directly as you have indicated?

Mr. Hell: You can use this method on all of the points that you have measured and you should choose representative input points. Perhaps you should use the one that gives the highest input values of the mounting points. I know that could be different and you should choose the best input points when you measure vibration.

Mr. Kana: If you have differences when you measure the input point at several locations, such as at the base of this instrument package, and you do indeed get differences in those inputs then it seems that you must allow for that since you really have a multiple source input. You must also allow for whether or not those sources are correlated or uncorrelated and that would influence the final outcome.

Mr. Hell: Yes, I think you are correct if there are quite different results from different input points. You should take care of that perhaps in the addition of safety factors. Our method is very simple in principle and you noticed the basic conditions for it to work in the first presentation. We showed that it should be working at almost each point in the same way and in one direction too. This is the first condition; but when you get away from this condition you have to take care of the safety factors.

Mr. Kana: Do you feel conceptually that it would work? It is just a matter of more complexity than in handling the different inputs.

Mr. Hell: Of course you can use more complicated mathematics too but we have tried to simplify it for standard use.

Mr. Sylwan: I should add that this is a problem also for the standard analog approach. We have not tried to solve this specific problem. I think if we had to use big matrices and thereby had to acquire a great deal of data this approach would not be practical.

Mr. Sattinger (Westinghouse): Would you expound a little on the definition on the H 21 transfer function? Is it a true impedance function or is it more of a transmissibility function? Is it a ratio of force to acceleration or acceleration to acceleration?

Mr. Sylwan: It is not a true impedance ratio it is a true transfer function, acceleration to acceleration; but it could be expressed as a ratio between two mechanical impedances.

Mr. Curtis (Hughes Aircraft): I would like to compliment the authors on their inovativeness of their approach. In response to Dr. Kana it seems to me that one could make that calculation if one had the psd's of various attachment points. Calculate the H 21 squared based on the power average of the input to the response psd at the selected point and then control the power average at those same points when running the test in the laboratory and at least on the average it will all come out in the wash.

Mr. Hell: It is true that if you can make measurements at the internal points and you have the best way to simulate the service environment. But it is often impossible to do that and then you have less spectra to use. We have used these methods in practice when measuring internal response points on a launcher. It was very difficult in this situation to determine the input points for that equipment from these measurements. We measured the response point and from that point we could calculate the best test levels.

Mr. Thomas (Air Force Flight Dynamics Laboratory): I suspect that this is still yet so new that you don't have the history to back it up yet. Have you been able to verify the legitimacy of the tests by actual experience in service?

Mr. Hell: No, this method is quite new. We are trying to implement it in our work and for further specification of the test levels on equipment; we have only done it on a few items of equipment.

VIBRATION ANALYSIS OF A HELICOPTER PLUS AN EXTERNALLY-ATTACHED STRUCTURE

D. J. Ewins, J. M. M. Silva*, G. Maleci**

Imperial College of Science and Technology

London

A vibration analysis has been made of a complex structure comprising a helicopter airframe, external carrier platform and a store, in order to construct a mathematical model for use in a design optimisation exercise. The model formed was based on impedance coupling of component substructures, using experimentally-derived modal data for the airframe and store, and a finite-element theoretical model of the carrier. Predictions for the complete assembly agreed well with data measured on the actual structure over much of the frequency range, although the accuracy was reduced at higher frequencies. Further investigation indicated that this effect was probably due to approximations made in the coupling conditions, rather than to limitations in the models of the substructures. The exercise demonstrates the usefulness of this type of analysis for complex engineering structures and also highlights some problems which may be encountered in applying theoretically-straightforward techniques to practical cases.

1. INTRODUCTION

1.1 Objective

The primary objective of the study reported in this paper was to establish the feasibility of constructing a mathematical model for the vibration analysis of a complex aerospace structure. The structure consisted of a helicopter airframe with an externally-attached carrier substructure and is illustrated in Figure 1.

The purpose of constructing this mathematical model was to provide the basis for a design optimisation exercise in which the vibration environment of the carried store could be improved by making suitable modifications to parts of the complete system. However, we are not concerned here with this eventual application; only with the processes involved in obtaining the necessary model.

1.2 Approach

Various constraints and requirements influenced the choice of the methods used for this study. Principal amongst these was the requirement that the output from any mathematical analysis of the structure should be expressed in terms of its forced vibration response characteristice (and not just of its modes of vibration) since these are the most directly related properties to the vibration environment of concern. A second constraint was the requirement that any design modifications should be confined to the carrier platform itself, or to the struts which support it, and so access was required to individual parts of the system model. Another consideration was the non-availability of a suitable theoretical model of the airframe.

Accordingly, the approach chosen for this study was impedance coupling of component models, in which the constituent parts of the overall system are each studied and modelled individually by whatever means is most appropriate - theoretical, numerical, experimental -

---

*Now at University of Lisbon, Portugal

**Now at Nuovo Pignone, Florence, Italy

and then these are assembled into a single system model by coupling their impedance properties at each junction. Such a method satisfies the main considerations listed above and also allows considerable flexibility throughout the whole process.

2. ANALYSIS METHOD

There are several methods available for the vibration analysis of coupled substructures which could be used in this type of application. Many of these are mathematically elegant and computationally efficient, but are best suited to the analysis of systems where every component is modelled theoretically. When one or more components must be represented by experimental data, as is the case here, it may be more appropriate to rely on the more direct and simpler approach of impedance coupling. The basic theory of this method is very simple and is summarised as follows, using 'mobility' to describe a velocity-per-unit-force frequency response function and 'impedance' to represent its inverse. (A more detailed description of the theory may be found in (1), and a previous practical application in (2).)

Consider two components, A and B, which are to be coupled in a single coordinate (i.e. one coordinate, or freedom, of A will be locked onto one of B). If the point mobility (or impedance) of each component separately in this coordinate is Y_A for A and Y_B for B (or Z_A and Z_B), then the corresponding point mobility after coupling A and B to form C, Y_C is given by:

$$Y_C^{-1} = Y_A^{-1} + Y_B^{-1} \qquad \text{or} \quad Z_C = Z_A + Z_B \qquad (1)$$

If more than one coordinate is involved in the coupling process, then each component's mobility properties will be contained in a matrix of individual mobilities and the coupling equation becomes:

$$[Y_C]^{-1} = [Y_A]^{-1} + [Y_B]^{-1}$$
$$[Z_C] = [Z_A] + [Z_B] \qquad (2)$$

The most general case arises when each component has several coordinates of interest, not all of which are involved in the coupling process (i.e. there are some points of A whose motion is of interest in the final analysis but which do not couple directly onto B). Here the impedance matrices must be partitioned, grouping together all those coordinates not involved in the coupling (x_a and x_b, say) and then all those which are (x_c). Thus:

$$\left[Z_A\right] = \left[Y_A\right]^{-1} \equiv \begin{array}{c} \begin{array}{cc} (x_a) & (x_c) \end{array} \\ \left[\begin{array}{c|c} Z_A & Z_A' \\ \hline Z_A' & Z_A'' \end{array}\right] \end{array} \begin{array}{c} \\ (x_a) \\ (x_c) \end{array} \qquad (3)$$

Similarly,

$$\left[Z_B\right] = \begin{array}{c} \begin{array}{cc} (x_c) & (x_b) \end{array} \\ \left[\begin{array}{c|c} Z_B & Z_B' \\ \hline Z_B' & Z_B'' \end{array}\right] \end{array} \begin{array}{c} \\ (x_c) \\ (x_b) \end{array}$$

The properties of the coupled system, C, are given by:

$$\left[Z_C\right] = \left[\begin{array}{c|c} Z_A & Z_A' \\ \hline Z_A' & Z_A'' \end{array}\right] + \left[\begin{array}{c|c} Z_B & Z_B'' \\ \hline Z_B' & Z_B'' \end{array}\right]$$
$$= \left[\begin{array}{c|c|c} Z_A & Z_A' & 0 \\ \hline Z_A' & Z_A'' + Z_B & Z_B' \\ \hline 0 & Z_B' & Z_B'' \end{array}\right] \qquad (4)$$

from which we can obtain:

$$\left[Y_C\right] = \left[Z_C\right]^{-1} \qquad (5)$$

Other components may be added by a simple extension of this process either simultaneously or sequentially, by repeating the coupling snown in (4) with another component. An advantage of the latter approach is that any coordinates used in joining A to B which are of no further interest can be deleted from Y_C simply by removing the corresponding row and column, thereby reducing the size of the matrices to be handled. It should be noted that deletion of coordinates from an impedance matrix has the effect of grounding those particular coordinates; a property which can be used to advantage, although not without care.

A general purpose program -

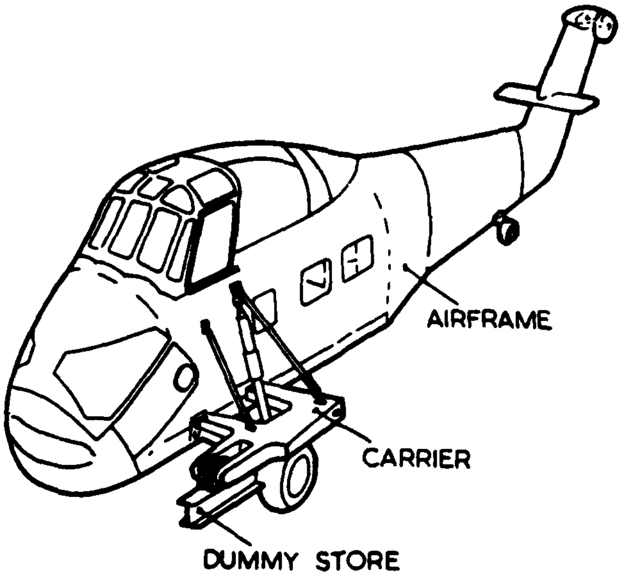

FIGURE 1 THE HELICOPTER/CARRIER STRUCTURE

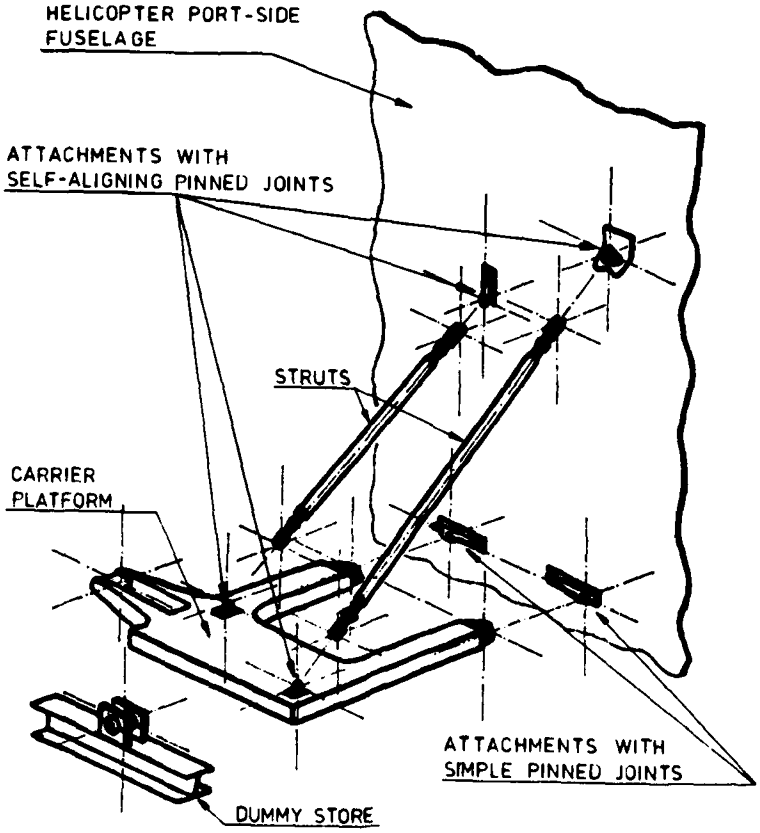

FIGURE 2 COMPONENTS OF SYSTEM MODEL

COUPLE 1 - has been developed to implement this impedance coupling principle, and this has been widely used for both academic and industrial projects, (2). This program is used extensively in the present study.

3. SYSTEM MODEL

3.1 Components

The first stage in the overall modelling process is that of identifying the best subdivision of the complete system into suitable components, and then deciding how each of these should be analysed and also how to represent their interconnection.

In this case, the subdivision is relatively obvious - airframe, platform, store, struts, as shown in Figure 2 - and the methods of analysing each were:

(i) airframe - experimental measurements of the mobility properties required for the analysis, followed by a curve-fitting process to make these data conform to a mathematically-consistent model;

(ii) platform - numerical (finite element) analysis guided by mobility measurements on the actual structure;

(iii) store - theoretical model, as a rigid body;

(iv) struts - theoretical model, using Timoshenko beam theory.

It was also decided that construction of the system model would be performed in two stages, partly to reduce the size of the matrices to be handled (as mentioned in Section 2), but also to provide an interim check on the progress of the analysis. Thus, in addition to the complete system, shown in Figure 1, some results are also given for the carrier structure subassembly, consisting of the platform plus the store, illustrated in Figure 3.

3.2 Modelling Details

The next stage is an examination of the system to ascertain what simplifications, if any, can be incorporated in order to economise the process. Of particular relevance are planes of symmetry which might permit a fully 3-dimensional analysis to be made in smaller stages. However, there is very little symmetry in the structure being studies here and so we have, at first sight, to include all 6 coordinates at each junction point, giving a 42 x 42 impedance matrix of the complete structure. However, because of the vast amount of data which such a complete model would demand, we shall seek to make some simplifying assumptions in order to reduce the size of the model.

(a) Airframe Since the initial plan was to measure all the mobility data required for the airframe, the 576 elements in the complete matrix describing the 4 attachment points were examined carefully to identify any which could be omitted from the analysis (see Figure 4). The struts which attach at the upper two points do so through ball-and-socket joints and so it might be assumed that no torques are transmitted between the airframe and struts, thereby obviating the need to include the three rotational coordinates at either of these points. Also, the lower attachments, to the platform, are made with pin joints so that one rotation coordinate, θ_Z, can be omitted at each of these two points. Further, since our interest is primarily in vibration in the vertical direction, it was decided that motion in the fore-and-aft direction, y and θ_X, would be of secondary importance and so the primary coordinates for the airframe model became:

$$x_1;\ x_2;\ x_3;\ x_4;\ \theta_{Y_2} \text{ and } \theta_{Y_3}$$

and all* the elements in the 6 x 6 mobility matrix were obtained. In addition, measurements were made of the point mobilities in coordinates

$$y_2;\ z_2;\ \theta_{X_2};\ y_3;\ z_3;\ \text{and } \theta_{X_3}$$

so as to include a representative stiffness in those directions.

(b) Platform Similar considerations applied to the platform dictated the coordinates to be included in its model, although as this component was modelled analytically, there was not the same incentive to eliminate coordinates as there was for the airframe. Thus, all the directions were included at the store attachment points.

---

*Symmetry assumed so that only 21 actual measurements were made.

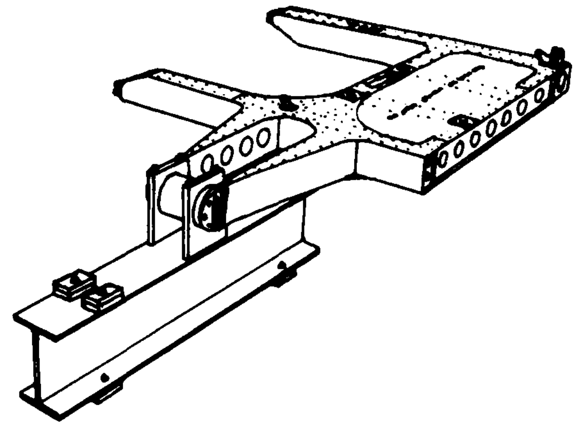

FIGURE 3 CARRIER SUB-ASSEMBLY

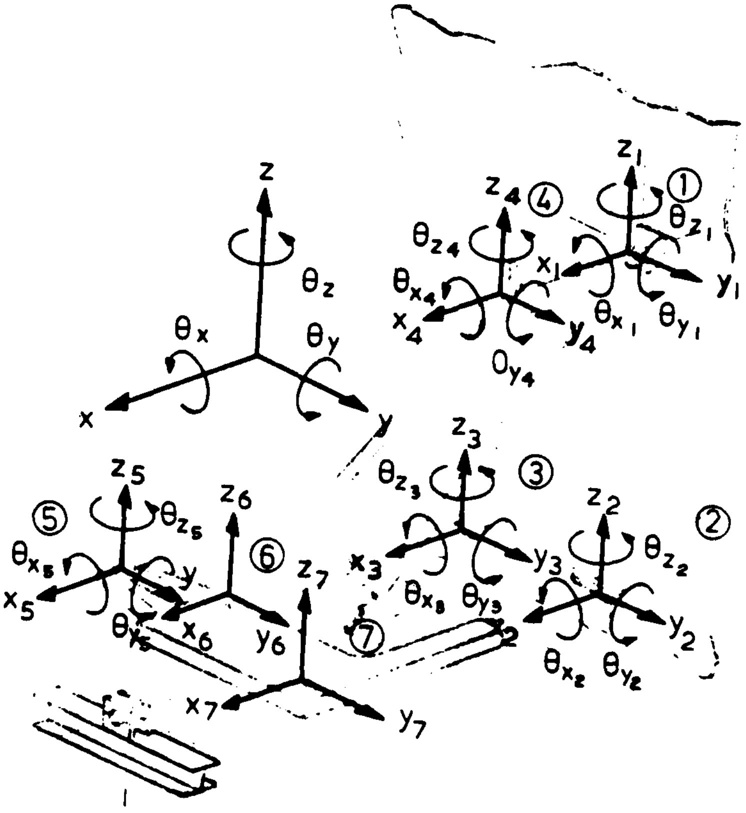

FIGURE 4 MODEL COORDINATE SYSTEM

4. COMPONENT MODELS

4.1 Airframe

Measurements were made of nearly 40 individual mobility plots on the airframe while it was supported at the rotor head by a soft suspension. The frequency range was limited for this component to the decade between 3 and 30 Hz, since that included the severest excitation conditions and, once again, considerations of time and economy were necessary. The measurement method used was a traditional stepped-sine steady-state excitation using a conventional electromagnetic shaker and piezoelectric transducers. Some of the mobilities required involved rotational coordinates and a specially-developed technique, reported previously (3), (4), was used to measure these properties. Some typical plots of both translation and rotation mobilities are shown in Figure 5.

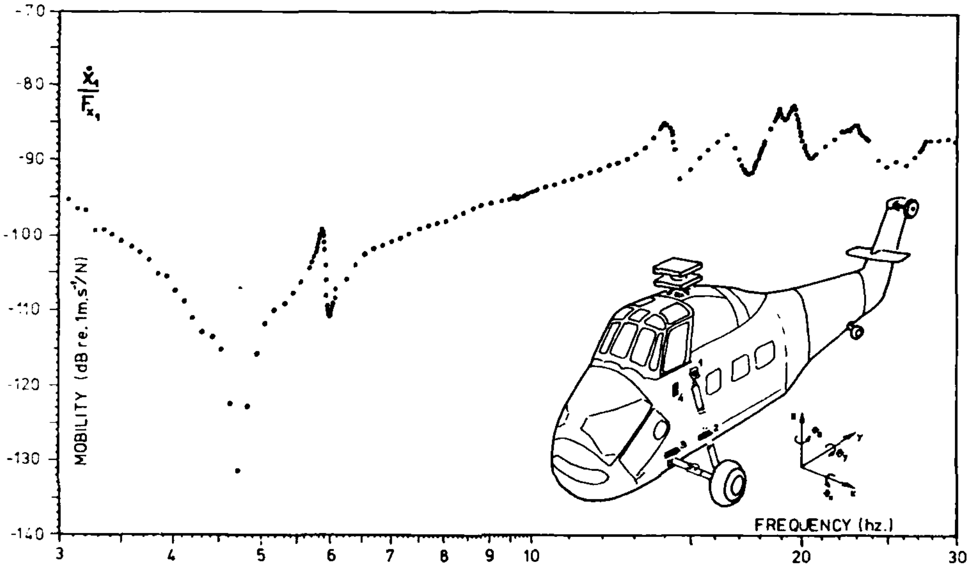

(a)
POINT
TRANSLATION

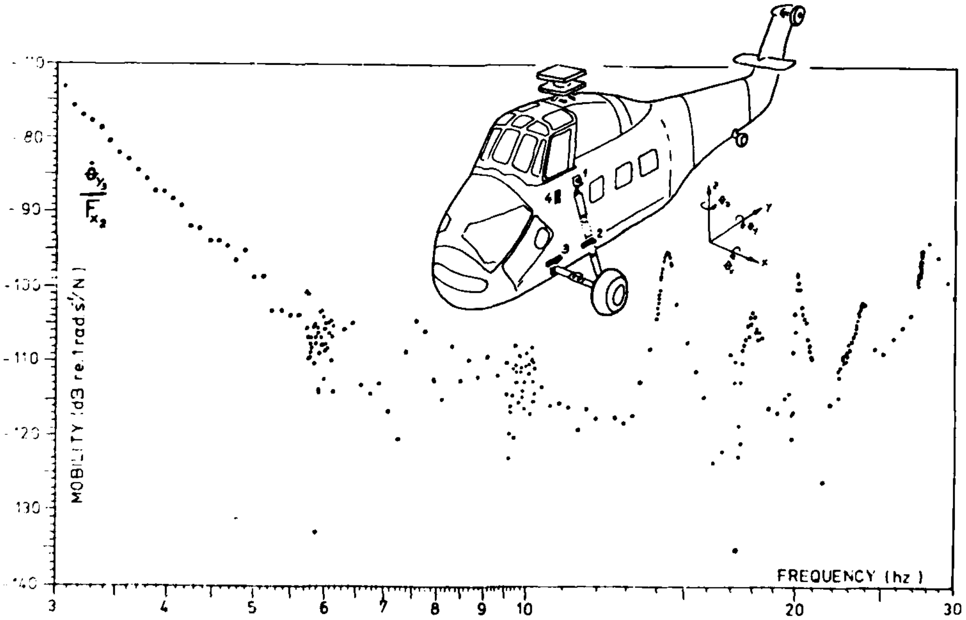

(b)
TRANSFER
ROTATION

FIGURE 5 TYPICAL MEASURED MOBILITY DATA

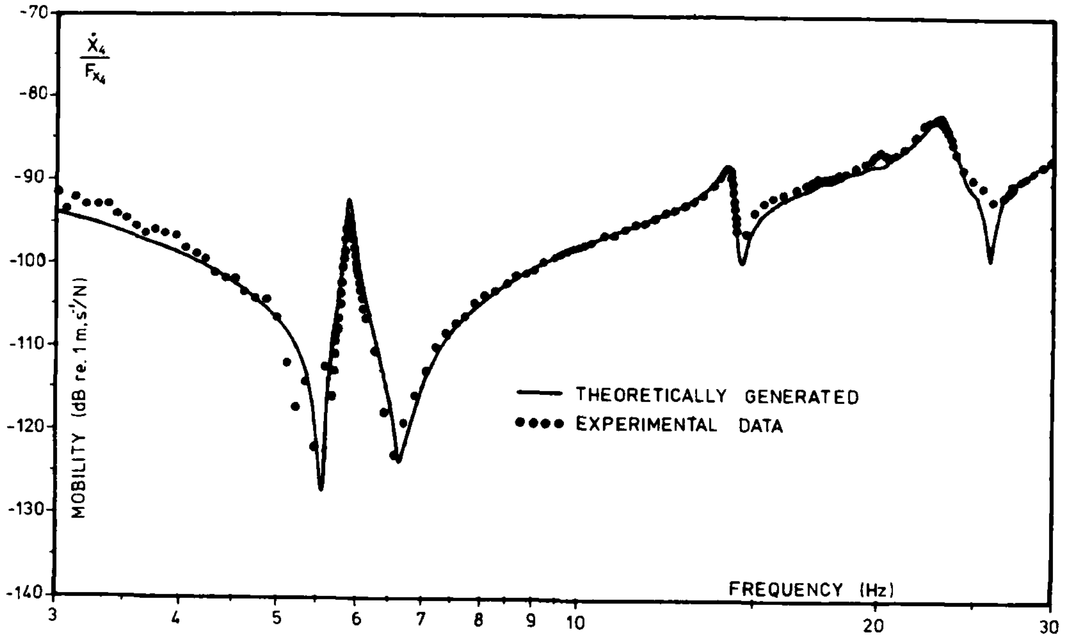

FIGURE 6 MOBILITY DATA REGENERATED BY MODEL

The measured data were processed by a modal analysis or curve-fitting procedure whereby a simple formula was devised to represent or 'regenerate' each of the measured curves. In addition to providing a considerable saving in the amount of data to be stored, these theoretical models of the mobility curves also serve to ensure that the complete model of the airframe is mathematically clean and that it conforms exactly to a linear multi-degree-of-freedom model. (The inclusion of the raw measured mobility data could lead to numerical ill-conditioning in the complete system model, due to the presence of inevitable experimental errors.) An example of a theoretically-regenerated mobility curve is presented in Figure 6. The method used for the curve-fitting process is described in detail in (5) and the helicopter mobility measurements themselves are presented in greater detail in (6).

4.2 Platform

Using detail drawings of the platform, a hybrid mathematical model was devised consisting of lumped masses, Timoshenko beams and plate finite elements, as shown in Figure 7. Attempts to use a simpler, beam-type model had failed and considerable effort was expended in ascribing appropriate values to the various elements of the model shown here. Calculations made for various of the mobility parameters required in the assembly analysis were compared with measurements made on the actual structure as a test of the model's validity. A sample mobility is shown in Figure 8, from which it can be seen that only moderate success has been achieved by the mathematical model of the platform.

4.3 Struts, Store

The remaining components (two struts and the store) were of sufficiently simple form to be amenable to direct theoretical modelling with confidence. The store was taken to be a rigid body, over the frequency range of interest, and the struts were analysed as uniform beams. The only additional data which were used were assessments of the local flexibility of the tongue and fork attachments at the ends of the struts to hold the self-aligning socket joints. Some mobility measurements were made with the strut attached to a heavy steel block via one such joint, and from these it was possible to deduce estimates for the flexibility of the attachments themselves.

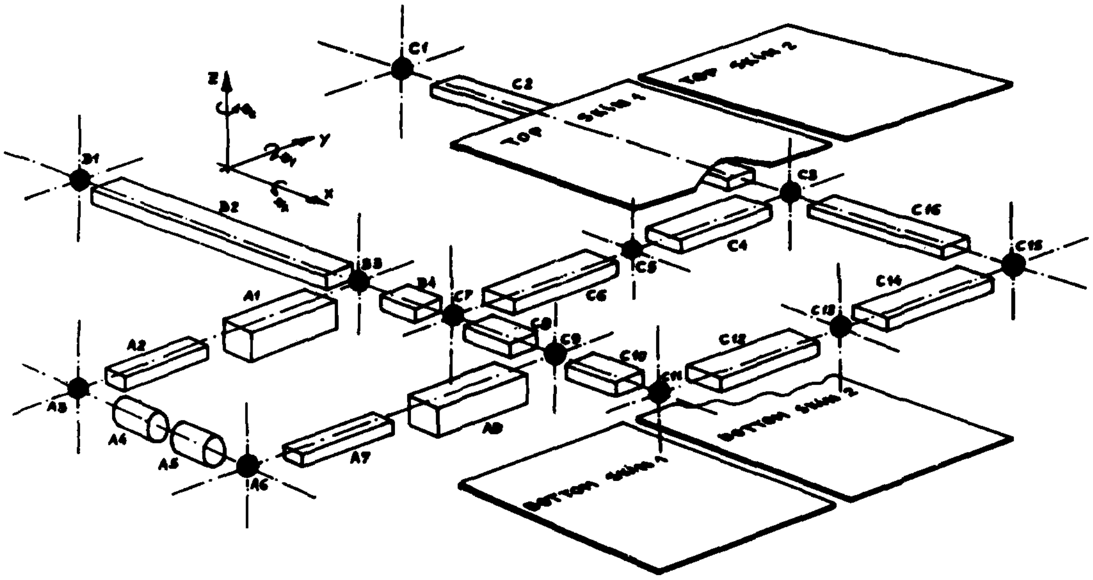

FIGURE 7 THEORETICAL MODEL OF CARRIER PLATFORM

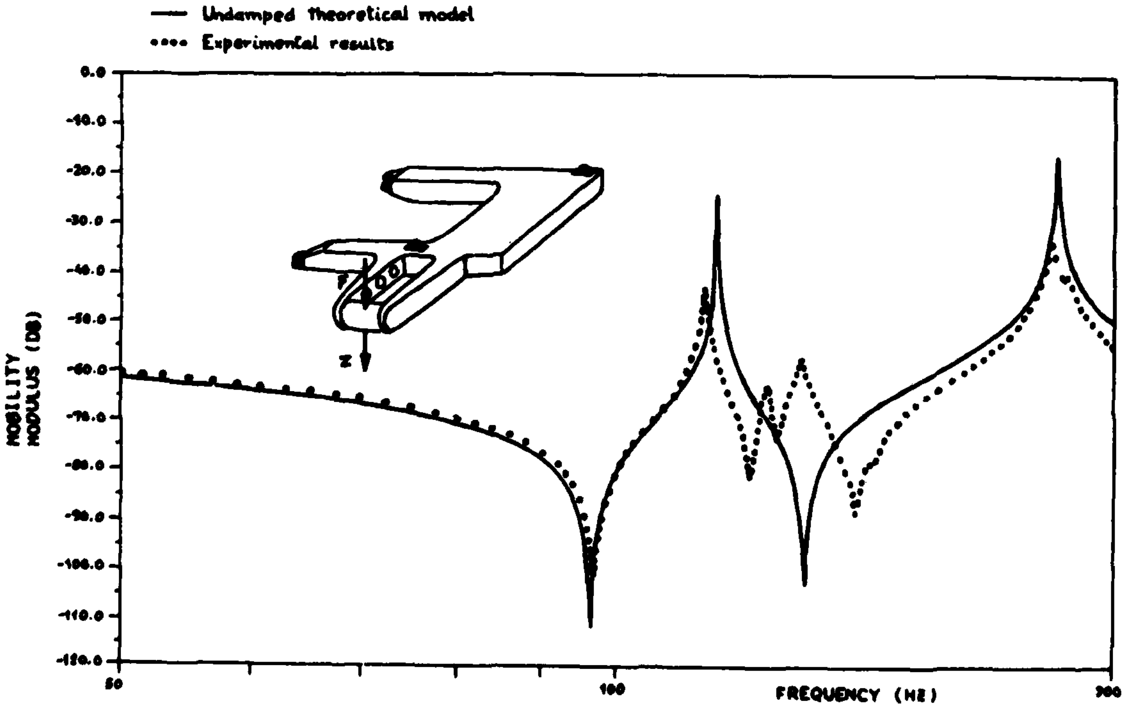

FIGURE 8 THEORETICAL AND MEASURED PLATFORM MOBILITIES

5. ASSEMBLY ANALYSIS

5.1 Carrier Structure Subassembly

An interim assessment of the modelling process was obtained by predicting and measuring the platform plus store subassembly. By coupling them in the 6 coordinates at their junction, a model was formed from which the two sample mobility plots, given in Figure 9, were computed. These mobilities are shown alongside the corresponding measured data and represent the best and the worst of the model's predictions. It should be noted that Figure 9(a) follows very closely the behaviour of a rigid mass, reflecting the dominance of the store's inertia in that point mobility, and is thus relatively insensitive to any discrepancies in the platform model. The transfer measurement across the structure, shown in Figure 9(b), is a much more demanding test of the validity of the model.

5.2 Complete Assembly

Undaunted by the shortcomings of the subassembly model, an analysis of the complete system was made and one mobility plot - the point mobility at the store attachment - is shown in Figure 10, alongside some measured data acquired at the same time as the bare airframe data. A companion plot is shown in Figure 11 for the configuration with the atore removed.

5.3 Discussion

It must be noted that the model developed for the platform is considerably less accurate in its representation of the dynamic properties of that component than are those for the other components and, as such, constitutes the weakest link in the model. This is emphasised by the results obtained for the carrier structure subassembly, when the platform is attached to a massive component which changes its vibration modes markedly.

Nevertheless, it must be noted that in the final assembly results, the predicted mobilities compare very favourably with the test results throughout 70 - 80% of the frequency range. Only at the 'higher' frequencies (above 20 Hz) does the model fail to predict accurately, but even then, it only fails on the assembly which includes the store.

One conclusion which might be drawn is that the complete system response is dominated by the airframe, whose properties are automatically included in the model with great accuracy. However, the removal of the store brings about a major change in behaviour (Figure 11 cf. Figure 10) and so it is established that the whole system <u>is</u> influenced by all its components and thus that the analysis and model are successful up to 20 Hz.

In an attempt to explain exactly what is responsible for the poorer performance at the higher frequencies, and also to explore the characteristics of the model, a series of further studies was made.

6. FURTHER INVESTIGATIONS

Two separate aspects of the analysis described above were examined by a series of additional studies made to aid the understanding of the performance of the model. These were:

(a) replacing the theoretical model of the carrier structure by one derived directly from modal tests (in order to remove the influence that an inadequate component model might exert); and

(b) replacing the airframe by a 'rigid' structure (to facilitate further full and partial assembly checks and to remove the possibility that the airframe dominates the final characteristics).

6.1 Revised Carrier Structure Model

By conducting a series of mobility measurements on the platform plus store assembly, and subjecting these to modal analysis procedures, it was possible to formulate a new model for the carrier structure and thus to enter the second phase of the complete system modelling procedure with full confidence in the models used for all components.

The required mobility matrix for the carrier subassembly was already prescribed by the chosen coupling conditions, and by measuring a limited number of these mobilities directly and decomposing them into a modal model, it was possible to regenerate the full mobility matrix for the subassembly. Two of the measured and analysed mobility curves are shown in Figure 12. The process used meant that all the elements of the mobility matrix could be regenerated, not only those actually measured, and as a check, Figure 13 shows a 'derived' mobility (derived from two other mobility plots) alongside the measured curve (which was measured purely as a check).

When this revised carrier model is

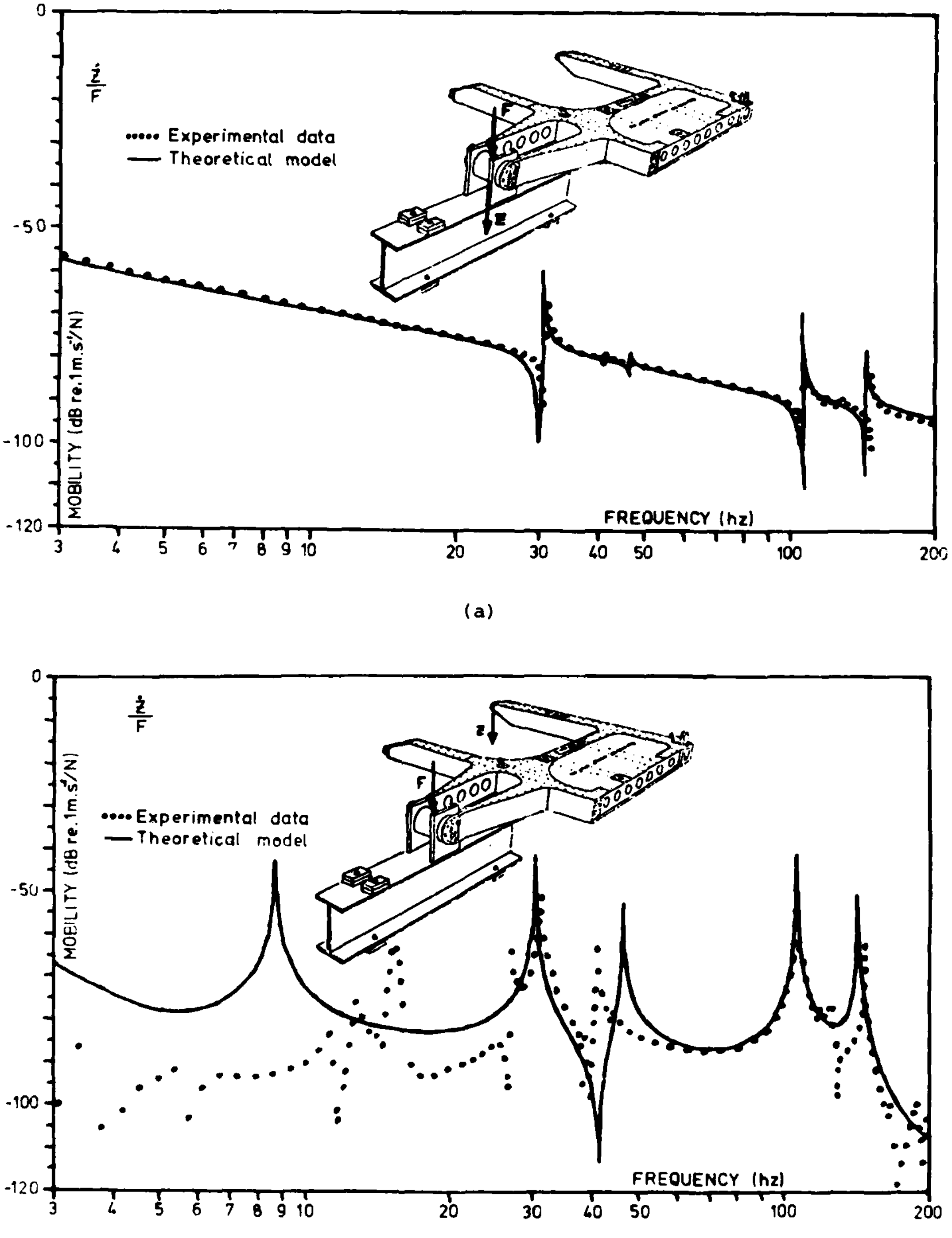

FIGURE 9 SYSTEM MODEL PREDICTIONS AND ACTUAL MEASURED DATA FOR CARRIER STRUCTURE

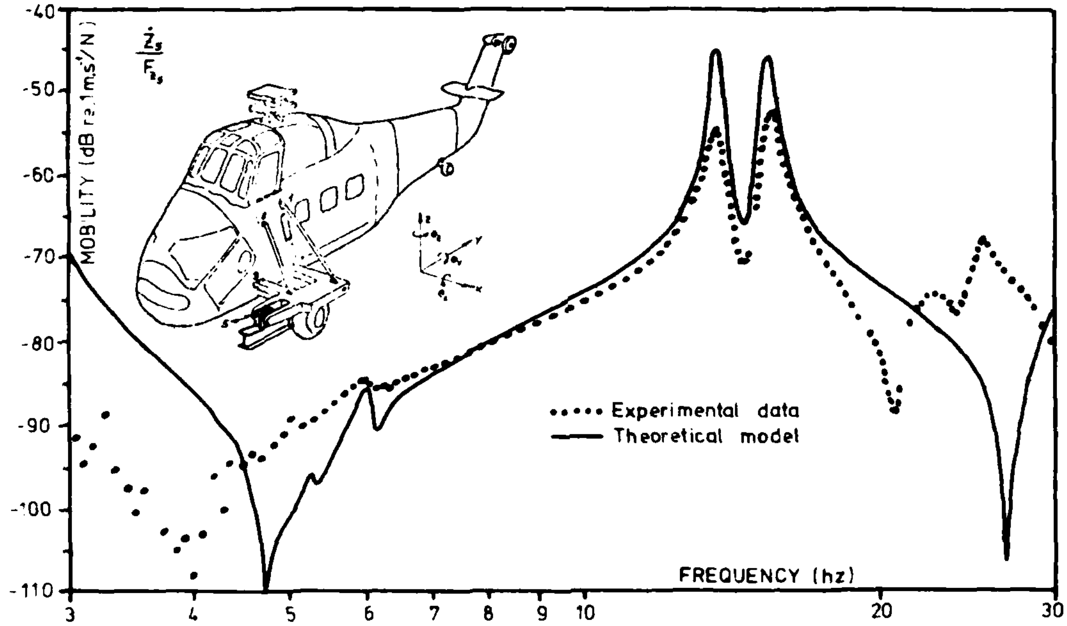

(a) MODULUS

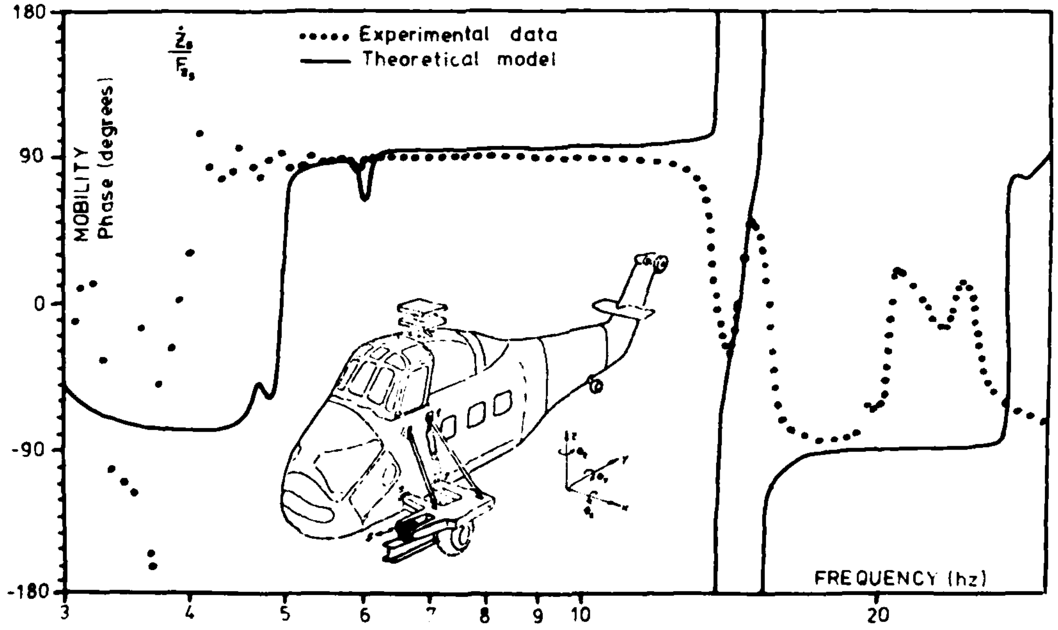

(b) PHASE

FIGURE 10 SYSTEM MODEL PREDICTIONS FOR COMPLETE ASSEMBLY PLUS MEASURED DATA

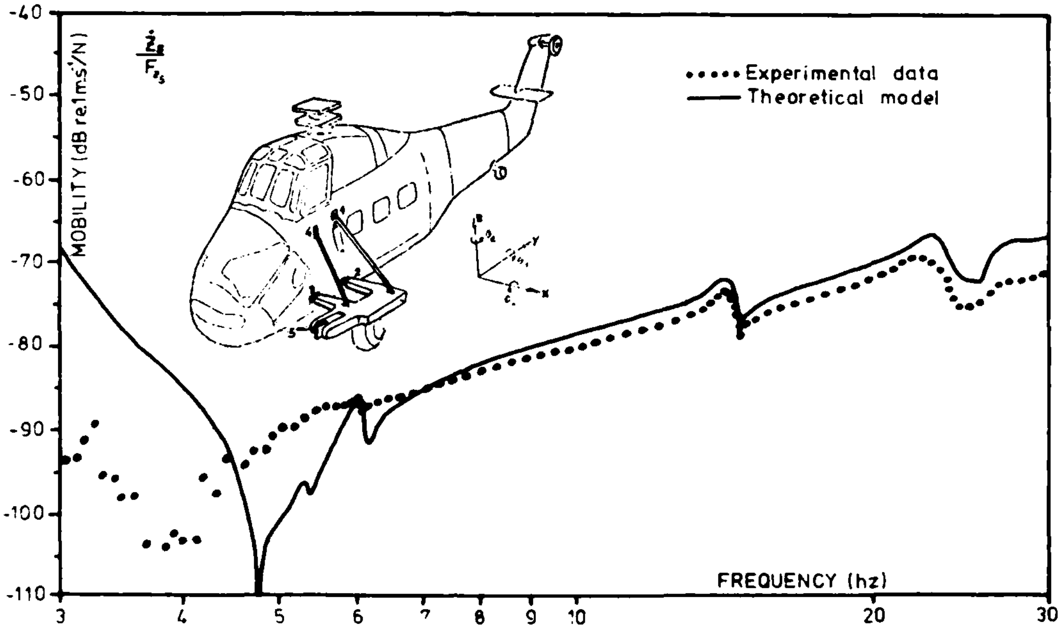

(a) MODULUS

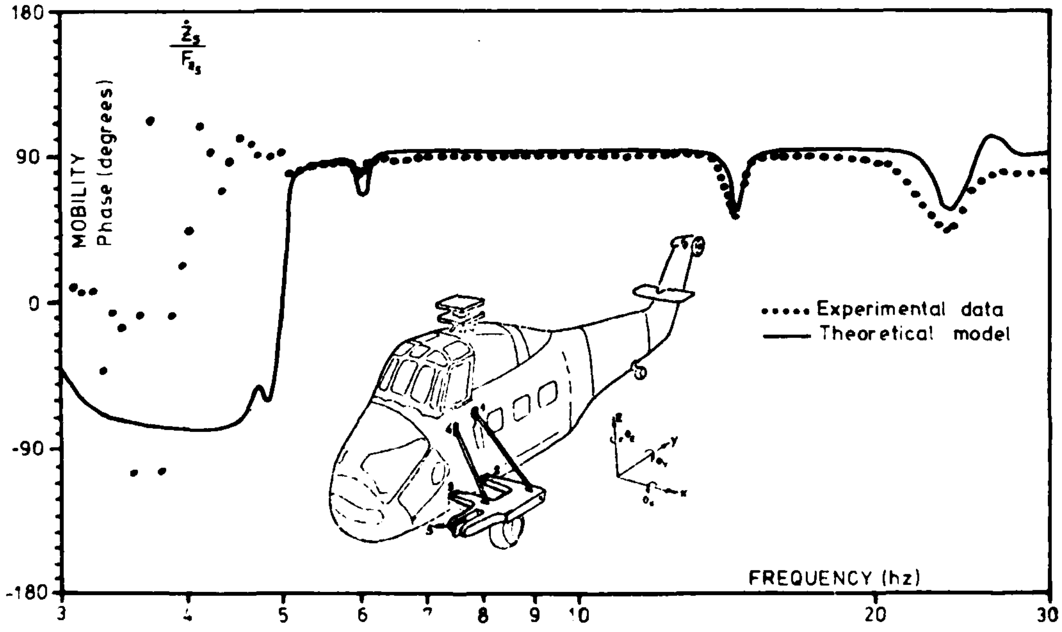

(b) PHASE

FIGURE 11 SYSTEM MODEL PREDICTIONS FOR COMPLETE ASSEMBLY (MINUS STORE) PLUS MEASURED DATA

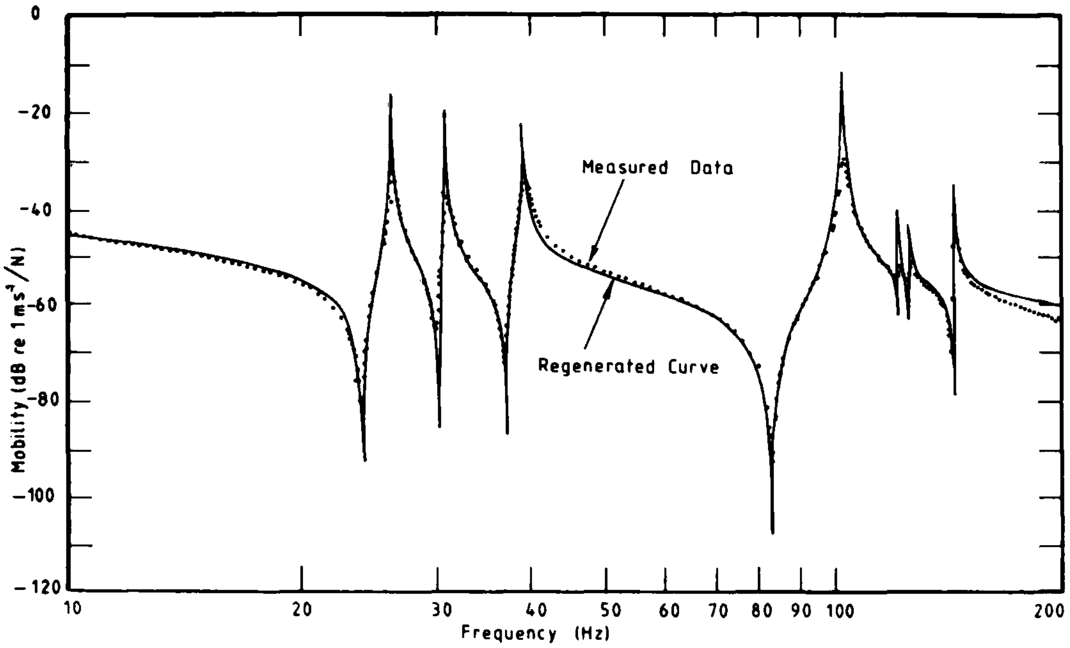

(a) TRANSLATION MOBILITY

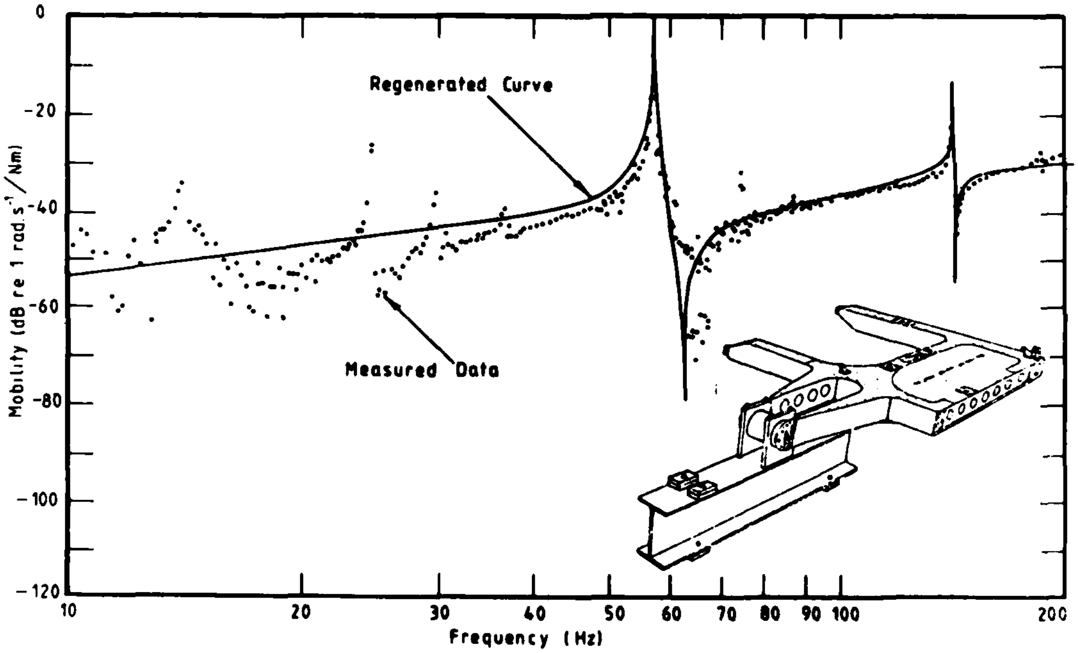

(b) ROTATIONAL MOBILITY

FIGURE 12 TYPICAL MOBILITY MEASUREMENTS ON CARRIER STRUCTURE PLUS CURVE-FIT REGENERATIONS

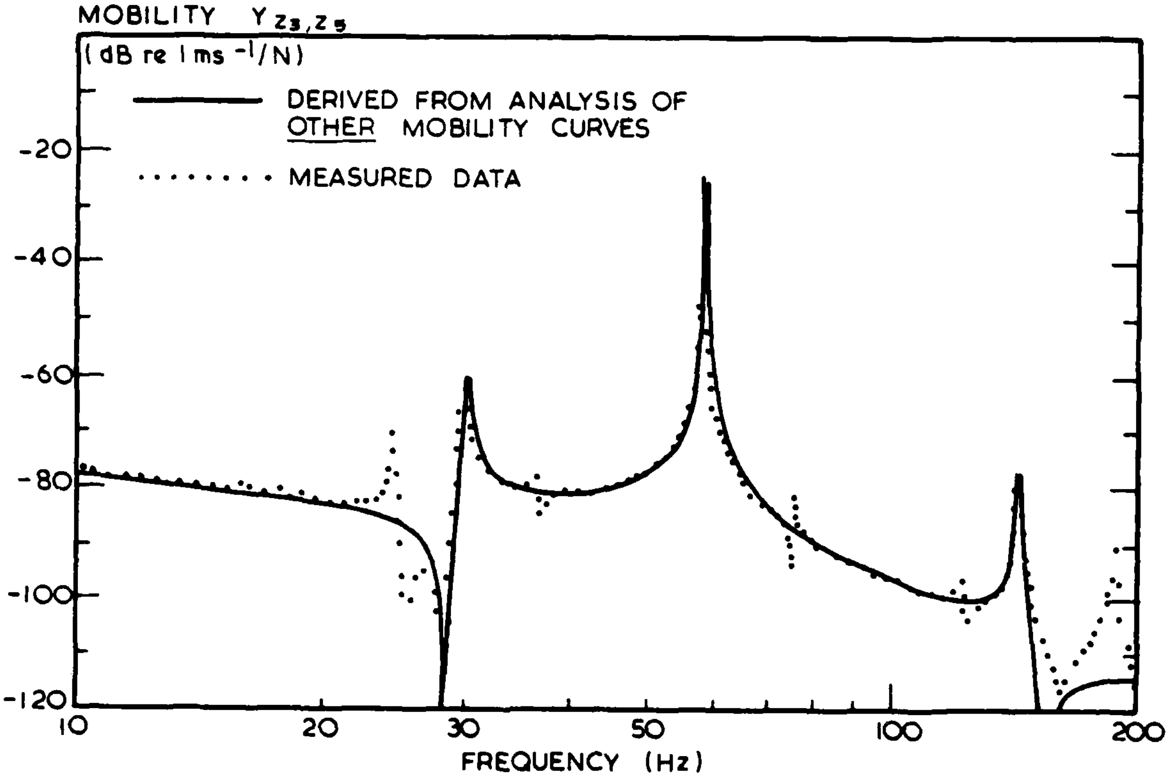

FIGURE 13 PREDICTED AND MEASURED CARRIER MOBILITY

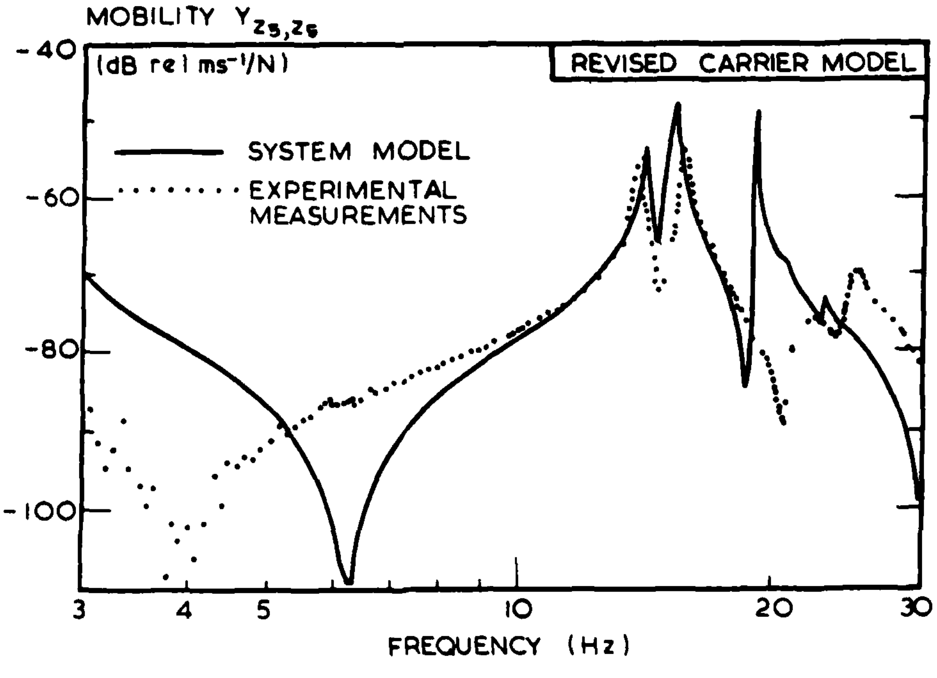

FIGURE 14 SYSTEM MODEL PREDICTIONS FOR COMPLETE ASSEMBLY (revised carrier model)

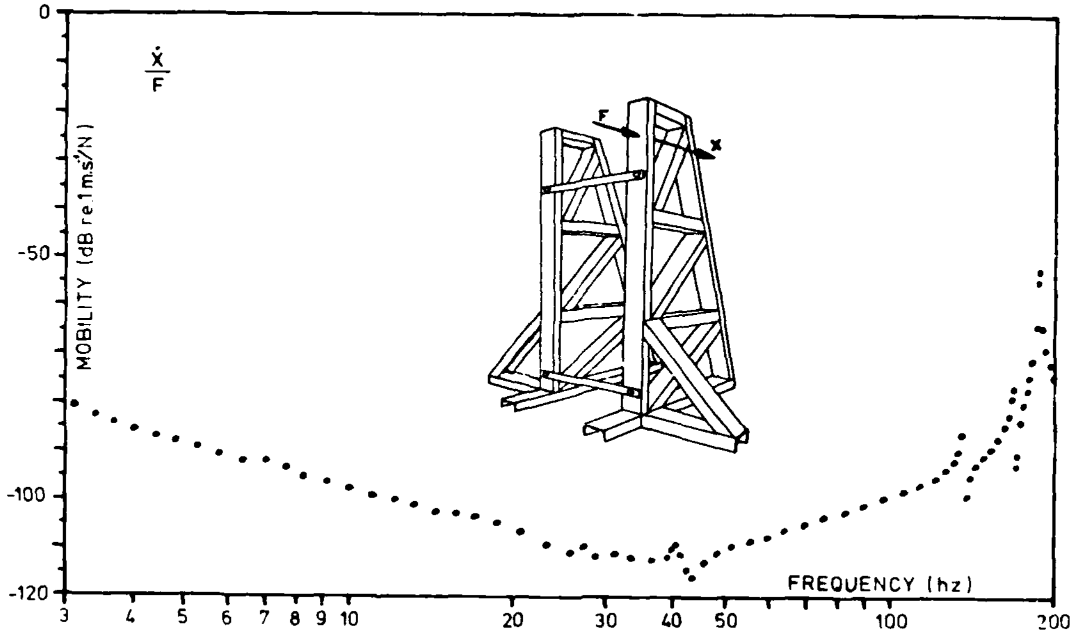

FIGURE 15 RIGID STRUCTURE AND TYPICAL MOBILITY

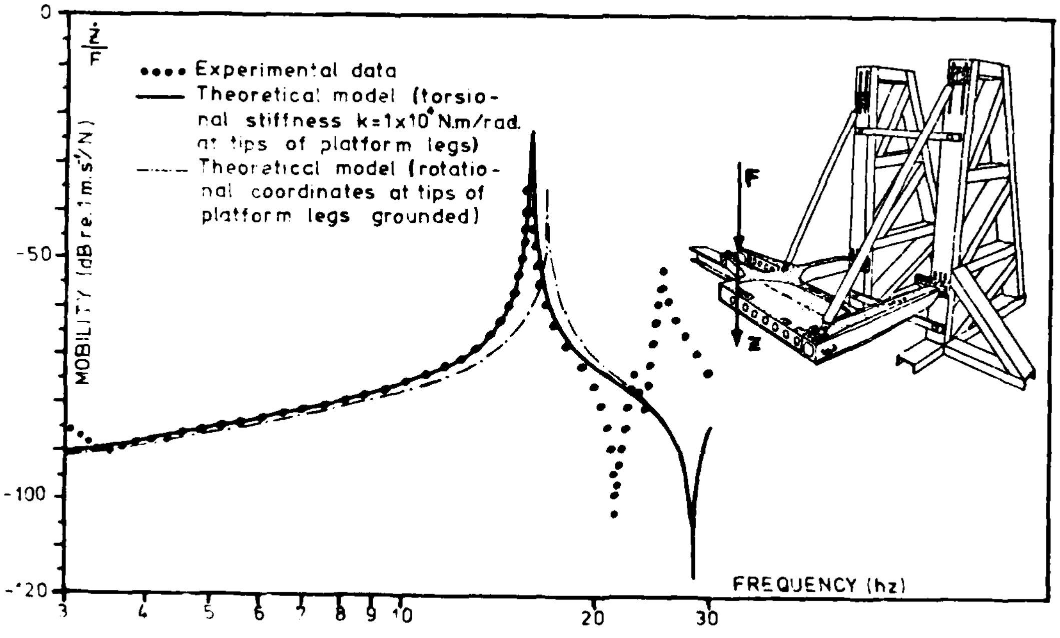

FIGURE 16 PREDICTED AND MEASURED MOBILITY OF
CARRIER ATTACHED TO RIGID STRUCTURE
(Theoretical carrier model)

incorporated into the complete system model, we obtain the results shown in Figure 14. This curve does show a slight improvement over the earlier prediction (Figure 10) in that one or more additional modes have been introduced above the fundamental ones. However, the improvement is not dramatic and, clearly, limitations to the carrier model were not solely responsible for the fall-off in its performance.

6.2 Rigid Foundation Structure

A massive and stiff framework was designed to provide a non-resonant and effectively-rigid base against which to connect the carrier structure and struts. Figure 15 shows the framework and a typical mobility measurement at one of the attachment points. A series of calculations were made in which the carrier structure plus struts were considered to be grounded at their extremities and these results were compared with measurements on the actual system.

The first result, shown in Figure 16, was made using the original theoretical model for the platform.

Subsequently, a second analysis was made using the revised carrier model, derived from measurements, and that resulted in the curve shown in Figure 17. Once again, the revised model represents an improvement, but does not provide quite the accuracy which might be hoped for.

There followed an extensive series of calculations in which various model parameters were varied, or omitted, to assess the sensitivity of the overall results. One of these variations is shown in Figure 18, in which the exact conditions of the joint between the platform and the rigid structure are modified. This curve shows a significant change from Figure 17, and, indeed, one of the most sensitive parameters was found to be the stiffness included for the joints themselves.

7. CONCLUDING REMARKS

It has been shown that a useful and practical vibration analysis may be made of a very complex engineering structure using component models and impedance coupling. However, it must be acknowledged that the conceptually-simple coupling technique requires some care in application to real structures. Previous studies (2) have shown the problems which can arise when experimental data are used in an analysis of this type and the necessity of constructing a mathematically-consistent model from the measured airframe mobilities has been fully recognised. Further problems arise when, as is inevitable in an industrial environment, simplifications or compromises have to be made in the cause of expediency. It is felt that one of the major conclusions from the studies reported here is that the omission of coordinates from the analysis must only be done with great care, and it is suspected that the rotational coordinates (which will often be the first to be abandoned because of the difficulty of measuring them) may well be critical ones.

Perhaps related to this last comment is the observation that the joints themselves may also play an important role in determining complete structures' characteristics, and they may be left out of all the individual component analyses. In this study, we have attempted to include their effects either by modifying the component models (as in the case of the struts) or by measuring component mobilities 'through' the joints (as was done on the airframe). However, we are conscious that joints may well be inadequately represented in our model.

So, in conclusion, we have obtained a satisfactory system model over most of the frequency range of interest. The reduced accuracy of the model at higher frequencies is thought to be caused by inadequacies in the modelling assumptions (i.e. choice of coordinates etc.) rather than by limitations in the individual component models.

8. ACKNOWLEDGEMENTS

The authors wish to acknowledge the technical and financial support of Westland Helicopters Ltd. and the Ministry of Defence (P.E.).

9. REFERENCES

1. R E D Bishop & D C Johnson:
'The Mechanics of Vibration'
Cambridge University Press 1960

2. M G Sainsbury & D J Ewins:
'Vibration Analysis of a Damped Machinery Foundation Structure using the Dynamic Stiffness Coupling Technique'
A S M E, J Eng Ind 96B 3 1974

3. D J Ewins & M G Sainsbury:
'Mobility Measurements for the Vibration Analysis of Connected Structures'
S V Bull 42 1 1972

4. D J Ewins & P T Gleeson:
'Experimental Determination of Multi-Directional Mobility Data for Beams'
S V Bull 45 5 1975

5. J M M Silva & D J Ewins:
'Identification of Modal Parameters from Measured Mobility Data'
(In preparation)

6. D J Ewins & J M M Silva:
'Measurements of Structural Mobility on Helicopter Structures'
RAE/R Aero Soc/ISVR Symposium:
"Internal Noise in Helicopters"
July 1979

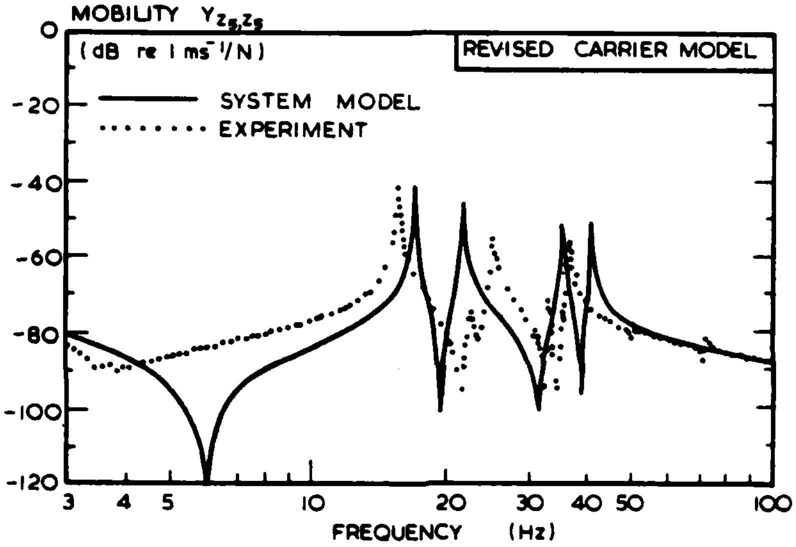

FIGURE 17 PREDICTION FOR CARRIER ATTACHED TO RIGID STRUCTURE

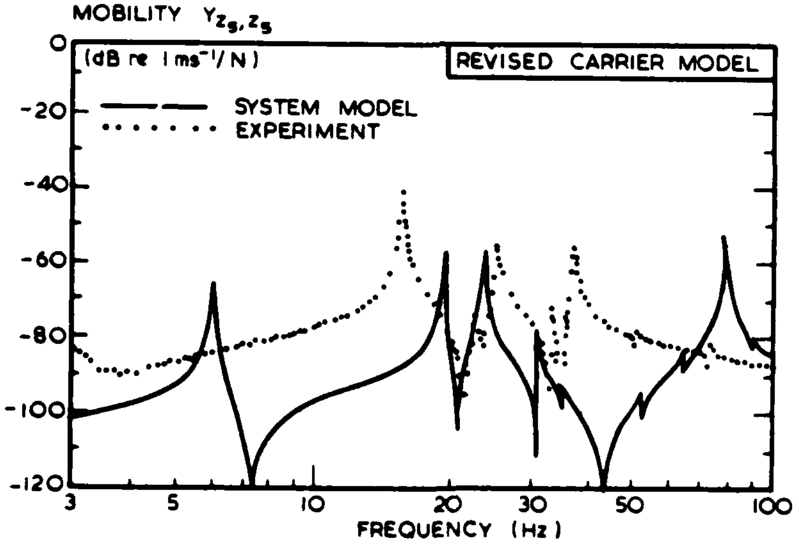

FIGURE 18 EFFECT OF RELAXING JOINT CONSTRAINT

IMPROVING VIBRATION TECHNIQUES FOR DETECTING WORKMANSHIP DEFECTS IN ELECTRONIC EQUIPMENT

JOHN W. BURT and MICHAEL A. CONDOURIS
TECHNICAL SUPPORT ACTIVITY, US ARMY ELECTRONICS COMMAND
FORT MONMOUTH, NEW JERSEY 07703

This report describes the results of a study made to evaluate the effectiveness of sine and random vibration for detecting workmanship defects in electronic equipment. The vibration test program was based upon the use of a fastener-cantilever beam device which effectively simulated workmanship defects that had first mode resonant frequencies between 27 and 880 Hz. It was found that both swept frequency sine and random vibration are very effective for detecting workmanship defects, but that sine vibration at a single non-resonant frequency, (2.2g at a fixed non-resonant frequency) is very ineffective. Whether to use swept sine or random vibration for burn-in depends on which type was used for design qualification. The same type of vibration used in design qualification should be used for burn-in. Further, it was found that the best results are achieved when burn-in vibration is done at the design qualification amplitude.

INTRODUCTION

Burn-in tests are run on electronics equipment when it is considered important that infant mortality type defects be detected and repaired before the equipments are subjected to additional in-plant tests such as qualification and reliability tests.

Burn-in tests usually consist of a combination of electrical stressing, temperature cycling and vibrations. Until recently, the vibration test mostly used by the military for burn-in testing of electronic equipments consisted of a 2.2g peak sinusoidal vibration at a fixed nonresonant frequency between 20 and 60 Hz. It has long been suspected that the single frequency 2.2g vibration burn-in test is not adequate to screen out the type of workmanship defects found in electronic equipments. The latest and more popular burn-in vibration tests include random, pseudo-random and sine sweep vibration. The users of these tests have reported better success in detecting workmanship defects than the fixed nonresonant sine vibration test. The study we undertook for detecting workmanship defects in electronic equipment evaluated the effectiveness of swept frequency sinusoidal vibration, random vibration, and sinusoidal vibration at a fixed resonant frequency.

The work described in this paper concerns itself with a laboratory experiment -- under closely controlled conditions -- with a goal to provide additional insight in the effectiveness of swept sine, random and single frequency vibration in detecting workmanship defects. The experiment was geared to show the effects of varied parameters of frequency, amplitude, sweep rates and type of vibration on a simple mechanical model. The effort was not intended to prove which type of vibration, swept sine or random, is better for detecting workmanship defects. The work was sponsored by the Army Materials Mechanics Research Center, Watertown, Mass, under the Materials Testing Technology Program.

DISCUSSION

Simulation of Workmanship Defects

Vibration in conjunction with thermal cycling and electrical stressing is used in the burn-in testing of electronic equipment to detect -- without damaging the equipment -- the type of workmanship defect that causes failure because (1) of mechanical fatigue (such as cold solder joints, nicked wires, and improperly attached high mass parts like capacitors or resistors) or because (2) of the loosening of fasteners. Both the loosening of fasteners and the fatigue failures of a cold solder joint result from stress reversals that occur during vibration. Normally, to get either the loosening type of failure or the fatigue failure, there must be a certain number of stress reversals occurring at a particular stress level. The higher the stress level, the lower the number of stress reversals needed to get a failure. We set out to relate this to workmanship defect detection.

At the start of the program we considered duplicating the various types of workmanship defects mentioned previously, and then subjecting them to different kinds of vibration. However, duplicating many of these workmanship defects in quantities sufficient for a large vibration test program was considered difficult to do within the program time and budget constraints. The reason for this is that workmanship defects (such as cold solder joints, dressed wires, etc.), have to be very nearly identical to get repeatable results from vibration testing. The even relatively small variations in the physical characteristics of the cold solder joints would produce an unacceptably large scatter in the vibration test results. It was then concluded that many of the actual workmanship defects that are usually detected in electronic equipment by using vibration would not be used.

After considerable analysis, we concluded that a system of improperly tightened fasteners could be controlled and used to simulate various workmanship defects that fail because of repeated stress reversals during vibration. We would also need a method of varying the first mode resonant frequency over a relatively wide frequency range to simulate the frequency of different types of defects. This was done by combining a cantilever beam with the improperly tightened fastener. The fastener was used to attach the cantilever beam to a vibration fixture.

The result is a test device that is simple, inexpensive, easy to set up, reusable, and one that produces repeatable results during vibration testing.

The fastener-cantilever beam was easy to tune to any desired first-mode resonant frequency over a relatively wide frequency range primarily by changing the length of the beam and, to a lesser extent, by changing the torque used to tighten the fastener. For this test program, the torque was held constant, and the length of the beam was changed to obtain the desired first-mode resonant frequency. By use of this method, fastener-cantilever beam devices with first-mode resonant frequencies from 27 to 880 Hz were successfully assembled and used for this test program.

Test Setup

For each vibration test, 20 fastener-cantilever beam devices were each attached with a number 8 machine screw and nut to a fixture that was mounted to a vibration table as shown in Figure 1. Before tightening the screw and nut, each beam was checked to make sure that it was free to rotate about the axis of the screw as the center of rotation. The axis of each screw was perpendicular to the vertical wall of the vibration fixture.

For the vibration test, each beam was secured in position at the top of the rotation circle. This is an unstable position, and when the fastener holding the beam in position loosened during vibration, the beam rotated very quickly 180 degrees to the bottom (stable) position of the rotation circle. Figure 2 shows some of the beams in the top position (workmanship defects not yet detected) and some of the beams in the bottom position (workmanship defects detected).

To simulate workmanship defects, fasteners were tightened using a torque of 4.5 in-pd. This number was selected because our early test efforts using torques above and below 4.5 in-pd showed that 4.5 in-pd was high enough to produce repeatable results during vibration and yet was low enough to be considered defective from a workmanship standpoint.

This latter point was demonstrated to be true by subjecting a group of fastener-cantilever beam devices to a full 9 hour vibration qualification test. This test and the test results are described in detail later in this report in the section called "Workmanship Defect Qualification Test".

During vibration, beams that came loose would be manually held in place in the bottom position so that they would not rattle around and perhaps strike nearby beams and thereby spoil the test results. Each vibration test was, therefore, stopped frequently so that all loose fasteners could be retightened with the beams in the bottom position.

Two different cantilever beam configurations were used, a "long beam" and a "short beam." Most of the tests were conducted using the "long beam."

The beams were steel and 0.097 inches thick. The first mode natural frequencies (Tables 1 & 2) are less than calculated values for ideal cantilever beams because the beam attachment to the fixture wall was not rigid as is assumed in the standard cantilever beam equations. Figure 1 shows the "long beam" configuration.

The second cantilever beam configuration was called the "short beam."

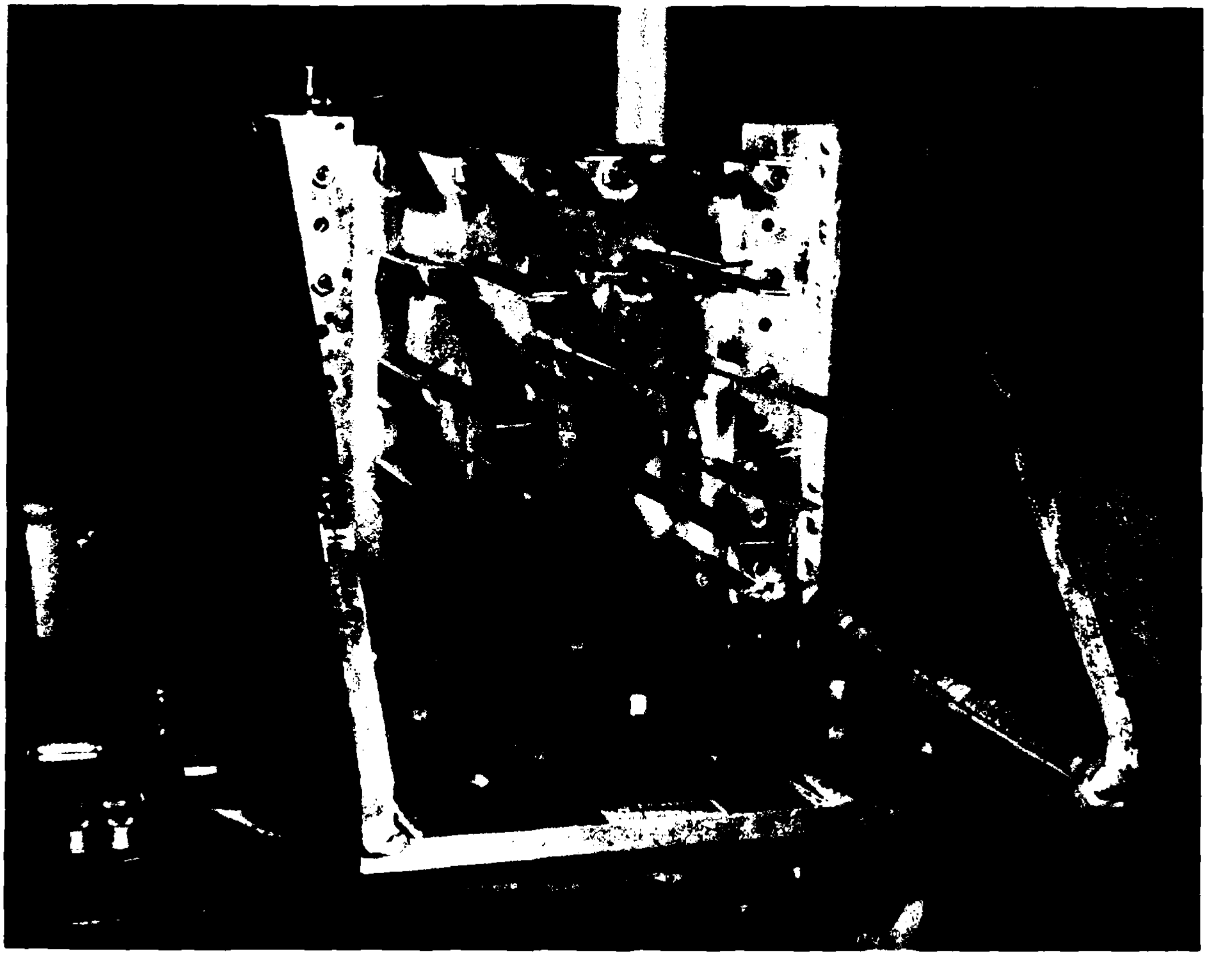

FIGURE 1. LONG BEAM SETUP, BEFORE VIBRATION

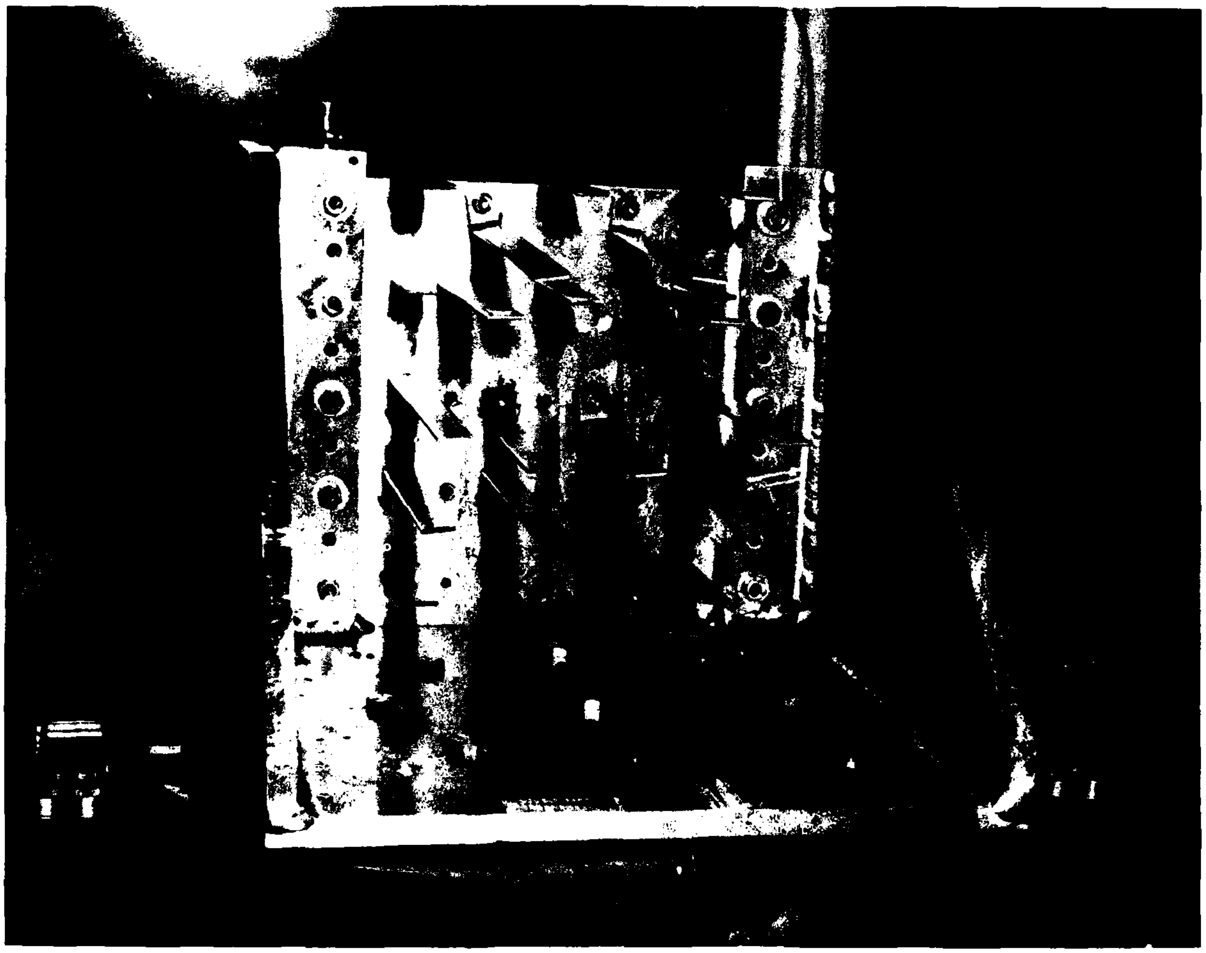

FIGURE 2. LONG BEAM SETUP, AFTER VIBRATION

TABLE 1. LONG BEAM CONFIGURATION

No. of Beams	Length of Beams (In.)	First Mode Natural Frequency (Hz)
2	9.75	27
2	9.00	31
2	8.25	35
2	7.50	43
2	6.75	52
2	6.00	65
2	5.25	79
2	4.50	97
2	3.75	140
2	3.00	198

TABLE 2. SHORT BEAM CONFIGURATION

No. of Beams	Length of Beams (In.)	First Mode Natural Frequency (Hz)
2	3.75	149
2	3.375	190
2	3.00	226
2	2.75	266
2	2.50	340
2	2.25	400
2	2.00	498
2	1.75	580
2	1.50	710
2	1.25	880

These beams were also steel and 0.097 inches thick. As can be seen from the tables, two sets of beams, the 3 inch and 3.75 inch, were common to both the long and short beam setups. One explanation for the difference in the first mode natural frequencies between the two tables for the same length beams can be explained because of a difference in mass loading on the vertical wall of the vibration fixture. The short beams taken as a group were lighter than the long beams and, therefore, the natural frequencies of the 3 inch and 3.75 inch beams will be slightly higher when measured with those beams in the short beam group than when they are in the long beam group. The short beam configuration is shown in Figure 3.

Vibration Test Program

The vibration test program was run using both the "long beams" in Table 1 and the "short beams" described in Table 2. A summary of the types of vibration used follows:

1. Swept frequency sine vibration was performed using various combinations of sweep rates, amplitudes and frequency ranges.

2. Fixed frequency, non resonant, sine vibration was performed using various combinations of amplitude and frequency.

3. Random vibration was performed using various combinations of power spectral density and frequency range.

Most of the tests were conducted with the vibration applied in the vertical axis.

Vibration was applied also in the X and Y axes to see if workmanship defects would be detected during "out of plane" vibration testing. That is, could workmanship defects whose primary excitation axis was the Z axis, be detected while vibration was applied in the X or Y axis.

The reason for doing this "out of plane testing" was to determine if it is necessary to vibrate an equipment in three principle axes to detect workmanship defects.

Vibration Apparatus and Control Unit

Fixed frequency sine, swept frequency sine, and random vibration were all performed using an MB Corporation C-25 vibration shaker. This machine has a force rating of 3000 pounds. The vibration control unit was a Hewlett Packard Fast Fourier Analyzer, Model 5451B, with vibration control options. The Signal Conditioner was a Model 610 FMG-3, manufactured by Unholtz Dickie Corporation. The accelerometers used to monitor vibration levels were Endevco Corporation Model 2213E.

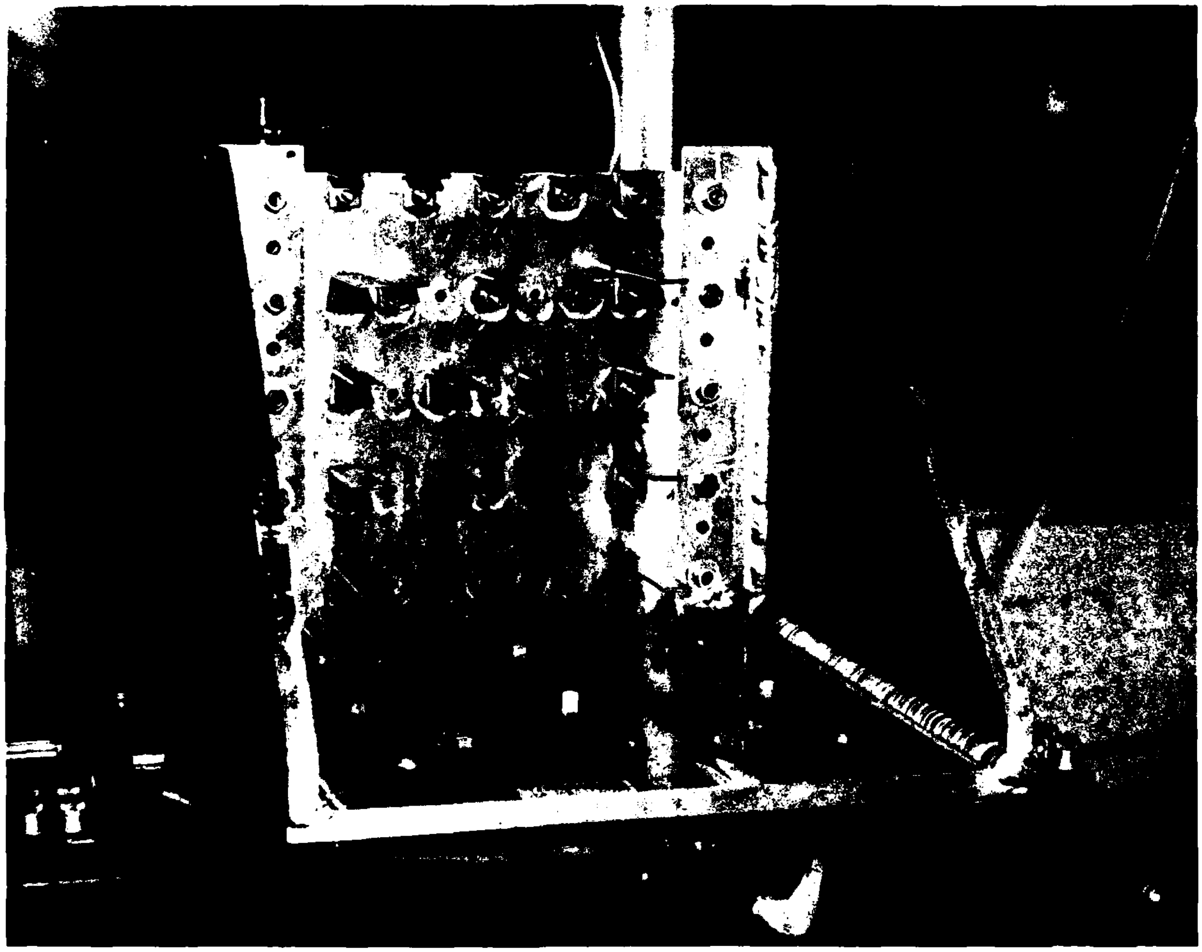

FIGURE 3. SHORT BEAM CONFIGURATION, BEFORE VIBRATION

Workmanship Defect Qualification Test

To verify that 4.5 inch pounds of torque on the fasteners does represent a workmanship defect, 10 pairs of fastener-cantilever beams were subjected to the standard 9-hr vibration qualification test for helicopter mounted equipment as given in MIL-STD-810C with a 500 Hz upper limit. Each pair consisted of two beams of the same length, but one fastener was torqued to 4.5 in-pd to simulate a workmanship defect and the other fastener was torqued to 20 in-pd to represent good workmanship. Each pair of beams varied in length with the shortest at 3 inches and the longest at 9.75 inches. First mode resonant frequencies varied from 27 Hz for the long beams to 198 Hz for the short beams.

The beams were vibrated as follows:

5 to 14 Hz	0.2 inch double amplitude
14 to 33 Hz	2g
33 to 55 Hz	0.036 inch double amplitude
55 to 500 Hz	5g

The sweep speed was logarithmic and such that it took 30 minutes to go from 5 to 500 to 5 Hz. Three hours of cycling was done in each of the three major axes for a total of nine hours of vibration. The results of this test were that all 10 of the fasteners torqued to 4.5 in-pd failed (workmanship defects detected) and all 10 of the fasteners torqued to 20 in-pd (good workmanship) successfully completed the vibration test with no failures. Eight out of ten failures occurred in the first 30 minutes of vibration and the other two between 180 and 210 minutes of vibration.

RESULTS

Repeatability of Test Results

The fastener-cantilever beam device produced results which were highly repeatable. Examination of Figures 4 and 5 shows this. Figure 4 shows the repeatability of five tests made on the "long beams" using swept sine vibration. The vibration test conditions were:

15 to 20 Hz	0.1 inch double amplitude
20 to 33 Hz	2g
33 to 55 Hz	0.036 inch double amplitude
55 to 500 Hz	5g

The sweep speed was 3.4 octaves/minute.

Figure 5 shows the repeatability of five tests made on the same "long beams" using random vibration. The vibration test conditions were:

15 to 60 Hz at 3 db per octave

60 to 500 Hz at $0.1g^2$ per Hz

Total rms g level was 6.865

Fixed Non-resonant Frequency Sine Vibration

Both the "long beam" setup and "short beam" setup were subjected to fixed non-resonant frequency sine vibration at various amplitude-frequency combinations as shown in Table 3. No workmanship defects were detected during a total of 27 hours and 8 minutes of vibration.

Swept Frequency Sine Testing

Swept frequency sine vibration at an assumed design qualification level was found to be effective for detecting workmanship defects as is shown in Figures 4 and 6. The vibration test selected was:

15 to 20 Hz	0.1 inch DA
20 to 33 Hz	2g
33 to 55 Hz	0.036 inch DA
55 to 500 Hz	5g

This particular vibration curve produced good results in terms of total numbers of workmanship defects detected in reasonable time periods (within 12 to 15 minutes of testing). However, it should be emphasized that the vibration test curve used for detection in a particular electronic equipment should always be related to the design qualification test curve.

Sine Sweep Speed Test Results

A comparison of two sweep speeds (3.4 octaves per minute and 1.7 octaves per minute) does not indicate any clear advantage for either. The faster sweep speed did detect slightly more workmanship defects during a 12 minute test duration than did the slower sweep speed (87 out of 100 for the faster sweep and 82 out of 100 for the slower sweep); this comparison was made using 5 vibration tests at the first sweep and 5 at the slow sweep. The results are shown in Figure 6. However, the above difference is considered too small to be statistically significant.

"Short Beam" Configuration Test Results

While the "short beam" included beams with first mode resonant frequencies up to 880 Hz, the highest first mode resonant frequency at which a defect was detected was 498 Hz (see Table 4). This occurred after 52 minutes of random vibration in Test No. 70. In the same test, after 60 minutes of vibration, a defect was detected that had a first mode resonant frequency of 400 Hz. These were the only detections of defects with first mode resonant frequencies above 340 Hz made during the entire test program. Also, these two detections were made after 52 and 60 minutes of random vibration, a time period much too long for use in a vibration burn-in test.

TABLE 3. Test Results for Fixed Non-resonant Frequency Sine Vibration

Test No.	Long or Short Beams	Axis of Vibration	g Level	Frequency Hz	Total Vibration Time	Number Workmanship Defects Detected
19	Long	Z	2.2	47	4 hrs + 15 min	None
20	Long	Z	5.0	120	4 hrs + 45 min	None
21	Long	Z	2.2	20	6 hrs + 48 min	None
26	Long	Z	2.2	20	4 hrs	None
27	Long	Z	2.2	20	2 hrs	None
36	Long	Z	2.2	20	3 hrs	None
78a	Short	Z	10.0	28	10 min	None
78b	Short	Z	10.0	42	30 min	None
78c	Short	Z	10.0	56	10 min	None
78d	Short	Z	10.0	70	20 min	None
78e	Short	Z	10.0	85	10 min	None
78f	Short	Z	10.0	100	10 min	None
78g	Short	Z	10.0	120	10 min	None
78h	Short	Z	10.0	160	10 min	None
78i	Short	Z	10.0	180	10 min	None
78j	Short	Z	10.0	205	10 min	None
78k	Short	Z	10.0	240	10 min	None
78l	Short	Z	10.0	290	10 min	None
78m	Short	Z	10.0	375	20 min	None
78n	Short	Z	10.0	455	50 min	None
78o	Short	Z	10.0	575	20 min	None

Figure 7 shows a comparison of swept sine vibration for three frequency ranges. It indicates that increasing the upper frequency limit does not significantly improve the effectiveness of swept sine vibration to detect workmanship defects that have relatively high first mode resonant frequencies.

Out of Plane Testing

Examination of Table 5 shows that for our model vibration in one axis did detect workmanship defects in the other two axes. This is true for both swept sine and random vibration. However, we feel that some or perhaps much of this, is due to transverse vibration inputs which are inherent, in an uncontrolled sense, in vibration systems which include the shaker, slip table, fixture and test specimen. Fixed frequency sine vibration (2.2g at a nonresonant frequency) as in previous tests did not detect any workmanship defects during a total of 6 hrs of vibration in any axis.

Random Vibration

The vibration test results in Figure 8 show that the effectiveness of random vibration for detecting workmanship defects is more dependent upon the acceleration spectral density in the frequency range immediately surrounding the first mode resonant frequencies of the workmanship defects than it is upon the overall rms "g" level. You will note that the 8.08g rms level was much more effective than was the 8.9g rms level, because it was concentrated over a bandwidth of 15 to 500 Hz while the 8.9g rms was spread over a much wider bandwidth of 15 to 2000 Hz. For example, the number of defects detected by the 8.9g rms vibration was 3 in 4.5 minutes of vibration with no detections during an additional 11.5 minutes of vibration, while the 8.08g rms of more concentrated vibration energy detected 15 defects in 3 minutes of vibration with no more defects detected during an additional 14 minutes of vibration. Figure 9 also illustrates this point.

CONCLUSIONS

1. The presently used vibration test for burn-in of army electronics equipments (2.2g at a fixed non resonant frequency) has no merit for detecting workmanship defects.

2. Swept frequency sine and random vibration are both effective for detecting workmanship defects in electronic equipment. The same type of vibration should be used for burn-in as was used for design qualification.

3. The amplitude of vibration is very important for the detection of workmanship defects for both swept frequency sine and random vibration. Because of the unknowns that are introduced, it is not advisable to vibrate at amplitudes higher than the design qualification level.

4. Any burn-in vibration test that is effective, will probably use up a small amount of the useful life of the equipment being tested because of fatigue. For example, army avionics equipments are normally subjected to

TABLE 4. "Short Beam Setup" Test Results.

Test No.	Type of Vibr	"g" Level	Frequency Range Hz	No. of Defects Detected	Highest Frequency Detected Hz	Total Test Time in Minutes
67	Swept Sine	5g	15 to 800	7 (all in 6.8 minutes)	266	95
67a	Swept Sine	5g	15 to 500	6 (5 in 9 minutes 1 in 50 minutes)	266	96
68	Swept Sine	5g	15 to 300	6 (all in 8.5 minutes)	266	75
70	Random	$0.1g^2$/Hz 6.865 grms	15 to 500	6 (3 in 1.5 minutes) 1 at 4.5 minutes 2 after 52 minutes)	498 at 52 min 400 at 60 min 340 at 4 min	77.5
71	Random	$0.065g^2$/Hz 7.37 grms	15 to 860	2 (1 at 60 seconds 1 at 34.5 minutes)	340 at 34.5 min 149 at 1 min	53
72	Random	$0.06g^2$/Hz 7.768 grms	15 to 2000	1 (in 60 seconds)	149	66
73	Random	$0.1g^2$/Hz 6.097 grms	20 to 400	2 (in 1.5 minutes 1 at 5.5 minutes	190	16.5
74	Swept Sine	5g	15 to 500	5 (3 in 4.5 minutes 1 at 9 minutes 1 at 15 minutes	226	57
75	Swept Sine	5g	15 to 500	4 (3 in 4.4 minutes 1 at 13 minutes)	266	52.8
77	Swept Sine	5g	15 to 500	5 (3 in 6 minutes 1 at 15 minutes 1 at 42 minutes)	226 at 15 min	42

NOTES:

1. All of the above tests were conducted in the vertical axis.
2. Fixed frequency non resonant sine test results are shown in Table 3.

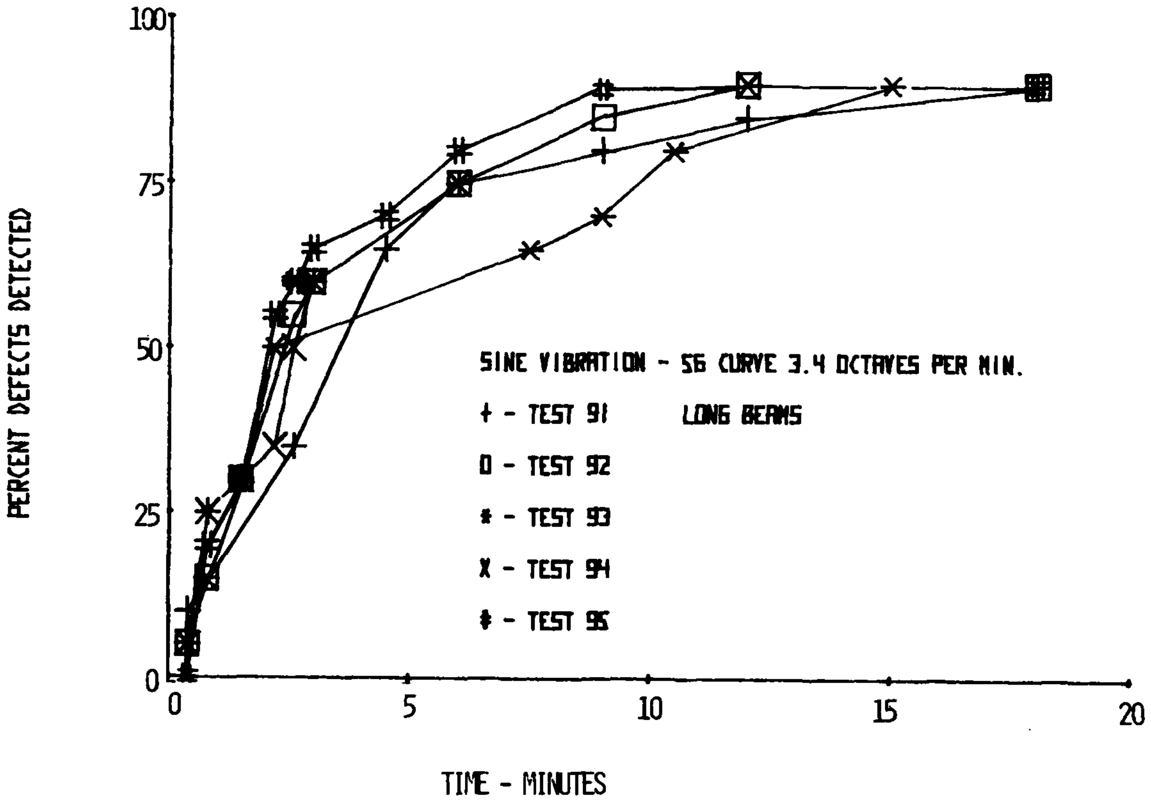

FIGURE 4 PERCENT DEFECTS DETECTED VS TIME - LONG BEAM
SINE VIBRATION, 5G CURVE

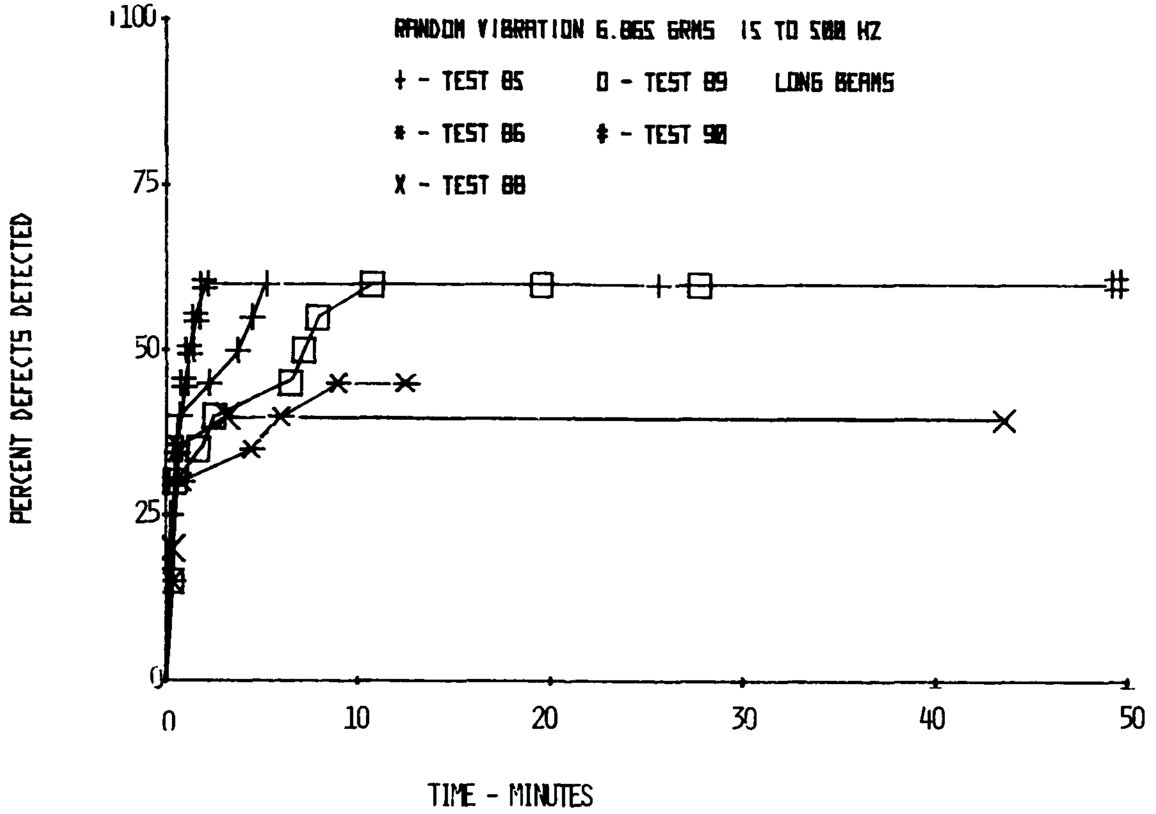

FIGURE 5 PERCENT DEFECTS DETECTED VS TIME - LONG BEAM
RANDOM VIBRATION 6.8 G's RMS

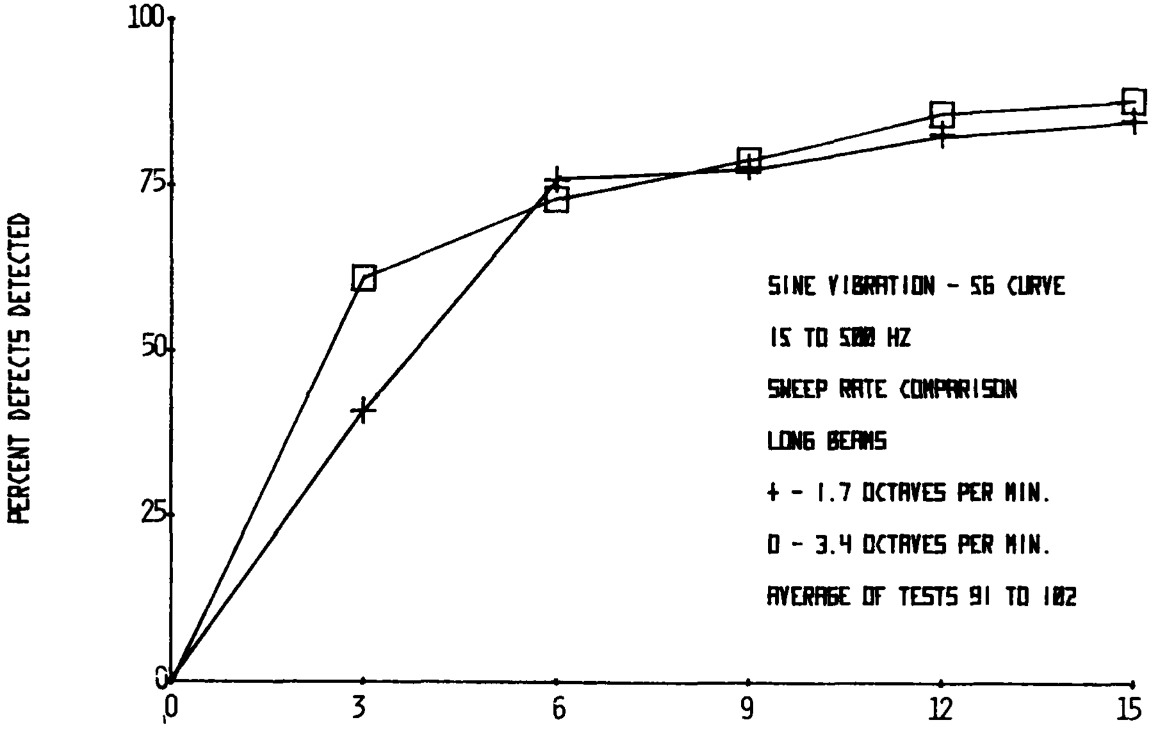

TIME - MINUTES

FIGURE 6 PERCENT DEFECTS DETECTED VS TIME - LONG BEAM
SINE VIBRATION, 5G CURVE

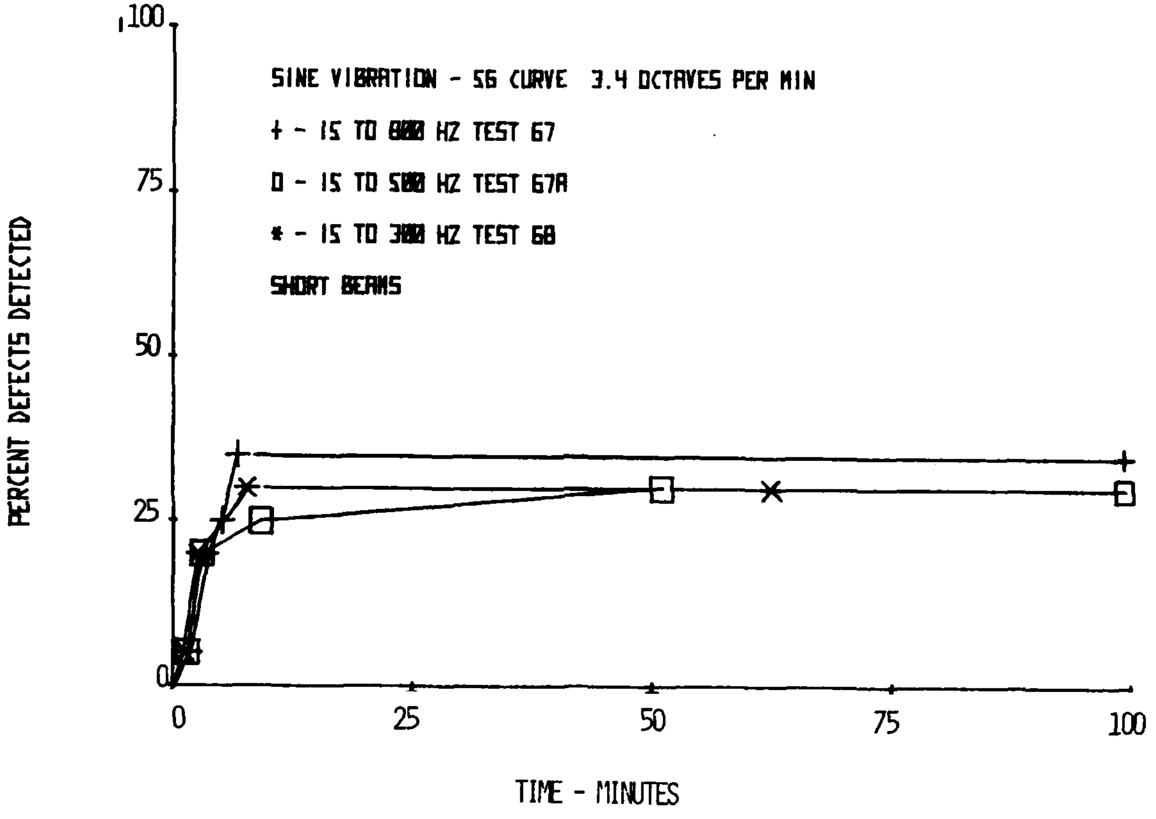

FIGURE 7 PERCENT DEFECTS DETECTED VS TIME - SHORT BEAMS
SINE VIBRATION 5G CURVE

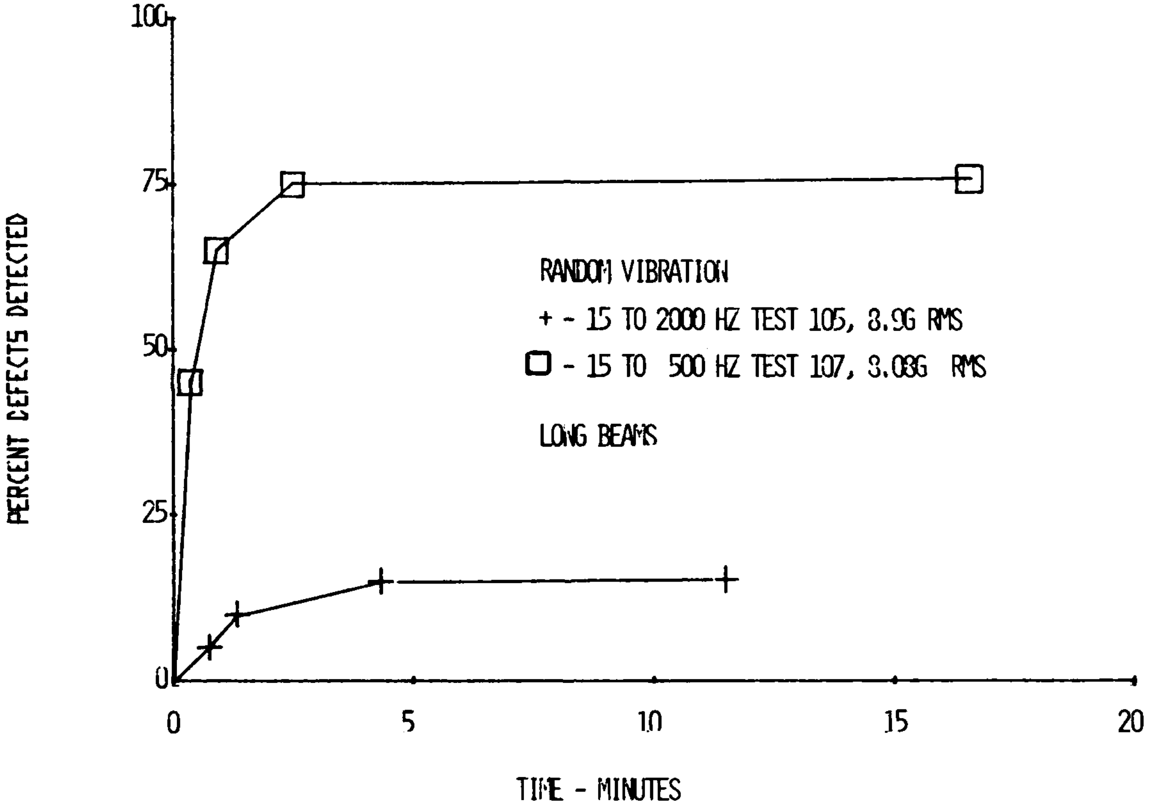

FIGURE 3 PER CENT DEFECTS DETECTED VS TIME - LONG BEAMS
RANDOM VIBRATION

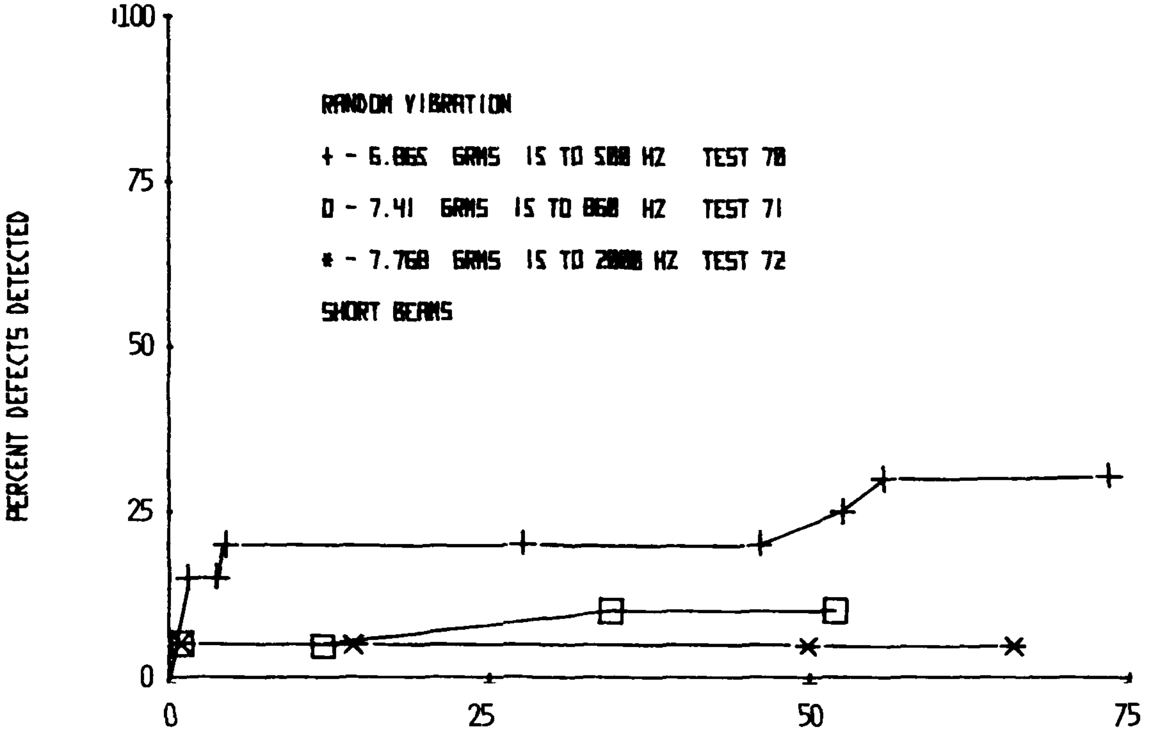

FIGURE 9 PERCENT DEFECTS DETECTED VS TIME - SHORT BEAMS
RANDOM VIBRATION

TABLE 5. Out of Plane Test Results

Test No.	Axis of Defects	Axis of Vibr	Type of Vibr	"g" Level	No. of Defects Detected	Frequency Range Hz	Total Test Time in Minutes
23	Z	X	Swept Sine	6g	16 in 4 minutes	20 to 300	6
24	Z	X	Random	$0.1g^2/Hz$ 5.3 grms	12 in 1 minute	20 to 300	60
25	Z	X	Swept Sine	5g	10 in 8 minutes	20 to 300	10
26	Z	X	Fixed Freq Sine	2.2g	None	Fixed Freq 20	240
27	Z	Y	Fixed Freq Sine	2.2g	None	Fixed Freq 20	120
28	Z	Y	Random	$0.1g^2/Hz$ 5.3 grms	13 in 2 minutes	20 to 300	2
29	Z	Y	Swept Sine	6g	18 in 3 minutes	20 to 300	4
31	Z	Y	Swept Sine	5g	18 in 7 minutes	20 to 300	8
32	Z	Y	Swept Sine	4g	16 in 10 minutes	20 to 300	10
33	Z	Y	Swept Sine	4g	17 in 6 minutes	20 to 300	6
34	Z	Y	Swept Sine	4g	1 in 6 minutes	300 to 600	6
35	Z	Y	Random	$0.1g^2/Hz$ 5.546 grms	1 in 10 minutes	300 to 600	10

NOTE: All of the tests in Table 5 were run using the "Long beam setup" a nine hour design qualification vibration test, using sinusoidal vibration. Our test results show that an effective vibration burn-in test for these equipments is to vibrate them at the full design qualification test level for a time of 15 to 16 minutes, which is a little less than 3% of the nine hour design qualification test.

5. In many cases vibration in one plane can be effective for detecting workmanship defects, provided that the equipment has a distinct design axis. However, if the major design axis cannot be easily selected, then the use of two or three axis vibration should be considered.

6. Our test results show that it was very difficult to detect workmanship defects which have first mode resonant frequencies that are high -- above 500 Hz, even though vibration inputs were as high as 2000 Hz.

RECOMMENDATIONS

1. Fixed frequency sine vibration should not be used for detecting workmanship defects.

2. Either swept frequency sine or random vibration should be used. Whether to use swept frequency sine or random vibration for workmanship defect detection depends upon which type was used for design qualification. The same type of vibration should be used for workmanship defect detection as was used for design qualification.

3. Additional investigation should be conducted into the vibration of more complex systems under controlled conditions to extend the detection techniques outlined in this report, particularly with respect to systems which have potential workmanship defects with high first mode resonant frequencies and equipments that have a truly non-predominant axis of design.

DISCUSSION

Mr. Kilroy (Naval Ordnance Station): Were the same fasteners reused or were different types of fasteners used?

Mr. Condouris: No, we kept one type of screw consistant throughout all of the testing. We might have changed the screws that wore out. The important thing is that we kept the screw and the clearence of the beam somewhat loose in order that it could rotate when it became loose so we were able to determine when the so called defect occurred.

Mr. Kilroy: That means you did not have a lock washer between the screw and the plate.

Mr. Condouris: No we did not. We had a nut in the back of the vibration plate. We essentially created a defect where somebody forgot a washer and we were anxious to get some response from the various types of vibration we were using; so we created a defect and we tried to extrapolate from that what could have happened if it were possibly another defect.

SINGLE-POINT RANDOM AND MULTI-SHAKER SINE SPACECRAFT MODAL TESTING

M. Ferrante, C. V. Stahle, D. G. Breskman
General Electric Company
Space Division
King of Prussia, Pennsylvania

This paper describes the modal test of the launch configuration of the DSC-III spacecraft which consists of a tandem spacecraft configuration with a DSCS-II atop a DSCS-III. Single-Point Random (SPR) was used as the basic test technique, and a new Multi-Shaker Sine (MSS) testing technique was used to validate it by measuring selected modes. Although the two DSCS-III solar arrays were removed and tested separately to eliminate clustered modes, the spacecraft exhibited a high modal density making accurate modal measurements difficult. Thirty-six modes below 50 Hertz were measured and the adequacy of the results was determined by the orthogonality of the modes. The SPR test of a solar array was acceptable with orthogonality between modes of less than 0.2. However, the spacecraft SPR results were marginal having orthogonality values as high as 0.4. The MSS test used up to four shakers to suppress modes adjacent to each target mode using a technique based on the generalized force determined from the measured modal deflections at the shaker locations. The MSS results for 15 modes were acceptable having orthogonality values of less than 0.2. The MSS results for these 15 modes were comparable with the SPR results except for two MSS modes which showed a marked improvement. During the test, major improvements in SPR procedures and data processing times were obtained by hardware and software changes. Data processing time was reduced by an order of magnitude. However, it is felt that additional refinements are needed before the SPR technique can be confidently applied to spacecraft testing. It does appear that SPR can be more cost effective than the MSS technique even for complex spacecraft modal testing.

INTRODUCTION

The purpose of this paper is to discuss our experience in implementing the random modal test technique (Reference 1, 2, 3, 4)* using the Hewlett Packard HP5451B Fourier Analyzer and to present results comparing the random technique and the multi-shaker sine technique when applied to the test of the launch configuration of the DSCS-III spacecraft. Modal testing of SAMSO spacecraft requires more precision than many applications because the measured modes are used directly in subsequent loads analysis and because spacecraft have a high modal density resulting in a large number of closely spaced modes. The random technique has not been accepted as a valid method of performing modal tests by SAMSO. Although many people feel that it will ultimately become the most effective, previous spacecraft results have met with limited success, (Reference 5 and 6). This paper discusses the results from this more recent application.

TEST OBJECTIVE AND CRITERIA

The objective of the test was to develop an experimental model of the launch configuration that includes all modes which are responsive to significant launch transients. The launch configuration of the spacecraft is shown in Figure 1 and consists of a DSCS-II spacecraft mounted atop a DSCS-III spacecraft. The modes responsive to launch transients are considered to be the major structural modes below 50 Hertz. From analytical predictions, it was anticipated that there would be approximately 70 modes in the frequency range from 10 to 50 Hertz resulting in many closely spaced modes. The two panel solar array stacks of the DSCS-III caused significant complexity in that the two solar array stacks caused groups of 4 closely spaced modes throughout the frequency range.

The criteria for evaluating the adequacy of the measured modes was that the modes be orthogonal, a necessary condition for use in subsequent loads analyses. Stated mathematically, the test criteria was

$$\phi_i^T M \phi_j = 1.0 \quad i = j$$
$$\le 0.1 \quad i \neq j$$

where ϕ is a mode shape vector defined by the instrumented points on the spacecraft and M is the mass matrix associated with these points. The value of 0.1 for the off-diagonal terms of the orthogonality matrix was a goal based on previous experience. It was anticipated that larger terms might result because of the difficulty in determining a mass matrix and an adequate set of instrumented points. Therefore, values of 0.20 were considered acceptable. The mass matrix was a full matrix obtained from a diagonal mass matrix transformed to the instrumented points with a Guyan transformation.

OVERALL APPROACH

The overall test approach was to simplify the test article, to use Single Point Random (SPR) as the primary method of modal measurement and to use Multi-Shaker sine (MSS) testing to validate the SPR results. To reduce the modal density and to eliminate the grouped solar array modes, the solar arrays were removed from the DSCS-III spacecraft and tested separately using the SPR technique.

---

*Numbers in parenthesis are listed as references at the end of this paper.

This eliminated the grouped solar array modes and reduced the number of desired modes by nearly half. The SPR technique was used with five different shaker locations to assure that all modes were excited; the resulting mode shapes were then edited to eliminate duplicate modes and provide a set which best satisfied the orthogonality criteria. To validate the SPR measurements, the MSS technique was used to measure 15 modes of the spacecraft stack. The selection of the modes (approximately 40% of total set) was on the basis of their significance to dynamic loading and to better define modes which were difficult to measure with the SPR technique.

Figure 1. DSCS III Launch Configuration

INITIAL TRAINING

Approximately 7 months before the modal testing began, the HP5451B system was obtained and training of personnel was begun. This training was used to familiarize laboratory technicians and engineers with the equipment and software, define and develop additional software not provided with the equipment, develop procedures and investigate problems and limitations caused by closely spaced modes. To accomplish this a simplified dual beam specimen was built and tested, Figure 2. The beam configuration was softly suspended and the beams were elastically coupled. The configuration provided a set of four relatively closely spaced low frequency modes with higher modes occurring in closely spaced pairs as indicated by the transfer function quadrature response curves shown in Figure 3. Analytical predictions were used to design the test specimen so that the specimen would present significant complexity due to close modal spacing and would provide modes in the frequency range of interest. The specimen was instrumented with 14 accelerometers. A force transducer was inserted in the shaker connection to measure the driving force.

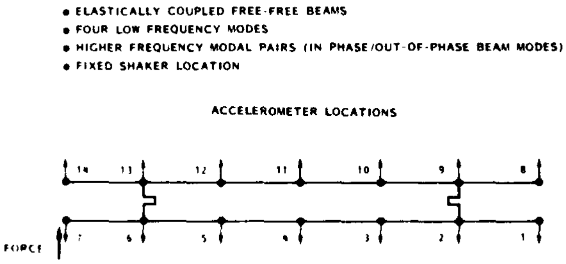

Figure 2. Dual Beam Test Configuration

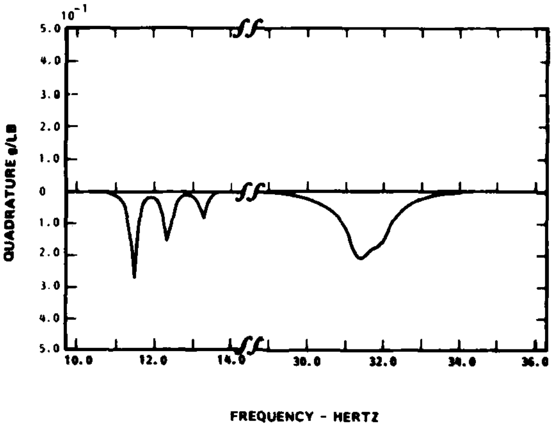

Figure 3. Dual Beam Test, Typical Transfer Function Quatrature Response

A number of software additions were made during this training period with the help of HP engineering personnel. These software additions included: (1) normalization tables to permit accelerometer sensitivities to be optimally set, (2) software to permit hard copies to be made of co/quad transfer functions, coherence functions and response PSD's, (3) corrections for accelerometer orientations, i.e. 0 or 180° phase, (4) data manipulation with multiplexing of channels, (5) analog plot capability for functions not readily available, and (6) software arrangements that enabled results from the HP5451B to be readily transmitted by magnetic tape to the large computer for subsequent manipulation and hard copy plotting. A significant effort was required to supplement the basic software with added capabilities required for efficient processing of the large quantities of data from the modal test. In addition to providing the basic training to the technicians and engineers, the identification of software needs and its implementation were an essential result of this initial experimentation.

The modal measurements using the beam specimen with the HP algorithms indicated that satisfactory results could be obtained but required some skillful manipulation by the analyst fitting the transfer functions. The basic algorithm provided for an automatic interactive fit of the transfer functions using modal parameters obtained from manually fitting a few selected stations. It was found that the automatic feature often resulted in unacceptable curve fitting and displayed significant variations in damping from station to station for a mode. Particular difficulty occured when the station had a small modal response and the resulting fit tended to diverge. With careful editing of results by the analyst, acceptable results were obtained with all off-diagonal orthogonality terms less than 0.2 for five different analysts.

At the completion of the training phase, there was a general feeling of readiness. Major improvements had been made in the software including the unattended generation of transfer functions with hard copies of the data. All were reasonably familiar with the new equipment with some having developed an ability to program and manipulate data.

TEST EQUIPMENT AND INSTRUMENTATION

The data acquision and analysis equipment were similar in all tests but several different shaker systems were used. The solar array was instrumented with 63 accelerometers while 196 accelerometers were used for the spacecraft. The accelerometers were recorded using a 100 channel analog multiplex system with a patch board arrangement for interchanging groups of 100 measurements. Kistler force transducers were used to measure the excitation force. Two Hewlett Packard HP5451B analyzers were used for data analysis. One unit was equipped with a 16 channel digital multiplex system for converting the analog data to digital form. Both HP5451B units were used for data analysis from digital magnetic tape. During the test, some difficulty was experienced in the operation of the digital multiplexer and, as a result, an HP5451C unit was obtained on a temporary basis during the spacecraft modal test. Data analysis for the solar array and for the early stages of the spacecraft test used the standard HP curve fitting algorithms with "zoom" capabilities. In order to reduce the data processing time, the final spacecraft data analysis used curve fitting algorithms supplied by the University of Cincinnati (Reference 7).

For the SPR tests, two shaker systems were used. For the solar array test, a Ling Model 370 shaker (70 pounds RMS force) was used and proved to be adequate. For the spacecraft test, the 70 pound shaker was used initially but was found to be inadequate. A Ling Model 385 shaker (500 pounds RMS force) had been obtained for the test and was found necessary to provide adequate broadband random excitation to the large spacecraft structure.

For the MSS test, four MB PM50 shakers were used. A single servo control unit with individual power amplifier gain controls was used to drive the shakers. A Spectral Dynamics (SD) Phaselock unit was used during resonant dwells to assure resonant excitation. Initial shaker system evaluations included individual shaker servo controls, but this was found to offer no particular advantages and made the control system much more complex.

SINGLE POINT RANDOM TESTING

The general procedure for the single point random test technique is shown in a block diagram in Figure 4. It consisted of attaching one shaker and its load cell at a single point on the test article, applying force to the structure using random excitation, acquiring data with the analog system, digitizing the analog data, generating transfer functions for all measurements and extracting modal parameters using special data curve fitting routines. The modal parameters for each mode were frequency, mode shape and damping characteristics, usually in percentage of critical. The final modal data was then evaluated by performing orthogonality checks and mode shape plots. The same procedure was used for each shaker location. The final data from the various shaker locations was edited to eliminate duplicate modes. The spacecraft test used five shaker locations, each with different force levels and spectrum shapes resulting in a final edited set of 36 modes. Similarly the solar array provided a set of 13 modes from three shaker locations.

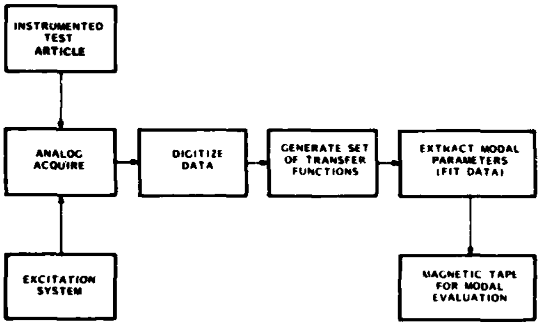

Figure 4. Single Point Random (SPR) Technique General Procedure

It is advantageous in the single point random test technique to excite a structure at more than one location to excite selected modes and to assure excitation of all modes. Also it was desired, as we established during the initial training, to shape the input force levels to enhance certain modes. The shaker locations were chosen based on results using analytical models. Analytical mode shape plots and response analysis using the analytical modes provided the basis for defining the best shaker locations to excite all modes of interest. For the solar array test detailed response analyses were performed before testing while for the spacecraft the schedule only allowed limited analysis. A major consideration in determining the maximum number of shaker locations was schedule and funding available because of the long data processing time based on the HP standard curve fitting routines. The University of Cincinnati curve fitting routine reduced the data processing time considerably and if these routines were considered in the original test planning more shaker locations would have been used especially for excitation of spacecraft component modes.

MULTI-SHAKER SINE TESTING

For the MSS testing, it was desired to use a technique which would result in a set procedure precluding the need for "artistic" tuning by the shaker operator. Because it was planned to use four shakers or less, the technique was not truly a multi-shaker technique. Techniques developed in the literature appeared to have no direct applicability in that the techniques were developed on the basis of a large number of shakers relative to the number of modes of interest. The technique which was used was based on the equation

$$\left\{F_S\right\} = \left[\phi^T_S\right]^{-1} \left\{F_q\right\}$$

where $\left\{F_S\right\}$ is the amplitude vector of the forces at the shaker locations, $[\phi^T{}_S]$ is the transpose of the modal amplitudes matrix at the shaker locations and $\left\{F_q\right\}$ is the vector of generalized modal forces equal to one for a target mode and zero for the others. After selecting a set of shaker locations on the basis of inspection of the mode shapes in the frequency range of interest, a first approximation of ϕ_S was obtained by driving one of the shakers and measuring the quadrature responses at all shaker locations in each of the modes in the frequency range of interest. The force distributions for up to four target modes were then determined from the equation (because the matrix size was limited to a 4 by 4, the matrix solution was readily obtained using a hand calculator or a desk side time sharing terminal). Using the calculated force distribution for a target mode, a frequency sweep was made, the mode was tuned by peaking the quadrature, and a second estimate for the ϕ_S matrix obtained. This was repeated for each target mode. These new force distributions were then used for a second set of sweeps to verify the purity of the target modes. For some modes the procedure was repeated again using the results obtained with force distribution to obtain a second estimate of ϕ_S and F_S. It was anticipated that the solutions would converge to a desired force distribution, however, only minor improvements were obtained after the second ϕ_S estimate was used to excite the modes.

The technique appeared to work rather well. The narrow band sweeps were generally similar to single degree-of-freedom responses but, as expected, often contained residual real responses at resonance due to the limited number of shakers being used. The technique is based on the suppression of up to 3 modes near the target mode rather than maximizing the response in the target mode. Figure 5 shows emphasis of quadrature response of individual modes when using three shakers. The force distributions were difficult to anticipate for more than 2 modes. The technique may have worked even better with another shaker system in that there were obvious problems with the shaker control system not holding shaker phase as the frequency was varied through resonance. This shaker phase problem was undoubtedly due to mechanical feedback from the spacecraft and was reduced by placing the shakers at points having relatively high mass and stiffness.

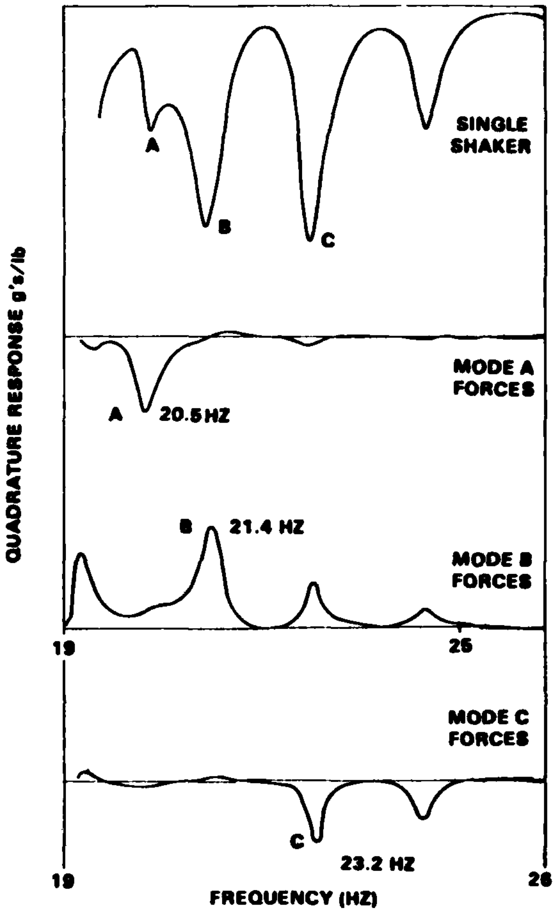

Figure 5. Multi-Shaker Quadrature Response

Although the original intent was to use the SPR results to select a portion of the modes for MSS measurement, the SPR data was not available prior to the MSS testing. The modes measured with the MSS technique were primarily the low frequency modes believed to be most important for spacecraft loading and some of the lower frequency component modes. The MSS modes were not necessarily the SPR problem modes because the SPR data was not available.

SOLAR ARRAY SINGLE POINT RANDOM MODAL TEST

The solar array was tested in the stowed configuration. It consisted of a yoke and two honeycomb panels joined together at the ends by hinges and latches and mounted to the spacecraft by four pyrotechnic fittings. The exploded view of the array, Figure 6, shows the accelerometer locations (uncircled numbers), the shaker locations (circled numbers), the five latch/hinge fittings, and the four spacecraft attachments. Because of accessibility limitations, all shaker locations were on the outboard panel.

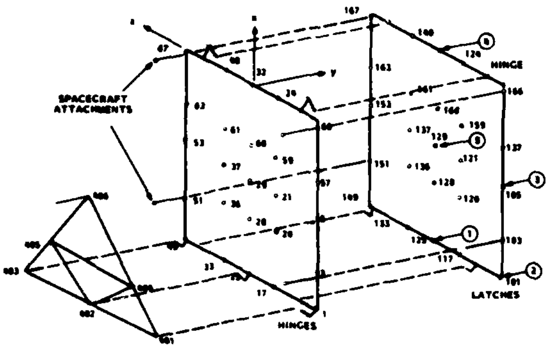

Figure 6. Solar Array Modal Test Accelerometer and Shaker Locations

Although all structural modes may be excited by a random force input at any point on the structure (except a node), a strategy was developed for the solar array configuration to obtain modal separation by choosing shaker locations which excited closely spaced modes from different shaker locations. With this strategy, it was hoped, subsequent data reduction would be significantly simplified and the modes would be more accurately measured. It was desired to find the minimum number of shaker locations from which all of the modes could be excited with reasonable separation.

The shaker locations were determined analytically using an 84 degree of freedom (DOF) NASTRAN finite element model. By analytically exciting the structure at different locations, the shaker locations which gave the best response could be determined. The criteria used to determine good shaker locations was the ratio of the quadrature response of the resonant mode to the quadrature response of the next largest mode and is shown pictorially in Figure 7. Since at resonance the modal response is in quadrature, this was felt to be a valid method of evaluation. These ratios were calculated for each perspective shaker location (circled numbers in Figure 6) and ranked as good, medium and poor as shown in Figure 7.

It was found all but one mode had a G rating at one or more of the proposed shaker locations. During the solar array test, data for only shaker locations 1, 2 and 5 was analyzed. The transfer functions from these shaker locations provided all data needed to define all modal characteristics for modal frequencies up to 70 Hertz.

The measured solar array mode frequencies using the single point random technique are summarized in Figure 8 along with the modal damping in terms of percent of critical. These 13 modes represent the final edited set using data from three shaker locations. The figure shows that these modes are for the most part well separated and no major problem was encountered in using the standard HP algorithims to extract the modal parameters.

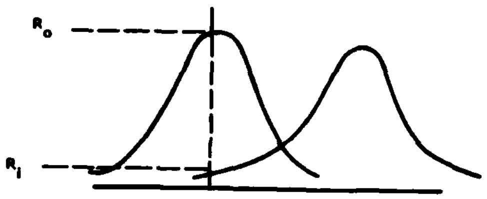

R_o = RESONANT MODE RESPONSE

R_i = LARGEST NON-RESONANT MODE CONTRIBUTION

Mode	Resonant Freq.	Shaker Location 1	2	3	4	5
1	25.686	O	M	G	G	G
2	27.805	G	O	O	O	G
3	28.391	O	M	M	M	O
4	34.553	O	G	G	G	G
5	43.282	O	G	G	M	O
6	43.93	G	O	O	M	G
7	49.379	O	G	M	G	G
8	49.938	M	O	O	O	O
9	56.247	G	O	O	G	G
10	65.307	O	O	G	O	G
11	66.131	O	O	O	G	O
12	73.609	O	M	G	O	G

<u>Rating</u>

G - R>5

M - R=3-5

O - R<3

Figure 7. Criteria for Examining Response

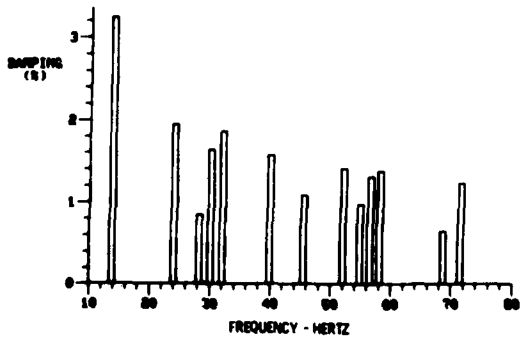

Figure 8. Solar Array Modal Frequencies and Damping Values

The orthogonality check summary for the 13 solar array modes is shown in Figure 9. The figure shows the largest off diagonal term in the orthogonality check matrix as a function of the number of modes having, at least one term with the value shown. For the full set of 13 modes, the largest off diagonal term was 0.191 and approximately 75% of the terms are below 0.10. Although all modes did not meet the initial goal of 0.1 they did meet the acceptable level of 0.20. This test was considered successful since the resulting modes exhibited reasonably good orthogonality.

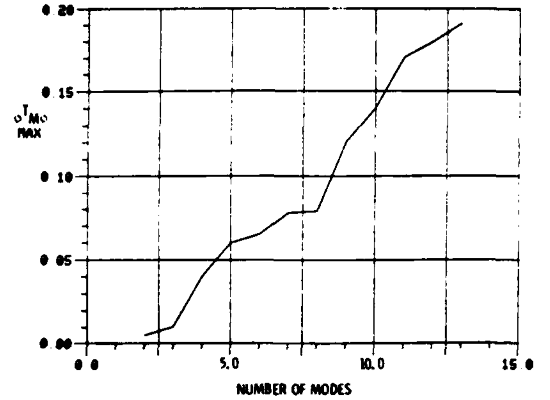

Figure 9. Single Point Random Test Solar Array Modes, Orthogonality Summary

SPACECRAFT SINGLE POINT RANDOM TEST RESULTS

The final edited set of modal frequencies for the spacecraft stack are summarized in Figure 10 along with its associated modal damping value. This set represents 36 modes from 5 shaker locations and this figure shows the high modal density especially in the frequency range above 30 Hertz. Extraction of modal parameters for this set of modes was very difficult and required a considerable amount of time for 196 channels of data with the use of the standard HP curve fitting algorithms. The data analysis was finally completed with the use of the more automated *University of Cincinnati curve fitting* algorithms which reduced the total data analysis time by approximately one order of magnitude. A similar time saving was obtained for the transfer function generation using the HP 5451C machine. Table 1 compares data processing times with the use of the standard HP algorithms, and the HP 5451C for transfer function generation to data processing time with the use of the University of Cincinnati algorithms and the HP 5451C for transfer function generation. The total processing time for one shaker location was reduced from 420 hours to 60 hours to generate a complete set of 36 modes in the frequency range from 5 to 50 Hertz with frequency resolution of 0.0488 Hz for 196 accelerometer measurements.

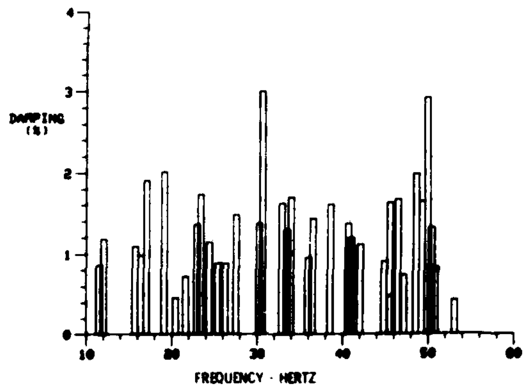

Figure 10. Spacecraft Modal Frequencies and Damping Values

Table 1. SPR Data Processing Times

Digitize Time* (Hrs)	TF Generation Time (Hrs)	Program	Curve Fit Time (Hrs)	Method
12	120	HP5451B Auto (32K)	288 (HP)	Manual
12	12	HP5451C Auto (64K)	36 (UC)	Least Squares

Processing Time Reduced From 420 Hrs to 60 Hours for one Shaker Location

The orthogonality check summary for the 36 spacecraft modes is shown in Figure 11. This summary indicates approximately two-thirds of the modes having off diagonal terms within the acceptable value of 0.2. Nine modes have terms greater than 0.2 but less than 0.3 and 6 modes have terms greater than 0.3 with the largest term approximately 0.4. The larger off diagonal terms occur in the higher frequency range where a higher modal density exists and more complex mode shapes are experienced. For more complex modes the mass matrix representation and instrumentation requirements become more critical. Also the spacecraft has many component modes which possibly need to be excited separately for better modal definition. Schedule restrictions did not allow further evaluation to determine the cause of the large off diagonal terms in the orthogonality check matrix.

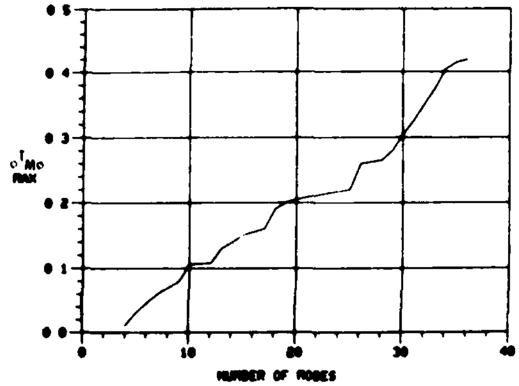

Figure 11. Single Point Random Spacecraft Modes, Orthogonality Summary

COMPARISON OF SPACECRAFT SINGLE POINT RANDOM AND MULTI-SHAKER SINE TEST RESULTS

The orthogonality check was used to compare the single point random test modes to the multi-shaker sine modes. Only 15 modes were measured using the multi-shaker sine test technique. The single point random technique included the set of 36 modes. First a cross orthogonality check between the two sets was run to establish the similarity between the common 15 modes. The coupling terms of the cross-orthogonality check $\phi^T_{SPR} M\phi_{MSS}$ are ideally equal to 1.0 for similar modes. A summary of the diagonal terms for the cross orthogonality check is shown in Table 2. This table shows that 7 modes have diagonal terms greater than 0.90 which indicates similar modes. Four modes have values between 0.8 and 0.9, two modes have values between 0.7 and 0.8 and two modes between 0.4 and 0.5. The similarity of these modes was further established by comparison of mode shape plots and modes with values between 0.8 and 0.9 can be considered similar. The two modes between 0.7 and 0.8 are more complex and similarity becomes harder to establish. The two modes which have the largest discrepancy are local antenna modes. For these two modes in the multi-shaker sine tests the antennas were excited locally and during the single point random tests these modes were excited from structural hard points. Review of the mode shape plots indicate that the antenna motions are similar but in the single point random modes these modes couple with other parts of the spacecraft, while in the multi-shaker sine modes only the antennas are responding.

Table 2. Multi-Shaker Sine (MSS) and Single Point Random (SPR) Modal Data Comparison

Mode No.		Frequency		
MSS	SPR	MSS (Hz)	SPR (Hz)	$\phi^T_{MSS} M\phi_{SPR}$
1	1	11.54	11.527	.965
2	2	11.97	12.069	.993
3	3	14.84	15.703	.800
4	4	16.16	16.412	.964
5	5	16.97	17.070	.987
6	6	19.16	19.144	.818
7	7	20.45	20.497	.945
8	8	21.55	21.698	.857
9	9	22.68	22.952	.975
10	12	25.44	25.44	.991
11	15	30.27	30.185	.823
12	16	31.24	30.614	.438
13	18	33.69	33.487	.712
14	20	35.35	35.907	.735
15	21	36.10	36.487	.444

No further tests were attempted to establish the reason for the difference but review of analytical results indicates that the single point random mode shapes agree more closely with the analytical predictions. Table 3 also shows good agreement between the frequencies for both tests. The largest difference is approximately 5 percent for the third mode while the difference for other modes is much less.

The 15 multi-shaker sine modes have off diagonal terms less than 0.2 and generally have lower off diagonal terms than the corresponding modes obtained using the single point random technique. This comparison is shown in Figure 12. This figure also shows that two of the SPR modes have terms greater than 0.2. We cannot conclusively say from these results that the MSS testing provides better results than the SPR technique. Only a partial set was obtained from the MSS test and this set includes modes only to approximately 35 Hertz while the complete set of modes includes many more complex modes above this frequency range. With the schedule restrictions no attempt was made to measure the high frequency modes with the MSS technique.

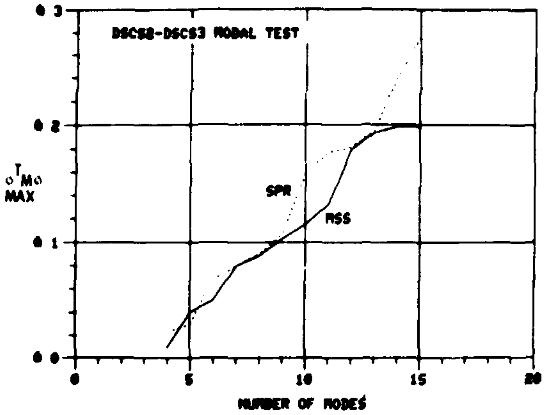

Figure 12. Comparison of MSS and SPR Orthogonality

CONCLUDING REMARKS

The multi-shaker sine technique used has not been fully developed to the extent that is can readily be implemented for spacecraft testing. The techniques which are described in the literature are based on a large number of shakers. This results in a complex test arrangement and considerable difficulty in adjusting shaker forces for pure mode excitation. It is farther complicated by shaker force amplitude and phase distortion resulting from the response at the shaker attachment making the adjustment of shakers even more difficult. Although the technique described in this paper appeared to enhance target modes and can be used with a small number of shakers, it also becomes complex and difficult to apply when modal density is high. It does, however, provide a systematic method of testing once a set of shaker locations have been selected.

At the time this test was performed, the SPR technique required farther development to measure modal characteristics of complex structures with sufficient accuracy to enable an experimental modal model to be confidently developed. Data processing times with the HP5451B computer were unacceptable but were reduced by more than an order of magnitude to acceptable times with the larger core HP5451C computer. For the simpler solar array test, satisfactory results were obtained using several excitation points and the algorithms provided with the computer. However, for the spacecraft test, the algorithms provided with the computer and those available from the University of Cincinnati were not adequate in those frequency ranges where the modal density was particularly high. Because of the long data processing times, the modes where defined from a limited number of excitation points. The results, though useable, were not as accurate as desired. Major problems still were encountered in determining resonances, particularly for component modes.

It is anticipated that the SPR technique will be the most effective modal test technique in the near future. The larger computer with the reduced data processing time permits more excitation points to be used than were used in this test. Similiarly, the larger core will permit improved accuracy by enabling more modes to be treated simultaneously by the curve fitting algorithms. The SPR technique also provides a more systematic method of extracting modes. It does not require as long a test period or the complex fixturing of the MSS test. On the basis of our experience using an HP5451C computer, the test duration should be reduced to one-fourth that of an MSS test and the cost should be reduced to approximately half that of the MSS test.

The SPR technique has high potential but additional development is needed before it can be confidently applied to the accurate measurement of the modes of complex structures.

REFERENCES

1. M. Richardson and R. Potter, "Identification of the Modal Properties of an Elastic Structure From Measured Transfer Function Data," ISA/ ASI 74250 (239-246), May 1974
2. M. Richardson, "Modal Analysis Using Digital Test Systems," Seminar on Understanding Digital Control and Analysis in Vibration Test Systems, Shock and Vibration Information Center Publication, U.S.A., May 1975
3. Ramsey, K.A., "Effective Measurements for Structural Dynamics Testing, Part I," Sound and Vibration, November 1975
4. Ramsey, K.A., "Effective Measurements for Structural Dynamics Testing, Part II," Sound and Vibration, April 1976
5. C.D. Knauer, A.J. Peterson, and W.B. Rendahl, "Space Vehicle Experimental Modal Definition Using Transfer Function Techniques," Presented at the SAE National Aerospace Engineering and Manufacturing Meeting, Culver City/ Los Angeles, California, November 17-20, 1975
6. E.L. Leppert, S.H. Lee, F.D. Day, P.C. Chapman, and B.K. Wada, "Comparison of Modal Test Results: Multipoint Sine Versus Single Point Random," SAE Paper No. 760879, Presented at the Aerospace Engineering and Manufacturing Meeting," San Diego, California, November 29 - December 2, 1976
7. D.L. Brown, R.J. Allemang, Ray Zimmerman, and M. Mergeay, "Parameter Estimation Techniques for Modal Analysis," SAE Paper No. 790221," Detroit, Michigan, February 26 - March 2, 1979.

BIAS ERRORS IN A RANDOM VIBRATION EXTREMAL CONTROL STRATEGY*

D. O. Smallwood
D. L. Gregory

Sandia Laboratories
Albuquerque, NM

This paper discusses the theoretical basis for an extremal control strategy in random vibration testing; except for special cases, this strategy results in bias errors. Formulas for estimating the bias are given, and methods for minimizing the error are suggested. The conclusion was reached that a sequential averager should not be used for this control strategy as its use will result in an unknown bias error.

*This work was supported by the United States Department of Energy.

NOMENCLATURE

N = number of control channels

m = number of frames of data averaged for each measurement

n = number of independent measurements

G = mean value of the spectral estimate at a given frequency

k = averages per loop on HP vibration control systems

$p(y)$ = probability density function of the spectral estimate Y

Y_i = spectral estimate of the random process, X_i

X_i = random process at ith control point

Z = extremal control random variable $Z = \mathrm{Max}[Y_1, Y_2, \ldots Y_n]$

$x_{ij}(t)$ = ith frame of data taken from Channel j

ℓ = index

μ_z = mean of the extremal control variable, Z

$\hat{\mu}_z$ = μ_z/G normalized mean of Z

i = index

$E[Z^2]$ = mean square value of Z

$\hat{E}[Z^2]$ = $E[Z^2]/G^2$ normalized mean square of Z

σ_z = standard deviation of Z

$\hat{\sigma}_z$ = σ_z/G normalized standard deviation of Z

$P(y)$ = $P(Y \le y)$ probability distribution function of Y

$P(z)$ = $P(Y \le z)$ probability distribution function of Y

$p(y)$ = $dP(y)/dy$ probability density function of Y

$p(z)$ = $dP(z)/dz$ probability density function of Z

Ω = intersection of probability subspaces.

INTRODUCTION

A method of control for random vibration tests of increasing popularity is extremal control. In this vibration-control strategy a number of channels are chosen and, on a frequency line-for-line basis, the channel with the highest spectrum is used for control.

This paper discusses the theoretical basis of this control strategy; the initial part will consider the general case of several independent and/or dependent control channels. The results will show bias except for some special cases.

THEORY

First consider the case of N control channels. The control channels are not required to represent independent processes. Each control channel is sampled with m frames of data. Assume that the sampling process is done so that each frame of data is independent of every other frame of the random processes (see Fig. 1). A spectral estimate will now be formed by averaging the raw spectra of m frames of data for each channel. It can be shown that the probability density of each spectral estimate is chi-squared with 2m degrees of freedom [1]. Each estimate will be referred to as a measurement in this paper. If two spectral estimates are independent, the two respective measurements will be referred to as independent measurements. The probability density of the spectral estimate Y corresponding to a random process X is given by (see Appendix A).

$$p(y) = \left(\frac{m}{G}\right)^m \frac{y^{m-1}}{(m-1)!} e^{-my/G} \qquad (1)$$

where G is the mean value of the spectral estimate at a particular frequency. Assume further that each of the random processes (X_i, i=1,...N) has the same distribution and mean. Each of the spectral estimates will also have the same distribution and mean as given by Eq (1). The spectral estimates will be called Y_i, i=1,...N. The extremal control random variable (Z) will now be defined as

$$Z = \text{Maximum } [Y_1, Y_2, \ldots Y_N] \qquad (2)$$

Remember that the variables Y are spectral estimates; i.e., they are functions of frequency. Likewise, Z is a spectral estimate and is a function of frequency.

Let n be the number of independent measurements for this case; since every frame is independent of every other frame, n=N.

It is shown in Appendix A that the probability density of Z is given by

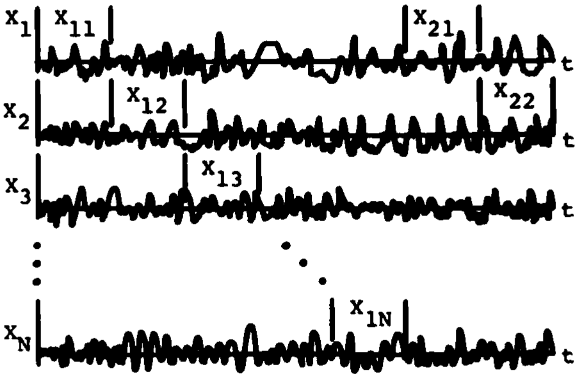

Fig. 1. Sequentially sampled data $x_{ij}(t)$ = the ith frame of data taken from Channel j.

$$p(z) = \frac{n}{(m-1)!} \left(\frac{m}{G}\right)^m z^{m-1} e^{-mz/G}$$

$$\cdot\left[1 - e^{-mz/G} \sum_{\ell=0}^{m-1} \left(\frac{m}{G}\right)^{\ell} \frac{z^{\ell}}{\ell!}\right]^{n-1} \qquad (3)$$

This function can then be used to calculate the mean and standard deviation of the extremal control variable, Z, as a function of n and m. If control of the random test is to be unbiased, the mean of the spectral estimates should be G. If the individual spectral estimates (Y_i) are unbiased, the extremal control variable will be equal to the mean of the individual spectral estimates which is the correct value. As the standard deviation of the extremal control variable decreases, the statistical confidence in the result will increase. To summarize, the most desirable condition is for the mean of the extremal control variable (μ_Z) to be

$$\mu_Z = G$$

and for the standard deviation (σ_Z) to be as small as possible. Table 1 tabulates normalized values for several values of n and m.

As can be seen from Table 1, only n=1 results in an unbiased estimate. Note also from Table 1 that, if the number of independent measurements (n) is reasonably large, the mean is significantly larger than one even when a

Table 1
The normalized mean, mean square, and standard deviation of the extremal control variable

n \ m		1	2	3	5	9
1	$\hat{\mu}_z$	1.0	1.0	1.0	1.0	1.0
	$\hat{E}[z^2]$	2.0	1.5	1.33	1.20	1.11
	$\hat{\sigma}_z^2$	1.0	0.707	0.574	0.447	0.333
2		1.5	1.375	1.313	1.246	1.185
		3.5	2.437	2.063	1.741	1.503
		1.118	0.739	0.582	0.434	0.314
4		2.0833	1.774	1.630	1.486	1.359
		5.7638	3.708	2.990	2.381	1.931
		1.19315	0.749	0.577	0.416	0.290
8		2.7178	2.180	1.945	1.715	1.520
		8.914	5.314	4.103	3.103	2.387
		1.236	0.749	0.566	0.402	0.277
16		3.381	2.587	2.254	1.935	1.672
		13.014	7.244	5.385	3.894	2.863
		1.2587	0.743	0.552	0.387	0.260

Footnotes:

n = number of independent measurements

m = number of frames of data averaged for each measurement

$\hat{\mu}_z$ = normalized mean, μ_z/G

$\hat{E}[z^2]$ = normalized mean square, $E[z^2]/G^2$

$\hat{\sigma}_z^2$ = normalized standard deviation squared, $(\sigma_z/G)^2$

large number of frames (m) are averaged to improve the estimate for each measurement. This implies that a significant bias error will result. Fig. 2 plots the normalized (with respect to G) mean and standard deviation for the special case m=1. As can be seen, the standard deviation quickly approaches an almost constant value while the mean continues to grow for increasing n.

Consider the case where the N control channels are simultaneously sampled as shown in Fig. 3. It will be assumed that each of the X_i, i=1,...N, are linearly related. That is, a constant linear relationship exists between the N control channels. This assumption is reasonable if the control channels are all mounted on the same linear structure and the data samples are taken from each channel with sample-and-hold circuits. In this case, the N spectral estimates will not be linearly independent. For example, if one spectral estimate is high, all the estimates will be high by a proportional amount. Therefore, this case corresponds to the previous case with n=1.

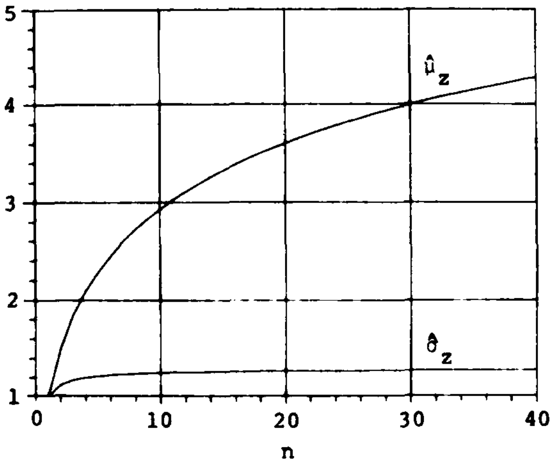

Fig. 2. Normalized mean and standard deviation of the extremal control variable for the special case m=1.

If the various inputs are only partially related, the results will be somewhere between the two extremes of total independence and total dependence. For example, let N=4 and m=3. If the inputs are independent, n=4 and the bias will be 1.63. If the inputs are completely dependent, n=1 and the bias will be 1.0. If the inputs are partially dependent, the bias will be between 1.0 and 1.63.

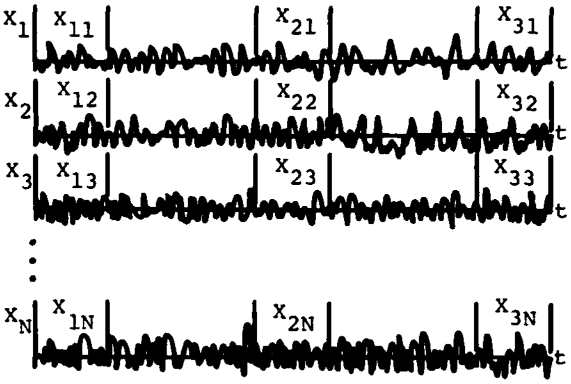

Fig. 3. Simultaneously sampled data.

Consider the case of a sequential sampler where the spectral levels are not the same at each of the N control points. The probability distribution of the extremal control variable now becomes

$$P(Z<z) = \prod_{i=1}^{n} P(Y_i<z) \qquad (4)$$

since n=N.

$$P(Z<z) = P(z)$$

$$= \prod_{i=1}^{n}\left[1 - e^{-mz/G_i}\sum_{\ell=0}^{m-1}\left(\frac{m}{G_i}\right)^{\ell}\frac{z^{\ell}}{\ell!}\right] \qquad (5)$$

where G_i is the mean value of the spectrum at the ith control point. As before, it is assumed that the spectra of each control point is measured independently. Since

$$p(z) = \frac{dP(z)}{dz} \quad , \qquad (6)$$

the mean and mean square can be evaluated from the relations,

$$\mu_z = \lim_{a\to\infty}\left[aP(a) - \int_0^a P(z)dz\right] \quad , \qquad (7)$$

$$E[Z^2] = \lim_{a\to\infty}\left[a^2P(a) - 2\int_0^a zP(z)dz\right] . \qquad (8)$$

For the special case where one particular spectrum (say P_j) is much larger than the rest

$$G_j >> G_i \quad i\neq j \quad ,$$

then P(z) will be dominated by that particular spectrum. Whenever $P(Y_j<z)$ is significantly larger than zero, all the other distributions, $P(Y_i<z;\ i=j)$, will be near one, hence

$$P(z) \approx \left[1 - e^{-mz/G_j}\sum_{\ell=0}^{m-1}\left(\frac{m}{G_j}\right)^{\ell}\frac{z^{\ell}}{\ell!}\right] \qquad (9)$$

This reduces the problem to the case of n=1 as previously developed. The two special cases (first, where all the G_i are the same; and, second, where one G_i is much larger than the rest) establish bounds on those cases where the G_i's are different but nearly the same. For example, if four channels are sampled sequentially with one frame per channel (m=1), the correct bias will be 2.08 (n=4) for frequencies where all the control channels are responding the same (rigid body behavior) and 1.0 (n=1) at those frequencies where one control channel dominates the rest. At frequencies where the spectrum is not the same at each of the control channels but also is not dominated by one channel, the bias will be somewhere in the range of 1.0 to 2.08. As can be seen, the bias is a function of frequency; this can be a difficult error to detect. The bias will look like a constant for a closed loop test (output = input) or for a test where all the control channels are responding the same. However, the bias can be significantly different when the system dynamics (different G_i's at the various control points) come into play. It is here that the system dynamics complicate the results, making the data more difficult to interpret.

EXPERIMENTAL RESULTS

The only experimental results that could be obtained in our laboratory using current equipment was for the case of m=1; i.e., the spectrum for each control channel was computed from one frame of data resulting in two statistical degrees of freedom. This is a current software limitation. Our system is limited to four control channels and are of the sample-and-hold variety. A sequential analog-to-digital converter was not available for testing. The test system was a HP5451C Fourier System with the vibration control option.[*] A parameter of interest on the available HP system is the number of averages per loop, k. On the HP system, the data is not averaged first and the extremal control variable is formed from kN frames of data. If the N control channels are hardwired such that all inputs are the same and a sample-and-hold digitizer is used, the number of independent spectral estimates (n) reduces to k. The observed bias was measured for a large number of n's.[**] The experimental bias and theoretical bias are plotted in Fig. 4. As can be seen, the experimentally determined bias is significantly less than theory indicates. To check this discrepancy, the experiment was repeated using an HP3722A noise generator[*] to replace the internal-noise generator of the vibration-control system. This time the experimental and the theoretical results were in close agreement. The difference has not been explained. Two possible explanations have been suggested. First, the output of the vibration-control system may not be truly Gaussian and, hence, the spectral estimates may not be chi-squared. Second, the time-domain randomization used to generate the output sequence may not result in frames of data that are truly independent of each other. In any event, it is clearly indicated that care should be taken to experimentally verify any results applied to a different system. Subtle differences in the "random" output can change the results significantly.

In our system the bias error can easily be corrected for linearly related control channels by simply introducing another bias in the opposite direction to cancel the bias introduced by the extremal-control strategy. A simple way to accomplish this is to multiply the channel sensitivity parameter by the experimentally determined bias factor (Fig. 4).

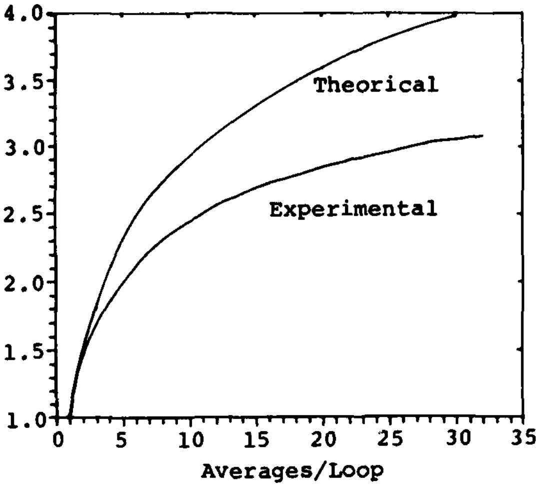

Fig. 4. Bias error.

CONCLUSIONS

A sequential averager should not be used for extremal control; if it is used, an unknown bias error will result. The bias error will be a function of the number of channels averaged, the number of degrees of freedom for each estimate, and the relative magnitude of each of the control channel spectrums. The last item implies that the bias error will be a function of frequency. All of the control channels should be sampled in parallel with sample-and-hold circuits. If the control channels are linearly related, extremal control can then be accomplished without bias if n=1. If m is also 1, the variance of the spectral estimates will be large, since there are only two degrees of freedom. Therefore, the convergence of the system will have to be slow; that is, a large correction to the drive spectrum cannot be made because of the uncertainty of the correction. The equalization will therefore be sluggish. If n is greater than one, the bias is a constant and can be corrected. The correction depends on the number of frames averaged (m) on the distribution and autocorrelation of the control time histories. If the distribution of the control time histories is Gaussian and the auto-correlation is zero between frames, the correction has been determined theoretically (Table 1). For many real systems the correction will need to be determined experimentally.

---

[*] This is not a recommendation or condemnation of this particular manufacturer's equipment; it simply reflects the available equipment. Similar equipment could be expected to have similar results.

[**] On the HP System the parameter (n) is called averages/loop.

If nonlinearities exist, a bias error can still exist. The error will always be conservative; i.e., the measured extremal spectrum will be greater than or equal to the true extremal spectrum. This residual bias error can be minimized by averaging frames (increasing m) before the extremal spectrum is formed.

APPENDIX A

The definition of a chi-squared distribution with n degrees of freedom is given by [1]

$$p(\chi^2) = \frac{(\chi^2)^{[(n/2)-1]} e^{-\chi^2/2}}{2^{n/2}\,\Gamma(n/2)} \qquad (A.1)$$

If n = an even integer, $\Gamma(n/2)$ can be replaced by $(n/2 - 1)!$. The mean value of this distribution is given by

$$\mu(\chi^2) = \int_0^\infty \chi^2 p(\chi^2)\, d(\chi^2) = n \qquad (A.2)$$

when the mean is given by G, a new variable (y) is defined where

$$y = \frac{G}{n}\chi^2 \qquad (A.3)$$

The probability density of y is given by

$$p(y) = \frac{n}{G}\, p(\chi^2)\Big|_{\chi^2 = \frac{yn}{G}}$$

$$p(y) = \frac{\frac{n}{G}\left(\frac{xn}{G}\right)^{[(n/2)-1]} e^{-yn/2G}}{2^{n/2}\,[(n/2)-1]!} \qquad (A.4)$$

Letting m=n/2

$$p(y) = \left(\frac{m}{G}\right)^m \frac{y^{m-1}}{(m-1)!}\, e^{-my/G} \qquad (A.5)$$

The probability that the random variable Y will be greater than y is given by

$$P(Y>y) = \int_y^\infty p(y)\,dy$$

$$= \int_y^\infty \left(\frac{m}{G}\right)^m \frac{y^{m-1}}{(m-1)!}\, e^{-my/G} dy$$

$$P(Y>y) = e^{-my/G} \sum_{\ell=0}^{m-1} \left(\frac{m}{G}\right)^\ell \frac{y^\ell}{\ell!}$$

$$P(Y<y) = 1 - P(Y>y)$$

$$P(Y<y) = 1 - e^{-my/G} \sum_{\ell=0}^{m-1} \left(\frac{m}{G}\right)^\ell \frac{y^\ell}{\ell!} \qquad (A.6)$$

The extremal control random variable Z will now be defined as

$$Z = \text{Maximum}[Y_1, Y_2, Y_3, \ldots Y_n]$$

The probability that the variable Z will be less than a value z is given by

$$P[Z<z] = P[Y_1<z \Omega Y_2<z \ldots \Omega Y_n<z]$$

Ω = intersection

If each of the measurements are independent and have the same distribution as Y,

$$P[Z<z] = [P[Y<z]]^n$$

or

$$P[Z<z] = \left[1 - e^{-mz/G} \sum_{\ell=0}^{m-1} \left(\frac{m}{G}\right)^\ell \frac{z^\ell}{\ell!}\right]^n \qquad (A.7)$$

The probability density of the extremal-control variable is then given by

$$p(z) = \frac{d}{dz} P(Z<z) \,,$$

$$p(z) = \frac{n}{(m-1)!}\left(\frac{m}{G}\right)^m z^{m-1} e^{-mz/G}$$

$$\cdot\left[1 - e^{-mz/G} \sum_{\ell=0}^{m-1} \left(\frac{m}{G}\right)^\ell \frac{z^\ell}{\ell!}\right]^{n-1} \qquad (A.8)$$

The mean (μ_z) and the standard deviation (σ_z) can now be found from the formulas

$$\mu_z = \int_0^\infty z p(z)\, dz$$

$$E[z^2] = \int_0^\infty z^2 p(z)\, dz$$

$$\sigma_z^2 = E[z^2] - \mu_z^2$$

For the special case of m=1, where n!=1 for n≤0

$$p(z) = \frac{n}{G} e^{-z/G}\left[1 - e^{-z/G}\right]^{n-1}$$

$$= \frac{n}{G} \sum_{i=0}^{n-1} (-1)^{i} \frac{(n-1)!}{i!(n-1-i)!} e^{-\frac{z(i+1)}{G}}$$

This gives

$$\mu_z = Gn! \sum_{i=0}^{n-1} \frac{(-1)^{i}}{(n-1-i)!(i+1)!(i+1)} \quad (A.9)$$

$$E[z^2] = 2G^2 n! \sum_{i=0}^{n-1} \frac{(-1)^{i}}{(n-1-i)!(i+1)!(i+1)^2} \quad (A.10)$$

The probability density for this case is plotted for several values of n as Fig. A.1.

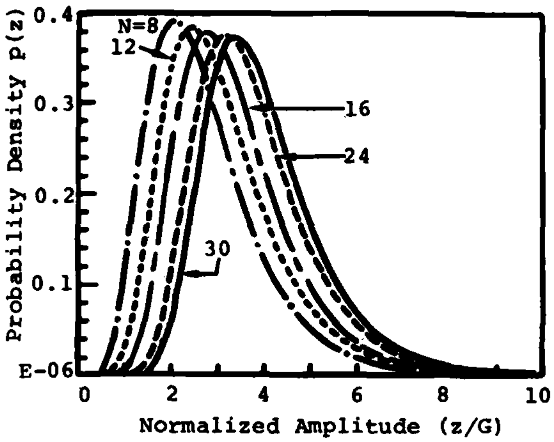

Fig. A.1. Probability density of the extremal control variable for the special cases m=1 and several n's

REFERENCE

1. J. S. Bendat and A. G. Piersol, Random Data: Analysis and Measurement Procedure, (New York: Wiley, 1971).

A NEW METHOD OF IMPROVING SPECTRA SHAPING IN REVERBERANT CHAMBERS

James N. Scott
NASA, Goddard Space Flight Center
Greenbelt, MD 20771

and

Raymond L. Burkhardt
Northrop Services, Incorporated
NASA, Goddard Space Flight Center
Greenbelt, MD 20771

This study involves the use of acoustic suppression to line the horn duct of a reverberant noise chamber in an effort to enhance the spectrum shaping capability of the chamber. This permitted the low frequency level to be increased to required values while attenuating the high frequency noise, thus achieving the required roll-off to simulate the Space Transportation System (STS) payload bay acoustic environment. This paper describes the construction of the liner and the evaluation of the liner to determine its attenuation characteristics.

INTRODUCTION

The required spectrum shape for simulating the acoustic environment in the payload bay of the STS was achieved inside the Goddard Space Flight Center (GSFC) 68 cubic meter reverberant noise chamber by placing acoustic suppression material inside the horn. This was accomplished by fabricating a sheet metal liner, shaped to fit the exponential horn and attaching the suppression material to the inside surface of the liner using a double sided adhesive tape. The suppression material is a 2.5 cm thick acoustic foam containing a lead septum. The liner is held in place in the horn by a special bracket attached to the chamber wall.

The development of this liner arose out of preliminary attempts at GSFC to achieve the predicted STS acoustic environment in the chamber. During these tests, it was found that the predicted spectrum could not be obtained in the GSFC facility by simply increasing the input power to the acoustic driver. Operating the driver at maximum power did provide the proper level of sound at low frequencies, but at frequencies above 400 Hz the sound level was much higher than necessary and the desired roll-off could not be achieved by the usual spectrum shaping procedure, thus requiring space systems to undergo high frequency test environments much more severe than necessary. From this was born the idea of using acoustic suppression in the horn duct to attenuate the sound above 300 Hz.

This paper will review the predicted acoustic environment for the STS payload bay and the difficulties encountered in simulating that environment for tests in the GSFC reverberant noise chamber. The facility limitations and circumstances leading to the development of the horn liner will then be discussed. This will be followed by a description of the liner itself and the mans by which it was evaluated. The results of the evaluation test will then be presented along with a discussion of additional applications of the concept.

SPACESHUTTLE ACOUSTIC ENVIRONMENT

The predicted acoustic environment for the payload bay of the STS (refs. 1, 2) is more severe than any previously experienced with expendable launch vehicles. The most significant difference between the space shuttle and expendable launch vehicles is that much of the noise generated during a shuttle launch is concentrated in the frequency range below 400 Hz with a relatively sharp roll-off beginning at about 125 Hz and dropping by about 20 dB at 2000 Hz. This spectrum is shown in Figure 1. It should be noted that these predicted levels are for the empty shuttle payload bay. Acoustic levels for specific payloads are dependent on geometry, configuration, surface area and acoustic absorption characteristics. Thus, as a result of reflections, resonant amplification or attenuation, the acoustic levels with payloads present could be significantly different than those for the empty payload bay. Consequently the shape, as well as the level of the acoustic spectra, encountered in the payload bay of the space shuttle will differ significantly from any previously encountered in expendable launch vehicles.

Space systems which are to fly aboard the shuttle must be tested to verify their ability to withstand the acoustic environment encountered during launch. This generally is accomplished by placing the system in a reverberant chamber and introducing an acoustic environment which simulates the launch environment.

Such a system is the thermal canister, part of the OSS-1 pallet to be flown on an early shuttle mission. This thermal

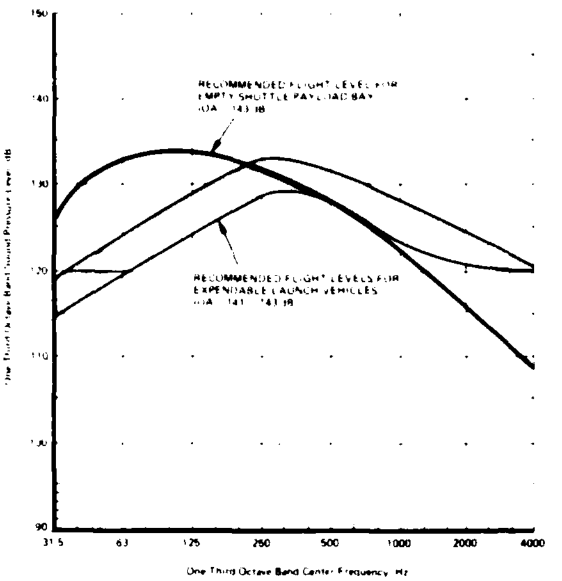

Fig. 1. Comparison of predicted shuttle empty payload bay acoustic environment with expendable launch vehicle acoustic environment

canister was tested in the GSFC 68 cubic meter reverberant noise chamber. During the preliminary calibration of the chamber for this test, several unsuccessful attempts were made to produce the predicted shuttle empty payload bay acoustic spectrum. The high level of low frequency noise was obtained by operating the acoustic driver at maximum power. This also produced very high levels of high frequency noise which could not be reduced by the usual method of electronically controlling the valve system which produces the noise. Hence, the proper roll-off with increasing frequency could not be obtained by controlling the acoustic driver.

To avoid the possibility of causing an unrealistic failure of a space system as a result of exposure to an environment more severe than necessary, the noise levels at frequencies above 250 Hz had to be reduced without significantly affecting the levels below 250 Hz. Since this could not be accomplished by controlling the acoustic driver, the use of acoustic suppression in the horn duct was considered.

ACOUSTIC SUPPRESSOR

Acoustic suppression has been used successfully in lining the inlet and exhaust ducts of jet aircraft engines to attenuate sound. In this case, certain frequencies, including discrete tones, may dominate the entire noise field. This has resulted in the development of techniques which permit acoustic suppressors to be designed or tuned to attenuate noise at a discrete frequency or in a given narrow bandwidth (ref. 3-6). Noise suppression analysis techniques have been developed for sound propagation in ducts with constant cross-section area. However, the frequency bandwidth of the attenuated noise can possibly be increased by applying suppression to a duct with varying cross section area such as the exponential horn. This belief is based on previous studies (ref. 6) which have shown a strong dependence of sound attenuation on frequency. This dependence occurs through the ratio of duct height to sound wavelength and has been verified for ducts of constant cross section. Intuitively it is expected that for a given suppression material in an exponential horn duct, the frequency attenuated would decrease with increasing cross-section, thus, attenuating a wider range of frequencies than would be attenuated in a duct of constant cross-section. This effect would of course vary with the frequency dependent absorption properties of the suppression material. The analytical details of this thinking are presently being investigated.

For purposes of achieving the desired acoustic spectrum in the GSFC reverberant chamber, a liner was fabricated from materials on hand. This liner is made of 6061-T6 aluminum sheet 3.2 mm thick, which is shaped to fit the horn of the GSFC reverberant chamber. The edges of the sheet are fastened at right angles with L brackets and machine screws from the inside. This sheet metal structure is lined with an acoustic foam containing a lead septum. This foam, which is attached with a double sided adhesive, is 25.4 mm thick. At the small end, the liner is 127.0 mm X 127.0 mm and expands with the exponential horn to 495.3 mm X 495.3 mm at the large end. The overall length of the liner is slightly over 1 meter. The liner is mounted using a special support and retaining bracket. The liner is shown in front of the horn in Figure 2 and Figure 3 shows the liner installed in the horn.

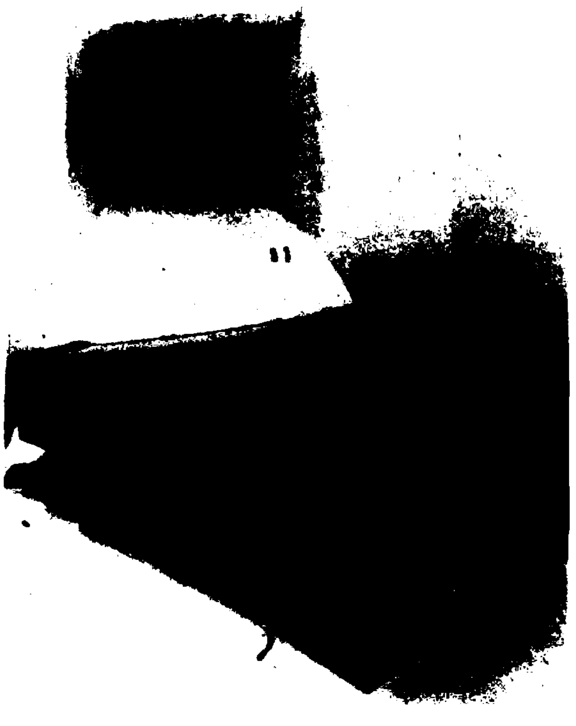

Fig. 2. Acoustic suppression horn liner in front of exponential horn

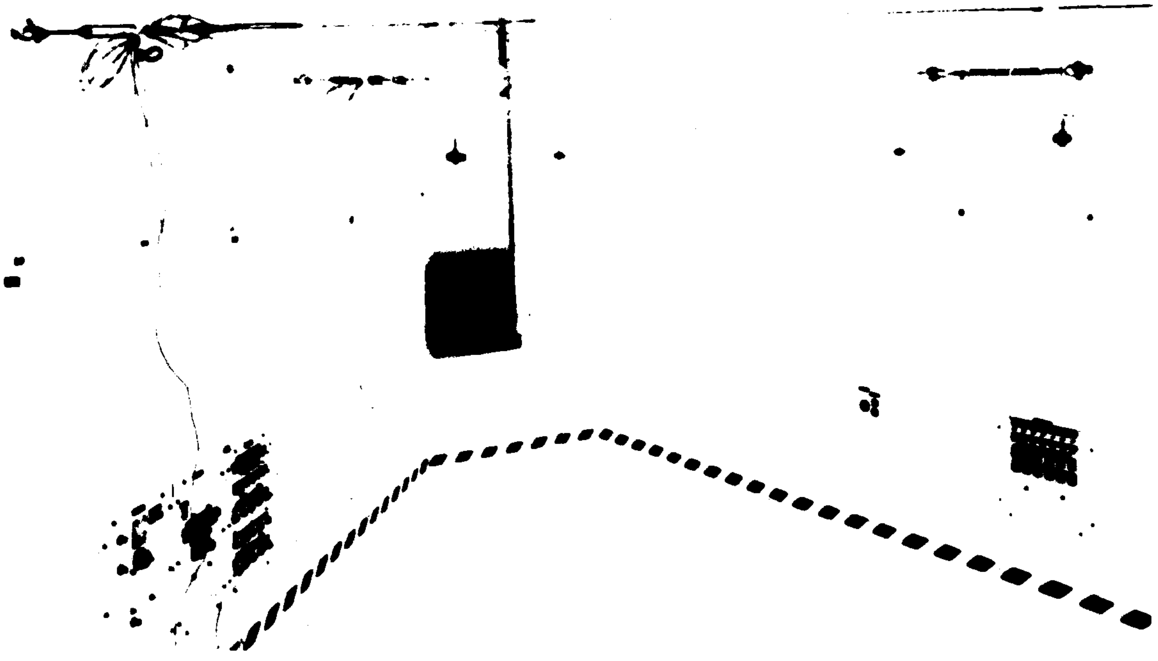

Fig. 3. Acoustic suppression horn liner installed in horn

DESCRIPTION OF TEST FACILITY

This description of the room, horn and driver is taken directly from reference 7.

Figure 4 is an isometric view of the reverberation noise test facility, which is a poured concrete chamber with an epoxy-painted interior. The interior volume of the reverberant room is approximately 68 m^3 with a total surface area of 102 m^2. The maximum orthogonal dimensions are 5.3 by 4.2 by 3.3 in the ratio 1.00:0.79:0.63, which has been suggested by Sepmeyer (ref. 8) for good chamber performance. The floor plan is basically rectangular, with two adjacent walls bisected vertically to form a fifth wall. The entrance to the reverberant chamber is a steel door 2.7 m high by 2.1 m wide. The practicability of this design was verified by a series of model studies conducted by Bolt, Beranek and Newman, Inc., as reported in reference 9.

The chamber, door, horn, and exhaust/silencer system have been designed for an overall noise reduction of 50 dB to the outside of the chamber, provided that the cable and plumbing penetrations are properly sealed. All dB notations are referenced to 20×16^{-6} N/m^2 unless otherwise noted.

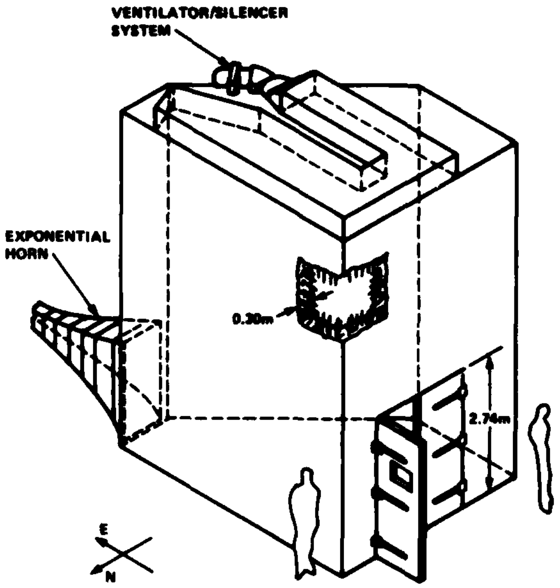

Fig. 4. Goddard reverberant noise chamber

Horn

The acoustic excitation is supplied to the reverberant chamber by an exponential horn which can be driven by either a Noraircoustic Mark V or a Ling EPT 1094B air-modulator acoustic driver. As shown in Figure 5 the exponential horn is coupled to the chamber through an opening 1.04 by 1.42 at one end of the chamber.

The exponential horn consists of a fiberglass and steel liner encased in 25 cm of steel reinforced concrete. The horn

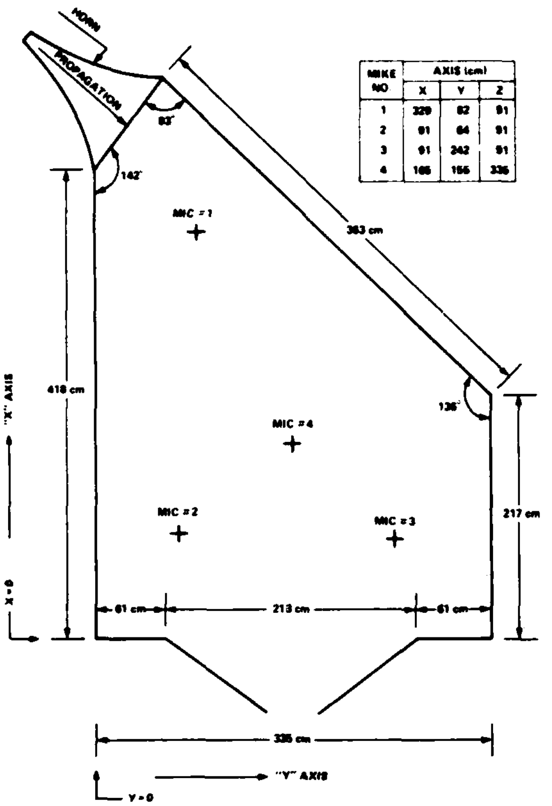

MIKE NO	AXIS (cm)		
	X	Y	Z
1	329	82	91
2	91	64	91
3	91	242	91
4	166	156	336

Fig. 5. Reverberant chamber layout and microphone locations

has an overall length (including the extension through the chamber wall) of 3.0 m and a flare coefficient of 0.02. The cutoff frequency of the horn is estimated to be 60 Hz.

Driver

The two acoustic generators used to drive the exponential horn are remotely programmable types. The input-output specifications for these generators are shown in table 1.

The Norairacoustic Mark V generator consists basically of an electro-hydraulically driven poppet valve which provides 100-percent modulation of the high pressure airstream. It can respond to many types of electrical inputs, such as single impulses, periodic or complex waveforms, and wideband random noise.

The Ling EPT 1094B acoustic generator is controlled by an electro-dynamically operated sleeve valve, and is also capable of reproducing impulse, periodic and random input signals. These noise sources have previously been evaluated and reported.

DATA ACQUISITION

To evaluate the horn liner, two different tests were performed, specifically a random noise test was run followed by a sine sweep test. The control and data acquisition systems differ slightly for each test. A description of the random noise test will be presented first and will be followed by a discussion of the sine sweep test.

Random Noise Test

For the random noise tests, the acoustic field in the GSFC reverberant chamber was excited by driving the horn (without the liner) with the Noraircoustic Mark V acoustic generator. An Allison Model 650R Random Noise Source provided the random noise signal to the acoustic generator. This random noise signal was shaped through a General Radio Model 1925 Third Octave Band Equalizer to provide a uniform sound power input to the chamber from 50 Hz to 800 Hz. Since this signal provides equal power for equal bandwidths, the power level increases at a rate of 3 dB per octave. Figure 6 shows a block diagram of this setup.

Table 1
Input-output Specifications for Noraircoustic Mark V and Ling EPT 1094B Noise Generators

Data	Noraircoustic Mark V	Ling EPT 1094B
Output Acoustic Power	50 kW	10 KW
Air Supply Pressure	827.36 N/m^2 x 10^3 (120 psig) 1,241.04 N/m^2 x 10^3 (180 psig)	275.78 N/m^2 x 10^3 (40 psig)
Air Flow Capacity	26.90 m^3/minute (950 scfm) 32.0 m^3/minute (1,130 scfm)	12.75 m^3/minute (450 scfm)
Hydralic Flow	22.70 x 10^{-3} m^3/min at 17.2 x 10^6 N/m^2 (6 gpm at 2,500 psi)	
Electrical Power	100 volt-amps	90 volt-amps

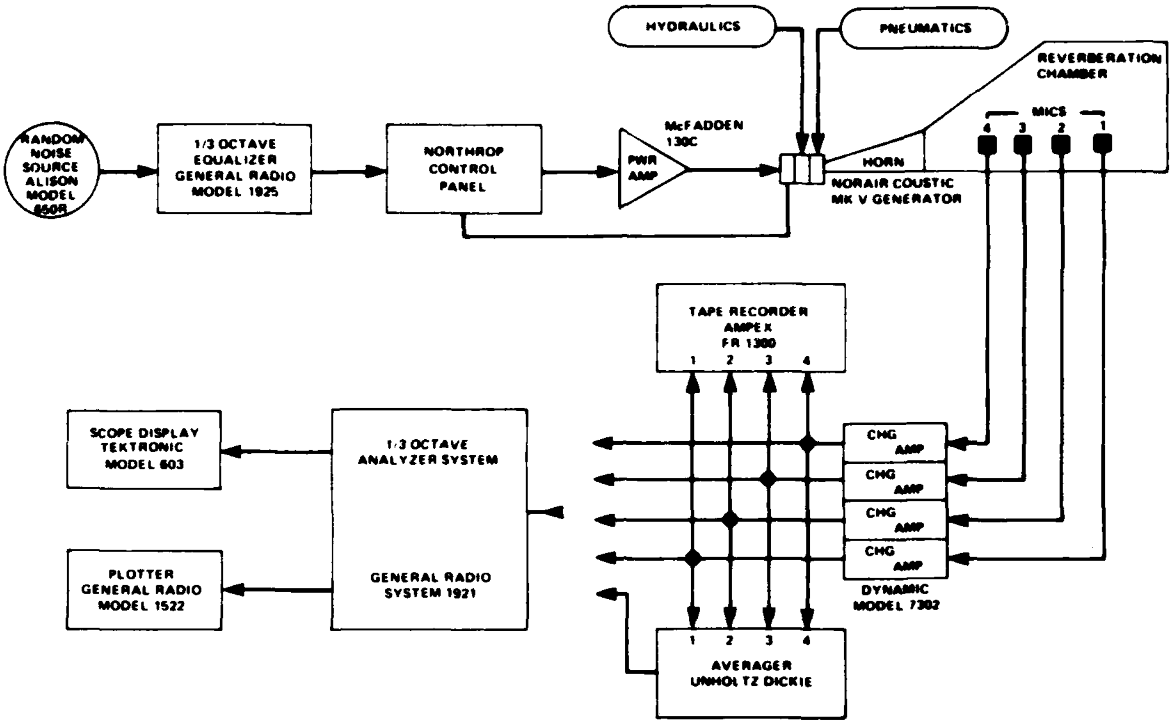

Fig. 6. Equipment setup for random noise test

Four Endevco Model 2510 microphones were positioned inside the reverberant chamber at selected locations. These microphones were used for monitoring the acoustic field in the chamber and for data acquisition. Figure 5 shows the microphone locations. The microphone signals were passed through Dynamics Model 7302 Charge Amplifier to a General Radio System 194 Real Time Analyzer. This Real Time Analyzer provides a 1/3 octave band plot of sound pressure level vs. frequency for each microphone. These plots are displayed on a CRT and on a paper strip chart recorder while the data is recorded on an Ampex FR1300 Tape Recorder. Some of these plots are shown in Figure 7 and 8. They will be discussed later. Upon completion of this procedure for the bare horn, the acoustic suppression liner was installed in the horn and the procedure was repeated using the same input control settings. The microphone signals were recorded as before.

Sine Sweep Test

The Ling 1094B Acoustic Generator was used to drive the horn (first without the liner) for the sine sweep test. The input to the generator system was supplied by a Spectral Dynamics Model 5070A Sweep Oscillator. This input signal consisted of a 1 volt rms sine wave which was initially put in at a frequency of 50 Hz. The frequency was then increased at a rate of 1 decade/min or 3.29 octave/min up to a frequency of 10 kHz while maintaining the 1 volt rms input level. Figure 9 shows a block diagram of the setup. The sound field inside the reverberant chamber was recorded on magnetic tape using the same microphones, charge amplifiers and tape recorder used in the random noise test. This sound field was plotted as sound pressure level vs. frequency on a Moseley Model 135 x-y plotter. This was done by putting the microphone signal through a Moseley Logarithmic Converter to convert the ac rms signal to the logarithmic dc (sound pressure level) signal as the y input to the plotter. The output of the sweep oscillator provided the x input (frequency) to the plotter. Plots were made for each of the four microphones, first without the liner in the horn and then with the liner in place. Typical plots are shown in Figures 10 and 11.

TEST RESULTS

Random Noise Test

Figure 7 and 8 show the 1/3 octave plots of the acoustic spectrum shape recorded on microphones 1 and 4 inside the reverberant chamber. Figures 7a and 8a show the sound field for the bare horn (without the liner) while 7b and 8b show the spectrum shape with the acoustic suppression liner in the horn. Since the plots for the remaining two microphones exhibit similar characteristics ,they are not shown. The similarity of the spectrum shape from all four microphones indicates that the sound field is uniform throughout the chamber and that the liner does not affect this uniformity. Hence, the effect of the liner is to attenuate the sound passing through it.

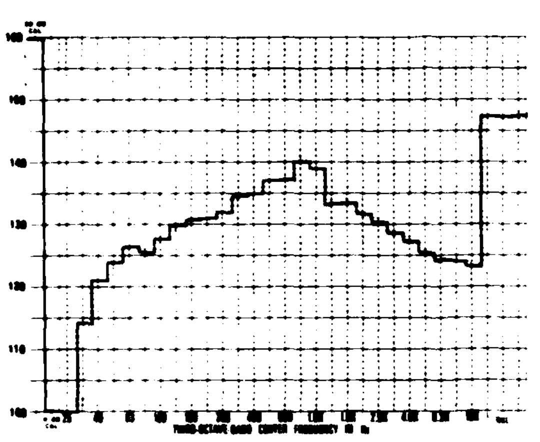

a. Without Acoustic Suppression Liner

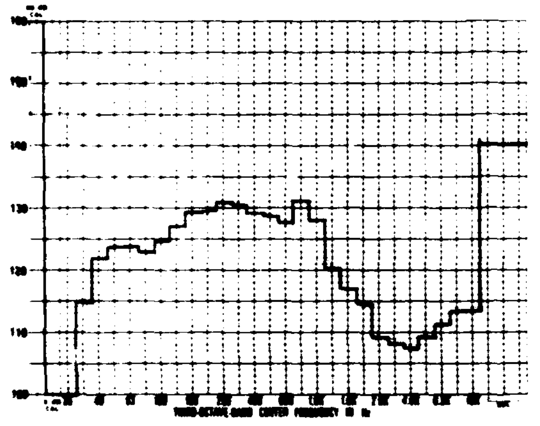

b. With Acoustic Suppression Liner

Fig. 7. Acoustic spectrum for random noise test
Microphone #1

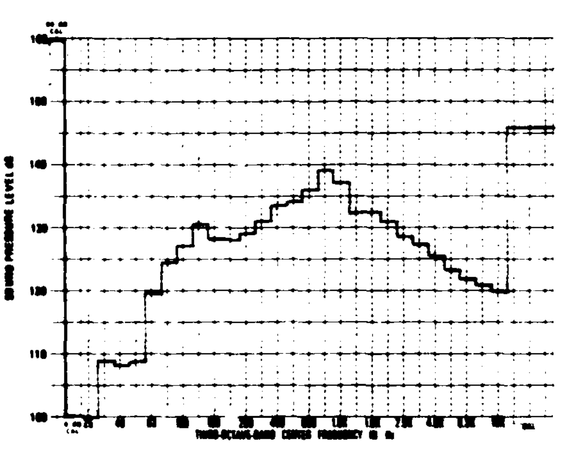

a. Without Acoustic Suppression Liner

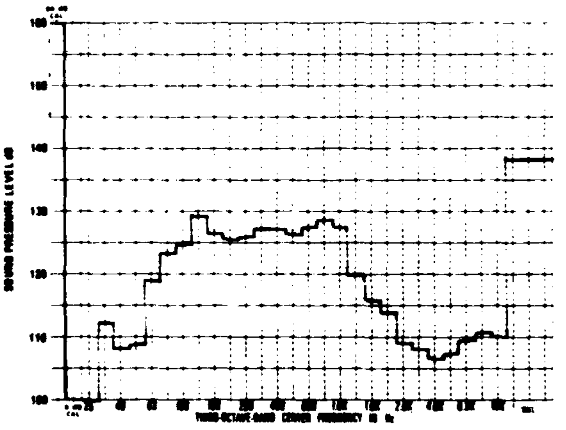

b. With Acoustic Suppression Liner

Fig. 8. Acoustic spectrum for random noise test
Microphone #4

Comparing the spectrum shpae with and without the liner reveals that below 250 Hz the attenuation is insignificant. This is in accordance with the desired effect of little or no attenuation below 250 Hz. At frequencies above 250 Hz the effect of the liner becomes apparent. Up to 250 Hz, the reduction in level is less than 3 dB while above this frequency the attenuation increases to a peak of about 20 dB at 2500 Hz as shown in Figure 12. The attenuation then drops back to about 7 dB at 10 kHz. If significant attenuation is considered to be 5 dB or more, then the effective bandwidth of this liner can be regarded as ranging from 400 Hz to 10,000 Hz with a peak attenuation at 2500 Hz.

Although the peak sound pressure level occurs at 800 Hz, both with and without the liner in place, the spectrum does not increase significantly between 50 and 800 Hz when the liner is in the horn. Without the liner the level at 800 Hz is about 140 dB. The liner reduces this level to about 130 dB. The roll-off above 800 Hz is about 5 dB/octave up to 4 kHz and about 11 dB/octave with the liner in the horn. The overall level of sound in the chamber is reduced from about 147 dB without the liner to about 140 dB with the liner. These values are based on 1/3 octave distributions and the frequencies given are the center frequencies of the 1/3 octave bands.

Sine Sweep Test

This test was performed to determine the sound attenuation at a given discrete frequency. This test was also of value in determining the peak attenuation frequency of the liner, as well as the attenuation bandwidth. Comparing the plots without the liner (Figures 10a and 11a) to those with the liner (Figures 10b and 11b) shows that the attenuation below 250 Hz was again less than 3 dB which is regarded as insignificant.

It should be noted that for the sine sweep the peak noise level without the liner is about 156 dB at 350 Hz. This peak shifts to about 153 dB at 250 Hz when the liner is placed in the horn. Significant attenuation begins to occur at about 400 Hz and increases to a peak attenuation of 17 dB at about 3150 Hz. The attenuation then drops back to about 10 dB at 6300 Hz and remains constant from there to 10,000 Hz. This is shown in Figure 13 which shows the variation of

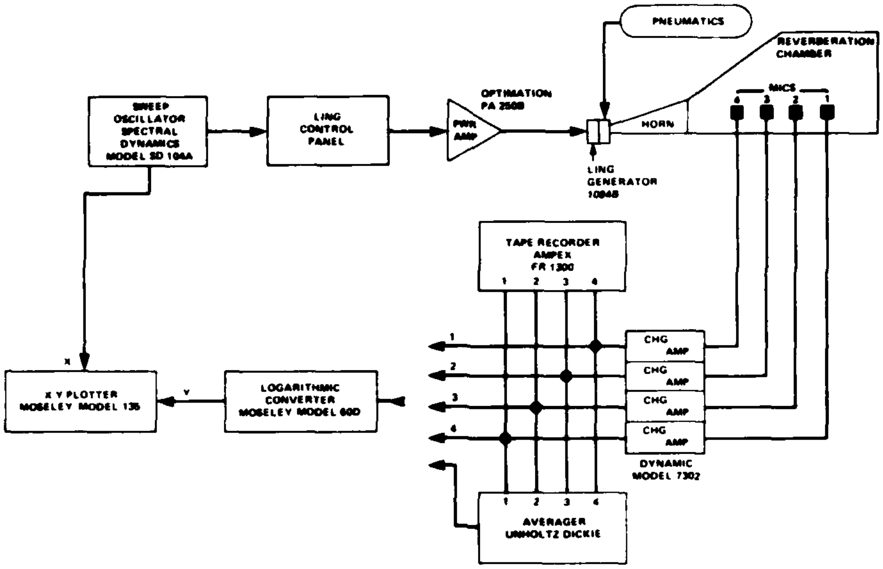

Fig. 9. Equipment setup for sine sweep test

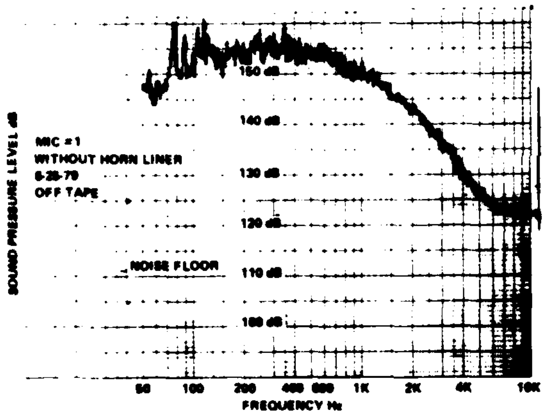

a. Without Acoustic Suppression Liner

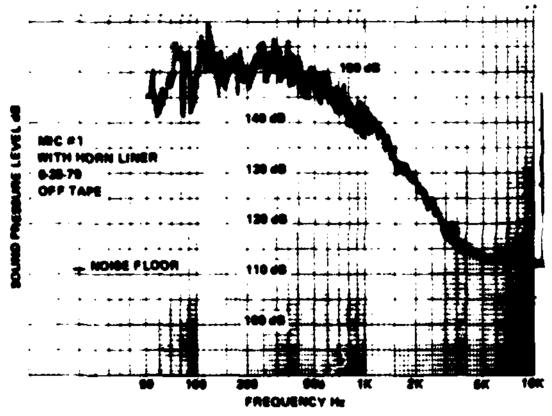

b. With Acoustic Suppression Liner

Fig. 10. Sound pressure level in reverberant chamber for sine sweep - Microphone #1

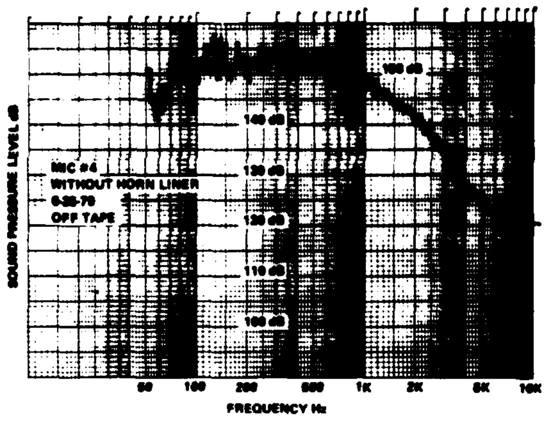

a. Without Acoustic Suppression Liner

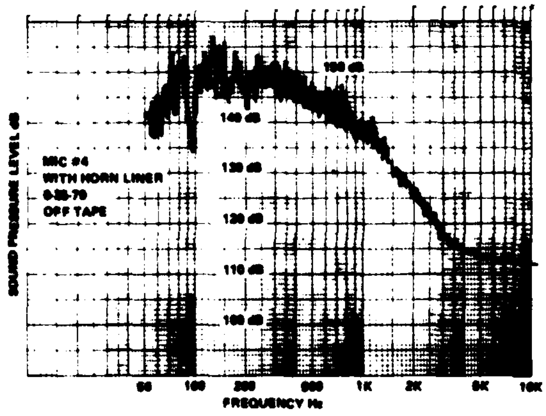

b. With Acoustic Suppression Liner

Fig. 11. Sound pressure level in reverberant chamber for sine sweep – Microphone #4

attenuation with frequency. Figures 10 and 11 also show that the level decreases more rapidly with frequency from 1000 Hz to 4000 Hz when the liner is in the horn. Without the liner, the drop is from 150 dB at 1 kHz to 130 dB at 4 kHz. With the liner the drop is from 140 dB at 1 kHz to 115 dB at 4 kHz.

In general, the information obtained from the sine sweep test was supportive of the random noise test results. Specifically, the tests showed that the liner has a relatively broadband of attenuation capability. The peak attenuation shown in the random noise test results occurs at a slightly lower frequency than that shown by the sine sweep. This is the result of more attenuation over a broad range of frequencies which are concentrated in the 2.5 kHz 1/3 octave. The single discrete frequency at which the greatest attenuation occurs lies just above the upper edge of the 2.5 kHz 1/3 octave; hence, the peak attenuation frequency differs slightly in Figures 12 and 13.

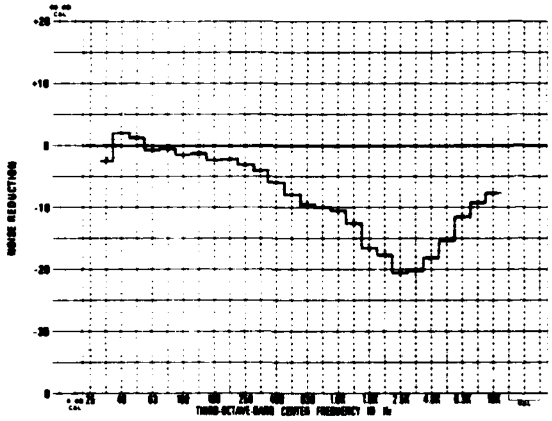

Fig. 12. Noise reduction due to liner for random noise test

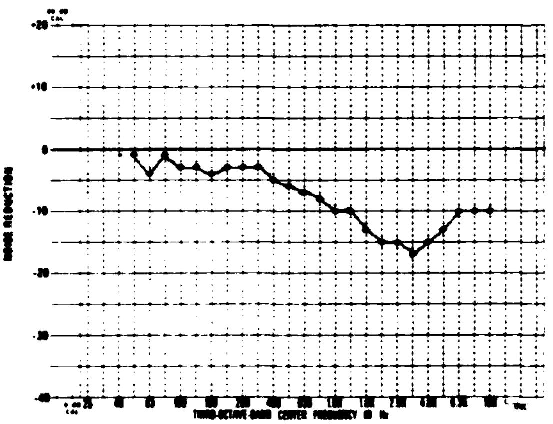

Fig. 13. Noise reduction due to liner for sine sweep test

SUMMARY AND CONCLUSION

The purpose of this acoustic suppression liner was to provide a capability of obtaining shuttle acoustic spectrum in GSFC reverberant chamber. This was accomplished successfully, providing insight into a potential method of obtaining different spectra shaping capabilities for reverberant chambers.

Evaluation of the liner by means of a random noise test and a sine sweep gave an idea of the characteristics of the liner, namely peak attenuation frequency and the noise reduction at that frequency. This, of course, is a function of the acoustic pressure, p, acoustic particle velocity v, normal to the wall (or in this case, liner surface). These properties control acoustic impedance ($Z = p/v$) which determines absorption or attenuation of the sound. As noted earlier, the attenuation is frequency dependent through the ratio of duct height to wavelength of sound.

This sort of device shows promise as a means of obtaining desired spectra shapes or special effects in reverberant chambers. Such liners can possibly be designed to attenuate sound at other frequencies and bandwidths and/or sound can be absorbed at a discrete frequency. This may be accomplished by using different types of suppression materials, that is, by changing the density of the foam or using fibers, or felts, or for discrete frequencies using Helmholtz resonator suppressors consisting of a perforated sheet backed by a honeycomb material.

With advent of the space shuttle, future acoustic environments are as yet uncertain and, in fact, may vary widely depending upon payload configuration and geometry. Development of this technology detailed in this paper could prove to be quite beneficial in achieving the environments required for the acoustic testing of future payloads.

REFERENCES

1. Piersol, A. G., Pope, L. D., Wilby, J. F., "Space Shuttle Payload Bay Acoustic Prediction Study," Report No. 3286, Bolt Beranek and Newman, Inc., August 1977.

2. Piersol, A. G., Rentz, P. E., "Prediction of Space Shuttle Orbiter Payload Bay Launch Acoustic Levels Based Upon OV101 Acoustic Tests," Report No. 3424, Bolt, Beranek and Newman, Inc., April 1977.

3. Morse, P. M., "The Transmission of Sound Inside Pipes," J. Acoust. Soc. Am. 11, 205, 1939.

4. Morse, P. M., "Vibration and Sound," Second edition, McGraw-Hill, New York, 1948.

5. Cremer, V., "Theory of Sound Attenuation in a Rectangular Duct with an Absorbing Wall and the Resultant Maximum Coefficient," Acustica, 3, 249-263, 1958.

6. Rice, E. J., "Attenuation of Sound in Soft-Walled Circular Ducts," in "Aerodynamic Noise," Ribner, H. D. ed., University of Toronto Press, pp. 229-249, 1969.

7. Cyphers, H. D., Munson, A. N., On, F. J., "Comparative Evaluation of Predicted and Measured Performance of a 68 Cubic Meter Truncated Reverberant Noise Chamber," NASA TN D-7755, January 1975.

8. Sepmeyer, L. W.,"Computed Frequency and Angular Distribution of the Normal Modes of Vibration in Rectangular Rooms," J. Acoust. Soc. Am., 37, 3, 1965.

9. Scharton, T. D., Rentz, P. E., Lubman, D., White, P. H., "Techniques for Improving the Low Frequency Performance of Small Reverberation Chambers," NASA NAS5-21003, NAS CR-112407, Bolt, Beranek and Newman, Inc., California, 1970.

DISCUSSION

Mr. Henderson (Air Force Materials Laboratory): In your testing I noticed that the liner has an 1/8 inch aluminum backing. Did you have any kind of a durability problem?

Mr. Scott: No.

Mr. Cole (Cambridge Acoustical Assoicates, Inc.): It is an interesting idea. I am wondering, in terms of efficiency of material, what the comparison would be between that and using small patches of the material inside the chamber of a similar material instead of affecting the field near the source and the propagation down the duct into the room?

Mr. Scott: That would be worth trying. I am not aware of anything that has been done along that line at this point.

THE VIBRATION TEST UNIT

A UNIQUE RAIL VEHICLE VIBRATION TEST FACILITY

R.O. Coupland and A.J. Nintzel
Wyle Laboratories
Colorado Springs, Colorado

This paper describes the Vibration Test Unit, a twelve shaker vibration system designed to vibrate a railcar to simulate the action of track/train dynamics. It includes a description of the system and a summary of its performance capabilities.

INTRODUCTION

The Transportation Test Center (TTC), located 25 miles northeast of Pueblo, Colorado, is a facility where research is conducted to develop and improve railroad and transit technology. Performance and reliability testing on the TTC's major tracks has helped researchers discover answers to many rail-related problems. As in other research disciplines, a controlled environment is necessary to achieve reliable results. In early 1975 the Federal Railroad Administration (FRA) decided to equip the Rail Dynamics Laboratory (RDL) with two highly advanced test machines to provide controlled conditions for rail vehicle dynamic testing. The machines are the Roll Dynamics Unit (RDU) and the Vibration Test Unit (VTU).

The RDU will be used to investigate the wheel/rail dynamics of acceleration, adhesion, braking, and hunting. The RDU simulates the forward motion of a vehicle on rollers rather than on conventional rails. It has the capacity to apply rotating forces or absorb forces from the wheels of a powered vehicle.

The subject of this paper, the Vibration Test Unit (VTU), is designed to vibrate a railcar to simulate the action of track/train dynamics using a hydraulic shaker system. Studies of suspension characteristics, rock and roll tendencies of rail vehicles, component and vehicle natural frequencies, ride comfort, lading responses, and simulation of full scale vehicle loads can be achieved on the VTU.

OVERVIEW

The VTU provides the capability for subjecting a rail vehicle weighing to 1428.57 kn (320,000 lb) to a controlled full scale vertical and lateral input at the rail/wheel interface. This will allow a realistic simulation of loads experienced by a rail vehicle in over-the-road service. A schematic of the VTU is shown in Figure 1.

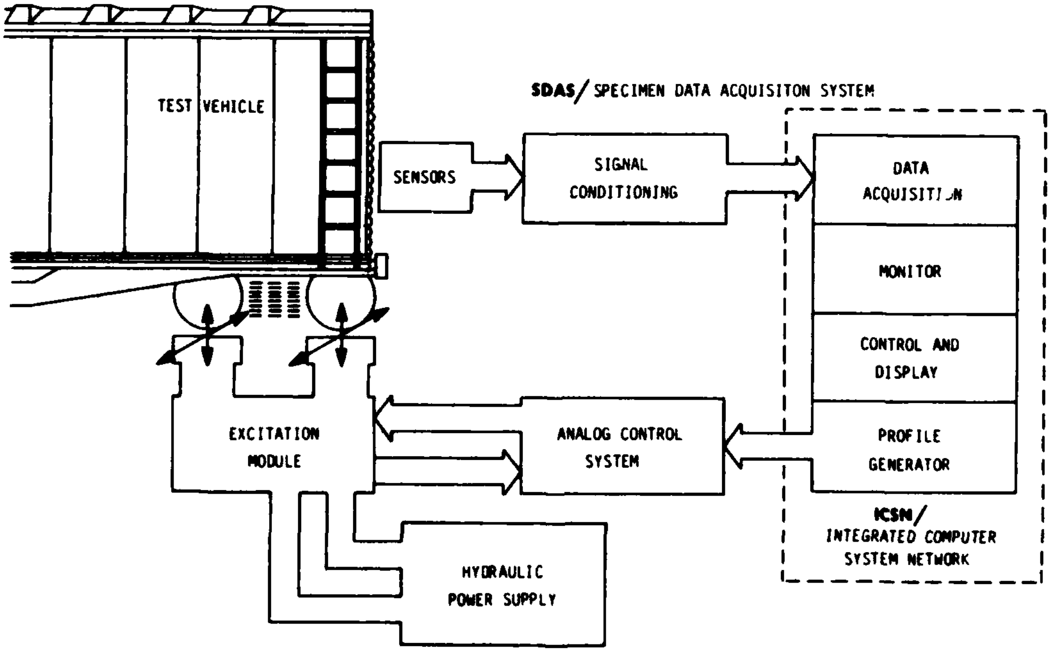

FIGURE 1 - SCHEMATIC OF VIBRATION TEST UNIT

The VTU consists of the excitation modules, the hydraulic power supply, the analog control system, the specimen data acquisition system (SDAS), and the integrated computer system network (ICSN). The excitation modules, hydraulic power supply, analog control system, and SDAS will be described in more detail later in this presentation. The ICSN, which is discussed fully in the paper following this one, has a profile generator which sends command signals to the analog control system. The control system shapes and amplifies the control signals and transmits them to the excitation modules. Displacements and accelerations of the excitation modules are fed back to the analog control system forming a tight closed loop excitation system. Vehicle responses, sensed with a variety of transducers, are signal conditioned, sent through analog to digital converters, and recorded on digital magnetic tape in the data acquisition portion of the ICSN.

The excitation modules are movable to accommodate different sized vehicles. The range of test vehicle sizes which can be accommodated on the VTU is shown below.

Vehicle Length (max)	27.43 m (90.0 ft)
Vehicle Width (max)	3.66 m (12.0 ft)
Vehicle Weight (max)	1428.57 kn (320,000 lb)
Axle Load (max)	357,14 kn (80,000 lb)
Truck Center Distance	
(min)	6.10 m (20.0 ft)
(max)	21.34 m (70.0 ft)
Truck Axle Spacing	
(min)	1.37 m (54.0 in.)
(max)	*2.79 m (110.0 in.)*
Gauge	
(min)	1.44 m (56.5 in.)
(max)	1.68 m (66.0 in.)

The VTU has four excitation modules and each excitation module supports one axle of a typical four-axle test vehicle. The excitation modules introduce test inputs at the rail/wheel interface. Each excitation module consists of two vertical excitation modules, an axle support system, a lateral excitation module, and various on-board hydraulic components. A sketch of two excitation modules supporting a hopper car is shown in Figure 2. Motion capabilities for each module under a 22.32-kn (5,000 lb) load are:

- VERTICAL
  - a. .0508 m peak (2.0 in.)
  - b. .635 m/s peak (25 in./s)
  - c. 4.0 G peak
  - d. 0.2 through 30 Hz
- LATERAL
  - a. .038 m peak (1.5 in.)
  - b. .38 m/s peak (15.0 in./s)
  - c. 3.1 G peak
  - d. 0.2 through 30 Hz

The capabilities of the VTU are shown on the plot in Figure 3. The 357.14-kn (80,000 lb) dynamic vertical load capability of each VTU excitation module is compatible with the load environments experienced by a rail vehicle. A typical rail vehicle load environment is shown as exceedance per mile versus side frame load in Figure 4. It is easily seen that each excitation module's dynamic load capability of 357.14-kn (80,000 lb) about the static load satisfies the spatial load spectra shown in Figure 4.

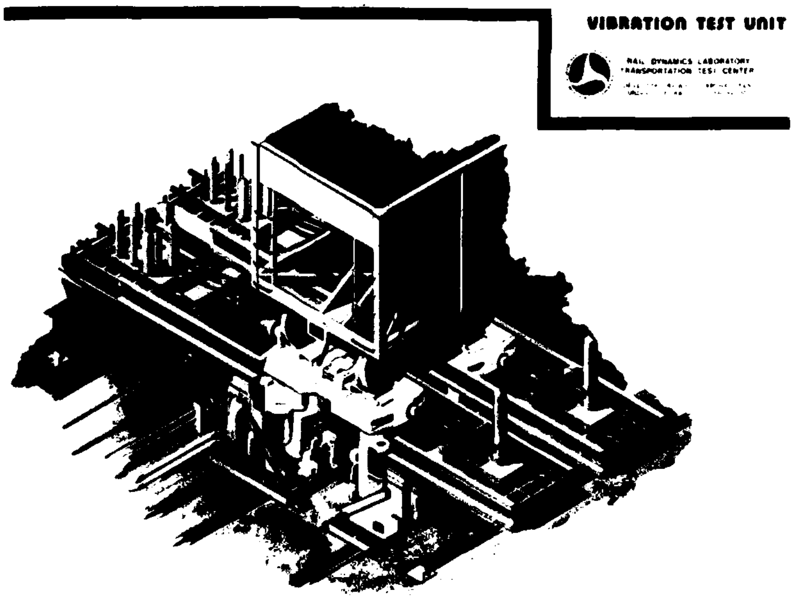

FIGURE 2 - VTU WITH HOPPER CAR

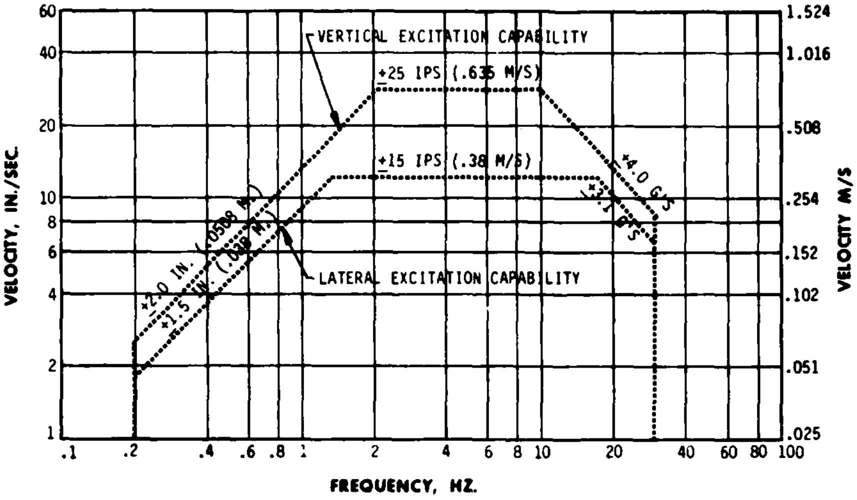

FIGURE 3 - VTU EXCITATION CAPABILITY

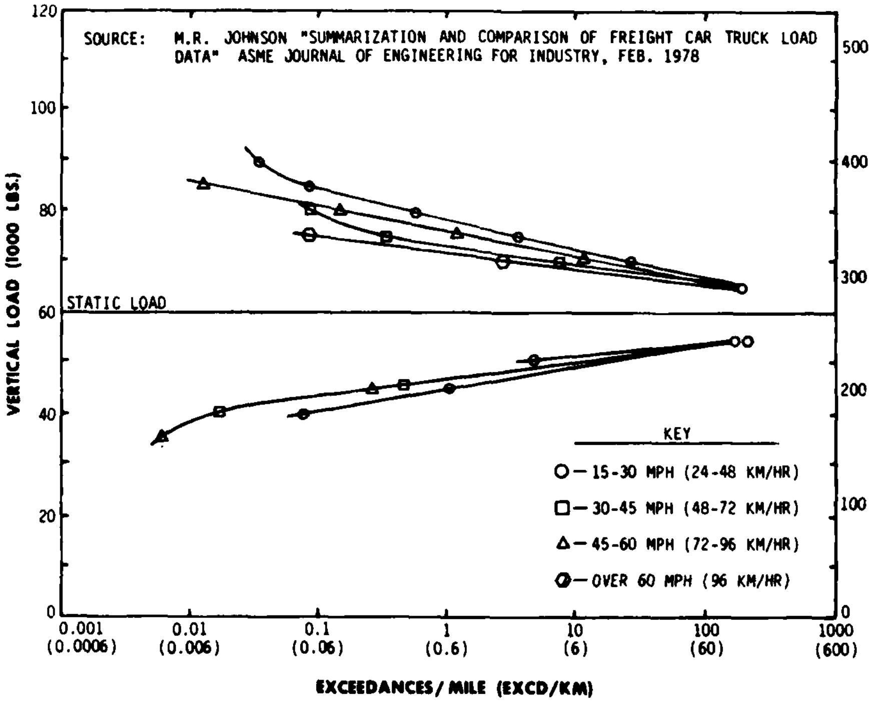

SOURCE: M.R. JOHNSON "SUMMARIZATION AND COMPARISON OF FREIGHT CAR TRUCK LOAD DATA" ASME JOURNAL OF ENGINEERING FOR INDUSTRY, FEB. 1978

FIGURE 4 - SIDE FRAME VERTICAL LOAD SPATIAL SPECTRA

The predominant vertical side frame loads of a typical rail vehicle are shown as a power spectral density (PSD) in Figure (5). This PSD can be easily duplicated by the VTU since it has an RMS of less than 45.0 kn (10,000 lb) from .5 to 30 Hz. Below 2.0 Hz, the VTU is amplitude limited to ±0.508m (±2 in.). This results in the force capability of the VTU being limited to a constant density of approximately $1x10^7 n^2$/Hz from .2 to .5 Hz with a 1160-kn (260,000 lb) vehicle on the VTU, which is very close to the required force density.

VTU SYSTEM DESCRIPTION

As mentioned above, the VTU consists of the following major elements:

- Excitation Modules
- Hydraulic Power Supply
- Analog Control System
- Integrated Computer System Network
- Specimen Data Acquisition System

The mechanical and hydraulic elements of the VTU are located in the high bay of the RDL. They are connected via control and instrumentation cables to the control, signal conditioning, and computer systems located in the RDL control room.

The excitation module can provide both vertical and lateral inputs to a rail vehicle. Each of the wheels of the railcar is driven vertically at the rail/wheel interface by a 178.57-kn (40,000 lb) vertical excitation module. Lateral inputs are supplied by a 133.93-kn (30,000 lb) lateral excitation module. Vertical and lateral loads are transmitted to the rail/wheel interface by the axle support system bearing assembly (ASSBA) which allows 5 degrees of freedom of motion and utilizes hydrostatic bearings to achieve a stiff, low friction, force transmission element. Each of these is shown in Figure 6 and will be described in detail below.

Each vertical excitation module has an actuator that is a double acting, double rod end .127-m (5 in.) diameter hydraulic cylinder with a working area of .013 m^2 (20 $in.^2$). The actuators use 67-centistoke (300 SSU) hydraulic fluid at 2.07 x 10^7 kn/m^2 (3000 $lb/in.^2$). A schematic of the vertical excitation modules is shown in Figure 7. Integral snubbers are incorporated at the ends of the bore to absorb velocities that may occur due to failure or overloads. The upper snubbing stroke is .016 m (0.62 in.). The longer snubbing stroke is .0325 m (1.28 in.) to accomodate gravitational and dynamic loads. Spherical hydrostatic bearings are located at the upper and lower ends of the actuator to accommodate side forces and to reduce the breakout force. The only friction experienced is due to viscous drag and friction of the upper rod wiper and seal.

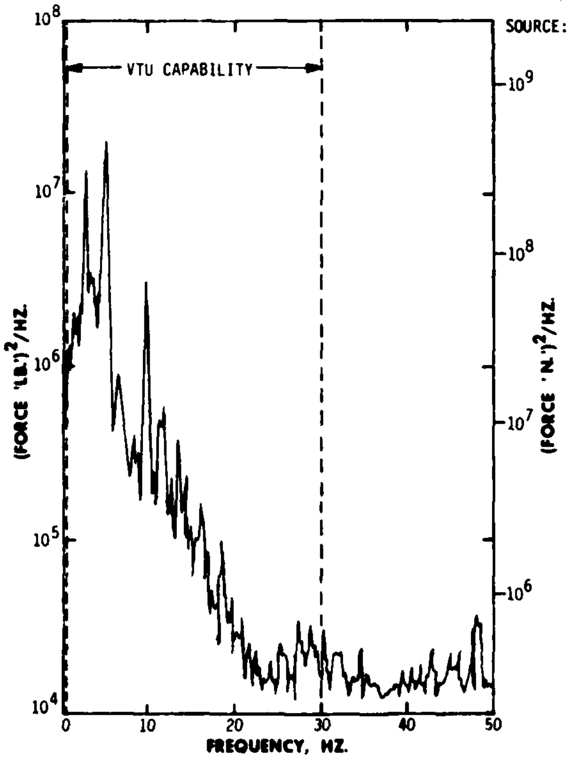

SOURCE: M.R. JOHNSON "SUMMARIZATION AND COMPARISON OF FREIGHT CAR TRUCK LOAD DATA" ASME JOURNAL OF ENGINEERING FOR INDUSTRY, FEB. 1978

FIGURE 5 - POWER SPECTRAL DENSITY OF SIDE FRAME LOAD AT 60 MPH (96 KM/HR)

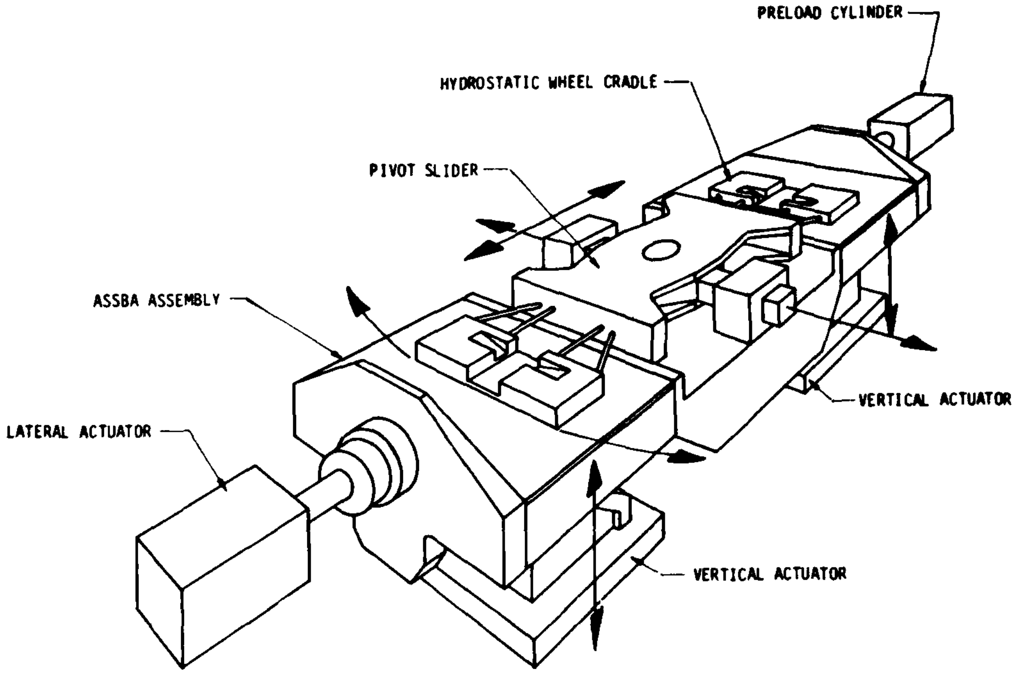

FIGURE 6 - VTU EXCITATION SYSTEM

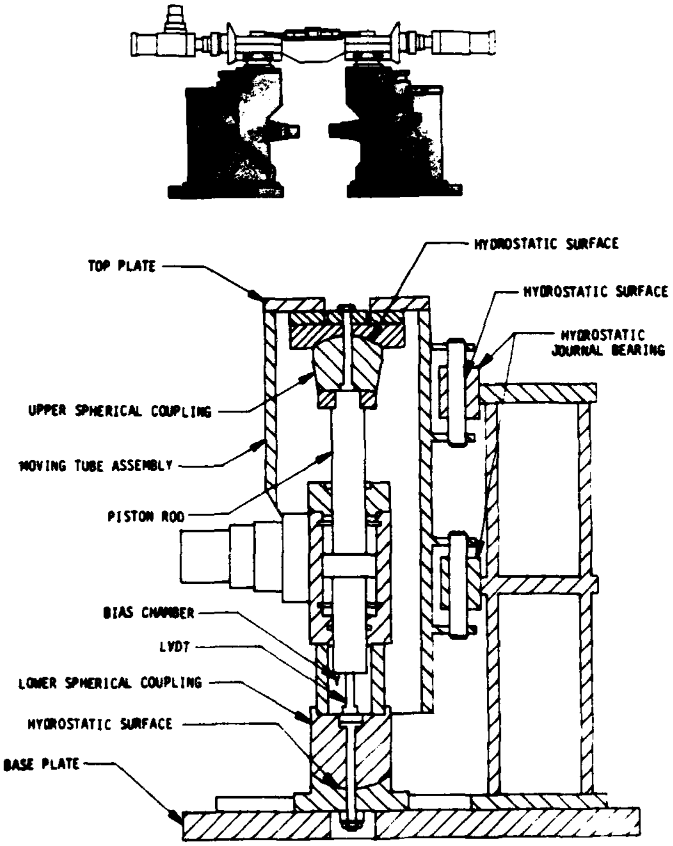

FIGURE 7 - VERTICAL EXCITATION MODULES

A pressure adjustable load bias system is in the lower portion of each vertical excitation module. The load bias system balances out the 1-G test vehicle loads to allow the full force capability to be used for excitation of the test vehicle. It was designed so that its natural frequency is well below the lowest frequency of excitation (0.2 Hz). The vertical actuator and spherical couplings are attached to a moving tube assembly by a top plate, forming a moving platform assembly. The moving platform assembly is attached by three linear hydrostatic journal bearings to a stationary structure. These bearings constrain the vertical excitation module to vertical in-line motion only.

The hydraulic actuator is driven by a two-stage .511 m^3/min (135 gpm) servovalve. The first stage is a pilot spool, a four-way closed center spool valve, driven by an electrodynamic voice coil and centered by preloaded springs. The second stage is a slave spool, a four-way closed center spool valve, driven by modulated fluid flow from the pilot valve. A linear variable differential transformer (LVDT) senses slave valve position, providing position feedback to the summing junction of servoamplifier electronics. This results in a servovalve with a bandwidth (-3 db) of approximately 100 Hz and a first order roll-off.

The vertical modules provide the vertical excitation input to each axle of a test vehicle. Mounted on top of the pair of vertical modules is the ASSBA. The ASSBA enables the system to provide combined vertical and lateral inputs by means of several hydrostatic bearings. It also accommodates vehicle bending and yaw motions. The ASSBA consists of two linear bearing assemblies, a center beam, a pivot slider, and two wheel cradles.

The top plate of the moving platform assembly attaches to two spherical hydrostatic couplings which are parallel to the longitudinal axis of the VTU. Figure 8 shows the linear bearing assembly portion of the ASSBA. The couplings allow relative motion between the vertical actuators, enabling roll motions to be input by the system. Longitudinal forces from carbody flexure are reacted on the bearing plates on the linear bearing assembly and into the spherical hydrostatic couplings. The upper portion of the spherical couplings attaches to two linear hydrostatic bearings, which accommodate the lateral motions input by the lateral actuator. The linear bearings of each axle's excitation system are attached to the center beam of the ASSBA.

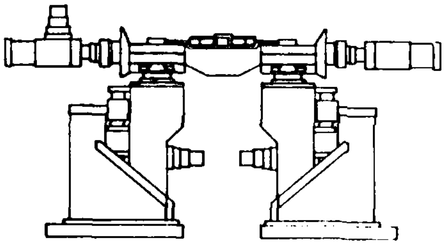

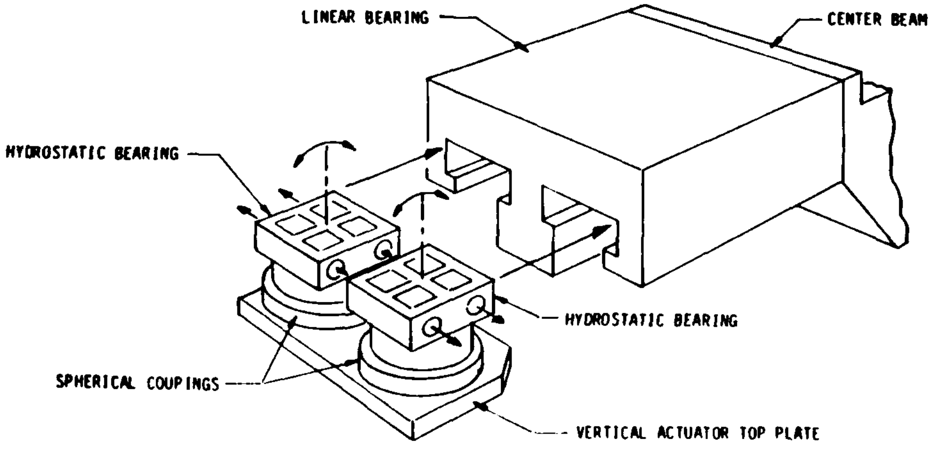

FIGURE 8 - LINEAR BEARING ASSEMBLY OF THE ASSBA

The pivot slider assembly mounts on the top surface of the center beam as shown in Figure 9. The pivot slider assembly includes a trunnion bearing which accommodates longitudinal motions due to test vehicle rigid body and flexing responses. The trunnion bearing is a hydrostatic linear bearing with spherical hydrostatic pads to allow for any misalignment. Attached to the pivot slider are wheel cradles which contain the test vehicle wheels in a cup-like housing.

The pivot slider bearing is a roller bearing which, in conjunction with hydrostatic bearings between the wheel cradle and wear plates on the center beam, allow yawing motions of the test vehicle trucks.

The ASSBA will accommodate the following test input motions: vertical translation, roll motions, and lateral translation. It will further accommodate longitudinal translation and yaw motions induced by a test vehicle. The ASSBA is thus the interface between the test vehicle and the vertical and lateral excitation modules. It transmits their vertical and lateral excitation inputs to the test vehicle.

The lateral excitation module provides the lateral vibration input to the ASSBA and, hence, to the test vehicle. The lateral excitation module includes a lateral actuator and preload assembly which contain the ASSBA under a 267.86-kn (60,000 lb) compressive load to prevent separation of the system during operation. The lateral actuator and preload assembly are not connected mechanically to the ASSBA, allowing the lateral actuator and preload assembly to remain stationary in the horizontal plane. The interface between the ASSBA and lateral excitation module is by means of spherical pad bearings, attached to the end of the lateral actuator and preload assembly, which slide on the vertical slider plate of the linear bearing assembly at each end of the ASSBA. The spherical pad bearings can pivot to accommodate out-of-plane motions of the ASSBA that arise, for example, during roll motions.

The lateral actuator which is shown in Figure 10 is a double acting, double rod end hydraulic cylinder with a working area of .0096 m^2 (15 in.^{2}) and a rod diameter of .152 m (6 in.). It uses 67-centistoke (300 SSU) hydraulic fluid at 2.07 x 107 kn/m^2 (3000 lb/in.^{2}). The lateral actuator bias system and the preload assembly provide the 267.86-kn (60,000 lb) compressive load on the ASSBA; the system is designed such that its resonance is well below the lowest frequency of excitation.

The nominal operational stroke of the lateral actuator is .045 m (1.78 in.) extend, and .052 m (2.04 in.) retract. This is based on .038 m (1.50 in.) of operational stroke, and .021 m (.82 in.) of lateral compensatory motion necessary to accommodate the varying geometry that results from the translation of the slider plate of the linear bearing assembly during ASSBA roll conditions.

Snubbers are incorporated at the end of the actuator base to absorb velocities at each end of the stroke. The retract snubbing stroke is .038 m (1.50 in.) and the extend snubbing stroke is .0063 m (.25 in.) for both cylinders. The retract snubbing stroke will absorb the kinetic energy of both cylinders plus the ASSBA. The extend snubbing stroke will absorb the kinetic energy of a single cylinder. Extend snubbing is not reached until full retract snubbing has occurred, maintaining the hydrostatic bearings in compression at all times.

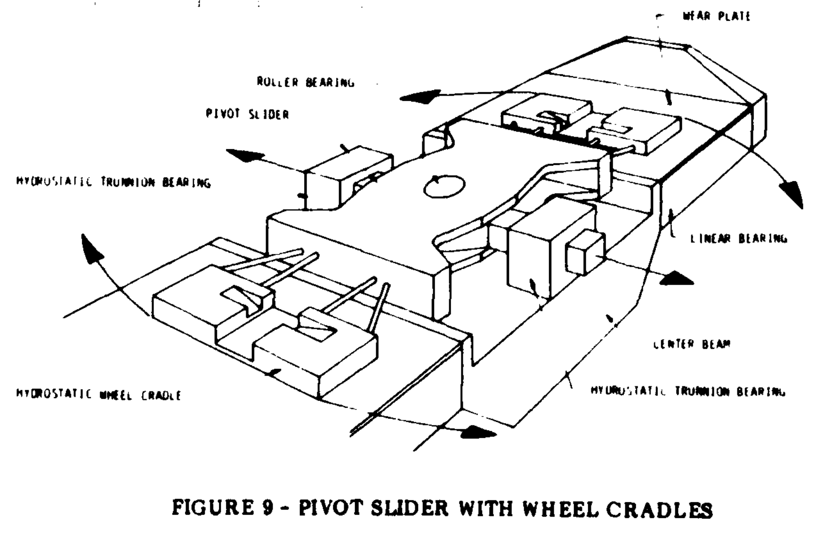

FIGURE 9 - PIVOT SLIDER WITH WHEEL CRADLES

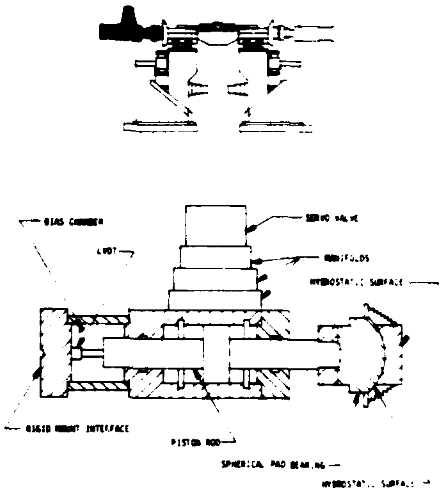

FIGURE 10 - LATERAL ACTUATOR

The preload cylinder shown in Figure 11 is nearly identical to the lateral actuator, except that no oil flows into the cylinder. The bias chamber is pressurized to maintain the 267.86-kn (60,000 lb) compressive load on the ASSBA. In the event of a hydraulic failure, an emergency dump air bag system is pressurized to prevent separation during the time the system goes to full retract.

The lateral servovalve is a two-stage .265 m^3/min (70 gpm) servovalve. The valve characteristics are identical to the vertical valve with the following exceptions:

1. Pilot stage mass is slightly lower.
2. Slave stage valve is destroked, giving lower maximum piston rates.

An LVDT senses valve position, providing position feedback to the summing junction of the servoamplifier electronics. This results in a servovalve bandwidth (-3 db) of approximately 80 Hz and a first order roll-off. The preload assembly does not require a servovalve since its function is to maintain the compressive load on the ASSBA.

The reaction loads of the lateral actuator and preload cylinder are taken by the lateral restraint system. This steel structure shown in Figure 12 extending across the VTU pit is necessary because the walls of the pit were not capable of withstanding the static and dynamic loads.

The longitudinal restraint system consists of two reaction masses, one at each end of the test vehicle. An A-frame structure mounted on the reaction masses contains a longitudinal preload rod that connects to the coupler draft gear on the test vehicle. This system is preloaded to 133.93 kn (30,000 lb) to restrain test vehicle longitudinal motion. Large test vehicle roll motions are prevented by a roll restraint system that is adjustable for individual vehicles and prevents roll motions greater than 8 degrees.

The vertical and lateral actuators and the hydrostatic bearings of the VTU have pressurized hydraulic fluid from seven .681 m^3/min (180 gpm) hydraulic pumps, operating at 2.07×10^7 kn/m^2 (3,000 lb/in.^{2}) pressure. A total of 4.769 m^3/min (1260 gpm) is available to the VTU. This amounts to 2,205 hydraulic horse power available for actuators and bearings of the VTU. The pump units are located at the RDU pit of the high bay, and a piping system distributes the hydraulic fluid to the actuators and bearings. The piping system can be reconfigured with crossover valves so that if a pump fails, testing can be continued with somewhat reduced capability. The piping system can be readily changed to accommodate vehicles of different lengths.

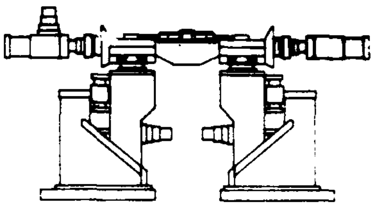

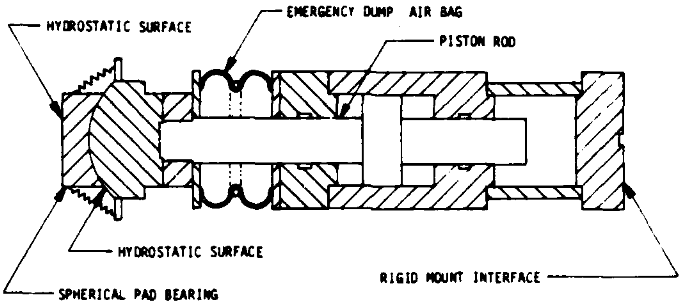

FIGURE 11 - PRELOAD CYLINDER

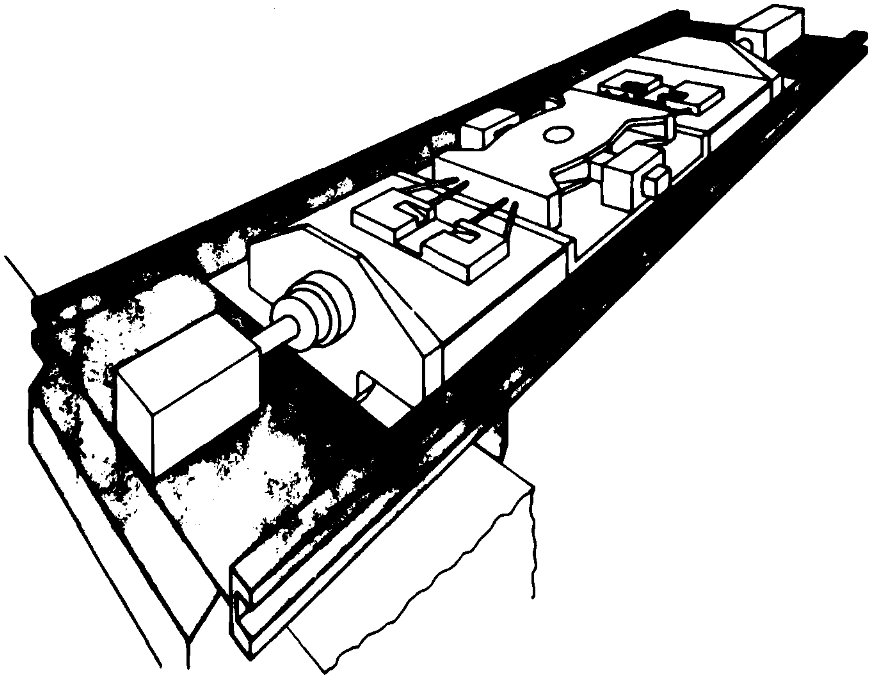

FIGURE 12 - LATERAL RESTRAINT STRUCTURE

The VTU analog control system provides closed loop displacement control of the wheel/rail interface on each excitation module (i.e., a given input voltage command provides a known piston displacement). Closed loop feedback control is used, since a hydraulic actuator is inherently unstable, to achieve wide bandwidth performance and to maintain good shaker response fidelity (+5% of commanded displacement) from 0.2 to 30 Hz. The control configuration utilizes servovalve slave displacement, piston displacement, and piston acceleration as feedback elements. Slave valve displacement feedback results in a high performance servovalve (80 to 100 Hz) which acts as an inner loop to the piston feedbacks. The piston displacement (an LVDT) feedback allows the desired system bandwidth to be attained. Piston acceleration feedback stabilizes the resonance caused by the ASSBA, the test vehicle mass, and the oil compressibility. For the vertical excitation modules this resonance occurs at 50 Hz with a damping ratio of about .08 open loop; for lateral excitation modules it occurs at 38 Hz with a damping ratio of about .10 open loop. The control system was designed using classical linear control theory.

The profile generator computer of the ICSN generates the command displacements for the four excitation modules. These twelve signals pass through digital to analog converters at a rate of approximately 500 samples/second/actuator and are low-pass filtered at 100 Hz, resulting in a high fidelity reconstructed analog signal being sent to the analog control system. The principal capability is for sinusoidal sweeps, dwells, and decays. The modes of vibration are shown in Figures 13 and 14. The modes of operation are vertical translation, pitch, roll, yaw, and lateral translation in any combination; and time delayed motions or arbitrary motions (where each wheel's vertical motion and each axle's lateral motion is independently controlled). The profile generator computer will accept a track geometry tape which will allow the VTU to replicate the conditions a test vehicle would experience in actual service.

Real-time limit checking of up to 36 data channels on the data acquisition computer ensures that no dangerous levels of stresses or motions are achieved. When a channel limit check occurs, a signal sent over the inter-computer communications link (ICCL) to the profile generator computer removes the test signal and initiates a controlled shutdown.

Data from the excitation modules and the test vehicle are conditioned and passed through anti-aliasing filters and analog to digital converters. Up to 128 channels of data can be acquired on magnetic tape at rates up to 400 samples/second/channel on the data acquisition computer.

SUMMARY

The VTU is a dynamic test machine which will allow users from the rail industry to evaluate vehicle dynamic response modes. It will be used for evaluation of suspension systems, model response evaluations, rock, roll, and bounce mode responses, ride comfort, and simulation of full scale vehicle loads. The VTU provides for vertical inputs at each wheel/rail interface and lateral inputs along each axle line at the rail/wheel interface. The VTU uses a dual minicomputer system for signal generation, data acquisition, and limit checking.

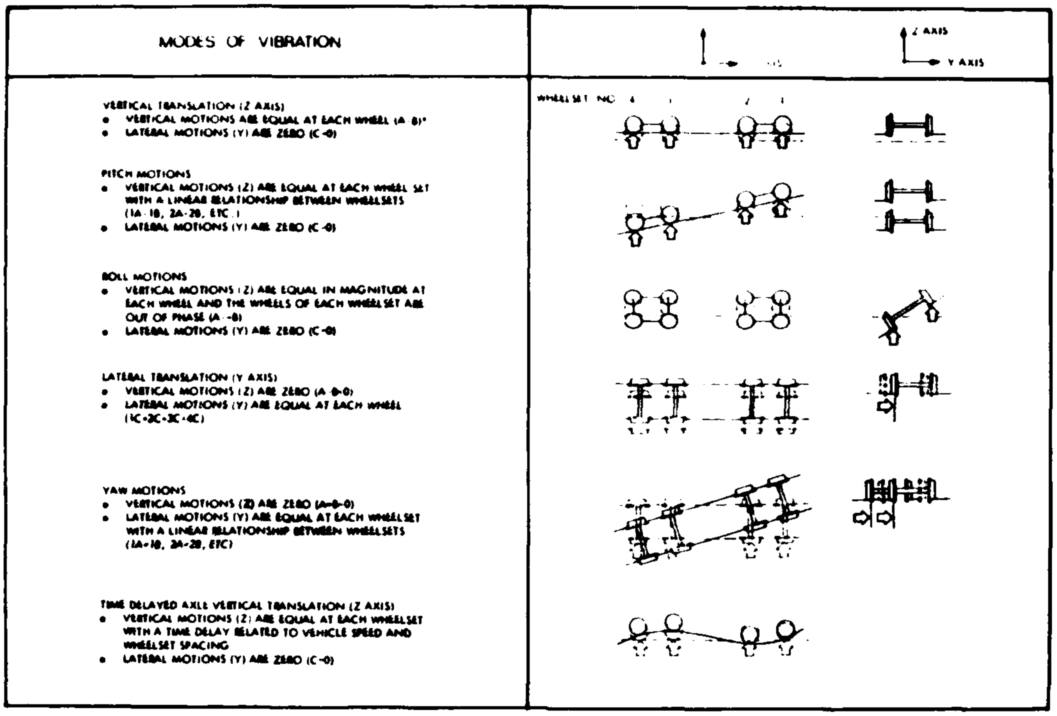

MODES OF VIBRATION

VERTICAL TRANSLATION (Z AXIS)
- VERTICAL MOTIONS ARE EQUAL AT EACH WHEEL (A-B)*
- LATERAL MOTIONS (Y) ARE ZERO (C-0)

PITCH MOTIONS
- VERTICAL MOTIONS (Z) ARE EQUAL AT EACH WHEEL SET WITH A LINEAR RELATIONSHIP BETWEEN WHEELSETS (1A-1B, 2A-2B, ETC.)
- LATERAL MOTIONS (Y) ARE ZERO (C-0)

ROLL MOTIONS
- VERTICAL MOTIONS (Z) ARE EQUAL IN MAGNITUDE AT EACH WHEEL AND THE WHEELS OF EACH WHEELSET ARE OUT OF PHASE (A--B)
- LATERAL MOTIONS (Y) ARE ZERO (C-0)

LATERAL TRANSLATION (Y AXIS)
- VERTICAL MOTIONS (Z) ARE ZERO (A-B-0)
- LATERAL MOTIONS (Y) ARE EQUAL AT EACH WHEEL (1C-2C-3C-4C)

YAW MOTIONS
- VERTICAL MOTIONS (Z) ARE ZERO (A-B-0)
- LATERAL MOTIONS (Y) ARE EQUAL AT EACH WHEELSET WITH A LINEAR RELATIONSHIP BETWEEN WHEELSETS (1A-1B, 2A-2B, ETC)

TIME DELAYED AXLE VERTICAL TRANSLATION (Z AXIS)
- VERTICAL MOTIONS (Z) ARE EQUAL AT EACH WHEELSET WITH A TIME DELAY RELATED TO VEHICLE SPEED AND WHEELSET SPACING
- LATERAL MOTIONS (Y) ARE ZERO (C-0)

FIGURE 13 - MODES OF VIBRATION

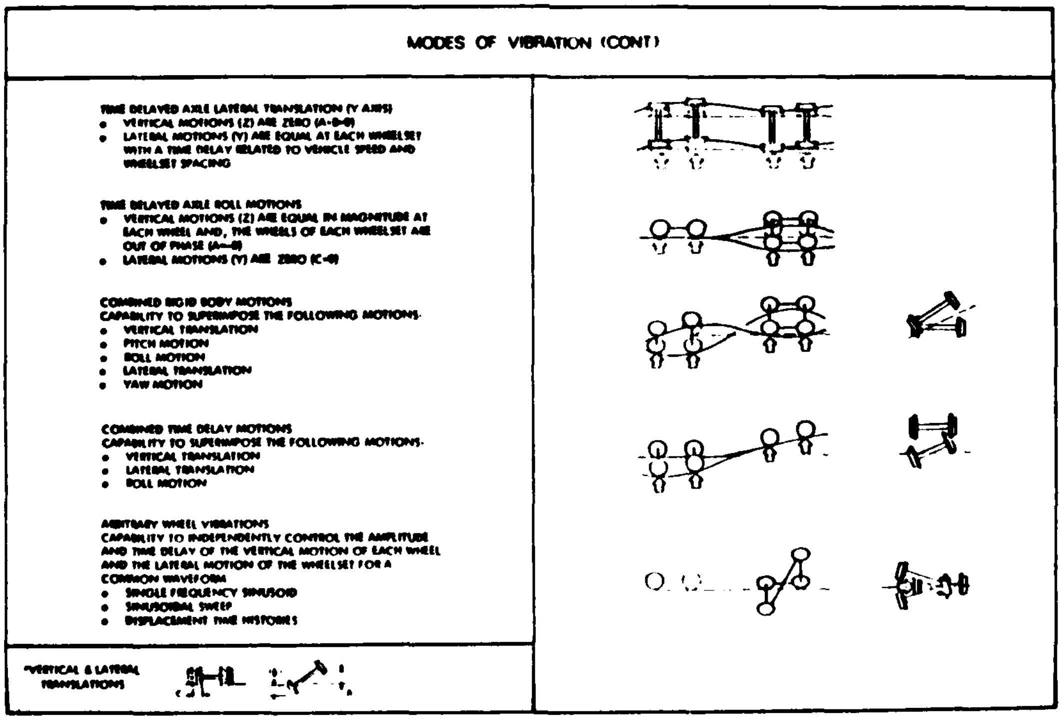

MODES OF VIBRATION (CONT)

TIME DELAYED AXLE LATERAL TRANSLATION (Y AXIS)
- VERTICAL MOTIONS (Z) ARE ZERO (A-B-0)
- LATERAL MOTIONS (Y) ARE EQUAL AT EACH WHEELSET WITH A TIME DELAY RELATED TO VEHICLE SPEED AND WHEELSET SPACING

TIME DELAYED AXLE ROLL MOTIONS
- VERTICAL MOTIONS (Z) ARE EQUAL IN MAGNITUDE AT EACH WHEEL AND, THE WHEELS OF EACH WHEELSET ARE OUT OF PHASE (A--B)
- LATERAL MOTIONS (Y) ARE ZERO (C-0)

COMBINED RIGID BODY MOTIONS
CAPABILITY TO SUPERIMPOSE THE FOLLOWING MOTIONS:
- VERTICAL TRANSLATION
- PITCH MOTION
- ROLL MOTION
- LATERAL TRANSLATION
- YAW MOTION

COMBINED TIME DELAY MOTIONS
CAPABILITY TO SUPERIMPOSE THE FOLLOWING MOTIONS:
- VERTICAL TRANSLATION
- LATERAL TRANSLATION
- ROLL MOTION

ARBITRARY WHEEL VIBRATIONS
CAPABILITY TO INDEPENDENTLY CONTROL THE AMPLITUDE AND TIME DELAY OF THE VERTICAL MOTION OF EACH WHEEL AND THE LATERAL MOTION OF THE WHEELSET FOR A COMMON WAVEFORM
- SINGLE FREQUENCY SINUSOID
- SINUSOIDAL SWEEP
- DISPLACEMENT TIME HISTORIES

*VERTICAL & LATERAL TRANSLATIONS

FIGURE 14 - MODES OF VIBRATION

THE APPLICATION OF COMPUTERS TO DYNAMIC RAIL VEHICLE TESTING

B. Clark
Wyle Laboratories
Colorado Springs, Colorado

A two-computer system is used to provide semiautomated test control and monitoring for a rail vehicle test facility at the Rail Dynamics Laboratory. The system provides control at 12 independent force transfer points, and a data acquisition capability of 100,000 samples per second. The computer equipment and the control and data acquisition computer software are described.

INTRODUCTION

The Rail Dynamics Laboratory (RDL), located at the Department of Transportation's Transportation Test Center in Pueblo, Colorado, is the world's largest rail dynamics test facility. The RDL houses two test machines and a computer network designed to permit vibration and roll dynamics testing of rail vehicles.

The computer system and the software developed for this system play a vital role at the RDL. They provide functions which automate many tedious and time consuming operations, and enable a degree of flexibility in the conduction of tests that would not be possible without the aid of computers. This paper describes the computer hardware used at the RDL and the functions performed by the computer software.

TEST MACHINES

The RDL is equipped with two rail vehicle test machines, the Vibration Test Unit (VTU) and the Roll Dynamics Unit (RDU).

The VTU consists of twelve servocontrolled hydraulic actuators: eight vertical actuators, one under each of the eight wheels of a mounted test vehicle, and four lateral actuators located in line with the four axles. The VTU can subject a stationary rail vehicle to vertical displacements of ±.0508 m (±2.0 in.) and to lateral displacements of ±.0381 m (±1.5 in.)

The RDU can support and drive the wheelsets of a four-axle rail vehicle or locomotive truck using eight rollers oriented to impart rotational motion to the wheels, one pair for each of the four axles of a test vehicle. The RDU can also absorb wheel rotation from a self-powered vehicle. It has the capacity to simulate a vehicle speed of over 230 kph (144 mph).

The VTU test machine and the control strategy used in this system are described in the paper, "The Vibration Test Unit - A Unique Rail Vehicle Vibration Test Facility" by R.O. Coupland and A.J. Nintzel, to be published.

COMPUTER HARDWARE

The computer network consists of two Varian V-73 minicomputers, selected for their high input/output rates, with an array of high performance peripherals. One computer is used for signal generation to drive the VTU. The second is used for acquisition and recording of test data from the VTU and RDU.

The two computers communicate with each other via an inter-computer communications link (ICCL) with a data transfer rate of 30,000 words per second. The ICCL is used to coordinate processing in the signal generation and data acquisition computers.

The required functional capabilities are distributed between the two computers, one of which has 65,536 words and the other 49,152 words of memory (16-bit). Both computers have 2.34 million words of disk storage, two 150-inch per second, 9-track, 1600-bits per inch tape drives, and a complement of printers, card readers, CRT terminals, and analog equipment. The analog equipment consists of 80 channels of 14-bit digital-to-analog converters (DACs) on the signal generation computer, and 256 channels of 14-bit analog-to-digital converters (ADCs) on the data acquisition computer.

This work was funded under contract with DOT-FRA Office of Research and Development.

Figures 1 and 2 illustrate the general relation of the computer network to the VTU and the RDU, respectively.

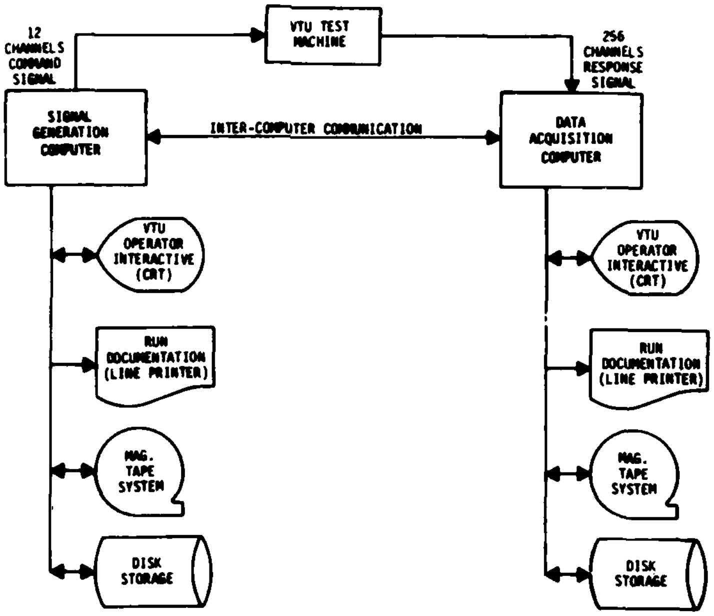

FIGURE 1 - VTU COMPUTER SYSTEM

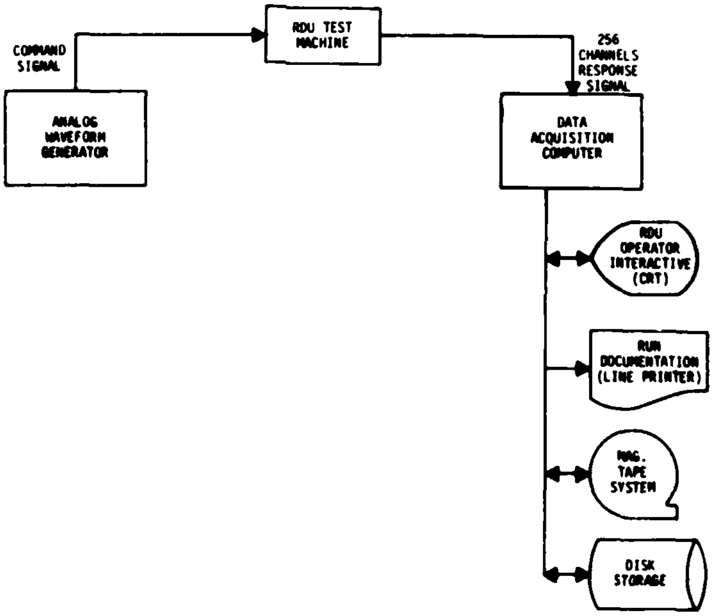

FIGURE 2 - RDU COMPUTER SYSTEM

Tables 1 and 2 list the computer equipment comprising the signal generation and data acquisition systems, respectively.

TABLE 1

Signal Generation System Equipment Configuration:

a. Varian V-73 Computer
   - Priority Interrupt Module, 4 Each
   - Hardware Fixed-Point Multiply/Divide
   - Power Failure/Restart
   - Real-Time Clock
   - Automatic Bootstrap Loader
   - Writable Control Store
   - 64K Word Core Memory (Dual Port)
   - Memory Protect
   - I/O Bus with Direct Memory Access
   - Direct Memory Interface
   - Buffer Interlace Controller, 4 Each
   - Teletype Controller (Modified for CRT)
   - Floating Point Processor

b. Infoton Vistar GT Teletype Compatible CRT, 2400 Baud

c. Data Products Model 2230 Line Printer, 132 Print Positions, 300 Lines/Minute

d. Documation M-200 Card Reader, 80 Column Cards, 300 Cards/Minute

e. Pertec Disc D3341
   - 2 Platters
   - 2200 BPI
   - 100 Tracks/Inch (203 Tracks Per Platter, Total)
   - 48 Sectors/Track, 120 Words/Sector
   - 2.34 Megaword Capacity (1.17 Megawords/Platter)

f. Tektronix Graphic Display (4010), and 4610 Hard Copy Unit

g. Potter Instruments Magnetic Tape Drives (2 each)
   - 1600 BPI
   - Phase Encoded
   - 150 In./Sec
   - 9 Channel

h. Phoenix Data, Inc. 80 Channel DAC

i. Intercomputer Communicator Interface

TABLE 2

Data Acquisition System Equipment Configuration:

a. Varian V-73 Computer
   - Priority Interrupt Module, 4 Each
   - Hardware Fixed-Point Multiply/Divide
   - Power Failure/Restart
   - Real-Time Clock
   - Automatic Bootstrap Loader
   - Writable Control Store
   - 48K Word Core Memory (Dual Port)
   - Memory Protect
   - I/O Bus with Direct Memory Access
   - Direct Memory Interface
   - Buffer Interlace Controller, 4 Each
   - Teletype Controller

b. Infoton Vistar GT Teletype Compatible CRT, 2400 Baud

c. Data Products Model 2230 Line Printer, 132 Print Positions, 300 Lines/Minute

d. Documation M-200 Card Reader, 80 Column Cards, 300 Cards/Minute

e. Pertec Disc D3341
   - 2 Platters
   - 2200 BPI
   - 100 Tracks/Inch (203 Tracks Per Platter, Total)
   - 48 Sectors/Track, 120 Words/Sector
   - 2.34 Megaword Capacity (1.17 Megawords/Platter)

f. Tektronix Alphanumeric Console (4023)

g. Potter Instruments Magnetic Tapes Drives (2 each)
   - 1600 BPI
   - Phase Encoded
   - 150 In./Sec
   - 9 Channel

h. Phoenix Data, Inc. 256 Channel ADC

i. Intercomputer Communicator Interface

j. Digital Input Module

k. Digital Output Module

COMPUTER SOFTWARE

The software for support of the VTU provides the following general functions:

- Signal Generation
- Data Acquisition and Recording
- Limit Checking
- Actuator Calibration
- Startup and Shutdown
- Data Base Maintenance
- Test Events Log

Only the data acquisition and recording and limit checking functions are used to support the RDU. Signal generation is provided by an analog subsystem built into the RDU Control System.

SIGNAL GENERATION

The signal generation function can provide the VTU with two distinct types of vibration profiles: sinusoidal and time history.

The sinusoidal waveform provides the capability to specify independent amplitude and phase relationships for each of the 12 actuators. The signal frequency may vary throughout the test run within the range from 0.2 to 30 Hz, but is the same for the 12 actuators. Tests can be performed in which the signal automatically sweeps continuously through any segment of the 0.2 to 30 Hz range, or the test personnel can manually select individual frequency and amplitude points and generate signals at only those points.

The second type of waveform is time history. These waveforms are obtained from magnetic tape recordings of actual track profiles. The signal generator can play back the track profiles over a wide range of speeds, and can accommodate test vehicles with truck axle spacings from 1.37 m (54.0 in.) to 2.79 m (110.0 in.) and truck center distances from 6.10 m (20.0 ft) to 21.34 m (70.0 ft).

Signal generation is accomplished by building a digital approximation of the desired waveform and outputting the profile through a digital-to-analog converter (DAC) to the VTU. All waveforms are stored in a 32k word area of core memory reserved for the signal generation process. The digital waveform data are multiplexed in memory, arranged into contiguous sets of data with each set containing a single amplitude displacement point for each channel of output signal. A complete signal profile segment is composed of as many as 1024 of these sets. The DAC accesses the data directly from the computer memory, and outputs one set of data in a burst (on the order of 10 microseconds per channel), followed by a time delay. The process repeats for each set until the entire segment is output. The time delay is software-selectable and is varied in order to control the rate at which data conversion occurs. Sinusoidal waveforms are output at rates between 500 and 1000 samples per second for each of the 12 channels. For time history waveforms, the rates are between 200 and 400 samples per second per channel.

A double buffering technique is used for signal generation with each buffer containing a complete segment of the waveform. When one buffer is being output by the DAC, the other buffer is being filled with the next segment. Generation of the time history signal requires this ping-pong method in order to process the data tape continuously. The sinusoidal waveform, however, does not.

The DAC is configured such that in the absence of a software command to switch to the second buffer, the first buffer is repeated. This feature is used to output a continuous sinusoid by storing a complete sine wave in one of the output buffers and allowing the DAC to output the same buffer for a period of time. This permits long dwells where the frequency and amplitude of the waveform do not change. Signal frequency changes are effected by changing the DAC output rate. Changes in amplitude require building a new buffer.

DATA ACQUISITION AND RECORDING

Analog data are acquired, digitized, and stored in buffers of the computer memory using analog-to-digital converters (ADCs). When a buffer fills, the data are written to magnetic tape. High speed controllers permit the acquisition and recording of up to 256 analog channels at data rates up to 400 samples per second per channel. The data acquisition computer has two tape drive units for recording data. When one fills, it automatically rewinds the tape and goes off-line, while data recording continues on the alternate tape unit. No data are lost.

Data acquisition is continuous throughout a test, but data recording may be turned off and on upon command to permit recording during selected time intervals. The software provides automatic control of recording on/off intervals in coordination with signal generation, or recording can be controlled manually at the discretion of the test personnel.

LIMIT CHECKING

During data acquisition, real-time limit checking is performed on up to 36 of the analog channels to ensure that the VTU is operating within safe limits. Whenever one of these monitored channels falls outside the permissible range of data values, the signal generation computer is notified via the ICCL and an emergency shutdown is performed. For sinusoidal vibration profiles, the shutdown time is one period at the current signal frequency. For time history, the time is a fixed interval specified prior to the start of testing.

The limit checking function provides the capability for test personnel to independently specify, for each channel, a frequency range, minimum and maximum limits, and a total number of out-of-limit counts causing an emergency shutdown.

ACTUATOR CALIBRATION

The VTU software supports two separate actuator calibration procedures.

The first procedure allows the VTU test personnel to measure and perform a tolerance check on the position of each actuator piston at zero displacement, full positive displacement, and full negative displacement, prior to testing. The tests provide a verification of static actuator position settings. These measurements are taken from analog channels connected to the actuator. The data are acquired, digitized, averaged, and checked for tolerance. A computer display is produced identifying actuators which are out of tolerance.

A second procedure calculates scale factors which relate a desired actuator displacement to a signal generation command signal. This procedure involves both a signal generation and a data acquisition function. A DC command signal of specified voltage is output to the VTU, and the resulting actuator displacement is read by the computers. Two such measurements are taken and processed, each at different voltages, to produce a linear scale factor for each actuator. A third measurement is also taken at some intermediate voltage to verify linearity.

STARTUP AND SHUTDOWN

In support of activities during startup and shutdown of the VTU, the software provides a computerized checklist of events occurring during these processes. Each step of the checklist is displayed in turn on the computer console identifying which activities must be performed next and specifying which crew is assigned to complete the task. This computerized checklist aids the test personnel to ensure the orderly process of starting up or shutting down the VTU.

With the completion of each step of the checklist, the computer writes an entry into a system log recording the time and nature of the step. Certain computer displays call for responses from the console operator. This response is also written into the system log.

DATA BASE MAINTENANCE

Several computer programs have been developed to provide for maintenance of the test data base. In most cases the programs use an interactive language developed specifically for the VTU system which enables the operator to create, modify, and store the data base files from the computer console. Hard copy listings of the data can be generated on a line printer providing a permanent record of the contents of all files.

One of the data base files contains room for 200 distinct descriptions of the signal generation process. Each descriptor specifies completely independent sets of test parameters including: signal frequency, actuator amplitudes and relative phase angles, rates, units, and other parameters which control various options of the signal generation process. Test runs can easily be defined to produce a variety of vibration motions to the VTU including vertical only, lateral only, pitch, yaw, roll, or a combination of these motions, each with or without time delays between different axles of the test vehicle.

Another data base file contains up to 20 different data acquisition configurations used to define on which analog channels data will be acquired, and of those channels, which ones will be limit checked and precisely what the limit check criteria will be.

TEST EVENTS LOG

The VTU software maintains a time-stamped, computerized log of events throughout the VTU calibration and testing activities. Entries written to the log include: the frequency and amplitude of the command signal at each data recording interval, the results of the actuator calibration along with the computer measurements, and a summary line at the completion of each step of the startup and shutdown checklist. The log also contains operator commands entered during a test, and messages identifying software-detected computer system failures. In addition to software-generated entries, the operator can enter remarks of any nature into the log.

TECHNICAL PROBLEMS

The significant problems that were faced during specification and development of the computer functions were related to the data throughput. The target throughput rates were 102,400 samples per second for data acquisition, and 12,000 samples per second for signal generation. The signal generation function also required frequent updating to allow amplitude and phase changes, and to enable track geometry data to be played out continuously. These problems were solved by allocating these activities to separate minicomputers and selecting special, extremely fast, input/output device controllers. These controllers are interrupt-serviced, and are capable of direct memory access, enabling data transfers to occur with a minimum of Central Processor Unit intervention. With this hardware configuration and the associated real-time device drivers, the target throughput rates were achieved.

SUMMARY

The Rail Dynamics Laboratory uses a two-minicomputer system to support testing of its two-rail vehicle dynamics test machines. The computer system and specially developed software provide functions related to digital signal generation, data acquisition and recording, limit checking, calibration, and other capabilities facilitating operation of the Vibration Test Unit and the Roll Dynamics Unit.

LOW FREQUENCY STRUCTURAL DYNAMICS OF THE SPACE SHUTTLE SOLID ROCKET BOOSTER MOTOR DURING STATIC TESTS

M. A. Behring and D. R. Mason
Thiokol Corporation/Wasatch Division
Brigham City, Utah 84302

Low frequency oscillations in measured thrust have occurred during static testing of the Space Shuttle Solid Rocket Booster Motor. These measured thrust oscillations are believed to be associated with oscillations in chamber pressure, but are much larger than can be directly attributed to observed pressure oscillations from a ballistic consideration only. This paper describes the development of a mathematical model simulating the motor in the test stand and describes analytical studies into the effects of small amplitude, chamber pressure oscillations on measured thrust.

INTRODUCTION

During the development of the Space Shuttle Solid Rocket Motor (SRM), four development motors (DM) were static fired in the Thiokol T-24 test facility. On each of these static tests, low frequency oscillations in measured thrust occurred. These oscillations have caused a great deal of interest in the low frequency dynamic characteristics of the SRM as installed in the static test facility. A mathematical model simulating the motor in the test facility was developed and studies were performed into the low frequency dynamic behavior of the structure. The intent of this paper is to summarize the analytical studies conducted to date on this problem and to present conclusions reached.

DISCUSSION

The SRM was developed by Thiokol Corporation/Wasatch Division in conjunction with the National Aeronautics and Space Administration (NASA) under contract NAS8-30490 and was sponsored by NASA/Marshall Space Flight Center.

The motor is approximately 125 feet long and 146 inches in diameter. Its weight is approximately 1,250,000 pounds at ignition and 140,000 pounds at end of burn. The motor develops a maximum thrust of approximately 3,000,000 pounds during its 120 second burn.

The motor is fabricated in four segments: a forward segment, two center segments, and an aft segment. The motor case is 0.5 inch thick, D6AC-steel. The propellant grain has a center port design with a star configuration in the forward end of the forward segment. When assembled, the motor is held in the test facility at the forward and aft skirt attach rings with all axial loads taken out by the forward support. Figure 1 shows the first development motor (DM-1) prior to static testing. Figure 2 indicates the arrangement of the test stand components and the load measurement devices.

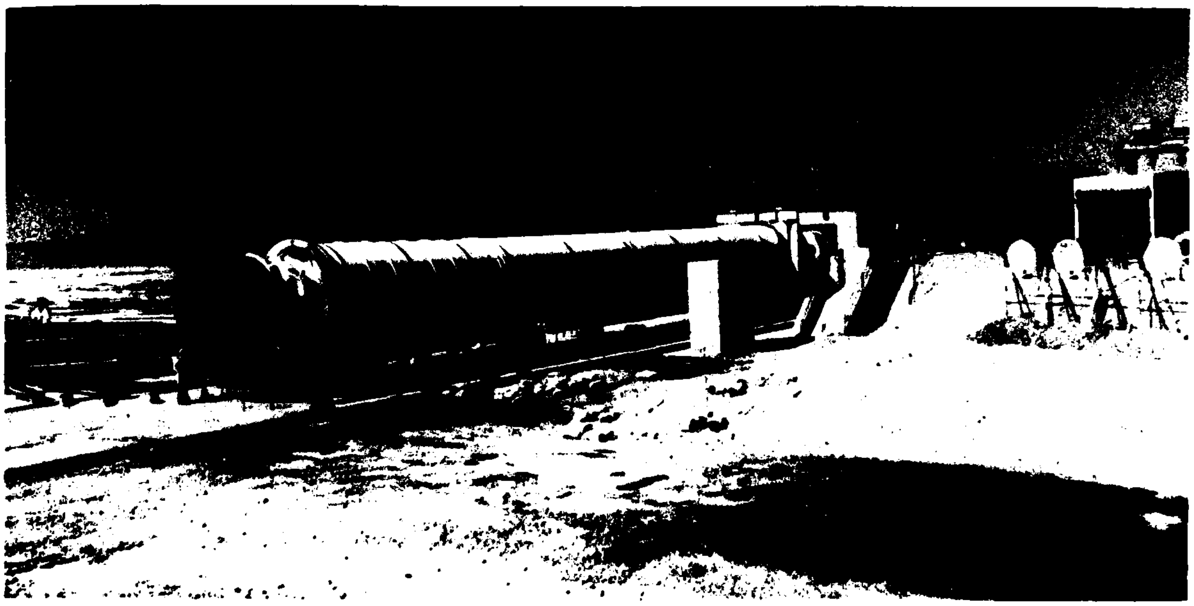

Figure 1. DM-1 Prior to Static Test

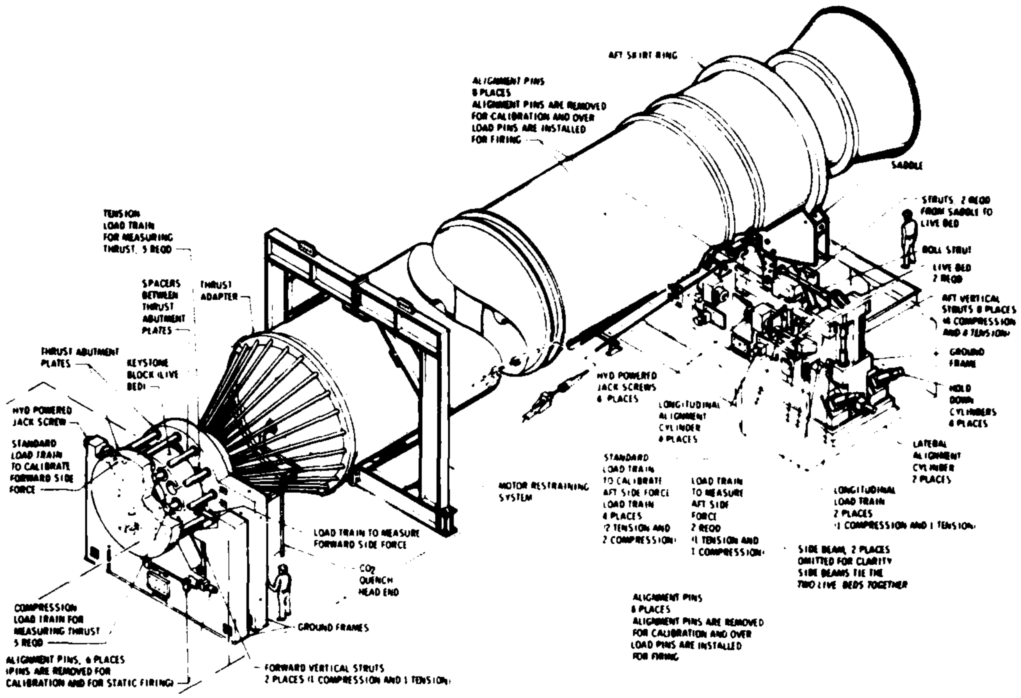

Figure 2. SRM Test Stand

A typical measured thrust trace is presented in Figure 3. Detailed examinations of thrust data revealed low frequency oscillations of a quasi-sinusoidal nature with maximum amplitudes from approximately 100,000 to 180,000 pounds peak to peak. Plots of amplitude versus frequency versus time (waterfall plots) are shown in Figure 4 for both pressure and thrust for the DM-3 test. These data are typical of all the static tests in which oscillations were apparent in measured thrust throughout the motor burn. For a more detailed discussion of the thrust oscillations observed during demonstration motor testing, see Reference 1. One band of oscillations occurred at 6 to 7 Hz at ignition and increased in frequency to 11 to 12 Hz near the end of burn. At approximately 70 to 80 seconds, another oscillatory band occurred at about 14 to 17 Hz. An examination of pressure data showed no apparent

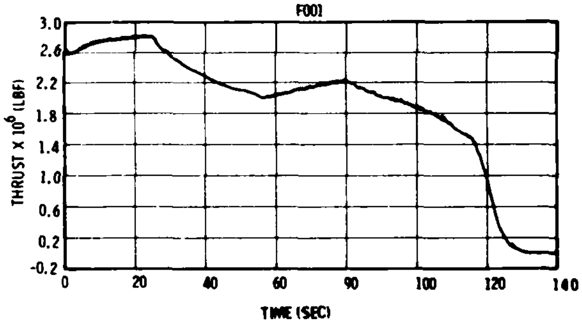

Figure 3. Measured Thrust (F001)

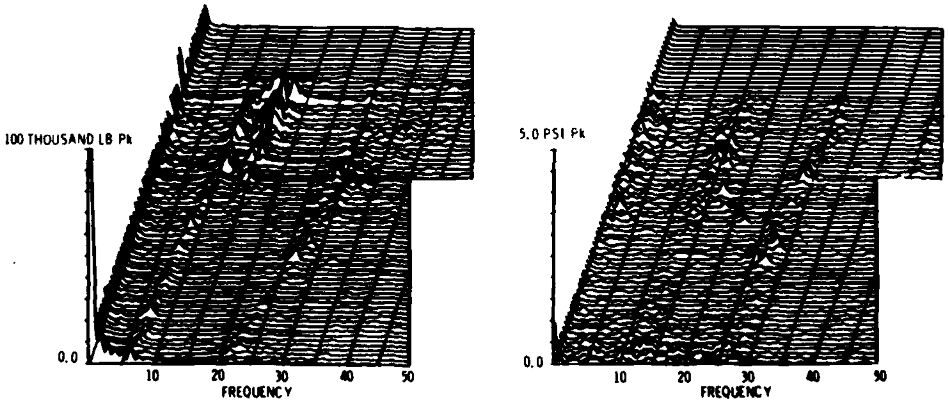

WATERFALL PLOT OF THRUST GAGE F001 DURING THE DM-3 TEST

WATERFALL PLOT OF PRESSURE GAGE P010 DURING THE DM-3 TEST

Figure 4. Waterfall Plots of Pressure Gage P010 and Thrust Gage F001 During DM-3 Test

oscillations in the 6 to 12 Hz range; however, during the latter part of the burn, pressure oscillations in the 14 to 17 Hz range became readily apparent. Other pressure oscillations were observed in the 25 to 30 Hz range; these were not considered in this study. The appearance of the 14 to 17 Hz oscillations in both thrust and pressure data suggested a correlation. Figure 5 presents a 2 second record of thrust and pressure from the DM-2 test in which this correlation is apparent.

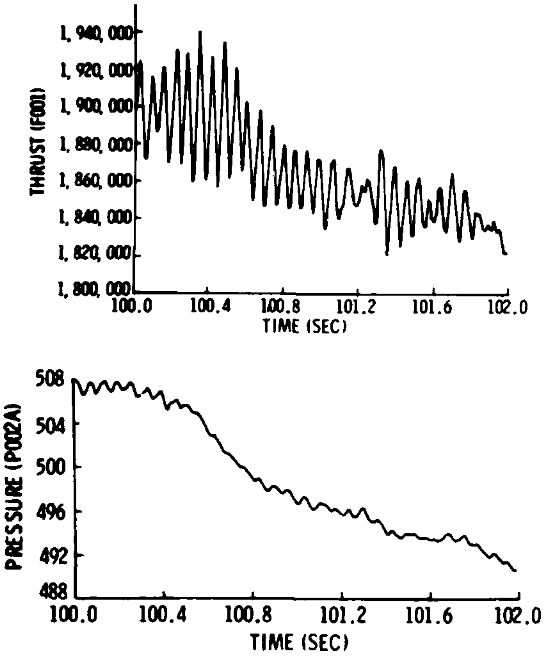

Figure 5. DM-2 Static Test Data

A mathematical model of the motor in the static test facility was developed using the NASTRAN computer program. The motor was modeled as a lumped parameter beam with the propellant connected rigidly to the motor case. The nozzle and exit cone assembly were treated as a concentrated mass connected to the motor case by scalar springs allowing it 5 degrees of freedom relative to the case. The static test facility was simulated with concentrated masses and scalar springs. The support of the motor in the test facility was modeled with a combination of rod and bar elements and scalar springs. A simplified sketch of the mathematical model is shown in Figure 6.

Following the DM-3 static test, a modal survey vibration test was conducted on the burned out motor while it was still in the test stand (Reference 2). This test was conducted by Structural Dynamics Research Corporation of San Diego, CA and coordinated by Rockwell International/Space Division. In this test, natural frequencies, mode shapes, and damping factors for modes up to 50 Hz were experimentally measured. The axial transmissibility of the system was also determined by monitoring the axial load cell (thrust measurement device) while exciting the motor at the aft end in the axial direction.

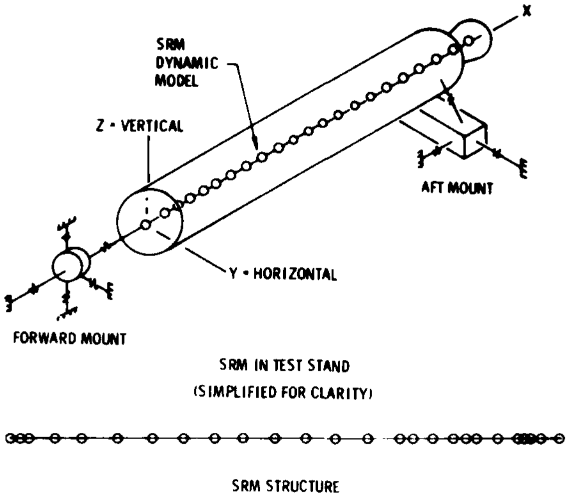

Figure 6. Mathematical Model Schematic

The mathematical model was altered to represent the configuration that existed during the modal survey test, and natural frequencies and mode shapes were calculated. The experimental results of the modal survey test were then used to refine the model until a reasonable correlation was achieved for modes up to 16 Hz. Not surprisingly, several modes of vibration were noted during the modal survey test that were not predicted by the model. Most of these, however, were dominated by shell activity which is not reproducible by a lumped parameter beam model. In the modal survey test, many of the beam modes are modified by shell activity and local deformations, but the basic beam mode shapes were obtained by the simplified model. Table I summarizes the natural frequencies and modal identifications for modes up to 16 Hz.

TABLE I

Measured and Calculated Natural Frequencies

TEST FREQUENCY (Hz)	ANALYSIS FREQUENCY (Hz)	MODE DESCRIPTION
4.44	4.5	LATERAL MODE
5.57	--	FIRST TORSION, SHELL
6.06	6.15	VERTICAL BENDING
6.86	5.41	FIRST ROLL
8.82	7.87	LATERAL MODE, SHELL, SKIRT FORE AND AFT
9.18	--	LATERAL MODE, SHELL
9.49	9.64	AFT SKIRT AND SADDLE FORE AND AFT, SHELL ACTIVITY
10.25	--	SHELL ACTIVITY
10.30	10.97	LATERAL MODE
11.24	--	SECOND TORSION, SHELL ACTIVITY
12.30	--	SHELL ACTIVITY
12.90	--	SHELL ACTIVITY
13.40	13.11	ISOLATED F&A MOTION OF AFT LIVE BED
13.57	--	AFT SADDLE; SKIRT, NOZZLE, AND KEYSTONE BLOCK MODE
15.30	16.34	FIRST AXIAL

A frequency response analysis was conducted with the model to simulate the effects of axial excitation applied at the aft skirt during the modal survey test. The axial constraint force at the forward end of the test stand per unit applied excitation was calculated and compared to the experimentally determined axial transmissibility function. Adjustments were made to the modal damping values in the model to bring the predicted response levels into agreement with the test data. The analysis damping value required for the fundamental axial mode was higher than that measured in the modal survey test. Other damping values were approximately those measured. The predicted and measured axial transmissibility functions are compared in Figure 7.

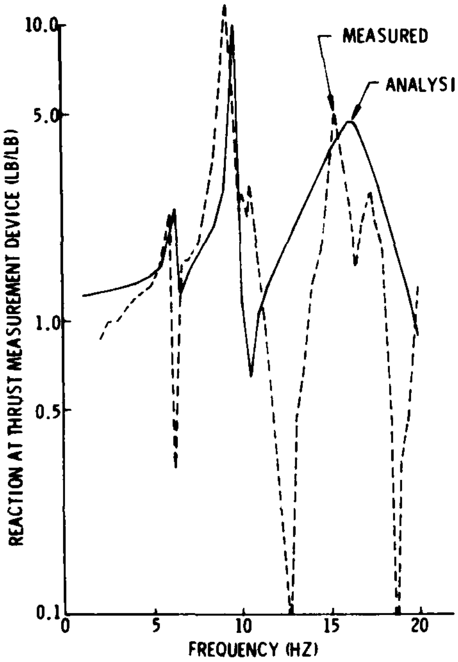

Figure 7. Axial Transmissibility

Models were then developed for several motor burn times: ignition, 50 seconds, 100 seconds, and end of burn. Natural frequencies and mode shapes were calculated for each of the burn times modeled. Figure 8 is a plot of natural frequencies versus burn time. The analytical modes that are dominated by axial motion correlate well with the frequency of thrust oscillations at various burn times. Correlation with the fundamental vertical bending mode was also shown.

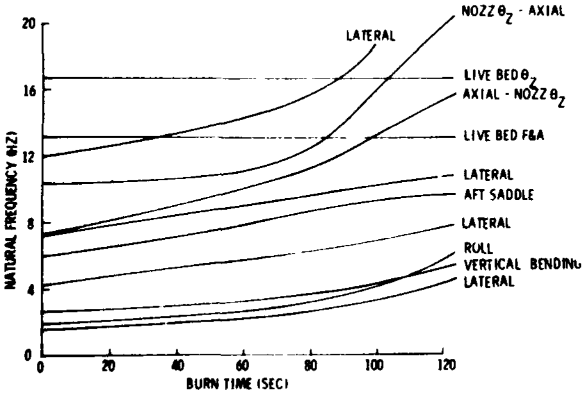

Figure 8. Natural Frequency vs Burn Time

An acoustic analysis conducted by the Naval Weapons Center (Reference 3) indicates the presence of a fundamental longitudinal acoustic mode of the rocket motor chamber at approximately 15 Hz. Figure 9 shows the calculated frequency of the first acoustic mode versus burn time.

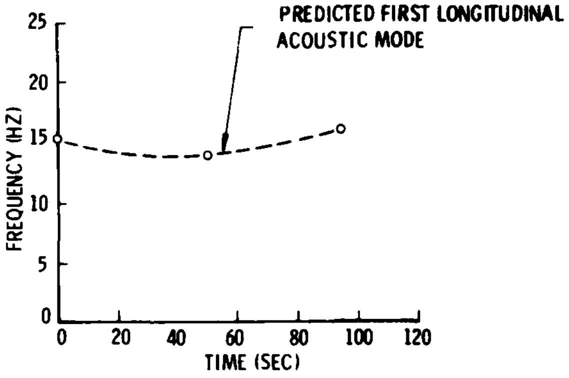

Figure 9. Acoustic Mode Frequency vs Burn Time (NWC Results)

A frequency response analysis was then conducted to simulate the sinusoidal excitation provided by the fundamental longitudinal acoustic mode. As shown in Figure 10, a unit chamber pressure oscillation was assumed at the head end of the motor, and the predicted acoustic pressure at the nozzle was applied at the motor aft end. As these pressures are out of phase for the first acoustic mode, the resulting forces are in phase. The forcing frequency was varied from 12 to 17 Hz, a range somewhat larger than the predicted range of the acoustic mode.

PRESSURE PROFILE

EXCITATION	P_H (PSI)	P_{SN} (PSI)
SINUSOIDAL	1.0	-0.96

Figure 10. Pressure Forcing Function for Response Analyses

Since the largest observed thrust oscillations occur during the latter part of the motor burn, the response analysis was conducted using the 100 second and end of burn models. The axial constraint force at the forward end of the test stand per unit chamber pressure is plotted versus frequency in Figure 11. As shown, a 1.0 psi pressure oscillation at 15 to 16 Hz results in a measured thrust oscillation of approximately 90,000 pounds near the end of burn. The expected thrust oscillation from a 1.0 psi pressure oscillation based solely on ballistic considerations is approximately 28,000 pounds. Due to the proximity of the fundamental axial mode of the motor structure in the test stand to the frequency of the acoustic mode pressure oscillation late in the motor burn, dynamic amplification of measured thrust of up to approximately three times can be attained. At 100 seconds on DM-2, a pressure oscillation of approximately 1.6 psi at 15.7 Hz resulted in a measured thrust oscillation of approximately 50,000 lb/psi, while the model predicts a thrust response of approximately 42,000 lb/psi under these conditions.

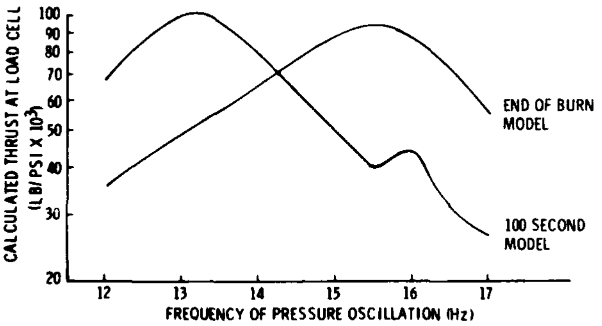

Figure 11. Calculated Thrust Response Due to Chamber Pressure Oscillation

CONCLUSIONS

The low frequency dynamics of the Space Shuttle SRM in the static test facility can be adequately represented by a beam model. Good correlation was achieved between mathematical model results and modal survey test results for low order bending modes and for the fundamental axial mode of the motor in the static test facility. The axial response of the model correlated well with the experimentally determined axial transmissibility of the SRM in the test facility over the frequency range of interest.

The analytical studies performed indicate that the observed oscillations in measured thrust can result from small chamber pressure oscillations. During static test, acoustic mode pressure oscillations can produce oscillations in measured thrust as much as three times greater than predicted by ballistic considerations alone. In a similar manner, thrust oscillation magnitudes in the mated vehicle will depend on interactions between the vehicle dynamics and the chamber pressure oscillations. An assessment of this situation is underway at Rockwell International/Space Division and elsewhere.

1. "Thrust Oscillations of the Space Shuttle Solid Rocket Booster Motor During Static Tests," D. R. Mason, S. L. Folkman, M. A. Behring, Paper 79-1138 presented at the AIAA 15th Joint Propulsion Conference, Las Vegas, Nevada, 18-20 June 1979.
2. "Test Results For Solid Rocket Motor DM-3 Modal Survey Ground Test," Structural Dynamics Research Corporation/Western Operations, SDRC Project No. 1531, 1 Dec 1978.
3. "Internal Acoustic Characteristics of the NASA Solid Propellant Booster Motor," H. B. Mathes, C. J. Bicker, Technical Memorandum 2822, Naval Weapons Center, November 1976.

VIBRATION ENVIRONMENT OF THE SPACE SHUTTLE SOLID ROCKET BOOSTER MOTOR DURING STATIC TESTS

D. R. Mason and M. A. Behring
Thiokol Corporation/Wasatch Division
P.O. Box 524, Brigham City, Utah 84302

During motor development, four Space Shuttle Booster solid rocket motors were static tested in the Thiokol T-24 facility. On these motor tests, the self-induced vibration environment was monitored at numerous locations on the motor. This paper summarizes the results of this vibration environment survey and compares results to flight criteria established by NASA for locations on the motor.

INTRODUCTION

The self-induced vibration environment was monitored during the four Space Shuttle SRM development motor static firing tests. This report documents vibration data from the DM-1, DM-2, DM-3, and DM-4 static tests in accomplishing this objective.

The Space Shuttle solid rocket booster motor (SRM) is approximately 125 ft long and 146 in. in diameter, weighs approximately 1,250,000 lb prior to ignition, and develops a maximum thrust of near 3,000,000 lb during the 120 sec motor burn. Between July 1977 and February 1979, four development motors (DM) were static tested.

A variety of dynamic instrumentation was located on the development motors during static testing. The emphasis of the vibration survey was on the accelerometer data acquired over the frequency range from 20 to 2,000 Hz. Power spectral density analyses of this data were performed for various motor burn times, and results were compared to determine environment variations from location to location on the motor for the four static tests. Comparisons to NASA flight vibration criteria were also made.

DISCUSSION

Instrumentation

Vibration instrumentation on the development motors consisted of accelerometers bonded to the motor structure at various locations. The approximate locations of the accelerometers are shown in Figure 1. Table I contains the specific location and orientation as well as the range of each accelerometer.

The accelerometers used were Unholtz-Dickie Model 5D21-8 with a low frequency response to 3 Hz and a resonant frequency of 40 kHz. Signal conditioning was by way of PCB Piezotronics charge amplifiers (Model 463M04) and charge converters (Model 422M34) with a frequency response of 5 Hz to 20 kHz. Data acquisition was by way of an Ampex FM tape recorder (Model FR3020) with frequency response on the band used of DC to 2,000 Hz.

Data Reduction

Each accelerometer channel was plotted on an oscillograph (acceleration versus time) for the entire duration of the firing. This format provided both a good overview of the data and a quick assessment of its validity. Obvious anomalies, such as signal dropout, were readily apparent as were overall trends in the data.

After a preliminary assessment was made based on the oscillograph records, power spectral density (PSD) plots (g^2/Hz vs Hz) were generated for each accelerometer for 2 sec time frames beginning approximately at the following times (T+0 is ignition):

1. T-5 sec
2. T+2 sec
3. T+15 sec
4. T+30 sec
5. T+60 sec
6. T+90 sec
7. T+120 sec

Although the data in general is non-stationary, over short time intervals the data were

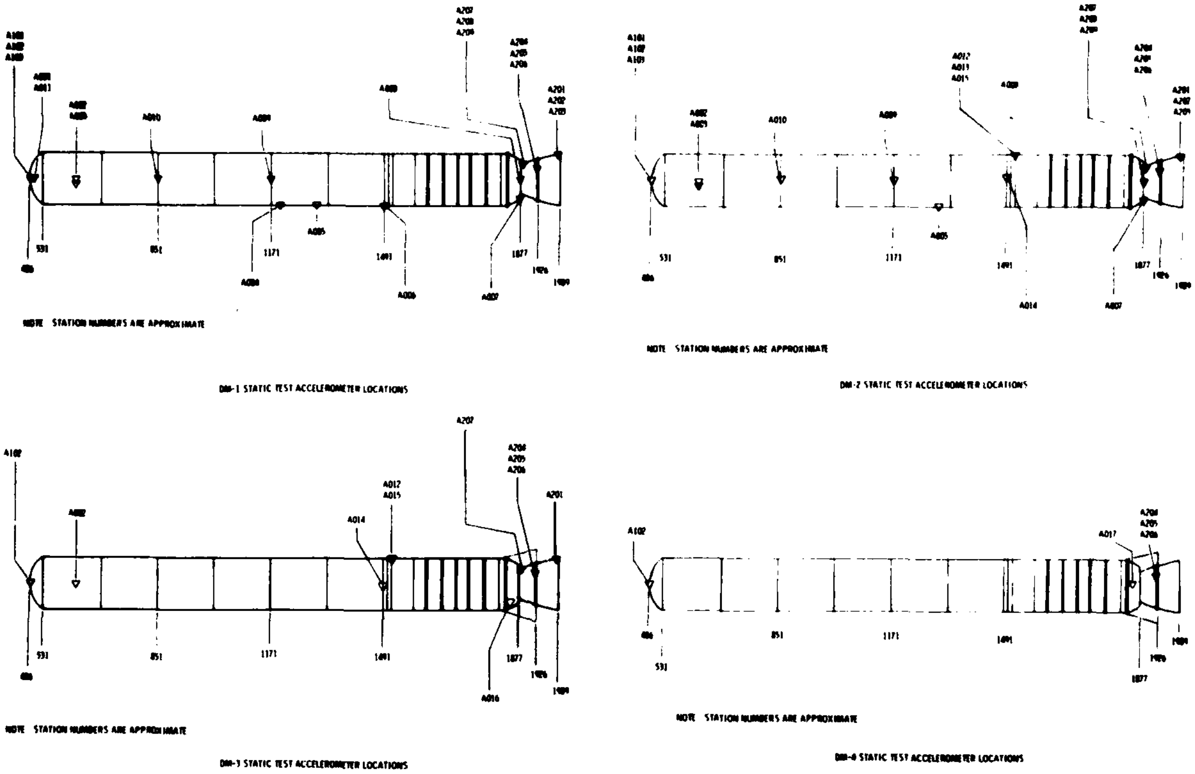

DM-1 STATIC TEST ACCELEROMETER LOCATIONS

DM-2 STATIC TEST ACCELEROMETER LOCATIONS

DM-3 STATIC TEST ACCELEROMETER LOCATIONS

DM-4 STATIC TEST ACCELEROMETER LOCATIONS

Figure 1. Test Accelerometer Locations

TABLE 1

TEST ACCELEROMETER LOCATIONS

PARAMETER	LOCATION	STATION, INCHES	ANGLE, DEGREES	ORIENTATION	RANGE, G ZERO TO PEAK*			
					DM-1	DM-2	DM-3	DM-4
A001	Forward Dome, Opposite Star Point	498.0	90	Normal to Surface	80	--	--	--
A002	Forward Segment, Opposite Star Point	625.0	90	Radial	80	25	25	--
A003	Forward Segment, Opposite Star Point	625.0	73.6	Radial	80	25	--	--
A004	Aft-Center Segment	1200.0	0	Radial	80	--	--	--
A005	Aft-Center Segment	1300.0	0	Radial	80	25	--	--
A006	Aft-Center Segment to Aft Segment Joint	1492.0	1	Radial	80	--	--	--
A007	Nozzle Fixed Housing To Aft Segment Joint	1877.0	0	Radial	80	25	--	--
A008	Nozzle Fixed Housing To Aft Segment Joint	1877.0	90	Radial	80	25	--	--
A009	Forward Center Segment To Aft Segment Joint	1172.0	91	Radial	80	50	--	--
A010	Forward Segment To Forward Center Segment Joint	852.0	91	Radial	80	50	--	--
A011	Forward Dome, Opposite Star Point	498.0	270	Normal to Surface	80	--	--	--
A012	ET Attach Stub	1511.0	180	Radial	--	25	25	--
A013	ET Attach Stub	1511.0	180	Tangential	--	25	--	--
A014	Aft Center Segment To Aft Segment Joint	1493.0	90	Radial	--	25	25	--
A015	ET Attach Stub	1511.0	180	Axial	--	25	25	--
A016	Aft Dome	1860.0	0	Normal to Surface	--	--	25	--
A017	Aft Dome	1860.0	90	Normal to Surface	--	--	--	25
A101	Forward Closure Input to S&A	486.355	270	Vertical	25	25	--	--
A102	Forward Closure Input to S&A	486.355	270	Axial	25	25	10	25
A103	Forward Closure Input to S&A	486.355	270	Horizontal	25	25	--	--
A201	Exit Cone, Forward of Exit Plane Reinforcement Ring	1983.0	180	Radial	80	100	100	--
A202	Exit Cone, Forward of Exit Plane Reinforcement Ring	1983.0	180	Tangential	80	100	--	--
A203	Exit Cone, Forward of Exit Plane Reinforcement Ring	1983.0	180	Axial	80	100	--	--
A204	Compliance Ring at TVC Actuator Attach	1924.0	135	Radial †	100	100	100	60
A205	Compliance Ring at TVC Actuator Attach	1924.0	135	Tangential †	100	100	100	60
A206	Compliance Ring at TVC Actuator Attach	1924.0	135	Axial	100	100	100	60
A207	Field Joint Flange	1884.6	180	Radial	100	100	100	--
A208	Field Joint Flange	1884.6	180	Axial	80	100	--	--
A209	Field Joint Flange	1884.6	180	Tangentail	80	100	--	--
A212	Flex Bearing Forward End Ring	1835.0	0	Normal to Surface	--	--	100	100

* If No Range Shown, Accelerometer Was Not On That Test

† Orientation On DM-1 Was Vertical And Horizontal

treated as stationary. The PSD plots provided a means of assessing the data for narrow band frequency content as well as energy distribution and overall composite root-mean-square (RMS) vibration levels. By generating PSD's at several time frames, an assessment of frequency content and energy distribution vs time was made. The T-5 time frame established a prefire instrumentation noise baseline against which subsequent data could be assessed.

The PSD plots presented in this report were generated by converting analog PSD plots to digital data using a digitizing tablet and then creating computer generated plots. The digital data were also used to calculate overall RMS vibration levels.

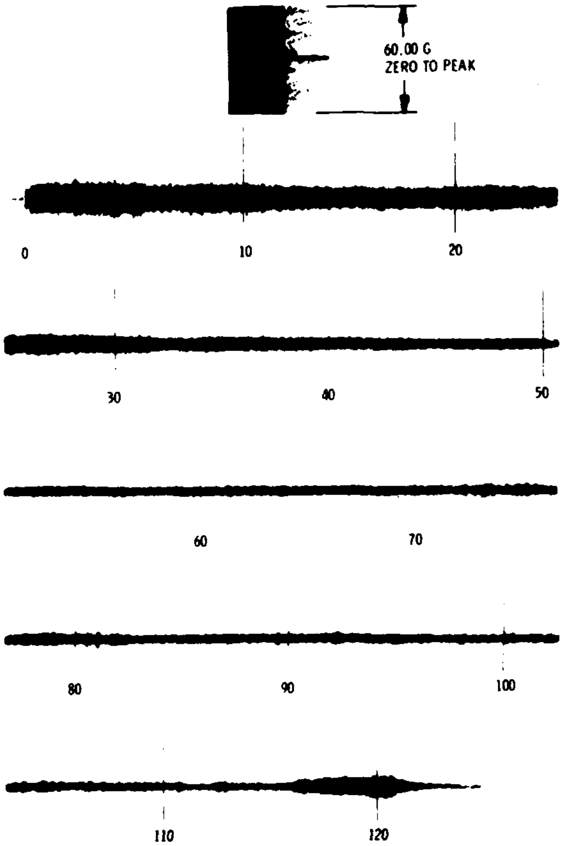

Figure 2. Oscillogram of Accelerometer A206 (DM- ()

RESULTS

Figure 2 shows a typical oscillograph record (A206 on the nozzle) and shows the overall vibration level vs time for the entire DM-4 firing. Some of the more obvious characteristics of the data can be noted on this oscillogram.

Several of the oscillograms (most notably A205, A206, and A212) contain many erratic bursts of significantly higher amplitude from approximately 60 sec until tailoff. No definite explanation of this phenomenon is known at this time.

A typical PSD plot (Figure 3) shows the energy distribution as a function of frequency

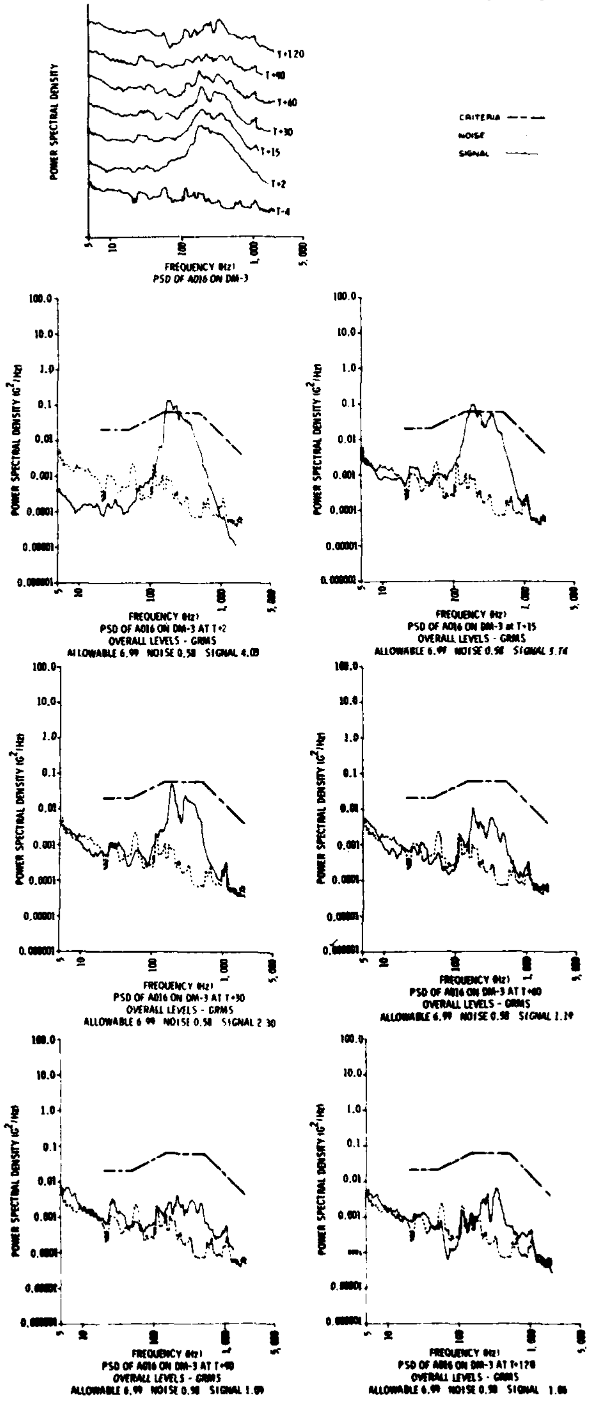

Figure 3. Power Spectral Density vs Frequency of Accelerometer A016 (DM-3)

for various times during the firing as well as a composite plot. The prefiring noise levels (which is an indication of the instrumentation noise) and the NASA flight criteria (per Reference 1) are also plotted for comparison. Spectral analysis of the data indicates, that for many parameters, a significant amount of the low frequency content is due to instrumentation noise. The overall composite RMS levels were also calculated for each criteria, noise level, and signal and appear on the applicable plots.

Power spectral density (PSD) analyses for the accelerometer measurements from the four static tests were documented in References 2 thru 5. The accelerometers were grouped into the four subzones shown on Figure 4 as was done in Reference 1. The PSD vs frequency plots for accelerometers in each subzone were grouped on the same plot as shown in Figures 5 thru 8. An envelope was then constructed which encompassed the maximum values (including instrumentation noise) to obtain the self-induced vibration environment for each subzone. These figures are a composite of the maximum amplitude determined for each accelerometer in a particular subzone for the four motor tests. Results are also presented in Figures 5 thru 8. For purposes of comparison, the NASA flight criteria from Reference 1 are also shown on these figures. Reference 1 has been updated by NASA for specific components based on static test data.

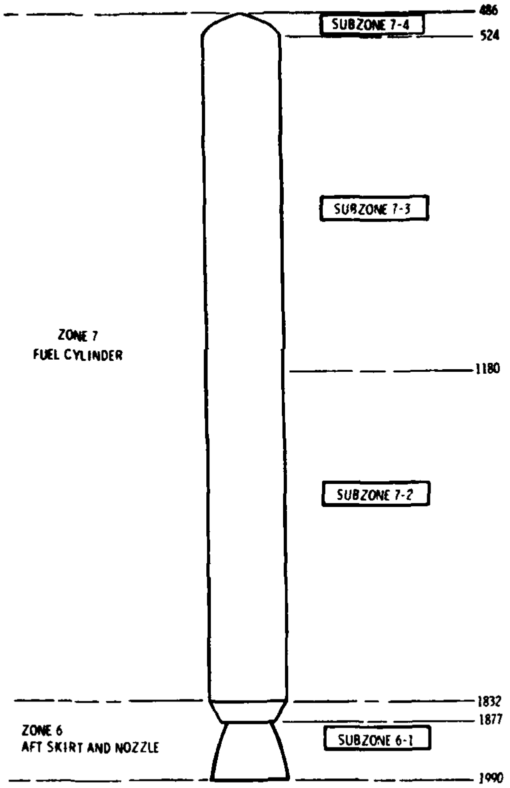

Figure 4. Solid Rocket Motor Zones

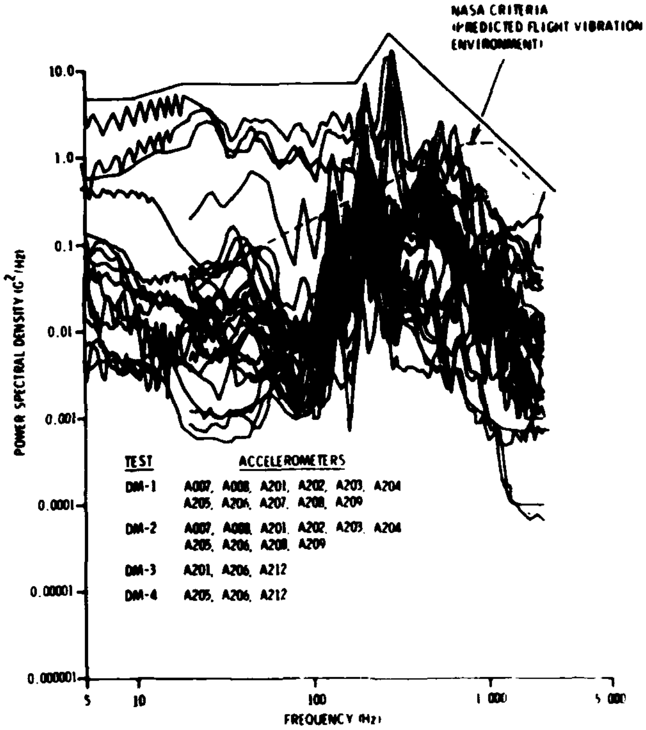

Figure 5. Power Spectral Density vs Frequency for Accelerometers in Subzone 6-1

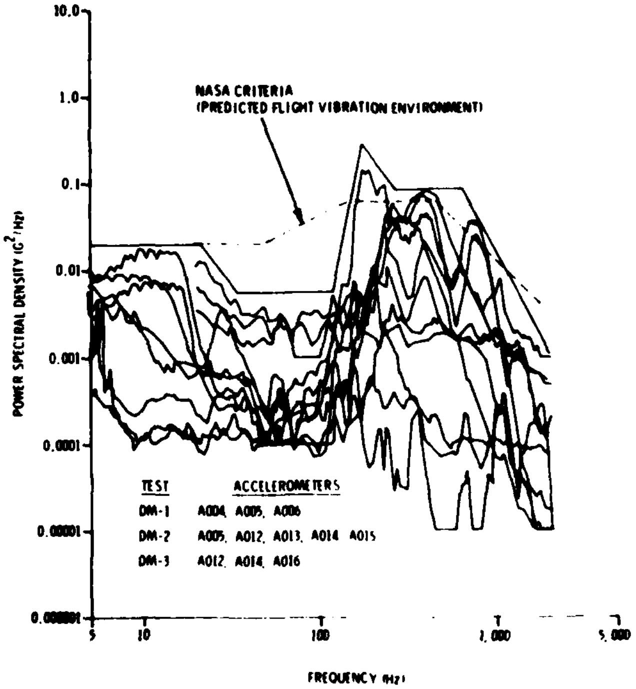

Figure 6. Power Spectral Density vs Frequency for Accelerometers in Subzone 7-2

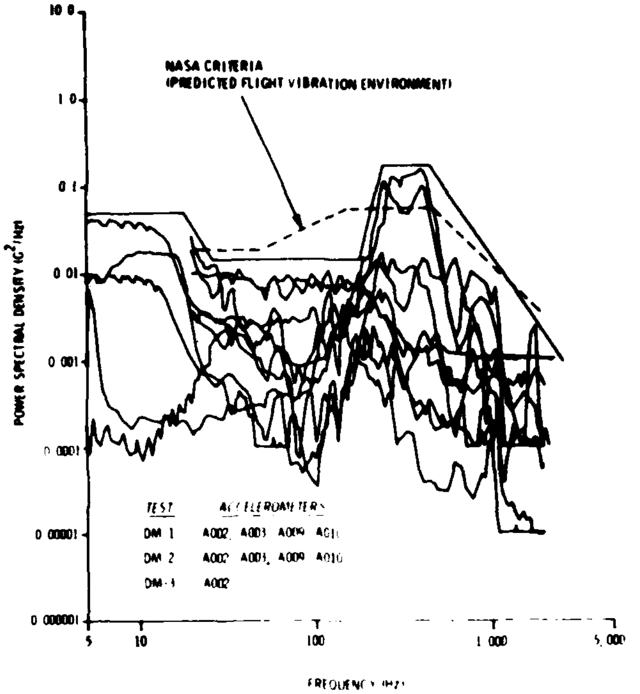

Figure 7. Power Spectral Density vs Frequency for Accelerometers in Subzone 7-3

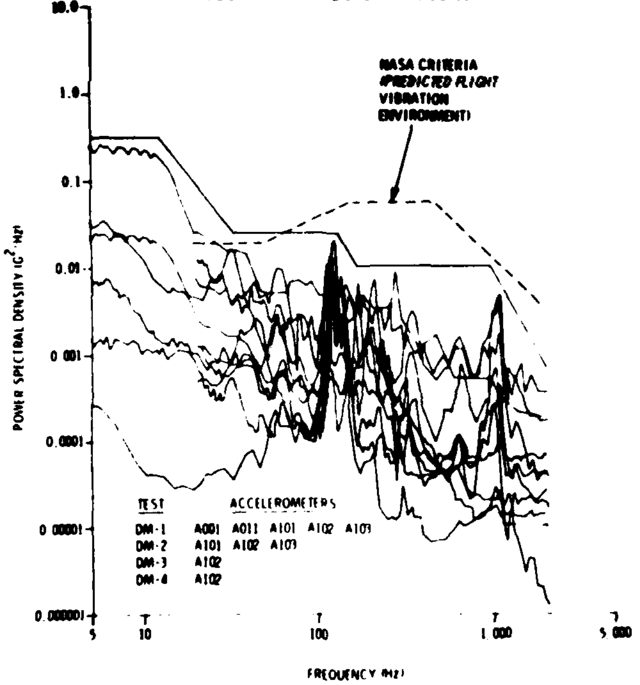

Figure 8. Power Spectral Density vs Frequency for Accelerometers in Subzone 7-4

Little of a definitive nature is ventured about the origins of the narrow band frequencies found at the various locations. Those noted on the nozzle and exit cone are probably indicative of exit cone shell modes. Most of these were above 100 Hz and are therefore outside the range of the vibration analysis conducted for the nozzle/exit cone assembly. Notable exceptions are the 25 Hz peak noted on DM-1 thru DM-4 which probably corresponds to a 2 wave circumferential mode calculated for the exit cone, and a peak near 35 Hz on DM-1 which probably is a 3 circumferential wave mode.

CONCLUSIONS

In general, the highest vibration levels were measured toward the aft end of the motor, with the highest amplitudes occurring just forward of the nozzle exit plane. Some locations, particularly on the nozzle and exit cone, displayed vibration levels somewhat in excess of the NASA criteria. However, the amplitudes observed do not compromise the integrity of the structure. Vibration levels diminish toward the forward end of the motor, with the forward dome region registering the lowest amplitudes.

REFERENCES

1. "Solid Rocket Booster Vibration, Acoustic, And Shock Design And Test Criteria," NASA document SE-019-049-2H, Revision A, 17 Dec 1976.
2. "Space Shuttle SRM DM-1 Vibration Data Summary," Thiokol/Wasatch document TWR-11843, M. Behring, 5 May 1978.
3. "Space Shuttle SRM DM-2 Vibration Data Summary," Thiokol/Wasatch document TWR-11964, M. Macocha and M. Behring, 8 Aug 1978.
4. "Space Shuttle SRM DM-3 Vibration Data Summary," Thiokol/Wasatch document TWR-12261, V. Call and M. Behring, 3 Apr 1979.
5. "Space Shuttle SRM DM-4 Vibration Data Summary," Thiokol/Wasatch document TWR-12294, V. Call and M. Behring, 23 Apr 1979.

ELIMINATION OF A DISCRETE FREQUENCY ACOUSTICAL PHENOMENON ASSOCIATED WITH THE SPACE SHUTTLE MAIN ENGINE OXIDIZER VALVE-DUCT SYSTEM

L. A. Schutzenhofer, J. H. Jones, R. E. Jewell, and R. S. Ryan
NASA/George C. Marshall Space Flight Center
Marshall Space Flight Center, Alabama 35812

In the development of the Space Shuttle Main Engines, various unpredictable dynamical phenomena were experienced which have resulted in engine shutdown or failures, e.g., fires. One such dynamical phenomenon consisted of an acoustical buzz at 7200 Hz in the vicinity of the main oxidizer valve. The method of isolating the buzz phenomenon, identifying the mechanism, and developing a fix to eliminate the buzz is presented together with supporting data. These data, i.e., fluctuating pressure and acceleration data, were obtained from hot firing engine tests and from liquid nitrogen flow simulation tests conducted at Marshall Space Flight Center.

INTRODUCTION

The Space Shuttle Main Engines (SSME) represent an advancement over the F-1 engines which were the engines that powered the Saturn/Apollo space vehicle. The SSME's are designed to be reusable for 55 missions; they are throttlable over a 2:1 range; they have high turbopump and chamber pressures; and the system has three combustion chambers and four turbopumps. Some additional characteristics associated with the SSME's are shown in Figure 1; for example, the area ratio is 77.5:1 and the full power level is 109 percent of the rated power level.

In the course of development of these engines, various unpredictable dynamical phenomena have occurred which have resulted in engine shutdowns or failures, i.e., fires. The purpose of this paper is to describe one phenomenon. This phenomenon was an acoustical buzz in the main oxidizer valve which resulted in high vibration levels and eventual failure of the main oxidizer valve (MOV). This buzz was at a frequency of approximately 7200 Hz and it was of such an amplitude that it caused: (1) fretting of mating surfaces in the liquid oxygen (LOX) environment that resulted in a fire, (2) degradation of seals in the MOV that resulted in LOX leakage, and (3) a continuous increase in fluctuating pressure and vibration levels from test to test which, if allowed to continue to grow, could have resulted in a catastrophic engine failure.

When the high amplitude vibration level at 7200 Hz was first detected, its origin was not known. Through detailed analysis of the hot firing engine data, it was determined that the source of the anomalous frequency was in the vicinity of the MOV. In addition to the anomalous buzz frequency, there were discrete frequency pressure fluctuations in SSME high pressure liquid oxygen pump (HPOP) at harmonics of the pump rotational frequency. The specific aspects of all these discrete frequencies will be delineated in subsequent sections.

To understand the mechanism associated with the valve buzz and to develop a fix, flow simulation tests were conducted at Marshall Space Flight Center (MSFC) without the high pressure LOX pump. This testing was accomplished in blowdown simulation tests using liquid nitrogen (LN_2) as the test medium instead of LOX. The results of this testing were complemented by an acoustical analysis. In this analysis, it was hypothesized that the buzz mechanism consisted of a shear layer instability that excited the MOV flange/HPOP duct flange cavity tangential acoustical frequencies. These frequencies were hypothesized to coalesce with the MOV longitudinal duct mode acoustical frequencies. This combination of coincidental shear layer/acoustical frequencies resulted in producing the buzz phenomenon. The data from the LN_2 tests substantiated the previously mentioned hypothesis. The development of a fix which suppressed the buzz phenomenon in the LN_2 tests and in hot firing engine tests was the final verification of the mechanism.

HARDWARE DESCRIPTION

The MOV of the SSME's is a fluidic switch in the LOX system that releases the flow of LOX from the HPOP to the main combustion chamber

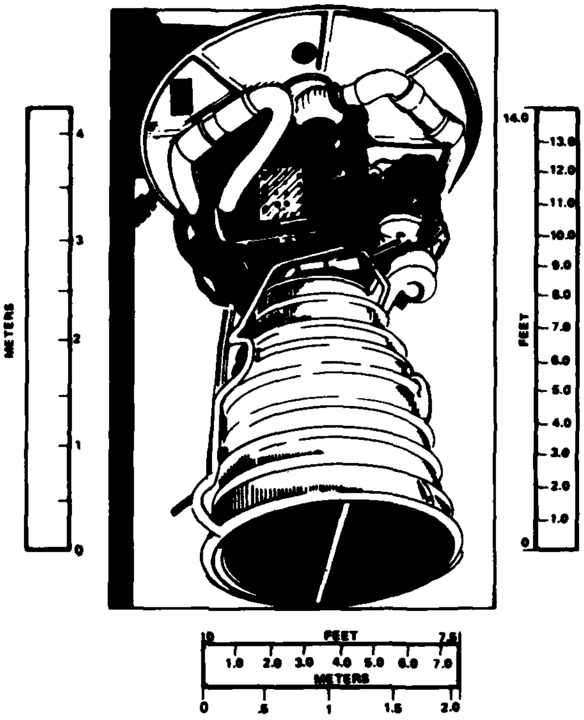

•THRUST		
•SEA LEVEL	375K	(1,668,000 N)
•VACUUM	470K	(2,090,000 N)
•FPL	109%	109%
•CHAMBER PRESSURE	2970 PSIA	2048 N/cm^2
•AREA RATIO	77.5	77.5
•SPECIFIC IMPULSE (NOM)		
•SEA LEVEL	363.2	3562 $\frac{\text{N sec}}{\text{kg}}$
•VACUUM	455.2	4464 $\frac{\text{N sec}}{\text{kg}}$
•MIXTURE RATIO	6.0	6.0
•LENGTH	167"	424 cm
•DIAMETER		
•POWERHEAD	105" x 95"	267 x 240 cm
•NOZZLE EXIT	94"	239 cm
•LIFE	7.5 HRS 55 STARTS	7.5 HRS 55 STARTS

Figure 1. Space Shuttle Main Engine characteristics.

(Figure 2). The MOV is a ball type valve, and it is fairly complex internally in that it is a system composed of seals, bellows, cams, sleeves, etc. On either side of the MOV there are ducts (approximately 4 inches in diameter) which converge such that the valve itself has a cross-section of approximately 2.5 inches in diameter. At the mating sections between the valve and the ducts, there are flanges (Figure 2) where the valve is bolted into the system.

The details of these converging sections are shown in Figure 3 together with the significant dimensions of the MOV. Figure 3 provides a description as to the overall size of the valve. Also shown is the flange gap between the duct flange and the valve flange (see detail A in Figure 3). This gap existed in the original design so that shims could be placed between the sleeve and the valve flange for final adjustments. It will be shown later that this flange gap is significant in relationship to the acoustical buzz phenomenon. Figure 3 (upper left) presents the press fit sleeve. This press fit sleeve was installed to provide additional strength to the sleeve to survive the acoustical buzz pressure fluctuations. A subsequent redesign is shown on the right. This redesigned sleeve is the first man orbital flight (FMOF) thick sleeve configuration, and it was developed to provide more strength. Neither of these modifications was sufficient to provide enough strength to withstand the acoustical buzz phenomenon. The dashed line in Figure 3 represents the thick sleeve for the FMOF configuration.

TYPICAL FLUCTUATING PRESSURE DATA

Typical fluctuating pressure data from a hot firing engine test are shown in Figures 4 and 5. The data presented in these figures represent high frequency data at various axial locations along the discharge duct from the HPOP to the main combustion chamber. The first measurement is HPOP discharge dynamic pressure. Then at the inlet to the MOV, there is a measurement designated as the MOV inlet dynamic pressure. Finally, downstream of these two measurements is the main combustion chamber LOX injector dynamic pressure. Data from all three of these positions are shown in Figures 4 and 5.

Figure 4 presents the RMS (root mean square) time histories of test 013 whose duration was approximately 25 seconds. Figure 4 also presents the engine power settings. It can be seen that the engine was ramped up to 90 percent power level. Then it was ramped to 95 percent, 100 percent, and back down to 90 percent power. The high amplitude of the system's RMS pressure fluctuations can clearly be seen from this figure. A typical instantaneous time history of the pressure fluctuations for the MOV

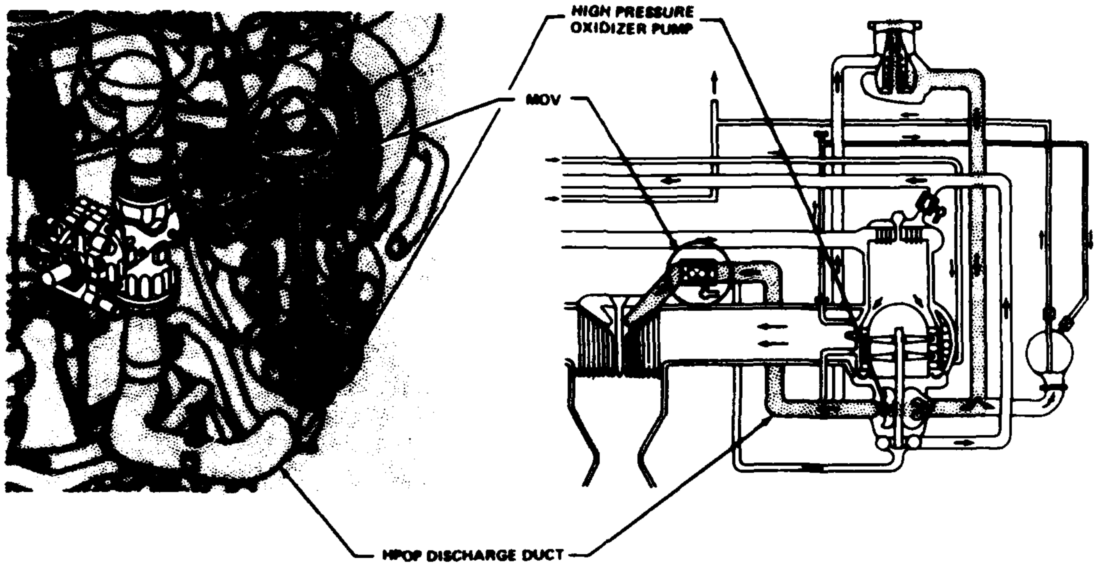

Figure 2. Location and function of main oxidizer valve.

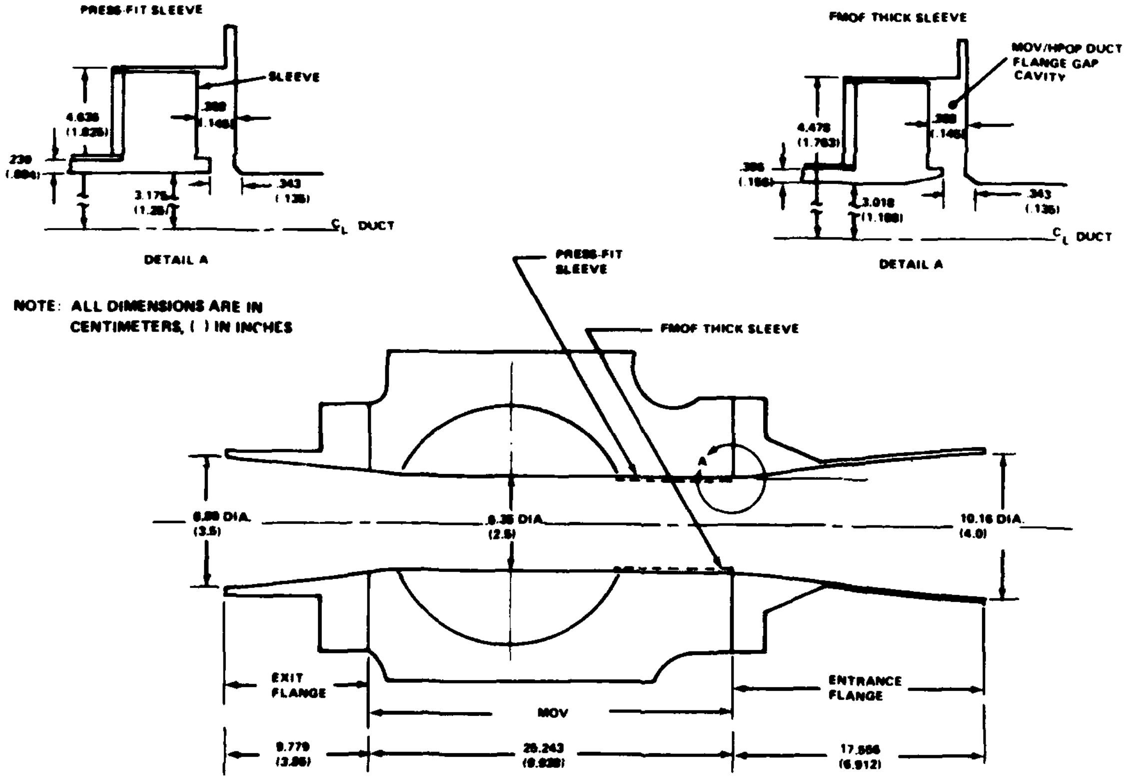

Figure 3. Nominal dimensions associated with main oxidizer valve.

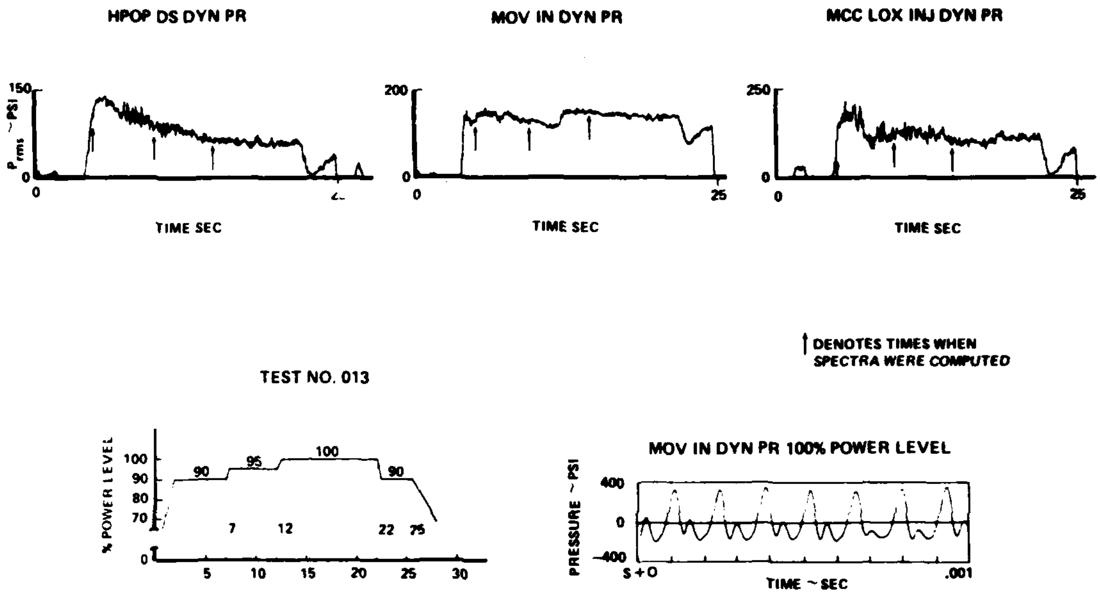

Figure 4. Fluctuating pressure variation (Test 013).

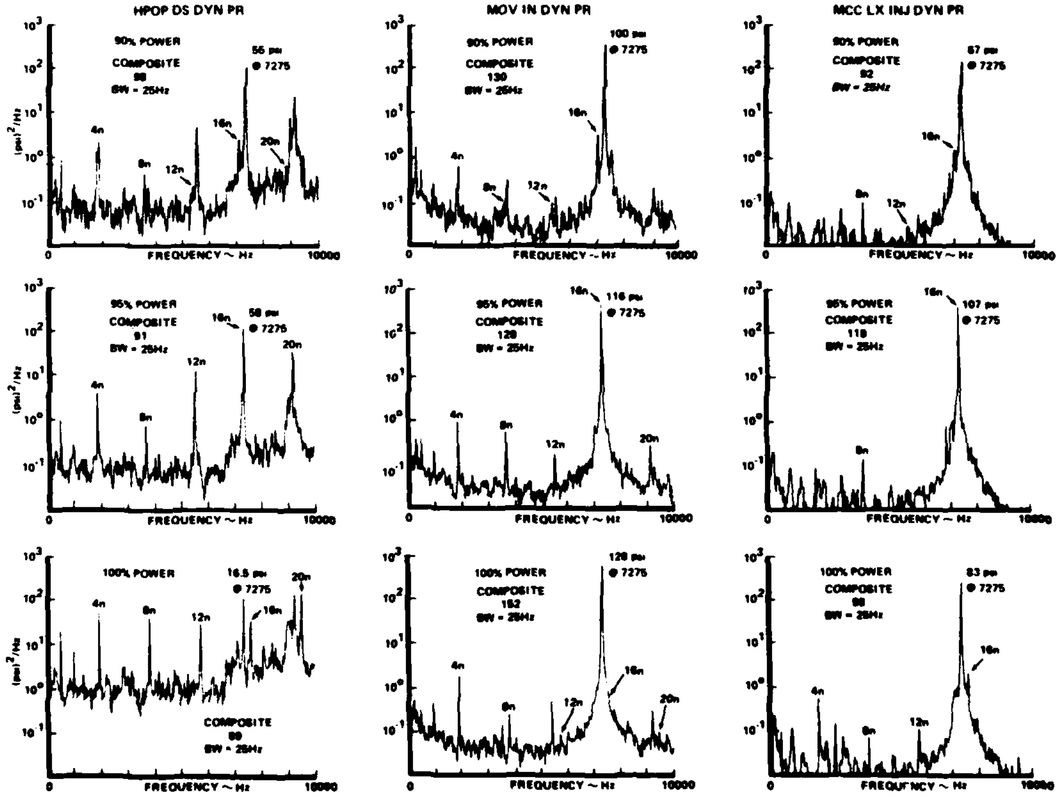

Figure 5. Typical fluctuating pressure spectral distribution (Test 013).

inlet is also shown on Figure 4 for a very small time increment. This waveform is typical of the MOV inlet measurement, and the discreteness of the buzz phenomenon can be seen.

Spectral data corresponding to these measurements are shown on Figure 5. These spectra were taken at consistent times which are designated by the arrows shown in Figure 4. These times correspond to engine power settings of 90 percent, 95 percent, and 100 percent of the rated power level for the SSME. Figure 5 indicates that there are a number of discrete frequencies and some of these are harmonics of the HPOP blade passage frequency. A significant feature of this figure is the increase in passage frequency. This 16n component starts below the 7275 Hz buzz frequency at the 90 percent power setting. Then, at 95 percent power, the 16n component coalesces with buzz frequency. Finally, at 100 percent power the 16n component increases above the buzz frequency. During these changes of engine power level, the buzz frequency remains approximately fixed at a frequency of 7275 Hz.

The amplitude of the buzz frequency is always highest at the MOV inlet in comparison to the other two axial positions. This indicated that the source of the buzz was in the vicinity of the MOV and was not emanating from the HPOP nor the main combustion chamber. Furthermore, it can be seen from Figure 5 that the amplitude at the buzz frequency is significantly higher than the amplitude at the pump blade passage frequencies at the MOV inlet and MCC LOX injector. Whenever the phenomenon occurred, the spectral data indicated not only the buzz frequency but also a strong second harmonic of the buzz frequency. This second harmonic is not shown in Figure 5 because the analysis is truncated at 10,000 Hz; however, it can be seen in a subsequent figure where the analysis is to 20,000 Hz.

SIMULATION OF BUZZ PHENOMENON IN LN_2

Flow simulation tests were conducted at MSFC to reproduce the buzz phenomenon without the high pressure LOX pump to determine: (1) whether or not the HPOP had any effect upon the generation of the anomalous frequencies, (2) the source of the anomalous frequencies, and (3) what type of fix could be implemented to eliminate the buzz phenomenon. These goals were accomplished in blowdown simulation tests using LN_2 as the test medium instead of LOX. Through the application of dynamic similitude theory, LN_2 flow conditions were established such that the anomalous frequencies that occurred in the LN_2 medium were scaled to reproduce the buzz phenomenon that was observed in the LOX hot firing engine tests.

The most significant simulation parameters between LN_2 and LOX to reproduce the buzz phenomenon were Strouhal number and Mach number. In the analysis, the Strouhal number was defined as fl/v, where f was the buzz frequency, l was the length of the opening of the flange gap cavity (0.135 inch), and v was the flow velocity. In addition, the Mach number was defined as the flow velocity, v, divided by the velocity of sound, c, of the medium. These dimensionless parameters are similar to those of References 1 and 2. A comparison of the dimensionless buzz frequencies is shown in Figure 6. It can be seen in this figure that LN_2 test data compare very well to the SSME hot firing engine data. The significant correlating parameter in this case is the Mach number. These data indicate that the dimensionless Strouhal number decreases as the Mach number increases. Furthermore, it can be seen that the second, third, and fifth value duct mode frequencies are the predominant frequencies. The correlation of these data was an important clue in regard to understanding the mechanism of the buzz phenomenon and developing a fix. The data shown in Figure 6 strongly suggest an acoustical cavity resonance phenomenon as delineated in References 1 and 2.

Based upon the data in Figure 6, it was hypothesized that the buzz mechanism consisted of a shear layer instability exciting the MOV inlet flange/HPOP duct flange cavity tangential mode acoustical frequencies. This cavity is shown in Figure 3 as detail A. These frequencies are then coalesced with the MOV longitudinal duct mode acoustical frequencies. This combination of coincidental shear layer/acoustical frequencies results in producing the buzz phenomenon. The verification of this mechanism is shown on Figure 7. Figure 7 presents a comparison of calculated frequencies from Rossiters' frequency equation [1] where γ is a quantity proportional to a phase angle difference between an acoustic wave and the shear layer wave propagation, the calculated HPOP/flange gap cavity tangential acoustical frequencies where j is an integer for the various modes, the calculated longitudinal duct mode frequencies where n is an integer for the various modes, and the measured buzz frequencies from LN_2 tests as a function of flow velocities. The results shown in Figure 7 pertain to LN_2 flow conditions and not the hot firing LOX data. From this figure, it is seen that the calculated longitudinal duct modes and the flange gap cavity tangential modes are nearly coincident. In the LN_2 blowdown tests, the velocity of the flow was varied linearly so that there existed the possibility of exciting many modes. The data shown in Figure 7 clearly show that the LN_2 experimental results consist of various acoustic modes which are excited at different velocities, and these measured values coincide with the calculated coalesced frequencies. Further, each acoustic mode (buzz frequency) is sustained over a range of flow velocities. For the 6800 Hz phenomenon (in LN_2), the flow velocity range where this frequency was generated was from 160 feet/second to 250 feet/second. This flow

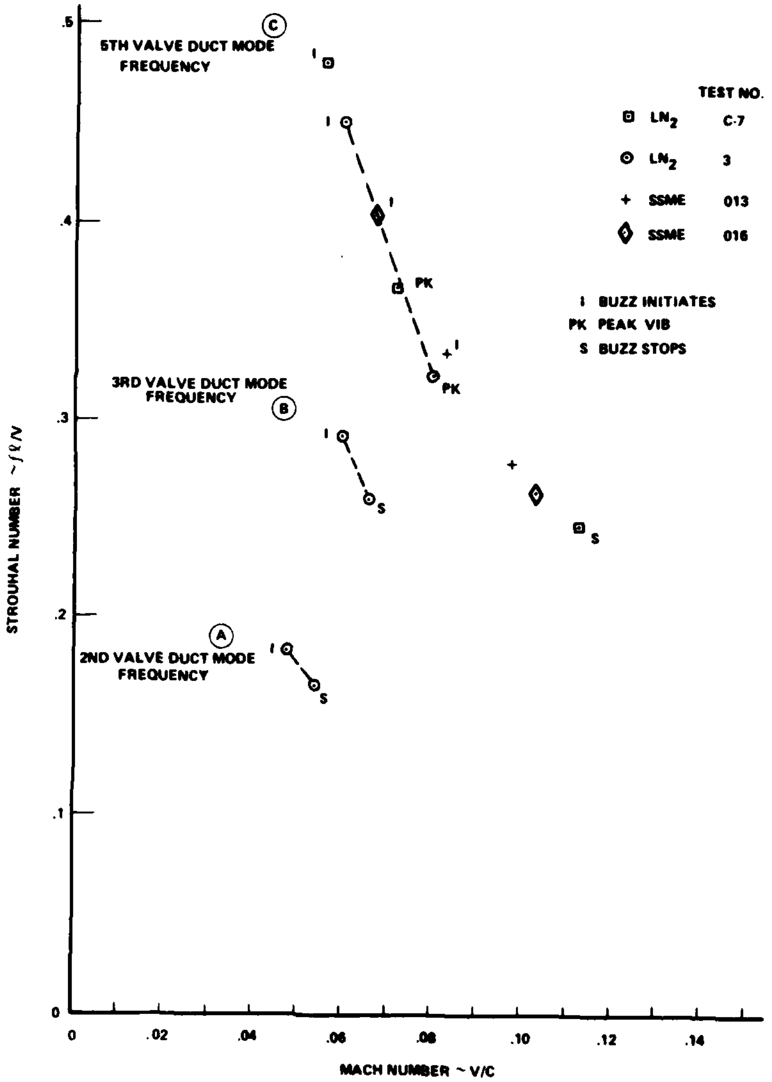

Figure 6. Functional variation of Strouhal number with Mach number.

regime, when scaled to LOX flow conditions, corresponds to the operating power levels where the 7200 Hz phenomenon was observed in the hot firing engine tests. The shaded portion of Figure 7 indicates the "on set" velocity conditions as determined from Rossiters' equation. The comparison to Rossiters' frequency equation is remarkable in consideration of the complexity of the geometry and flow. All these analytical results and experimental verification substantiate the hypothesized mechanism.

During the LN_2 flow test series, various configurations were tested for the developmental valve and the FMOF valve. The main results from the most significant tests utilizing these configurations are shown in Figure 8. This figure presents the RMS acceleration obtained from an accelerometer located on the MOV inlet flange. These RMS accelerations are shown for various configurations for the buzz flow conditions. Figure 8 shows that the press-fit, damped, and thick sleeve all experience the buzz phenomenon. When the MOV flange/HPOP flange gap cavity (see detail A, Figure 3) was plugged with a shim, the buzz phenomenon was completely eliminated for all valve configurations as indicated by Figure 8. Although the fix of plugging the flange gap cavity with a shim worked in LN_2, it remained to verify this fix in a hot firing test. Figure 9 presents a comparison of hot firing engine MOV axial accelerations for a configuration with the shim fix and without the shim fix. This figure dramatically verifies that the shim fix eliminates the 7200 Hz buzz phenomenon. It can be seen that the composite acceleration goes from 338 g without the fix to 33 g with the fix. Additionally, this figure

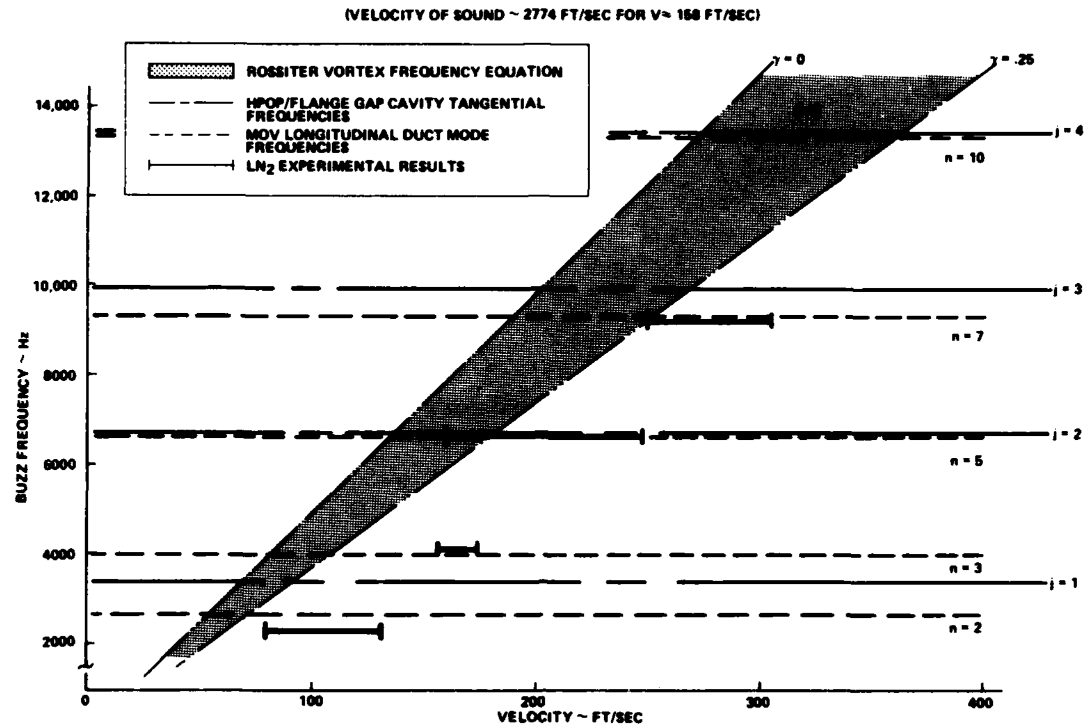

Figure 7. Buzz frequency mechanism.

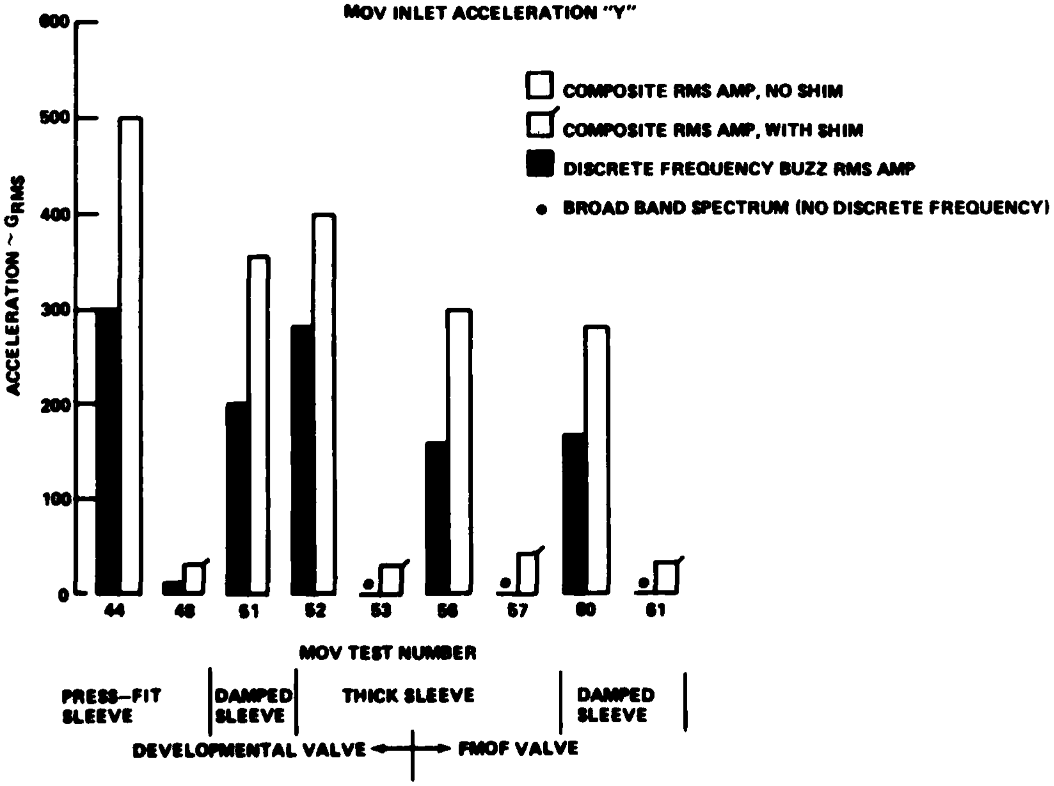

Figure 8. Summary of results of MSFC LN_2 MOV flow tests.

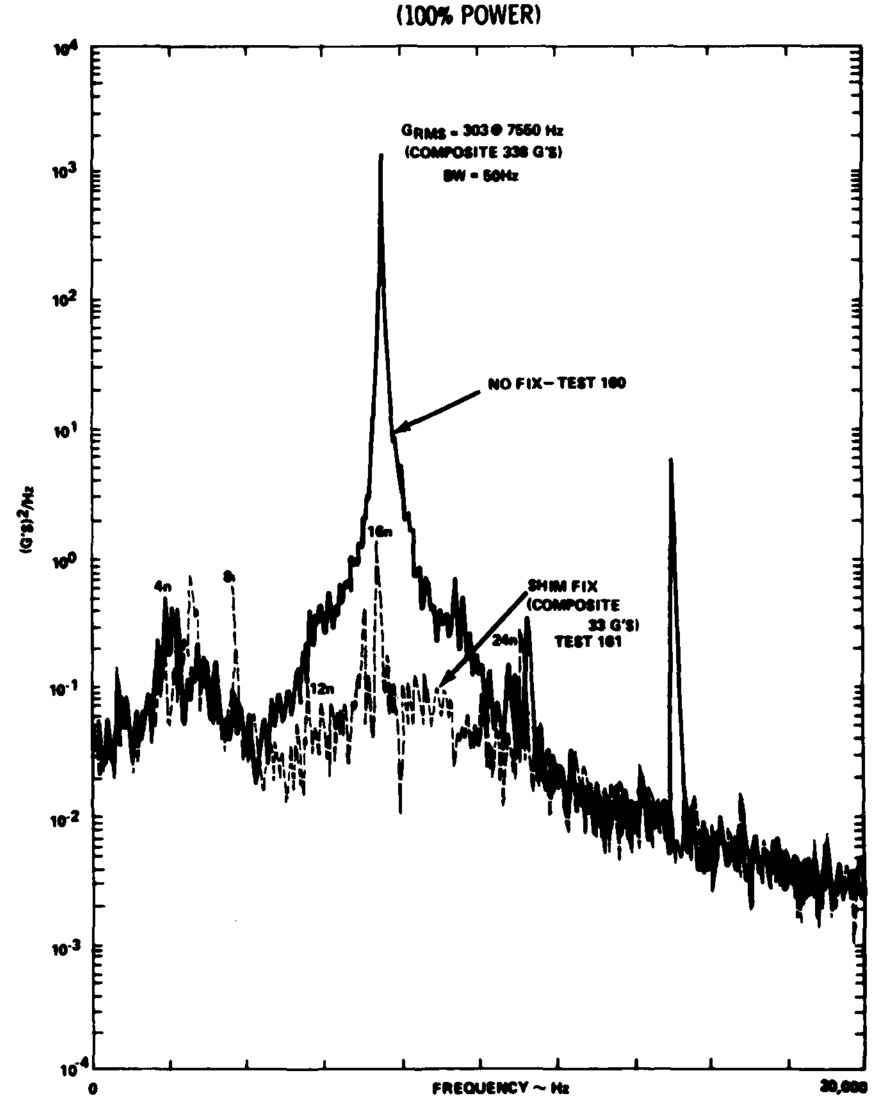

Figure 9. Comparison of hot firing MOV AX ACC with/without shim fix.

shows that the 7200 Hz buzz frequency has a second harmonic. This harmonic is typical of all the data where the buzz exists.

As a final verification of the LN_2 testing and simulation method, a comparison of the LN_2 blowdown test data and LOX data is shown in Figure 10. These results are compared in dimensionless form and for the condition with the shim. These data were normalized to their respective RMS values and the frequency was scaled for a unit length and the velocity of sound in the respective media. The velocity of sound is the appropriate velocity to scale with for this case because the fluctuations are acoustically induced and are propagated with the velocity of sound. This comparison indicates that the basic background fluctuations in the HPOP discharge duct and valve scale as they should and that the harmonic components of the pump pressure fluctuations stand out.

CONCLUDING REMARKS

The damage that occurred during hot firing testing of the SSME's as a result of a 7200 Hz discrete frequency was caused by an acoustical buzz phenomenon. The location of this buzz was at the cavity formed by the mating of the MOV and HPOP duct flanges. The mechanism was a shear layer/acoustical resonant condition that resulted from the coalescing of the shear layer instability frequency with the longitudinal duct mode frequency and the flange gap tangential frequency. This mechanism was substantiated in LN_2 blowdown testing. A shim fix was developed to plug

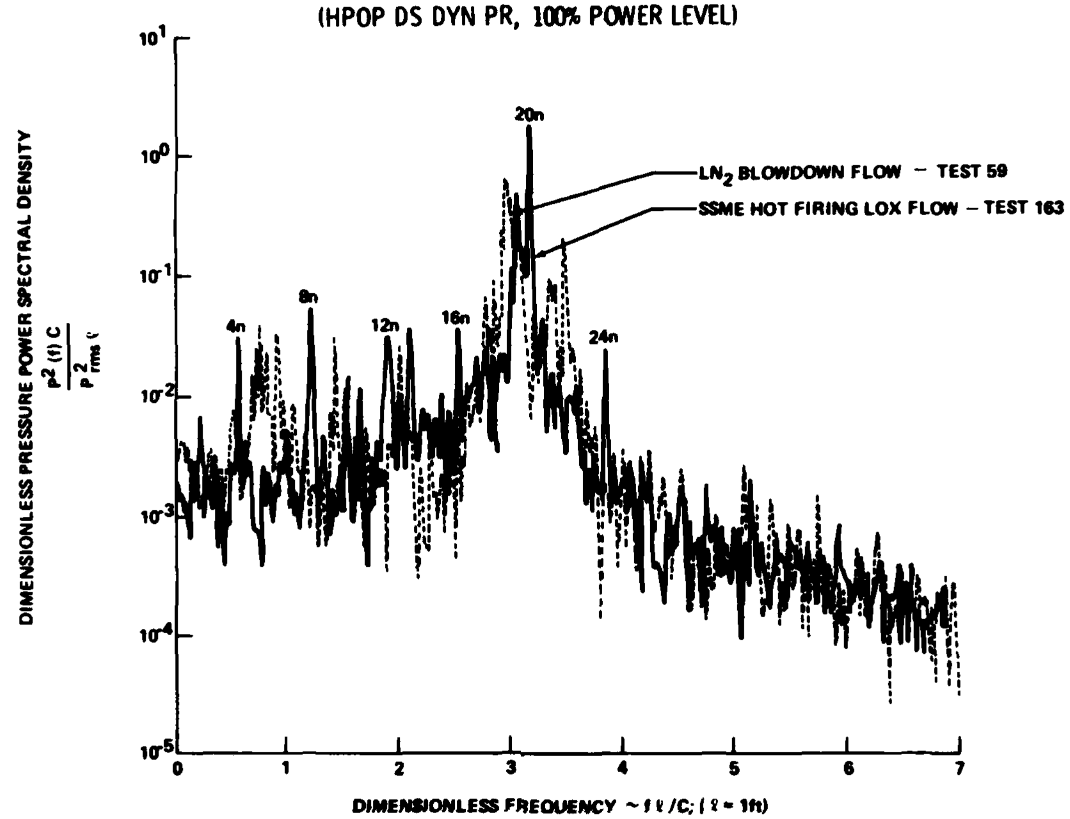

Figure 10. Dimensionless comparison of hot firing LOX flow and LN$_2$ blowdown flow with shim fix.

the flange gap cavity. This fix eliminated the oscillations associated with the buzz phenomenon in the LN$_2$ tests and in hot firing engine testing.

REFERENCES

1. Rossiter, J. E., "Wind Tunnel Experiments on the Flow Over Rectangular Cavities at Subsonic and Transonic Speeds," Royal Aircraft Establishment Technical Report No. 64027, October 1964.

2. Tam, C. K. and Block, P. J. W., "On the Tones and Pressure Ocillations Induced by Flow Over Rectangular Cavities." Journal of Fluid Mechanics, Vol. 89, Part 2, pp. 373-399, 1978.